Unraveling Molecular Gas Conditions across Nearby Galaxies with CO Isotopologues

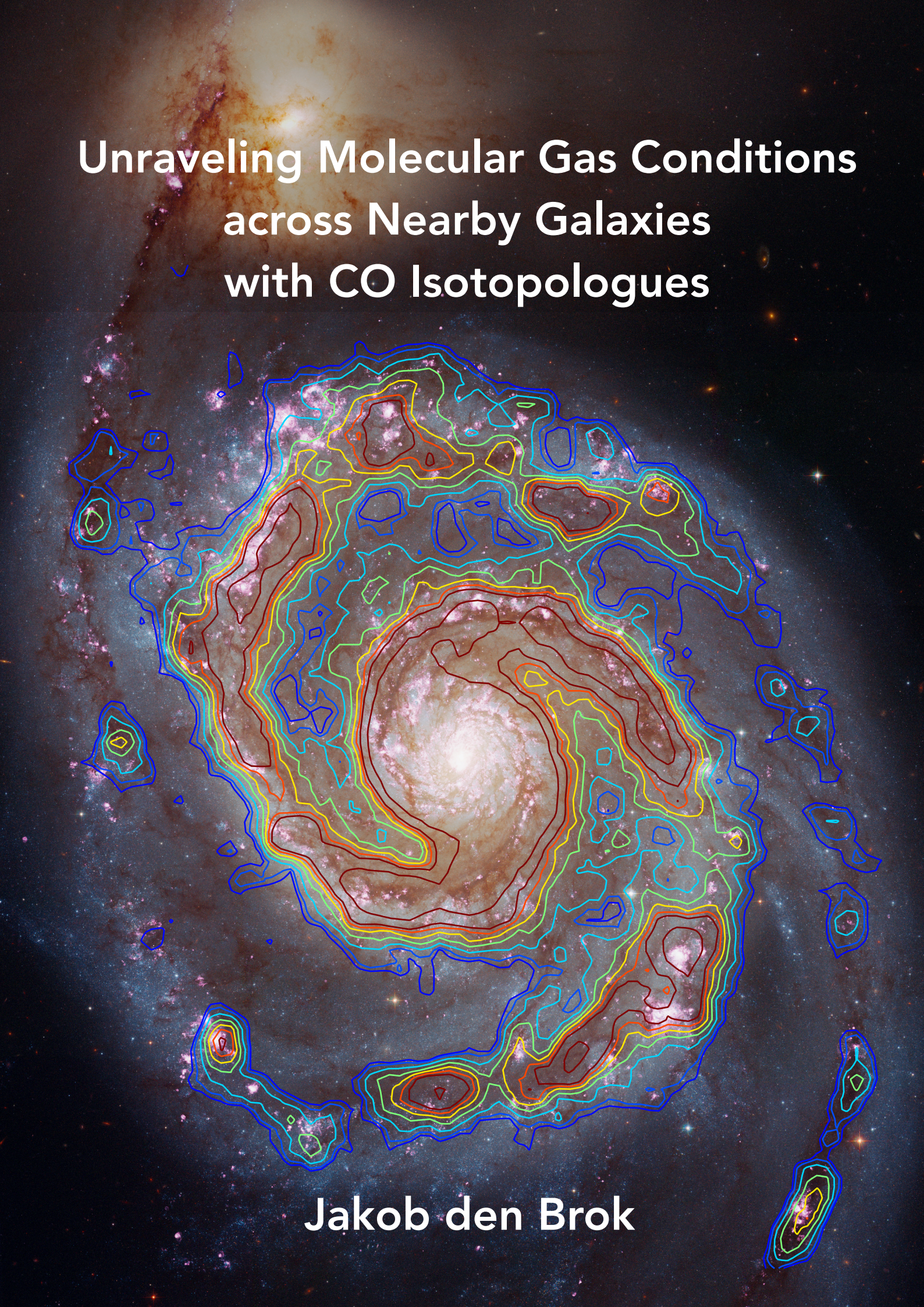

Jakob den Brok

Unraveling Molecular Gas Conditions across Nearby Galaxies with CO Isotopologues

Dissertation
zur
Erlangung des Doktorgrades (Dr. rer. nat.)
der
Mathematisch-Naturwissenschaftlichen Fakultät
der
Rheinischen Friedrich-Wilhelms-Universität Bonn

von
Jakob Sebastiaan den Brok
aus
Mainz, Rheinland-Pfalz, Deutschland

Bonn, 24.11.2022

Angefertigt mit Genehmigung der Mathematisch-Naturwissenschaftlichen Fakultät der Rheinischen Friedrich-Wilhelms-Universität Bonn

1. Gutachter:	Prof. Dr. Frank Bigiel
2. Gutachter:	Prof. Dr. Karl M. Menten
Tag der Promotion:	24.11.2022
Erscheinungsjahr:	2022

To my mother and father

I looked into the spectroscope. No spectrum such as I expected! A single bright line only! ...
The riddle of the nebula was solved. The answer had come to us in the light itself, read:
Not an aggregation of stars, but a luminous gas.
Stars, after the order of our own Sun, and of the brighter stars, would give a different spectrum;
the light of this nebula had clearly been emitted by a luminous gas.

William Huggins, 19th century astronomer, identifying the existence of gas in interstellar space.

Abstract

In general, we associate large spatial scales, heavy massive objects, and great distances with the scientific study of Astronomy. However, in this thesis, we study the tiny hydrogen molecule, H_2, which populates interstellar space. An intricate interplay exists between the molecular gas in the interstellar medium (ISM) and its capacity to form stars. Gaining insight into the composition of the molecular gas as well as its physical and chemical conditions is crucial to comprehending how star formation proceeds and how galaxies evolve. However, H_2 is difficult to observe directly under the commonly cold ISM conditions. Nowadays, Carbon Monoxide (CO) emission has become the most accessible tracer of the bulk molecular ISM distribution. In combination with various CO isotopologues, we can start to grasp the full extent of molecular gas conditions.

This thesis analyses CO and its isotopologue line emission within and across entire nearby galaxies. We draw on observations from various large programs of millimeter observatories, such as the IRAM 30m telescope and ALMA. The first scientific project investigates the $R_{21} \equiv {}^{12}\mathrm{CO}\,(2{-}1)/(1{-}0)$ line ratio. It is common to rely on ${}^{12}\mathrm{CO}\,(2{-}1)$ to trace molecular gas mass after converting it down to the $J = 1 \rightarrow 0$ transition using R_{21}. This line is advantageous because its brightness and frequency allows more efficient mapping. However, R_{21} varies due to its sensitivity to the temperature and density of the gas. This project presents a major systematic analysis of the line ratio across nine nearby galaxies on kiloparsec-scales. We show that it is important to account for R_{21} variation, in particular, toward the center of galaxies, where the line ratio generally increases by 10–20% to the galaxy-wide average.

The second project presents the first insights from the CLAWS IRAM 30m large program that targets M51. We present the first resolved detection of numerous faint CO isotopologues, such as ${}^{13}\mathrm{CO}$, $\mathrm{C}^{18}\mathrm{O}$, and even $\mathrm{C}^{17}\mathrm{O}$, across the full disk of a regular star-forming galaxy. We assess the CO isotopologue line ratio trends and conclude that selective nucleosynthesis and optical depth effects dominate the observed kpc-scale variation across M51. Overall, the project provides a benchmark study on kpc-scales and opens the way for future CO isotopologue studies in nearby galaxies.

The thesis also presents a wide-field IRAM 30m study of CO isotopologues M101. Using SED-fit-based dust mass estimates, we systematically estimate the CO-to-H_2 conversion factor across the galaxy. This study goes beyond recent research by combining the conversion factor analysis across a full nearby galaxy with the investigation of R_{21} variation. We find that the center shows significantly lower conversion values by a factor 10. This highlights the need to account for a variable α_{CO} value when we derive molecular gas mass scaling relations, such as the Kennicutt-Schmidt law.

Throughout the thesis projects, we take special care in understanding telescope systematics that hamper the sensitivity and quality of the observations. We investigate flux calibration stability and the error beam contribution for the 30m telescope. We find that an uncertainty of 10–15% needs to be considered when dealing with millimeter single-dish observations. Such an in-depth observation uncertainty analysis is

rarely found in the literature. But it is essential and helps us to correctly interpret the line emission and ratio trends.

We have investigated the main tracer for molecular gas across entire nearby galaxies. We also assessed relevant systematic effects that can hamper our observations. As such, the thesis projects offer detailed diagnostics on accurately accounting for and interpreting the variation of CO-derived properties of the molecular ISM. Furthermore, this research helps to advance future studies toward higher resolution observations that will help us understand the small-scale mechanisms that regulate star formation and connect them to the large-scale dynamical processes across galaxies.

Zusammenfassung

Im Allgemeinen assoziieren wir mit Astronomie große räumliche Skalen, schwere massive Objekte und weite Entfernungen. In dieser Arbeit untersuchen wir im Gegensatz dazu das winzige Wasserstoffmolekül, H_2, welches wir im interstellaren Raum zu finden ist. Im interstellaren Medium (ISM) findet ein kompliziertes Wechselspiel zwischen den verschiedenen Komponenten, dem molekularen Gas und seiner Fähigkeit, Sterne zu bilden, statt . Ein Verständnis der Zusammensetzung des molekularen Gases, sowie seiner physikalischen und chemischen Bedingungen, ist entscheidend um zu begreifen, wie Sterne enstehen und Galaxien sich entwickeln. Unter den üblicherweise kalten ISM-Bedingungen können wir jedoch den molekularen Wasserstoff nur schwer direkt beobachten. Daher wird heutzutage vor allem die Emission von Kohlenmonoxid (CO) benutzt um die Verteilung des molekularen ISMs zu studieren. In Kombination mit verschiedenen CO-Isotopologen können wir die verschiedenen molekularen Gasbedingungen erfassen.

In dieser Dissertationsarbeit analysieren wir CO-Emission und CO Isotopologlinien in nahen Galaxien. Wir stützen uns dabei auf Beobachtungen aus verschiedenen Large Programs von Millimeter-Observatorien, wie dem IRAM 30m-Teleskop und ALMA. Als erstes untersuchen wir das $R_{21} \equiv {}^{12}\mathrm{CO}\,(2{-}1)/(1{-}0)$-Linienverhältnis. Es ist üblich ${}^{12}\mathrm{CO}\,(2{-}1)$ zu benutzen, um die Masse des molekularen Gases zu ermitteln, nachdem man es mit Hilfe von R_{21} in den $J = 1 \rightarrow 0$-Übergang umgerechnet hat. Diese Linie ist vorteilhaft, da ihre Helligkeit und Frequenz eine effizientere Beobachung ermöglicht. Allerdings variiert R_{21} aufgrund seiner Empfindlichkeit auf Temperatur und Dichte des Gases. In dieser Studie führen wir eine umfassende und systematische Analyse des Linienverhältnisses in neun nahen Galaxien durch. Wir zeigen, dass es wichtig ist, R_{21}-Variationen zu berücksichtigen, insbesondere in Richtung des Zentrums von Galaxien, wo das Linienverhältnis im Allgemeinen um 10-20% gegenüber dem galaxienweiten Durchschnitt ansteigt.

Das zweite Projekt präsentiert die ersten Erkenntnisse aus dem CLAWS IRAM 30m Large Program, welches M51 beobachtet. Wir präsentieren die ersten Beobachtungen zahlreicher leuchtschwacher CO-Isotopologe, wie ${}^{13}\mathrm{CO}$, $\mathrm{C}^{18}\mathrm{O}$ und sogar $\mathrm{C}^{17}\mathrm{O}$, über die gesamte Scheibe einer regulären sternbildenden Galaxie. Wir untersuchen die Trends der CO-Isotopolog-Linienverhältnisse und kommen zu dem Schluss, dass selektive Nukleosynthese und optische Tiefeneffekte die beobachtete Variation auf kpc-Skalen dominieren. Insgesamt stellt das Projekt eine Richtswert-Studie auf kpc-Skalen dar und öffnet den Weg für zukünftige CO-Isotopolog-Studien in nahen Galaxien.

In dieser Arbeit präsentieren wir auch eine IRAM-30m-Studie von CO-Isotopolog Emission in M101. Unter Verwendung von SED-basierten Staubmassenschätzungen bestimmen wir systematisch den CO-zu-H_2-Konversionsfaktor in der gesamten Galaxie. Diese Studie geht über die bisherige Forschung hinaus, indem sie die Analyse des Konversionsfaktors mit der Untersuchung der R_{21}-Variation kombiniert. Wir finden, dass das Zentrum signifikant niedrigere Konversionswerte um einen Faktor 10 aufweist. Dies unterstreicht die Notwendigkeit, einen variablen α_{CO}Wert zu berücksichtigen, wenn wir allgemeine Skalierungsrelationen, wie zum Beispiel das Kennicutt-Schmidt-Gesetz, aus den Beobachtungen herleiten.

Während des gesamten Projekts achten wir besonders darauf, die sysetmatischen Ungenauigkeiten des Teleskops zu verstehen, welche die Empfindlichkeit und Qualität der Beobachtungen beeinträchtigt. Wir untersuchen die Stabilität der Flusskalibrierung und den Beitrag der Error Beams des 30-Meter-Teleskops. Wir stellen fest, dass bei Millimeter-Beobachtungen eine Unsicherheit von 10 bis 15% berücksichtigt werden muss. Eine derart detaillierte Analyse der Beobachtungsunsicherheit finden wir selten in der Literatur. Sie ist jedoch für das korrekte Verständnis und die Interpretation der Linienemission und derer Linienverhältnisse unerlässlich. Daher hilft uns diese Analyse, die Unsicherheiten unserer nachfolgenden Messungen abzuschätzen, und ermöglicht uns eine genauere Interpretation unserer Ergebnisse.

In dieser Dissertation haben wir den wichtigsten Indikator für molekulares Gas in nahen Galaxien untersucht. Wir haben auch relevante systematische Effekte untersucht, die unsere Beobachtungen beeinträchtigen können. So bieten die Projekte der Dissertation detaillierte Diagnosen zur genauen Erfassung und Interpretation von CO-abgeleiteten Eigenschaften des molekularen ISM. Darüber hinaus trägt diese Forschung dazu bei, künftige Studien zu höher aufgelösten Beobachtungen voranzutreiben, die uns helfen werden, die kleinräumigen Mechanismen zu verstehen, welche die Sternentstehung regulieren, und sie mit den großräumigen dynamischen Prozessen in Galaxien zu verbinden.

Acknowledgements

A PhD thesis project constitutes a monumental task and journey. The path would have been impossible to accomplish without the dedication, invaluable help, and indispensable support from countless mentors, friends, and family. In the following sentences, I try to put to words and express my deepest gratitude to all the people along my 3 year PhD journey.

Firstly, I like to thank my supervisor Frank for offering me the PhD position in his group and providing exciting and interesting research projects and opportunities. Also, I am extremely thankful for Frank's guidance throughout the project, helping me to see and focus on the relevant issues and science questions, which helped to bring projects to a conclusion, being always available for feedback up to the last minutes of a deadline and supporting me during the difficult COVID-19 related home-office time. Furthermore, I would like to express my gratitude for the invaluable support from Ashley and Johannes, who always managed to make time for support and answer questions despite their busy research, work, and life schedules. I also like to thank Ivana for her show of incredible passion and motivation for astronomical research. I remember when I visited the group in January 2019, the conversation with Ashley and Ivana helped me to see immediately that I had chosen the right group. A big thank you also goes to Cosima, the best "office buddy". Unfortunately, it lasted way too short since we had to go into home-office mode after the first six months of our PhD. Cosima's skills to communicate and visually present data are something that I aspired to and helped me grow as a researcher. In addition, I like to express my gratitude to Lukas whose care for detail, and due diligence also helped me to better understand my own research.

Moreover, the whole project would not have been possible to complete without the support, mentoring, and input my collaborators abroad. I am extremely grateful to Adam Leroy, Eva Schinnerer, and Antonio Usero. I am thankful for their constant constructive input and contribution with new ideas to my research. I am certain that also, because of them, I now have the opportunity to continue doing research in academia.

I also want to express my sincerest gratitude to Mike Koss and Benny Trakhtenbrot for their incredible continued support, mentoring and patience for our continued collaboration after I had started my PhD. I stand were I am today also because of them.

Besides academic and work-related support, I am also incredibly thankful for the personal and mental help throughout my PhD thesis from various people. I want to thank my father for his remarkable eye for detail and teaching to go beyond just superficial questions and answers. Also, I want to thank my mother and step-father for their unconditional support during the difficult time since the spring of 2020, but also before and after, with their constant encouragement that helped me navigate through the PhD journey. Moreover, I am thankful to Sonja, who unconditionally supported me throughout this time, even though it meant sacrificing a weekend skiing together in the mountains or a night out because of constant deadlines or work-related stress. I am looking forward to spending more time together, even if it first will take another three years and an ocean apart. Ich möchte mich auch herzlich bei Opa und Oma bedanken, die immer für mich da sind und mich unterstützen. Zudem bedanke ich mich bei Hilla, die mich schon von klein auf unterstützt und an mich geglaubt hat. También quiero dar las gracias a mi hermano, que siempre me ha

enseñado el significado de seguir los sueños. Last but not least, I want to thank my co-PhD students and friends at AIfA, in particular Maude, Toma, Christos, Tsan-Ming, Prachi, Abel, Kevin, and Ankur, who made feel welcome and at home in Bonn.

List of Publications

Relevant First-Author Publications

The following list indicates the relevant first-author publications that are discussed and presented in this thesis. These thesis research project culminates in two peer-reviewed and published research publications. In addition one more manuscript is in preparation for submission to the Astrophysics & Astronomy journal.

1. **den Brok J. S.**, Chatzigiannakis D., Bigiel F., Puschnig J., Barnes A. T., Leroy A. K., Jiménez-Donaire M. J., Usero A., Schinnerer E., Rosolowsky E., Faesi C. M., Grasha K., Hughes A., Kruijssen J. M. D., Liu D., Neumann L., Pety J., Querejeta M., Saito T., Schruba A., Stuber S. (2021), *New constraints on the ^{12}CO(2-1)/(1-0) line ratio across nearby disc galaxies*, Monthly Notices of the Royal Astronomical Society, 504, 3221.

   Author's Contribution: J.d.B. performed the scientific analysis, including the investigation of the combined IRAM and ALMA dataset and looking into the flux calibration stability, under the supervision of F.B., A.B., A.L., J.P., E.R., E.S., and A.U.. D.C. performed an early data exploration, which however was not used in this draft. An initial version of the short paragraphs on the literature comparison was compiled by J.P. The other co-authors helped to interpret the results and provided comments and edits to the final manuscript.

2. **den Brok J. S.**, Bigiel F., Sliwa K., Saito T., Usero A., Schinnerer E., Leroy A. K., Jiménez-Donaire M. J., Rosolowsky E., Barnes A. T., Puschnig J., Pety J., Schruba A., Bešlić I., Cao Y., Eibensteiner C., Glover S. C. O., Klessen R. S., Kruijssen J. M. D., Meidt S. E., Neumann L., Tomičić N., Pan H.-A., Querejeta M., Watkins E., Williams T. G., Wilner D. (2022), *A CO isotopologue Line Atlas within the Whirlpool galaxy Survey (CLAWS)* , Astronomy & Astrophysics, 662, A89.

   Author's Contribution: J.d.B. performed the scientific analysis under the supervision of F.B., A.B., A.L., J.P., T.S., E.S., and A.U. J.d.B. prepared the data products for the public data release, and wrote the manuscript. Contribution of the other co-authors amounted to help in the interpretation of the results and edits/comments regarding the manuscript.

3. **den Brok J. S.**, Bigiel F., et al., (2022), *Multi-CO Emission and New Constraints on the CO-to-H_2 Factor across M101*, in prep.

   Author's Contribution: J.S.d.B performed the IRAM 30m observations, the scientific analysis, and wrote the manuscript under the supervision of F.B, J.P., A.T.B, A.L, A.U, and E.S.

Relevant Co-Authored Publications

The following list indicates submitted and published work that are complementary and related to results and analysis presented in this thesis. The author of this dissertation has contributed as co-author to these papers throughout the duration of the thesis project.

1. Neumann L., Gallagher M. J., Bigiel F., Leroy A. K., Barnes A. T., Usero A., **den Brok J. S.**, Belfiore F., Bešlić I., Cao Y., Chevance M., Dale D. A., Eibensteiner C., Glover S. C. O., Grasha K., Henshaw J. D., Jiménez-Donaire M. J., Klessen R. S., Kruijssen J. M. D., Liu D., Meidt S., Pety J., Puschnig J., Querejeta M., Rosolowsky E., Schinnerer E., Schruba A., Sormani M. C., Sun J., Teng Y.-H. and Williams T. G., *The ALMOND Survey: Molecular cloud properties and gas density tracers across 25 nearby spiral galaxies with ALMA*, subm. to Monthly Notices of the Royal Astronomical Society.

   Author's Contribution: J. S. d. B. contributed edits that helped to improve the manuscript. In addition, J. S. d. B helped with the data analysis and discussed in-depth the results and interpretation with the lead-author.

2. Barnes A. T., Chandar R., Kreckel K., Glover S. C. O., Scheuermann F., Belfiore F., Bigiel F., Blanc G. A., Boquien M., **den Brok J. S.**, Congiu E., Chevance M., Dale D. A., Deger S., Kruijssen J. M. D., Egorov O. V., Eibensteiner C., Emsellem E., Grasha K., Groves B., Klessen R. S., Hannon S., Hassani H., Lee J. C., Leroy A. K., Lopez L. A., McLeod A. F., Pan H.-A., Sánchez-Blázquez P., Schinnerer E., Sormani M. C., Thilker D. A., Ubeda L., Watkins E. J., Williams T. G., (2022), *Linking stellar populations to H II regions across nearby galaxies. I. Constraining pre-supernova feedback from young clusters in NGC 1672*, Astronomy & Astrophysics, 662, L6.

   Author's Contribution: J. S. d. B. contributed edits that helped to improve the manuscript.

3. Leroy A. K., Rosolowsky E., Usero A., Sandstrom K., Schinnerer E., Schruba A., Bolatto A. D., Sun J., Barnes A. T., Belfiore F., Bigiel F., **den Brok J. S.**, Cao Y., Chiang I.-D., Chevance M., Dale D. A., Eibensteiner C., Faesi C. M., Glover S. C. O., Hughes A., Jiménez Donaire M. J., Klessen R. S., Koch E. W., Kruijssen, J. M. D., Liu D., Meidt S. E., Pan H.-A., Pety J., Puschnig J., Querejeta M., Saito T., Sardone A., Watkins E. J., Weiss A., Williams T. G., (2022), *Low-J CO Line Ratios from Single-dish CO Mapping Surveys and PHANGS-ALMA*, The Astrophysical Journal, 927, 2.

   Author's Contribution: J. S. d. B. contributed edits that helped to improve the manuscript.

4. Eibensteiner C., Barnes A. T., Bigiel F., Schinnerer E., Liu D., Meier D. S., Usero A., Leroy A. K., Rosolowsky E., Puschnig J., Lazar I., Pety J., Lopez L. A., Emsellem E., Bešlić I., Querejeta M., Murphy E. J., **den Brok J. S.**, Schruba A., Chevance M., Glover S. C. O., Gao Y., Grasha K., Hassani H., Henshaw J. D., Jimenez-Donaire M. J., Klessen R. S., Kruijssen J. M. D. Pan, H.-A., Saito T., Sormani M. C., Teng Y.-H., Williams T. G., (2022), *A 2-3 mm high-resolution molecular line survey towards the centre of the nearby spiral galaxy NGC 6946*, Astronomy & Astrophysics, 659, A173.

   Author's Contribution: J. S. d. B. contributed edits that helped to improve the manuscript. In addition, J. S. d. B helped with the data analysis and discussed in-depth the results and interpretation with the lead-author.

5. Leroy A. K., Schinnerer E., Hughes A., Rosolowsky E., Pety J., Schruba A., Usero A., Blanc G. A., Chevance M., Emsellem E., Faesi C. M., Herrera C. N., Liu D., Meidt S. E., Querejeta M., Saito T.,

Sandstrom K. M., Sun J., Williams T. G., Anand G. S., Barnes A. T., Behrens E. A., Belfiore F., Benincasa S. M., Bešlić I., Bigiel F., Bolatto A. D., **den Brok J. S.**, Cao Y., Chandar R., Chastenet J., Chiang I.-D., Congiu E., Dale D. A., Deger S., Eibensteiner C., Egorov O. V., García-Rodríguez A., Glover S. C. O., Grasha K., Henshaw J. D., Ho I.-T., Kepley A. A., Kim J., Klessen R. S., Kreckel K., Koch E. W., Kruijssen J. M. D., Larson K. L., Lee J. C., Lopez L A., Machado J., Mayker N., McElroy R., Murphy E. J., Ostriker E. C., Pan H.-A., Pessa I., Puschnig J, Razza A., Sánchez-Blázquez P., Santoro F., Sardone A., Scheuermann F., Sliwa K., Sormani, Mattia C., Stuber, Sophia K., Thilker, David A., Turner, Jordan A., Utomo D., Watkins E. J., Whitmore B., (2021), *PHANGS-ALMA: Arcsecond CO(2-1) Imaging of Nearby Star-forming Galaxies*, The Astrophysical Journal Supplement Series, 257, 2.

Author's Contribution: J. S. d. B. contributed to the data reduction and data quality assessment.

6. Bešlić I., Barnes A. T., Bigiel F., Puschnig J., Pety J., Herrera Contreras C., Leroy,A. K., Usero A., Schinnerer E., Meidt S. E., Emsellem E., Hughes A., Faesi C., Kreckel K., Belfiore F. M. C., Chevance M., **den Brok J. S.**, Eibensteiner C., Glover S. C. O., Grasha K., Jimenez-Donaire M. J., Klessen R. S., Kruijssen J. M. D., Liu D., Pessa I., Querejeta M., Rosolowsky E., Saito T., Santoro F., Schruba A., Sormani M. C., Williams T. G., (2021), *Dense molecular gas properties on 100 pc scales across the disc of NGC 3627*, Monthly Notices of the Royal Astronomical Society, 506, 1 .

   Author's Contribution: J. S. d. B. contributed edits that helped to improve the manuscript. In addition, J. S. d. B helped with the data analysis and discussed in-depth the results and interpretation with the lead-author.

Contents

CHAPTER 1

Introduction

> For what could be more beautiful than the heavens which contain all beautiful things.
>
> N. Copernicus – 16th century astronomer

Overview

At first glance, the vast space between the stars in our night sky presents itself as empty and devoid of any matter. For millennia, the study of astronomy focused exclusively on describing and predicting the motion of stars and planets across the seemingly barren sky. But upon close inspection, one will find, in fact, a rich presence of gas and interstellar dust that permeates these seemingly empty regions. Today, we not just know about the existence of this so-called *interstellar medium* (ISM), but we also start to grasp the far-reaching impact and effect this material has on its host galaxy. The ISM is not just a simple component that makes up part of a complete galaxy, but it is the key galactic reservoir from which stars form and into which they end up injecting their energy and spreading their enriched material. Understanding the ISM is indispensable for a complete picture of galaxy formation and evolution.

Figure 1.1 shows one of the first observations taken with the James Webb Space Telescope. This infrared (IR) image depicts the nearby, star-forming region NGC 3324 situated within the Carina Nebula. The dark clouds at the bottom half consist mainly of cold molecular hydrogen and interstellar dust. Hidden deep inside, we will find newborn stars. The exterior is exposed to scorching UV light emitted by nearby massive stars. As a result, the outer layers slowly erode due to photodissociation and photoevaporation. This process manifests itself by the blue glow.

This thesis focuses on a particular aspect of the ISM: The cold and molecular gas phase, which builds the fuel for star formation. Using emission originating from the *carbon monoxide* (CO) molecule, we obtain fundamental insight into the physics and chemistry of this particular phase of the ISM. The following sections will briefly introduce the ISM, the processes regulating it, and describe the methods and techniques to study it. If not mentioned otherwise, the primary sources of reference in the introductory sections are the textbooks by Tielens (2010), Choudhuri and Smoot (2011), Draine (2011), Wilson et al. (2013) and Williams and Viti (2014) and the reviews by Kennicutt and Evans (2012), Krumholz (2015) and Klessen and Glover (2016).

Figure 1.1: **The Carina Nebula.** This IR image, one of the first taken by the James Webb Space Telescope, shows a nearby and young star-forming region. Credit: NASA, ESA, CSA, STScI Heritage Team (STScI/AURA).

1.1 The Interstellar Medium

Historically, the discovery and study of the ISM date back to the 19th and early 20th centuries. While the notion of an *interstellar substance* traces back to the 17th century (e.g., *aether interstellaris*; Bacon and Rawley, 1670), the space was initially thought to be void and empty. By the 19th century, after steady advances in telescope design and performance, it became apparent that other astronomical objects exist in the Universe besides stars and planets. For instance, the first detection of spectral lines within an emission nebula pointed to the existence of gaseous material between stars (Huggins and Miller, 1864; Huggins, 1865), and opened the field of ISM studies.

Nowadays, after more than a century of research, we consider the ISM the primary galactic repository of mass and energy, as it provides the matter from which stars are formed. Far from being simple, the ISM is a turbulent, multi-phase, and multi-scale medium. On the one hand, to understand the large-scale dynamics of the ISM, it is crucial to know about the underlying physics that regulates the small scales, such as stellar evolution and cloud-scale dynamics. But on the other hand, local, small-scale properties, such as the ability of the gas to cool, collapse and form stars, are all affected by dynamical processes on large galactic scales, e.g., the large-scale galactic dynamics or the environmental effects of bars and galactic centers. Consequently, the spatial scales studied for understanding the ISM range from the size of whole galaxies to the small clouds of gas that form individual stars. In addition, the physics of the ISM truly incorporates a multitude of physical fields, ranging from quantum physics and chemistry to magnetohydrodynamics, plasma physics, and gravitational dynamics. The far-reaching effects and these connections to various aspects of physics make the study of the ISM essential for numerous fields of astronomy. With a broad set of methods and techniques, it becomes possible to disentangle the various processes, constraints, and aspects that together shape the ISM.

1.1.1 Constituents of the ISM

In the Milky Way, about 10–15% of the visible (baryonic) matter resides within the ISM, while the rest is primarily incorporated within stars and stellar remnants, such as white dwarfs, neutron stars, or black holes. By far the most common element in the ISM, in terms of mass fraction, is hydrogen (H) with ~70%, followed by Helium (He) with 28%. Heavier elements, which astronomers commonly refer to as *metals*, only constitute a mere 2% of the overall mass. The ISM itself is composed of various constituents, all of which contribute to an intricate interplay between each other. Following Draine (2011), we can list the subsequent components:

1. **Interstellar Gas:**
   The interstellar gas is undoubtedly the major component of the ISM in terms of its influence on galaxy formation and evolution. It includes ions, electrons, atoms, and molecules that all exist in the gaseous phase. Empirically speaking, we find that the thermal and chemical state of the gas covers a wide range of temperatures and densities (see Table 1.1). Generally, the observed densities and temperatures can be categorized by a set of distinct *phases*. In the 1950s, after the groundbreaking detection of H I via the 21cm transition (Ewen and Purcell, 1951), the idea of a multi-phase medium in thermal equilibrium arose (Spitzer, 1956). A more precise model was put forward by Field et al. (1969), who suggested that two thermally stable gas phases coexist, namely the so-called hot, neutral medium (HNM; with $T \sim 10^4$ K) and cold neutral medium (CNM; with $T < 300$ K). These two phases are present because, at those two temperatures, the gas will remain in thermal equilibrium. Gas with temperatures between these two phases becomes thermally unstable and will either cool down by increasing its density and become part of the CNM, or it will heat up, reducing its density and becoming part of the WNM.

   A few years later, McKee and Ostriker (1977) suggested the presence of another gas phase, the hot ionized medium (HIM), after studying supernovae. Observations showed that supernovae produced ionized bubbles that are filled with extremely hot gas, heated by shocks to around $T \sim 10^6$ K. Due to its low density, the HIM has a very large filling factor. Approximately half of the MW disk is filled by HIM, despite it contributing to only a small fraction of the total ISM mass.

   Soon after, however, it became evident that these three phases still do not adequately describe the total variation of the interstellar gas. After observing the dispersion of radio signals from pulsars (e.g. Reynolds, 1989) and free-free absorption of the Galactic synchrotron background (e.g. Hoyle and Ellis, 1963), it became apparent that another phase, the Warm Ionized Medium (WIM; Reynolds 1985), is present. Newest estimates postulate that around 90% of the total ionized gas in the ISM is situated within the WIM (Haffner et al., 2009). Massive type O and B stars are the primary radiation source that ionizes the gas in the WIM.

   Finally, it became clear that the CNM itself can be even further separated into two key sub-components: the atomic and the molecular CNM. A large fraction of galactic disks consists of cold neutral atomic hydrogen, HI (Wolfire et al., 2003). Emission from HI is crucial to mapping the kinematics of the atomic gas in the Milky Way (Binney and Merrifield, 1998). However, at the thesis' heart is the focus on the other sub-component of the CNM: the molecular gas. The particular interest in this component arises from the fact that we observe the presence of molecular gas to be tightly linked to star formation. Since the molecular gas is denser, self-shielding is effective so that molecular hydrogen in the form of H_2 can be abundant.

   We note that even further, more detailed subdivisions of individual phases exist in the literature.

Table 1.1 lists the five most relevant phases. In Section 1.3, the properties of molecular gas clouds, which host most of the molecular gas, are discussed in further detail.

Table 1.1: Characteristic Phases of Gas in the ISM. Table adopted from Klessen and Glover (2016).

Gas Phase	Temperature (K)	Density (cm^{-3})	Fractional Ionization
Hot Ionized Medium (HIM)	10^6	$10^{-2} - 10^{-3}$	1
Warm Ionized Medium (WIM)	8000	0.5	1
Warm Neutral Medium (WNM)	$\sim 10^4$	0.5	~ 0.1
Cold Neutral Medium (CNM)	~ 100	$20 - 50$	$\sim 10^{-4}$
Molecular gas	$10 - 20$	$> 10^2$	$\leq 10^{-6}$

2. **Interstellar Dust:**
Distributed within the interstellar gas are also small, solid particles. Measurements suggest that these particles range in size from $\sim 0.02 - 20\,\mu$m. The presence of interstellar dust articulates itself, particularly in the form of reddening of starlight crossing the ISM. Such reddening occurs because the ultraviolet light is scattered and absorbed more dominantly than the optical and infrared wavelengths (Rayleigh scattering). Generally, only a small amount of the total ISM mass is locked in dust particles. Measurements from the local ISM suggest that approximately 1% of the total mass of the ISM resides in dust particles. Nonetheless, we should not underestimate dust's influence on ISM processes. Dust grains play a crucial role since they catalyze the formation of H_2 and more complex molecules on their surfaces which are eventually injected into the ISM. Moreover, by absorbing UV radiation, dust grains help to shield molecules from photodissociation. Furthermore, interstellar dust can play a dominant role in the energy budget of the ISM. On the one hand, it acts as an efficient cooling agent due to emission of infrared emission. On the other hand, it heats the surrounding gas due to the absorption of ultraviolet starlight. The formation of dust grain takes place in the outer layers of Red giant stars or planetary nebulae.

3. **Electromagnetic Radiation:**
Photons permeate the ISM from numerous sources and different origins. In sum, the ensemble of photons with different energies all together comprise the *interstellar radiation field* (ISRF). The ISRF regulates various processes in the ISM, including (i) the chemical state of the gas as high energy radiation leads to photodissociation of molecules and ionization of atoms, (ii) photoelectric heating due to energetic electrons that are ejected from dust grains that have absorbed UV radiation (iii) thermal equilibrium of interstellar dust in case the absorption of ISRF radiation and the thermal re-emission of this energy balance.

   Looking at the ISRF in the solar neighborhood, we can distinguish different components tracing diverse origins. Figure 1.2 illustrates the key components of the local ISRF. The three most dominant components are radiation originating from the cosmic microwave background (CMB) in the microwave regime, thermal emission in the infrared by dust grains, and stellar emission that dominates the visible and UV wavelength range. In addition, X-ray radiation exists that originates from hot plasma in the ISM and from galactic synchrotron emission by relativistic electrons. However, this radiation is less dominant in the solar neighborhood. Locally, the ISRF can vary dramatically. For instance, in the vicinity of young and hot type O and B stars, the UV radiation will increase, or the X-ray emission will be significantly enhanced near active galactic nuclei.

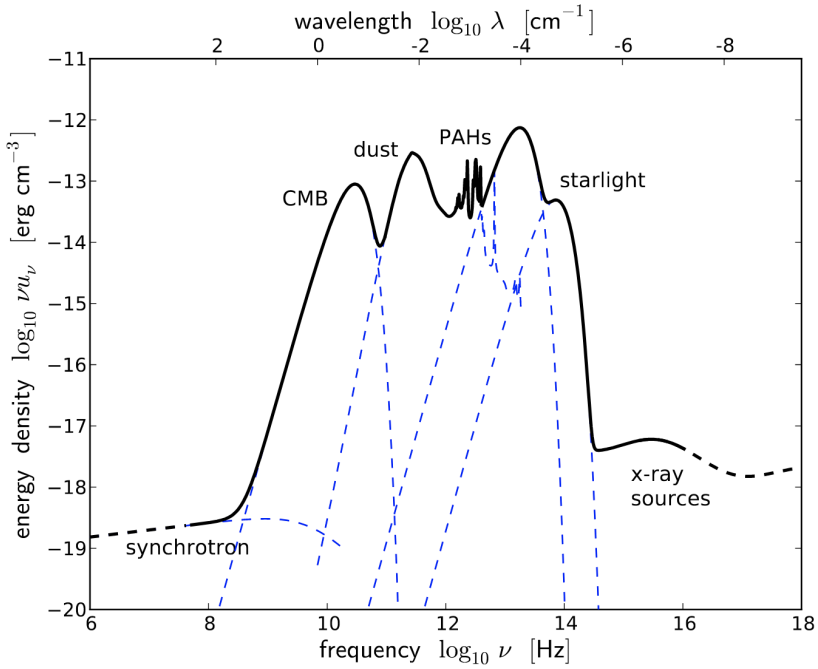

Figure 1.2: **The interstellar radiation field (ISRF) in the solar neighborhood.** The sketch illustrates the composition of the ISRF as function of photon energy. Credit: Figure taken from Klessen and Glover (2016)

4. **Cosmic Rays:**
   The ISM is also filled with relativistic charged particles, such as predominantly protons but also electrons or heavier nuclei. Their kinetic energy ranges from 100 MeV up to more than 1 TeV. Since these particles are charged, they will be deflected by magnetic field lines across the galaxy. Consequently, the particles will scatter within the Galactic disk, leading to a relatively uniform local cosmic ray energy density (except for most highly energetic cosmic rays because they are not significantly deflected).

   In the more dense ISM, where the ISRF becomes too weak, cosmic rays constitute an important ionization source. Furthermore, they act as an important gas heating source by injecting their kinetic energy into the electrons that were ejected by the ionization. Hence, they play a crucial role in affecting the chemistry of the ISM. The rate of cosmic rays drops steeply as a function of their kinetic energy. Consequently, the majority of the heating and ionization of the gas is due to less energetic cosmic rays (∼100 MeV).

5. **Magnetic Fields**:
   The ISM is permeated by magnetic fields that arise from electric currents by charged particles. These fields affect the trajectories of cosmic rays and, in the case of strong magnetic fields, also gas dynamics of the ISM and the onset of star formation. From observations it is estimated that the average magnetic field strength in the Milky Way is around 3 μG (Planck Collaboration et al., 2016a). The intensity varies with the density of the gas and follows a power law $B \propto n_{\mathrm{H}}^{\alpha}$. Initially, star-forming theories suggested that magnetic fields in the ISM will actually prevent to certain degrees the collapse of molecular clouds that would form stars (Shu et al., 1987). More recent studies, however, suggest magnetic fields are rather not strong enough to stabilize the clouds as a whole (Hennebelle and

Inutsuka, 2019). But they remain a major agent during the collapse of clouds by removing angular momentum (Tan et al., 2014; Planck Collaboration et al., 2016b).

6. **Gravitation Fields and (hypothetical) Dark Matter Particles**:
   Gravitational fields that regulate the dynamics, kinematics, and collapse of the ISM constitute another relevant component for the description of the ISM. Since only 10% of the galaxy's mass is enclosed within the ISM, the gravitational potential is mainly dominated by stars, stellar remnants, and dark matter. But in the dense molecular gas, the gravitational field can, in fact, locally be dominated by the molecular gas itself, leading to self-gravitating clouds.

   The hypothetical dark matter particles do not play any considerable role, apart from their contribution to the gravitational field. So far, non-gravitational interactions of dark matter particles with the baryonic matter have not yet been indisputably detected and remain speculative in the context of ISM studies. Hence, in this thesis, we do not consider the presence of dark matter particles in our interpretations of the ISM.

1.1.2 Galaxy Evolution and the ISM

The history and development of the ISM are tightly linked to the formation and evolution of the galaxy itself. The full extent of this co-evolution is captured by the *baryonic life cycle*. The various stages of the cycle and the subsequent transitions are illustrated in Figure 1.3. Baryonic matter in the Galaxy is constantly being transferred from one phase to the other. Diffuse clouds constitute the first step of the cycle. They are mostly made out of neutral hydrogen. Eventually, these diffuse clouds will contract further and shape the breeding grounds where star formation occurs. In addition, dust grains are produced in the outer regions of red giants and eventually fill up the ISM. Ultimately, once the stars have reached their end, their stellar remnants will again replenish the ISM with heavier elements or with energy and momentum from shocks or stellar winds.

Diffuse clouds consist mainly of atomic gas but also contain a small fraction of molecules (Snow and McCall, 2006). At low densities ($n \leq 10^4\,\mathrm{cm}^{-3}$), the gas is fully exposed to the galactic ISRF. Consequently, photodissociation will destroy a significant fraction of the molecules in the medium. While atomic hydrogen remains mainly neutral, atoms with lower ionization potential than hydrogen, such as atomic carbon (11.3 eV), will be ionized. At higher attenuation of the ISRF ($A_V{\sim}1$), H_2 can remain present in substantial amounts. Other molecules, such as CO, however, are still photodissociated by UV radiation penetrating deep enough into the cloud layer. The dust grains also play a crucial role in the enrichment of molecular H_2. Molecular hydrogen can only be formed in high-density gas through 3-body reactions on the surface of dust grains. Furthermore, dust grains are needed for the absorption of the excess energy of the reaction. Because H_2 has a symmetric dipole moment, this excess in energy cannot radiate away efficiently, leaving the synthesized molecule otherwise in the excited state, H_2^* (Wakelam et al., 2017). At even higher attenuations ($A_V > 1$), atomic carbon or molecular CO can be present in substantial amounts (this phase is often referred to as the *translucent cloud phase*; van Dishoeck and Black 1989).

At higher densities ($n \geq 10^4\,\mathrm{cm}^{-3}$), the core of the cloud will be completely shielded against the ISRF. In these regions, carbon and oxygen will be captured in the form of CO in significant amounts, making this molecule the second most abundant after H_2 (abundance fraction of $[\mathrm{CO/H_2}] \approx 10^{-4}$). These dense molecular clouds are of particular interest due to their ability to form stars by gravitational collapse. Furthermore, they host rich chemistry, with only cosmic rays penetrating deep enough to dissociate the molecules.

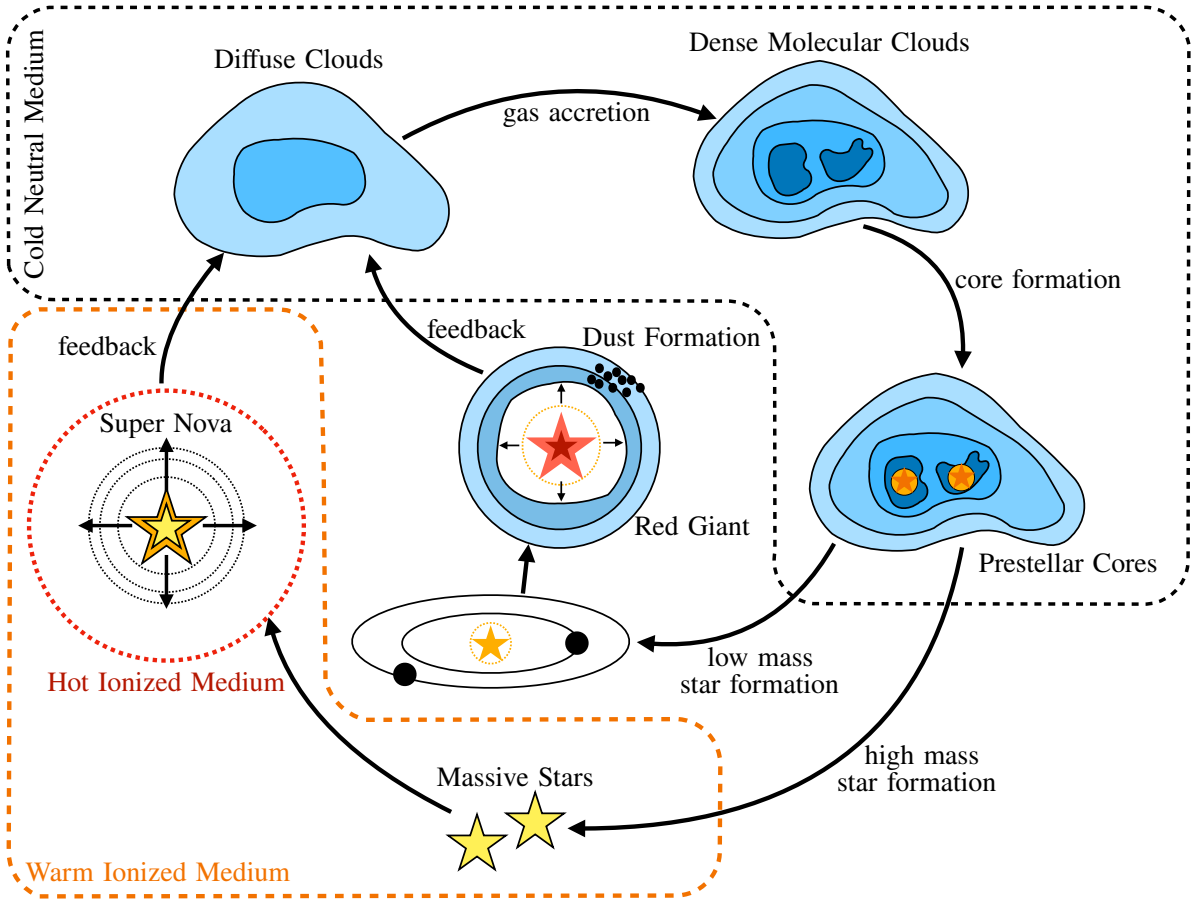

Figure 1.3: **The ISM Baryonic Life-Cycle.** This sketch illustrates the main evolutionary steps of the cycle. Diffuse clouds will eventually condense and form dense molecular clouds and ultimately prestellar cores, where star formation occurs. After stars have formed, the resulting stellar remnant will depend on the initial mass of the stars. Supernovae happen as the result of a core-collapse of massive stars, while the red giant phase is also reached by less massive stars. These stellar remnants affect the cold neutral medium in terms of energy input, replenishing heavier elements and enrichment of dust. In turn, dust acts as a major catalyst for the formation of H_2 in the ISM. This illustration is inspired by a figure shown in Demyk (2011).

Finally, the baryon cycle finishes with star formation and their respective end products. Regarding star formation, we differentiate between high-mass and low-mass star formation. A difference lies in the stellar remnant after the death of the stars. High-mass star formation will produce bright O and B stars that photodissociate their surrounding gas and form the WIM. In fact, they will destroy their molecular environment before they fully form due to their hard radiation field (i.e., radiation with a large fraction of photons with $E_\nu > 13.6\,\mathrm{eV}$). Finally, a supernova will replenish the ISM with heavier elements produced either inside the star due to nuclear fusion or in processes during the core collapse of the star. Furthermore, the resulting shocks of the supernova will dissipate energy in the surrounding, heating the gas. Less massive stars will form into red giants before turning into white dwarfs. The red giant phase is relevant for the formation of dust grains as heavier elements freeze out in their stellar winds.

This completes the full baryonic cycle in the galaxy. Star formation is closely linked to the reservoir of

molecular gas, which in turn is affected by feedback mechanisms of the stellar remnants. Hence, the galaxy evolution of stellar populations is tightly intertwined with the ISM evolution itself.

1.2 Observing the ISM in mm Wavelengths

Because of the multi-phase and multi-component nature of the ISM, various strategies have to be devised to obtain information about the underlying processes and interactions. Multi-wavelength observations are necessary to assess all aspects of the ISM. In this thesis, the focus lies on the molecular gas component. Because the gas in the dense molecular gas phase is relatively cold (~10 K), radio and mm-wavelengths from rotational transitions of different molecules constitute a major pathway to studying the medium. Chapter 2 will give more details about the particular ways to obtain information about astronomical systems in general with telescopes and detectors.

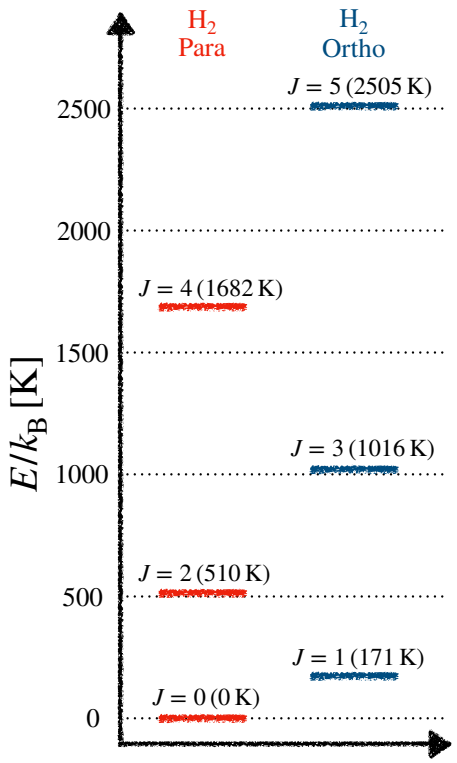

Figure 1.4: **Rotational level diagram of H_2** The levels are separated between the para and ortho H_2. Level energy values taken from Goldsmith et al. (2010).

1.2.1 Challenges Observing H_2 Directly

When studying the state of the molecular gas, we are generally interested in grasping the distribution of the molecular hydrogen H_2, since it constitutes the most abundant molecule. But as a significant impediment for ISM astronomers, H_2 is extremely difficult to observe directly. This is not the case for atomic hydrogen. The hyperfine transition due to a spin-flip of the electron from parallel to anti-parallel to the proton emits radio waves at 21cm (~1.4 GHz). Because the transition energy is extremely small, the state is even excited in the coldest parts of the ISM. Hence this emission is very easy to observe in the Milky way and across extragalactic sources. It was one of the first transitions that was postulated to be observable in the radio regime (van de Hulst, 1945). The first actual detection dates back to the early 1950s (Ewen and Purcell, 1951). Since then, the 21cm HI line has become a workhorse tracer of the cold atomic medium.

However, in colder and denser molecular clouds, most hydrogen is captured in H_2, making the HI 21cm line an unreliable tracer. In fact, within spiral galaxies, a significant fraction of the non-stellar baryonic mass resides within H_2, where it acts as an important coolant of warmer diffuse gas, cooling it down to temperatures of around 100 K (Williams, 1999). What makes H_2 so difficult to observe under normal molecular cloud conditions? Because H_2 is a symmetric molecule, it is classified as a so-called *homo-nuclear diatomic* molecule. For molecules, we can distinguish between three types of excitation:

1. *electronic*, when one or more electrons of the molecule get excited;
2. *vibrational*, when the vibrational state of the two nuclei gets excited;

3. *rotational*, when the state of the two nuclei's rotation around the center of mass gets excited.

Under general dense molecular cloud conditions, the characteristic temperature is around $10 - 20\,\mathrm{K}$. This is not high enough to excite electronic and vibrational transitions and just barely rotational transitions. Rotational transitions occur when the angular momentum due to motion around the center of mass of the molecule changes. For a diatomic molecule, the corresponding energy difference is given by:

$$\Delta E_J = \frac{\hbar^2}{2\mu R_0^2} J \times (J+1), \tag{1.1}$$

with the reduced Planck constant $\hbar$, the equilibrium separation distance R_0, the reduced mass of the system μ, and the rotational quantum number J. The rotational levels of H_2 for different quantum number Js are shown in Figure 1.4. For a homo-nuclear molecule, like H_2, transitions with $\Delta J = 1$ are forbidden since no process turns a hydrogen molecule in an even J state into an odd J state. Consequently, the lowest energetic transition possible is given by the $J = 2 \rightarrow 0$ transition, with an upper level energy of $E/k_\mathrm{B} \approx 510\,\mathrm{K}$. However, in molecular clouds with $T \approx 10\,\mathrm{K}$, only a negligible fraction of H_2 will be in the excited state. It is only feasible at a temperature of $T \geq 100\,\mathrm{K}$ to observe H_2 in rotational emission. In rare specific galactic environments, such high-temperature conditions are feasible. But studies observing H_2 rotational lines from such regions generally only capture about 1%–30% of the total molecular gas (Roussel et al., 2007). Vibrational transitions of H_2 are similarly challenging to observe. The lowest vibrational transition, $v = 1 \rightarrow 0$, lies at $\lambda = 2.2\,\mu\mathrm{m}$, with an upper energy level at $E/k_\mathrm{B} = 6\,471\,\mathrm{K}$. This transition is valuable for studying the molecular gas in shocked regions, such as in outflows of young stellar objects or photodissociation regions (Shull and Beckwith, 1982). Nonetheless, this transition captures again only a fraction of the total H_2 amount. Similarly, electronic transitions of H_2, which lie typically in the far-UV regime, are generally limited to the emission from the diffuse ISM. There, the stellar UV background is less attenuated by dust, generating the conditions necessary for electronic excitation (first detections of H_2 from such regions made by Carruthers, 1971).

Given these limitations, it is impossible for all practical purposes to detect H_2 directly and reliably under the characteristic cold molecular ISM conditions. To facilitate the observation of the distribution of H_2, astronomers rely on detection by using a proxy, such as dust or molecular line emission by other molecular species.

1.2.2 CO as Indirect Bulk Molecular Gas Tracer

Luckily, the medium consists not purely of H_2 due to enrichment by heavier elements produced in massive stars and supernovae. In the cold and dense molecular ISM, the C and O atoms predominantly combine to form CO, making it the second most abundant molecule (relative abundance of $[\mathrm{CO}/\mathrm{H_2}] \approx 10^{-4}$). The CO molecule has a weak permanent dipole moment and low excitation energy of around $E/k_\mathrm{B} \approx 5\,\mathrm{K}$. Hence, the rotational ground transition $J = 1 \rightarrow 0$ is easily excited and thermalized under characteristic dense and cold molecular ISM conditions. An additional advantage is that the lowest transition with a frequency of $\sim$115 GHz (2.6 cm) is within an atmospheric window, meaning that the transition is observable from the ground (see discussion in Section 2.1). Since it is more easily observable than H_2, CO has become one of the most commonly used tracers of the bulk molecular gas distribution within the Milky Way and in extragalactic sources.

CO was the first interstellar molecule whose rotational $J = 1 \rightarrow 0$ ground transition was observed at $\lambda = 2.6\,\mathrm{mm}$ in the nearby Orion Nebula (Wilson et al., 1970). In the subsequent years, molecular clouds throughout the Milky Way were surveyed in more detail using their 2.6 mm CO emission (e.g., Solomon

et al., 1972; Wilson et al., 1974; Burton et al., 1975; Scoville and Solomon, 1975). These first studies found that the distribution of molecular CO resembles more closely that of compact HII regions and not that of the more widespread atomic hydrogen gas. At the same time, studies targeting nearby and bright extragalactic sources also found a widespread presence of CO molecular gas (e.g., Rickard et al., 1975; Solomon and de Zafra, 1975). Using CO emission, attempts were made to estimate the total molecular gas mass in extragalactic systems (Young and Scoville, 1982). At first, extragalactic observations were hampered by low angular resolution compared to Milky Way studies. However, with advances in instrument and telescope design, the first resolved detections of molecular gas were achieved using interferometers (e.g., Vogel et al., 1987; Wilson et al., 1988).

1.2.3 Remaining Challenges of Molecular ISM Observations

The low-J CO rotational transitions have become a workhorse tracer of the bulk molecular mass in the Milky Way and extragalactic sources. However, there still remain challenges when relying on CO to properly assess and trace the molecular ISM under certain specific conditions. The two most notable challenges are that (a) the emission of CO is optically thick, and that (b) the presence of large amounts of so-called CO-dark gas will hamper its use to estimate the bulk molecular mass distribution.

1. **Optical Depth:**
   The emission from the CO $J = 1 \rightarrow 0$ transition line is optically thick[1] (e.g., Shetty et al., 2011). This poses a major challenge for the use of CO to estimate the underlying H_2 column density. Due to optical depth effects, we generally expect the quantitative relation between CO luminosity and H_2 amount to break (e.g. Seifried et al., 2020; Bisbas et al., 2021). To take the analogy from Kennicutt and Evans (2012), using CO as the molecular gas tracer is akin to using the presence of a brick wall to estimate the depth of the building behind it. In particular, the brightness temperature we observe from the CO transition is related to the surface layer where the optical depth is $\tau_{CO} \leq 1$. As a consequence, the peak CO emission does not necessarily overlap with regions where the H_2 column density is highest (Shetty et al., 2011). Furthermore, the observed CO line width will correspond to velocity dispersion dominating the outer surface layers of the molecular cloud. This makes it difficult to assess the underlying velocity dispersion of the full molecular clouds that are not virialized.

2. **CO-dark gas:**
   Recent studies using γ-ray flux originating from interactions of cosmic rays with molecules (e.g., Strong and Mattox, 1996; Grenier et al., 2005) as well as dust emission and absorption measurements (e.g., Reach et al., 1994; Reach et al., 1998; Planck Collaboration et al., 2011a) suggest that additional gas is present that cannot be accurately accounted for by HI and CO emission alone. It is generally suggested that the so-called *dark gas* stems from molecular gas lacking bright enough CO emission. This is further supported by detections of interstellar molecules, such as OH and CH, toward the line of sights that do not show any CO emission (e.g., Wannier et al., 1993; Magnani and Onello, 1995; Allen et al., 2015). The presence of molecular gas without corresponding CO emission is also expected because H_2 can exist in layers of a molecular cloud further out than the CO region. The explanation is that the CO has a smaller self-shielding threshold than H_2 and will consequently be photodissociated faster. The layer between the outer H_2 cloud and the inner gas region will mark the CO-dark molecular gas in such clouds. So atomic HI and CO emission measurements are not enough to account for all the hydrogen gas in the ISM. Using the lack of CO emission at face

[1] A more detailed discussion about the optical depth, τ will be given in Section 1.6

value for the non-presence of molecular gas, it has been found that generally 12% up to 100% of the actual molecular gas present will be missing when relying solely on CO as a tracer (Liszt and Pety, 2012). Metallicity is expected to play a key role. Past studies of galactic systems with lower metallicities, such as the Large Magellanic Cloud (e.g Hughes et al., 2010) or low-metallicity galaxies (e.g. Galametz et al., 2009; Cormier et al., 2014) showed disproportionate lower CO emission than expected from scaling relations such as the Kennicut-Schmidt relation (see Subsection 1.5.1). Commonly used alternative tracers of molecular gas include emission from neutral ([CI] emission from C) or ionized ([CII] emission from C^+) carbon. However, these tracers also come with their own unique challenges. For instance, both [CI] and [CII] are expected to trace not just molecular,but also atomic gas to various degrees (e.g., Franeck et al., 2018; Li et al., 2018; Vizgan et al., 2022).

1.3 Properties of Molecular Clouds

The molecular gas is predominantly located within cold ($T \sim 10-20$ K) and dense ($n > 10^3$ cm^{-3}) so-called *giant molecular clouds* (GMC; Sanders et al. 1985). Broadly, we can define GMCs just as over-densities in the molecular gas. They do not necessarily have to be gravitationally bound (Chevance et al., 2020). In terms of total mass, they contain approximately the same fraction as confined within the atomic gas phase in galaxies (Young and Scoville, 1991). Molecular clouds show an intricate and complex morphology and substructure, which is revealed by high-resolution observations of clouds in the Milky Way (e.g., Pety et al., 2017; Rosen et al., 2020; Stanke et al., 2022). Figure 1.5 shows a qualitative illustration of a molecular cloud and its key substructure components.

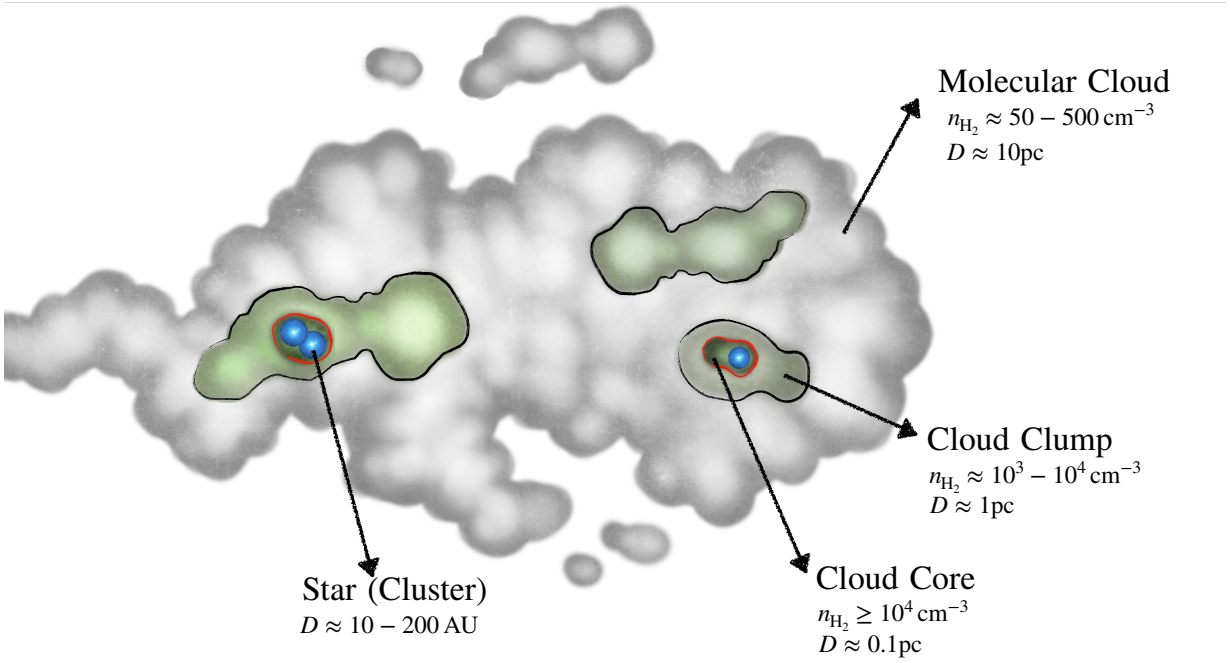

Figure 1.5: **Structure of a Giant Molecular Cloud (GMC).** The illustration sketches the sub-components of GMCs. The labels indicate the average densities and sizes components. This sketch builds on a Figure from Pokhrel et al. (2018).

CO emission reveals well the overall extent of the bulk molecular cloud. GMCs have a characteristic size of tens of parsec and incorporate, on average, a mass of $10^4 - 10^6\,M_\odot$ (Murray, 2011). Across such a molecular cloud, the density is not distributed homogeneously. Locally, denser substructures will form in a hierarchical manner. Regions of enhanced density are referred to as molecular, star-forming *clumps*. They are smaller (size of ∼1 pc) and denser by a factor of 10 – 100 than the rest of the cloud. But they actually hold most of the mass of the overall cloud (Blitz, 1987; Bertoldi and McKee, 1992). The further fragmentation of these clumps into (pre-stellar) *cores* (e.g. André et al., 2014) constitutes another fundamental step in the evolutionary process of star formation (e.g., André et al., 2010). Such cores have an average size of 0.1 pc and can host the formation of single stars or stellar clusters. Since they are typically more gravitationally bound, they tend to be more spherical than the overall molecular cloud or the clumps. Toward the denser regions of the cloud, the gas properties will change. For example, while the overall GMC is supersonically turbulent (due to the influence of hierarchical gravitational collapse and feedback-driven outflow; Chevance et al. 2020), measurements of the gas velocity dispersion in the cores indicate more subsonic gas (Lada et al., 2008; André et al., 2014). In contrast, high-mass star-forming regions show dominant non-thermal gas motion and accompany large, pc-scale gas flows toward these star-forming cores (e.g, Wyrowski et al., 2016; Sokolov et al., 2018). Such turbulent gas dynamics are a crucial element of models that predict large accretion rates to support high stellar-mass formation (McKee and Tan, 2003).

The boundary of molecular clouds is commonly defined using a certain CO emission threshold. Alternatively, a certain level of extinction of the galactic ISRF or from light emitted by background stars can also be used to delimit the boundary of molecular clouds (Kennicutt and Evans, 2012). The so-called photon-dissociation regions (PDRs, Tielens et al. 1993; Hollenbach and Tielens 1999) are an important part of the boundary layer of molecular clouds. A PDR is a stratified layer surrounding GMCs and results from far-UV photons from the ISRF or nearby hot stars that photodissociate the molecules up to a certain layer into the cloud. Figure 1.6 shows a cross-section into a GMC. Inside the cloud, at high attenuation (A_V), the CO is well enough shielded and abundantly present. However, CO will be photodissociated at lower attenuation, leading to layers where H_2 is still the dominant species, without any significant CO emission. This region is referred to as CO-dark gas (Meyerdierks and Heithausen, 1996; Grenier et al., 2005, see also Subsection 1.2.3). Here, carbon will almost exclusively be present in atomic form. At the exposed, most outer layer, also H_2 will photodissociate, marking the transition to the atomic interstellar gas phase.

1.3.1 CO Isotopologues

Different isotopes of the heavier elements populate the ISM. In particular, the C, N, and O elements and their isotopes are of interest when investigating the chemical evolution of galaxies. The star formation history, the evolution of the individual stars, and the enrichment of gas by stellar remnants all affect the spatial distribution and relative abundance of the various isotopes. We find molecules with different isotopic compositions, so-called *isotopologues*, in the molecular ISM. For example, carbon monoxide is most abundantly found as a composite of $^{12}C^{16}O$ (which is generally just abbreviated as "CO"). The second most abundant CO isotopologue in regular nearby galaxies is $^{13}C^{16}O$ (abbreviated as ^{13}CO) and then $^{12}C^{18}O$ (abbreviated as $C^{18}O$). Observing these isotopologues makes it possible to measure the C and O isotope abundances. Studies investigating such isotope abundances and their ratios have been extensively carried out in clouds within the Milky Way (e.g. Langer and Penzias, 1990; Wilson and Matteucci, 1992; Henkel et al., 1994; Wilson and Rood, 1994; Milam et al., 2005). With recent advances in telescope and instrumentation design, it has become possible to obtain spatially resolved observations of CO isotopologue emission in extragalactic systems as well (e.g., Martin et al., 2010; Henkel et al., 2014; Jiménez-Donaire

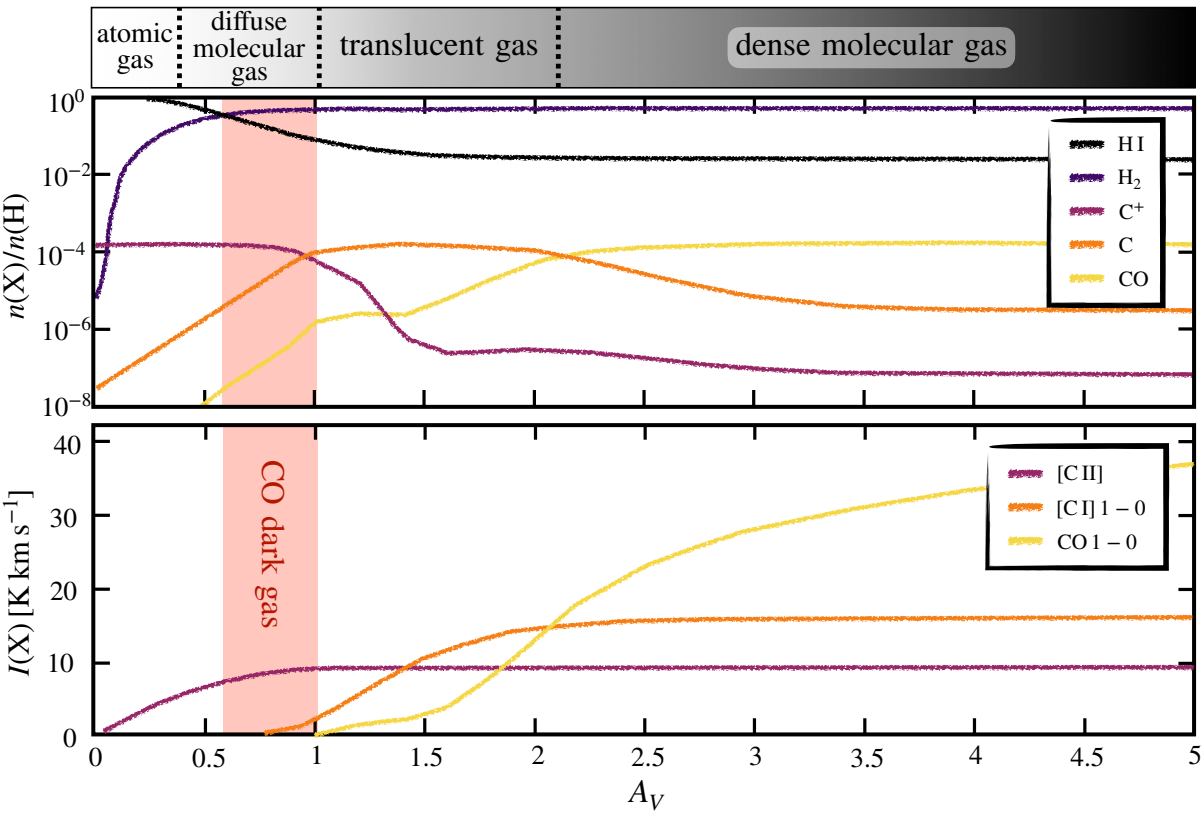

Figure 1.6: **Abundance and Emission at the GMC Boundary.** The two panels show the abundance fraction and emission of certain molecules as a function of optical depth into the cloud. The model to calculate the abundances/line intensities uses a constant H density $n_{\rm H} = 3 \times 10^3$ cm^{-3} a radiation field which is 30 times the radiation field described in Draine (1978), and a cosmic-ray ionization rate of 2×10^{-16}s^{-1} per hydrogen nucleon. Credit: Abundance and intensity profiles adopted from Bolatto et al. (2013).

et al., 2017a; Jiménez-Donaire et al., 2017b; Teng et al., 2022). In summary, CO isotopologue observations are commonly used to probe one of the following aspects of the molecular ISM (White, 1997):

- **Molecular Abundances – Chemical Evolution and Star Formation History**
  Under certain physical and chemical conditions of the gas, the C, N, and O isotopes or the CO isotopologue species will be formed or destroyed. By investigating the abundance variations of the different CO species, we can make conclusions, for example, about the star formation processes and the stellar evolution, both of which affect the isotopic abundances directly.

  For instance, the ^{12}C, ^{13}C, and ^{18}O isotopes can be used to distinguish between primary and secondary processing of the elements in stars. The ^{12}C atom is directly produced via the triple-α process (Salpeter, 1952) in massive stars (Timmes et al., 1995). Similarly, the ^{18}O isotope is also primarily produced by massive stars (Sage et al., 1991; Meyer et al., 2008). In contrast, the ^{13}C and ^{17}O isotopes are a byproduct of the so-called CNO cycle and are both converted into ^{14}N (Weizsäcker, 1937; Weizsäcker, 1938). As a consequence, massive stars do not significantly enrich the ISM with ^{13}C and ^{17}O isotopes (Prantzos et al., 1996). But low and intermediate-mass stars do, in fact, enrich the ISM with these particular isotopes, since during their red giant phase, ^{13}C and ^{17}O will be pulled

to the star's surface from the core by convection. Stellar winds then eject these species into the ISM (Wilson and Matteucci, 1992). Since these isotopes will be locked in molecules, CO isotopologue studies have been used to attempt to study the stellar populations and compare high to low-mass star-forming sites based on the $^{13}C/^{12}C$ and $^{17}O/^{18}O$ isotope ratios (e.g. Henkel and Mauersberger, 1993; Zhang et al., 2018; Brown and Wilson, 2019). We refer to abundance variations due to the stellar processing of the C and O isotopes as *selective nucleosynthesis* (Casoli et al., 1992).

Besides abundance variations of the isotopes, the isotopologue molecules themselves can also undergo changes in their relative amounts. For instance, there exist chemical processes that convert the ^{12}CO into the ^{13}CO isotopologue via an exothermic reaction (so called *chemical fractionation;* Watson et al., 1976; Keene et al., 1998):

$$^{13}C^{+} + {}^{12}CO \rightarrow {}^{12}C^{+} + {}^{13}CO + \Delta E. \tag{1.2}$$

This process occurs predominantly in cold regions ($T \leq 20\,\mathrm{K}$), since higher temperatures would lead to more rapid ion exchange, negating the effects of this reaction. Theoretical models predict that this process can enhance the ^{13}CO abundance by a factor of $2-3$ relative to ^{12}CO in molecular clouds under the right conditions (Szűcs et al., 2014).

Finally, the ISRF can also have a non-negligible effect on the relative isotopologue abundances. Hard UV radiation will photodissociate the CO molecules. Because ^{12}CO is relatively abundant in the molecular gas, self-shielding is more relevant. The other CO isotopologues, however, are less abundant, so they are less well self-shielded up to much deeper depth into the cloud (Bally and Langer, 1982). The relevance of the so-called *selective photodissociation* has lately, however, been put into question. Szűcs et al. (2014) simulated molecular clouds. Their models suggest no significant variation of the isotopologue ratios due to selective photodissociation.

So by investigating relative CO isotopologue abundance variations, we open a window to the chemical enrichment and evolution of the ISM in galaxies. For instance, due to selective nucleosynthesis, different stellar populations can be traced. Such observations are commonly used to assess the stellar evolution history of galaxies and investigate the universality of the initial mass function of stars (Brown and Wilson, 2019) across nearby galaxies.

- **Molecular Cloud Mass:**
  A fundamental understanding of the star formation processes requires assessing the distribution of molecular gas since it constitutes the main reservoir out of which stars are formed. However, properly evaluating the total column of H_2 is challenging (see Subsection 1.2.1 and Section 1.4). Because CO isotopologues, such as ^{13}CO and $C^{18}O$, are less abundant, they remain optically thin across nearby galaxy (Tan et al., 2011). Hence, they are a good tracer of the total CO isotopologue species column density. If the abundance ratio of H_2 to the specific isotopologue is known, we can estimate the total molecular gas mass of an individual or an ensemble of clouds (see, e.g., Cormier et al., 2018). Further details regarding this technique are given in Subsection 1.4.2.

- **ISM Thermodynamics – Changes in the Physical Conditions**
  If the conditions of the gas, such as the temperature, density, or opacity, vary, they will impact the emissivity of the CO transitions (e.g., Pineda et al., 2008; Wong et al., 2008; Davis, 2014). We expect these conditions to vary across and between different galaxies. For example, the center of certain spiral galaxies shows more turbulent gas, pushing down the CO-emitting gas's opacity. This will affect more dramatically the optically thick ^{12}CO emission (Sandstrom et al., 2013; Krieger

et al., 2017; Mangum et al., 2019). So by studying CO isotopologue emission ratios of lines with different optical depths, we can obtain insight into changes in the underlying physical conditions of the gas. In addition, the different CO isotopologues likely trace separate structures or phases of the gas. While ^{12}CO traces well the overall bulk molecular gas, ^{13}CO will be more confined to the denser and colder molecular gas, where the conditions permit efficient emission of the line (Cormier et al., 2018). In addition, different J transitions of the various isotopologues will trace the changes in the excitation conditions (such as temperature and density).

So, in summary, the CO isotopologues and their different rotational J transitions provide an excellent tool to trace various aspects of the physical and chemical conditions of the molecular ISM in galaxies. A challenge remains to disentangle the numerous processes that act in parallel and change the observed CO emission or their ratios.

1.4 The CO-to-H_2 Conversion Factor

CO line emission surveys of the Milky Way and beyond demonstrate their use to trace the distribution and physical conditions of the molecular gas. A conversion factor is needed to relate the observed CO integrated intensity, $W_{\rm CO}$, to the bulk molecular gas mass. The so-called CO-to-H_2 conversion factor is either defined via the H_2 column density, $N_{\rm H_2}$ (referring to the conversion factor as $X_{\rm CO}$):

$$\frac{N_{\rm H_2}}{\rm cm^{-2}} = X_{\rm CO} \times \frac{W_{\rm CO}}{\rm K\,km\,s^{-1}}, \tag{1.3}$$

or the molecular gas mass surface density $\Sigma_{\rm mol}$ (referring to the conversion factor as $\alpha_{\rm CO}$)[2]:

$$\frac{\Sigma_{\rm mol}}{\rm M_\odot\,pc^{-2}} = \alpha_{\rm CO} \times \frac{W_{\rm CO}}{\rm K\,km\,s^{-1}}. \tag{1.4}$$

Benchmarking studies of molecular gas in the solar neighborhood found an average conversion factor at $X_{\rm CO} = 2\times10^{20}\,{\rm cm^{-2}}\,({\rm K\ km\ s^{-1}})^{-1}$ (Solomon et al., 1987; Strong and Mattox, 1996). This value translates, after also accounting for contribution of helium, to $\alpha_{\rm CO} = 4.4\,{\rm M_\odot\,pc^{-2}}\,({\rm K\,km\,s^{-1}})^{-1}$. Recent studies find similar values across nearby spiral galaxies (Sandstrom et al., 2013). Properly calibrating these conversion factors remains challenging since the bulk molecular gas mass must be determined independently of the CO line intensity. The following section provides an overview of the techniques used to estimate the bulk H_2 mass. A more detailed description of the various methods is given by Bolatto et al. (2013).

[2] Throughout this thesis, we will interchangeably refer to the conversion factor as $\alpha_{\rm CO}$, or $X_{\rm CO}$. They are directly related to each other via the following formula:

$$\frac{\alpha_{\rm CO}}{M_\odot\,{\rm pc^{-2}}\,({\rm K\,km\,s^{-1}})^{-1}} = 2.18 \times \frac{X_{\rm CO}}{10^{20}{\rm cm^{-2}}\,({\rm K\,km\,s^{-1}})^{-1}}$$

1.4.1 Theoretical and Empirical Considerations

Under a set of assumptions on the emitting gas, we can make first-order estimates to relate the emitted CO emission to the underlying mass of the cloud. Following Bolatto et al. (2013), we can list the subsequent assumptions:

(i) The molecular cloud is virialized. This means that the potential energy is equal to twice the internal kinetic energy. For such a cloud, its (virial) mass, $M_{\rm vir}$, can be estimated following Solomon et al. (1987):

$$M_{\rm vir} = \frac{3(5-2k)}{G(3-k)} R \times \sigma^2, \tag{1.5}$$

with the projected radius R (in parsec), the 1D velocity dispersion along the line of sight σ (in $\mathrm{km\,s^{-1}}$), the gravitational constant G and the power-law index for a spherical volume density distribution of the cloud mass, $\rho(r) \propto r^{-k}$. Generally, for a first-order approximation, $k = 1$ is used.

(ii) The mass of the molecular cloud is dominated by H_2. In this case, following the first assumption, the Virial mass, $M_{\rm vir}$, is a good approximation of the total molecular gas mass.

(iii) The cloud follows a size-velocity dispersion relation. A relation between the molecular cloud's line width (which is linked to the velocity dispersion σ) and size has been empirically established in past studies (Larson, 1981; Heyer et al., 2009):

$$\sigma = C \times \sqrt{R}. \tag{1.6}$$

The coefficient has been calibrated to $C \approx 0.7\,\mathrm{km\,s^{-1}\,pc^{-0.5}}$ (Solomon et al., 1987; Roman-Duval et al., 2010). This relation likely holds under normal molecular gas conditions and is derived from equilibrium supersonic turbulence conditions occurring within a highly compressible medium (McKee and Ostriker, 2007). The general application is further supported by observations in extragalactic sources, where a similar size-line width relation has been established (e.g., Rubio et al., 1993; Bolatto et al., 2008).

(iv) The condition of the molecular cloud have approximately a constant temperature.

For a molecular cloud, the emitted CO luminosity will be related to its projected area onto the plane of the sky (πR^2) and the integrated intensity ($T_{\rm B}\sqrt{2\pi}\sigma$, assuming a Gaussian profile; for further details about surface temperature T_B, see Section 2.1):

$$L_{\rm CO} = \sqrt{2\pi^3} T_{\rm B} \times \sigma \times R^2 \tag{1.7}$$

Combining Equation 1.5, Equation 1.6, and Equation 1.7, solving for $M_{\rm vir}$ by substituting σ and R, and assuming $k = 1$ yields:

$$M_{\rm vir} \approx M_{\rm mol} \propto \left(C^{1.5} \frac{L_{\rm CO}}{T_{\rm B}} \right)^{4/5} \tag{1.8}$$

For molecular clouds that follow our assumptions, we can relate the mean mass surface density to C via $\Sigma_{\rm mol} = M_{\rm mol}/(\pi R^2) \propto C^2$ (Bolatto et al., 2013). So in conclusion, we can derive the following relation for the CO-to-H_2 conversion factor:

$$\alpha_{\rm CO} \equiv \frac{M_{\rm mol}}{L_{\rm CO}} \propto L_{\rm CO}^{-0.2} \times T_{\rm B}^{-0.8} \times \Sigma_{\rm mol}^{0.6} \tag{1.9}$$

From this simple theoretical derivation alone, we see that the conversion factor is expected to vary as a function of the local ISM environment. Indeed, previous theoretical and empirical studies confirm and support that the CO-to-H_2 conversion factor depends on the particular molecular cloud properties, including temperature, density, gas turbulence, and metallicity (e.g. Wolfire et al., 2010; Shetty et al., 2011; Gong et al., 2020). As a consequence, $X_{\rm CO}$ will vary within and across different types of galaxies. For example, looking at Equation 1.9, observations have showed that $\Sigma_{\rm mol}$ varies within the Galactic center (Oka et al., 2001) or within more extreme environments in starburst galaxies (Rosolowsky and Blitz, 2005). This agrees well with the fact that also a larger variation of $X_{\rm CO}$ has been found in these environments (e.g., Papadopoulos et al., 2012; Sandstrom et al., 2013).

There are three distinct galaxy environments where large deviations from the canonical Milky Way $X_{\rm CO}$ conversion factor have been previously found:

- **Galactic Centers:**
  Studying a larger sample of nearby spiral galaxies, Sandstrom et al. (2013) found a clear depression of $X_{\rm CO}$ toward certain galaxy centers. The conversion factor is 5–10 times lower than the disk's average value. A number of physical drivers could be responsible for lower $X_{\rm CO}$ values including (i) more turbulent, (ii) hotter, or (iii) more diffuse gas (e.g., Oka et al., 1998; Liszt et al., 2010). The CO emissivity will increase for a fixed molecular gas mass in these scenarios. Furthermore, more emission could stem from a more optically thin diffuse phase, which increases the overall observed CO brightness.

- **Starburst and (Ultra) Luminous Infrared Galaxies:**
  Starburst and (ultra) luminous infrared galaxies (ULIRGs) show significantly lower $X_{\rm CO}$ values than regular spiral galaxies (Downes and Solomon, 1998; Papadopoulos et al., 2012). In these systems, the assumption that the velocity dispersion accurately reflects the underlying mass of the cloud due to self-gravity is no longer accurate. So an increase of the line width in excess of self-gravity can explain the observed lower $X_{\rm CO}$ values. Other processes, such as the feedback from star formation or merging of systems, will enhance the gas temperature and also increase the velocity dispersion of the gas (Narayanan et al., 2011).

- **Low Metallicity Systems:**
  High $X_{\rm CO}$ values are found in dwarf systems (Schruba et al., 2012). These systems show very low metallicities ($Z < 0.5 Z_{\odot}$). Due to a lower presence of heavier elements, the dust-to-gas ratio will decrease. Due to lower dust attenuation, CO will be shielded less well. The decreased CO abundance will also make self-shielding less effective. In contrast to CO, molecular hydrogen is less affected due to more effective self-shielding. The actual region inside the molecular cloud where CO is found will shrink toward the center. Hence the CO emission will decrease. Because still significant amounts of H_2 are present, but the CO gas becomes fainter, $X_{\rm CO}$ has to increase to compensate for this effect.

1.4.2 Calibration Techniques for the CO-to-H_2 Factor

Different techniques exist to independently measure the molecular gas mass in order to calibrate the precise value of the $X_{\rm CO}$. The following paragraphs provide a broad overview of different approaches and discuss

their individual strengths and potential limitations.

1. **Virial Technique:**
   Assuming that the molecular clouds are virialized, their mass can be determined from the gas velocity dispersion. Assuming the CO is well mixed with the H_2, its line width can be used to estimate the gas velocity dispersion. Empirical studies have established a relation between the CO luminosity L_{CO} and the Virial mass, M_{Vir}. Studying GMCs in the Milky Way Solomon et al. (1987) find a tight relation of $M_{vir} = 37.9 \times L_{CO}^{0.82}$. This is close to the theoretical dependence on L_{CO} (see Equation 1.9). The Virial method has, however, two major limitations. First, it requires resolved GMC observations to obtain their individual properties. In particular, in extragalactic studies, this is very challenging since several GMCs get convolved within our beam due to the limited resolution. Secondly, using CO to trace the Virial mass requires that it accurately samples the full cloud. In low-metallicity regions, CO might not be abundant enough and only be present toward the center of the cloud. Consequently, its velocity dispersion does not accurately sample the full extent of the GMC.

2. **Column Density Estimation with Dust Emission:**
   Reprocessed dust emission in the far-infrared is another commonly used tracer of the molecular gas distribution in the ISM (e.g., Dame et al., 2001; Sandstrom et al., 2013). Since this technique is independent of the CO emission, it is less sensitive to the fundamental assumption that CO traces the full molecular gas extent. Using the so-called dust-to-gas ratio (DGR), one can convert the observed dust mass surface density (Σ_{dust}) to a total gas mass surface density (Σ_{gas}):

   $$\frac{\Sigma_{dust}}{DGR} = \Sigma_{gas} \equiv \Sigma_{HI} + \Sigma_{mol} \tag{1.10}$$

   So by including also 21cm HI observations, it is possible to obtain molecular gas mass estimates since we can disentangle the two components of Σ_{gas}. But this technique requires a robust constraint on the DGR, since this parameter can depend on the ISM's specific atomic or molecular phase. Observations of dust emission in the Galactic plane using the *Planck* telescope find, however, no clear radial dependence or variation of DGR (Planck Collaboration et al., 2011b).

   In fact, since the total gas mass is traced by dust with little bias, dust-based measurements constitute likely the most direct way to estimate the CO-to-H_2 conversion factors. The only limitations of this method remain the potential existence of a gas phase not well traced by dust emission or significant variations in the DGR with specific environments. Studies have shown that the DGR is correlated with metallicity (Draine et al., 2007; Muñoz-Mateos et al., 2009a; Chiang et al., 2021), giving us another lever to constrain this parameter and hence obtain more robust conversion factor estimates.

3. **Gamma-Ray Observations:**
   Collisions of energetic cosmic rays with interstellar nucleons are a relevant process in the ISM that gives rise to γ-radiation. By measuring the strength of the resulting γ-radiation, we can deduce the amount of nucleons present. This makes it possible to assess the amount of molecular gas (Lebrun et al., 1983; Strong and Mattox, 1996; Abdo et al., 2010). However, this technique is challenging and has only been successfully performed in Galactic clouds or the Magellanic Clouds since the resolution ofγ-ray observations are coarse and sensitive measurements are required. Hence, this technique is not used in extragalactic studies so far. Furthermore, recent observations suggest that better knowledge of the underlying cosmic ray distribution is required to adequately evaluate the γ-ray emission. For instance, Murphy et al. (2012) find that the γ-ray emission does not peak where

most gas is expected to be distributed. In this case, cosmic-ray injection by other sources might seriously hamper the robustness of this technique.

4. **Column Density Estimation with Optically Thin Emission Lines:**
Optically thin molecular lines are commonly used as tracer of the total H_2 column as well (Israel, 2009a; Israel, 2009b; Cormier et al., 2018). In particular, emission from the CO isotopologue ^{13}CO is favorable since it is relatively bright and remains optically thin across the galaxy (except for the high-density cores of GMCs; McKee and Ostriker 2007). The column density is then related to the integrated intensity of the line, $I(^{13}\mathrm{CO})$, following (Jiménez-Donaire et al., 2017b):

$$N(^{13}\mathrm{CO}) = \frac{3 \times 10^{14}}{1 - \exp\left(-5.29/T_{\mathrm{exp}}\right)} \frac{\tau_{13}}{1 - \exp\left(-\tau_{13}\right)} I(^{13}\mathrm{CO}) \tag{1.11}$$

The optical depth correction term, $\tau_{13}/(1 - \exp(-\tau_{13}))$ will be approximately equal to 1 for optically thin emission (i.e. $\tau_{13} \ll 1$), making the column density directly linear to the integrated intensity (for a constant excitation temperature T_{exc}). The ^{13}CO conversion factor can be converted to a corresponding H_2 column density by applying canonical CO isotopic ratios. In principle, this technique does also work identically for other CO isotopologues, such as C^{18}O. However, their emission is generally fainter in the ISM than ^{13}CO (due to lower abundances of these isotopologue species), thus requiring higher sensitivity observations to reach similar S/N.

As a limitation, however, past studies find that ^{13}CO-based molecular mass estimates seem to systematically underestimate total H_2 column densities by a factor of 2-3 (Meier et al., 2008; Cormier et al., 2018). Several suggestions have been put forward to explain this discrepancy. For instance, optically thick ^{13}CO could be mixed within the observed line of sight. Such ^{13}CO emission at a higher optical depth has been observed in the Milky Way on small scales (e.g. Jakob et al., 2007). An alternative explanation is the fact that ^{12}CO and ^{13}CO likely do not trace gas under the same conditions. Since ^{12}CO is optically thick, the critical density of the line will be reduced due to line trapping. Hence ^{12}CO will also trace the low-density gas, as opposed to ^{13}CO emission, which is weaker because it is sub-thermally excited and traces the more dense gas (Goldsmith et al., 2008; Leroy et al., 2017). Hence, ^{13}CO could underestimate the total molecular mass.

1.5 Empirical Star Formation Scaling Relations

When studying star formation, we are not just interested in the origin of stars and planetary systems, but we also attempt to understand its connection to galaxy formation and evolution. Understanding the various processes that regulate star formation is currently an active field of research in astronomy. It remains challenging to reconcile the numerous processes that act on different relevant scales (from ISM dynamics on large galactic scales to turbulence and cloud fragmentation on small sub-pc scales). So far, several correlations between star formation and (molecular) gas content and its physical conditions have been established. In particular, the strong connection between the star formation rate (SFR) and the molecular gas content makes molecular ISM studies crucial for understanding the onset of star formation across galaxies.

1.5.1 The Kennicutt-Schmidt Law

An empirical connection between the gas amount and the rate of star formation has first been suggested by Schmidt (1959) after studying the distribution of atomic gas and different stellar populations in the solar neighborhood. Expanding upon this work, Kennicutt (1989) and Kennicutt (1998) investigated global SFR and gas mass for a larger sample of nearby spiral and starbursts galaxies. This study lays the foundation for the so-called Kennicutt-Schmidt (KS) law, which directly relates the molecular gas surface density, $\Sigma_{\rm gas} \equiv \Sigma_{\rm HI} + \Sigma_{\rm mol}$ (mass per area), and the SFR surface density, $\Sigma_{\rm SFR}$ (mass per year per area) in the form:

$$\Sigma_{\rm SFR} \propto \left(\Sigma_{\rm gas}\right)^{N} \tag{1.12}$$

To measure both surface densities, Kennicutt (1998) used HI and CO observations in combination to trace the total gas surface density, $\Sigma_{\rm gas}$, and extinction-corrected Hα to estimate the SFR surface density $\Sigma_{\rm SFR}$. The resulting power law index measured $N = 1.4 \pm 0.2$. Figure 1.7 illustrates the global surface densities derived by Kennicutt (1998) for a set of ~100 nearby sources. It indicates the close correlation between the two parameters. Even more interestingly, the KS relation presented in Figure 1.7 also shows data points that are systematically offset above or below the main $N = 1.4$ relation. For instance, metal-poor galaxies, indicated by the open circles, deviate from the main line toward higher SFR values or lower gas surface densities. In addition, observations by Wyder et al. (2009) of low surface brightness galaxies also show a break. These sources lie systematically below the main trend (indicated by cross symbols in Figure 1.7). Such systematic offsets could reflect physical changes in the star formation law itself. Or it indicates that the particular method of determining the SFR and gas surface densities is not well calibrated for all types of sources or environments. To construct accurate star formation models, it is important to understand which of the two explanations is more likely: actual physical reasons or issues related to the methodology of measuring the individual quantities themselves.

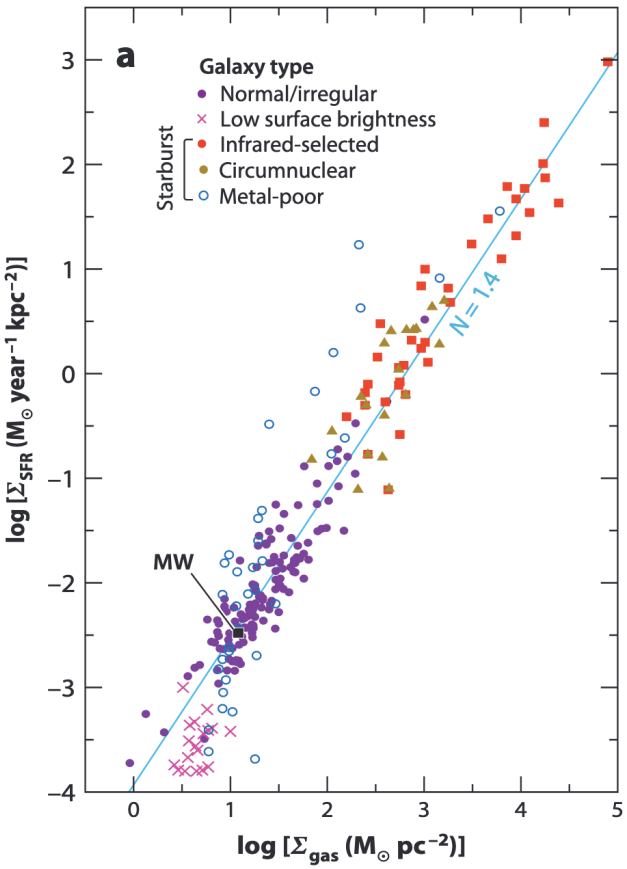

Figure 1.7: **The Kennicutt Schmid (KS) law.** A close relation between the total gas mass surface density on the x-axis and the SFR surface density on the y-axis is apparent. Credit: Figure taken from Kennicutt and Evans (2012)

Since both the gas mass and SFR surface densities are not measured directly, they will depend on the specific choice of model to convert the observed CO emission to a gas mass or the Hα emission to an SFR

measurement. Kennicutt (1998) uses a constant X_{CO} when determining the gas mass surface densities. However, as described in Subsection 1.4.1, the conversion factor will vary with the ISM environment. For example, X_{CO} is expected to be higher in low-metallicity systems. Using an updated X_{CO} would hence lead to higher gas mass surface densities. Similarly, starburst and galactic centers, where high SFRs are detected, tend to have lower X_{CO}, thus leading to lower gas mass surface densities. By correcting for X_{CO} variation, the slope actually shifts from $N_{\mathrm{fix,\,X_{CO}}} = 1.4$ to a steeper $N_{\mathrm{free,\,X_{CO}}} = 1.7 - 1.8$ (Narayanan et al., 2012). Similarly, also the SFR measurements are subject to serious differences depending on the particular prescription used. Especially at high-resolution observations, substantial variation in the estimated SFR can occur due to an incomplete sampling of the stellar IMF and a non-continuous star formation across different lines of sight (Kennicutt, 1998).

To summarize, the KS law captures that gas acts as input for star formation. The evidence that the SFR and gas mass surface densities do not correlate linearly implies that the star-forming efficiency in the ISM varies. So far, we have established the relation using mass and SFR *surface* densities since they reflect more closely the measurements we obtain from observations when we look at integrated emission along a line of sight. More fundamentally, an even closer relationship can be expected for the *volume* densities of star formation and gas mass. Connecting surface density measurements to volume densities is challenging, as it requires knowledge about the distribution of the material along the line of sight. For galaxies, for instance, by assuming certain scale heights of the disk, we could translate surface to volume densities. Alternatively, non-LTE modeling of CO emission can be used to constrain the necessary volume density of the gas to reproduce the observed emission. Another challenge for correctly interpreting the KS relation is that based on the particular selection of SFR tracer, different timescales can play a role. CO traces the current molecular gas amount. In contrast, Hα is related to the sum of stars that have formed within the last ~5 Myr. At coarse (~kpc) scales, the telescope beam will still encompass several clouds at several evolutionary stages, mitigating the discrepancies. At higher resolution, however, the scaling relations can break since we observe the gas and SFR at different evolutionary stages (Kruijssen and Longmore, 2014). In the context of this thesis, we mainly deal with kpc-scale observations. However, the issue of time-scale-dependent variation has to be kept in mind when we push toward higher GMC-scale resolutions.

1.5.2 Correlation of SFR with Molecular Gas

We can now study resolved SFR and gas mass across nearby galaxies with advances in telescope and instrumentation design since the beginning of the 21$^{\mathrm{th}}$ century. While studies before were limited to only global SFR and gas mass values, it was now possible to investigate lines of sight with different fractions of gas components or varying SFR all within a single galaxy. Several large-scale studies investigated resolved gas mass and SFR surface densities across nearby galaxies (e.g., Schuster et al., 2007; Leroy et al., 2008; Gratier et al., 2010; Schruba et al., 2011; de los Reyes and Kennicutt, 2019; Kennicutt and De Los Reyes, 2021). A wide variety of KS indices, N, was found, ranging from 1.4 up to 3.1. Such a large variation challenges the notion of a global star formation law that is valid across all galaxies.

To better understand the cause and extent of the measured power-law indices variation, the focus shifted on differentiating Σ_{gas} into its components of atomic gas, $\Sigma_{\mathrm{H\,I}}$, and molecular gas, Σ_{mol}. Initially, the results were inconclusive on whether $\Sigma_{\mathrm{H\,I}}$ or Σ_{mol}, in fact, show a tighter correlation with the SFR surface density. For instance, early results initially suggested a stronger correlation of the SFR surface density with the molecular gas surface density (e.g. Wong and Blitz, 2002; Komugi et al., 2005; Kennicutt et al., 2007). In contrast, other studies found only weak correlations with the molecular gas surface density (e.g., Crosthwaite and Turner, 2007; Schuster et al., 2007).

In essence, the use of different molecular gas and SFR prescriptions made a cross-sample comparison

difficult. To overcome these challenges, a series of studies (Leroy et al., 2008; Bigiel et al., 2008; Bigiel et al., 2010; Schruba et al., 2011) combined ^{12}CO observations from HERACLES (Heterodyne Receiver Array CO Line Extragalactic Survey, Leroy et al., 2009), HI data from THINGS (The HI Nearby Galaxy Survey, Walter et al., 2008), and IR images from SINGS (Spitzer Infrared Nearby Galaxies Survey, Kennicutt et al., 2003) for a sample of seven nearby massive star-forming galaxies. Their main result can be distinguished into two regimes: (i) at low-densities (HI dominated), the gas mass is uncorrelated with the SFR and (ii) in the higher-density regime (H_2 dominated), the SFR is tightly correlated with gas density following a constant star formation efficiency (SFE $\equiv \Sigma_{\rm SFR}/\Sigma_{\rm H_2}$). Since then, the tight correlation between molecular gas and SFR has further been verified by numerous studies (e.g. Verley et al., 2010; Azeez et al., 2016; Kennicutt and De Los Reyes, 2021) and is supported by theoretical work (e.g. Krumholz et al., 2012; Hu et al., 2021; Whitworth et al., 2022).

Still, uncertainties connected to the molecular gas mass estimation methodology remain a major challenge for studies investigating the KS relation in extragalactic sources. For example, many studies rely on observations of higher J CO transitions, which first need to be down-converted to $J = 1 \rightarrow 0$ rotational transition (e.g., Tacconi et al., 2008; Genzel et al., 2012; Jiang et al., 2015; Bicalho et al., 2019; Pessa et al., 2021) before applying the $X_{\rm CO}$ conversion factor. This introduces another uncertainty factor: the CO line ratio. For future ISM studies, it is essential to constrain changes in CO line ratio and $X_{\rm CO}$ within and across galaxies to properly evaluate the variation of the derived scaling relations and implications for star formation in the ISM.

1.6 Radiative Transfer and Molecular Line Emission

In astronomy, we observe electromagnetic radiation propagating through various media in space. We describe the radiation in terms of brightness per unit frequency, which constitutes the so-called *specific intensity* (also spectral intensity or spectral brightness), which we denote by I_ν. It is defined in terms of flow of energy per unit time, $\mathrm{d}P$, per infinitesimal surface area, $\mathrm{d}A$, that the radiation crosses, the angle θ between the incoming ray of radiation and the plane of the surface, the frequency band width, $\mathrm{d}\nu$, and an infinitesimal solid angle, $\mathrm{d}\Omega$, as measured from an observer:

$$I_\nu = \frac{\mathrm{d}P}{(\cos\theta \mathrm{d}A)\mathrm{d}\nu\mathrm{d}\Omega} \quad \left[\mathrm{W\,m^{-2}\,sr^{-1}\,Hz^{-1}}\right] \tag{1.13}$$

Absorption, emission, and scattering processes all affect the resulting radiation we will measure on Earth. *Radiative transfer equations* provide the mathematical framework to describe the interactions of the radiation with the material it permeates. We assess the propagation of the radiation by describing the infinitesimal change in the specific intensity, $\mathrm{d}I_\nu$, along an infinitesimal propagation path, $\mathrm{d}s$. For light propagating through empty space, the intensity will not change[3]:

$$\frac{\mathrm{d}I_\nu}{\mathrm{d}s} = 0 \tag{1.14}$$

If the radiation propagates through matter, we have to account for two processes. On the one hand, the radiation can be increased by emission that arises within the medium. This can be treated mathematically with the introduction of the so-called *emission coefficient*, j_ν. On the other hand, the specific intensity can

[3] This might be counterintuitive, but we note that the specific intensity I_ν describes brightness per solid angle, so it constitutes a surface brightness. At a higher distance, the source's intensity falls with the square, but the apparent angular size also decreases with the square. Consequently, the surface density stays constant.

decrease due to scattering and absorption by matter along the line of sight. The amount of decrease has to be proportional to the specific intensity itself. This can be described by the absorption coefficient α_ν. Combining these terms of absorption and emission, we can lay the foundation for the understanding of the interaction between radiation and matter with the following equation:

$$\frac{\mathrm{d}I_\nu}{\mathrm{d}s} = j_\nu - \alpha_\nu I_\nu \tag{1.15}$$

The absorption potential of a medium can also be described using the optical depth. In the case of only absorption (i.e. $j_\nu = 0$), the radiative transfer equation can be solved via integration and yields:

$$\frac{\mathrm{d}I_\nu}{\mathrm{d}s} = -\alpha_\nu I_\nu \quad \Rightarrow \quad I_\nu(s) = I_\nu(0) \times \exp\left(-\int_s \alpha_\nu(s)\mathrm{d}s\right) \tag{1.16}$$

The term inside the exponential is denoted as the optical depth $\tau_\nu \equiv \int_s \alpha_\nu(s)\mathrm{d}s$. We distinguish between two limiting cases:

1. **Optically Thin Case ($\tau_\nu \ll 1$):** transparent, the electromagnetic radiation does not decrease significantly.
2. **Optically Thick Case ($\tau_\nu \gg 1$):** opaque, the light of a background source gets extinguishes.

In the case of local thermodynamic equilibrium, the ratio of the absorption and emission coefficients is independent of the material. It only depends on the temperature following Kirchhoff's law $S_\nu(T) = j_\nu/\alpha_\nu \equiv B_\nu(T)$ (where $B_\nu(T)$ describes the Planck radiation function). This term is denoted as the *source function*. If we can describe the source function along the full path of the ray, we can find the following solution to the radiative transfer equation

$$I_\nu(s) = I_\nu(0)e^{-\tau_\nu(s)} + \int_0^{\tau_\nu(s)} S_\nu(T(\tau))e^{-(\tau_\nu(s)-\tau)}\mathrm{d}\tau \tag{1.17}$$

This expression provides the general solution to the radiative transfer equation. Again, the first term on the right side of the equation expresses the attenuation of the background radiation by a factor $e^{-\tau_\nu}$, and the second term indicates the added emission $S_\nu \mathrm{d}\tau$, which via effective absorption along the path itself gets attenuated by a factor $e^{-(\tau_\nu-\tau)}$. For an isothermal medium, where $T(s) = T = \text{const.}$, the integral can be solved explicitly. If we express the source function in terms of the $B_\nu(T)$, we find

$$I_\nu(s) = I_\nu(0)e^{-\tau_\nu(s)} + B_\nu(T)\left(1 - e^{-\tau_\nu(s)}\right) \tag{1.18}$$

So in the case of a high optical depth ($\tau_\nu \gg 1$), the radiation field will be described by the Planck function: $I_\nu = B_\nu(T)$.

1.6.1 Line Emission

This thesis project aims at the observation and interpretation of molecular line emission. Line emission is the result of an energy transition from an upper energy level, E_u, to a lower energy level, E_l. The excitation temperature, T_{exc}, describes the ratio of the level population density via the Boltzmann equation:

$$\frac{n_u}{n_l} = \frac{g_u}{g_l} e^{-(E_u-E_l)/(k_\mathrm{B}T_{\mathrm{exc}})} \tag{1.19}$$

where g_u and g_l describe the level degeneracies. In the context of rotational transitions, the excitation temperature is commonly also referred to as *rotational temperature*. The Einstein coefficients (Einstein, 1916) are a useful way of describing the emission and absorption capacities of atoms or simple molecules. The emission of a photon will lead to a depopulation of the energy levels. The main pathway of emission are either spontaneous emission (described by the Einstein coefficient A_{ul}), stimulated emission due to an external radiation field (the rate is described by the Einstein coefficient B_{ul} and is also linear to the average external radiation field[4]) and collisional de-excitation (rate denoted by γ_{ul} and proportional to the level population and collider density n_c) with one of the more abundant colliders in the ISM (mainly e^-, H, H_2, or He). The following equation can express the rate of depopulation:

$$\left(\frac{\mathrm{d}n_u}{\mathrm{d}t}\right)_{u\to l} = -n_u(A_{ul} + B_{ul}\bar{I} + \gamma_{ul}n_c) \tag{1.20}$$

Similarly, the upper-level population can increase due to absorption of background photons (described with the Einstein coefficient rate B_{lu}, again proportional to the average background radiation field $\bar{I}$) and due to collisional excitation (descried by the coefficient γ_{lu}):

$$\left(\frac{\mathrm{d}n_u}{\mathrm{d}t}\right)_{l\to u} = n_l(B_{lu}\bar{I} + \gamma_{lu}n_c) \tag{1.21}$$

If the system is in equilibrium, the Einstein coefficients are related to each other according to the following set of equations:

$$A_{ul} = \frac{2h\nu^3}{c^2}B_{ul} \qquad g_lB_{lu} = g_uB_{ul} \tag{1.22}$$

For such a two-level system in thermodynamic equilibrium, the level population density is time-independent ($\mathrm{d}n/\mathrm{d}t = 0$). There is a balance between the various excitation and de-excitation processes. For the steady-state case, also the collisional and de-collisional reaction rates are related and depend on the kinetic temperature of the gas as follows:

$$\gamma_{ul} = \frac{g_l}{g_u}\gamma_{lu}e^{h\nu/(k_\mathrm{B}T)} \tag{1.23}$$

where $\nu = \Delta E_{ul}/h$ and T indicates the kinetic temperature of the gas. Combining Equation 1.20 and Equation 1.21, under the assumption of thermodynamic equilibrium, we can find an expression for the level population density ratio. In the absence of a background radiation field $\bar{I}$, the ratio is given by

$$\frac{n_u}{n_l} = \frac{g_u}{g_l}\frac{1}{1 + (A_{ul}/\gamma_{ul}n_c)}e^{-h\nu/(k_\mathrm{B}T)} \tag{1.24}$$

So the ratio of the level population would describe a Boltzmann distribution if no spontaneous emission occurs ($A_{ul} = 0$). However, since some species will, in fact, de-excite due to spontaneous emission, the upper-level population will decrease, which explains the deviation from a pure Boltzmann distribution.

The Einstein coefficients are also useful in the context of the radiative transfer equations (Equation 1.15). The number of spontaneous transitions per unit volume per unit time is given by n_uA_{ul}. The transitions then emit a total energy given by $h\nu n_uA_{ul}$. So we can describe the emission coefficient j_ν as follows (Mangum

[4] $\bar{I} \equiv 1/4\pi \int I_\nu\phi(\nu)\mathrm{d}\nu\mathrm{d}\Omega$ for a given line profile described by a profile function $\int \phi(\nu)\mathrm{d}\nu = 1$

and Shirley, 2015):

$$j_\nu = \frac{1}{4\pi} h\nu A_{ul} \phi(\Delta\nu) \tag{1.25}$$

where $\phi(\Delta\nu)$ describes the line profile and the 4π term comes from the fact that the energy is emitted per unit solid angle. Similarly, assuming local thermal equilibrium (LTE), we can describe the attenuation as follows:

$$\alpha_\nu = \frac{1}{4\pi} h\nu \left(n_l B_{lu} - n_u B_{ul}\right) \phi(\Delta\nu) \tag{1.26}$$

Using this expression for the attenuation coefficient, we can also describe the optical depth, τ, in terms of the Einstein coefficients and the level population densities:

$$\tau_\nu = \int \alpha_\nu \mathrm{d}s = \frac{1}{4\pi} h\nu \int (n_l\, B_{lu} - n_u B_{ul}) \phi(\Delta\nu) \mathrm{d}s \tag{1.27}$$

This means that the optical depth depends on the ratio of the level populations. Using Equation 1.19 and the relation between the Einstein coefficients in Equation 1.22, we can simplify Equation 1.27 further and obtain:

$$\tau_\nu = \frac{1}{4\pi} h\nu B_{ul} \left(e^{h\nu/(k_\mathrm{B}T)} - 1\right) \phi(\Delta\nu) \underbrace{\int n_u \mathrm{d}s}_{\equiv N_u} \tag{1.28}$$

where the last term defines the column density $N_u \equiv \int n_u \mathrm{d}s$, which indicates the density of material along the line of sight. From an observational standpoint, the expression above provides a way of determining the column density by measuring the frequency integrated line intensity, W:

$$N_u \propto \left(\frac{\tau_\nu}{1 - e^{-\tau_\nu}}\right) \times W \tag{1.29}$$

In Subsection 2.1.5, this formula will be discussed in further detail in the context of the brightness temperature, which is commonly used in radio astronomy to express the specific brightness.

^{12}CO emission line

The rotational transition of ^{12}CO is one of the key molecular emission lines studied in this thesis. For a rotational transition $J \longrightarrow J-1$, the Einstein coefficient is given by the following expression (Draine, 2011):

$$A_{J\to J-1} = 1.07 \times 10^{-7} \frac{J^4}{J + \frac{1}{2}} \left[\mathrm{s}^{-1}\right] \tag{1.30}$$

The $J = 1 \longrightarrow 0$ line has a frequency of ~115 GHz and the Einstein coefficient is $A_{10} = 7.16 \times 10^{-8}\,\mathrm{s}^{-1}$. For a common molecular cloud, we can derive an approximation of the optical depth. A detailed derivation can be found in (Draine, 2011).

$$\tau \approx 50 \left[\frac{n(\mathrm{CO})/n_\mathrm{H}}{7 \times 10^{-5}}\right] \left[\frac{2\,\mathrm{km\,s}^{-1}}{\sigma_v}\right] \tag{1.31}$$

where σ_v indicates the velocity dispersion. In molecular clouds, this expression generally yields, $\tau \gg 1$, meaning the CO is predominantly optically thick. Only for highly turbulent (high σ_v) or very diffuse gas (low $n(\mathrm{CO})$) will the optical depth drop to lower opacities.

1.6.2 Critical Density and LTE-Conditions

Equation 1.29 yields an expression to measure the upper-level population of any atomic or molecular species by observing the line emission. In general, however, we are more interested in obtaining information about the total number density of a species, including all the level populations. Under a set of certain assumptions, it is possible to derive estimates about the total level population density based on the observation of a single emission line. For example, if the system is in LTE, a simple relation exists between individual level populations. However, assuming that the system is in LTE is not always justified, which means other ways have to be found to describe the total level populations (so-called non-LTE case).

In case a system follows LTE conditions, which means the thermodynamical properties have thermodynamic equilibrium values set to the local temperature and pressure of the gas, the level populations are related according to the following equation:

$$\frac{N_u}{N_{\mathrm{tot}}} = \frac{g_u}{Z} e^{-E_u/(k_{\mathrm{B}} T_{\mathrm{exc}})} \tag{1.32}$$

where Z describes the partition function for a given species. LTE generally applies when the collisional transition rates of any given transition line dominate over radiative transitions. This occurs when the gas density exceeds a certain threshold, the so-called *critical density* n_{crit}. For a two-level system, following Equation 1.24, the critical density is defined as the ratio of the radiative and collisional transition (see also Shirley 2015):

$$n_{\mathrm{crit}} \equiv \bar{\beta} \frac{A_{ul}}{\gamma_{ul}} \tag{1.33}$$

where $\bar{\beta}$ describes the directional averaged photon escape fraction (for an optically thin medium $\bar{\beta} = 1$)[5]. In case the density of a level population exceeds the critical density, the upper state's depopulation is mainly due to collisional de-excitation. The excitation temperature will be driven toward the kinetic temperature of the gas. We say that the emission is *thermalized* and it will be observable. If the density is significantly below the critical density, the upper level will not be highly populated. The excitation temperature will be driven toward the background radiation temperature. As a consequence, the emission line will be significantly weaker. Generally, due to line trapping, the decay rate of radiative emission is lowered, decreasing the critical density. This effect is captured by the escape fraction coefficient $\bar{\beta}$. LTE conditions generally only apply to homogeneous regions. For unresolved observations, the beam encompasses a range of densities and temperatures. Hence, LTE conditions are unlikely to hold, and any of the calculations we performed before in this chapter under LTE assumption will only yield crude approximations.

1.6.3 Modelling non-LTE Conditions

In case the medium is not thermalized, we cannot describe the level populations relative to the total population density with a single temperature. In this case, the density cannot be estimated using Equation 1.32. The different level population ratios each follow the Boltzmann equation with a different excitation temperature. However, it is possible to obtain estimates of gas temperature and density based on observed emission by locally solving the radiative transfer equations. Nevertheless, such calculations remain challenging since the radiative transfer equations describe a non-linear and nonlocally coupled set of relations. Various tools exist that help to solve this set of equations. For example, `RADEX` (van der Tak et al., 2007) is a commonly used

[5] Often, the critical density is defined explicitly with $\bar{\beta} = 1$, while introducing the escape fraction yields the *effective* critical density (see discussion by Shirley 2015).

non-LTE radiative transfer code. The code solves for a converged solution of the excitation and radiation field under the assumption of a homogeneous medium. The escape probability calculation, relevant to constrain $\bar{\beta}$, follows the formalism described by Sobolev (1960). The final solution is approximated iteratively: The code starts with level populations derived under LTE conditions. Then it computes the resulting escape fraction and optical depth. From these estimates, the energy level populations are updated, and the calculation steps are repeated until convergence is reached. In Chapter 7, we describe and apply the novel `Densegastoolbox` (DGT; Puschnig et al., 2020), which builds on `RADEX`, but can account for gas with a distribution of densities. Accounting for a distribution of densities is relevant for kpc-scale observations, where the beam will include a mix of gas at different phases.

1.7 Outline of Thesis and Science Questions

The previous sections introduce the general scientific background on the objectives and questions addressed in this thesis. Broadly speaking, the thesis can be split into a technical analysis and three parts, focusing on different scientific aspects. The scientific aspects are all connected by the use of millimeter CO and isotopologue observations to characterize the chemical and physical conditions of the molecular gas in nearby spiral galaxies on ~kpc scales.

Technical Part: Telescope Flux Calibration and the Error Beam
Chapter 2 provides the necessary background information on the particular telescopes and instruments we rely on for this thesis. Due to systematic uncertainties associated with the instruments' design, it is challenging to adequately interpret the resulting data. For example, studying the observing stability using line calibrators, Jiménez-Donaire et al. (2019) found a flux calibration uncertainty of ~10% for the IRAM 30m telescope and EMIR instrument. Leroy et al. (2009) found an even higher calibration uncertainty of ~20% for the IRAM 30m telescope using the HERA receiver instrument. In Chapter 3 we describe the analysis of IRAM 30m telescope performance. We use pointing observations in selected regions in the nearby massive star-forming galaxy M51 and assess the scan-by-scan stability of the instrument. Furthermore, we present methods to estimate the contribution from the telescope's error beams, which can seriously affect the measured intensities. This analysis is rarely done in the literature, but is essential to properly interpret observe line emission.

Science Part 1: CO excitation and the CO Line Ratio

Science Questions (Part 1):

- How does the ^{12}CO(2−1)/(2−1) ≡ R_{21} line ratio vary across and within a sample of nearby spiral galaxies?
- In what way can we parameterize changes in R_{21}?
- How does R_{21} variation affect molecular gas mass scaling relations assuming a constant ratio?

CO has become the workhorse tracer of the bulk cold molecular gas in the ISM (see Section 1.4). Regularly, the ^{12}CO transition is targeted in galactic surveys since it can be observed more efficiently and at a higher resolution than the $J = 1 \rightarrow 0$ transition using the same telescopes. However, the observed ^{12}CO(2-1) intensity first needs to be "down-converted" to the ^{12}CO(1-0) intensity, which is commonly done using a canonical and constant R_{21} line ratio. To assess R_{21} variation in the most systematical way possible, we use a sample of nine nearby spiral galaxies that are part of the EMPIRE survey (EMIR Multiline Probe of the ISM Regulating Galaxy Evolution, Jiménez-Donaire et al., 2019). We complement the ^{12}CO(1-0) data with ^{12}CO(2-1) observations from PHANGS-ALMA (The Physics at High Angular resolution in Nearby GalaxieS – ALMA Leroy et al., 2021b) and HERACLES (Leroy et al., 2009). Combining these datasets, Chapter 4 discusses and presents the significant variation of R_{21} we observe within and across the nine galaxies. For example, certain galaxies show a clear enhancement of R_{21} towards the center. Such variations can affect the derived molecular gas mass scaling relations when using a constant R_{21}. Furthermore, for sources where we have CO(2-1) observations from both PHANGS-ALMA and HERACLES, we find significant discrepancies in the measured intensities order 20-30%. This implies that the potential instrumentation uncertainties, such as flux calibration or error beam contribution, must be properly constrained for future CO studies.

Part 2: Resolved faint CO isotopologue emission across M51

Science Questions (Part 2):

- How does the rotational line emission of CO isotopologues vary across M51?
- To what degree does the CO isotopologue line variation trace temperature, column and volume densities and the CO-to-H_2 conversion factor in M51?

CO isotopologue line emission traces the chemical enrichment of the molecular ISM (see Subsection 1.3.1). As part of the CLAWS (Chapter 5) project, we obtained deep IRAM 30m telescope observations of M51 in the 1mm and 3mm wavelength regime were obtained. This dataset provides for the first time the opportunity to study resolved isotopic variation across the full molecular disk of a regular nearby galaxy. Already earlier studies found strong internal variation, such as a prominent arm–interarm difference in CO emission in M51 (e.g. Koda et al., 2012). Moreover, the galaxy is molecular gas-rich and interacts with a companion galaxy. This makes the galaxy a suitable candidate for such a pilot study to investigate the variation of resolved CO isotopologue emission across the galaxy. Based on the observed trends, we relate the observed line ratio variation to nucleosynthesis and changes in the optical depth (due to increased turbulence or the presence of more diffuse gas).

Part 3: Studying the CO-to-H_2 Conversion Factor Variation across M101

Science Questions (Part 3):

- How does the ^{13}CO emission vary across M101?
- To what extent is the CO-to-H_2 conversion factor variable across M101?
- How consistent are CO-to-H_2 conversion factor estimates from different techniques?
- To what extent do the molecular gas mass scaling relations differ when accounting for a variable R_{21} and CO-to-H_2 conversion factor?

We obtained 30m telescope wide-field ($10'\times10'$ field-of-view) ^{12}CO(1-0) and ^{13}CO(1-0) observations across M101. The project consists of (i) investigating the variation of CO isotopologue ratios across the galaxy and combining this with (ii) obtaining resolved α_{CO} conversion factor estimates using the scatter minimization technique (Leroy et al., 2011; Sandstrom et al., 2013). The galaxy due to its strong metallicity gradient. Metallicity is a proposed key parameter driving changes in the conversion factor. We find a significant variation of α_{CO} towards the center of the galaxy with values 10 times lower compared to disk values. This has implications for the derived scaling relations. For instance, the lower α_{CO} value toward the center results in much higher derived star-forming efficiencies. Finally, we assess that a set of three variables can be used to describe the observed variation in the conversion factor across the galaxy. The work is presented in Chapter 6.

Furthermore, Chapter 7 will provide details about open questions and future projects, focusing on non-LTE line modeling in M51 using the CLAWS dataset and pushing towards multi-CO studies at higher resolutions. Finally, Chapter 8 concludes with the main results and findings of this thesis.

CHAPTER 2

Observation, Methods and Analysis Techniques

> Nothing has such power to broaden the mind as the ability to investigate systematically all that comes under thy observation in life.
>
> M. Aurelius – 2nd century AD Roman emperor and philosopher

Overview

In astronomy, the majority of our discoveries derive from electromagnetic radiation. Other information carriers, such as meteorites, cosmic rays, or probes returned from space missions, constitute only a minor fraction. Historically, astronomers have been limited to only the narrow range of the visible (also called *optical*) part of the electromagnetic spectrum (see Figure 2.1). Still today, the optical wavelength regime is valuable for studying hot thermal sources such as stars, galaxies, or warm gas ionized by surrounding stars. However, to properly understand the full interplay of the ISM, it is indispensable to employ a multi-wavelength approach. This thesis project builds, in particular, on the observation of micrometer and radio waves, which includes wavelengths around $\lambda \approx 10 - 15\,\mathrm{m}$ down to shorter wavelengths around $\lambda = 0.3\,\mathrm{cm}$.

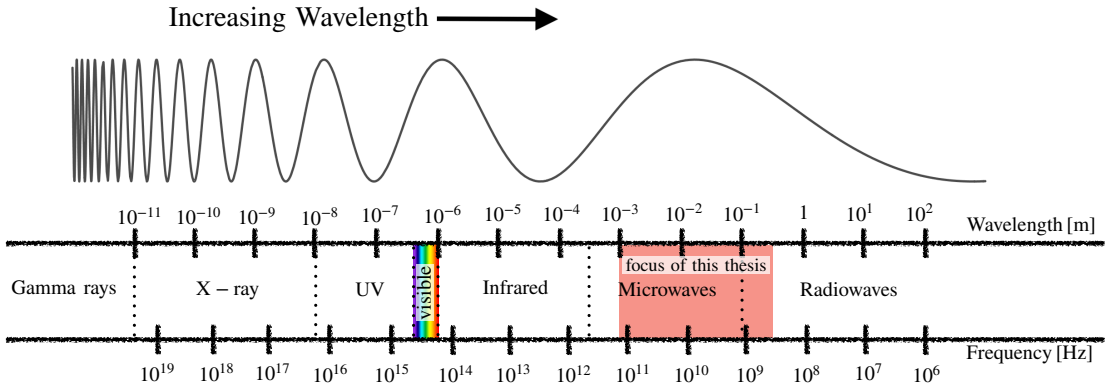

Figure 2.1: **Full Range of Electromagnetic Spectrum.** The visible range is only a small part of the full spectrum. The thesis focus are wavelengths from 1 mm to 21 cm (approximate range shaded in red).

While certain aspects of the description of electromagnetic radiation are independent of the wavelength, the techniques used to measure the diverse wavelength bands differ significantly. This chapter introduces the fundamentals of radio astronomy. I rely mainly on Wilson et al. (2013), Burke and Graham-Smith (2014) and Condon and Ransom (2016) for general references on telescope and instrument background. Furthermore, a description of the telescopes and instruments design, which is crucial for successful observations, follows. The final sections discuss the specific data analysis techniques used for this thesis.

2.1 Fundamentals of Radio Astronomy

The very beginning of radio astronomy can be traced back to the first half of the 20$^{\text{th}}$ century. In the 1930s, it became evident that extraterrestrial sources emit electromagnetic radiation in the radio wave regime after Karl Jansky used a direction-sensitive antenna array pointed at the sky (Jansky, 1933). The discovery was actually serendipitously, as they aimed to investigate static in the atmosphere that could interfere with short wave transmissions across the Atlantic. First deliberate attempts to detect radio waves from extraterrestrial origin date back earlier. In the late 19$^{\text{th}}$ century, efforts were made by various scientists to detect radio emission from the Sun (e.g., Wilsing and Scheiner, 1896; Nordmann, 1905). However, the detection proved difficult due to the technical limitations of the instruments. A real breakthrough in the scientific field occurred later, after World War II when experience gained in the development of radar systems helped develop more sensitive instruments and telescopes for astronomical purposes.

2.1.1 Flux Density and Brightness Temperature

Put simply, when observing an astronomical object, the telescope's detector measures the radiation strength as a function of direction in the sky (i.e., mapping) and frequency (i.e., spectroscopy). Other quantities, such as time-dependent variation or the light's polarization, are often considered as well.

All photons collected with a telescope contribute to the total brightness, which we describe with the specific intensity (refer to Section 1.6). The *flux density* is defined as the spectral power received by a detector with a unit projected area, i.e., integrating the specific intensity over the solid angle of the source Ω_s (and assuming that the angular size of the source is small, $\theta \ll 1$ rad, which means $\cos\theta \approx 1$):

$$f_\nu = \int_{\Omega_s} I_\nu \mathrm{d}\Omega \quad \left[\mathrm{W\,m^{-2}\,Hz^{-1}}\right] \tag{2.1}$$

The flux density has SI-units of $\mathrm{W\,m^{-2}Hz^{-1}}$. However, astronomical radio sources are usually weak and located far from us, leading to very small flux density values. It has become practical to define and work with the unit *Jansky*:

$$1\,\text{Jansky} = 1\,\text{Jy} \equiv 10^{-26}\mathrm{W\,m^{-2}Hz^{-1}} \tag{2.2}$$

Still, only a small fraction of astronomical sources are as bright as 1 Jy or above. E.g., for reference, a source of 1 Jy still only produces a signal of 10^{-15} W at a 100 m telescope, such as the Effelsberg radio telescope near Bonn. Hence, extremely sensitive instruments are necessary to detect radio emission originating from astronomical sources.

Alternatively, it is widespread in radio astronomy to describe the specific intensity in terms of a brightness temperature, T_b, given in Kelvin. On the one hand, the motivation for introducing the brightness temperature is of technical nature since radio telescopes are often calibrated by so-called absorbers of known temperatures. On the other hand, the temperature of a radio source is generally of physical interest.

Under local thermodynamic equilibrium (LTE) and assuming a large optical depth of the emitting source, the spectral intensity becomes a function of the temperature as described by the Planck function:

$$I_\nu \equiv B_\nu(T) = \frac{2h\nu^3}{c^2}\frac{1}{e^{h\nu/(k_\mathrm{B}T)} - 1} \tag{2.3}$$

We then define the *brightness temperature*, T_b, as the temperature of a hypothetical black body that radiates at I_ν:

$$T_b \equiv \frac{h\nu/k_\mathrm{B}}{\ln\left(1 + 2h\nu^3/(c^2 I_\nu)\right)} \tag{2.4}$$

In the radio regime, where we are generally dealing with small frequencies, we can approximate the Planck function in terms of the Raleigh-Jeans limit ($h\nu \ll k_\mathrm{B}T$)[1], $I_\nu = B_\nu^\mathrm{RJ}$. This is more convenient since it provides a linear relationship between the brightness temperature and the specific intensity. Consequently, the brightness temperature, which is in the RJ limit generally referred to as the antenna temperature, T_A, is defined as:

$$\boxed{T_A(\nu) = \frac{c^2}{2k_\mathrm{B}\nu^2} I_\nu} \tag{2.5}$$

The antenna temperature should not be confused with the actual physical temperature of an object. In fact, the antenna temperature is frequency-dependent. Consequently, the antenna temperatures of thermal sources is generally lower than their physical temperatures. Only for a true black body object, observed at low frequencies, would the antenna temperature match its actual physical temperature.

2.1.2 Telescope Design

A radio telescope is designed to collect and detect faint radiation coming from extraterrestrial sources. In simplest terms, the design of radio telescopes tries to optimize two criteria: observing sensitivity and angular resolution. The sensitivity of a telescope can be improved by increasing the collecting area and minimizing factors that lead to increased noise (which can be achieved by improving, for example, the quality of the receiving system). The angular resolution depends on the telescope size (or the baseline for interferometers). The most common design for singe-dish telescopes operating in the mm regime is a parabolic antenna that reflects the incoming radiation onto a focal point. There the radiation is detected using a receiver. However, a telescope will be sensitive not just to radiation from the point it is directed at. Also, radiation will enter the receiver from other directions, mainly due to irregularities on the reflecting surface or scattering from the structure holding the secondary mirror. The directional contribution of radiation is described using a frequency-dependent beam pattern function $P_\nu(\theta, \phi)$, which is normalized to its maximum peak. The angles θ and ϕ are polar coordinates,

A significant challenge of telescope design is reducing the contribution of radiation from the side and back lobes since they reduce the efficiency of the observation. The telescope beam solid angle expresses the total directional contribution of radiation by an ideal isotropic source.

[1] E.g., for a common temperature in the cold molecular ISM of 20 K, this limit would correspond to frequencies below $\nu < 400$ GHz. In this thesis, the lines we look at sit right at the edge of this limit. For instance, we have ^{12}CO (1−0) at ~115GHz and ^{12}CO (2−1) ~230GHz.

We can express it by integrating over the entire beam pattern, P_ν following:

$$\Omega_A = \int_\Omega P_\nu(\theta, \phi) \mathrm{d}\Omega \tag{2.6}$$

indicating the direction with respect to the telescope's main pointing axis (see Figure 2.2).

Similarly, the main beam solid angle, Ω_{mb}, is defined by integrating only over the main beam lobe. We can approximate the main beam lobe using a 2D Gaussian profile with a full width half maximum, θ_{FWHM}, that defines the angular resolution of the telescope. The resolution of the instrument is generally dependent on the observed frequency, ν, and size of the telescope, D: $\theta_{\mathrm{FWHM}} \propto (D \times \nu)^{-1}$. The ratio of the main beam solid angle over the full beam angle provides an estimate of the telescope's beam efficiency, i.e., the relative importance of the main beam lobe over the side lobes:

$$B_{\mathrm{eff}} = \frac{\Omega_{\mathrm{mb}}}{\Omega_A} \tag{2.7}$$

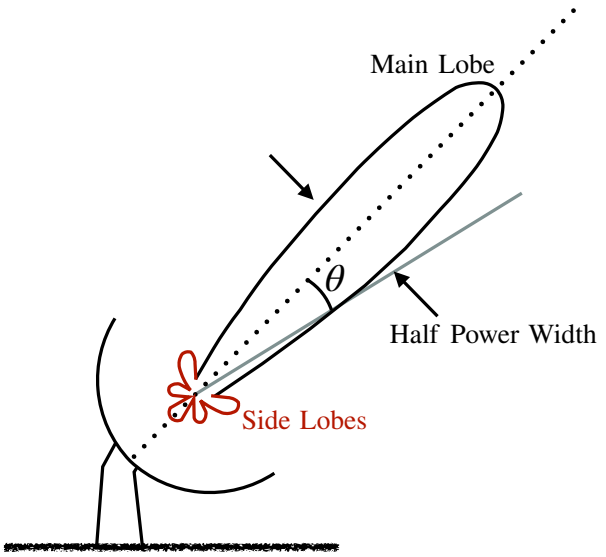

Figure 2.2: **Radio Antenna Response Pattern** Illustration of the beam pattern $P_\nu(\theta, \phi)$ indicating the main lobe and the side lobes. The parameter θ describes the angle from the telescope's pointing axis (dotted line) and ϕ the rotational direction perpendicular to the axis. Notice that the beam is symmetric with respect to ϕ.

The goal of telescope design is to maximize the main beam efficiency by minimizing the contribution of stray light entering the observations via the side lobes. The beam response $P_\nu(\theta, \phi)$ is also relevant for describing the power received by an antenna for a given spectral intensity:

$$W_\nu = \frac{1}{2} A_{\mathrm{eff}} \int_\Omega I_\nu(\theta, \phi) P_\nu(\theta, \phi) \mathrm{d}\Omega \overbrace{=}^{\text{isotropic } I_\nu} \frac{1}{2} A_{\mathrm{eff}} I_\nu \times \Omega_A \quad \left[\mathrm{W\,Hz^{-1}}\right] \tag{2.8}$$

where the factor $1/2$ accounts for the fact, that we consider the radiation to be unpolarized, and $A_{\mathrm{eff}} = \lambda^2/\Omega_A$ describes the telescopes effective collecting area. If we substitute the spectral intensity with the Raleigh Jeans approximation (Equation 2.5) we obtain a simple expression

$$W_\nu = k_{\mathrm{B}} \times T_A(\nu) \tag{2.9}$$

Therefore, the received power by the antenna is directly proportional to the antenna temperature. This expression is known by the *Nyquist approximation* (Nyquist, 1928) and is relevant for receiver design. When a resistor is placed in a thermal bath, its temperature is connected to the received power in an equivalent way. So, in other words, we can relate the antenna temperature to the temperature of a matched resistor whose thermally generated power equals that produced by the antenna. This notion links back to the concept of T_A via black body radiation, as previously introduced (see Equation 2.5).

From a scientific standpoint, we are not necessarily interested in the measured quantity T_A itself but rather in the actual emission coming from the target, denoted as the main beam temperature T_{mb}. We want

to correct for the rear-side lobe using the forward beam efficiency ($F_{\rm eff}$) and, at the same time, we only want to account for the main beam lobe using the main beam efficiency ($B_{\rm eff}$):

$$T_{\rm mb} = \frac{F_{\rm eff}}{B_{\rm eff}} \times T_A \tag{2.10}$$

For astronomical observational purposes, we often find the antenna temperature in this equation denoted by the *corrected* antenna temperature, T_A^*. It describes the intensity after correcting for atmospheric attenuation and radiative loss. Furthermore, we note that throughout the thesis projects, we are referring to the main beam temperature when talking about the brightness temperature.

2.1.3 Receiver Design

Heterodyne Receivers

The principle behind a heterodyne receiver consists of shifting the frequency of incoming radiation to lower frequencies that are easier to process with current instrumentation. This is done by injecting a stable second frequency through a mixer. The schematics are illustrated in the left panel of Figure 2.3. The radio frequency is mixed with a frequency from a local oscillator (LO). The result is the intermediate frequency (IF) and is generally at a lower frequency of ~10 GHz (instead of the >100 GHz when observing mm lines). This is convenient since designing electronic circuits that are used to analyze high radio frequencies is extremely challenging. So a heterodyne receiver helps us to down-convert the incoming signal from high frequencies where electronic devices would fail. In addition, by generating the IF, it is possible to operate at a fixed frequency independent of the targeted radio frequency. This makes it possible to optimize detector circuitry to only a small range of frequencies, while a wider range in actual radio frequencies can be observed.

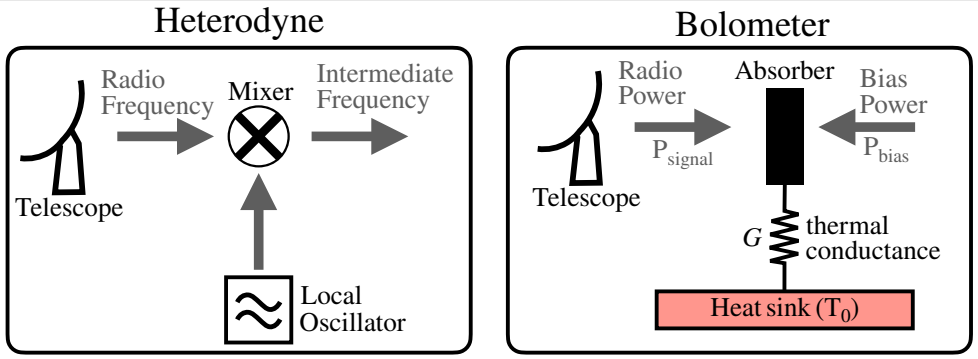

Figure 2.3: **Receiver Design Schematics** (*Left*) Schematic illustration of a heterodyne receiver, where a local oscillator frequency is used to shift down the radio frequency to an intermediate frequency that is more easily processable (*right*) Illustration of a bolometer.

Bolometers

Bolometers are devices that measure the strength of a signal with the help of an absorber. The absorber consist of a material whose resistance changes with an increase in temperature by heating of the incoming photons. By measuring the resistance R, the temperature of the absorber can be accurately determined.

The right panel in Figure 2.3 illustrates the basic principle. The absorber is connected to a heat bath of temperature T_0. By exposing the absorber to a constant bias power, the temperature change can be attribute to the incoming radiation via

$$T_{\rm abs} = T_0 + (P_{\rm signal} + P_{\rm bias})/G \tag{2.11}$$

where G represents a system-dependent conversion factor. In contrast to the heterodyne receiver, a bolometer is not sensitive to the actual frequency of the incoming radiation. Hence, such a detector is more common for the use of imaging using bandpass filters. A challenge, however, is the requirement to cool the bolometers down to almost absolute zero (to ~0.1 K) to achieve sufficiently good sensitivities.

2.1.4 Observing Noise and Sensitivity

We can quantify the strength or significance of a measurement with the *signal to noise ratio* (S/N). For telescope observations, the S/N will be:

$$\mathrm{S/N} = \frac{1}{\sqrt{2}} \frac{T_A}{T_{\rm sys}} \tag{2.12}$$

where $T_{\rm sys}$ indicates *noise temperature* (also called system temperature), which describes the added noise of the system. The $\sqrt{2}$ term accounts for a S/N if only noise is present[2].

The noise temperature can be expressed as a sum of different components that a receiver will pick up in emission. In units of brightness temperature, the individual (noise) contributing components are independent, and we can separate the total energy into the source temperature itself (T_A) and the noise temperature:

$$T_{\rm tot} = T_A + T_{\rm sys} = T_A + \underbrace{T_{\rm bg} + T_{\rm sky} + T_{\rm spill} + T_{\rm cal} + T_{\rm rx}}_{=T_{\rm sys}} \tag{2.13}$$

We can separate the noise temperature into components, such as

- the noise contribution from the galactic backgrounds, $T_{\rm bg}$;
- the noise contribution from atmospheric emission, $T_{\rm sky}$;
- noise contribution from ground radiation (so called-spillover), $T_{\rm spill}$;
- noise contribution due to injected noise, $T_{\rm cal}$;
- receiver noise temperature, $T_{\rm rx}$.

Generally, the system temperature, $T_{\rm sys}$ amounts to several tens to hundreds of K. In contrast, the source temperature of astrophysical objects is on mK-level (i.e., usually, $T_{\rm sys} \gg T_A$). So designing receivers that can filter out the relevant source temperature from the dominant system temperature is challenging. However, the source signal will be correlated from one observation sample to the next. The noise is generally not correlated between successive observations. Hence, increasing the number of observed samples makes it possible to reduce the noise.

So, back to the S/N (Equation 2.13), we can also express it in terms of the observed bandwidth, $\Delta\nu$, and the observed time, τ. By raising the number of independent measurements, N, the S/N will increase with

[2] More correctly, the S/N for a signal V is defined as $\mathrm{S/N} \equiv \frac{\langle V \rangle}{(\mathrm{Var}(V))^{1/2}}$, where $\langle V \rangle$ indicates the mean and $\mathrm{Var}(V)$ the variance of the signal. In case that the signal V is just *noise*, then the ratio boils down to $1/\sqrt{2}$.

$\sqrt{N}$. Following the Nyquist theorem, we require a sampling rate of $2 \times \tau/N$ to reconstruct a frequency range $\Delta\nu$ as an independent sample. This leads to the *radiometer equation* describing the S/N:

$$\mathrm{S/N} = \frac{T_A}{T_{\mathrm{sys}}} \times (\Delta\nu\tau)^{1/2} \tag{2.14}$$

Therefore, by increasing the observing time, τ, or the total bandwidth, $\Delta\nu$, it is possible to improve the significance of the observed target signal.

2.1.5 Brightness Temperature and Radiative Transfer Equations

Section 1.6 introduces the radiative transfer equations in terms of the spectral intensity, I_ν. More relevant for this thesis is the use of brightness temperature. The general solution of the radiative transfer equations, Equation 1.17, can be converted to units of brightness temperature, since $B_\nu(T) \propto I_\nu \propto T_A$ (e.g., see Equation 2.5):

$$T_A(s) = T_A(0)e^{-\tau_\nu(s)} + \int_0^{\tau_\nu(s)} T(s)e^{-\tau}\mathrm{d}\tau \tag{2.15}$$

where we denote the thermodynamic temperature of the medium at the position s as $T(s)$. If the medium is isothermal ($T(s) \equiv T_{\mathrm{exc}} = \text{const.}$), then we can solve the integral expression and obtain (refer to Equation 1.18)

$$T_A(s) = T_A(0)e^{-\tau_\nu(s)} + T_{\mathrm{exc}}(1 - e^{-\tau_\nu(s)}) \tag{2.16}$$

where the first term corresponds to the background temperature ($T_A(0) \equiv T_{\mathrm{bg}}$).

Generally, we are interested in finding an expression for the emitted intensity of a molecular cloud that emits due to a given transition. The antenna temperature of such a source can be expressed by (Williams and Viti, 2014):

$$T_A = \frac{hc^2 N_u A_{ul}}{2k_{\mathrm{B}}\nu^2\Delta\nu}\left(\frac{\Omega_s}{\Omega_A}\right)\left(\frac{1 - e^{-\tau_\nu}}{\tau_\nu}\right) \tag{2.17}$$

The terms in the first bracket describe the solid angles of the source (Ω_s), the antenna or telescope itself (Ω_A), and the line bandwidth is described by $\Delta\nu$. We can solve the expression of Equation 2.17 for the upper-level population N_u column density, giving us a way to estimate the amount of material based on an observed emission line:

$$N_u = \frac{2\nu^2}{hc^2 A_{ul}}\left(\frac{\Omega_A}{\Omega_s}\right)\left(\frac{\tau_\nu}{1 - e^{-\tau_\nu}}\right) W \tag{2.18}$$

where $W \equiv \int T_A \mathrm{d}\nu \approx T_A\Delta\nu$ describes the frequency integrated brightness temperature of an emission line. This expression is also key for molecular gas line emission modeling since it links the observed emission to the amount of molecular gas (see also Subsection 1.6.2). The expression in Equation 2.18 can be further simplified for two scenarios:

1. **Resolved Source:** If the source is resolved and the observed emission fills the telescope beam, the expression in the first bracket (the so-called beam filling factor) will tend to 1 and hence can be neglected. This is also the case for diffuse emission. If the source is not resolved, the so-called beam filling factor will deviate from unity. Consequently, the emission will be spread out over a larger area, so the beam filling factor will correct for this effect of reduced emission.

2. **Optically Thin Source:** In case the emission of the source is optically thin ($\tau_\nu \ll 1$), then the optical depth correction factor (term in the second bracket) will tend to unity and can be neglected. However, if the optical depth is significant, not all photons emitted by the cloud will be observable since a considerable amount will be absorbed or scattered. As a consequence, the observed emission will be reduced.

For resolved, optically thin sources, where both simplifications apply, the level population density will be directly proportional to the integrated intensity W of the emission line.

2.2 Radio and mm Telescopes

Throughout the thesis project, we rely on several different telescopes and instruments to collect the relevant data that we need to address specific science questions. For radio telescopes, we differentiate between single dish telescopes with a single continuous collecting area and interferometers that combine several single dish antennae as an array. Ideally, we want single dish telescopes to be as big as possible to improve the angular resolution and maximize the collecting area. Single dish telescopes are, however, constrained in their size due to gravitational bending and wind. This means that in order to guarantee high-quality observations, single-dish telescopes generally do not surpass a certain size. Otherwise, the performance would suffer since it becomes increasingly challenging to construct a reliable steering mechanism and ensure that the reflective surface smoothed to a fraction of the observed wavelength. As a consequence, current single dish observations do not supersede angular resolutions of $\sim 10''$ in the mm-regime. This is relatively coarse compared to ground-based optical observations that reach angular resolutions of $\leq 1''$. With so-called *interferometers*, combining observations of several antennas spread out over an area, it is possible to achieve high angular resolutions comparable to optical instruments.

2.2.1 Atmospheric Transition Window

A major challenge that ground-based observations of any wavelength face is the interference of the Earth's atmosphere due to scattering or absorption of incoming photons. This effect is illustrated in Figure 2.4, which shows the transmission of the atmosphere as a function of wavelength. The IR regime, UV, and higher energy radiation all suffer dramatically under atmospheric opacity. At the shorter-wavelength end of the radio ($\lambda < 1$ mm) regime, there are numerous vibrational transitions of atmospheric molecules such as CO_2, O_2, and H_2O that absorb most extraterrestrial mid to far-infrared radiation. Rotational transitions are responsible for absorption at mm wavelengths, where the FIR regime goes over into the radio regime. The atmosphere then becomes mostly transparent again at longer wavelengths. Only at very low frequencies of $\nu < 300$ MHz, ionospheric refraction will again hamper ground-based observations. Therefore, for the most part, radio frequencies are accessible to ground-based telescopes. As an additional advantage, the Sun is not a strong radio source. Consequently, radio observations are regularly performed during the day and at night. The molecular lines we study in this thesis are right at the upper-frequency limit of the radio regime (at around 1mm). In this range we find significant telluric absorption by rotational transitions of O_2 and H_2O. By placing mm observatories at high altitudes in dry climates, we can minimize the telluric absorption by these molecules and observe the extraterrestrial molecular line emission more efficiently.

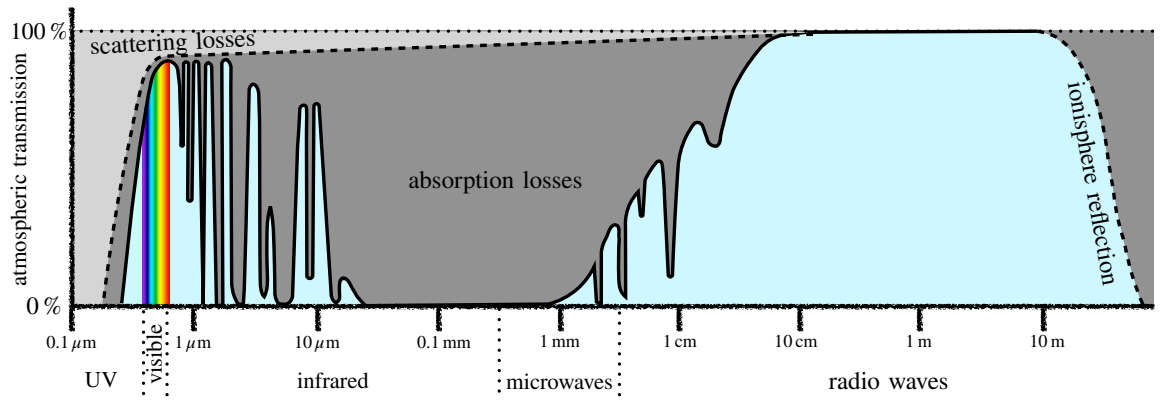

Figure 2.4: **Atmospheric Transition of Electromagnetic Radiation.** Only at certain wavelength, such as in the optical and radio regime, is the atmosphere transparent to extraterrestrial radiation. In contrast, due to absorption, scattering and reflection effects, the atmosphere can become opaque.

2.2.2 The IRAM 30m Telescope

The 30m telescope on the Pico Veleta in the southern Spanish Sierra Nevada mountain range is operated by the *institute de radioastronomie Millimétrique* (IRAM) and was built in the early 1980s. It is one of the largest and most sensitive radio telescopes operating in the millimeter wavelength regime. It consists of a single parabolic dish with a surface precision of 55 μm. It sits at an altitude of ~3000 m. In addition to the good weather condition, the atmospheric water content is minimal, making an efficient detection of millimeter wavelengths possible. The telescope operates in the wavelength regime from around 80 to 350 GHz. It is equipped with heterodyne receivers and a continuum camera. The most commonly used receiver is the *Eight MIxer Receiver* (EMIR). Past studies also relied on observations made with the *HEterodyne Receiver Array* (HERA).

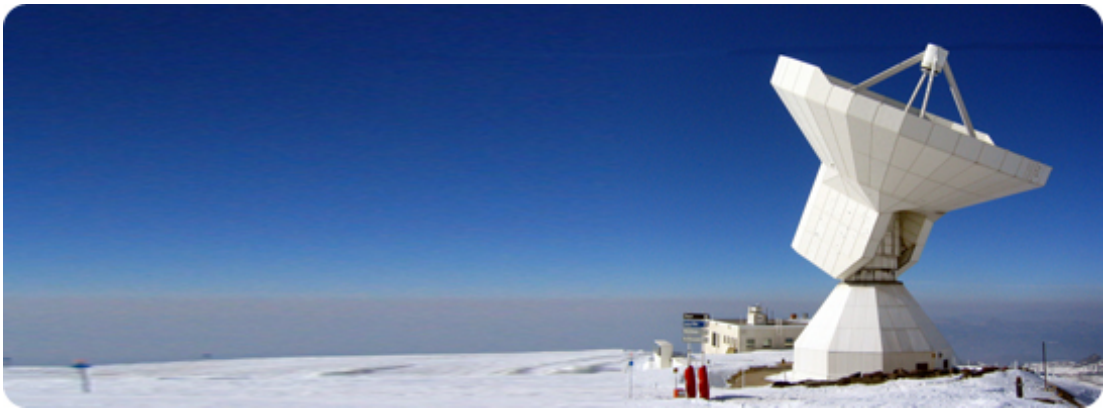

Figure 2.5: **The Institute de Radioastronomie Millimétique (IRAM) 30m telescope** Image Credit: IRAM.

EMIR: The EMIR receiver provides spectral coverage with four different bands ranging from 73 to 350 GHz. It offers very stable and low noise temperatures and a wide bandwidth of 8 GHz per side-band (Carter et al., 2012) for two orthogonal linear polarizations. It was commissioned in early 2009. For the instrument,

IRAM overhauled the calibration system from previous generation receivers. External warm optics provide an ambient temperature load. The beam is then passed back to the cold load at 15 K. The calibration accuracy is expected to be within an uncertainty of 10% when observing under stable conditions.

HERA: This is a multi-pixel heterodyne receiver consisting of two arrays of 3×3 pixels (Schuster et al., 2004). It operates in the range of 215 to 272 GHz. Because it is a multi-beam spectral line receiver, it is very efficient for rapid raster and on–the–fly imaging of spectral lines. The calibration proved to be more difficult, with an uncertainty ranging up to 20% (Leroy et al., 2009). Since 2021, HERA has been decommissioned.

2.2.3 Single Dish Observing Strategy

Single dish observations, particularly from the IRAM 30m telescope, build an integral part of this thesis project. Following Equation 2.13, a successful observation strategy aims to correctly assess the signal received from a source after accounting for the many uncertainties that arise from the receiver, telescope or variation of atmospheric conditions. This section provides a brief overview of the observing strategy when using the IRAM 30m telescope.

I) Signal Calibration: The receiver output (generally referred to as *voltage*, V, or *counts*, C) needs to be converted into a meaningful quantity, such as the physical brightness temperature. To accurately convert, we need to calibrate using sources with a known temperature brightness. A standard procedure for heterodyne receivers, which are installed on the IRAM 30m telescope, is the so-called *chopper wheel* method (Penzias and Burrus, 1973). The method consists of contrasting sky observations (using an *ON* and *OFF* position) and loading a cold source and hot source (source at room temperature) in front of the detector. Figure 2.6 illustrates the general principle of the chopper wheel method by means of the different spectral measurements. The antenna temperature T_A' (where the prime indicates correction for atmospheric extinction) can then be expressed, to first order, in terms of

$$T_A' = T_{\rm cal} \times \frac{V_{\rm ON} - V_{\rm OFF}}{V_{\rm hot} - V_{\rm cold}} \tag{2.19}$$

where $V_{\rm OFF}$ indicates the measured off source voltage (Figure 2.6, panel (i)), $V_{\rm ON}$ the on source voltage (Figure 2.6, panel (ii)), and $V_{\rm hot}/V_{\rm cold}$ the voltage when exposed to the hot/cold load. Notice that the off position voltage, $V_{\rm OFF}$, is identical to the combination of cold load and receiver noise signal ($V_{\rm OFF} = V_{\rm cold} + V_{\rm rx}$, with $V_{\rm rx}$). $T_{\rm cal}$ is the calibration term, which includes the beam forward efficiency and is calibrated to convert voltage into brightness temperature units. The method requires observing the source (the *ON*) and a position without any emission (*OFF*).

A key strategy for a successful and efficient calibration is to obtain systematic measurements of the baseline via the *OFF* point without significantly reducing the time observing the (more scientifically interesting) *ON* position. The IRAM 30m telescope employs the following observing strategies to ensure repetitive *ON* and *OFF* measurements:

- **Position Switching:** The pointing of the telescope's antenna switches between the source and an area in the sky where no emission is expected. The ON and OFF position separation should not be too large to ensure that the atmospheric conditions are similar between the two pointings. Also, position switching is only feasible if the rate of variation of the atmospheric conditions is smaller than the time it takes the telescope to move between the ON-OFF positions.

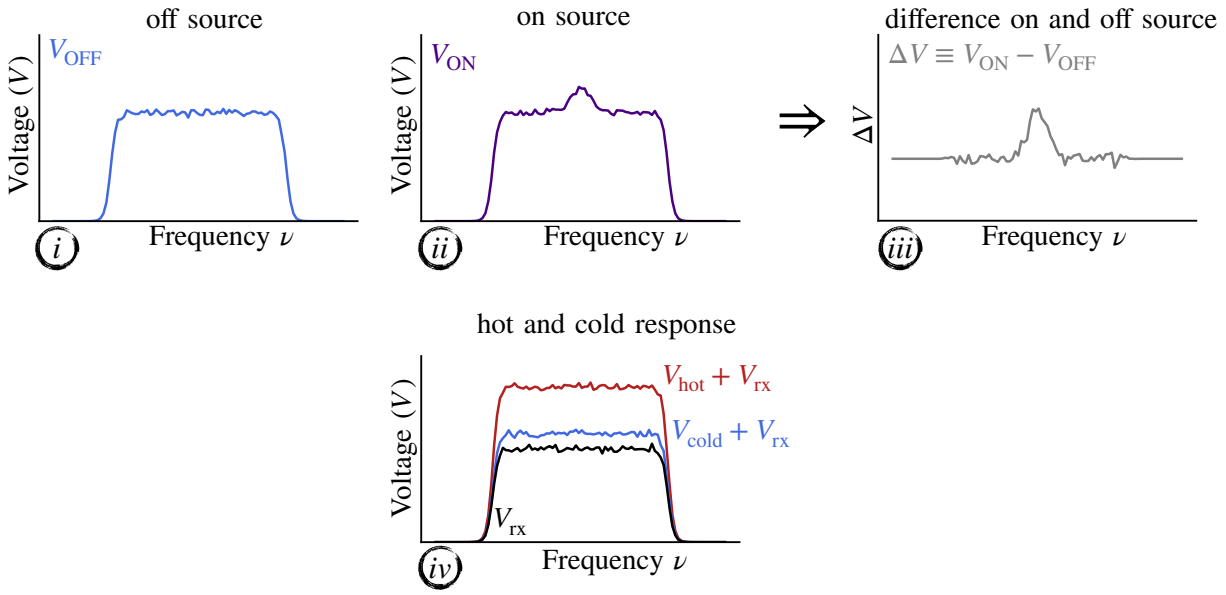

Figure 2.6: **Chopper Wheel Method** (i) The voltage $V_{\rm OFF}$ is the signal when no source is present. The panel shows the voltage over a range of frequencies. (ii) When the telescope is pointed toward a source, we measure $V_{\rm ON}$. (iii) The difference of the *ON* and *OFF* signal measures the source emission. (iv) To convert voltage to brightness temperature, we use a hot and cold load. The system noise voltage is indicated by $V_{\rm rx}$.

- **Wobbler Switching:** This technique is, in principle, identical to position switching. Not the antenna, but the secondary mirror gets re-positioned. This is more time-efficient. However, the range of movement of the secondary mirror is limited (no more than $240''$). For extended sources, the maximal possible wobbler ON-OFF separation might not be enough to cover a region without any emission.
- **Frequency Switching:** Alternatively, instead of re-positioning the pointing of the telescope, it remains in the ON position, but the tuning frequency is cyclically changed between two phases. The *OFF* tuning should be selected such that the resulting spectrum does not show any source emission. This method is also very time efficient since the telescope does not need to be re-positioned. However, the system's stability as a function of frequency could vary significantly, or atmospheric lines could hamper an accurate calibration.
- **Background Subtraction:** In principle, no *OFF* position is needed if we can obtain a well-behaved baseline fit from the *ON* observation. By fitting the baseline within the targeted spectral region, we can obtain an equivalent to an *OFF*-source observation. This method requires, however, that the baseline does not include emission from the source or other spurious artifacts that make fitting a baseline impossible.

II) Pointing and Focus: Throughout the observing run, it is necessary to ensure that the pointing direction of the telescope is stable. In regular intervals, a correction needs to be performed. The calibration is performed by scanning over an unresolved source for which we know the coordinates. Any potential offset can be used to correct the pointing of the telescope. Generally, the pointing for the IRAM 30m telescope should be checked every ~40 – 60 min. Also, the focus of the telescope observations varies with time and needs constant calibration. The focus can be adjusted by changing the primary and secondary mirror

separation. The optimal distance is determined such that the PSF response is minimal when observing a point source. The focus needs to be checked ~3-4 h or if atmospheric conditions have changed significantly (e.g., after dawn or dusk).

III) On-the-Fly (OTF) Mapping: With the OTF technique, it is possible to efficiently map larger areas in the sky (relative to the beam size). The result is a 3D data cube, i.e., a 2D map where each pixel contains a spectrum (see Figure 2.8). Instead of iteratively switching between an *ON* and *OFF* position, the telescope scans smoothly and rapidly across a path over the sky. After completing each track, the *OFF* position is then targeted. This significantly reduces the telescope's overhead.

2.2.4 Atacama Large Millimeter Array (ALMA)

Besides the single dish IRAM 30m telescope, we also rely on ALMA, which is an astronomical interferometer (Wootten and Thompson, 2009). In terms of sensitivity and resolution, it has revolutionized radio astronomical observations. It combines a total of 66 radio telescopes that have 12m and 7m diameters. It is situated in the Atacama Desert at an altitude of 5 000 m, yielding excellent atmospheric observing conditions. The instrument is operated by the European Southern Observatory (ESO). It operates in the range of 31 to 1000 GHz. The antennas can be set up in different configurations, achieving different sensitivities and angular resolutions. The baseline can be extended up to 16 km, making angular resolutions of $<0.1''$ possible. Due to its high-quality instrumentation design, it offers a very accurate calibration of <3% (Francis et al., 2020). This makes ALMA observation particularly interesting to compare to observations made with other telescopes, such as the 30m telescope, and investigate flux calibration uncertainties.

Figure 2.7: **Atacama Large Millimeter Array (ALMA).** Image Credit: ESO/ALMA.

2.2.5 Other relevant Telescopes and Instruments

Data from several other telescopes and observatories are included in this thesis project. The observations range across a vast regime of wavelengths from the optical to the lower frequency radio waves. The following list provides a brief overview of the more relevant observatories for this thesis project. These telescopes and instruments are essential to derive ancillary physical parameters, such as the star formation rate, dust mass, or atomic hydrogen distribution, all of which cannot be traced by mm observations alone. Further details regarding the technical specifications are given in the relevant chapter.

- **Karl G. Jansky Very Large Array (VLA):** The interferometer consists of 27 antennas, each with a diameter of 25 m. It is located in New Mexico, USA, and operates at frequencies of 1 to 50 GHz. The configuration of the antennas can change, yielding different angular resolutions.

- **45m Nobeyama Radio Observatory (NRO):** The single dish telescope is located in Japan and is operated by the National Astronomical Observatory of Japan. It was constructed in 1982. With a diameter of 45m, it currently constitutes one of the largest single dish mm radio telescopes. It operates at 80 to 116 GHz.
- **Submillimeter Array (SMA):** The interferometer consists of eight 6-meter antennas and is located on Mauna Kea in Hawaii. The baseline can vary between 16 to 508 meters. It operates at higher submillimeter frequencies of 194 to 408 GHz. Combining both sidebands from heterodyne receivers yields a large bandwidth of 48 GHz, making it an ideal instrument to study a suite of molecular lines simultaneously.
- **Herschel Space Observatory (HSO):** Operated by the European Space Agency (ESA), HSO was in operation from 2009 to 2013 and covered the infrared wavelength regime from 55 μm to 672 μm. The satellite is equipped with a 3.5 m primary mirror. In this thesis, we rely on observations made with the Photodetecting Array Camera and Spectrometer (PACS) and Spectral and Photometric Imaging Receiver (SPIRE) instruments. Due to the depletion of liquid helium, which is necessary to cool the systems, the telescope mission ended in 2013.
- **Spitzer Space Telescope (SST):** The infrared SST observatory was launched in 2003. The satellite carried three instruments that together covered the wavelength range of 3.6 μm to 160 μm. Despite running out of liquid Helium as coolant in 2009, the observatory continued to operate until 2020 using only the two shorter wavelength bands (3.6 μm and 4.5 μm).
- **Hubble Space Telescope (HST):** Launched in 1990, HST is a space observatory in low-earth orbit. It has a primary mirror diameter of 2.4 m and operates with five main instruments that can observe ultraviolet, visible, and near-infrared light.

2.3 Astronomical Data Analysis

Most millimeter observations are provided in the form of so-called 3D data cubes. The following sections describe how we can describe and scientifically analyze such datasets.

2.3.1 2D and 3D data Analysis Techniques

Astronomical data cubes, which we extensively use in this PhD project, consist of two spatial (x and y axis) and a frequency axis (z axis). This means that we obtain the main beam temperature in terms of $T_{\rm mb}(x, y, v)$ (so-called *voxels*). It is common to describe the spectral axis in terms of a velocity relative to the rest-frame frequency of an emission line using the Doppler shift. We can derive a range of data products for any given astronomical cube. These help us to disentangle, visualize and properly analyze the various information encapsulated within the cube. Table 2.1 summarizes the key 2D data products and provides the prescription to derive them. To improve the significance of the data, it is common to define a mask, $M(x, y, v)$, that indicates what voxels belong to the emission line and what voxels are only noise related.

The integrated intensity (moment-0) or peak intensity map best describes the strength of the emission line. The moment-0 is one of the key parameters when describing the radiative transfer equations. It is obtained by integrating the cube (also called *collapsing*) along the velocity axis. In order to optimize the S/N, voxels outside the mask are set to 0. Since the line width information is removed, there is a degeneracy in moment-0 maps regarding broad lines with a low peak and narrow lines with a high peak. In contrast,

the peak intensity looks at the maximum brightness temperature for a given line of sight, but it again loses information about the line width.

Information regarding the kinematics of the emitting gas is best captured by the mean velocity (moment-1) and velocity dispersion (moment-2) maps. The mean velocity describes the bulk motion of the emitting gas element along the line of sight. Due to the Doppler shift, the peak emission frequency will shift towards bluer or redder wavelengths. Since we observe an ensemble of gas particles, the individual velocities will vary. The moment-2 map estimates the line width, which is linked to the gas velocity dispersion. Figure 2.8 illustrates a data cube example and shows the key 2D products.

Table 2.1: Summary of key 2D Data Products used in this thesis project, adopted from (Leroy et al., 2021a)

Map	Mathematical Prescription	Unit
Integrated Intensity (Moment-0)	$W(x,y) = \sum_i T_{\rm mb}(x,y,v_i) M(x,y,v_i) \delta v$	K km s^{-1}
Peak Intensity	$I_{\rm peak}(x,y) = \max_{v_i}\left[T_{\rm mb}(x,y,v_i)\right]$	K
Mean Velocity (Moment-1)	$\bar{v}(x,y) = \frac{1}{W(x,y)} \sum_i v_i T_{\rm mb}(x,y,v_i) M(x,y,v_i) \delta v$	km s^{-1}
rms line width (Moment-2)	$\sigma_v(x,y) = \left(\frac{1}{W(x,y)} \sum_i (v_i - \bar{v})^2 T_{\rm mb}(x,y,v_i) M(x,y,v_i) \delta v\right)^{1/2}$	km s^{-1}

Note: $M(x,y,v_i)$ indicates a Boolean mask that indicates whether the line is detected or not. δv indicates the channel width.

2.3.2 The PyStructure

To efficiently analyze multi-line and multi-wavelength datasets, we use a pipeline that first homogenizes the complete dataset in terms of resolution and spatial coverage. The particular pipeline is called PyStructure and is based on IDL scripts used to obtain bias-free measurements of molecular cloud properties (Rosolowsky and Leroy, 2006). The following section briefly outlines the key aspects of this routine.

1. **Data Convolution:** We use observations from various telescopes and at different frequencies for the final analysis. Consequently, the angular resolutions do not necessarily match. To homogenize the full dataset, we convolve all data cubes and maps to the common (i.e., largest) beam size. For this step, we assume that the convolution kernel of the data is sufficiently well described by a 2D Gaussian function, for which the width is defined by the difference in quadrature ($\theta_{\rm kernel} = \sqrt{\theta^2_{\rm target} - \theta^2_{\rm source}}$).

2. **Hexagonal Grid Sampling:** In our analysis, we usually want to compare the emission of different lines for a common line of sight. Hence we need to regrid all cubes and maps to a common sampling grid. The PyStructure code performs a half-beam sized hexagonal sampling instead of a Cartesian sampling. Using a hexagonal sampling is commonly done in the literature (e.g. Bigiel et al., 2011; Sandstrom et al., 2013; Kawana et al., 2022). As opposed to a Cartesian sampled grid, the data points are all equidistant in a hexagonally sampled grid. This ensures a more uniform sampling. The oversampling factor, which is defined as the ratio of the beam area relative to the pixel size ($N_{\rm s} = (1.13 \times \theta^2_{\rm FWHM})/A^{\rm hex}_{\rm pix}$), is also minimized[3], while still ensuring Nyquist sampling.

[3] Note that if the pixel spacing is equal to the beam size then there is no oversampling.

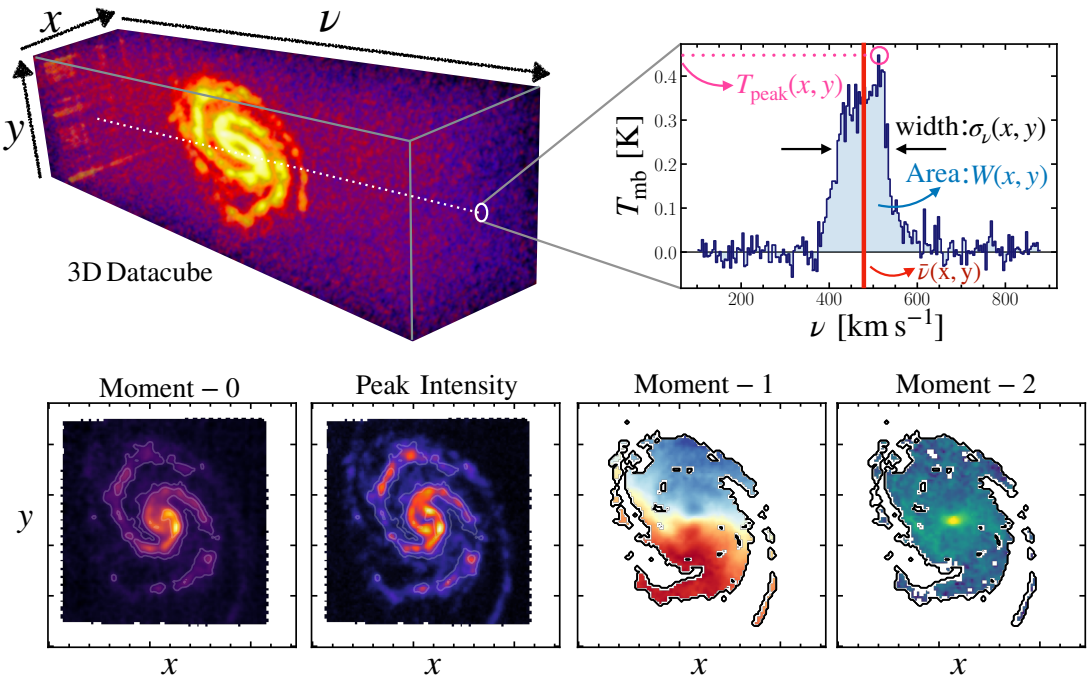

Figure 2.8: **Example Data Cube and Key Products.** Example of CO(2-1) observation made with the IRAM 30m telescope of galaxy M51. The top left illustrates a 3D datacube, where the colors indicate the brightness temperature. The three axes are labeled. The line illustrates the spectral axis for a random pixel (x, y). The spectrum is shown on the top left, where the key derived parameters are indicated. The peak temperature (in pink) is the brightness temperature corresponding to the largest value of the spectrum. The moment-0 is equivalent to the area under the spectral curve. The red vertical line indicates the mean velocity, $\bar{\nu}$, (also referred to as moment-1). The moment-2 corresponds to the width of the line. The bottom panels show the 2D data products, which we obtain after processing the spectral axis of each pixel.

3. **Cube rms and Masking Routine:** To improve the S/N of the derived data products, we determine a 3D mask that indicates voxels that contain line emission. In simple terms, the mask consists of voxels that have a value above a certain threshold factor of the line rms. The rms is determined from the signal-free part of the spectrum using the median absolute standard deviation (concept dating back to Gauss, 1816), which is more robust toward outliers than the general standard deviation. The mask is created using a set of previously defined *reference* lines. These should be bright enough so that we do not lose emission for all other lines on which we apply the mask. We generate the mask by combining a so-called high mask with a high threshold and a low mask with a low rms threshold. In essence, the high mask is expanded into the low mask to recover areas of low rms emission belonging to the high rms core. This ensures that the final mask does not contain noise peaks while not being too strict and missing a significant amount of the line voxels.

4. **Data Product Generation:** The convolved and hexagonally sampled data cubes are processed to obtain the key data products described in Subsection 2.3.1. The corresponding error is computed based on Gaussian error propagation.

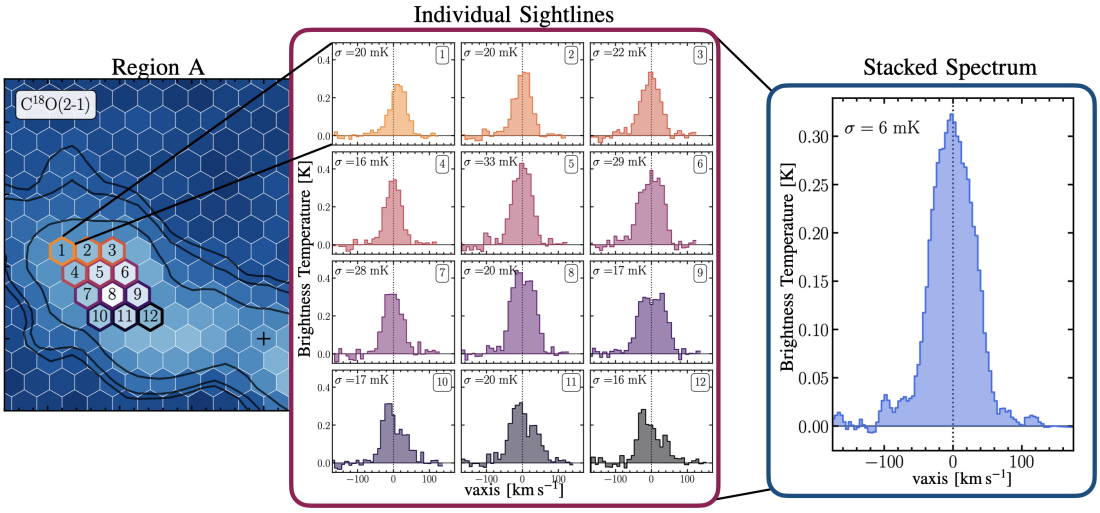

Figure 2.9: **Spectral Line Stacking.** Here, we select twelve sightlines corresponding to a specific region in the center of galaxy M82 center (see left panel). The central panel shows each individual spectrum. The corresponding root-mean-squared (rms) at 10 km s^{-1} is indicated in each panel. We have shifted each spectrum such that they are centered at the same velocity (using the brighter ^{12}CO(2-1) emission). When stacking n spectra, the rms will decrease by a factor of $\sim\sqrt{n}$. The right panel shows the stacked spectrum of the twelve sightlines. The rms clearly decreased from ~20 mK to ~6 mK.

2.3.3 Spectral Line Stacking

Throughout this thesis project, we deal with faint molecular emission in certain regions of the galaxy. We use the so-called *spectral line stacking* technique to improve the S/N of the detection. This technique is commonly used in the literature (e.g. Schruba et al., 2011; Walsh et al., 2016; Cormier et al., 2018; Loomis et al., 2021). Figure 2.9 illustrates the basic principle. Since the noise is uncorrelated, the signal can be improved by combining several spectra. However, since the spectra from different lines of sight have likely different velocity shifts, we first need to regrid each spectrum along the velocity axis so that the local peak velocity corresponds to $v = 0$ km s^{-1}. Given a set $\mathcal{B} = \{i | i \text{ in some bin}\}$ which defines the indices of a predefined bin:

$$T_{\rm mb}^{\rm stack}(v_{\rm shift}) = \frac{1}{|\mathcal{B}|} \sum_{i \in \mathcal{B}} T_{\rm mb}(x_i, y_i, v_{\rm shift}) \tag{2.20}$$

By shifting the spectra to their local zero-point, we remove the large-scale velocity gradient and ensure that spectra from different parts of the galaxy will average coherently. Commonly, we use the following bins:

- *Radial Stacking:* We often are interested in establishing whether a radial trend of some sort exists across a galaxy. We refer to *radial* stacking when we bin the data using concentric rings of a fixed width and increasing radius.
- *Regional Stacking:* We can commonly distinguish between different galaxy regions, such as the center and disk or the spiral arm and interarm.
- *Stacking by Quantity:* We can bin the lines of sight by any other quantity, such as stellar mass surface density, dust mass surface density, CO velocity dispersion, etc. For example, when stacking by $\Sigma_{\rm SFR}$,

we have binned the individual sightlines by their SFR surface density.

When stacking n spectra, the noise will generally improve by a factor $\sim\sqrt{n}$ for uncorrelated noise. We note that spectral line stacking is not to be confused with binning integrated line intensities.

CHAPTER 3

IRAM 30m Telescope Performance Analysis

Things usually look better if you're doing something right.

M. Reid to K. M. Menten – 20th/21st century astronomers

Overview

Data obtained with the IRAM 30m telescope build an integral part of the PhD thesis project. Uncertainties and limitations associated with the observations must be well understood to ensure that we properly analyze the dataset. While essential, such an analysis is something we rarely find being performed in the literature. By 2020, we had obtained ^{12}CO(1-0) and ^{12}CO(2-1) OTF observations from various observing programs and telescopes for a sample of nine nearby spiral galaxies[1]. Upon close inspection of the datasets, we note large discrepancies when comparing observations of the same line in the same galaxy. To quantify the robustness and performance of observations obtained with IRAM 30m telescope EMIR receiver, we aim to systematically assess the flux calibration stability. For that purpose, we requested director's discretionary time (DDT) to observe selected pointings across M51. The details are presented in Section 3.1. Overall, we find a consistent scan-to-scan variation of 10%. Only for fainter lines, the intensity can vary by >50% between different scans. Another relevant effect can be emission contribution from the error beams that introduce additional uncertainty. While most emission enters the telescope via the main beam, a non-negligible fraction of emission comes from side lobes. Techniques exist to estimate and quantify such error beam contribution. In particular, the interarm region suffers more significantly, with >10% of the measured intensity originating, in fact, from emission via the side lobes.

3.1 Flux Stability Analysis

Combining datasets from different telescopes for a multi-line and multi-transition study is challenging. Variation in the overall performance, observing stability, and noise handling can lead to systematic differences in the obtained intensity measurements. This is particularly relevant when investigating line ratios, where the dynamical range is small (e.g., the CO(2-1)/(1-0) line ratio we observe in M51 has a

[1] We investigated resolved CO line ratio, R_{21}, variation across and within these nine galaxies (see Chapter 4). These were part of the EMPIRE sample (Jiménez-Donaire et al., 2019).

range of $R_{21} = 0.5 - 1.0$). Systematic errors can be minimized when simultaneously observing the two CO transitions with the same instrument. But when combining CO observations from two different telescopes, the resulting ratio can vary significantly depending on the telescope's performance. In the context of CO line ratio studies, this issue has become more relevant with recent work on resolved nearby galaxies (e.g. Yajima et al., 2021; den Brok et al., 2021; Leroy et al., 2022). Particular reasons for the instabilities of observed fluxes are manifold. Most commonly, the performance of a radio telescope can suffer from the following aspects:

1. **Different or Unstable T_{sys}:** The system temperature is defined in Equation 2.13 as the part of the observed intensity related to the noise. It consists of several different components (mainly related to noise injected by the receiver).

2. **Variable S/N:** The reached sensitivity can vary for a single observation or between observations of two different lines due to their respective signal strength.

3. **Scanning Artifacts:** When performing on-the-fly (OTF) observations, it is possible that bad scans can impact the resulting observations.

4. **Varying Atmospheric Conditions**: Changes in atmospheric opacity or differences in the average airmass (linked to telescope's pointing elevation) also affect the resulting flux intensity, if not properly calibrated.

5. **Bad Intensity Calibration:** The intensity calibration is performed using the chopper wheel method (see Subsection 2.2.3), which consists of oscillating observations that are exposed to either a cold and a hot load. Systematic uncertainties in the calibration procedure can affect the resulting observation.

6. **Improper Error Beam Handling:** Emission entering via the side lobes of the beam lead to a larger observed intensity. The beam pattern differs by telescope, but is also frequency dependent, making it challenging to properly account for when combining multi-telescope datasets.

By relying only on a dataset of two lines observed with the same telescope at the same time, several of these issues will cancel out when taking the line ratio. By comparing the resulting variation, we can study the impact of flux stability issues on other line surveys. This section focuses exclusively on the CO(2-1)/(1-0) line ratio variation in the nearby spiral galaxy M51.

3.1.1 Introduction – The IRAM 30m DDT Project #E02-20

One of the main reasons that motivated the in-depth analysis of the IRAM 30-m performance analysis was our recent study (Chapter 4 of this thesis; den Brok et al., 2021), where we find an arm-interarm CO line ratio trend that is conflicting with previous work. Counter-intuitively, we measure higher R_{21} line ratio values in the interarm compared to the spiral arm regions. This result opposed previous studies of the same galaxy (Koda et al. 2012). We narrow down the discrepancy to the use of different CO(1-0) and CO(2-1) datasets. Substituting the different CO(1-0) datasets resulted in an inverted arm-interarm trend. For reference, we use the PAWS CO(1-0) map from Pety et al. (2013), while Koda et al. (2012) use data from Koda et al. (2011)). In addition to internal variation, M51 shows a very large averaged line ratio when compared to other nearby galaxies (R_{21}~0.9 for M51, while the average across nearby galaxies is 0.64; den Brok et al., 2021). In den Brok et al. (2021), we perform various analyses to understand the uncertainties of the IRAM 30m PAWS data. We now suggest that the discrepancy is caused by the NRO CO(1-0) data, which has improper error beam handling, different or unstable T_{sys}, variable S/N, or scanning artifacts.

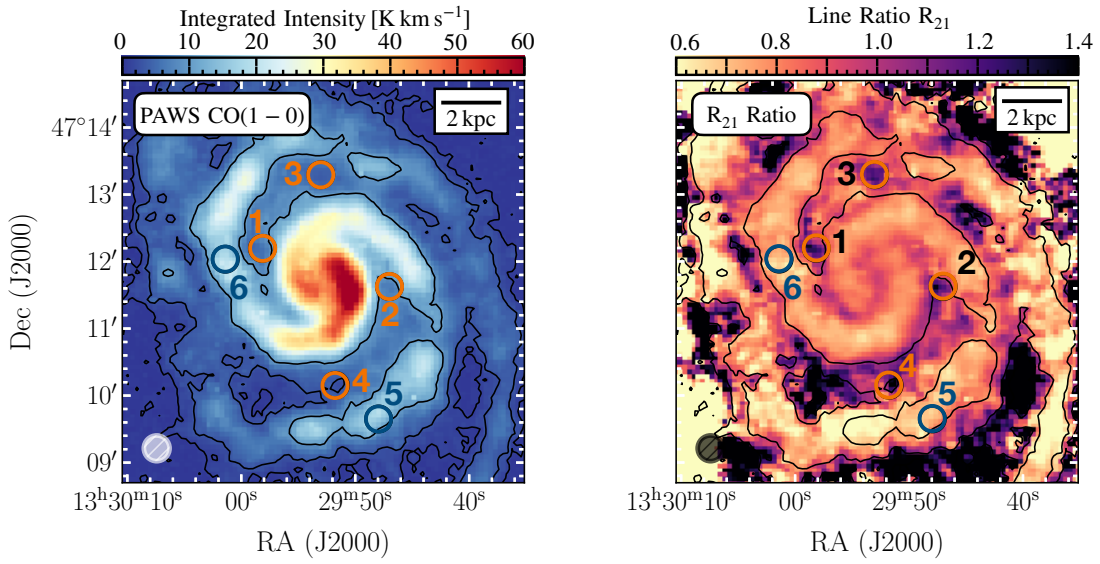

Figure 3.1: **Pointing Selection for DDT Program #E02-20.** (*Left*) PAWS OTF integrated CO(1-0) map of galaxy M51 with the six selected pointings highlighted. Interarm pointings (1-4) are color-coded in orange, and spiral arm pointings (5-6) in blue. (*Right*) The CO line ratio R_{21} using PAWS CO(1-0) and CLAWS CO(2-1) data. The interarm pointings are selected around regions with enhanced R_{21}.

However, as a definitive experiment to confirm the robustness of previous IRAM 30m measurements, we proposed observing four selected pointings in the interarm (labeled 1-4) and two pointings in the spiral arm region (labeled 5-6). Figure 3.1 shows the CO(1-0) OTF emission (from PAWS) together with the 6 proposed pointings. The selection of the individual pointings is based on assessing the R_{21} map and finding where the variation is strongest in the interarm regions.

Table 3.1: Summary of the six pointings observed as part of the project #E02-20.

N^o	**RMS [mK]**		**S/N**		Obs. Date (in 2021)	$N_{\rm scans}$
	(1-0)	(2-1)	(1-0)	(2-1)		
1	7	7	50	33	8/9 Mar.	6
2	7	9	39	19	8/9 Mar.	6
3	6	9	33	18	27 Feb. + 8/9 Mar.	8
4	5	6	20	13	27 Feb. + 8/9 Mar.	9
5	6	11	108	37	8/9 Mar.	6
6	6	8	119	67	27 Feb. + 8/9 Mar.	8

The observations of the DDT project #E02-20 were carried out over the course of two separate nights. On the night of February 27$^{\rm th}$, severe weather conditions limited the window of possible observing time to only 3 h. Due to this limited time-constrained, only 3/6 proposed pointings were initially observed (pointings 3, 4, and 6). Another observing run was carried out on the night of March 8/9$^{\rm th}$. All six pointings could be observed with a total of 6 h, telescope time over the two nights. A summary of the complete DDT program dataset is given in Table 3.1. The final CO(1-0) and CO(2-1) spectra are presented in Figure 3.2.

Since changing atmospheric conditions or calibrations variation can significantly affect the resulting

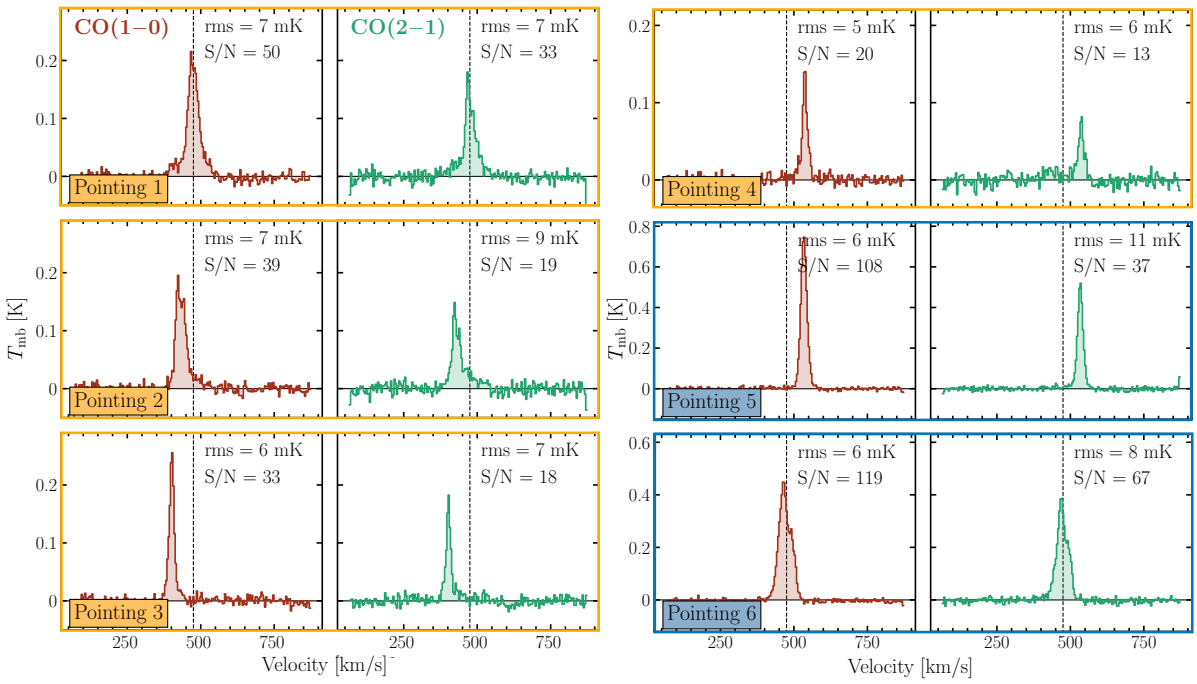

Figure 3.2: **CO(1-0) and CO(2-1) Spectra for Individual Pointings**. The CO(1-0) spectra are in the left panels (red) and the CO(2-1) in the right panels (green). Position 1 – 4 (yellow) are from the interarm and positions 5 – 6 (blue) are from the spiral arm regions. The dashed line indicates the systemic velocity of M51 at ~471 km s^{-1} (Shetty et al., 2007). Each panel indicates the rms of the line-free part of the spectrum and the S/N of the integrated emission.

intensity measurements, we looped through the pointings several times. We observed each pointing for 6 min, before moving to the next. This ensured that the spectra of the different pointings are approximately uniformly affected by any potential instability. As a result, we have several scans for each pointing (the number of scans per pointing is listed in the last column of Table 3.1).

3.1.2 Further Relevant Observations

We use OTF maps to complement the data performance analysis. PAWS covered the central region of M51 at 1 arcsec resolution (Pety et al., 2013; Schinnerer et al., 2013). For short-space corrections, the full disk of M51 is also observed. These IRAM 30m observations have a resolution of 23 arcseconds. In addition, we use IRAM 30m large program data from CLAWS. This survey covered the emission of several CO isotopologues across the full disk of the M51. The OTF maps are used to produce mock pointing observations. Using the apertures corresponding to the proposed pointings, we can extract the spectra by only combining lines of sight within each aperture.

3.1.3 Data Assurance Checks

In combination with the OTF maps, we do a couple of consistency checks to characterize the performance of the 30m telescope. In this subsection, we address issues from which the telescope performance can suffer in the following order:

I. **Compare Different Observing Nights:** For three pointings, we can compare the spectra observed on 27th of February and 8/9th of March. This makes it possible to assess the calibration stability since the observing conditions differ between the two nights.

II. **Differences between Individual Scans:** Due to the looping over the pointings, we have several scans per position. In case of adequate performance, we expect the different scans not to show any substantial line variation.

III. **Elevation of Telescope Pointing:** The airmass will vary with elevation. We can assess the impact by comparing any potential scan-to-scan variation to the elevation of the telescope pointing.

IV. **OTF Extracted Spectra:** The OTF maps can be used to create mock pointing observations. We compare such spectra extracted from the OTF maps to the #E02-20 pointing observations.

V. **Pointing Error Analysis** By shifting slightly the aperture used to extract the mock spectra from the OTF data, we can simulate a pointing error and assess its impact.

I) Consistency Check between Different Observing Nights

The observations of the six pointings are split over two nights. Three selected pointings were observed on both nights. This includes the interarm regions 1 and 2 and the spiral arm region 6. Figure 3.3 shows the spectra for CO(1-0) and CO(2-1) from both observing nights as well as their residual (the observation of the first night are plotted below the observation on the second night). Table 3.2 lists the relative difference of the integrated intensity. In general, the integrated intensity variation varies of order 10-20% between the two different observing nights. Such a degree of variation is consistent with the finding of previous studies investigating the stability of line calibrators (e.g. Jiménez-Donaire et al., 2019). The CO(2-1) emission for pointing 4 shows, however, a very big difference (~40%). The observation of the 27th of February seems to be affected by a bad scan, resulting in lower detected emission.

Table 3.2: Comparison of the line intensities of the same position over the two observation runs.

Pointing N^{o}	**Difference ($R_{27/09}$)**	
	(1-0)	(2-1)
3	1.20	1.04
4	0.98	0.61
6	0.93	1.17

During both nights, we also observed the line calibrator IRC+10216. This makes it possible to estimate the calibration stability of the telescope. Figure 3.4 shows the comparison of the CO lines of the line calibrator for both nights. From these measurements, the 3mm observations seem less stable since they show a ~ 15% variation between the two nights for the integrated line intensity. The 1.3mm observation appears to be more stable, with only a 2% difference in integrated intensity between the two measurements. IRAM generally reports a calibration uncertainty of around 10% for good observing conditions[2]. The line calibrator variation of ~ 15% could explain the observed variation of the CO(1-0) measurements in pointing 3 and 6 (see Figure 3.3).

II) Consistency Check between Individual Scans

Since we obtained numerous scans for the individual pointing (see Table 3.1), we can study the consistency

[2] https://publicwiki.iram.es/EmirforAstronomers/#Telescope_efficiencies (06/16/2022)

of the resulting spectra. The integrated intensity of the individual scans for both lines is indicated in Figure 3.5. Figure 3.6 and Figure 3.7 show the individual scans for all the pointings for CO(1-0) and CO(2-1) respectively. Scans 1-4 were observed on the 27th of February (only pointing 3, 4, and 6). Scans 5-11 were obtained on the night of 8/9th of March (for all pointings). Looking at Figure 3.5, we can see that the CO(1-0) scan-by-scan variation seems to be within the margin of error of the integrated intensity measurements for most scans. Only for pointing 3, 4, and 6, does the scan #2 seem to show a bigger difference. In contrast, the variation of the CO(2-1) line emission scans shows stronger scan-to-scan variation, with >50% for certain instances. The variation of the scans taken on the first night likely relates to the unstable weather conditions. Strong winds forced the suspension of any further observations after 3 h. In some instances, the scan-to-scan variations seem to be connected between the CO(1-0) and CO(2-1) emission line (e.g., scan #1 for pointing 5 and 6 both show a significantly higher intensity than scan #1, or scan #8 and #9 have both larger intensities than the average in pointing 5). Such a correlation likely indicates sources of variation not linked to the observing frequency (we stress again that both the CO(1-0) and CO(2-1) lines were observed simultaneously per pointing). In other cases, for a given scan, CO(1-0) and CO(2-1) are affected differently. The fact that the CO(2-1) shows stronger variation can be linked to several possibilities: For CO(2-1) at 1.3 mm, the atmospheric opacity is stronger, the main beam efficiency is smaller, and the line intensity is smaller (depending on the line ratio R_{21} than CO(1-0) at 3 mm.

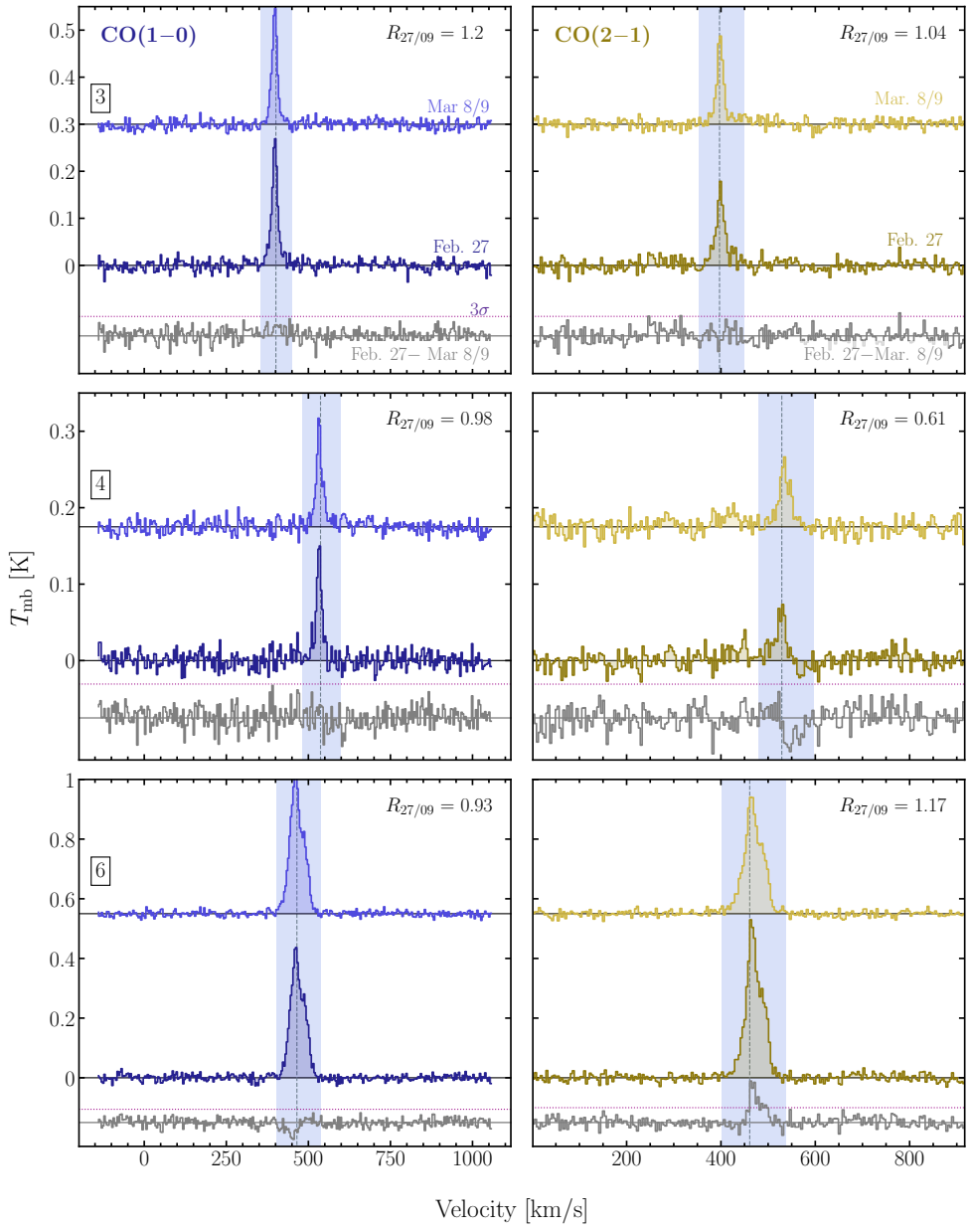

Figure 3.3: **Day-by-Day Comparison.** For three pointings we have observations from both observing nights. The top spectrum shows the March 8/9 observation, the middle spectrum the data from the 27th of February, and the grey line indicates the residual. The integrated intensity ratio of the two days is indicated in each panel.

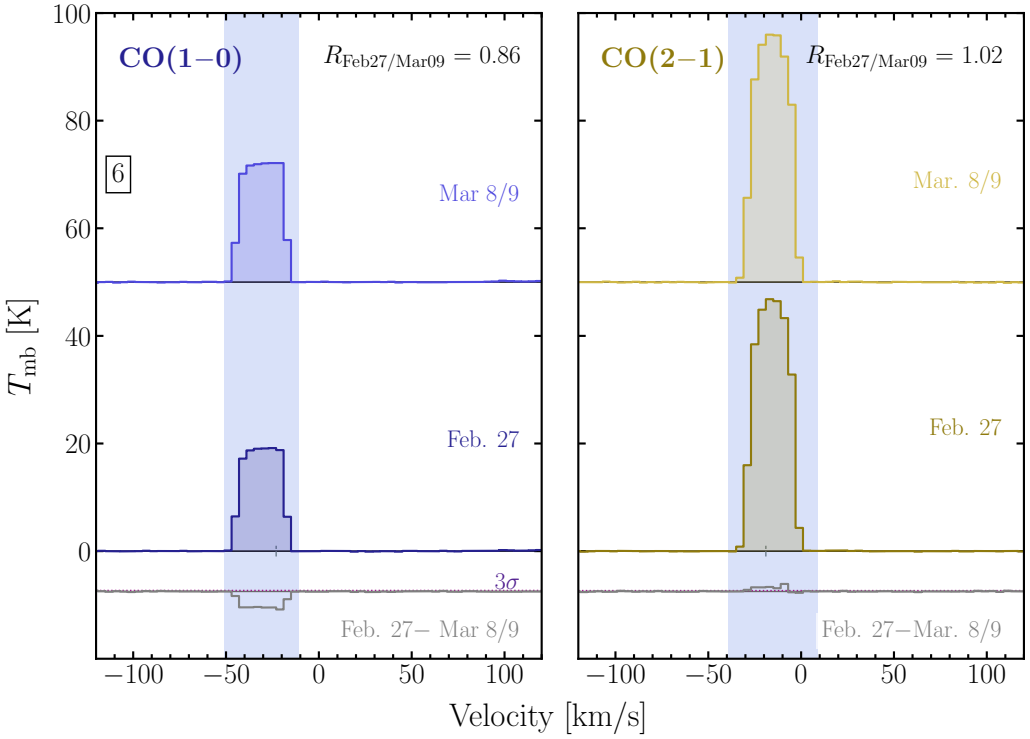

Figure 3.4: **Line Calibrator IRC+10216.** Comparison of the line calibrator's CO(1-0) and CO(2-1) emission. Residual shows the spectrum of the second night subtracted from the first night. The ratio between the two observations is given in each panel. In particular, the CO(1-0) emission differs by 14% between the two nights.

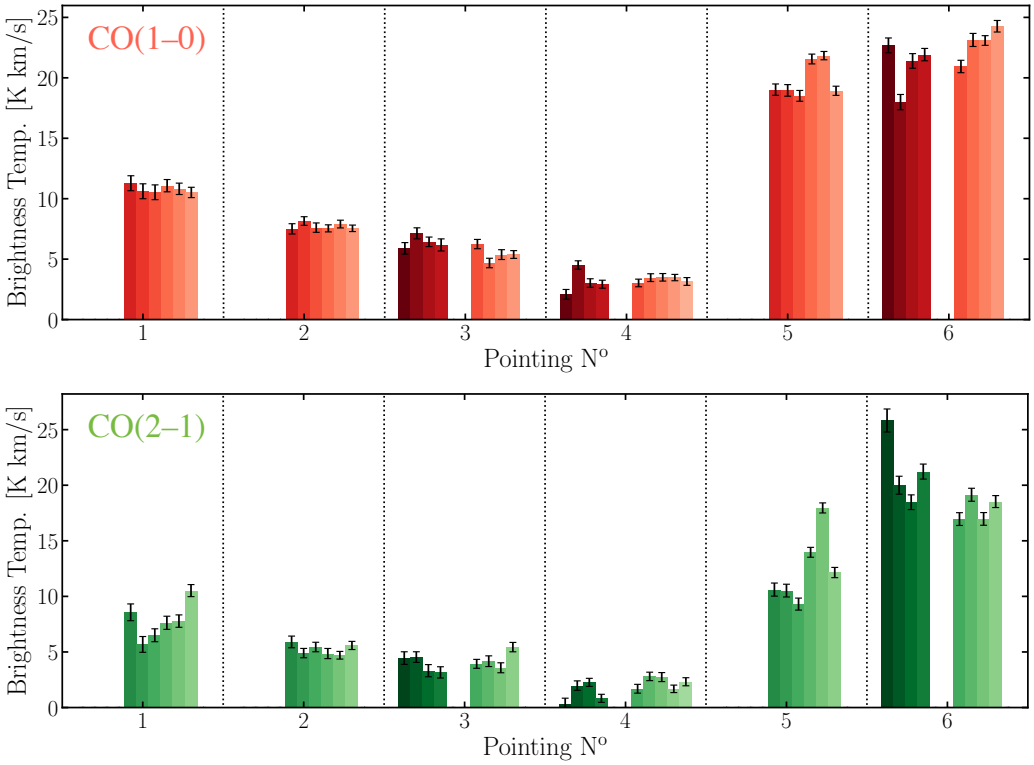

Figure 3.5: **Scan-by-Scan Variation.** We iterated through the different pointings several times. Consequently, we have for each pointings numerous scans. These panels show the comparison of the line intensity of our program for each individual scan (1 in darkest green/red, 11 in lightest green/red), separated by pointing number. The top panels show the CO(1-0) line intensity, and the bottom panels show the CO(2-1). Scan 1-4 are only taken for pointing 3, 4, and 6. Scan 5-6 are only taken for pointing 1, 2, and 5.

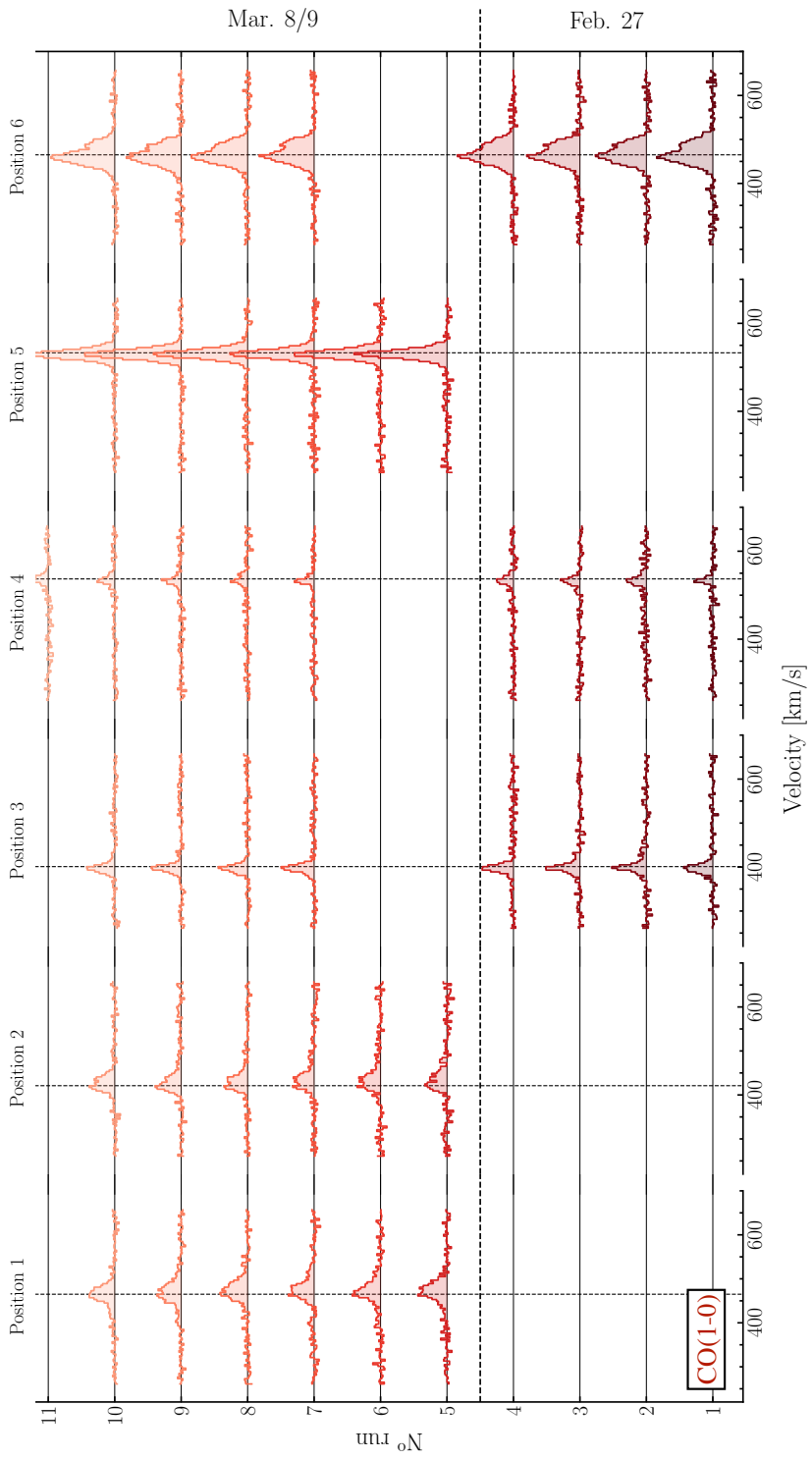

Figure 3.6: Individual CO(1-0) scans of the different pointings. On the first night, we only observed pointings 3, 4 and 6.

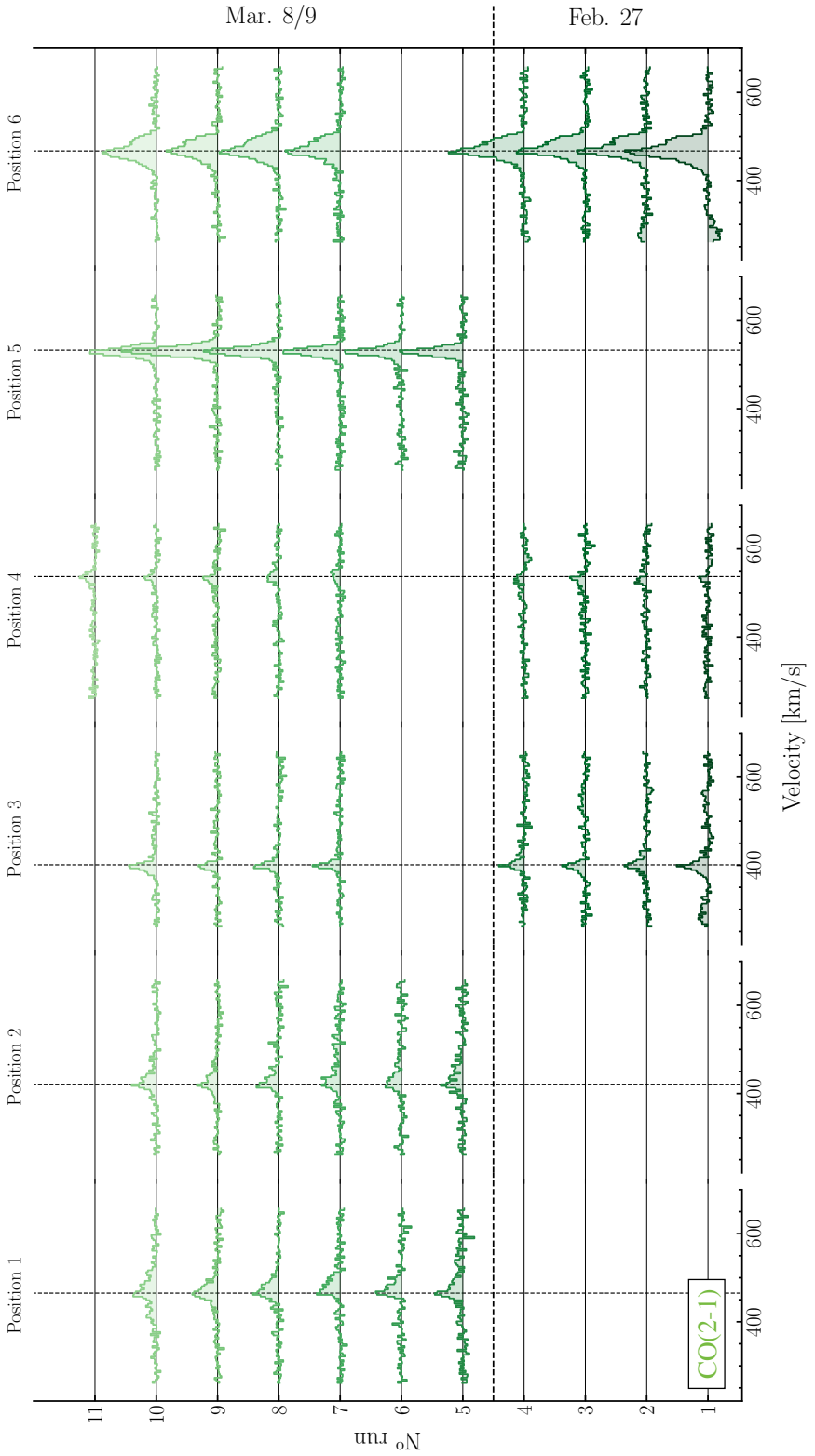

Figure 3.7: Individual CO(2-1) scans of the different pointings. On the first night, we only observed pointings 3, 4 and 6.

III) Elevation of the Telescope

The airmass of the observation changes with the elevation of the telescope's pointing direction. With decreasing angle, the source emission travels through a thicker layer of the atmosphere, hence increasing its impact on the resulting observation through absorption and scattering by turbulence cells. Also, the telescope's beam pattern will likely change with the elevation since gravitational stress will bend or stretch parts of the antenna to a small degree. The telescope's ideal source elevation that minimizes any such effects is at 45°. Our dataset can investigate whether there are any systematic trends in the measured CO brightness temperature with the source's elevation in the sky. In Figure 3.8, we plot the CO(1-0) and CO(2-1) intensities for all the individual scans (colored by the pointing number) versus the elevation of the source. The top panels show a trend with elevation for each pointing. In the bottom panel, we normalize by the average intensity of each pointing (i.e., the intensity of the spectrum of the combined scans for each pointing number, as in Figure 3.2). In addition, we bin the data to indicate any potential trend with the source elevation. No significant trends are seen for the CO(1-0) and the CO(2-1) line emission for any given pointing. Scan-by-scan variation from a different origin seems to dominate. Only the normalized CO(2-1) binned intensities seem to increase with the elevation slightly, but the scatter of ~20% remains dominant. We concluded that for our purposes, the performance of the telescope is not significantly affected by elevation changes.

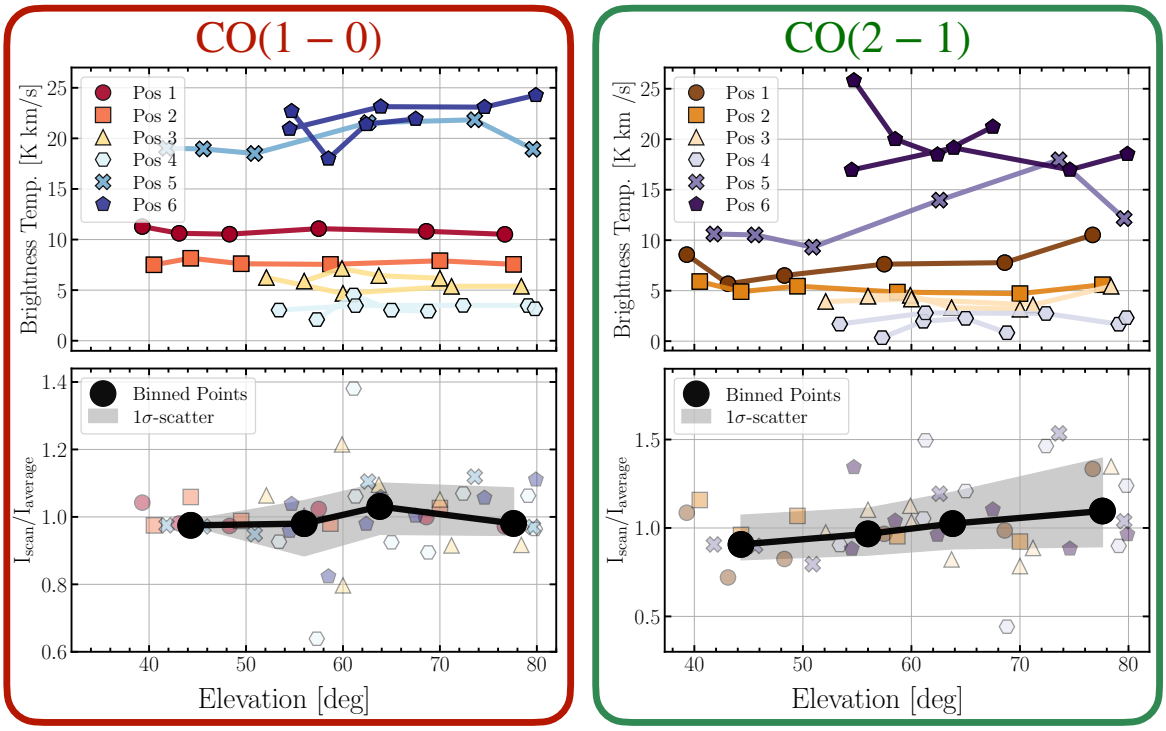

Figure 3.8: **Flux Calibration Stability with Elevation.** (*Top panels*) The intensity of the individual scans compared to the elevation pointing of the telescope. For pointing 3, 4, and 6, we have observations from two nights. (*Bottom panels*) Normalized intensities of the individual scans (i.e., divided by the brightness temperature of all scans of each pointing combined). We binned the data (black data points) to see any systematic trend with elevation. The left shows the CO(1-0) and the right the CO(2-1) data.

IV) Comparison to PAWS and CLAWS OTF Maps

Using a beam-size aperture, it is possible to create mock pointing observations with the OTF maps from PAWS for CO(1-0) and CLAWS for CO(2-1). We then compare them to the spectrum from the DDT program. The mock spectra are obtained by averaging over the lines of sight within the beam aperture of a given pointing. Comparing these simulated observations, we can check for consistency of the telescope's pointing and observations between the different projects. Figure 3.9 compares the integrated intensity from the extracted spectra and the DDT observations for the six different pointings. The bars indicate the line intensity ratio from the pointing to the mock observation $R_{\mathrm{E02\text{-}20/OTF}}$. There is a clear tendency that the CO(1-0) brightness temperature we observed as part of #E02-20 is systematically higher than that from PAWS (brown bar, by ~10-20%). Such a strong difference likely stems from a flux calibration issue that globally affects either the PAWS data cube or our CO(1-0) observations. Such a significant offset of the intensities between different observing programs will affect the accuracy of R_{21} line ratio studies (this will be further assessed in Chapter 4). In contrast, the #E02-20 pointing observations seem to slightly underestimate the CO(2-1) intensity compared to the CLAWS data (green bar; ~ 5%). As stated by IRAM, a difference of 5% is within the 10% expected from the general calibration uncertainty of the telescope.

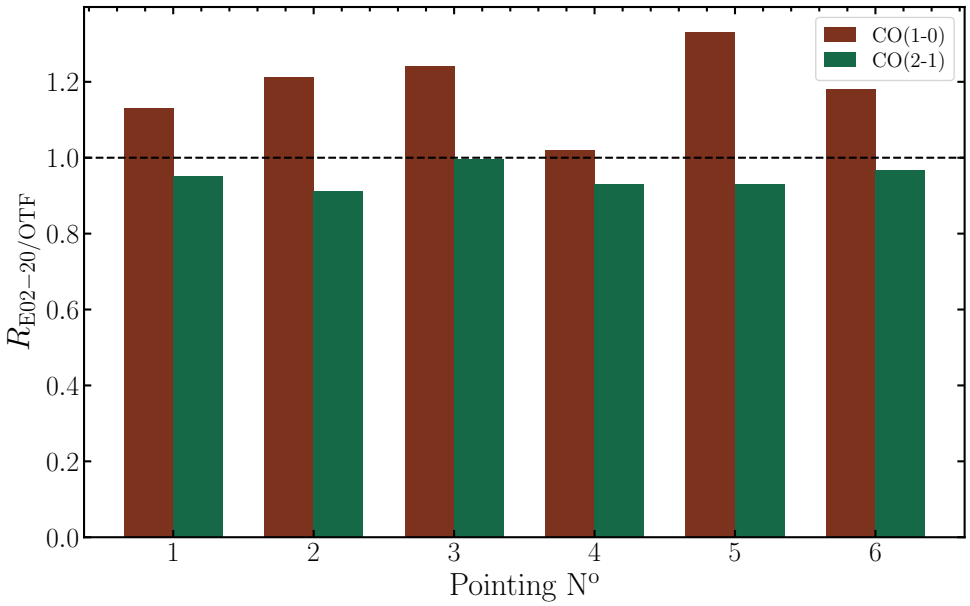

Figure 3.9: **Comparison of #E02-20 and OTF map Intensities.** The integrated intensity ratio from the #E02-20 program and PAWS (brown) or CLAWS (green). If the lines were exactly similar, we would expect a ratio of 1. We see that for CO(1-0), the #E02-20 program detects systematically brighter lines (by ~ 20%), while detected CO(2-1) emission is about 5% fainter than from the CLAWS mock emission.

V) Telescope Pointing Error Analysis

Another source of uncertainty is the pointing accuracy of the telescope itself. The accuracy is stated to be $<1''$ according to IRAM[3]. However, larger pointing offsets are found throughout the night after observing a point calibrator every ~1 h. We generally found a variation of $3''$ between iterative pointing calibrations. To investigate whether the difference in the measured line intensity between the two nights and the difference compared to PAWS/CLAWS can be explained by pointing error, we use the PAWS/CLAWS OTF maps and

[3] https://www.iram-institute.org/EN/content-page-58-7-55-58-0-0.html (06/16/2022)

shift around the aperture to create the mock spectra by 3" in each direction. With the help of these pointing simulations, we can look at how the line shape varies and see if this effect explains the differences. The result is shown in Figure 3.10 for pointing #6. The same method is applied to the other pointings. Generally, we see that the line intensity does only vary up to 10%. We thus conclude that a pointing error cannot fully explain the variation of up to 20%, which we find comparing the different scans (seen in Figure 3.9).

Furthermore, we looked at how the CO intensities vary if we displace the aperture by half-beam-sized steps (see Figure 3.11). For this analysis, we again use the PAWS CO(1-0) and CLAWS CO(2-1) OTF cubes, projected onto a hexagonal grid with half-beam spacing using the `PyStructure` (see Subsection 2.3.2). We performed this analysis for all six pointings (see the bottom panel for the illustration of the complete galaxy and the location of the individual pointings). In the top left panel, we look at the variation of CO(1-0) relative to the central pixel of our aperture. The color scale shows the variation of each pixel to the central pixel (indicated in green). We perform the same analysis for the CO(2-1) emission (illustrated in the top right corner of Figure 3.11. We see that already after about a beam-size displacement, the variation is of order >200% for CO(1-0) and CO(2-1). The bottom panels show the variation of the line ratio, R_{21}, when keeping either the CO(1-0) or CO(2-1) fixed (i.e. use the value of the central pixel, indicated in green). Again, we see that already quite fast, no further than a beam size separation from the center, we get significant variation in the CO line ratio value. We conclude that the pointing performance is more than sufficient for our purpose, and uncertainties related to the pointing accuracy cannot explain the discrepancies we see for the integrated line intensities when comparing different observing runs.

3.1.4 Conclusion – #E02-20 Project

This report provides an overview of several diagnostic plots that we use to analyze the IRAM 30m telescope's stability and performance. For that purpose, we used IRAM 30m DDT observations for six different pointing in the arm and interarm region of M51 as part of project #E02-20. The CO(1-0) and CO(2-1) spectra were observed simultaneously. This way, systematic uncertainties will minimize when looking at line ratios. We investigated different causes that could significantly affect the observed line intensities, such as line calibrator stability, source elevation changes, and the telescope's pointing accuracy. Furthermore, we complemented the #E02-20 dataset with spectra extracted from previous IRAM 30m OTF maps. We found significant scan-to-scan variation in certain instances, mainly in pointing 4, which showed the faintest CO emission line (scan-to-scan variation of order >50%). Furthermore, the different observing programs also showed systematic offsets of the line intensity of order 5% (for CO(2-1)) up to ~ 20% (for CO(1-0)), which, currently, we cannot account for. With our analysis, we can exclude issues with pointing accuracy or source elevation. The flux calibration stability can, however, vary up to 15%. One of the potential sources of inaccuracy remains error beam contribution, which affects the CO(1-0) and CO(2-1) lines differently. Overall, we suggest expecting an uncertainty of order ~15% when comparing data from different IRAM 30m observing runs. However, when studying ratios of lines observed at the same time by the same telescope, the uncertainty is likely at around ~5%.

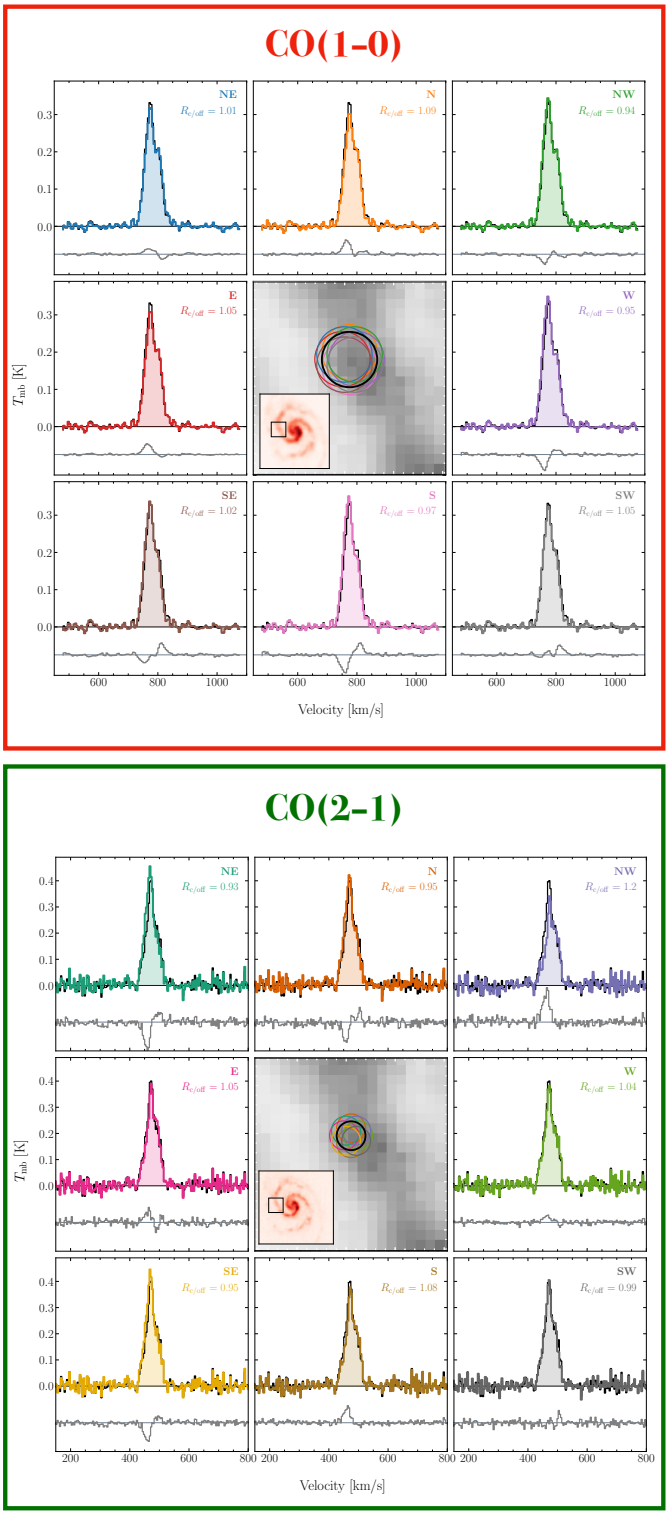

Figure 3.10: **Pointing Accuracy Analysis for Pointing 6** The spectra are extracted from the OTF maps (PAWS for CO(1-0) and CLAWS for CO(2-1). We shift the aperture around in various directions (indicated in the top right corner of each panel) by 3 arcsec. The black spectra shows the spectrum extracted from the central aperture and colored spectra shows the exctraction after shifting the aperture. The black circle and spectrum is the central pointing, the coloured ones indicate the offset apertures.

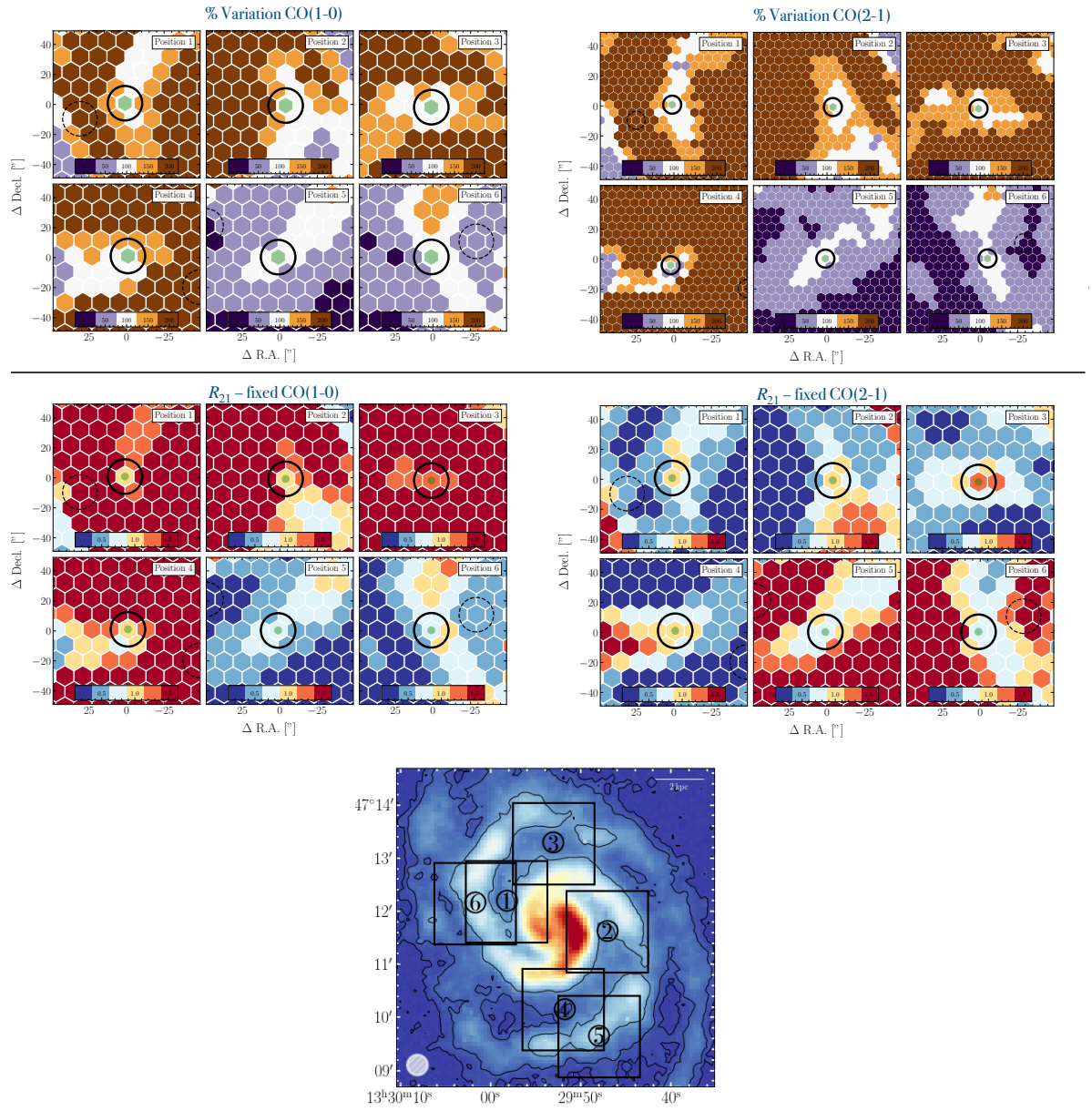

Figure 3.11: **PyStructure Pointing Accuracy Analysis.** (*Top Right*) Variation of the CO(1-0) intensity in percent, relative to the central pixel (indicated in green). (*Top Left*) Percentage Variation in CO(2-1). (*Center Left*) Variation of R_{21}. Each pixel shows it's CO(2-1) intensity divided by the CO(1-0) intensity of the central pixel (marked in green). (*Center Right*) Same, but with fixed CO(2-1). (*Bottom*) PAWS CO(1-0) intensity map illustrating the position of the six pointings.

3.2 Error Beam Analysis

As part of the general IRAM performance analysis, we also investigate ways to describe and correct emission contribution from the so-called error beams or side lobes. A precise correction requires a good understanding of the telescope's response pattern to external radiation. As discussed in Subsection 2.1.2, the beam pattern of the telescope can be separated into key components. Figure 3.12 shows a more detailed illustration of the beam pattern, $P(\theta, \phi)$, as a function of polar coordinates. The *main beam*, $\Omega_{\rm mb}$, is the component in the direction of the pointing of the telescope. In general, it holds most of the total observed power with respect to the other beam components. The width of the main beam characterizes the angular resolution of the instrument. Moreover, additional side lobes contribute a small fraction to the total received power. The width of both the main beam and error lobes scales with the observed frequency.

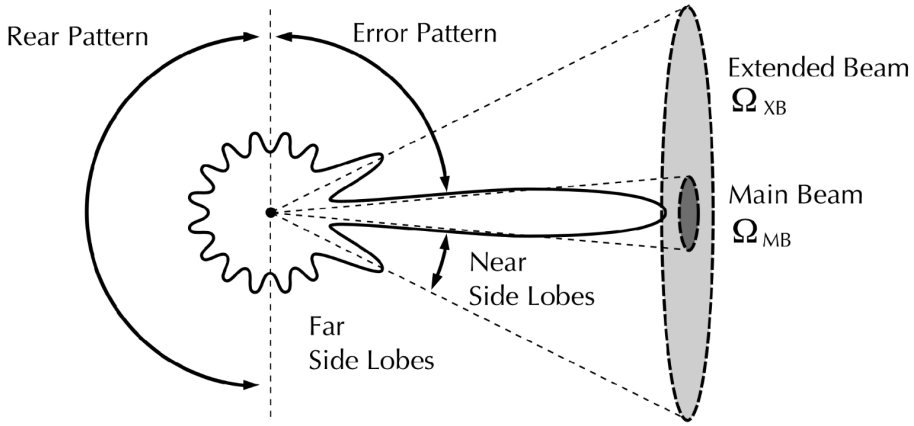

Figure 3.12: **Telescope Beam Pattern and Error Beams.** Image Credit: Figure taken from presentation by J. West, 2017 (https://www.atnf.csiro.au/research/radio-school/2017/lectures/west-single-dish-astronomy-2017.pdf)

Kramer et al. (2013) extensively studied and characterized the beam pattern of the IRAM 30m. The authors determined the beam shape of the telescope by measuring changes in total power scans across the limb of the Moon. The beam can be approximated with a set of 2D Gaussian shapes with different widths. In the case of the IRAM 30m telescope, a set of three error beam components is suggested to describe the full beam pattern. The three components each represent different degrees of distortions of the antenna or dish:

- **1st Component:** The gravitational bending of the full telescope dish leads to large-scale deformations. As a consequence, stray light enters the detection via the side lobes. Kramer et al. (2013) found that in 1997, the power contribution from this error component would vary significantly between different observations up to 25%. After upgrades to the dish, their latest observations from 2010 showed a more well-behaved performance with variations only at 5%. It is now possible to approximate the 1st error beam component using a 2D Gaussian with a frequency-dependent width.
- **2nd Component:** The dish of the telescope is fitted with reflecting panels. Misalignment of these panels leads to a larger side lobe.

- **3rd Component:** Inconsistencies and defects of the telescope dish panels themselves will lead to further side lobes with an even larger FWHM.

The full beam pattern of the 30m telescope with the different components is illustrated in Figure 3.13. At small angular distances from the telescope's pointing axis, the beam is dominated by the main beam component, but at larger angular distances, the different components contribute with varying impact.

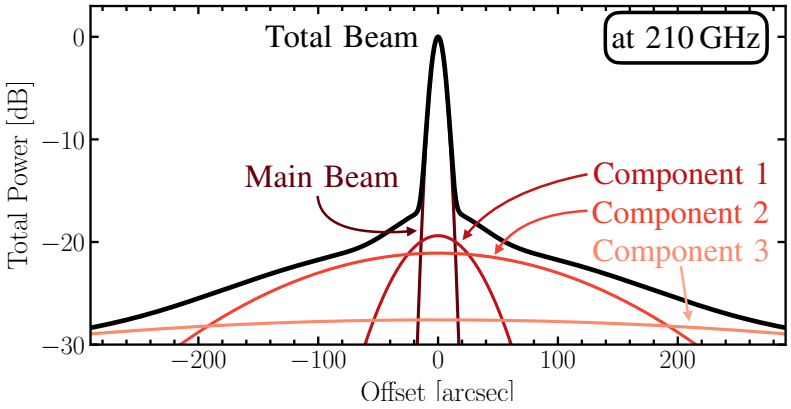

Figure 3.13: **IRAM 30m Telescope Beam at 210 GHz.** Telescope response curve to a point source. The beam parameter values are adopted from Kramer et al. (2013).

Past studies have investigated methods and techniques to describe and determine the contribution of the different error beam components (e.g., Garcia-Burillo et al., 1993; Bensch et al., 2001; Pety et al., 2013; Leroy et al., 2015). Such an analysis is also part of the thesis project described in Chapter 5 (den Brok et al., 2022). The following sections will go into more detail about the mathematical framework of the error beam correction. We focus specifically on IRAM 30m telescope since a prescription for the beam pattern by a set of 2D Gaussian profiles with varying widths exists.

3.2.1 Key Definitions and Notation

Our description of the error beam components and parameters follows the key definitions and notation by Kramer et al. (2013). A key source for the following error beam analysis is a private communication with and a summary manuscript written by A. Usero.

Beam Profile Parameters

- $\{G_i\}$, with $i = 0, 1, 2, 3$.
  We assume the beam is described by 2D Gaussian beam profiles G_i. The index of the main beam is $i = 0$. The Gaussian beam G_i is normalized ($\int_{\mathrm{sky}} G_i \mathrm{d}\Omega = 1$).

- $\{\theta_i\}$ and $\{\Omega_i\}$, with $i = 0, 1, 2, 3$.
  The beam component FWHM is described by the parameter θ_i. The corresponding solid angle is labeled with $\Omega_i \equiv \pi/(4 \log 2)\theta_i^2$.

- $\otimes$: The 2D convolution is indicated by this symbol.

- $\{\tilde{G}_i\}_{i>0}$ and $\{\tilde{\theta}_i\}_{i>0}$.
  Since we are interested in the error beam convolution, we deconvolve the main beam from the full beam profile. We indicate the 2D Gaussian kernel and the corresponding FWHM after deconvolution with $\tilde{G}_i$ and $\tilde{\theta}_i$. The following relation holds between the original and deconvolved kernel (for $i > 0$):

$$G_i \equiv \tilde{G}_i \otimes G_0 \qquad \text{with } \tilde{\theta}_i^2 \equiv \theta_i^2 - \theta_0^2 \tag{3.1}$$

- δ^{2D}
  The Dirac 2D distribution, which constitutes the unit element regarding 2D convolution with the following characteristics:

$$G_i = \delta^{2D} \otimes G_i \qquad \text{and} \qquad \int_{\text{sky}} \delta^{2D} \mathrm{d}\Omega = 1 \tag{3.2}$$

Beam Power and Efficiency Parameters
Note that some of the following parameters have already been defined in Subsection 2.1.2:

- F_{eff}: The forward beam efficiency which is defined as the ratio of the forward facing beam and the full antenna beam solid angle,

$$F_{\text{eff}} \equiv k_0 \frac{\Omega_{\text{F}}}{\Omega_A} = k_0 \left(\int_{\text{forward } 2\pi} P_n(\theta, \phi) \mathrm{d}\Omega \Big/ \int_{4\pi} P_n(\theta, \phi) \mathrm{d}\Omega \right), \tag{3.3}$$

  where k_0 indicates the resistive loss factor of the telescope (in Chapter 2 we consider $k_0 = 1$) and $P_n(\theta, \phi)$ the normalized 2D beam pattern.

- B_{eff}: The main beam efficiency is defined as the ratio of main beam solid angle over the antenna solid angle $B_{\text{eff}} \equiv k_0 \Omega_{\text{mb}} / \Omega_A$

- η_{rrs}: The rearward spillover and scattering efficiency. It is defined as the emission from the small positive lobes towards the backside of the antenna: $\eta_{\text{rrs}} \equiv 1 - F_{\text{eff}}$.

- $\{P_i'\}$: Set of beam component efficiencies. For the main beam (component $i = 0$), this is equal to the main beam efficiency: $P_0' = B_{\text{eff}}$.

- η_{fss}: The forward spillover and scattering efficiency. The forward beam efficiency is the sum of the beam component efficiencies as well as smaller scattering and spillover effects:

$$F_{\text{eff}} = \sum_{i=0}^{3} P_i + \eta_{\text{fss}} \tag{3.4}$$

- $\{P_i\}$: Set of relative beam component power (i.e. the integration over the Gaussian profile):

$$P_i \equiv \frac{P_i'}{\sum_{j=0}^{3} P_j'} \tag{3.5}$$

Since they describe the relative power contribution, the sum of the full set equals to 1:

$$\sum_{j=0}^{3} P_j = 1 \tag{3.6}$$

An important relation between the relative beam power and the beam efficiencies is the connection between the main beam efficiency to the sum of all beam efficiencies via:

$$\frac{B_{\text{eff}}}{P_0} = \sum_{j=0}^{3} P'_j \tag{3.7}$$

- $\{\epsilon_i\}$ for $i > 0$: Set of the relative beam component amplitudes, defined as

$$\epsilon_i \equiv \frac{P_i}{P_0} = \frac{P'_i}{B_{\text{eff}}} \tag{3.8}$$

The beam efficiency, power amplitude and widths were measured by Kramer et al. (2013) for the 30m telescope. Table 3.3 provides a summary of the key components and their values.

Table 3.3: Beam width and relative power for different frequencies as measured by Kramer et al. (2013)

	86 GHz, 3.49 mm		**145 GHz, 2.07 mm**		**210 GHz, 1.43 mm**		**280 GHz, 1.07 mm**	
	θ_i	P_i	θ_i	P_i	θ_i	P_i	θ_i	P_i
Main Beam	29″	0.87	16″	0.81	11″	0.72	8.4″	0.63
1st Error Beam	0	0	85″	0.02	65″	0.05	50″	0.04
2nd Error Beam	550″	0.07	350″	0.10	250″	0.13	175″	0.14
3rd Error Beam	2000″	0.06	1200″	0.07	860″	0.10	620″	0.19

Using cubic interpolation, we obtain the beam width and relative power for frequencies beyond the pivot frequencies in Table 3.3 at which the beam pattern was measured. Figure 3.14 shows the interpolation of the beam width and relative power. From the IRAM website[4], we obtain values for the beam efficiencies (see Table 3.4).

Table 3.4: **Beam Efficiencies for 30m Telescope.** Table adopted from Kramer et al. (2013)

Frequency	B_{eff}	P'_1	P'_2	P'_3	F_{eff}
86	81	0	7	6	95
115	78	1	8	6	94
145	73	2	9	6	93
210	63	4	11	9	94
230	59	4	11	11	92
280	49	3	11	15	87

[4] https://publicwiki.iram.es/Iram30mEfficiencies (06/18/2022)

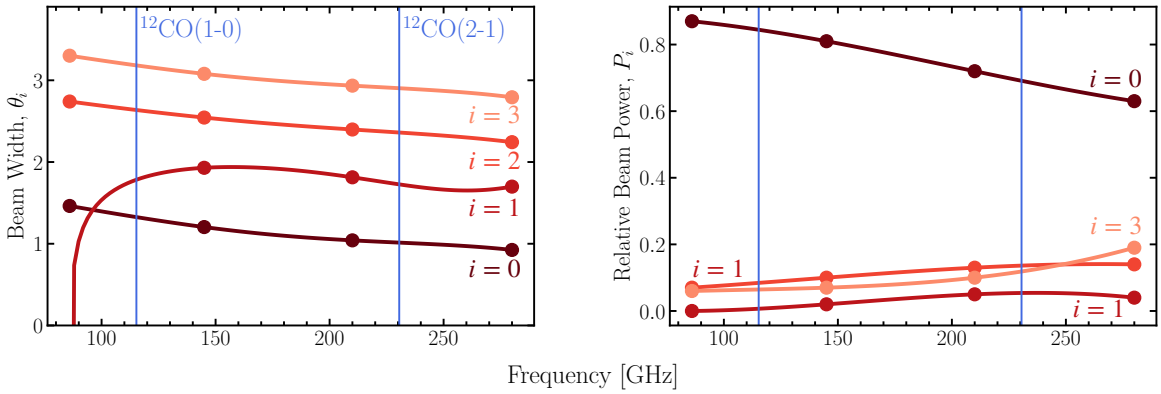

Figure 3.14: **Interpolated Beam Width and Relative Power.** Using cubic interpolation, the parameters can be extrapolated to frequencies other than the pivot points measured by Kramer et al. (2013) (see Table 3.3). The blue vertical lines indicate frequency of ^{12}CO(1-0) and ^{12}CO(2-1) emission at 115.3 GHz and 230.5 GHz respectively.

Brightness Temperature

- T_s: The source ideal brightness temperature distribution on the sky.
- T_A^*: The measured source brightness temperature in the sky. Because of instrumental effects, this constitutes a convolution of the actual (ideal) source brightness temperature with the full beam pattern following:

$$T_A^* = M \times \frac{1}{F_{\text{eff}}} \underbrace{\left(\sum_{i=0}^{3} P_i' \cdot G_i \right)}_{=\tilde{K}} \otimes T_s \tag{3.9}$$

  Here, M indicates a 2D mask that defines the boundaries of the map (i.e., states whether a line of sight on the full sky is inside or outside of the map). The term $\tilde{K}$ defines the so-called convolution kernel. Equation 3.9 can be rewritten in a more useful from using the relations between the different beam efficiencies:

$$T_A^* = M \times \frac{B_{\text{eff}}}{F_{\text{eff}}} \left(G_0 + \sum_{i=1}^{3} \epsilon_i \cdot G_i \right) \otimes T_s \tag{3.10}$$

- T_{mb}: The main beam temperature, as defined already in Subsection 2.1.2: $T_{\text{mb}} = (F_{\text{eff}}/B_{\text{eff}})T_A^*$.
- $\hat{T}_{\text{mb}}$: The *error beam free* main beam temperature. When assessing errorbeam contribution, we compare T_{mb} and $\hat{T}_{\text{mb}}$. It is defined as

$$\hat{T}_{\text{mb}} \equiv G_0 \otimes T_s \tag{3.11}$$

  Combining this equation with Equation 3.10, we can decompose the main beam temperature in the

error beam free component and the error beam contribution:

$$T_{\rm mb} = M \times \left(\hat{T}_{\rm mb} + \underbrace{\left(\sum_{i=1}^{3} \epsilon_i G_i \right) \otimes T_{\rm s}}_{\text{errb. contribution}} \right) \tag{3.12}$$

where the second term indicates error beam contribution (labeled as errb. contribution). This equation thus indicates that using the general form of the main beam temperature, one likely overestimates the true brightness temperature of the source by a factor of $1/P_0$ (for an infinitely large map). Generally, the true difference is likely smaller because we are dealing with maps of a limited extent. However, since the relative main beam power decreases with frequency (see Figure 3.14, right panel), it means that higher frequency observations are more affected by error beam effects.

3.2.2 Deconvolution with the Main Beam

Since the beam components can be approximated with 2D Gaussian profiles that are well behaved, we can deconvolve the main beam from the full beam kernel. This gives us a cleaner way of separating out the error beam contribution. After deconvolution with the main beam G_0, we can write Equation 3.12 in the form of

$$T_{\rm mb} = M \times \left(\delta^{\rm 2D} + \sum_{i=1}^{3} \epsilon_i \tilde{G}_i \right) \otimes \hat{T}_{\rm mb} \tag{3.13}$$

By deconvolving this expression, we have a way of deriving the error beam free brightness temperature term $\hat{T}_{\rm mb}$ from the measured main beam temperature . We can simplify the expression by (i) assuming that the beam size is smaller than the extent of the map, thus dropping the M term, and (ii) defining the kernel $K \equiv \sum_{i=1}^{3} \epsilon_i \tilde{G}_i$:

$$T_{\rm mb} = \left(\delta^{\rm 2D} + K \right) \otimes \hat{T}_{\rm mb} \tag{3.14}$$

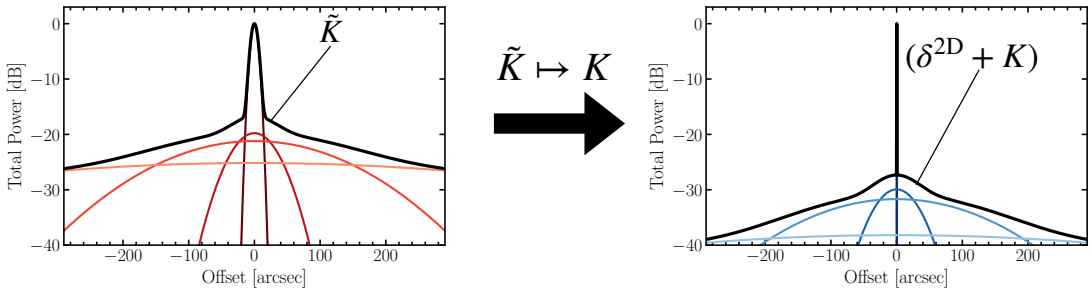

Figure 3.15: **Kernel Convolution for Beam at 210 GHz.** Converting the standard beam kernel $\tilde{K}$ to the kernel after devonvolution with the main beam, K. In relative units of dB.

3.2.3 Methods of Estimating Error Beam Contribution

We discuss and compare two different methods to deconvolve Equation 3.14 and extract the error beam free main beam temperature, $\hat{T}_{\mathrm{mb}}$.

1. **Direct Solution: Fourier Transform Deconvolution**

   We define the 2D Fourier transform, $\mathcal{F}$, of a function or map, $f(x, y)$, by the equation:

   $$\mathcal{F}(f)(u, v) = \int_{-\infty}^{\infty} \int_{-\infty}^{\infty} f(x, y)^{-2\pi i(ux+vy)} \mathrm{d}x\mathrm{d}y \tag{3.15}$$

   Introducing the Fourier transform in the context of the error beam analysis is helpful since, according to the *convolution theorem*, under suitable conditions, a convolution of two functions can be treated as a point-wise multiplication in the Fourier space:

   $$f \otimes g(x, y) = \mathcal{F}^{-1}\Big(\mathcal{F}(f)(u, x) \times \mathcal{F}(g)(u, x)\Big)(x, y) \tag{3.16}$$

   Applying the Fourier transformation onto Equation 3.14, we obtain[5]

   $$\mathcal{F}(T_{\mathrm{mb}}) = (1 + \mathcal{F}(K)) \times \mathcal{F}(\hat{T}_{\mathrm{mb}}) \tag{3.17}$$

   We can solve for the error beam free brightness temperature, which yields the following expression:

   $$\boxed{\hat{T}_{\mathrm{mb}} = \mathcal{F}^{-1}\left(\frac{1}{1 + \mathcal{F}(K)} \cdot \mathcal{F}(T_{\mathrm{mb}})\right)} \tag{3.18}$$

   Since the Kernel K is a sum of Gaussian profiles, we can find a simple form of its Fourier transform. The term $1/(1 + (F)(K))$ can be expressed as:

   $$\frac{1}{1 + \mathcal{F}(K)} = \frac{1}{1 + \sum_{i=1}^{n} \epsilon_i \mathcal{F}(\tilde{G}_i)} = \frac{1}{1 + \sum_{i=1}^{n} \epsilon_i e^{-\pi\tilde{\Omega}_i(u^2+v^2)}} = \begin{cases} \frac{1}{1+\sum_{i=1}^{n} \epsilon_i} = P_0 < 1 & u, v \ll 1 \\ \approx 1 & u, v \gg 1 \end{cases} \tag{3.19}$$

   Consequently, the full term on the right side, of which we have to take the inverse Fourier transform, is generally well defined and does not diverge to infinity for small or large spatial frequencies u and v.

2. **Iterative Solution: Truncated Series**

   An alternative approach is iteratively subtracting the map convolved with the error beam kernel K from the original map. The method is similar to the technique applied by Leroy et al. (2015). The following recursive formula captures the idea:

   $$T_{\mathrm{mb}|N} = T_{\mathrm{mb}} - K \otimes T_{\mathrm{mb}|N-1} \tag{3.20}$$

   where $T_{\mathrm{mb}|N}$ describes the N^{th} iteration approximation of the main beam brightness temperature,

[5] Note that $\mathcal{F}(\delta^{2\mathrm{D}}) = 1$

with $T_{\mathrm{mb}|0} \equiv T_{\mathrm{mb}}$. The formula can also we expressed in an explicit form:

$$T_{\mathrm{mb}|N} = \begin{cases} T_{\mathrm{mb}} & N = 0 \\ \left(\delta^{\mathrm{2D}} + \sum_{s=1}^{N} (-K)^s\right) \otimes T_{\mathrm{mb}} & N > 0 \end{cases} \tag{3.21}$$

In the equation, we define $(-K)^s \equiv \underbrace{(-K) \otimes \ldots \otimes (-K)}_{s \text{ times}}$. With increasing N, we improve the characterization of the the difference between the approximate solution $T_{\mathrm{mb}|N}$ and the exact one $\hat{T}_{\mathrm{mb}}$. Generally, the iteration converges with $\lim_{N\to\infty} T_{\mathrm{mb}|N} = \hat{T}_{\mathrm{mb}}$.

We can derive the expression for the iterative approach mathematically using the geometric series expansion:

$$1 + \sum_{s=1}^{N} (-x)^s = \frac{1 - (-x)^{N+1}}{1 + x} \tag{3.22}$$

If we convolve the factor $\left(\delta^{\mathrm{2D}} + \sum_{s=1}^{N} (-K)^s\right)$ onto both sides of Equation 3.14, we get

$$\left(\delta^{\mathrm{2D}} + \sum_{s=1}^{N} (-K)^s\right) \otimes T_{\mathrm{mb}} = (\delta^{\mathrm{2D}} - (-K)^{N+1}) \otimes \hat{T}_{\mathrm{mb}} \tag{3.23}$$

Combining the equation with Equation 3.20 yields an expression for the iterative solution in terms of the error beam free main beam temperature:

$$T_{\mathrm{mb}|N} = \hat{T}_{\mathrm{mb}} - \left((-K)^{N+1} \otimes T_{\mathrm{mb}}\right) \tag{3.24}$$

The precise condition for converges can be determined from integrating both sides of Equation 3.24 over the whole sky:

$$\int_{\mathrm{sky}} T_{\mathrm{mb}|N} \mathrm{d}\Omega = \left(\int_{\mathrm{sky}} \hat{T}_{\mathrm{mb}}\right) \times \left(1 - (-1)^{N+1} \left(\frac{1 - P_0}{P_0}\right)^{N+1}\right) \tag{3.25}$$

where we used the relation $\int_{\mathrm{sky}} K \mathrm{d}\Omega = (1 - P_0)/P_0$. As long as $P_0 > 0.5$, the iterative approach will converge towards the error beam free emission. This is equivalent to the condition, that the majority of the power stored in the full beam must be from the main beam.

3.2.4 Application and Comparison of Error Beam Estimation

The previous section described two different approaches that can be used to estimate the error beam free main beam temperature $\hat{T}_{\mathrm{mb}}$. The following section will investigate error beam contribution for CO(1-0) and CO(2-1) line emission respectively within the six pointings presented in Section 3.1 (see Figure 3.1). The contribution of the error beam for the different pointings is analyzed as part of the CLAWS project (Chapter 5; den Brok et al. 2022). Here, I will complement my previous analysis and focus on (i) the performance of the two approaches and (ii) if both techniques converge to the same error beam free main

beam temperature $\hat{T}_{\mathrm{mb}}$. Note that there are two important caveats regarding the following analysis:

1. The methods of the error beam analysis so far discuss 2D convolution. In our analysis, we are working with 3D data cubes. Therefore, we are also dealing with a spectral axis. When convolving and deconvolving, we perform the operation channel-by-channel. Hence, we ignore any line-spread effects. The error beam affects the spatial scales dominantly, so the channel-by-channel approach is still valid.

2. The error beam is not constant but can vary significantly with deformations of the telescope (e.g., due to gravitational bending when the telescope is moving into another position). Performing the error beam analysis can only provide a qualitative assessment of the impact on the resulting flux measurement. Quantitative results should be interpreted cautiously and should be seen as upper limits.

Convergence of Iterative Approach

The iterative approach technique estimates the error beam free main beam temperature by iteratively convolving the error beam kernel. Figure 3.16 shows the relative difference of the $T_{\mathrm{mb}|N}$ values between iteration steps n and $n+1$ for CO(1-0) and CO(2-1) respectively. We see that in both cases, the series converges. Each iteration decreases the difference below a predefined threshold (in the example set at 10^{-5}). The convergence is slightly slower for the CO(2-1) map. This is because P_0 decreases with increasing frequency. So at higher frequencies, the error beams will hold an increasing fraction of the total power, thereby increasing their contribution.

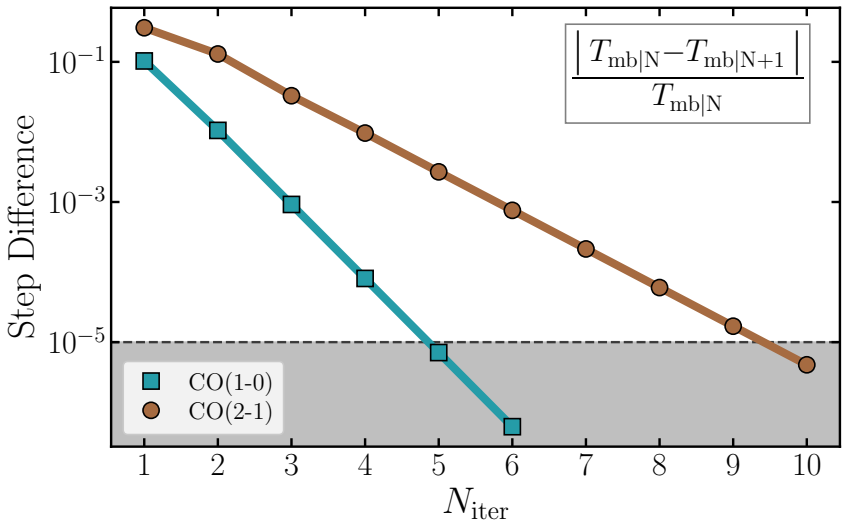

Figure 3.16: **Convergence of Iterative Approach.** The iterative main beam temperature converges for both the CO(1-0) and CO(2-1) intensity maps. The grey area shows the threshold of a difference of 10^{-5}. Since P_0 is smaller for the CO(2-1) line, it converges slower. This is due to the error beams holding a slightly more significant power fraction than at the CO(1-0) emission line frequency.

In the case of our CO(1-0) and CO(2-1) map, we see that we have reached the predefined threshold already after a small number of iterations. This means that the method can be implemented quite efficiently.

Comparing the Different Methods

We compare the results from both error beam estimation techniques as a consistency check. We expect the result to converge to the same error-free main beam temperature in the case of a good performance. Figure 3.17 compares the error beam contribution using both methods. The example is for a CO(2-1) spectrum in the interarm region in M51. The analysis is performed using the spectra extracted from a beam-sized aperture of 12″ diameter around Pointing 1 (see Figure 3.1).

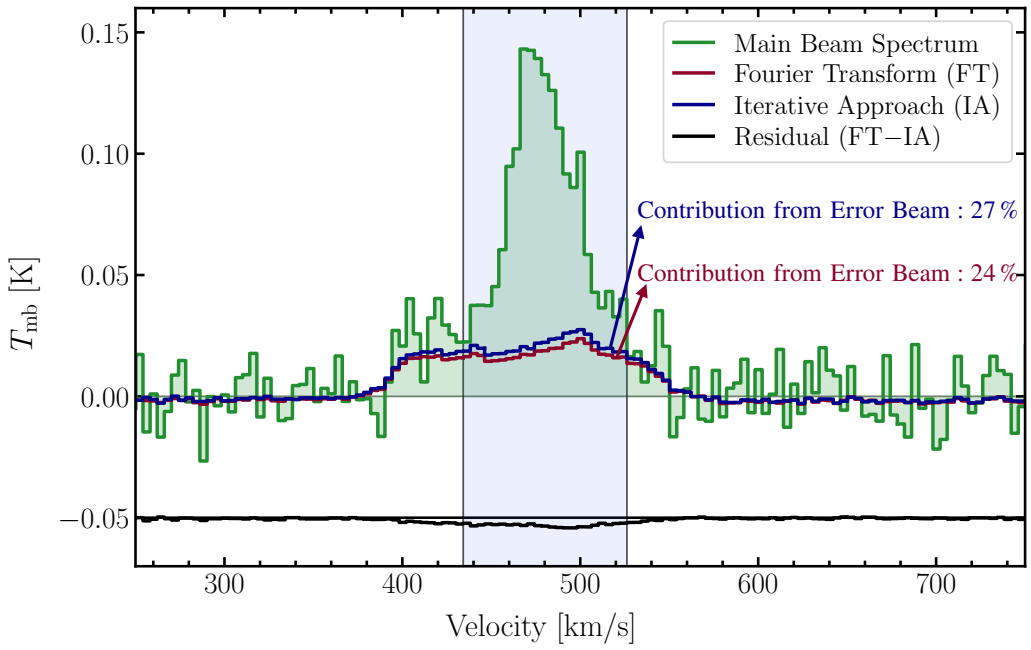

Figure 3.17: **Comparing Error Beam Contribution to CO(2-1) using two Different Methods.** The green spectrum is extracted from a beam-sized aperture (12″) at Pointing #1. The red line shows the contribution of the error beam determined using the Fourier transform technique. Within the masked region, the contribution constitutes 24% of the total intensity. The blue line shows the contribution estimated using the iterative approach. It yields a slightly higher contribution of 27%. The residual comparing the result from both methods is indicated and shifted down by 0.05.

The error beam contribution is estimated by integrating the emission within a given mask (shaded in blue in Figure 3.17) and comparing what fraction can be attributed to the error beam. Both methods show a similar amount of error beam contribution. In the example above, the contribution we obtain with the iterative approach is slightly higher with a fraction of 27% of the total intensity. In contrast, the Fourier transform method yields a contribution estimate of 24%. Such minor discrepancies are likely linked to the initial assumptions and simplifications of both methods. For instance, we neglected the effect of limited map size in the formulas. And the Fourier Analysis might also slightly suffer from the fact that the 3rd error beam component leads to large-scale convolutions, which are not captured anymore within a limited map size. Overall, however, both methods agree within a margin of a few percentage points, also for the other pointings in M51. We refer the reader to the paper presented in Chapter 5 for the complete set of error beam estimations across M51.

3.2.5 Conclusion – Error Beam Analysis

The error beam analysis shows that contributions from the side lobes are not negligible for single dish observations. Since the total power held in the side lobes increases with the frequency, the contribution will also increase for lines at shorter wavelengths. Consequently, the CO(2-1) line is more heavily affected than the CO(1-0) emission line. Furthermore, the effect is more prominent when looking at fainter regions embedded in brighter ones (e.g., the interarm region). However, accurately quantifying the impact is challenging because the error beam is not constant but changes with varying telescope conditions. We perform the preceding analysis only for IRAM 30m data, where the beam shape has been mapped extensively for different frequencies. Other telescopes are also affected by error beam contribution. However, performing the error beam analysis without an accurate (first-order) estimation of the entire beam pattern is infeasible. For example, we expect that observations of M51 using the 45m NRO telescope will also be affected by error beam contribution. The main beam efficiency is smaller for the NRO telescope, and we expect that gravitational bending will cause even more significant deformations due to the larger size of the telescope dish than the IRAM 30m telescope. So we expect NRO observations to suffer more significantly from error beam contribution. But without beam pattern estimates, we cannot quantify the exact extent. For the IRAM 30m telescope, we generally conclude from our error beam analysis that particularly the faint regions embedded in bright spiral arms might suffer ~20%.

CHAPTER 4

EMPIRE CO(2–1)/(1–0) Line Ratio

New constraints on the ^{12}CO(2-1)/(1-0) line ratio across nearby disc galaxies
J. den Brok, D. Chatzigiannakis, F. Bigiel, J. Puschnig, A. Barnes, A. Leroy, M. Jiménez-Donaire, A. Usero, E. Schinnerer, E. Rosolowsky,C. Faesi, K. Grasha, A. Hughes, J. M. D. Kruijssen, D. Liu,L. Neumann, J. Pety, M. Querejeta, T. Saito, A. Schruba, S. Stuber,
2021, MNRAS, 504, 3

Overview

The ^{12}CO emission line has become a workhorse tracer of the bulk molecular gas mass and distribution in and across nearby spiral galaxies (see description and discussion in Section 1.4). In recent years, several large surveys have been undertaken to systematically observe, in particular, the higher-J CO(2-1) emission line. Especially with ALMA, observing the CO(2-1) line is faster by a factor ~2 than mapping CO(1-0) due to the line's brightness, its higher frequency and the efficiency of Band 6 coverage of the instrument. In an attempt to benchmark variations of the $R_{21} \equiv$ CO(2-1)/CO(1-0) line ratio with environments across and within different galaxies, we employ data from various kpc-scale millimeter wavelength surveys. At an angular resolution of $26''$ (corresponding to ~1-2 kpc in physical distance), resolved variation across the individual galaxies can be studied. The combined dataset of CO(2-1) and CO(1-0) includes large program observations from the IRAM 30m telescope (from EMPIRE, HERACLES, PAWS, and CLAWS) and the ALMA telescope (from PHANGS survey). A goal is to find a prescription for R_{21} variation without the need to observe both CO transitions. Thereby, also future studies will benefit from constraints on R_{21} across the nearby galaxy population.

This work was published at MNRAS in 2021. The paper den Brok et al. (2021) is provided in its entirety in original form in Appendix A. The following sections provide an overview and summary of the main science points. These consist and focus exclusively on my own contributions to the paper. This includes the assessment of R_{21} variation across and within the individual galaxies, the correlation with other galactic properties, such as the SFR surface density or CO intensity, and the cross-comparison to check the robustness of R_{21} measurements when substituting the data from different observing programs.

4.1 The EMPIRE Survey

For this study, we select nine nearby massive star-forming galaxies that all are part of the EMIR Multi-Line Probe of the ISM Regulating Galaxy Evolution (EMPIRE; Bigiel et al., 2016; Jiménez-Donaire et al., 2019) survey. EMPIRE is a 30m telescope large program with more than 500 h observing time to target high molecular density tracers along with ^{12}CO and its isotopologues ^{13}CO and C^{18}O in the 3mm window (at a frequency of ~100 GHz). The survey's primary scientific motivation is to investigate how the dense gas fraction correlates to the environment within and among nearby galaxies. Hence, high-density tracers, such as CN(1–0), HCO$^+$(1–0), and HNC(1–0), were targeted. The CO(1-0) line is also targeted to obtain total molecular gas mass and distribution estimates.

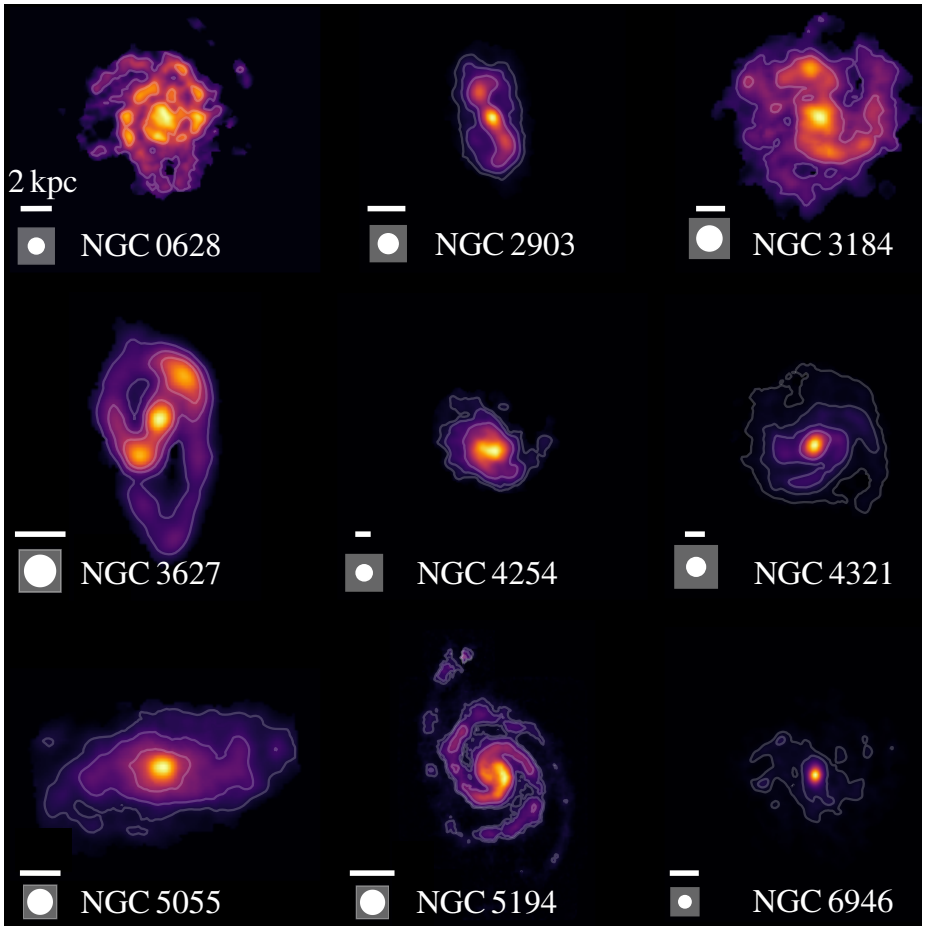

Figure 4.1: **EMPIRE Survey Sample of Galaxies.** Color scale and contours indicate the CO(1-0) intensity at different arbitrary scales for each galaxy to help illustrate morphological features. The circle at the lower left side of each galaxy indicates the angular resolution of 26″. The white line above each beam size indicates a physical distance of 2 kpc. The CO intensity maps are computed and provided as part of the EMPIRE public data release (Jiménez-Donaire et al., 2019).

Figure 4.1 illustrates the nine nearby star-forming galaxies that make up the EMPIRE sample. These sources all are well-resolved galaxies that are nearby (D~10 pc) and face-on ($i \leq 60^\circ$). These selection criteria ensure that the molecular gas will be bright enough to obtain significant detection of dense gas

tracers. Furthermore, the galaxies span a broad range of physical properties and morphological as well as dynamical features. For instance, the SFR surface density range is a full order of magnitude with around $3 - 20 \times 10^{-3}$ $M_\odot$ yr^{-1} kpc^{-2} (see Table 4.1). In addition, the different galaxy morphologies and environments include, (i) clearly resolved spiral arms (in NGC 0628, 2903, 3184, 3627, 5194, and 6946), (ii) barred galaxies (NGC 2903 and 3627), (iii) nuclear burst galaxies (NGC 2903, 4321, 6946), (iv) or interacting galaxies (NGC 3627, 4254, and 5194). As such, this sample can act as a useful template for extrapolations to the wider nearby galaxy population.

Besides millimeter observations from the EMPIRE survey and ALMA, we can rely on various multi-wavelength datasets from different surveys. As such, a wealth of ancillary data makes it possible to assess potential drivers of line ratio variation by comparing trends with, e.g., the SFR surface density or the dust mass or temperature.

4.2 Line Ratio Variation

R_{21} is the ratio of the two lowest rotational transitions of the primary CO molecule. These are among the brightest mm lines that are observable in nearby galaxies. Main physical drivers of R_{21} variation are changes in temperature, density, and opacity of the gas (Sakamoto et al., 1994; Sakamoto et al., 1997; Peñaloza et al., 2017; Peñaloza et al., 2018). Studies of the line ratio in the Milky Way (e.g., Hasegawa et al., 1997; Yoda et al., 2010) or within individual galaxies (Eckart et al., 1990; Lundgren et al., 2004; Koda et al., 2012; Vlahakis et al., 2013; Law et al., 2018) exist. These studies indicated, for example,

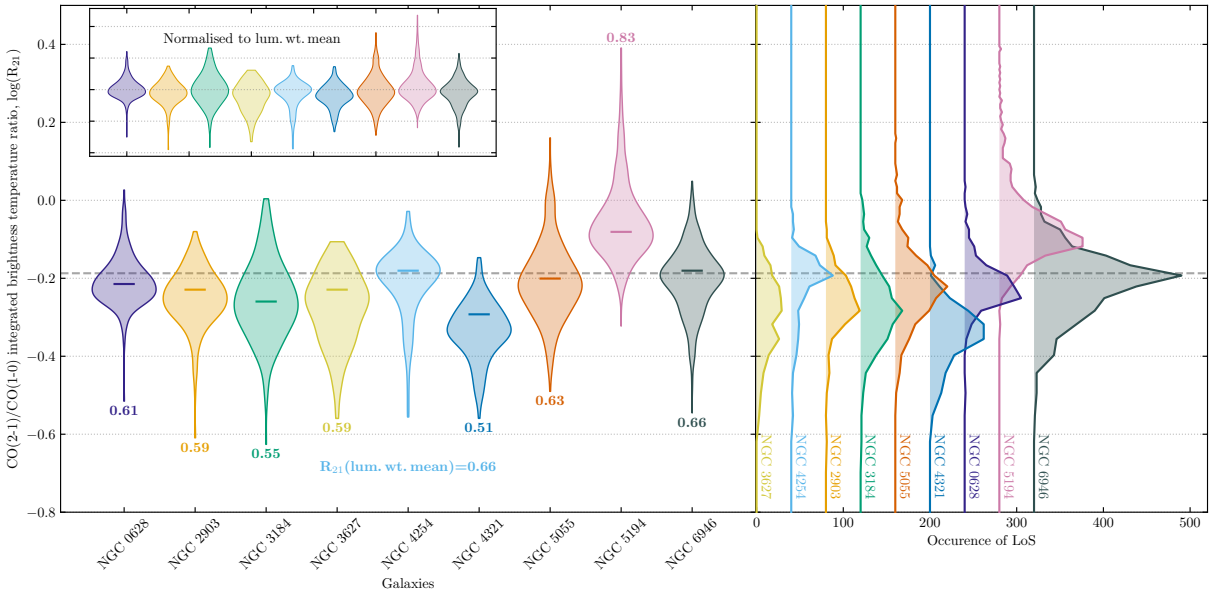

Figure 4.2: **Histogram of R_{21} distribution per galaxy**. (*left panel*) Violins indicate the log(R_{21}) distribution for the individual galaxies. For these histograms, only sightlines with S/N > 3 detection for both lines are considered. The colored horizontal bar inside each violin indicates the *luminosity-weighted mean* R_{21} (*inset panel*) Normalized log(R_{21}) violin histograms for each galaxy. (*right panel*) Histogram instead of violin plot of log(R_{21}) distribution. The dashed grey line across all panels indicates the area-weighted line ratio of $\langle R_{21} \rangle = 0.65$ across the full sample. Figure taken from den Brok et al. (2021).

Table 4.1: EMPIRE galaxies, their properties and intensity-weighted R_{21} measurements (adopted from den Brok et al. 2021).

Galaxy	Distance [kpc]	$M_\star$ [$10^{10}\,M_\odot$]	$\langle\Sigma_{\rm SFR}\rangle$ [$10^{-3} M_\odot\,{\rm yr}^{-1}\,{\rm kpc}^{-2}$]	R_{21}
NGC 0628	9.0	1.0	4.0	$0.61^{+0.06}_{-0.06}$
NGC 2903	8.5	1.3	5.7	$0.59^{+0.11}_{-0.07}$
NGC 3184	13.0	1.6	2.8	$0.55^{+0.09}_{-0.09}$
NGC 3627	9.4	3.2	7.7	$0.59^{+0.12}_{-0.11}$
NGC 4254	16.8	3.2	18	$0.66^{+0.05}_{-0.05}$
NGC 4321	15.2	4.0	9.0	$0.51^{+0.09}_{-0.07}$
NGC 5055	8.9	3.2	4.1	$0.63^{+0.09}_{-0.09}$
NGC 5194	8.4	3.2	20	$0.83^{+0.08}_{-0.09}$
NGC 6946	7.0	3.2	21	$0.66^{+0.07}_{-0.08}$

Note: The galaxy's average SFR surface density is measured by Leroy et al. (2013). The galaxy's integrated stellar mass is derived from 3.6 μ m emission by Dale et al. (2007) and Dale et al. (2009).

that changes of R_{21} are connected to decreasing gas densities within clouds, or increased gas temperature toward the center of galaxies, as expected from theoretical considerations.

We find an average (intensity weighted) line ratio and 16$^{\rm th}$–84th percentile range across all EMPIRE galaxies of $\langle R_{21}\rangle = 0.64^{+0.09}_{-0.09}$. However, we also see significant changes within and among the different galaxies. To describe trends, we rely on spectral line stacking (see Subsection 2.3.3) to improve the quantification of any potential trends in the data and recover the detection toward the outer region of the galaxies.

Galaxy-to-Galaxy Variation: We find significant offsets between the average R_{21} values for the different galaxies by around 0.2 dex. This is of a similar order to the internal trends that some of the galaxies show. The offsets are also apparent in Figure 4.2 by the violins, or in Figure 4.3, as the trend lines for the different galaxies are clearly shifted with regard to each other toward smaller or higher line ratios. However, we do not find any clear global galaxy property, such as stellar mass, SFR, metallicity, inclination, distance, and morphological type, that accurately predicts or correlates with the global R_{21} value. The observed galaxy-to-galaxy scatter strongly demands a high quality of the observations used. Since the observed dynamical range of R_{21} is small (~0.3 dex full scatter of all sightlines), a high signal-to-noise ratio and high precision absolute flux calibration are needed to improve our understanding of R_{21} variation.

Radial Trends: Already past line ratio studies of individual galaxies or the Milky Way found an enhancement of the value toward the center (e.g., Eckart et al., 1990; Braine and Combes, 1992; Saito et al., 2017; Koda et al., 2020). Figure 4.3 shows the radial trends for the individual galaxies from the EMPIRE sample. The line ratio can clearly be seen to increase by 10−15% within the central 2 kpc with respect to the galaxy-wide average value. Saito et al. (2017) found that models based on RADEX yield a radial kinetic temperature gradient toward the center that could explain the increased line ratio. Alternatively, the higher line ratio could also come from the presence of an AGN in certain galaxies (e.g., NGC 3627, 4321,

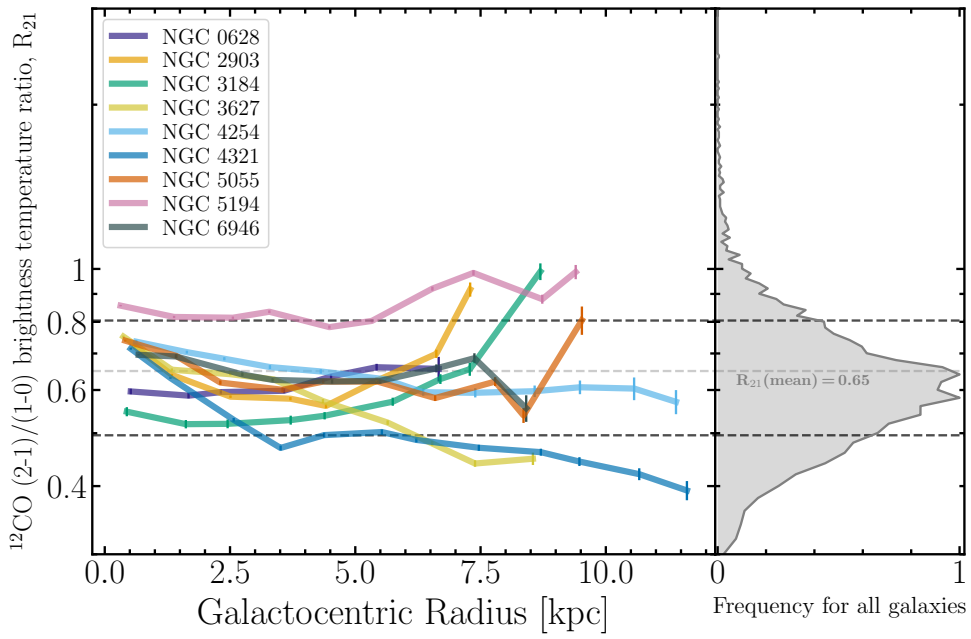

Figure 4.3: **EMPIRE R_{21} Radial Trends for Individual Galaxies** The colored lines show the radially stacked CO line ratio trends for the different galaxies. The grey horizontal lines indicate the mean line ratio of $R_{21} = 0.65$ and the corresponding 1σ scatter. The histogram on the right shows the line ratio distribution using all sightlines within all nine galaxies. We see that the ratio increases significantly toward the center of several galaxies. Significant galaxy-to-galaxy offsets are also apparent. For example, M51 (NGC 5194) shows a systematically higher R_{21} by ~30%. Figure taken from den Brok et al. (2021).

or 5194). In the disk itself ($r \geq 0.2r_{25}$), we find a relatively flat R_{21} trend without any apparent systematic radial changes.

Outlier NGC 5194 (M51): The line ratio trends we find in the spiral galaxy NGC 5194 (M51) are, in several regards, an outlier with respect to the full sample. We find a systematically higher average line ratio of $\langle R_{21}^{\mathrm{M51}} \rangle = 0.83^{+0.08}_{-0.09}$. Furthermore, the galaxy shows a strong arm-interarm contrast in the R_{21}. Values in the spiral arm region are significantly lower (R_{21}~$0.8 - 0.9$) than in the interarm region (R_{21}~$0.9 - 1$). At face value, higher line ratios in the interarm suggest the presence of more highly excited gas, which is more diffuse, warmer, and more optically thin. Already past studies concluded that a minor fraction of optically thin gas could significantly push the emissivity of CO(2-1) more than for the CO(1-0) emission line, hence driving up R_{21} (Wiklind et al., 1990). A more thorough investigation of M51 will follow in Chapter 5, where we use numerous CO isotopologues to further constrain the molecular gas conditions.

4.3 Parameterization of the Line Ratio

We look for ways to parameterize R_{21}. Such a parameterization makes it possible to predict line ratio variation for extensive surveys that rely on, for example, only CO(2-1) observations, such as PHANGS-ALMA. We also find a clear trend in the line ratio with the total infrared (TIR) intensity. The TIR represents repossessed emission and traces the heating of the ISM. In addition, denser gas is likely also traced by higher TIR surface densities since high-density gas is linked to regions with higher SFR (Usero et al., 2015;

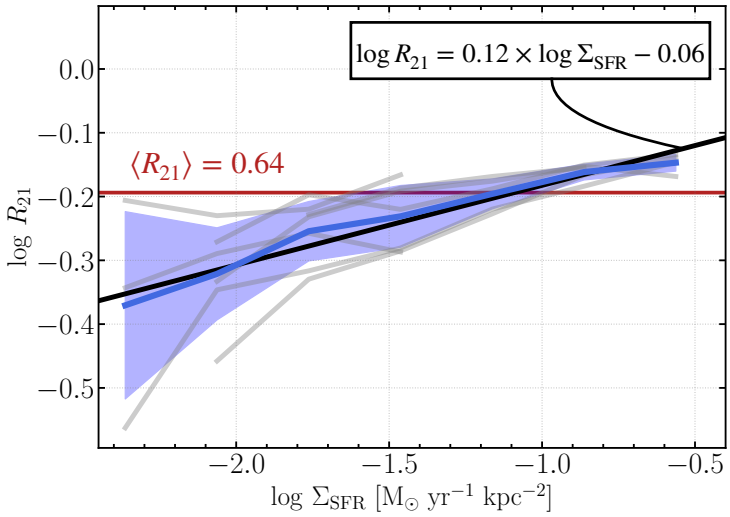

Figure 4.4: **Trend and Parameterization with SFR surface density.** Stacked line ratio trends with SFR surface density for the individual galaxies are shown in light grey. Blue indicates the average when combining all galaxies. The black line indicates a linear fit to the stacked trend. The red horizontal line indicates the intensity weighted average R_{21} for the complete EMPIRE sample. We note that NGC 2903 does not have Herschel IR coverage, based on which we estimate the SFR surface density. Hence it is not included in this figure.

Gallagher et al., 2018; Jiménez-Donaire et al., 2019). Using the prescription by Galametz et al. (2013), we can translate the TIR into an SFR surface density estimate. Given the theoretical expectations regarding TIR, we expect an increasing R_{21} with an increasing Σ_{SFR}.

Figure 4.4 illustrates the correlation between the stacked R_{21} values with SFR surface density for the individual galaxies (in grey) and the combined dataset (in blue). We indeed find a positive correlation between the two quantities, agreeing with our theoretical prediction. Performing a linear least-squared fit to the combined stacked dataset, we can parameterize the line ratio trend as follows[1]:

$$\log R_{21} = 0.12 \times \log \Sigma_{SFR} - 0.06 \tag{4.1}$$

Previous studies have also noted a trend of CO with SFR surface density (e.g. Bayet et al., 2009; Yajima et al., 2021; Leroy et al., 2022). In particular Leroy et al. (2022) find a similar relation when analyzing R_{21} trends in the PHANGS-ALMA sample. They find a slope of 0.13, which is only marginally higher than our slope of 0.12. Generally, using Σ_{SFR} offers a consistent first-order estimation to variations of R_{21}. It is also compatible with the increase of the line ratio toward the center of galaxies, where we generally find the most intense star formation activity.

[1] In the paper, we just describe the correlation between the SFR surface density and the line ratio qualitatively. The precise prescription is exclusively computed for the scope of this thesis.

4.4 Implication of CO Line Ratio Variation

Our finding of a systematic dependence of R_{21} on the SFR surface density has implications for the slope of derived molecular gas mass scaling relations, such as the Kennicutt-Schmidt law (KS law or KS relation; see Subsection 1.5.1). Based on the parameterization, we expect to find different indices when either using CO(1-0) or CO(2-1) and assuming a constant R_{21}. Yajima et al. (2021) find that, indeed, the indices change when using either CO(1-0) or CO(2-1). R_{21} is higher than the canonical value of 0.7 in high star-forming regions and lower in regions with decreased star formation. As a consequence, the molecular gas mass will be either overestimated (in case real R_{21} is higher) or underestimated if one uses CO(2-1) and a fixed R_{21}. Therefore, the actual KS indices become smaller. We can estimate the extent of change in the KS indices with the dynamical range of R_{21} and $\Sigma_{\rm SFR}$ we find in the EMPIRE sample. As seen in Figure 4.4, the line ratio increases by ∼40% for a 100 fold increase of $\Sigma_{\rm SFR}$. As a result, the slope of the KS relation should decrease by $\Delta N \approx 0.07$ (around 5-10% decrease). Such a decrease is within the margin of error that Yajima et al. (2021) find for their sample. We note that a similar trend of overestimated KS indices is also observed for a ^{12}CO(3-2) derived KS relation (Morokuma-Matsui and Muraoka, 2017).

However, the case is not straightforward whether indeed the R_{21} variation has an actual impact on the CO(2-1) derived molecular gas mas scaling relations. Changes in the R_{21} value are linked to the variation of the underlying physical conditions of the gas. However, such changes in temperature, density, or opacity of the gas will also likely impact the CO-to-H_2 conversion factor, which could counteract any bias assuming fixed R_{21}. So R_{21} alone is not enough to fully constrain the extent to which the scaling relations are affected. Furthermore, we note that R_{21} does not deviate significantly from a fixed canonical R_{21} value since the line ratios do saturate at ∼1 and also do not drop to arbitrarily low values (Leroy et al., 2022). Hence, effects of varying $X_{\rm CO}$, for which a larger dynamical range is observed (up to one order of magnitude; Sandstrom et al., 2013), could even dominate.

4.5 Investigating Issues with Flux Calibration

A significant source of uncertainty remains issues with flux calibration and general inconsistencies with the overall telescope performance when taking observations (refer back to Section 3.1). Based on the reported flux calibration stability of the individual survey programs, we can estimate that around 10–20% of the scatter in R_{21} stems from calibration uncertainty alone. Hence flux calibration uncertainty can also explain the galaxy-to-galaxy variation we find in our sample, which is of a similar order of magnitude. However, we expect flux calibration to affect the telescope observations consistently across the map, leading to a general offset and not variation within the map itself. But substantial discrepancies within certain regions are also found when comparing IRAM 30m HERACLES and ALMA-PHANGS ^{12}CO(2-1) maps of the same galaxy. Figure 4.5 illustrates the CO(2-1) intensity ratio for the individual lines of sights in NGC 3627 using ALMA and IRAM 30m observations. The grey band indicates the 20% flux calibration uncertainty range. The red points show the ratio based on the radial stacks. Indeed, we find that there seem to be global offsets between the two CO(2-1) intensities in the disk ($r > 2$ kpc) of order 20%. However, towards the center ($r < 2$ kpc), the ratio increases significantly, indicating that the IRAM 30m data seems to underestimate the CO(2-1) intensity significantly by almost a factor 2. Given these locally confined strong intensity discrepancies, we suspect they arise from HERA pixel gain variations. These variations then likely induce second-order local calibration uncertainties.

We have ALMA-PHANGS and IRAM-HERACLES coverage for five sources, so we can compare the CO(2-1) maps to assess flux stability. Indeed, while we find global offsets in CO(2-1) intensities between

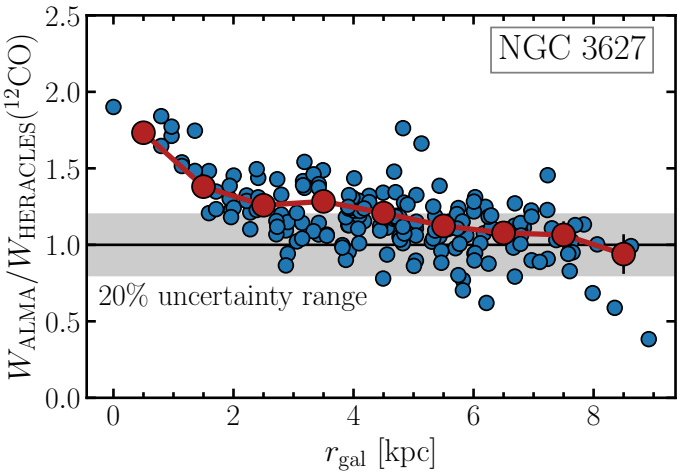

Figure 4.5: **Comparison of CO(2-1) intensities from ALMA and IRAM 30m for NGC 3627.** Blue points indicate the ratio of CO(2-1) intensities for individual lines of sight. The red points show the ratio using the radial stacks. Grey shaded region shows 20% uncertainty range around the 1:1 relation.

the individual galaxies and even some galaxies show strong local discrepancies, the average R_{21} estimate across all galaxies is not significantly affected. Only looking at galaxies with overlapping CO(2-1) datasets, we find $\langle R_{21}^{\rm HERA} \rangle = 0.62 \pm 0.14$ with HERA and $\langle R_{21}^{\rm ALMA} \rangle = 0.59 \pm 0.11$ with ALMA CO(2-1) data. These agree with each other within the margin of error. Thus, we conclude that the overall amplitude scale of HERA CO(2-1) intensities is not significantly biased relative to ALMA.

4.6 Summary and Conclusion

This project culminated in measuring and analyzing R_{21} variation on kpc-scales across and within a set of nine nearby spiral galaxies from the EMPIRE survey sample. We use the latest CO(1-0), and CO(2-1) maps to ensure a systematic analysis. Regarding the main science questions, we conclude with the following answers:

- **How does the R_{21} line ratio vary across and within a sample of nearby spiral galaxies?**
  We find various degrees and ways R_{21} varies: There are global offsets of the average line ratio across the individual galaxies, and we see an enhancement of R_{21} toward the center of the galaxies. Furthermore, $\Sigma_{\rm SFR}$, which traces the to some degree density and temperature changes of the gas, seems to be a good predictor of the R_{21} increases. However, we also found that a significant source of scattering in R_{21} measurements is related to flux calibration issues. This implies that care needs to be taken to ensure a correct reduction of the datasets. This way, uncertainties originating from technical and instrumental effects can be minimized.

- **In what way can we parameterize changes in R_{21}?**
  We find a linear trend of R_{21} with $\Sigma_{\rm SFR}$ in logarithmic space. This makes it possible to derive a relation of the form

$$\log R_{21} = 0.12 \times \log \Sigma_{\rm SFR} - 0.06. \tag{4.2}$$

With a slope of 0.12, the correlation is not very strong. With only a narrow dynamical range of SFR surface densities, likely scatter in R_{21} will dominate over any systematic trend. The relation we find is only calibrated for SFR surface densities commonly found in nearby spiral galaxies. The slope is in agreement with studies of larger samples (e.g., Leroy et al. 2022), but in the case of extreme galaxies with very high or low $\Sigma_{\rm SFR}$ values, the relation could easily break. For example, we expect a flattening since R_{21} likely saturates at ∼1. Hence further observations of other types of galaxies are necessary to calibrate the $R_{21} - \Sigma_{\rm SFR}$ relation to a broader dynamical range of SFR surface densities.

- **How does R_{21} variation affect molecular gas mass scaling relations assuming a constant ratio?** The molecular gas mass is commonly estimated using an $X_{\rm CO}$ factor that is calibrated on the CO(1-0) transition line. If only CO(2-1) observations are at hand, often a constant R_{21} is used to down-convert to the CO(1-0) intensity. However, taking the variation of R_{21} and how it is related to $\Sigma_{\rm SFR}$ into consideration, the molecular gas mass will be underestimated in high SFR regions and overestimated in low SFR regions. This will impact scaling relations, such as the Kennicutt-Schmidt law, where the power-law slope will be flatter if accounting for R_{21} variation when using CO(2-1) based molecular gas estimates. However, also the $X_{\rm CO}$ factor likely varies and could counteract any changes in the slope induced by R_{21} variation. Hence it is crucial to obtain estimates about changes in the CO-to-H_2 conversion factor since R_{21} alone is not enough to constrain the potential impact of the molecular gas mass scaling relations.

In conclusion, the project showed that significant R_{21} variation exists within and across individual galaxies. We stress that because we include observations from nine nearby galaxies, we have obtained very systematic constraints of resolved R_{21} across nearby galaxies. Earlier literature has limited similar investigations to unresolved studies or focused only on brighter regions inside galaxies. The observed scatter in R_{21} can induce a significant degree of uncertainty for accurate molecular gas mass estimates if one relies on CO(2-1) intensities alone. In this study, we focused on kpc-scale variation, which is important to understand large-scale dynamical processes in the ISM. We note that at higher angular resolution, the picture might be different when we start to resolve individual GMCs. Furthermore, variation of other parameters, such as $X_{\rm CO}$, also induces uncertainties and might even dominate over scatter related to inaccurate R_{21} estimations. The goal of the next project is to further constrain the physical conditions in the molecular gas at kpc resolution. We address this question using large program IRAM 30m observations of M51 (Chapter 5). Furthermore, in Chapter 6, we also address the question of a variable $X_{\rm CO}$.

CHAPTER 5

The CO Line Atlas Whirlpool galaxy Survey: CLAWS

A CO isotopologue Line Atlas within the Whirlpool galaxy Survey (CLAWS)
J. den Brok, F. Bigiel, K. Sliwa, T. Saito, A. Usero, E. Schinnerer, A. Leroy, M. Jiménez-Donaire, E. Rosolowsky, A. Barnes, J. Puschnig, J. Pety, A. Schruba, I. Bešlić, Y. Cao, C. Eibensteiner, S. Glover, R. Klessen, J. M. D. Kruijssen, S. Meidt, L. Neumann, N. Tomičić, H.-A. Pan, M. Querejeta, E. Watkins, T. Williams, D. Wilner
2022, A&A, 662, A89

Overview

The *CO Line Atlas of the Whirlpool Galaxy Survey* (CLAWS) is an IRAM 30m Large Program that targets a suite of molecular lines in the 1.3 mm and 3mm wavelength regime. Using this rich set of lines, particularly the low-J CO isotopologues, our goal is to constrain CO excitation and chemistry across M51. This will help determine the local physical conditions of the molecular CO bright gas. With an observing time of 149 h, we reached a very high sensitivity of observations. For the first time, multiple transitions of several CO isotopologues, including ^{12}CO, ^{13}CO, C^{18}O, and even C^{17}O are detected across an external galaxy and resolved beyond its central region (i.e., beyond r>2 kpc). Before, such CO isotopologue studies in M51 were only limited to individually selected bright regions (e.g. Schinnerer et al., 2010; Tan et al., 2011; Watanabe et al., 2014; Watanabe et al., 2016). The previous project (Chapter 4) already marked M51 as an interesting case to study because it shows, for example, a clear R_{21} variation between different environments, such as spiral arm and interarm regions. In addition, due to the galaxy's close proximity (D~8.6 Mpc) and high molecular gas surface density, it is routinely observed across different wavelength regimes, giving us a wealth of ancillary data sets to work with.

We find clear trends and variations for all combinations of CO isotopologue ratios with SFR surface density and galactocentric radius. Since we include optically thin and thick lines, we can deduce variation due to various physical drivers, in particular changes in the optical depth of the gas and relative abundance variations due to selective nucleosynthesis.

The following work was published at A&A in 2022. The paper den Brok et al. (2022) is provided in its entirety in original form in Appendix B. All the analysis steps presented in the paper have been performed by myself, with helpful advice and input on improving certain aspects of the methodology from the wider

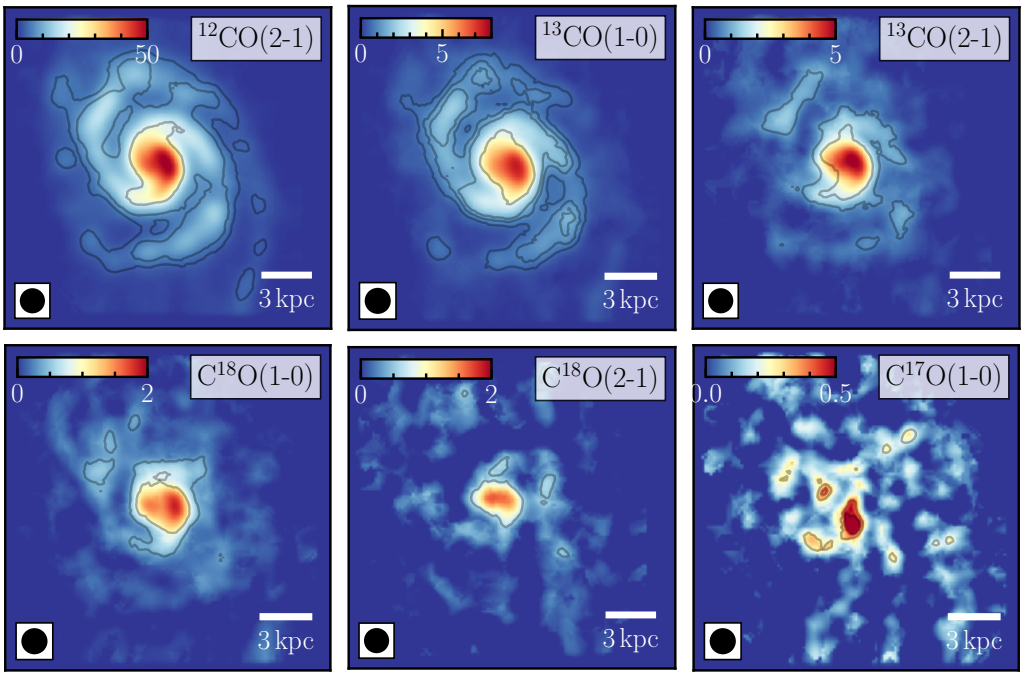

Figure 5.1: **Intensity maps of CO Isotopologues covered by CLAWS.** The moment-0 intensity maps convolved to 33″. Colorbar indicates the intensity in K km s^{-1}. The contours indicate arbitrary S/N> 5 levels.

field of co-authors. In addition, I generated the products for the public data release that included 3D cubes and moment maps for the main CO isotopologues. The following sections provide an in-depth commentary about the relevant science questions addressed by the project.

5.1 Catalogue of Observed Molecular Lines

A total of eleven molecular lines have been observed in the 1.3mm and 3mm window as part of the CLAWS large program. All observations were carried out using the IRAM 30m telescope EMIR instrument. The result is a 4.4′×4.4′ OTF map. Table 5.1 provides an overview of the lines covered by the program, separated by their respective wavelength regime. Figure 5.1 shows the intensity maps for the CO isotopologues covered as part of the CLAWS observing program.

We complement this dataset with ^{12}CO(1-0) IRAM 30m observations from the PAWS survey (Pety et al., 2013) and JCMT ^{12}CO(3-2) cubes from the *Nearby Galaxy Survey* (NGLS; Wilson et al., 2012). This gives us a total of eight low-J CO isotopologue lines we can use to assess the molecular gas.

5.2 M51's Arm–Interarm Trend

In Chapter 4, we remark the striking arm-interarm difference in the R_{21} ratio. As part of that project, we performed a logarithmic spiral decomposition quantified the higher line ratios in the interarm (R_{21}~0.9 – 1) as opposed to the spiral arm region (R_{21}~0.8 – 0.9). With the CLAWS dataset, we can look for similar trends using the other CO isotopologue line emissions, which trace different underlying physical properties

Table 5.1: **Summary of the lines covered in CLAWS.** Table adopted from den Brok et al. (2022).

Setup	Band	Line	$\nu_{\rm rest}$	Beam size	
			[GHz]	[″]	[kpc]
	(1)			(2)	(2)
1	E0 (3 mm)	CN(1-0)	113.250	26.1	1.1
		$C^{17}O$(1-0)	112.359	26.3	1.1
		^{13}CO(1-0)	110.201	26.8	1.1
		$C^{18}O$(1-0)	109.782	26.9	1.1
		CS(2-1)	97.981	30.2	1.3
		CH_3OH(2-1)	96.700	30.6	1.3
		N_2H^+(1-0)	93.173	31.7	1.3
		HC_3N(10-9)	90.897	32.5	1.4
2	E2 (1.3 mm)	^{12}CO(2-1)	230.538	12.8	0.53
		^{13}CO(2-1)	220.399	13.4	0.56
		$C^{18}O$(2-1)	219.560	13.5	0.56

Notes: (1) The EMIR band used for the observation (2) Beam size of the final data cube after reduction.

than R_{21}. Figure 5.2 shows five selected line ratios after stacking all sightlines within the spiral arm[1] (panels on the left) and the interarm region (panels in the center). The right panels show whether the line ratio increases or decreases from arm to interarm region (green: increase, red: decrease). We see that R_{21}, $R_{13/12}\equiv{}^{13}CO/^{12}CO$(1-0), and $R_{13/18}\equiv C^{18}O/^{13}CO$(1-0) all show higher ratios in the interarm region, while $R_{21}^{13}\equiv{}^{13}CO$(2-1)/(1-0) and $R_{32}\equiv{}^{12}CO$(3-2)/(2-1) does show higher values in the spiral arm region.

As a reminder, the various line ratios trace different physical or chemical aspects of the molecular gas conditions. R_{21} and R_{32} trace the excitation conditions of the CO gas, which are generally linked to changes in the temperature or density and the opacity of the gas (Shirley, 2015; Peñaloza et al., 2017). Given that interarms do not likely hold higher density molecular gas (Sun et al., 2020), the trends probably indicate hotter gas or changes to the opacity. Since R_{32} shows an opposite trend, it does more likely hint at changes to the opacity of CO bright gas, potentially due to the presence of a more diffuse gas component (which would be in accordance with the diffuse component predicted by Pety et al. 2013). The $R_{13/12}$ line ratio can potentially give insight into changes in the ^{12}CO optical depth since ^{13}CO is mostly optically thin. The line ratio increases toward the interarm region. If the variation is purely driven by opacity, this would actually indicate more optically thick gas in the interarm region since ^{12}CO(1-0) is in the denominator of the ratio. But it is also likely that $R_{13/12}$ is driven by changes in the relative abundance of ^{13}CO. The relative abundances vary according to the $R_{18/13}$ trend, as both are optically thin emission lines. The trend we see is in agreement with selective nucleosynthesis. More active star formation in the center and spiral arm will lead to an *inside-out* star formation history (Nelson et al., 2012; Frankel et al., 2019). Hence a higher number of intermediate-mass stars will have formed that increase the relative abundance of ^{13}CO.

Overall, given the sense of the line ratio trends we find, we are limited to a qualitative discussion of potential drivers. More J-transitions would be useful to properly assess the excitation conditions of the gas for the different CO isotopologues. Using the `DenseGasToolbox` (Puschnig, 2020), which builds on non-LTE modelling of line emission with `RADEX`, it can be possible to assess the conditions of the gas (see

[1] The environmental mask we used is illustrated in den Brok et al. (2022) in Figure 10 (see Appendix B).

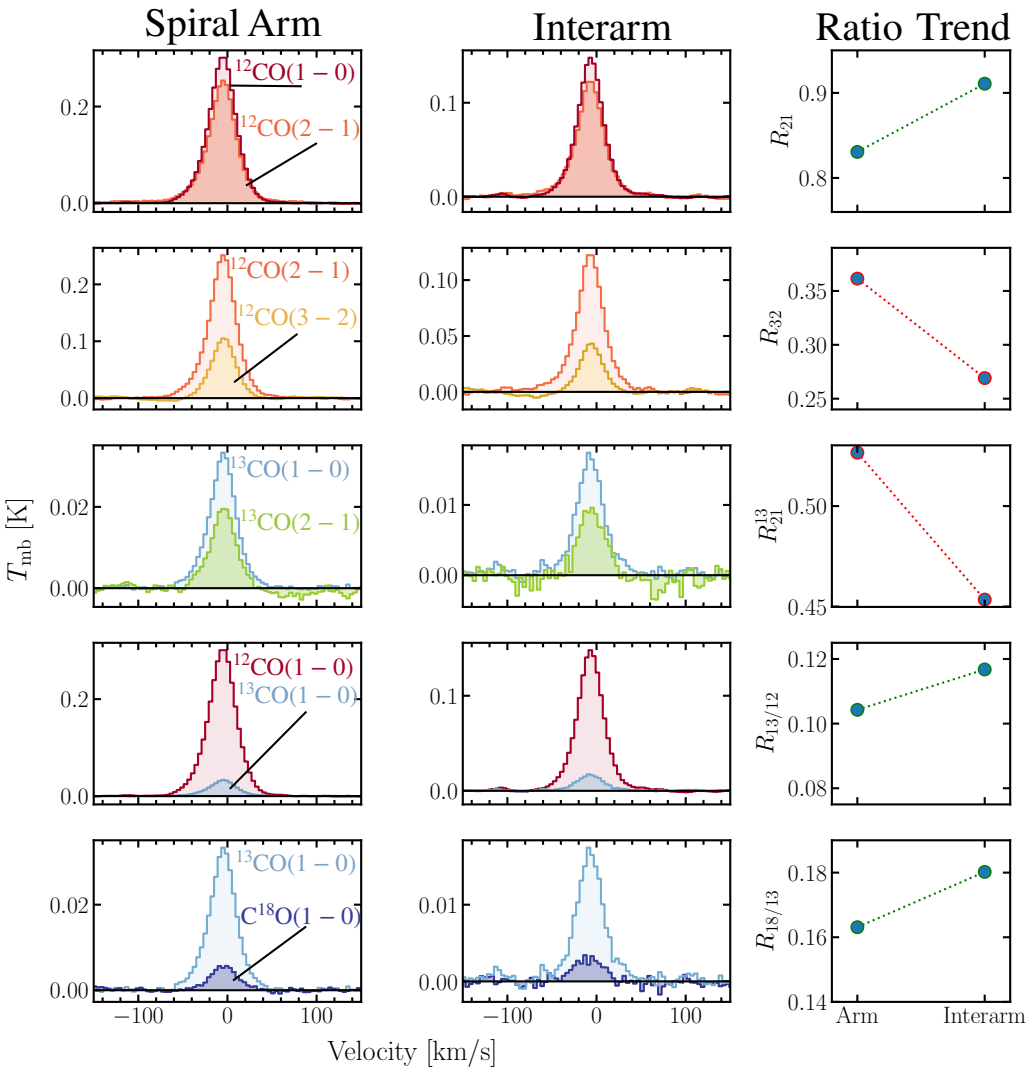

Figure 5.2: **Various CO ratio Arm–Interarm Trend in M51.** We stack the line of sights by either spiral arm or interarm region. The left panels show the stacked spiral arm spectra, and the central panels show the stacked interarm spectra. The right panels compare the variation of the line ratio. In case the line ratio is larger in the interarm, it is indicated in green, else in red.

Subsection 1.6.3). However, in this survey paper, we did not go beyond the qualitative description, and the line modeling will be part of a future project (see Chapter 7).

5.3 CO Isotopologue Line Ratio Trends

It can be useful to investigate potential line ratio trends with $\Sigma_{\rm SFR}$, since star-forming activity correlates, loosely speaking, with denser (leading to star formation) or warmer (via feedback) gas. In Figure 5.3 we look at four different CO isotopologue line ratio variations. The points are derived from stacking the lines of sight after binning by $\Sigma_{\rm SFR}$. For comparison, the average ratios for different galaxy types (or samples)

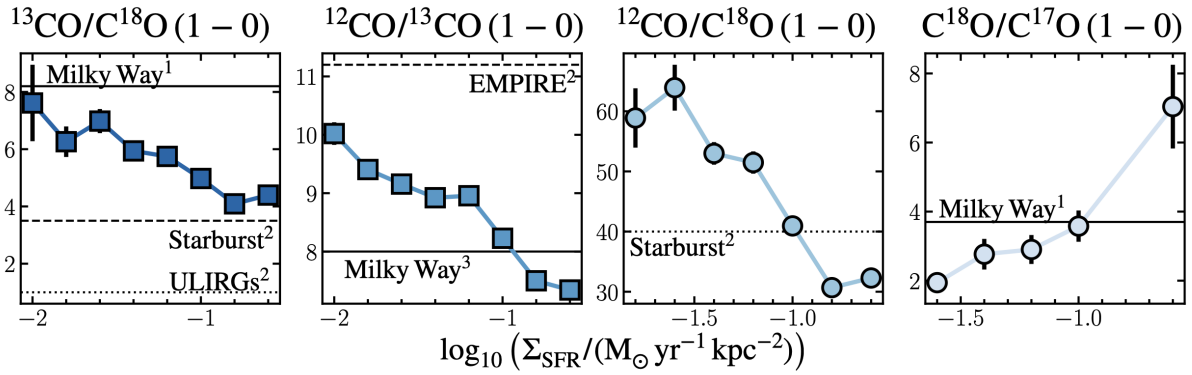

Figure 5.3: **Various CO ratio Arm–Interarm Trend in M51.** The various panels show the line ratio trends of the CO emission lines stacked by SFR surface density. For comparison, average line ratio values for different types and samples of galaxies are indicated in the individual panels. Source of the reference line ratio values are (1) Wouterloot et al. (2005), (2) Jiménez-Donaire et al. (2017b), and (3) Cormier et al. (2018).

are shown in each panel. All ratios show a clear increasing or decreasing trend with SFR surface density, with an increase or decrease of >50%. We again can use these trends to make qualitative deductions on any global physical drivers of the CO line ratio (see Subsection 1.3.1 for a discussion of potential drivers).

We conclude that the main drivers are the optical depth effect (mainly affecting the ^{12}CO emission) and selective nucleosynthesis (mainly pushing the chemical abundance of ^{13}CO where active star formation has occurred due to inside-out star formation). Likely, a combination of these effects and further impact by the SF history and chemical enrichment of the ISM all shape the line ratio trends we see.

As a side note, we like to highlight the trend of the C^{18}/C^{17}O(1-0) line ratio. Generally, the detection of C^{17}O(1-0) in extragalactic sources is only confined to the centers of galaxies or bright systems, such as starburst galaxies (e.g. Martin et al., 2021). We find an increasing ratio in the range of $2-8$, similar to the solar neighborhood Milky Way value (Wouterloot et al., 2005).

5.4 Summary and Conclusion

This paper summarizes the data and observations of the CLAWS IRAM 30m large program. The focus lies in describing the trends we find, particularly the low-J multi-CO line emission. Of particular interest are the following science questions:

- **How does the CO isotopologue line emission vary across M51?**
  Different combinations of line ratios trace many physical or chemical aspects of the molecular gas. In general, we find clear trends in the CO isotopologue line emission. Environmental trends (arm-interarm, center–disk) and systematic changes with the SFR surface density are particularly insightful. We conclude that the most likely explanation is a combination of drivers with selective nucleosynthesis and changes in the opacity being the most relevant ones.

- **To what degree does the CO isotopologue line emission variation trace temperature, column and volume densities and the CO-to-H2 conversion factor in M51?**
  The changes we observe in the CO line ratios of different J transitions (such as R_{21}, R_{32}, and R_{21}^{13}) all carry information about changes in the excitation conditions. This is linked to changes in the

temperature or density of the gas. However, to more accurately combine all the information of the numerous line ratios, we require modeling attempts beyond this project's scope. This will be addressed in a future project, where we will perform non-LTE analyses using modeling tools that build on `RADEX` (see Section 7.1). This will also allow us to gain constraints on the CO-to-H_2 conversion factor.

The CLAWS project constitutes a fundamental step toward describing and investigating molecular gas conditions and the chemical enrichment using CO isotopologues (^{12}CO, ^{13}CO, C^{18}O, and C^{17}O) across a nearby regular galaxy. Similar investigations by earlier studies either focused on the nuclear region or looked into resolved emission within starburst galaxies, where the molecular gas is brighter. The significant variation and trends of various CO isotopologues clearly indicates that they are a valuable diagnostics tool for the underlying molecular gas physics and chemistry on kpc-scales.

CHAPTER 6

Wide-Field Multi-CO Emission Across M101

Multi-CO Emission and New Constraints on the CO-to-H_2 Factor across M101
J. den Brok, F. Bigiel, A. Leroy, K. Sandstrom, E. Schinnerer, A. Usero, J. Chastenet, T. Saito, E. Rosolowsky, A. Barnes, J. Puschnig
in preparation

Overview

In the two projects presented in Chapter 4 and Chapter 5, we discuss the implications of varying CO excitation on commonly derived molecular gas mass scaling relations. However, so far, we did not account for the variation of the CO-to-H_2 conversion factor, α_{CO}. We know that the conversion factor is not constant but varies within and across galaxies as a function of metallicity, gas opacity, excitation, and other factors (see Section 1.4). In early 2021, we obtained ~70 h IRAM 30m telescope time to observe a wide-field $10' \times 10'$ map of the galaxy M101. We targeted the 1mm and 3mm ^{12}CO, ^{13}CO, and C^{18}O emission lines across the full galaxy. Due to its strong metallicity gradient (-1.1 dex/r_{25}; Berg et al. 2020), it offers a great leverage to study metallicity dependent variation. Using existing H I and IR SED-fit-based dust mass maps, we perform the so-called scatter minimization technique that yields an estimate of α_{CO} across the galaxy. The conversion factor from the scatter minimization technique has been studied systematically in nearby galaxies before (Sandstrom et al., 2013). However, in this work, we go beyond the previous research by relying on CO(1-0) directly, also investigating the implications of R_{21} variation, and connect insight from CO isotopologue line ratios on the molecular gas conditions across M101. The following chapter consists of the current manuscript *Multi-CO Emission and New Constraints on the CO-to-H_2 Factor across M101*, which is in preparation and will be submitted to A&A.

6.1 Introduction

The low-J rotational transitions of carbon monoxide (CO) are key tracers of the bulk molecular gas mass in the interstellar medium (ISM) within and across galaxies. While ^{12}CO is only the second most abundant molecule after molecular hydrogen, H_2, it has a permanent dipole moment and low moment of inertia. Consequently, ^{12}CO has low energy rotational transitions, leading to excitation and detectable emission at low temperatures – unlike H_2 – which is generally not observable in emission under typical cold molecular interstellar medium (ISM) conditions. Hence, in particular, at low temperatures (T~10 K)

and number densities above $n_{\rm H}$>10^2 [cm^{-3}], CO is regularly used as an effective tracer of the molecular ISM. The conversion from ^{12}CO emission to the amount of molecular gas relies on the application of an appropriate CO–to–H_2 conversion factor (see review by Bolatto et al., 2013). H_2 column densities, $N_{\rm H_2}$ [cm^{-2}], are derived from ^{12}CO integrated intensity, $W_{^{12}\rm CO}$ [K km s^{-1}] using the conversion factor $X_{\rm CO}$ [cm^{-2} (K km s^{-1})$^{-1}$]:

$$N_{\rm H_2} = X_{\rm CO} \times W_{^{12}\rm CO(1-0)}. \tag{6.1}$$

Equivalent to the factor $X_{\rm CO}$, but in different units, $\alpha_{\rm CO}$ [M$_\odot$ pc^{-2} (K km s^{-1})$^{-1}$], converts the integrated intensity into the total molecular gas mass surface density (including contribution of heavier elements), $\Sigma_{\rm mol}$ [$M_\odot$ pc^{-2}], via:

$$\Sigma_{\rm mol} = \alpha_{\rm CO} \times W_{^{12}\rm CO(1-0)}. \tag{6.2}$$

The specific numerical value of $\alpha_{\rm CO}$ varies with the ISM environment. In low-metallicity regions, for example, there can be a significant presence of CO-dark H_2 since dust shielding against photodissociation of CO is reduced (Maloney and Black, 1988; Israel, 1997; Leroy et al., 2007; Wolfire et al., 2010; Glover and Mac Low, 2011; Leroy et al., 2011; Bolatto et al., 2013; Schruba et al., 2017). In addition, previous studies find that $\alpha_{\rm CO}$ tends to decrease toward the centers of galaxies (Sandstrom et al., 2013; Cormier et al., 2018; Israel, 2020). The fact that centers of galaxies are regions with elevated temperature and gas turbulence (e.g., Israel, 2020; Teng et al., 2022) likely connects to the observed decrease in $\alpha_{\rm CO}$. Given that CO is so straightforwardly observable, a concrete prescription for $\alpha_{\rm CO}$ as a function of the environment remains a longstanding goal.

Obtaining robust $\alpha_{\rm CO}$ calibrations is challenging since the molecular gas mass must be measured independently of CO intensity. One commonly used technique consists of using dust emission to trace the total gas distribution in the ISM (e.g. Thronson et al., 1988; Israel, 1997; Leroy et al., 2011; Sandstrom et al., 2013). From an empirical standpoint, dust seems to be well mixed with the gas at the kpc-scales relevant to this paper. In addition, the dust emission remains optically thin across most nearby spiral galaxies. Using IR or (sub)mm emission, we can model the dust spectral energy distribution and obtain an estimate of the dust optical depth. We can translate the optical depth to a total gas column or mass surface density using a dust-to-gas ratio. The total gas consists of atomic gas (traced by HI) and molecular gas. By separating the total gas into its components, we can estimate $\alpha_{\rm CO}$. A strength of the dust technique is that the method traces the total gas with little bias. Consequently, it offers a direct way of measuring the molecular gas mass. However, there are two potential limitations of the method worth discussing: (i) gas that evades detection via dust emission and (ii) changes in dust emissivity. We can separate the total gas into an atomic component traced by H I and the molecular component we want to trace with CO emission. However, H I 21cm could miss a significant fraction of the ionized atomic gas. Heiles and Troland (2003) suggested that the contribution from the ionized component could be up to 20%. More recently, however, Planck Collaboration et al. (2011b) concluded that only a minor fraction of the dust emission originates from regions associated with ionized atomic gas. Overall, the contamination to $\alpha_{\rm CO}$ estimates from dust mixed with other invisible components seems negligible in nearby star-forming galaxies. This is further underpinned by the fact that $\alpha_{\rm CO}$ estimates derived from other techniques than dust emission find similar values (Bolatto et al., 2013). Besides, emissivity changes will manifest in inaccurately translating the observed dust emission into a dust column density. Past studies showed a link between metallicity and dust emissivity (e.g. Draine et al., 2007; Muñoz-Mateos et al., 2009b). However, in nearby spiral galaxies, usually, we do not observe too extreme metallicity values. Furthermore, we stress that, generally, by allowing the dust-to-gas ratio to vary, both limitations can be accounted for to some degree.

CO line ratio and conversion factor variation have implications for studies beyond nearby galaxies. For

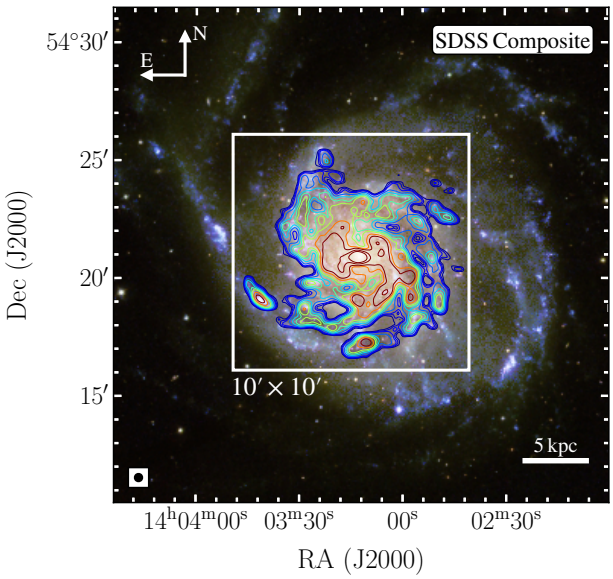

Figure 6.1: **SDSS RGB Image with ^{12}CO (1−0) overlay**. Colour image using public SDSS data from the 16th data release (Ahumada et al., 2020). We combined the u, g, and r filter bands. The IRAM 30m ^{12}CO (1−0) integrated intensities (at a resolution of 23″(∼800 pc), indicated by the black circle in the lower left) is shown in contours. The $10' \times 10'$ field-of-view of our IRAM 30m observation is indicated by the white rectangle.

instance, high redshift observations often focus on higher-J CO transitions, and therefore such studies depend on down conversion to the ^{12}CO (1−0) transition as well (Tacconi et al., 2008; Genzel et al., 2012; Narayanan and Krumholz, 2014; Cañameras et al., 2018). Often, CO line ratios are adopted, which are based on measurements in the local universe (e.g. Tacconi et al., 2008). But also, the observed CO line emission of different transitions varies with other galactic properties, including metallicity and the radiation field (Greve et al., 2014; Daddi et al., 2015). In particular, dust shielding is tied directly to metallicity (Byrne et al., 2019) and can affect the CO line ratio. Furthermore, metallicity correlates indirectly with the radiation field (Kewley et al., 2019) and the star formation intensity (Yates et al., 2012), both of which also impact the CO line ratio. Since galaxies will enrich heavy elements over cosmic time scales (see for example De Cia et al., 2018), it is also of interest to calibrate CO excitation against metallicity and the radiation field.

CO isotopologue emission can be used to study the molecular gas conditions in nearby galaxies (e.g. Davis, 2014; Israel, 2020; Teng et al., 2022). The low-J ^{12}CO transitions usually remain optically thick, whereas the ^{13}CO and C^{18}O are optically thinner. Consequently, comparing optically thin ^{13}CO and C^{18}O lines to the optically thick ^{12}CO lines gives insights into optical depth. Moreover, contrasting two optically thin lines offers an understanding of changes in relative abundances of the different isotopologue species (Davis, 2014). Several mechanisms can lead to differences in the relative abundance of the species. The various C and O isotopes originate from processes, such as nucleosynthetic and chemical processes (Henkel et al., 1994; Timmes et al., 1995; Prantzos et al., 1996). Hence, studying several CO isotopologues can provide insight into the chemical enrichment of the molecular gas.

M101 (NGC 5457) is a well-studied, massive, face-on, nearby (D = 6.65 Mpc; Anand et al. 2021), star-forming spiral galaxy in the northern hemisphere. In addition to its proximity, the galaxy has a low inclination (i = 18°), which allows for well-resolved, extended studies across the full galactic disc. M101 has a considerable apparent size across the sky with an extent of the disc in the optical of $\sim 20' \times 20'$ (Paturel

et al., 2003). It is tidally interacting (Waller et al., 1997) with nearby companion galaxies. Furthermore, M101 is of particular interest due to its well-documented metallicity gradient (Kennicutt et al., 2003; Croxall et al., 2016; Berg et al., 2020) based on auroral line measurements. The gradient is stronger than compared to other nearby spiral galaxies ($-1.1\mathrm{dex}/\mathrm{r}_{25}$; Berg et al., 2020). In Figure 6.1, we show an optical composite image using observations from the *Hubble Space Telescope* (HST). In addition, we show the ^{12}CO (1−0) line map presented in this paper using overlayed contours. The galaxy has a wealth of ancillary data across all wavelength regimes. As part of the IRAM 30m large program HERACLES (Leroy et al., 2009), wide-field ^{12}CO (2−1) observations exist, which complement our observations of the 3mm CO lines. Table 6.1 lists key properties of the galaxy derived from previous surveys and studies.

Table 6.1: Properties of M101.

Property	Value
Name	M101 (NGC 5457)
R.A. (J2000)[(a)]	14^{h}:03^{m}:$12^{\mathrm{s}}.6$
Decl (J2000)[(a)]	54°:$20'$:$57''$
i[(b)]	18°
P.A.[(b)]	39°
r_{25}[(a)]	$12.0'$
D[(a)]	6.65 Mpc
V_{hel}[(a)]	$237\,\mathrm{km\,s^{-1}}$
Morphology[(a)]	SABc
SFR[(c)]	$3.4\ \mathrm{M_\odot\,yr^{-1}}$
$\log_{10}(M_\star/\mathrm{M_\odot})$[(c)]	10.39

Notes:
(a) Anand et al., 2021;
(b) Sofue et al., 1999;
(c) Leroy et al., 2019.

This paper presents our newly obtained IRAM 30m wide-field ∼kpc multi-CO line observations of M101. They complement the IRAM 30m large program CLAWS (den Brok et al., 2022), which obtained deep multi-CO kpc-scale observations of the galaxy M51. Hence, we can investigate differences and similarities in molecular gas conditions traced by CO emission between these two massive, star-forming spiral galaxies. M51 is a suitable candidate to compare α_{CO} trends and variation since

(i) it is nearby ($D_{\mathrm{M51}} = 8.6$ Mpc; McQuinn et al. 2016);

(ii) the galaxy is similarly face-on ($i_{\mathrm{M51}} = 22^\circ$; Colombo et al. 2014) as M101;

(iii) as opposed to M101, it has a flatter metallicity gradient ($-0.23\mathrm{dex}/\mathrm{r}_{25}$; Berg et al. 2020). We note that despite the flatter trend in M51, we find a similar dynamical range in metallicities to M101. This is because in M51, we detect CO at larger radial distances from the center (as measured in r_{25} units).

6.2 Observations and Data Reduction

6.2.1 Observations

As part of an IRAM 30m observing program (#160-20), we used the EMIR receivers to map line emission in the 1 mm (220 GHz) and 3 mm (100 GHz) windows in dual polarisation from the disc of M101 for a total of ~80 h (~65 h on-source time) in the time period of January to March 2021. The receiver bandwidth was 15.6 GHz per polarization. We carried out the observations simultaneously in the E90 and E230 bands using both the upper-inner (UI) and upper-outer (UO) bands. We used the Fast Fourier Transform spectrometers with 195 kHz spectral resolution (FTS200). The spectrometer yielded a spectral resolution of ~0.5 km s^{-1} for the E090 and ~0.2 km s^{-1} for the E230 band. Table 6.2 lists the key lines we targeted.

Table 6.2: Summary of the lines targeted as part of the IRAM 30m observing program. Several observational parameters and key characteristics of the extracted data products are included.

Band	Line	$\nu_{\rm rest}$	Beam size		$\langle$rms$\rangle$	On-source time	$\langle T_{\rm sys}\rangle$	$\langle$pwv$\rangle$
		[GHz]	[″]	[kpc]	[mK]	[hr]	[K]	[mm]
			(1)	(1)	(2)	(3)	(4)	(5)
E0 (3 mm)	^{12}CO (1−0)	115.271	25.6	830	13.7	65.4	217	4.6
	^{13}CO (1−0)	110.201	26.8	860	7.4			
	C^{18}O (1−0)	109.782	26.9	870	7.3			
E2 (1.3 mm)	^{12}CO (2−1)	230.538	12.8	410	21.8	37.4	211	1.1

Notes: (1) Beam size of the final data cube after reduction. (2) Average rms measured for a 4 km s^{-1} channel width. (3) Total on-source time, including only the subset of data finally used to generate the cubes after reduction. The scanning speed was 8″/sec. While we simultaneously observed bands E0, and E2, the on-source time for the ^{12}CO (2−1) is shorter because we also dedicated time to target the $J = 2 \rightarrow 1$ transitions of ^{13}CO and C^{18}O, which required another tuning. However, we do not detect any (2−1) emission of these CO isotopologues in the 1mm regime. (4) Average system temperature (for a subset of data used for the final cube). (5) Average precipitable water vapor (pwv) during observations (for a subset of data used for the final cube).

For the mapping, we used a similar approach to the one from the EMPIRE survey (see Jiménez-Donaire et al., 2019). Using the on-the-fly/position switching (OTF-PSW) mode, we mapped a field of 10 arcmin × 10 arcmin (corresponding to ~20 kpc × 20 kpc or 0.83 r_{25} × 0.83 r_{25}). In addition, we included two emission-free reference positions (OFF position) offset by 300″ towards the North and East of M101's center. We scanned the field in RA and DEC directions using multiple straight paths that are each offset by 8″ from each other. After an iteration over the full field, we shifted the scanned box by $\sqrt{2} \times (0, 2'', 4'', 6'')$ along the diagonal. This guarantees that, in the end, we cover M101 with a much finer, 2″, instead of 8″, grid. We set the read-out dump time to 0.5 s, and the final spacing between data points reaches 4″. A typical observation session had a length of 6−9 h during the night, with 11 sessions in total. The telescope's pointing and focus were determined at the beginning of each session using observations of a bright quasar. We corrected the focus after 4 h of observing, and the pointing of the telescope was adjusted every 1−1.5 h using a nearby quasar. To ensure a proper antenna temperature ($T_{\rm a}^{\star}$) calibration, we did a chopper-wheel calibration every 10−15 minutes using hot-/cold-load absorber and sky measurements. Finally, to monitor systematic errors in amplitude and flux calibration, we observed line calibrators (IRC+10216 or W3OH) at the beginning or end of each observing session.

6.2.2 Data Reduction

The following steps summarize the data processing and reduction. For these individual routines, we employ the scripts used for the HERACLES and EMPIRE pipeline (see description in Jiménez-Donaire et al., 2019) and basic calibration steps by `MRTCAL`[1].

1. First, we convert the spectrum to the corrected antenna temperature scale ($T_a^\star$) by scaling each science scan using to most recent previous calibration scan.
2. We then subtract the most recent OFF measurement from the calibrated spectrum. This concludes the most basic calibration steps.
3. Next, using the *Continuum and Line Analysis Single-dish Software* (`CLASS`[2]), we extract the target lines and create the velocity axis given the rest frequency of the relevant line.
4. To subtract the baseline, we perform a constant linear fit. For the fit, we account for the systemic velocity of M101. We omit the range of 100 to 400 km s^{-1} around the center of the line (which corresponds to the velocity range of the galaxy).
5. Finally, we regrid the spectra to have a 4 km s^{-1} channel width across the full bandpass. Such a spectra resolution is sufficient to sample the line profile, as shown by previous observations and IRAM 30m surveys, such as HERACLES, EMPIRE, and CLAWS. The spectra are then saved as a FITS file.

To estimate the flux calibration stability, we observed spectra of line calibrators (e.g. IRC+10216) on several nights. We find a maximum day-to-day variation in amplitude of ∼5 per cent across all observations, which is consistent with the more extended analysis of the stability of the line calibrators in Cormier et al., 2018 done for the EMPIRE survey. The average actual noise in the cube data is listed in Table 5.1.

We perform a more sophisticated final data reduction using an `IDL` routine, which is based on the HERACLES data reduction pipeline (Leroy et al., 2009). With this pipeline, we can remove bad scans and problematic spectra. Furthermore, the routine performs a *platforming correction* at the edges of the FTS units. This ensures that the various sub-band continua are at a common level. We note that the receiver's tuning was chosen so that no target line is affected by potential offsets due to platforming. After the platforming correction, we perform a baseline fitting again. We start by excluding a generous line window using the ^{12}CO (1−0) line emission. We place a window extending in both spectral directions around the mean ^{12}CO (1−0) velocity. The window's full width for each pixel depends on the specific velocity range of the galaxy's emission derived from HERACLES CO(2-1) data. It ranges between 50 and 300 km s^{-1} for each pixel. We place two windows of the same width adjacent to the central window on both sides. The pipeline then fits a second-order polynomial to the baseline in these windows. The routine finally subtracts the resulting baseline from the full spectrum.

Bad scans and spectra are removed by sorting the remaining spectra by their rms. The pipeline determines the channel-rms from line-free windows after the baseline subtraction. We remove the spectra in the highest 10$^{\text{th}}$ percentile.

For the ensuing analysis, we will use the main beam temperature (T_{mb}). The main beam temperature is connected to the corrected antenna temperature scale ($T_a^\star$) via

$$T_{\text{mb}} = \frac{F_{\text{eff}}}{B_{\text{eff}}} T_a^\star \ . \tag{6.3}$$

[1] https://www.iram-institute.org/medias/uploads/mrtcal-check.pdf
[2] https://www.iram.fr/IRAMFR/GILDAS/doc/html/class-html/class.html

with the forward ($F_{\rm eff}$) and beam ($B_{\rm eff}$) efficiencies, which depend on the observed frequency. We determine the value of the efficiencies using a cubic interpolation of the efficiencies listed in the IRAM documentation[3]. For the $F_{\rm eff}/B_{\rm eff}$ ratio we find an approximate value of 1.2 for the 3 mm regime and 1.6 for the 1 mm regime.

Finally, we generate science-ready data cubes by gridding the spectra onto a $2''$ spaced Cartesian grid. We note that the final angular resolution is 20% coarser than the IRAM 30m native resolution. The final beam of each data cube, given in Table 5.1, represents the convolution of our gridding kernel and telescope beam (Mangum et al., 2007). The average noise in the cube data is listed in Table 5.1.

This work does not account for flux contamination due to error beam contribution. We note that M101 shows no strong arm-interarm contrast in CO emission (as opposed to other similar spiral galaxies, such as, for example, M51). Therefore, the magnitude of error beam contribution is expected to be minor. In den Brok et al., 2022, the effect of error beam contributions are discussed in detail. In particular, in the presence of strong contrast between bright and faint regions, the faint region can suffer from significant error beam contributions. The exact contribution is difficult to quantify as the exact shape of the error beam of a single-dish telescope fluctuates depending on the telescope's elevation. That is why only first-order estimates on the extent of the contribution can be made. IRAM provides estimates of the full 30m telescope beam pattern in their reports (e.g. Kramer et al., 2013). The 1 mm regime is more strongly affected by such error beam contributions, since the telescope's main beam efficiency is lower ($B_{\rm eff}^{3\,\rm mm} = 78$ and $B_{\rm eff}^{1.3\,\rm mm} = 59$). While den Brok et al., 2022 find in general contributions to be <10% in M51, it can in certain interarm regions reach up to 40%. In particular, regions with strong contrast are affected. For M101, we do not expect the error beam to contribute more than 10%, given the overall low contrast across its disk.

6.2.3 Ancillary Data and Measurements

For a complete analysis, we use archival and ancillary data sets. In this section, we briefly describe the additional data sets used in the analysis. For our $\alpha_{\rm CO}$ estimation approach, we particularly require robust dust mass surface density and atomic gas mass surface density maps.

Dust Mass Surface Density Maps

The dust surface density maps are the products of emission spectral energy distribution (SED) fitting from Chastenet et al. (2021). They used a total of 16 photometric bands, combining mid- and far-IR maps at 3.4, 3.6, 4.5, 4.6, 5.8, 8.0, 12, 22, 24, 70, 100, 160, 250 from the Wide-field Infrared Survey Explorer (WISE; Wright et al., 2010), Spitzer (Fazio et al., 2004; Rieke et al., 2004; Werner et al., 2004), and Herschel Griffin et al., 2010; Pilbratt et al., 2010; Poglitsch et al., 2010. For the M101 dust mass map they relied on Herschel data from KINGFISH (Kennicutt et al., 2011), Spitzer data from Gordon et al. (2007), and WISE maps from the z0mgs survey (Leroy et al., 2019). Chastenet et al. (2021) used the Draine et al. (2007) physical dust model to fit the data, with the `DustBFF` fitting tool (Gordon et al., 2014). The free parameters for dust continuum emission fitting are the minimum radiation field heating the dust, $U_{\rm min}$, the fraction of dust grains heated by a combination of radiation fields at various intensities, γ, the total dust surface density, $\Sigma_{\rm dust}$, the fraction of grains with less than 10^3 carbon atoms, $q_{\rm PAH}$, and a scaling factor for stellar surface brightness, Ω_*. Details on image preparation, fitting procedure and results can be found in Chastenet et al. (2021).

[3] http://www.iram.es/IRAMES/mainWiki/Iram30mEfficiencies

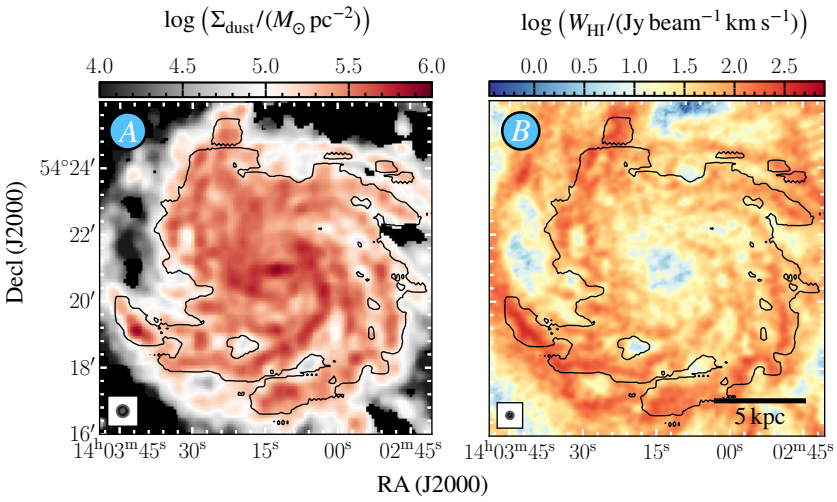

Figure 6.2: **Ancillary Data Set**. (*A*) The dust mass surface density map at *Herschel*/SPIRE 250 resolution (18″). The dust mass is estimated from SED fitting using the Draine et al., 2007 dust model (Chastenet et al., 2021). (*B*) THINGS H I moment 0 map after short-space correcting using Effelsberg EBHIS single-dish data (Winkel et al., 2016). Each panel shows the 0.5. K km s^{-1} contour of our ^{12}CO (1–0) IRAM 30m observation. Maps are shown at native resolution before hexagonal resampling.

Radial Metallicity Gradients

We employ radial metallicity gradient measurements from Berg et al., 2020. They derive the chemical abundances from optical auroral line measurements in HII regions across M101. Their observations are part of the CHemical Abundances Of Spirals (CHAOS) project (Berg et al., 2015). We use the slope and intercept of the gradient provided by Berg et al., 2020 (see Table 2 therein, we correct the slope since we use an updated value for M101's r_{25}):

$$12 + \log(\mathrm{O/H}) = \begin{cases} (8.78\pm0.04) - (1.10\pm0.07) R_g[r_{25}] & \text{for M101} \\ (8.75\pm0.09) - (0.27\pm0.15) R_g[r_{25}] & \text{for M51} \end{cases} \tag{6.4}$$

Atomic Gas Surface Density

To estimate the atomic gas surface density (Σ_{atom}), we use archival H I 21 cm line emission data from *The H I Nearby Galaxy Survey* (THINGS; Walter et al., 2008). The data were observed with the Very Large Array (VLA). We use the natural weighted data. These have an angular resolution of ∼11″(∼350 pc) and a spectral resolution of ∼5 km s^{-1}. We note that the THINGS data suffer from filtering artifacts. To improve the data, we feathered the interferometric VLA data using an Effelsberg single dish observation from the *The Effelsberg-Bonn H I Survey* (EBHIS; Winkel et al., 2016). We use the CASA version 5.6.1 `feather` function. We convert the H I line emission ($I_{\mathrm{H\,I}}$) to atomic gas surface density via (Walter et al., 2008):

$$\begin{aligned} &\Sigma_{\mathrm{H\,I}}[M_\odot\,\mathrm{pc}^{-2}] \\ &\quad = 1.36 \times (8.86 \times 10^3) \times \left(\frac{I_{\mathrm{H\,I}}[\mathrm{Jy\,beam}^{-1}\,\mathrm{km\,s}^{-1}]}{\mathrm{B_{maj}}[''] \times \mathrm{B_{min}}['']} \right), \end{aligned} \tag{6.5}$$

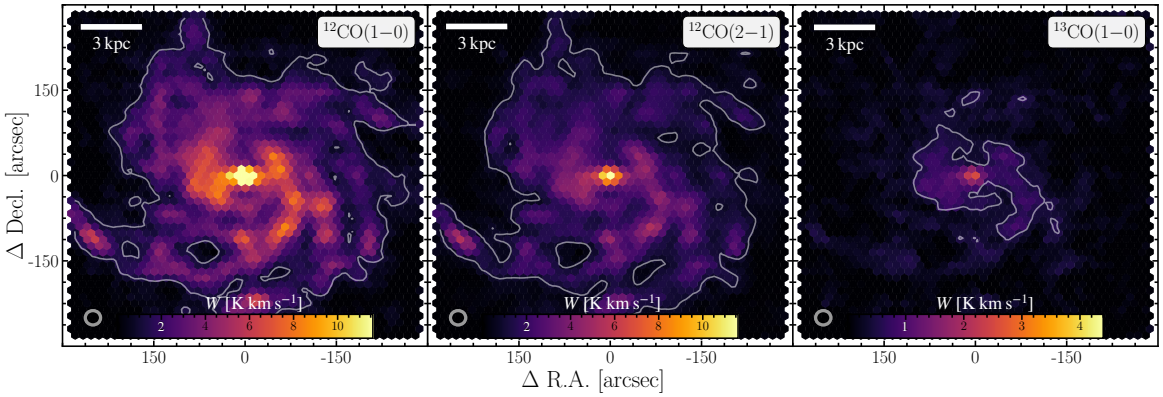

Figure 6.3: **Integrated Intensities**. All maps have been convolved to a common beamsize of 26″(the beamsize is indicated by the circle in the lower left corner). Color scale in units K km s^{-1}. Contour indicates S/N=5 of the respective CO isotopologue transition. We do not provide the C^{18}O (1−0) emission line map since we do not detect significant emission across the galaxy.

where the factor 1.36 accounts for the mass of helium and heavy elements and assumes optically thin 21cm emission. B_{max} and B_{min} are the FWHM of the major and minor axes of the main beam mentioned above. We provide further details on the feathering and how it affects the subsequent H I measurements in Section C.1.

Stellar Mass and SFR Data

We employ stellar mass and SFR surface density maps from the z0mgs survey (Leroy et al., 2019). The SFR surface density is estimated using a combination of ultraviolet observations from the Galaxy Evolution Explorer (GALEX; Martin et al., 2005) and mid-infrared data from the Wide-field Infrared Survey Explorer (WISE; Wright et al., 2010). We use the SFR maps with the combination FUV (GALEX)+ WISE4 (WISE).

We use the stellar mass surface density maps computed with the technique utilized for sources in the PHANGS-ALMA survey (Leroy et al., 2021b). In short, the $\Sigma_\star$ estimate is based on near-infrared emission observations at 3.6 μm (IRAC1 on Spitzer) or 3.4 μm (WISE1). The final stellar mass is then derived from the NIR emission using an SFR-dependent mass-to-light ratio.

6.2.4 Final Data Product

For the analysis in this paper, we homogenize the resolution of the data. We convolve all observations to a common angular resolution of 26″(=840 pc), adopting a Gaussian 2D kernel. We regrid all data onto a hexagonal grid where the points are separated by half the beam size (13″). We perform these steps using a modified pipeline, which has been utilized for IRAM 30m large programs before (EMPIRE, Jiménez-Donaire et al. 2019; CLAWS, den Brok et al. 2022).

We use the HERACLES/EMPIRE pipeline to determine the integrated intensity for the individual pixels in the regridded cube for each line, including H I. The goal is to create a signal mask that helps to optimize the S/N of the derived integrated intensities. The masked region over which to integrate is determined using a bright emission line. We use the ^{12}CO (1−0) line for the mask determination for pixels with a galactocentric radius $r \leq 0.23 \times r_{25}$. We select the factor 0.23, because, based on observations of star-forming galaxies, the CO surface brightness drops, on average, by a factor of $1/e$ at this radius

(Puschnig et al., 2020). This ensures that ^{12}CO is still detected significantly relative to the H I emission line. For lines of sight at larger galactocentric radii, the routine employs the H I emission line to determine the relevant spectral range. We make a mask where emission is detected at S/N > 4 and then expand the resulting mask into regions with S/N > 2 detections. Finally, we pad the mask by ±2 channels in velocity. The integrated intensity is then computed by integrating over the channels within the mask. Indicating the number of channels within the mask by $n_{\rm chan}$, the routine computes as follows:

$$W_{\rm line}\,[{\rm K\,km\,s^{-1}}] = \sum^{n_{\rm chan}} T_{\rm mb}(v)\,[{\rm K}] \cdot \Delta v_{\rm chan}\,[{\rm km\,s^{-1}}] \tag{6.6}$$

where $T_{\rm mb}$ is the surface brightness temperature of a given channel and $\Delta v_{\rm chan}$ is the channel width. Table 6.4 shows the integrated intensity for the ^{12}CO10, ^{12}CO21, and ^{13}CO10 emission lines. The integrated intensity maps The uncertainty of the integrated intensity for each sightline is computed using the final convolved and regridded cubes with the following equation:

$$\sigma_W\,[{\rm K\,km\,s^{-1}}] = \sqrt{n_{\rm chan}} \cdot \sigma_{\rm rms}\,[{\rm K}] \cdot \Delta v_{\rm chan}\,[{\rm km\,s^{-1}}] \tag{6.7}$$

We indicate the position-dependent 1σ root-mean-squared (rms) value of the noise per channel with $\sigma_{\rm rms}$. Our approach does not assume any variation of the noise with frequency for each target line. To determine the channel noise, the routine computes the median absolute deviation across the signal-free part of the spectrum scaled by a factor of 1.4826 (to convert to a standard deviation equivalent). Figure 6.3 shows the CO line intensity maps derived from this pipeline.

6.3 Analysis

In this study, we utilize observed quantities (i.e., integrated intensities or their ratios) and in certain instances also derived physical quantities (such as, for example, molecular gas mass surface density, $\Sigma_{\rm mol}$, or the star formation rate surface density, $\Sigma_{\rm SFR}$). We note that the conversion of observed quantities to derived ones is subject to additional uncertainties (e.g., Kennicutt and Evans, 2012; Bolatto et al., 2013; Usero et al., 2015).

6.3.1 $\alpha_{\rm CO}$ Estimation

We assume that dust and gas are connected via the following relation:

$$\frac{\Sigma_{\rm dust}}{\rm DGR} = \Sigma_{\rm H\,I} + \Sigma_{\rm H_2} = \Sigma_{\rm H\,I} + \alpha_{\rm CO} \times W_{^{12}{\rm CO}(1-0)}, \tag{6.8}$$

where DGR is the dust-to-gas ratio and $\alpha_{\rm CO}$ is the CO-to-H_2 conversion factor, which converts the CO integrated intensity into a molecular gas mass surface density. There are, however, two unknown quantities in Eq. (6.8): The key parameter $\alpha_{\rm CO}$ and the DGR value. Both parameters are expected to vary with galactic environment and are likely also linked to each other. To estimate both parameters, we introduce some modifications to the approach developed in Leroy et al., 2011 and Sandstrom et al., 2013. The idea is to simultaneously solve for $\alpha_{\rm CO}$ and DGR. The approach makes the following assumptions:

1. Gas and dust are well mixed. This ensures that Eq. (6.8) is valid.
2. DGR remains constant on ∼ 1.5kpc scales.
3. DGR does not change with atomic or molecular phases.

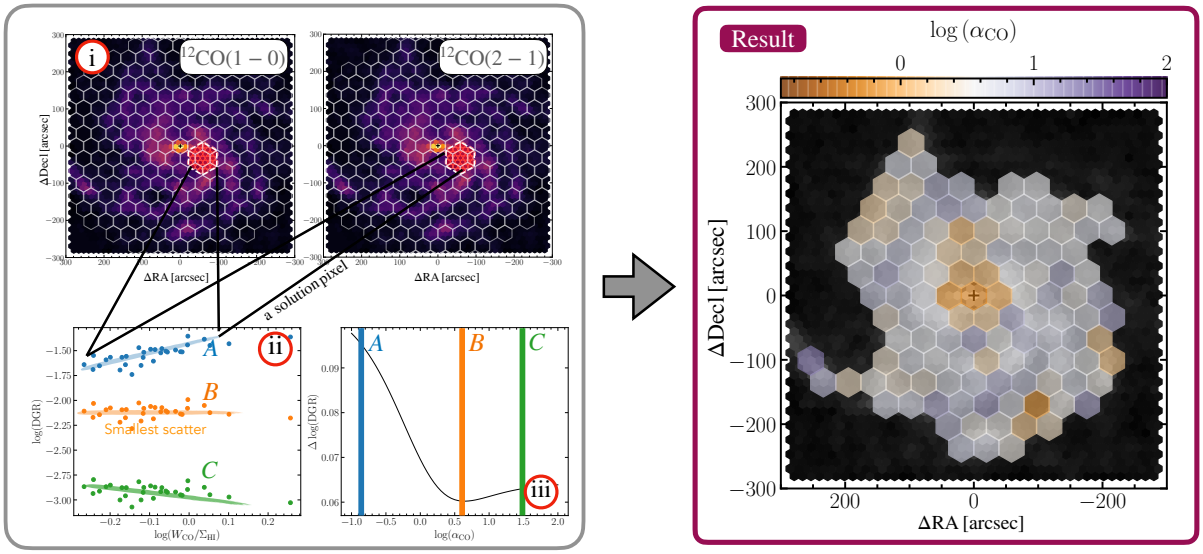

Figure 6.4: **Solution Pixel Approach to Estimate α_{CO}.** (*Left*) From the scatter minimization approach, described by Leroy et al., 2011 and Sandstrom et al., 2013, we obtain estimates of α_{CO} and DGR. The top panels (*i*) show the hexagons that illustrate the individual solution pixels for both ^{12}CO (1–0) and (2–1) transmission. The solution pixels consist of 37 underlying, half-beam spaced lines of sight. We note that the underlying hexagon tiling is meant to show the results in each solution pixel (the actual solution pixels have 40% overlap). In the maps, we highlight an individual solution pixel. We vary α_{CO} and compute the DGR following equation (6.8). We select the value for which the variation in DGR is minimal. The bottom right panel (*iii*) shows the variation of the DGR as a function of different α_{CO}. In the bottom left panel (*ii*), we combine all significant points from the solution pixel from both CO lines. We correct the ^{12}CO (2–1) data with the average line ratio of the solution pixel. The panel illustrates the differences in DGR for three selected α_{CO} (labeled *A*, *B*, and *C*). The variation for the selected solution pixel is minimal for α_{CO} labeled *B*. We perform this analysis for each solution pixel. (*Right*) The resulting α_{CO} value for each solution pixel based on the combined ^{12}CO (1–0) and ^{12}CO (2–1) emission line.

4. A negligible fraction of dust is present in the ionized gas phase.

The idea is that we find a value for α_{CO} which – given a set of measurements of Σ_{HI}, Σ_{dust} and $W_{^{12}CO}(1-0)$ – yields the most uniform distribution of DGR values over a certain (∼1.5kpc size) area. With this approach, we make no assumptions about the values of α_{CO} and DGR. We require, however, that there is a variation in the $W_{^{12}CO(1-0)}/\Sigma_{HI}$ ratio, since otherwise, there is no leverage by varying α_{CO} to find the minimum variation in the DGR values. We look for α_{CO} which yields the minimum scatter in DGR.

For a more detailed description of the implementation of the approach, we refer to Section 3 in Sandstrom et al., 2013. Here, we summarize how we construct a '*solution pixel*'. The approach requires a large enough set of sightlines, such that a variation in $W_{^{12}CO(1-0)}/\Sigma_{HI}$ ratio is present. But the region selected should also be small enough so that the assumption of a uniform DGR is still reasonable given the metallicity gradient (<0.1 dex/solution pixel). We split the galaxy into hexagonal regions containing 37 half-beam sampled data points (we flag and dismiss solution pixels where less than 15 sub-pixels show > 3σ CO emission). The solution pixels are separated center-to-center by 1.5 times the beam size. We note that

the solution pixels overlap (share ∼40% of the area with their neighboring solution pixel). Consequently, they are not fully independent from each other. We illustrate the solution pixel in Figure 6.4 (because the solution pixels are overlapping, it is difficult to illustrate. The pixel colored in red illustrates the full extent of a solution pixel). We estimate the uncertainty of the $\alpha_{\rm CO}$ value by performing a Monte Carlo test. For each measurement ($\Sigma_{\rm H\,I}$, $\Sigma_{\rm dust}$ and $W_{^{12}{\rm CO}(1-0)}$) we add random noise proportional to the their measurement errors. We repeat this 100 times. Our final $\alpha_{\rm CO}$ value and corresponding uncertainty are determined via bootstrapping. Iterating with $n_{\rm iter} = 1000$, we draw $n_{\rm sample} = 1000$ samples from the Monte Carlo iterations and take the mean and standard deviation.

We implement a slight improvement of the aforementioned $\alpha_{\rm CO}$ estimation method: For our data set, we have the advantage of the availability of two ^{12}CO rotational transitions to make our results more robust. We combine data points from both transitions simultaneously. When minimizing the scatter of the DGR to determine $\alpha_{\rm CO}$, we correct the ^{12}CO (2−1) data with the average R_{21} of each solution pixel. This introduces the assumption that R_{21} remains constant over the scales of a solution pixel. This is justified given the generally flat line ratio trends found across nearby galaxies, with only mild increases of 10% toward some galaxy centers (den Brok et al., 2021). By combining both CO lines, we effectively use all of our data.

We note that we do not account for systematic uncertainties in dust mass measurements. Phase-dependent depletion is observed, and the DGR is likely higher in dense, molecular regions (Jenkins, 2009). On the other hand, the dust appears to emit more effectively in dense regions (Dwek, 1998; Paradis et al., 2009; Köhler et al., 2015). These are discussed in detail in Sandstrom et al., 2013. They find that variation in DGR and dust emissivity could lead to a bias of $\alpha_{\rm CO}$ towards higher values (by a factor of ∼2). In contrast, uncertainties of cold dust in the SED modeling could bias $\alpha_{\rm CO}$ towards lower values (again by a factor of ∼2). However, recent work by Chiang et al. (2018) and Chiang et al. (2021) suggests that the variation of the dust-to-metals ratio and the emissivity could be larger. Such effects could be considered by updates to the scatter minimization technique in future work.

6.3.2 Metallicity, Z

We assume a solar abundance of $12 + \log_{10}({\rm O/H})_\odot = 8.69$ (Asplund et al., 2009) and convert the oxygen abundance to a metallicity ($Z = \Sigma_{\rm metal}/\Sigma_{\rm gas}$, where $\Sigma_{\rm gas}$ includes the mass of He as well). The following equation relates the fractional metallicity, Z, to the oxygen abundance:

$$Z = \frac{1}{M_{\rm O}/M_{\rm metal}} \frac{m_{\rm O}}{1.36\, m_{\rm H}} 10^{(12+\log_{10}({\rm O/H}))-12}. \tag{6.9}$$

We assume a fixed oxygen-to-metals ratio, $M_{\rm O}/M_{\rm metal} = 0.51$ (Lodders, 2003). The atomic masses for oxygen and hydrogen are indicated by $m_{\rm O}$ and $m_{\rm H}$ respectively. The factor 1.36 is used to convert the hydrogen mass to total gas.

6.4 Results

6.4.1 CO Emission Across M101

In Figure 6.3, we show the moment-0 maps of the ^{12}CO (1−0) and (2−1), and the ^{13}CO (1−0) emission lines. We detect significant ^{12}CO (1−0) and (2−1) emission across the full $10' \times 10'$ field-of-view. We see elevated emission clearly tracing the galaxy's bar and spiral arms. We also find higher integrated intensity values relative to the surroundings at the Eastern tip of the southern spiral arm. We find significant

^{13}CO (1−0) emission within $r_{\rm gal} \lesssim 5$ kpc. The emission clearly follows the bar and spiral arms. The C^{18}O (1−0) is too faint, and we do not detect any emission at S/N>3.

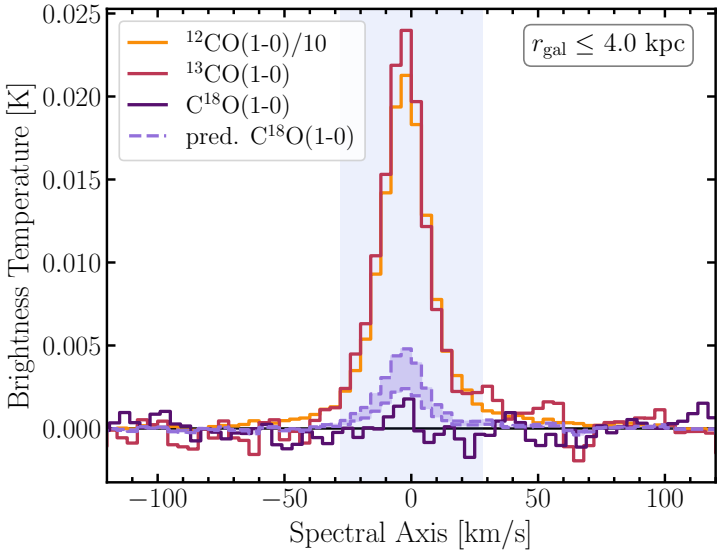

Figure 6.5: **Radially stacked CO spectra for $r_{\rm gal} \leq 4$ kpc.** We stack over the central 4 kpc. Furthermore, the predicted C^{18}O (1−0) emission line is shown, based on the ^{13}CO (1−0) emission line and assuming a line ratio of $0.2 > R_{18/13} < 0.1$ (Jiménez-Donaire et al., 2017a). The C^{18}O (1−0) in M101 seems to be fainter than we would expect based on values from EMPIRE. The blue shaded background indicates the line mask over which we integrate the spectrum.

For a full reference, Figure C.2 in Section C.3 shows the radially stacked spectra of the ^{12}CO (1−0) and ^{13}CO (1−0) emission line. We stack the spectra in radial bins with a step size of 1.25 kpc out to 10 kpc. Thanks to the improved S/N in the stacked spectra, we do find significant (S/N > 3) ^{13}CO (1−0) emission out to $r_{\rm gal} \leq 8$ kpc. However, C^{18}O (1−0) emission remains undetected for our 1.25 kpc radial bins and even when stacking all central 4 kpc sightlines (Figure 6.5). In the Figure 6.5, we show for comparison the expected range of line emission based on the ^{13}CO (1−0) emission and the assumption of a line ratio commonly found in spiral galaxy of $0.2 > R_{18/13} > 0.1$ (Langer and Penzias, 1993; Jiménez-Donaire et al., 2017a). The integrated intensity differs by a factor 2 to 4 from the predicted range ($W^{\rm ul} = 0.04$ K km s^{-1} and $W^{\rm pred.} = 0.1 - 0.2$ K km s^{-1} with an average uncertainty of 0.01 K km s^{-1}). We derive an 2σ upper limit of $R_{18/13} < 0.07$. For comparison, ratios commonly found in the literature range from $R_{18/13} > 1$ in ULIRGs (Brown and Wilson, 2019), to $R_{18/13}$~0.3 in starburst (Tan et al., 2011), and $R_{18/13}$~0.1 in the Milky Way (Langer and Penzias, 1993).

6.4.2 CO Line Ratios

We reiterate that we refer to the integrated intensity ratio between two lines simply as *line ratio*. The ^{12}CO (1−0) and (2−1), as well as the ^{13}CO (1−0) emission, is bright enough so that we can investigate its

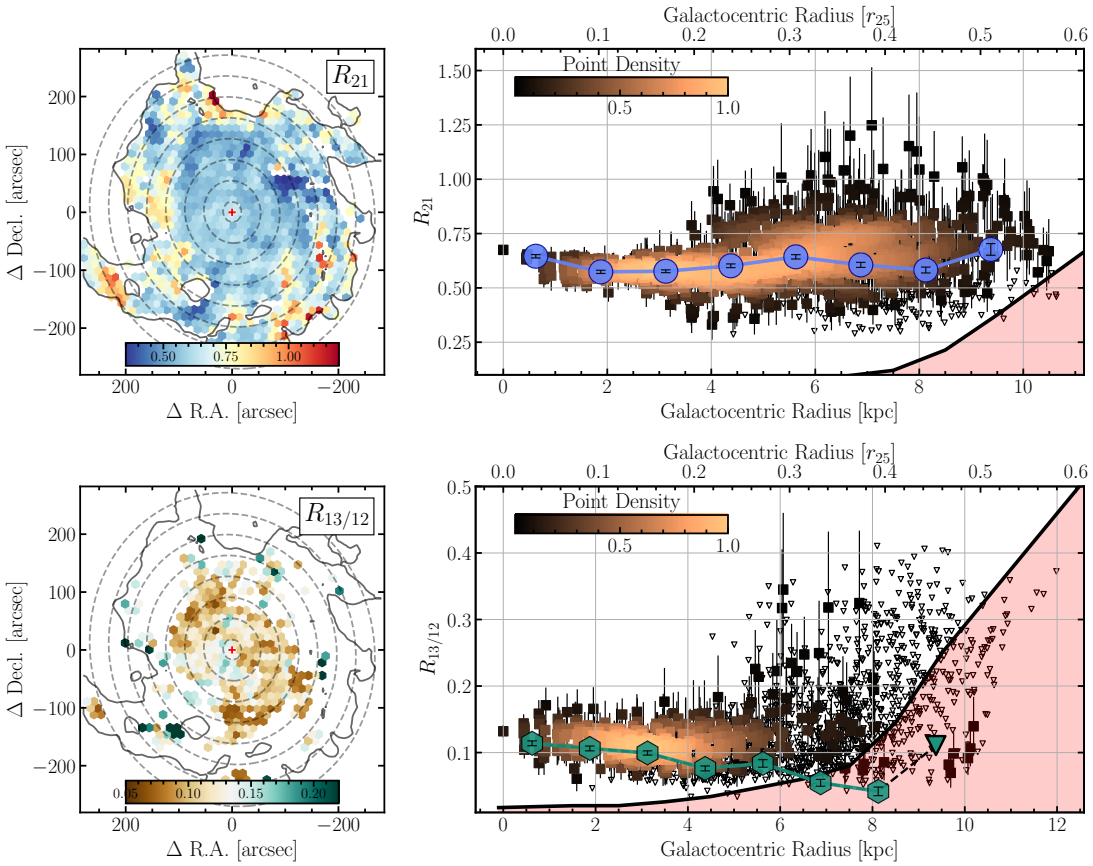

Figure 6.6: **Spatial and Radial Variation of the CO Line Ratio.** Top row shows the R_{21} line ratio while the bottom row shows the $R_{13/12}$ line ratio. The maps (left panels) show the spatial distribution of the line ratios. The 5σ contour of the ^{12}CO (1–0) emission is shown by the solid contour. The dashed circles indicate the radial bins used for the stacking. The radial plots (right panels) show the radial trends of the line ratios. The line ratio based on the stacked line brightness is indicated by the larger, blue circles and green hexagons. Triangles indicate 3σ upper limits. The uncertainty of the points is indicated, but it is generally smaller than the point size. The censored region is shown by the red (1σ) shaded region. The region indicates where due to the lower sensitivity of one observation set, we do expect to find a certain number of significantly detected data points.

variation across the field-of-view. In particular, the following line ratios are of interest to us:

$$R_{21} \equiv \frac{W_{^{12}\mathrm{CO}\,(2-1)}}{W_{^{12}\mathrm{CO}\,(1-0)}} \tag{6.10}$$

$$R_{13/12} \equiv \frac{W_{^{13}\mathrm{CO}\,(1-0)}}{W_{^{12}\mathrm{CO}\,(1-0)}} \tag{6.11}$$

We illustrate the spatial variation of these two line ratios as well as their radial trends in Figure 6.6. We show the line ratio of the individual sightlines as well as the radially stacked ones discussed in Subsection 6.4.1, which have a radial bin size of 1.25 kpc. Furthermore, we introduce a censored region. These indicate regions in the parameter space where we do not expect line ratio detections due to differences in the S/N of

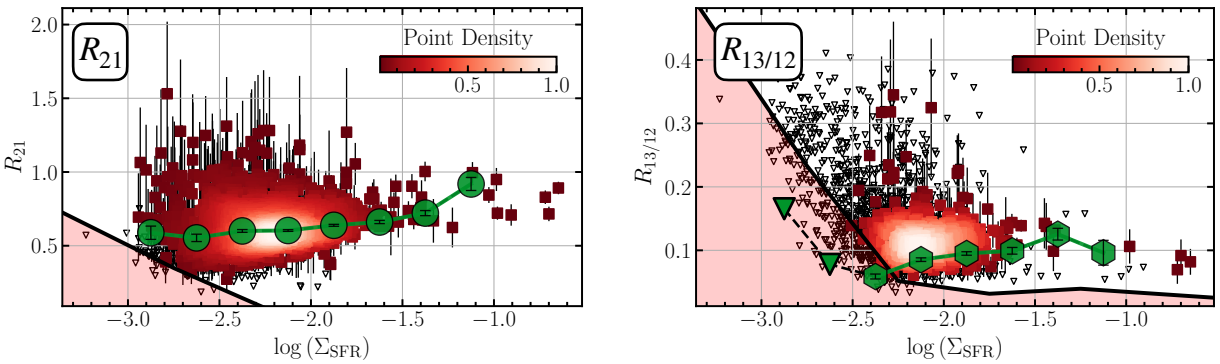

Figure 6.7: **CO Line Ratios as function of star formation surface density (Σ_{SFR}).** Panels show trends with the ^{12}CO (2−1)/(1−0) (R_{21}) ratio (left) and the ^{13}CO/^{12}CO (1−0) ratio ($R_{13/12}$) (right). Panel description follows right panels in Figure 6.6.

Table 6.3: **Mean values and Kendall's τ rank correlation coefficient (p-value given in parenthesis).** Measured for the line ratios of stacked spectra as function of galactocentric radius and SFR surface density (see Figure 6.6 and Figure 6.7).

Line Ratio	$\langle R \rangle$	$\langle R \rangle^{\rm equal}$	Kendall's τ rank correlation coefficient	
			Radius	Σ_{SFR}
	(1)	(2)		
R_{21}	$0.60^{+0.07}_{-0.11}$	$0.62^{+0.08}_{-0.14}$	0.36 (0.3)	0.92 (4×10^{-4})
$R_{13/12}$	$0.11^{+0.03}_{-0.02}$	$0.12^{+0.03}_{-0.03}$	−0.90 (0.003)	0.73 (0.06)

Notes: The value in parentheses indicates Kendall's τ p-value. We consider any correlation with $p \leq 0.05$ significant. (1) $\langle R \rangle$ indicates the average line ratio weighted by ^{12}CO (2−1) integrated intensity. The uncertainty for each line ratio is given by the weighted 16th and 84th percentiles range. (2) The ^{12}CO(1-0) intensity weighted median line ratio and 16th and 84th percentiles (since all pixels have the same size, this corresponds to weighing all points equally).

the two different line detections of the ratios (see Section C.2 for a description of the censored region). In addition, we compare the line ratio trends to Σ_{SFR}, which traces changes in temperature and density of the gas (Narayanan et al., 2012). Previous studies found a trend of R_{21} with the SFR surface density, which would make it a potential tracer of line ratio variation (Sawada et al., 2001; Yajima et al., 2021; Leroy et al., 2022, e.g.). Figure 6.7 illustrates the trends of CO lines stacked by Σ_{SFR}.

In Figure 6.8, we furthermore compare the average line ratio value R_{21} and $R_{13/12}$ we determined across the full field-of-view (see Table 6.3) with values measured in the literature.

R_{21} Line Ratio

For R_{21} we find a flat radial trend for the individual lines of sight as well as the stacked values. The Kendall's τ correlation coefficient does not indicate any correlation (see Table 6.3). We find a ^{12}CO (1−0) brightness weighted average ratio of $\langle R_{21} \rangle = 0.60^{+0.07}_{-0.11}$. This agrees well to within 1σ with the ratio of

$\langle R_{21}^{\mathrm{Leroy2022}} \rangle = 0.52^{+0.19}_{-0.13}$ reported for this galaxy by (Leroy et al., 2022), based on IRAM 30m HERA and NRO data. There seems to be only a mild increase of the ratio within the central region ($r_{\mathrm{gal}} < 1$ kpc), with a line ratio of 0.69 for the central sightline.

When comparing to the full EMPIRE survey, which consist of nine nearby spiral galaxies, we find an almost identical median value: den Brok et al., 2021 report $\langle R_{21}^{\mathrm{EMPIRE}} \rangle = 0.63^{+0.09}_{-0.09}$. In addition, our value agrees well with the average line ratio for a set of literature single-pointing measurements of nearby spiral galaxies, namely $\langle R_{21}^{\mathrm{literature}} \rangle = 0.59^{+0.18}_{-0.09}$, which den Brok et al., 2021 have compiled. Yajima et al., 2021 find an average $\langle R_{21}^{\mathrm{Yajima}} \rangle = 0.64^{+0.18}_{-0.18}$, which agrees with our finding in M101 within the error margins. Recently, Leroy et al. (2022) investigated R_{21} on kpc-scales for galaxies part of the PHANGS-ALMA survey. They report an average-wide line ratio of $\langle R_{21}^{\mathrm{PHANGS}} \rangle = 0.61^{+0.21}_{-0.11}$. Also, the center of NGC 6946 shows a similar dynamical range (Eibensteiner et al., 2022). M51 with ratio $\langle R_{21}^{\mathrm{M51}} \rangle = 0.89^{+0.11}_{-0.07}$ remains an outlier to all these studies as already noted by den Brok et al. (2022). Finally, we find that the average value derived from xCOLD GASS measurements (Saintonge et al., 2017) is slightly higher than the value we find. We note that the xCOLD GASS includes galaxies with high star formation rates, which could be associated with enhanced R_{21}. Overall, we see that our average value found in M101 agrees well with those derived from a larger set of nearby spiral galaxies.

Figure 6.7 shows the distribution of the line ratios for the individual sightlines with the SFR surface density. We also show the stacked line ratio to better illustrate the trends. When looking at the stacked points, we find, on the one hand, a significant ($p = 4 \times 10^{-4}$) positive ($\tau = 0.92$) correlation for R_{21} with the SFR surface density, Σ_{SFR}. Such a positive correlation with SFR surface density is also reported by Leroy et al. (2022), who studying the PHANGS-ALMA sample, found a Spearman's rank correlation coefficient of $\rho = 0.55$ for the galaxy-wide, normalized binned R_{21} to the normalized SFR surface density.

$R_{13/12}$ Line Ratio

For $R_{13/12}$ we find a clear negative radial trend when looking at the stacked data points (Kendall's coefficient of $\tau = -0.90$ and a p-value of $p = 0.003$. We consider a correlation with a p-value below 0.05 to be significant). We can sample the censored region with the stacked points, as we have significant ^{13}CO (1–0) emission out to ~8 kpc (see Subsection 6.4.1 and Figure C.2). The trend is less obvious when looking at individual sightlines, as the scatter seems to be significant over the radial trend, and we are limited by the censored region. We find an average line ratio of $\langle R_{13/12} \rangle = 0.11^{+0.03}_{-0.02}$. The stacked integrated intensities decreases from $R_{13/12}|_{r_{\mathrm{gal}}=0} = 0.113 \pm 0.004$ down to $R_{13/12}|_{r_{\mathrm{gal}}=8\,\mathrm{kpc}} = 0.055 \pm 0.005$ further out.

When stacking over the ^{13}CO mask, we compute the line ratio by integrating over a fixed window with a width of $\Delta v = 120\,\mathrm{km\,s^{-1}}$ centered at $v = 0\,\mathrm{km\,s^{-1}}$. We find $R_{21}^{^{13}\mathrm{CO}} = 0.60 \pm 0.01$ and $R_{13/12}^{^{13}\mathrm{CO}} = 0.115 \pm 0.003$.

The average ratio of $\langle R_{13/12}^{\mathrm{M51}} \rangle = 0.12^{+0.02}_{-0.072}$ found in M51 (den Brok et al., 2022) is consistent within the error margin of the average ratio we find in this study, however, its scatter is slightly larger. Cormier et al., 2018 studied the ^{12}CO-to-^{13}CO line ratio for the nine EMPIRE galaxies. Converting their finding to $R_{13/12}$, they obtain $\langle R_{13/12}^{\mathrm{EMPIRE}} \rangle = 0.09^{+0.01}_{-0.01}$, again consistent with our finding. Similarly, studying centres of around 10 nearby galaxies, including AGN and central starburst a range of $0.06 < R_{13/12} < 0.13$ is found by Israel, 2009a; Israel, 2009b. For comparison, we also show measurements from the Milky Way (Paglione et al., 2001). For galactic radii larger than 2 kpc, they find an average value of $\langle R_{13/12}^{\mathrm{MW}} \rangle = 0.10^{+0.02}_{-0.02}$. Also studying this ratio in the Milky Way, Roman-Duval et al., 2016 find a radial gradient of the ratio decreasing from $R_{13/12} = 0.16$ at 4 kpc to $R_{13/12} = 0.1$ at 8 kpc radial distance. Both Milky Way findings agree well with our finding in M101.

In addition, we investigate the distribution of the CO line ratio across the disk of the galaxy with respect

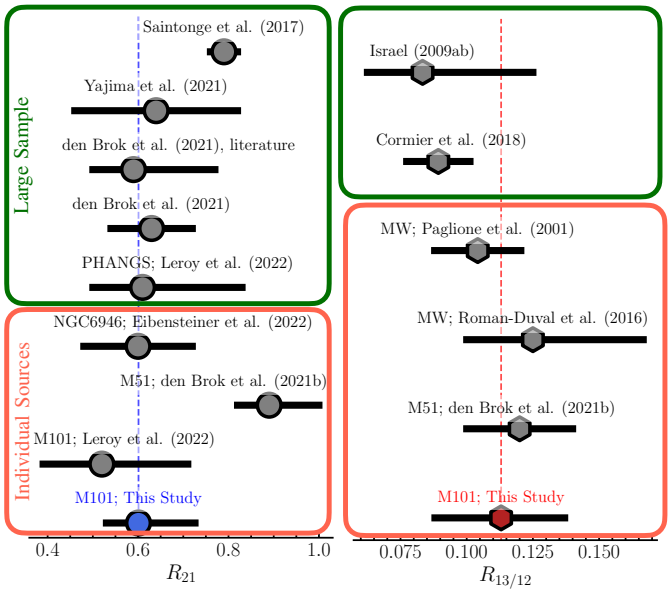

Figure 6.8: **CO Line Ratio Comparison to Literature Values.** We compare the average R_{21} and $R_{13/12}$ values estimated from the distribution of the M101 data points to literature values. Errorbars indicate the 1σ distribution of sample values. In case the literature value corresponds to the value for a specific galaxy, the name of the source is provided. (*Left*) Collection of R_{21} distributions. Our range of detected R_{21} agrees well with previous studies of M101. We also note that M51 shows higher line ratio values than M101. (*Right*) The $R_{13/12}$ distribution is shown. Our finding agrees well with results M51 and the Milky Way.

to the SFR surface density (see bottom panels of Figure 6.7). $R_{13/12}$ shows only a mild positive trend ($\tau = 0.73$) with the SFR surface density ($p = 0.06$).

6.4.3 Trends in $\alpha_{\rm CO}$ Distribution

The result panel in Figure 6.4 shows the spatial distribution of the estimated $\alpha_{\rm CO}$. From a qualitative assessment alone, we find towards the center of the galaxy a decrease in $\alpha_{\rm CO}$ and an increase of the DGR. Figure 6.9 shows the radial trend of $\alpha_{\rm CO}$ as well as the residual. The result clearly illustrates the lower $\alpha_{\rm CO}$ values towards the center, while it has a relatively constant value inside the disk (for the central solution pixel, we have $\alpha_{\rm CO}^{\rm center} = (0.43 \pm 0.03)\,{\rm M}_\odot\,{\rm pc}^{-2}\,({\rm K\,km\,s}^{-1})^{-1}$, while the average value in the disk amounts to $\langle\alpha_{\rm CO}\rangle|_{\rm disk} = (4.4{\pm}0.9)\,{\rm M}_\odot\,{\rm pc}^{-2}\,({\rm K\,km\,s}^{-1})^{-1}$). We find, however, a large 1σ point-to-point scatter in $\alpha_{\rm CO}$ inside the disk ($r > 2\,{\rm kpc}$) of ~0.3 dex. Based on our Monte Carlo implementation of iteratively computing $\alpha_{\rm CO}$, we find that the propagated uncertainty of $\alpha_{\rm CO}$ is ~0.1 dex. Figure 6.4 lists the $\alpha_{\rm CO}$ values using different binnings.

Our finding of low $\alpha_{\rm CO}$ values toward the center is consistent with other studies targeting larger samples of galaxies and found conversion factors 5−10 times lower than the average MW factor in the center of nearby spiral galaxies (Israel, 1997; Sandstrom et al., 2013). Past studies found such low values for extreme starbursts like galaxies, such as LIRG (e.g. Downes and Solomon, 1998; Kamenetzky et al., 2014; Sliwa et al., 2017). We note that, in particular, the low value we find for the center of M101 is consistent with the optically thin ^{12}CO emission limit. In the presence of highly turbulent gas motions or large gas velocity dispersion, it is possible that the low-J ^{12}CO emission turns optically thin. Under representative molecular ISM conditions with an excitation temperature of $T_{\rm ex} = 30\,{\rm K}$, a canonical CO abundance of

Table 6.4: **Median α_{CO} values for M101 and M51.**

	M101			M51		
α_{CO}[a]:	binned[b]	num. wgt[c]	lum. wgt[d]	binned[b]	num. wgt[c]	lum. wgt[d]
All	$4.3^{+0.9}_{-0.9}$	$4.4^{+3.1}_{-2.2}$	$4.1^{+2.7}_{-3.0}$	$3.3^{+0.6}_{-0.6}$	$3.2^{+3.0}_{-1.5}$	$3.1^{+0.4}_{-1.4}$
Center[e]		0.43			3.1	
Disk	$4.4^{+0.9}_{-0.9}$	$4.5^{+3.2}_{-1.8}$	$4.5^{+3.2}_{-1.6}$	$3.7^{+0.6}_{-0.6}$	$3.5^{+3.3}_{-1.8}$	$3.1^{+1.6}_{-1.5}$

Notes: (a) Conversion factor in units $M_\odot$ kpc^{-2} (K km s^{-1}), (b) binning together all the datapoints. Uncertainty represents the binned propagated uncertainty. (c) Median with 16th and 84th percentile scatter (d) ^{12}CO (1–0) intensity weighted median with 16th and 84th percentile scatter. (e) Center consists only of one solution pixel.

$\left[\mathrm{CO/H_2}\right] = 10^{-4}$, and assuming LTE, we expect $\alpha_{CO}^{\text{opt. thin}} \approx 0.34\,M_\odot\,\mathrm{pc}^{-2}(\mathrm{K\,km\,s^{-1}})^{-1}$, which is very close to the value we find for the center of M101.

We note that M101 is also included in the sample investigated by Sandstrom et al., 2013. They find a central α_{CO}value of $\log(\alpha_{CO}^{\text{center}}) = -0.45 \pm 0.2$, which lies within the margin of error of the value we find ($\log(\alpha_{CO}^{\text{center}}) = -0.4 \pm 0.05$). However, they find an average value of $\langle\alpha_{CO}^{S13}\rangle = 2.3$, which is a factor 2 lower than the value we find in this study. To test the impact of different data sets, we repeat the α_{CO} estimation using a different combination of ^{12}CO (2–1) (CLAWS and HERACLES) and H I (non-feathered and feathered) data sets. This way, we can assess how the difference in datasets affects the resulting α_{CO} values. For details on the comparison, we refer to Section C.5. The discrepancy can be traced back to the fact that they relied on ^{12}CO (2–1) observations from IRAM 30m/HERA, used a constant $R_{21} = 0.7$ ratio to convert between the $J = 2 \rightarrow 1$ and $J = 1 \rightarrow 0$ transition and used THINGS H I data that have not been short-space corrected. On the one hand, we find from our analysis that substituting the CLAWS data with the HERACLES ^{12}CO (2–1) observations does not significantly affect the average α_{CO} distribution. On the other hand, using the non-feathered H I data systematically lowers the α_{CO} measurements by 0.1 dex. We also find that using a constant R_{21} and only relying on the HERACLES ^{12}CO (2–1) observations, we

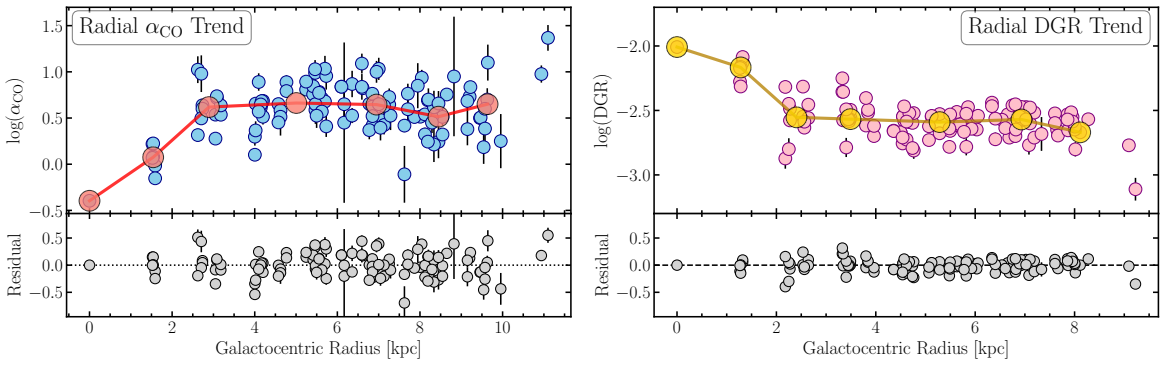

Figure 6.9: **Radial α_{CO} and DGR trend in M101** The left panel shows radial α_{CO} trend, and the right panel illustrates radial DGR dependency. (*Top*) Smaller blue (pink) points show the individual α_{CO} (DGR) measurements for the various solution pixels. Larger red (yellow) points show the derived trend based on binning the data. (*Bottom*) Residual α_{CO} or DGR values after subtracting the radial trend based on linearly interpolating the binned data trend.

further systematically lower α_{CO} by 0.2 dex, hence reproducing the results from Sandstrom et al. (2013). Compared to the full sample of spiral, star-forming galaxies investigated in Sandstrom et al., 2013, the value of α_{CO} we find is slightly above the sample-wide average value of $\alpha_{CO} = 3.1$.

Contrasting our finding to results from studies using another α_{CO} estimation approach, we find that our median α_{CO} value for the disk of M101 is, in fact, consistent with Virial mass dependent measurements. For example, Rebolledo et al., 2015 studied the conversion factor in certain brighter regions of M101 and found, on average, values close to the MW average.

After subtracting the radial dependence from α_{CO} we do not find any significant correlation with any of the parameters we investigate. Both the slope and the correlation coefficients are consistent with zero.

6.4.4 α_{CO} based on Multi-Line Modelling

Using the ^{13}CO (1–0) emission line, we can perform a simple LTE modelling attempt to obtain further independent estimates of α_{CO}, which we refer to hereafter as α_{CO}^{LTE}. Given LTE, one can estimate the conversion factor using the following equation

$$\alpha_{CO}^{LTE} = \left[\frac{H_2}{^{13}CO}\right] \times \frac{\eta_{12}}{\eta_{13}} \times \frac{6.5 \times 10^{-6}}{1 - \exp(-5.29/T_{exc})} \times R_{13/12}. \tag{6.12}$$

In this formula, $R_{13/12}$ captures the optical depth, T_{exc} indicates the excitation temperature of ^{13}CO and $\left[\frac{H_2}{^{13}CO}\right]$ describes the relative ^{13}CO abundance. We refer to Jiménez-Donaire et al. (2017a) for a more detailed derivation of the equation.

Figure 6.10 shows the derived α_{CO}^{LTE} values as a function of the galactocentric radius. For comparison, we also include the radial trend obtained from the scatter minimization technique. We use two different approaches to estimate the input parameters besides $R_{13/12}$ in Equation 6.12:

(i) We assume constant LTE conditions so that the lines are thermalized across M101 following values provided in Cormier et al. (2018). In particular, we fix the excitation temperature $T_{ex} = 20$ K, the beam filling factor ratio $\eta_{12}/\eta_{13} = 1$, and the ^{13}CO abundance $[H_2/^{13}CO] = 1 \times 10^6$ (for the disk, we assume a lower value than provided in Dickman, 1978). The result is indicated by the grey points in Figure 6.10. We find a relatively flat trend with $\langle \alpha_{CO}^{LTE} \rangle = 3.5^{+0.7}_{-0.9}$.

(ii) Because the molecular gas conditions are likely not constant across the galaxy, we perform the α_{CO}^{LTE} calculation again, but this time, we vary simultaneously the excitation temperature, beam filling factor ratio, and abundance ratio between the center and the disk, thus mimicking a two-phase model. We use a convenient sigmoid function to vary the parameters between the disk and center limit as a function of galactocentric radius. In particular, we use the limit values used in Cormier et al. (2018). We vary the ^{13}CO excitation temperature, T_{ex}, between 20 K (disk) and 30 K (center). Such values are in line with findings in the Milky Way (Roueff et al., 2021). Roman-Duval et al. (2016) find that the ^{13}CO-emitting gas is denser towards the center, which motivates us to use higher excitation temperatures towards the center, in line with finding higher ^{13}CO excitation temperatures in the denser regions of molecular clouds. The increase of the abundance towards the center is motivated by our finding that $R_{13/12}$ enhanced towards the center (see Subsubsection 6.5.1 for further discussion). Finally, we also vary the beam filling factor η_{12}/η_{13} between a value of 1 (disk) and 2 (center). The beam filling factor can particularly differ since we expect ^{12}CO to trace more the bulk diffuse phase, hence filling the beam, while ^{13}CO is more confined to the dense molecular gas phase. The measurements are shown as red points in Figure 6.10. The top panels of Figure 6.10 show the radial trend for the individual parameter we use as input for Equation 6.12. In fact, using this approach,

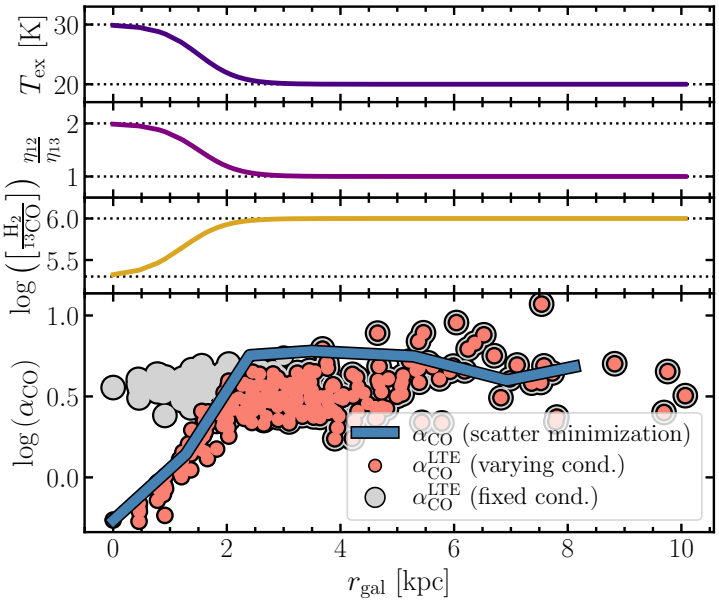

Figure 6.10: **^{13}CO Derived α_{CO}^{LTE}** We estimate the conversion factor under LTE assumptions using the ^{12}CO (1–0) and ^{13}CO (1–0) emission. We perform two iterations: (i) keeping the conditions fixed across the galaxy apart from the $R_{13/12}$ ratio and (ii) varying the ^{13}CO excitation temperature,T_{ex}, the beam filling factor ratio, η_{12}/η_{13}, and the ^{13}CO abundance between disk and center using a sigmoid function. (*Top three panels*) Variation of input parameters for α_{CO} derivation. (*Bottom Panel*) Radial Trend in α_{CO}^{LTE}. Grey points indicate measurements under fixed conditions. Red points indicate α_{CO}^{LTE} assuming a variation of input parameters as shown in the top three panels. The blue line shows the radial trend derived from the scatter minimization technique.

we can reproduce the depression of the conversion factor toward the center of the galaxy. For the disk ($r > 2$ kpc), we find $\langle\alpha_{CO}^{LTE,disk}\rangle = 2.8^{+1.1}_{-0.7}$, while in the center, we find $\langle\alpha_{CO}^{LTE,center}\rangle = 0.6^{+0.2}_{-0.1}$.

We note that with our ^{13}CO approach, we obtain α_{CO} values in the disk that are systematically lower by a factor 2 than the values we find with the scatter minimization approach. Such a finding of systematically lower α_{CO} values based on ^{13}CO is consistent with previous studies (e.g., Meier et al., 2001; Meier and Turner, 2004; Heiderman et al., 2010; Cormier et al., 2018). Similarly, Szűcs et al. (2016) show by using numerical simulation of realistic molecular clouds that total molecular mass predictions based on ^{13}CO are systematically lower by a factor of 2–3 due to issues related to chemical and optical depth effects. Cormier et al. (2018) conclude that the systematic offset between ^{12}CO and ^{13}CO based α_{CO} estimates likely derive from the simplifying assumption of a similar beam filling factor of the two lines across the disk. Such a difference is expected since ^{12}CO is tracing the diffuse molecular gas phase, while ^{13}CO is more confined to the more dense molecular gas phase. The fact that for the depression of α_{CO} both estimates agree likely also reflects that our simplified assumptions of the variation of the parameters to the center reflect the actual physical gas conditions more properly. To robustly and quantitatively constrain the parameters, such as the excitation temperature and abundance, the observations of other ^{13}CO rotational transitions would be necessary.

In principle, we could match both prescriptions with just slightly different parameter profiles for the LTE-based α_{CO} estimation. So far, for instance, we have adopted a MW-based ^{13}CO abundance in the disk. If we assume that abundance values in the disk are larger by a factor 2 in M101 than in the MW, we will

recover the same α_{CO} trend from both prescriptions. However, further observations are needed to constrain the actual ^{13}CO abundance in M101.

So generally, our LTE-based α_{CO} estimates offer valuable qualitative insight into potential drivers for the CO-to-H_2 conversion factor variation. Quantitatively assessing the α_{CO} values is difficult due to the underlying assumptions that need to be taken for the input parameters (excitation temperature, beam filling factor, and ^{13}CO abundance). By allowing variation of the parameters toward the center, the depression of α_{CO} is somewhat accurately described. This method provides an estimate of the order of magnitude change of the input parameters.

6.4.5 The DGR across M101

Based on our scatter minimization approach, we also derive estimates of the DGR for the individual solution pixels. The right panel in Figure 6.9 shows the radial trend in DGR. Similarly to α_{CO} we find a clear difference of the value towards the center (larger values by 0.5 dex), while the disk shows a relatively flat trend of $\log \mathrm{DGR} = (-2.6 \pm 0.5)$. Furthermore, the disk shows a relatively small point-to-point scatter of only 0.2 dex. The values we find for the DGR are significantly lower than the average Milky Way solar neighborhood ($\mathrm{DGR}^{\mathrm{MW}} = 0.01$, which is off by 0.5 dex; Frisch and Slavin 2003) and nearby spiral galaxies ($\mathrm{DGR}^{\mathrm{spiral}} = 0.014$, which is off by 0.6 dex;Sandstrom et al. 2013).

However, in their comprehensive study of the DGR in M101, Chiang et al. (2018) find values in agreement with our DGR results. They find a linear metallicity dependence of the DGR, with values ranging from 10^{-3} (at $12 + \log(\mathrm{O/H}) = 8.3$) to 10^{-2} (at $12 + \log(\mathrm{O/H}) = 8.6$). We cover a dynamical range in metallicity ($12 + \log(\mathrm{O/H})$) of 0.3 dex between center and disk of M101. Chiang et al. (2018) find a twofold dynamical range in DGR with respect to the metallicity range. Based on this, we would expect to find a 0.6 dex variation of DGR, which is close to the actual 0.5 dex we find.

6.4.6 Comparison of DGR and α_{CO} trends in M51 and M101

In the left panel of Figure 6.11, we compare the α_{CO} trend with galactocentric radius in the nearby massive star-forming galaxy M51 (NGC 5194). Figure 6.4 lists the α_{CO} values for M51 using different binnings.

We estimate α_{CO} in M51 as described in Subsection 6.3.1. We use CO (1−0) data from PAWS (Pety et al., 2013), CO (2−1) from CLAWS (den Brok et al., 2022), H I observations from THINGS (Walter et al., 2008) and dust mass maps using the Draine et al., 2007 model. We note that we do not perform a short-space corrections for the H I data, since upon visual inspection of the spectra, we find that the M51 are less affected by filtering issues than the M101 observations. Figure 6.11 shows the trend of α_{CO} determined from the scatter minimization technique for both M101 and M51 as a function of galactocentric radius, R_{21}, and $R_{13/12}$. For reference, we show the α_{CO} map for M51 in Appendix C.6.

(i) *Galactocentric Radius:* We do not find any significant trend of α_{CO} with galactocentric radius in M51. Across the disk of the galaxy, we find an average value of $\langle \alpha_{CO}^{M51} \rangle = 3.7 \pm 0.6 \mathrm{M}_\odot\,\mathrm{pc}^{-2}/(\mathrm{K\,km\,s}^{-1})$. This is slightly lower but within the scatter margin for the value found by Leroy et al. (2017). In that study, the authors performed a slightly different version of the scatter minimization technique: They selected a range in α_{CO} that yields a constant DGR trend across the disk of M51. With this technique, they find the following range $\alpha_{CO}^{L17} \approx 4.5 - 5.0\,\mathrm{M}_\odot\,\mathrm{pc}^{-2}/(\mathrm{K\,km\,s}^{-1})$.

(ii) *Line Ratio R_{21}:* This particular CO ratio is expected to trace variations in density, temperature, and potentially the opacity of the molecular gas (Peñaloza et al., 2017). Previous studies also find a correlation of R_{21} with the star formation rate surface density, Σ_{SFR} (Koda et al., 2020; den Brok et al., 2021; Leroy et al., 2022). As the middle panel of Figure 6.11 shows, M51 covers higher R_{21} values than M101.

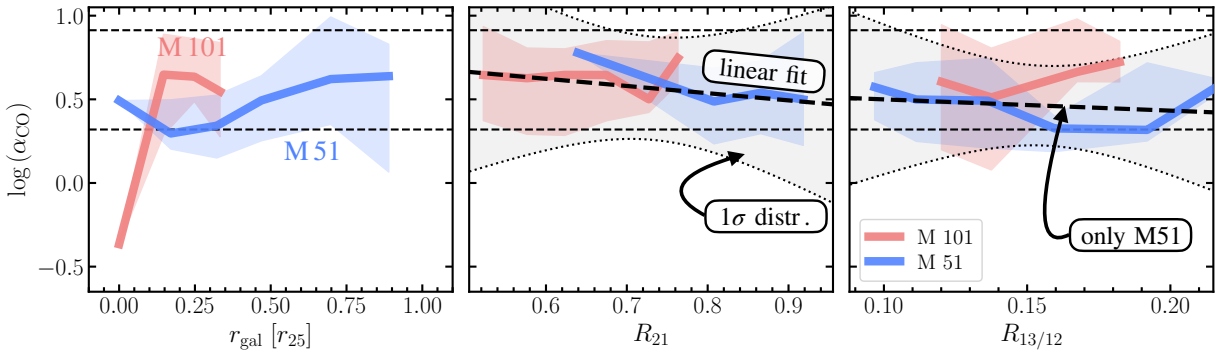

Figure 6.11: **Comparing α_{CO} Trends in M101 and M51.** Comparison of radial α_{CO} trend in M101(red) and M51(blue). Each panel shows the trend line for both galaxies separately. The trend is determined by binning the α_{CO} values of the individual line of sights. The shaded region around the trend line shows the respective 1σ scatter of the respected trend lines. (*Left*) Trend of α_{CO} with galactocentric radius normalized by r_{25}. (*Center*) ^{12}CO line ratio R_{21} correlation. The thick-dashed line shows a linear regression to the stacked data points (combining M51 and M101). The grey shaded region between the dotted curves indicates the 1σ confidence interval of the fit. (*Right*) Trend with the ^{13}CO-to-^{12}CO line ratio, $R_{13/12}$. The linear regression only fits the trend for M51 since no clear trend is seen for M101.

Combining the sightlines from both galaxies, we cover a dynamical range in line ratio values, we cover a range of R_{21}~$0.5 - 0.9$. This range is similar to the full range of line ratio values commonly found across a sample of nearby spiral galaxies (Yajima et al., 2021; Leroy et al., 2022). We find a negative correlation with a slope of $m = -0.5 \pm 2$. This is close to the predicted value based on 3D magnetohydrodynamics simulations of the ISM as given in Gong et al. (2020). However, our finding is limited by a large uncertainty. In conclusion, despite the range in R_{21}, we do not obtain strong constraints from our observations on any possible trends between the line ratio and the conversion factor. This limits the use of R_{21} as a predictor of α_{CO} variation for extragalactic studies on kpc scales.

(iii) *Line Ratio $R_{13/12}$:* Assuming optically thin ^{13}CO (1−0) emission, $R_{13/12}$ traces a combination of the ^{12}CO optical depth and abundance variations of the ^{13}CO species (see Subsubsection 6.5.1). We expect optically thin gas to have lower α_{CO} values (Bolatto et al., 2013). Consequently, if $R_{13/12}$ is driven by opacity changes, we expect lower line ratios to have low α_{CO}. In Figure 6.11, we only perform a linear fit to the trend of M51 since we cover a wider range of line ratios for that galaxy ($R_{13/12}$~$0.1 - 0.2$). While we do not find any significant trend, we do find a slight decreasing variation of α_{CO} with $R_{13/12}$ in M51. This is contrary to the sense of the relationship if changes in opacity are the main driver of $R_{13/12}$ variation. Hence, we conclude that this indicates that abundance effects also play a crucial role in the variation of this particular CO line ratio.

(iv) *Arm-Interarm Variation*: As opposed to M101 (see Section C.4), we find strong arm-interarm variation in R_{21} (Koda et al., 2012; den Brok et al., 2022) in M51, reflecting likely changes in the optical depth or temperature and density of the molecular gas. By decomposing our solution pixels by spiral phase, we can investigate whether α_{CO} shows arm-interarm dependence in M51 as well. Figure 6.12 shows α_{CO} binned by spiral phase (spiral phases belonging to the Northern spiral arm are shown in red, and blue indicates the spiral phases that define the southern arm). We decompose the spiral bins using a logarithmic spiral to describe the shape. The technique is described in detail in Koda et al. (2012). We find a significant variation of α_{CO} as a function of the spiral phase. The conversion factor is lower in the interarm than the spiral arm region by about ~0.5 dex. The variation is stronger than for the binned radial trend (see Figure 6.12).

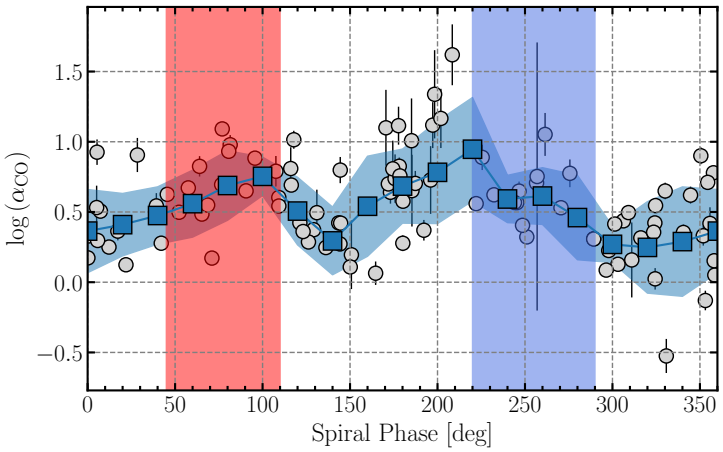

Figure 6.12: **Arm-Interarm Variation of α_{CO} in M51** The graph shows the ^{12}CO (1−0) intensity binned by spiral phase. The blue points show the stacked line ratio by spiral phases in steps of 20°, increasing counter-clockwise.

However, the radial bins are intensity weighted, so we expect the α_{CO} trend of the spiral arm to dominate. The arm–interarm trend is consistent with the presence of a more prominent diffuse CO component that enhances the CO emissivity. At the same time, it would decrease the required conversion factor to translate the CO intensity to molecular gas mass. The presence of a diffuse component has previously been suggested by Pety et al. (2013). On the basis of comparing GMC-scale (∼100 pc) and large scale (∼1 kpc) observations, they suggest that ∼50 % of the total CO emission could originate from such a diffuse component. Future work using high-resolution observations of the central region of M51 will provide further insight into the mechanism that produces these strong environmental changes in the line ratio and conversion factor (S. Stauber et al., in prep.). In contrast, we also note that we do not find any clear arm–interarm variation in α_{CO} for M101.

6.5 Discussion

6.5.1 Implications from CO Isotopologue Line Ratio Trends

With the IRAM 30m wide-field M101 program, we have observations of the $J = 1 \rightarrow 0$ transition of three CO isotopologue species: ^{12}CO, ^{13}CO, and C^{18}O. Comparing various CO line ratios will provide insight into the conditions of the gas on ∼kpc scales and investigate the physical and chemical drivers for variation.

R_{21} Ratio

The R_{21} ratio is sensitive to variation in gas temperature and density (Peñaloza et al., 2017). We see a mild increase of the line ratio towards the center of the galaxy (∼10% increase with respect to the galaxy-wide average). Such an increase has been observed by previous CO mapping surveys (Leroy et al., 2009; Leroy et al., 2013; Yajima et al., 2021; den Brok et al., 2021). The increase is attributed to the increased density and temperature, which is observed in the presence of nuclear star-forming regions, which will elevate R_{21}. In a similar way, the observed enhancement of R_{21} with Σ_{SFR} is expected from physical considerations. Leroy et al. (2022) noted that such an increased line ratio could follow from either higher-density gas (as discussed, e.g. Usero et al., 2015; Jiménez-Donaire et al., 2019; Gallagher et al., 2018) or stronger radiation fields and higher cosmic-ray densities. These drivers all lead to the presence of warmer gas and consequently affect the observed line ratio. Also, we do not find any significant variation between the spiral arm and interarm regions. For comparison, in other galaxies, a clear arm and interarm variation has been observed (Koda et al., 2012; Koda et al., 2020; den Brok et al., 2022). For example, M51 showed a clear

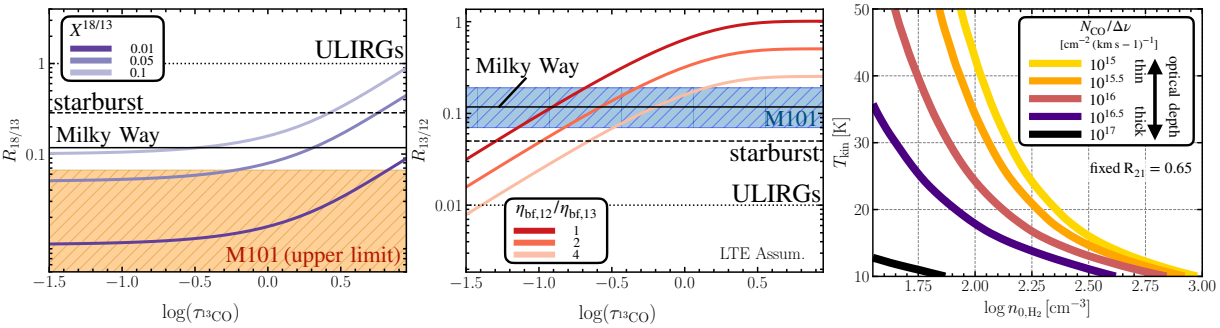

Figure 6.13: **Effect of ^{13}CO Optical Depth on CO line ratios under LTE Conditions.** We assume optically thick ^{12}CO and optically thin C^{18}O emission. (*Left*) Variation of $R_{13/12}$ with $\tau_{^{13}CO}$ for different beam filling factor ratios between the ^{12}CO and ^{13}CO emission, η_{12} and η_{13}. The blue band shows the range of measured $R_{13/12}$ values in M101. Average MW value (solid line), starburst (dashed line), and ULIRGs (dotted) is shown. (*Centre*) Variation of $R_{18/13}$ with $\tau_{^{13}CO}$ for different abundance ratios of the ^{13}CO and C^{18}O species. We do not significantly detect C^{18}O in the center of the galaxy. The orange shaded region hence shows the region where the line ratio in M101's central 4 kpc region could fall. (*Right*) We use the line ratio model calculation provided in Leroy et al. (2022). These are based on model calculations with RADEX (van der Tak et al., 2007) an used a lognormal density distributions described in Leroy et al. (2017). We fix the ratio at $R_{21} = 0.65$ and use a lognormal density distribution width of $\sigma = 0.6$. The color-coded lines show the trends for different total CO column densities per line width ($N_{CO}/\Delta v$). We note that we assume a common excitation (density, temperature) for all species and LTE for the left and middle panel.

enhancement of R_{21} in the interarm region of order $20-30\%$. In M101, however, no such variation is observed. On average, we find a line ratio attributed to the spiral arm regions of $R_{21}^{\rm arm} = 0.6 \pm 0.1$ and similarly, for the interarm-region, $R_{21}^{\rm interarm} = 0.6 \pm 0.1$. We discuss the precise analysis to quantify the arm and interarm regions using logarithmic spirals in Section C.4. We note that since the spiral structure is less pronounced in M101 than in M51, we also expect the difference in α_{CO} to be shallower.

CO Isotopologue Ratios

Generally, CO isotopologue line ratio variation across nearby galaxies is either linked to changes in the relative abundances of the isotopologue species or variation in the physical properties of the gas, such as its opacity, temperature, or density (Davis, 2014). Since the ^{13}CO (1–0) and C^{18}O (1–0) transitions are generally optically thin (see review by Heyer and Dame, 2015), they help us to constrain any potential changes in the relative abundances.

(i) Changes in CO isotopologue abundances: Processes that vary the CO isotopologue abundances can be selective nucleosynthesis (Sage et al., 1991; Wilson and Matteucci, 1992), chemical fractionation (Watson et al., 1976; Keene et al., 1998) or selective photodissociation (van Dishoeck and Black, 1988). These three mechanisms either locally enhance the ^{13}CO abundance (chemical fractionation), increase the ^{12}C and ^{18}O isotope abundances (selective nucleosynthesis), or lead to more photodissociation of certain species due to lower shielding and different differences in molecular structure (selective photodissociation). Line ratio trends then give us insight into whether any of these mechanisms act as global drivers and, more importantly, whether abundance variations can explain observed CO isotopologue line ratio trends in the first place. The left panel in Figure 6.13 illustrates the effect of relative abundance variations on the observed line ratio.

(ii) Optical Depth effects: Because, in particular, the ^{12}CO emission, and potentially the ^{13}CO emission

is optically thick, changes in the optical depth will then lead to a variation of the observed line ratio. Due to sufficiently low abundance, ^{18}CO generally remains optically thin. This way, it is possible to assess optical depth variation of ^{12}CO and ^{13}CO.

In Figure 6.13 we show the expected $R_{13/12}$ and $R_{18/13}$ trends with changing ^{13}CO (1−0) optical depth, $\tau_{^{13}\mathrm{CO}}$, under LTE assumption. The top panel shows the variation of $R_{13/12}$ for different beam filling factor ratios for ^{12}CO (1−0) and ^{13}CO (1−0). We note that when assuming a beam filling factor ratio of $\eta_{12}/\eta_{13} \leq 2$, the observed range in line ratio values found in M101 is in agreement with optically thin ^{13}CO emission (i.e. $\tau_{^{13}\mathrm{CO}} < 1$). Since we only derive upper limits for $R_{18/13}$, the left panel in Figure 6.13 highlights the ratio of possible line ratio values up to the upper limit. For optically thin ^{13}CO emission, $R_{18/13}$ traces the abundance ratio between these two CO isotopologues, $X^{18/13}$. Our upper limit of the line ratio hence suggests an upper limit of the abundance ratio of $X^{18/13} < 0.06$. In Figure 6.13, we illustrate the dependence of R_{21} on the temperature (kinetic temperature; T_{kin}) and density (collider density; $n_{0,\mathrm{H_2}}$). We use the model calculations given by Leroy et al. (2022), which employ multiphase RADEX model calculations (van der Tak et al., 2007) with density layers weighted by a lognormal profile and a common temperature, T_k, and column density per line width, N_{CO}/D_v, (Leroy et al., 2017). To illustrate the trends, we fix $R_{21} = 0.65$ and show different CO column densities per line width. The resulting trends illustrate the temperature–density degeneracy. We expect the column density per line width to increase toward the center. Consequently, fixing R_{21}, would indicate either an increase of the temperature (for constant density), or higher density (for constant temperature) toward the central region of M101.

So given optically thin ^{13}CO, the negative trend we find in $R_{13/12}$ with galactocentric radius either derives from changes in the optical depth of ^{12}CO or changes in the relative abundance of ^{13}CO (or a combination of these two factors). An increase of the $X^{13/12}$ abundance ratio toward the center would be consistent with such observed trends in the Milky Way (Milam et al., 2005) and other nearby spiral galaxies (Cormier et al., 2018). Such trends can be explained by selective nucleosynthesis: Inside-out star formation scenarios (Tang et al., 2019) will lead to an increased accumulation of ^{13}CO sooner towards the center of the galaxy, thus enhancing there the $R_{13/12}$ ratio. Such a scenario is also supported by the increase of $R_{13/12}$ with the star formation rate surface density (see Figure 6.7).

In contrast, the optical depth of ^{12}CO is expected to decrease in the presence of diffuse emission or increased turbulence. This would boost the emission of ^{12}CO relative to ^{13}CO and lead to a decreasing $R_{13/12}$. If changes in the optical depth were the main driver for line ratio variation, the increasing trend of $R_{13/12}$ toward the center of M101 would indicate higher optical depth in the center. Given our nearly flat R_{21}, higher optical depths would mean less dense or colder gas (as can be seen in Figure 6.13). We hence conclude that particularly the trend in $R_{13/12}$ derives to some parts from changes in the relative abundance of ^{13}CO. However, to properly disentangle the contribution of abundance variations and optical depth changes to the line ratio, at least another ^{13}CO transition is required to achieve a non-LTE modeling analysis.

6.5.2 Implications of α_{CO} Variation on Scaling Relations

The Kennicutt-Schmidt (KS) law (Schmidt, 1959; Kennicutt, 1989) relates the star formation surface density and the gas surface density, and its slope likely reflects the underlying processes of star formation (Elmegreen, 2002; Krumholz and McKee, 2005). The molecular KS law follows:

$$\log\left(\frac{\Sigma_{\mathrm{SFR}}}{M_\odot\ \mathrm{yr}^{-1}\ \mathrm{kpc}^{-2}}\right) = N \times \log\left(\frac{\Sigma_{\mathrm{mol}}}{M_\odot\ \mathrm{pc}^{-2}}\right) + C \tag{6.13}$$

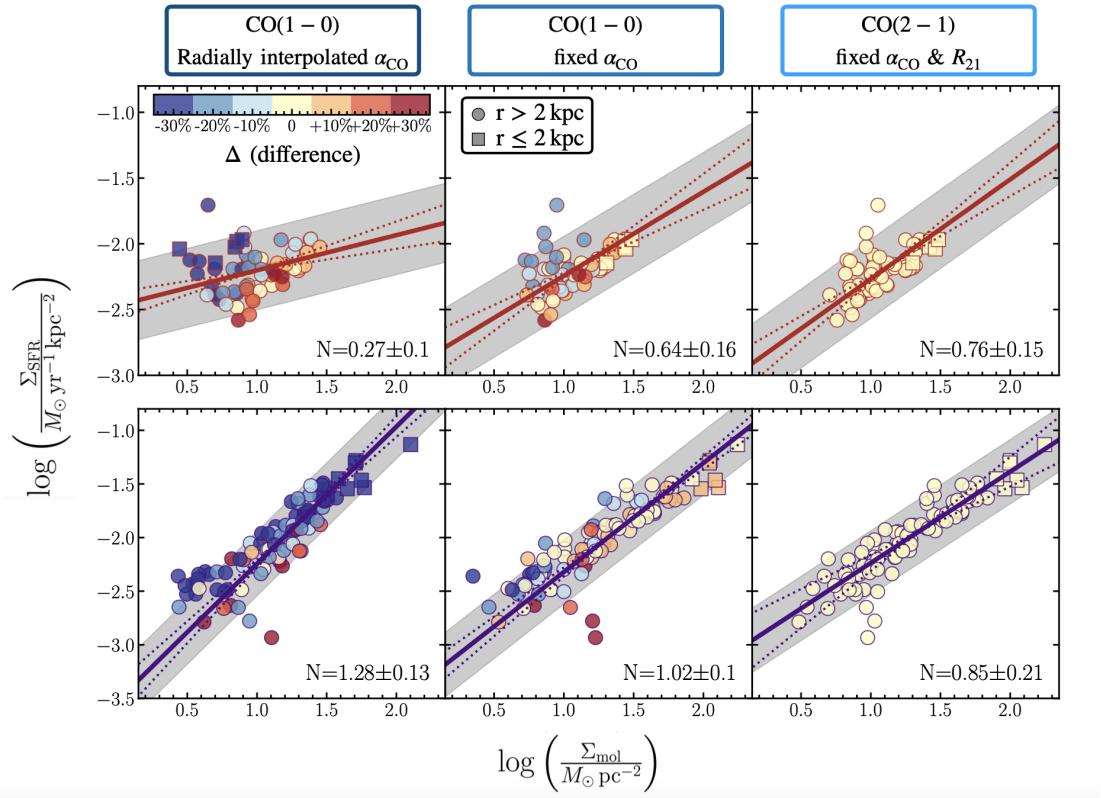

Figure 6.14: **Implication of Varying R_{21} and α_{CO} on the Kennicutt-Schmidt Relation** We compare the KS relation using three different ways of estimating the molecular gas mass, Σ_{mol}: (i) ^{12}CO (1–0) and a radially interpolated α_{CO} (ii) ^{12}CO (1–0) and a fixed $\alpha_{CO} = 4.3\,M_\odot\,pc^{-2}/(K\,km\,s^{-1})$, and (iii) ^{12}CO (2–1) and a fixed $R_{21} = 0.6$ (and $R_{21} = 0.9$ in M51; den Brok et al. 2022). The resulting KS index, N, is determined using an orthogonal distance regression (fit indicated by solid line) and indicated in each panel with its 1σ uncertainty. The grey shaded region shows the ±0.30 dex dispersion that Kennicutt and Evans (2012) find for a larger sample of galaxies. The points, which represent the individual solution pixels, are color coded by their difference in Σ_{mol} to the molecular gas mass determined using method (iii), which is shown in the right panel. Squares indicate the central points ($r \leq 2$ kpc).

where N, the key parameter, indicates the KS slope and C the normalization offset. Not only do the underlying physical processes lead to variations of the relation, but it has also been found that the slope will vary with spatial resolution (Onodera et al., 2010; Sanchez-Garcia et al., 2022). The "breakdown" of the relation at high resolution likely reflects that the underlying initial-mass function is not sampled well enough anymore.

When estimating the molecular gas surface density, Σ_{mol}, it is common to rely on higher-J ^{12}CO transitions, in particular ^{12}CO (2–1) (e.g., Cicone et al., 2017; Noble et al., 2019; Leroy et al., 2021b; Pereira-Santaella et al., 2021), and assume a constant line ratio to down-convert to the $J = 1 \rightarrow 0$ transition. Yajima et al. (2021) show, however, that the KS is underestimated by 10-20% when relying on ^{12}CO (2–1) and a constant R_{21}. However, also α_{CO} is subject to variation, so in Figure 6.14, we compare the different derived KS slopes, N, in M101 and M51 based on (i) using ^{12}CO (1–0) and a radially interpolated α_{CO} (ii) ^{12}CO (1–0) and a fixed $\alpha_{CO} = 4.3\,M_\odot\,pc^{-2}/(K\,km\,s^{-1})$, and (iii) ^{12}CO (2–1) and a fixed $R_{21} = 0.6$ (and $R_{21} = 0.9$ in M51; den Brok et al. 2022). The points, which show the solution pixels, are color-coded by

the percentage difference compared to the molecular gas mass derived from ^{12}CO (2−1) according to (iii):

$$\Delta[\%] = (\Sigma_{\rm mol} - \Sigma_{\rm mol}^{\rm fix\ \alpha_{CO}\ \&R_{21}})/\Sigma_{\rm mol}^{\rm fix\ \alpha_{CO}\ \&R_{21}} \times 100\%$$

.

Each panel also indicates the KS index, N (including the 1σ uncertainty). The index is determined using an orthogonal distance regression, which is more robust than the more commonly used linear regression. The right-most panel shows the relation based on method (iii). We find an index $N < 1$ for both galaxies. While the KS relation predicts a close relation between $\Sigma_{\rm SFR}$ and $\Sigma_{\rm gas}$, an overall dispersion from this relation is expected (±0.30 dex; Kennicutt and Evans, 2012) and connected to physical drivers. Regarding fixed and free R_{21}, we find an increase in N for M51 ($N = 0.85$ to $N = 1.02$), but a slight decrease for M101 ($N = 0.76$ to $N = 64$). We generally expect an increase of the index since R_{21} increases towards the center, leading to an overestimation of the molecular gas mass. We see that in M101, the points with higher $\Sigma_{\rm SFR}$ (connected to the center) also show a negative (blue) difference in molecular mass. The impact by R_{21} is generally, however, limited since we expect the line ratio to saturate at R_{21}~1. Also, we do not expect very low line ratio values (generally $R_{21} > 0.4$). So the dynamical range in R_{21} is very limited in general extragalactic studies (see, for example, also Yajima et al., 2021; Leroy et al., 2022).

We expect the impact by varying $\alpha_{\rm CO}$ to be larger since we observe a variation of the conversion factor of a factor of 5−10. When estimating the molecular gas mass using the radially interpolated $\alpha_{\rm CO}$ value (left column in Figure 6.14), we see a further increase in N for M51 and a decrease for M101. Since values with higher surface density seem to show a depression of $\alpha_{\rm CO}$ (e.g., the center), we expect that points with higher $\Sigma_{\rm SFR}$ have slightly overestimated molecular gas masses. Correcting this effect by accounting for $\alpha_{\rm CO}$ variation will push these points to lower $\Sigma_{\rm mol}$. This can be seen in M101, where the squared points (for which $r \leq 2$ kpc) are bluer than for fixed R_{21}. The other high-SFR points stem from the bright HII region toward the southeast. Given the fact that we overestimate Σmol when not accounting for varying R_{21} and $\alpha_{\rm CO}$(in particular for the center), we would expect the KS to increase. However, we still find very shallow KS indices, even when accounting for the variation in R_{21} and $\alpha_{\rm CO}$. This is because (a) the dynamical range in the SFR surface density is small (~0.5 dex) and (b) the points from the center of the galaxy are pushed off the linear relation (b) the HII region (NGC 5461) at high-SFR shows points offset from the main relation. Hence, a linear fit does not capture the entire trend of the relation.

To study the implications of varying $\alpha_{\rm CO}$ and R_{21} values on the scaling relations but also account for environmental variation, we investigate how the molecular gas depletion time $\tau_{\rm dep}$ varies as a function of radius across both galaxies. The depletion time is defined as follows:

$$\tau_{\rm dep} \equiv \frac{\Sigma_{\rm mol}}{\Sigma_{\rm SFR}} \tag{6.14}$$

Figure 6.15 shows the radial trend of $\tau_{\rm dep}$ for either fixed R_{21} and $\alpha_{\rm CO}$, or a radially interpolated $\alpha_{\rm CO}$. Both galaxies show relatively flat depletion times in their discs, independent of the $\Sigma_{\rm mol}$ method. This is in agreement with previous studies of nearby galaxies that also found constant depletion times (e.g. Bigiel et al., 2011; Leroy et al., 2017). Using radial $\alpha_{\rm CO}$ and CO(1-0), we find an average depletion time of $\tau_{\rm dep}^{M101} = 1.9$ Gyr and $\tau_{\rm dep}^{M101} = 1.9$ and $\tau_{\rm dep}^{M51} = 1.5$ Gyr with a scatter of 0.2 dex for both galaxies. As evident from the panel on the right of the figure, both galaxies show similar depletion times. In this panel, we combine the sightlines from both galaxies. We also note that the value for the average depletion time agrees well with the value of 1.6 Gyr found for M51 by Leroy et al. (2013) using PAWS CO(1-0) data. Using the constant $\alpha_{\rm CO}$ and R_{21}, we find a slightly higher depletion time in M51 by about 500 Myr (which

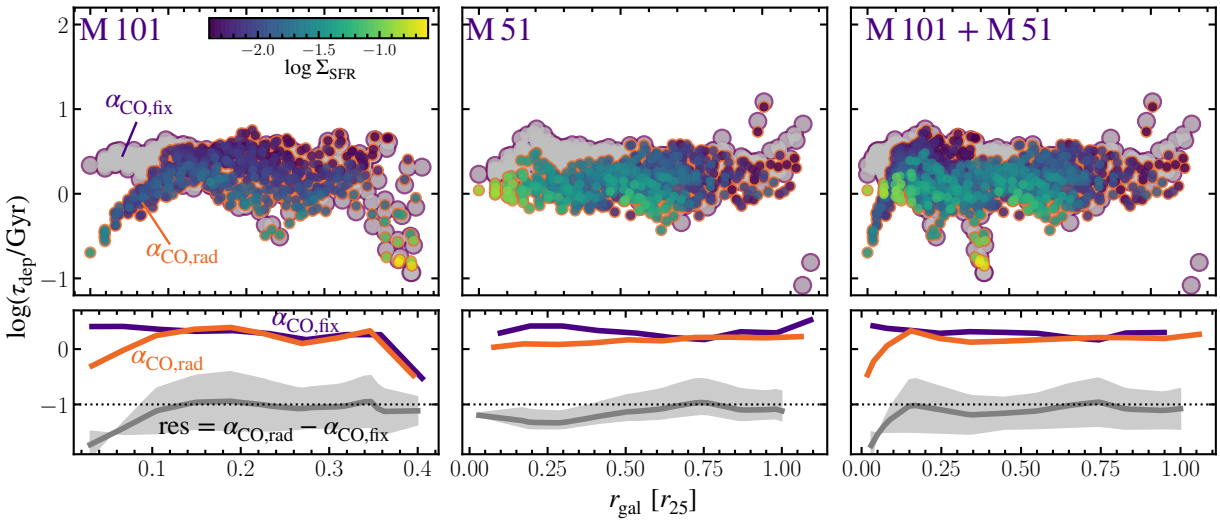

Figure 6.15: **Implication of Varying R_{21} and α_{CO} on the Molecular Gas Depletion Time** The top panels show the radial trend of the depletion time for M101 (left), M51 (center), and for the combination of the sightlines from both galaxies (right). The depletion time depends on a measurement of the molecular gas mass. The grey points (with purple edge color) show the measurements using CO(2-1) and fixed R_{21} and α_{CO} values. The points color-coded by SFR surface density are from using CO(1-0) and a radially interpolated α_{CO}. The bottom panels compare the radially binned trends of both measurements. The grey line indicates the residual of the two trend lines.

constitutes a ~50% increase). Such constant depletion times are thought to represent evidence that nearby spiral galaxies have disks populated by GMCs that form stars at a uniform pace (Bigiel et al., 2011). This is the case if the GMC properties are universal rather than sensitive to the local environment (Leroy et al., 2008).

While M51 shows a constant depletion time across the galaxy, independent of the method used, we see an apparent decrease of τ_{dep} toward the center of M101 when we use a radially interpolated α_{CO}. In the center, the constant trend seems to break, and we find $\tau_{dep} \approx 150 - 300$ Myr, which is an order of magnitude lower than the disk-wide average. Furthermore, M101 shows lower depletion times (again by almost one order of magnitude) in the bright HII region toward the southeast of the galaxy (NGC 5462). Sightlines within this region incidentally show also high SFR surface densities. The lower depletion times in the galaxy's center indicate a higher star formation efficiency (SFE). Utomo et al. (2017), studying galaxies from the EDGE-CALIFA survey, also found decreased depletion times toward the center of galaxies and suggested that when accounting for α_{CO} variation, the extent of the drop in τ_{dep} will be amplified. Such an increased SFE could be driven by increased gas pressure. Increased star-forming activity will lead to higher feedback rates. According to the star formation self-regulated model, the SFR will adjust to the feedback from massive stars and will counter the turbulent energy dissipation and cooling (e.g. Ostriker et al., 2010; Ostriker and Shetty, 2011; Kim et al., 2011).

The excessive decrease in the depletion time toward the center of M101 places strong constraints on star formation models to accurately account for the increased SFE. Observations of dense gas tracers, such as HCN, could shed light on whether a higher SFE could connect to a more elevated fraction of dense gas in the center.

6.5.3 Parameterizing α_{CO}

Ultimately, we hope to acquire a prediction for α_{CO} variation based on the observed galactic properties. Various α_{CO}-prescriptions have been proposed in the literature for a wide range of galaxy types, including low-metallicity dwarfs and bright metal-rich ULIRGs. Such prescriptions are mostly based on first order on the metallicity, Z (e.g. Schruba et al., 2012), but also incorporate further key parameters such as the surface brightness (e.g. Bolatto et al., 2013) or the CO line ratio, R_{21} (e.g. Gong et al., 2020). From theoretical considerations, we expect two major drivers of α_{CO} variation, which we need to account for:

1. Temperature and velocity dispersion effects seem to drive down the value in more extreme environments, such as the center of certain galaxies (e.g., in M101).

2. Large fraction of CO-faint gas will lead to an increase of α_{CO}.

In the case of the galaxies M101 and M51 point (1) seems relevant since we see a significant depression of α_{CO} toward the center. The second driver, CO-faint gas, appears to be more appropriate in, e.g., low-metallicity dwarfs, where much higher α_{CO} values are found (e.g. Israel, 1997; Schruba et al., 2011), than in regular spiral galaxies.

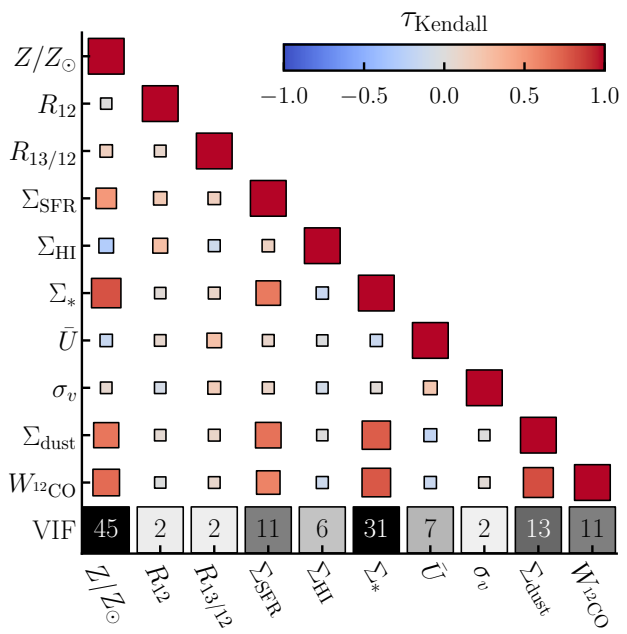

Figure 6.16: **Cross-Correlation of Feature Variables.** The correlation is computed in log-space. The empirical correlation is estimated using Kendall's τ correlation coefficient. The size of the boxes and color indicates the strength of the correlation. The VIF is an indicator of multicollinearity for a set of variables. Higher VIFs indicate a stronger mutual correlation between the selected variable and the other parameters.

Given the multitude of ancillary data for M101, we attempt to perform a multivariate analysis to find an expression for α_{CO} for a set of input parameters (so-called *feature variables*, $\{X_{ij}\}$, where $i = 1, 2, ..., n$ is the index of the data point, and $j = 1, 2, ..., m$ the index of the set of feature values.). The set of feature parameters is indicated in Figure 6.16. Besides the parameters already introduced in the previous chapter, we include the ^{12}CO (1–0) velocity dispersion, σ_v, (as measured by the 30m telescope), and the mean radiation field, $\bar{U}$, which is derived from the dust-SED fits used to measure the dust mass. The set of parameters is multi-correlated. Hence, we require a variable selection technique that allows us to choose the relevant variables only. Figure 6.16 shows a cross-correlation matrix for the various parameters. The correlation is quantified using Kendall's τ correlation coefficient. In addition, the figure lists the variable inflation factor (VIF). The VIF indicates the multicollinearity of a variable. Higher values indicate a stronger cross-correlation to other parameters. Consequently, the variation of one variable can be explained by the set of other independent variables. Generally, VIF > 5 indicates multicollinearity (e.g. Sun et al., 2022).

We convert all parameters to logarithmic space, so that we can build a linear predictive model of the

form:

$$\hat{y}_i = \beta_0 + \sum_{j=1}^{m} \beta_j X_{ji} \tag{6.15}$$

To select the relevant features, we perform a *lasso* feature fit (Santosa and Symes, 1986). We refer to Appendix C.7 for further details on the method and definitions. We create the sample by bootstrapping the original set of $\alpha_{\rm CO}$ values from the scatter minimization technique for the fitting procedure. We use a CO intensity weighted probability density function for the bootstrapping. The new dataset consists of $n = 1000$ data points (instead of just ~100 solution pixels). This way, we can ensure that the center is also captured in the fitting procedure. If we just use the normal area-weighted fit (i.e., because the disk holds more lines of sight), the depression would not be relevant for the fit.

We find a *preferred* power-law model using three parameters: $\Sigma_\star$, σ_v, and $\Sigma_{\rm HI}$. After incorporating an increasing number of parameters, the subsequent lasso path is illustrated in Figure 6.17. The model scatter (dex scatter in $(\hat{y}_i - y_i)$) reduces from the overall sample of 0.4 dex to ~0.2 dex after including the parameters. After three features, the scatter is not significantly reduced any further upon adding additional components to the model. The best fit model we find for M101 is given by

$$\alpha_{\rm CO} = 10^{5.2} \times \left(\frac{\Sigma_\star}{M_\odot\,{\rm pc}^2}\right)^{-0.55} \times \left(\frac{\sigma_v}{{\rm km\,s}^{-1}}\right)^{-1.6} \times \left(\frac{\Sigma_{\rm SFR}}{M_\odot\,{\rm pc}^2}\right)^{0.6} \tag{6.16}$$

The parameters for all models of the lasso regression up to the preferred model are given in Table 6.5.

Regarding the two primary drivers of $\alpha_{\rm CO}$ variation (temperature/velocity dispersion and CO faint gas), we see that the three parameters the lasso regression selected mostly relate to the first point. We note, however, that the underlying physical reason for $\alpha_{\rm CO}$ variation is tight to the fraction of CO emission arising from molecular gas in contrast to the fully extended, non-self-gravitating component as a constraint by the total mass of the system (Bolatto et al., 2013). In our prescription, $\Sigma_\star$ traces a significant fraction of the overall baryonic mass surface density, excluding the atomic and molecular ISM. The velocity dispersion and SFR surface density terms (σ_v and $\Sigma_{\rm SFR}$) trace, loosely speaking, temperature, density, and opacity

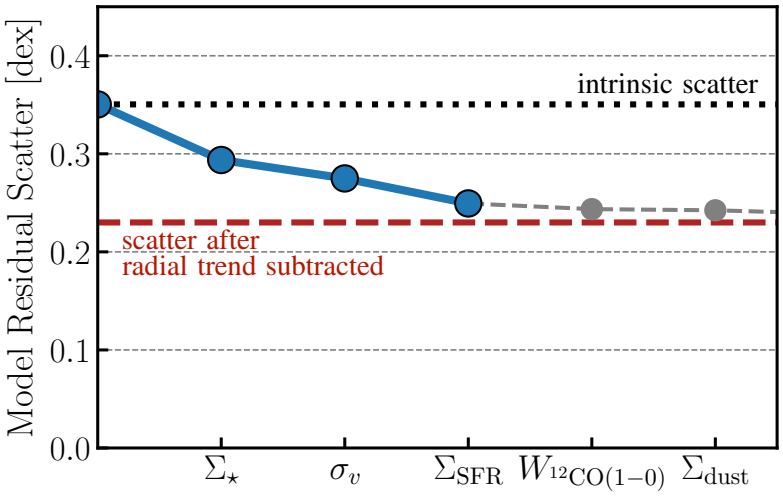

Figure 6.17: **Feature Selection *Lasso* Path** The residual scatter for using an increased number of features is shown. The preferred model (last blue point) is determined using the Bayesian Inference Criterion (BIC).

Table 6.5: **Summary Predictive Power-Law α_{CO} Models**

N_{comp}	Model	Residual [dex]	R^2	Δ BIC
1	$\alpha_{CO} = 10^{1.7\pm0.1} \times \left(\frac{\Sigma_\star}{M_\odot\,pc^{-2}}\right)^{-0.58\pm0.05}$	0.29	0.65	87
2	$\alpha_{CO} = 10^{2.8\pm0.1} \times \left(\frac{\Sigma_\star}{M_\odot\,pc^{-2}}\right)^{-0.46\pm0.05} \times \left(\frac{\sigma_v}{km\,s^{-1}}\right)^{-1.0\pm0.2}$	0.27	0.78	35
3	$\alpha_{CO} = 10^{5.2\pm0.1} \times \left(\frac{\Sigma_\star}{M_\odot\,pc^{-2}}\right)^{-0.55\pm0.08} \times \left(\frac{\sigma_v}{km\,s^{-1}}\right)^{-1.6\pm0.1} \times \left(\frac{\Sigma_{SFR}}{M_\odot\,yr^{-1}\,pc^{-2}}\right)^{0.6\pm0.1}$	0.25	0.81	7.7
Modified	$\alpha_{CO} = 10^{3.0\pm0.1} \times \left(\frac{Z}{Z_\odot}\right)^{-1.3\pm0.3} \times \left(\frac{\sigma_v}{km\,s^{-1}}\right)^{-1.9\pm0.1}$	0.26	0.8	–

Notes: The first column indicates the number of features selected for the model fit. The feature selection occurs using a *lasso* regression. The second column lists the model prescription in form of a power-law. The third column lists the model residual fit (i.e. scatter in dex of $y_i - \hat{y}_i$). The fourth column lists the coefficient of determination. This indicates the fraction of α_{CO} variation explained by the model. The fifth column lists the BIC difference between the selected model and the model with the smallest BIC. In general, the difference should not exceed 10 for a good performance (Sun et al., 2022).

variation. We note as a caveat, however, that we observe the kpc-scale velocity dispersion with our IRAM 30m telescope observations. This does not necessarily trace the underlying turbulence velocity dispersion of the molecular gas. Due to the coarse resolution, the line width might also increase due a dispersion of the bulk motion of several molecular clouds that are convolved within a single beam. Using a combination of the velocity dispersion σ_v and the stellar mass surface density $\Sigma_\star$, it is possible to account for the central depression of α_{CO} toward the center of the galaxy.

For comparison, we also used a customized two-component model consisting of the terms for metallicity ($Z/Z_\odot$) and ^{12}CO (1–0) line width. The selection of these two quantities is directly linked to the two tracers of α_{CO} variation we expect from theory: The line width traces the turbulence or optical depth of the gas, and the metallicity connects well to the prevalence of CO-dark gas. The coefficient of the fit and the performance in terms of model residuals are listed in Table 6.5.

The top panels in Figure 6.18 show a comparison of the α_{CO} trend found from the scatter minimization technique (indicated in color) and using the 3-component model derived from the *lasso* regression on the solution pixels of M101 for all sightlines (in grey) for both M51 and M101. For M101 (left; red), we see that the trend from the scatter minimization and from the three-component model are in good agreement (less than 0.1 dex discrepancy). The three-component model also produces a more flat α_{CO} trend toward the disk. Applying the model derived from M101 on M51, we find, in fact, also a good agreement in the disk between the scatter minimization and the 3-component model. Only for the innermost solution pixel ($r < 2$ kpc) the model predicts a depression of α_{CO}, which is not observed in the scatter minimization technique. We note that M51 holds an AGN, which likely affects the conditions of the molecular gas in its close vicinity (e.g. Kakkad et al., 2017; Esposito et al., 2022). Regarding the influence radius, Querejeta et al. (2016) find that the AGN feedback likely does not extend further radially outward than 0.5 – 1 kpc. Besides AGN, the center of M51 is also affected by strong tidal interaction with its iconic companion source (NGC 5195). Such interactions create strong internal gas flows. Consequently, the dynamical pressure will also increase towards the center of the galaxy (Meidt et al., 2013).

In conclusion, our α_{CO} prescription can likely break in the innermost regions of galaxies with conditions similar to M51 (AGN + interaction). Furthermore, we also stress that we do not cover low metallicity, so the prescription from our 3-component model also is likely only well-calibrated for approximately solar

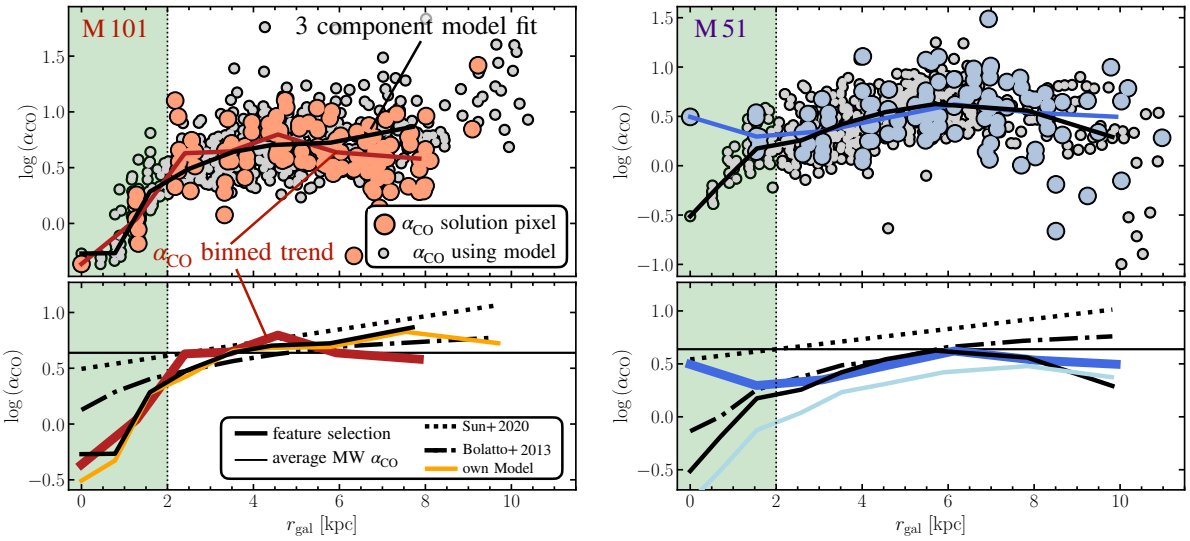

Figure 6.18: **CO-to-H_2 Conversion Factor Model and Prescription Comparison** (*Top Panels*) Comparing the radial α_{CO} trend derived from binning the data (in color) and the trend derived from applying the 3-component power-law model on the individual sightlines (see the model parameter in Table 6.5). The model is calibrated using the solution pixels from M101. The right panels show the model applied to the galaxy M51. (*Bottom Panels*) Comparison of the derived trend when applying the α_{CO} prescription used Sun et al. (2022) (dotted line), from Bolatto et al. (2013) (dash-dotted line), and our own two-component model based on metallicity and the ^{12}CO (1−0) velocity dispersion (orange/light blue). The thin horizontal line illustrates the average local solar neighborhood α_{CO} value. The green shaded region is an approximate illustration of the central region of the galaxy, where conditions potentially change dramatically to the overall disk.

metal abundances.

We compare our prescription to other commonly used ones. In particular, we test the prescription from Bolatto et al. (2013) and prescription from Sun et al. (2020) (which describes α_{CO} in terms of a power-law on metallicity, similar to Schruba et al. 2012; Amorin et al. 2016). The bottom panels of Figure 6.18 show a comparison of various radial trends of α_{CO} for the different prescriptions and the trend based on the scatter minimization technique. We also include our two-component model based on the metallicity and velocity dispersion (shown in light orange for M101 and light blue for M51). Our two-component in M101 agrees with the trend from the scatter minimization technique throughout the galaxy. However, for M51, the same prescription systematically underestimates $\alpha_{CO}$by 0.2 dex. In the disk, the prescription based on metallicity alone (dotted line; Sun et al. 2020) describes the range of α_{CO} approximately well in M101 and is slightly offset in M51 toward larger values (by about 0.3 dex). However, this prescription does not predict the depression of α_{CO} toward the center of the galaxy in M101. In contrast, we see that the prescription by Bolatto et al. (2013), which accounts for regions with high total mass surface density, also describes a mild depression of α_{CO} toward the center of both galaxies. However, the extent of the decrease is only ∼0.5 dex with respect to the average disk value, and not ∼1 dex, as we see in M101. The prescription by Bolatto et al. (2013) also finds a decreasing trend in M51. This finding suggests that the reason is linked to

the peculiarity mentioned above of M51, such as the AGN in the center or its strong interaction with the companion galaxy NGC 5195.

6.6 Conclusions – M101 Project

This study presents new wide-field IRAM 30m low-J CO observations of M101. We address two key aspects of the molecular gas physics in the galaxies M101 and M51: i) How well do CO isotopologue line emissions capture changes in the molecular gas overall characteristics, and ii) how does $\alpha_{\rm CO}$ vary with environmental parameters across the galaxy.
Based on our CO isotopologue analysis we find:

1. An average line ratio of $\langle R_{21} \rangle = 0.60^{+0.07}_{-0.11}$, which is consistent with previous studies of similar, nearby star-forming galaxies. The ratio stays predominantly flat across the disk of M101, with only a mild increase of 10% towards the central 1.5 kpc region.

2. Using spectral stacking, we can constrain an upper limit for $R_{18/13} < 0.07$ for the central 4 kpc region (by radius). Such low line ratios are more predominantly found in the outskirts of star-forming galaxies and indicate very low relative abundances of the $C^{18}O$ species.

3. Given the observed trend in $R_{13/12}$, which increases toward the center, we conclude that changes in abundances due to nucleosynthesis are a major driver on galaxy-wide scales. Changes in the opacity of ^{12}CO do not seem to be the major driver, since the optical depth generally decreases toward the center, which would result in an opposite $R_{13/12}$ trend.

Besides an in-depth analysis of the 3mm CO isotopologue line ratios, we investigate the variation of the CO-to-H_2 conversion factor, $\alpha_{\rm CO}$ across M101. We use a modified version of the scatter minimization technique. The method is based on the dust mass approach, and we use both the ^{12}CO (1−0) and (2−1) emission lines to estimate $\alpha_{\rm CO}$. Our main results and conclusion can be summarized as follows:

4. We find an average conversion factor of $\langle \alpha_{\rm CO} \rangle = 4.4 \pm 0.9$ across the disk of galaxy M101, with an apparent decrease of the value towards the galaxy's center by a factor of ∼10. The reduction of the conversion factor towards the center of the galaxy follows the expectation that the turbulence increases, hence decreasing the optical depth, which enhances the ^{12}CO emission. We also perform a scatter minimization approach in M51. We find a relatively flat $\alpha_{\rm CO}$ trend in M51 across the disk and center of the galaxy.

5. Using the optically thin ^{13}CO emission, we perform an LTE-based $\alpha_{\rm CO}$ estimation in M101. Generally, the conversion factor determined using this approach is lower by a factor 2−3 compared to the scatter minimization technique. The discrepancy is likely due to the simplifying assumption of a similar beam filling factor of the two lines and using constant excitation temperature. Using a two-component model of a galaxy by changing the conditions in the center and disk, we derive a depression of $\alpha_{\rm CO}^{\rm LTE}$ of similar order as the scatter minimization derived $\alpha_{\rm CO}$.

6. We find that accounting for R_{21} and $\alpha_{\rm CO}$ variation, the scaling relations from CO(2-1) alone significantly overestimate the molecular gas mass, particularly in the center of galaxies. The Kennicutt Schmidt relation index increases by ∼50% in the case of M51. Also, the molecular gas depletion time seems to be significantly overestimated in the center, if not accounting for $\alpha_{\rm CO}$ variation. Such low depletion

times imply a very high star-formation efficiency, which is likely connected to processes in the nuclear region of the galaxy.

7. Using a *lasso* regression feature selection for the trend in M101, we find a parameterization of $\alpha_{\rm CO}$ based on the stellar mass surface density, the atomic gas mass surface density, and the ^{12}CO (1−0) line width. These three components trace the two expected main drivers of $\alpha_{\rm CO}$ variation: (i) the turbulence of the gas and (ii), to some extent, the fraction of CO-faint gas. A power-law model combining these three components can explain 80% of the variation observed in $\alpha_{\rm CO}$. Applying the model to M51, we find that we can accurately estimate the $\alpha_{\rm CO}$ value in the disk. However, the model also predicts a depression in $\alpha_{\rm CO}$, which we do not observe from the scatter minimization technique.

Overall, our result shed new light on the degree of variation of $\alpha_{\rm CO}$ and the corresponding trends with key galactic properties. In particular, we stress that the points near the galaxy centers need to be treated with care when employing commonly used $\alpha_{\rm CO}$ prescriptions, as the depression of the value is not yet fully captured or understood.

CHAPTER 7

Outlook and Open Questions

> Même je remarquais, touchant les expérience, qu'elles sont d'autant plus nécessaires qu'on est plus avancé en conaissance
>
> R. Decartes – 17th century philosopher, mathematician, and scientist

Overview

This PhD thesis addresses various aspects of the multi-CO line emission study across nearby spiral galaxies. With the CLAWS large program, we observed a rich dataset of the J=2 → 1 and J=1 → 0 transitions of various CO isotopologues (Chapter 5). This dataset helps us to qualitatively assess variation in molecular gas conditions for the first time across and within a regular nearby galaxy beyond the nuclear region. Moreover, for M101 and M51, we perform a so-called scatter minimization technique to estimate α_{CO} using a combination of CO, H I, and IR dust emission observations (Chapter 6). All of these variations affect our ability to assess the molecular gas conditions. For example, when accounting for α_{CO} variation toward the center, we derive significantly different molecular gas depletion times and star-forming efficiencies. In this thesis, we have addressed the specific conditions of the molecular gas that can explain the observed variation. This is not just relevant for predicting how specific parameters (such as α_{CO}, or R_{21}) will change across the galaxy but is also critical for calibrating star formation theories. However, several scientific questions remain open. And in addition, new science questions naturally emerge from ongoing research. This chapter discusses, in more detail, the current work in progress of two distinct projects that build on the results obtained by my thesis. On the one hand, modeling the line emission is a fundamental next step to obtaining a more quantitative assessment of kpc-scale molecular gas condition variation. On the other hand, new higher-resolution observations will be necessary to expand our insight toward small-scale molecular cloud physics and connect it to the dynamical processes on larger galactic scales. At the end of the chapter, further open questions and potential new research directions are discussed.

7.1 CLAWS Line Modeling

Chapter 5 presents the CLAWS IRAM 30m Large Program survey. Combining with the PAWS ^{12}CO(1-0) (Pety et al., 2013) and NGLS ^{12}CO(3-2) (Wilson et al., 2012) observations, we obtain a total of eight resolved CO emission lines across the galaxy. To what degree does CO isotopologue line emission variation

trace changes in temperature, column, and volume densities and the CO-to-H_2 conversion factor in M51? In the study, we find that particularly the spiral arm and interarm region are of great interest due to the distinct R_{21} difference, with significantly higher line ratio values in the interarm than spiral arm region. So far, we have tried to identify and qualitatively describe the potential physical drivers of the CO line ratio variation (which results in our suggestion of selective nucleosynthesis and changes in opacity as the main reason for the observed changes). However, with the number of CO isotopologues, it now becomes possible to solve the radiative transfer equations and obtain more quantitative estimates of the underlying gas conditions, such as temperature and column density. In general, we are dealing with the following potentially interconnected parameters that describe the conditions of the gas:

- column density, N;
- volume density, n;
- excitation temperature, $T_{\rm ex}$;
- (relative) chemical abundance of the species, X;
- density distribution width (hereafter "density width"), σ;
- optical depth, τ.

These parameters differ from molecular species to species and line-to-line transition. For instance, we commonly deal with a temperature/velocity dispersion degeneracy, which we can only break with multiple-J line ratios. The parameters are connected with a non-linear system of equations. With tools like `RADEX` (van der Tak et al., 2007), it becomes possible to construct a parameter space, solve the radiative transfer equation and compare the resulting modeled line ratios to observed ones (we refer back to Subsection 1.6.3 regarding radiative transfer and line emission modeling). With eight CO isotopologues, we have a large enough set of emission lines to constrain a significant amount of degrees of freedom of the parameters mentioned above. Various tools exist to perform the line modeling. In a future study, we will employ tools beyond simple `RADEX` models. A particular such tool is the *Dense Gas Toolbox* (DGT; Puschnig et al., 2020). This tool offers a novel non-LTE molecular line radiative transfer code. The escape probabilities are calculated via a large velocity gradient (LVG) method. Fundamentally, the DGT is based on `RADEX`. However, the advantage of the DGT over `RADEX` is that it calculates line emissivities for an isothermal gas ensemble that comprises a distribution of densities (including lognormal or lognormal+power law distribution). For comparison, `RADEX` itself computes the line emissivity just for a single zone. Hence, the DGT is more suitable to model line ratios derived from extragalactic observations that, due to resolutions worse than several (k)pc, cannot be described accurately by just a single zone. We use fixed molecular species abundances and line optical depths for the DGT analysis to reduce the degrees of freedom. The fixed values are derived from the analysis results of the EMPIRE survey (Cormier et al., 2018; Jiménez-Donaire et al., 2019). The DGT computes and derives the following physical parameters: gas temperature, the (mass-weighted) mean density, and the width of the density distribution. The robustness of the modeled parameters is estimated using Bayesian inference (MCMC), which computes a probability distribution function for the derived quantities.

7.1.1 Spectral Line Stacking of Arm and Interarm

In principle, we can model the CO line ratios for the individual sightlines where we detected significant emission for several CO isotopologues. This would help us gain insight into the spatial variation of the

underlying physical properties. However, in this section, we focus on describing the conditions within the spiral arm and interarm region of M51. Using spectral line stacking will ensure significant emission also for the fainter CO isotopologue lines (including $C^{18}O$ (2−1) and potentially even $C^{17}O$ (1−0)). Figure 7.1 shows the derived spectra after stacking all sightlines attributed to the spiral arms. We use the environmental mask derived for the CLAWS survey (see Figure 10 in den Brok et al., 2022), which separates sightlines into different environments such as center, arm, and interarm. The integrated intensity is measured above 3σ uncertainty for almost all lines. Only $C^{17}O$ (1−0) is barely detected at S/N~3.

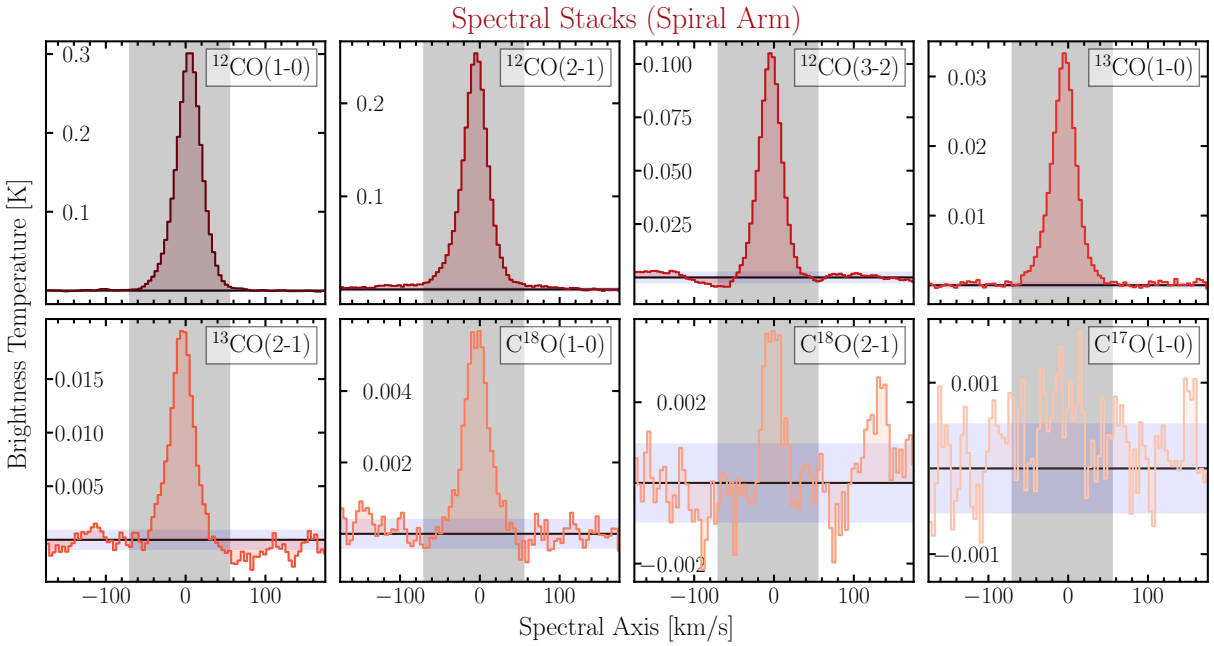

Figure 7.1: **Stacked Spiral Arm CO Isotopologue Emission.** The panels show the spectral stack for all sightlines attributed with the spiral arm in M51. The blue shaded regions show the spectral 1σ rms per line. The grey shaded regions show the velocity range over which the line is integrated to obtain an intensity measure.

Similarly, we can stack all sightlines attributed to the interarm region of M51. The result for the various CO isotopologue lines is shown in Figure 7.2. Because the interarm region is fainter, the S/N of the detections is generally lower. We detect all lines with S/N > 3 except for $C^{18}O$ (2−1). All the integrated line intensities and corresponding uncertainties are listed in Table 7.1 for both arm and interarm stacks.

7.1.2 Results from DGT Line Modelling

With the help of the DGT, we can obtain constraints on the volume density, n, temperature, T, and density width, σ, of the molecular gas that reproduces the observed multi-CO line ratio variations. Note that for the subsequent arm-interarm analysis, we remove the $C^{17}O$ emission. While its integrated intensity is detected above 3σ, its peak brightness temperature is not. Furthermore, for the input of the DGT, we increase the line intensity uncertainty to a 10% error if the actual error is lower. We run the DGT for both the arm and interarm region. The result for the probability density distribution based on the MCMC run of the derived total molecular gas temperature, volume density, and density width is shown in Figure 7.3. The contours show the PDF distribution.

Table 7.1: Line Intensity Measurements from Spectral Stacking.

		^{12}CO			^{13}CO		C^{18}O		C^{17}O
		(1−0)	(2−1)	(3−2)	(1−0)	(2−1)	(1−0)	(2−1)	(1−0)
W [K km s^{-1}]	A	12.06	10.20	3.56	1.268	0.69	0.207	0.08	0.06
	I	5.51	5.17	1.28	0.66	0.31	0.11	<0	0.05
σ_W [K km s^{-1}]	A	0.02	0.04	0.05	0.009	0.02	0.009	0.02	0.01
	I	0.02	0.05	0.06	0.01	0.03	0.01	0.03	0.01
S/N	A	500	250	65	140	35	23	4	5
	I	200	100	23	51	12	9	< 0	3

Note: The intensity is integrated over the velocity range indicated in Figure 7.1 and Figure 7.2. The integrated line intensity (W), line uncertainty (σ_W), and S/N ratio (S/N) are listed for spiral arm (A) and interarm (I) stacks.

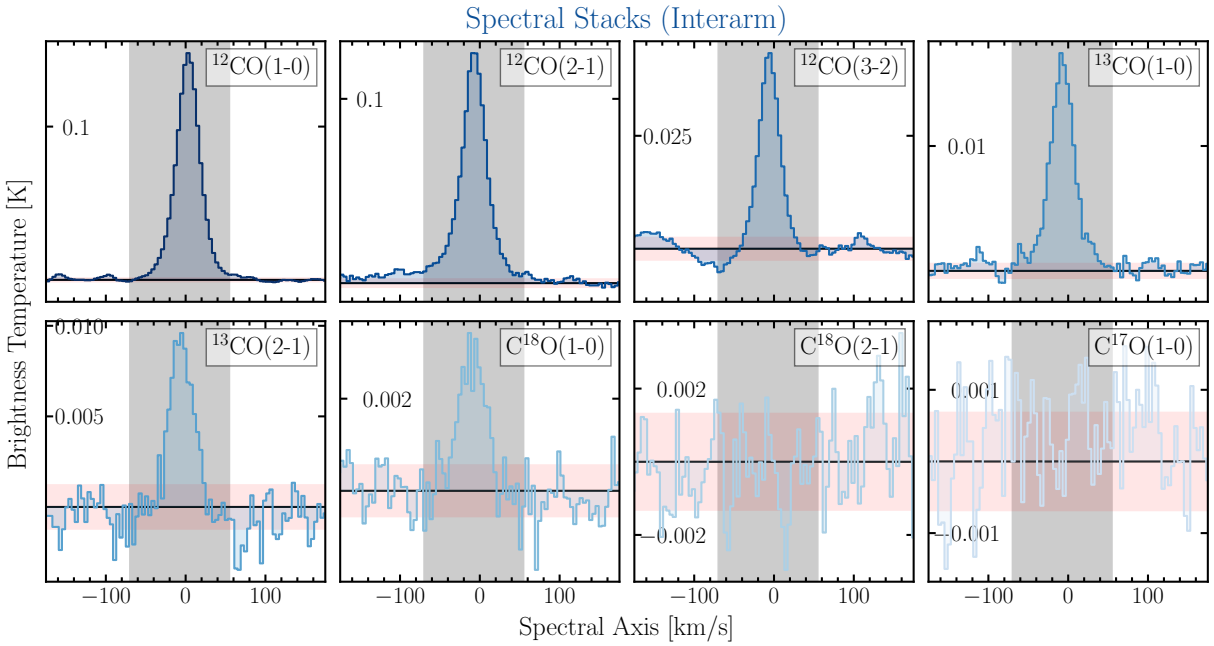

Figure 7.2: **Stacked Interarm CO Isotopologue Emission.** Panel description follows Figure 7.1.

We notice that the conditions are clearly distinct between the arm and interarm region. The spiral arm shows higher density, cooler temperatures, and a larger density width than the interarm region. The density width spans a more extensive dynamical range for the arm (0.5 ± 0.3 dex) than the interarm (0.2 ± 0.1 dex) region. Furthermore, for the interarm region, we see a clear bimodal distribution of densities (see the left panel in Figure 7.3). This means that the parameter solution derived from the MCMC modeling oscillates back and forth between two cases. One solution lies at higher temperatures and lower densities, while the other solution lies at temperatures comparable to the spiral arm region solution. This is also evident from the histograms at the top and right side of each panel for the volume density and temperature. To a lesser extent, a similar bimodal distribution for temperature and density is true for the spiral arm region.

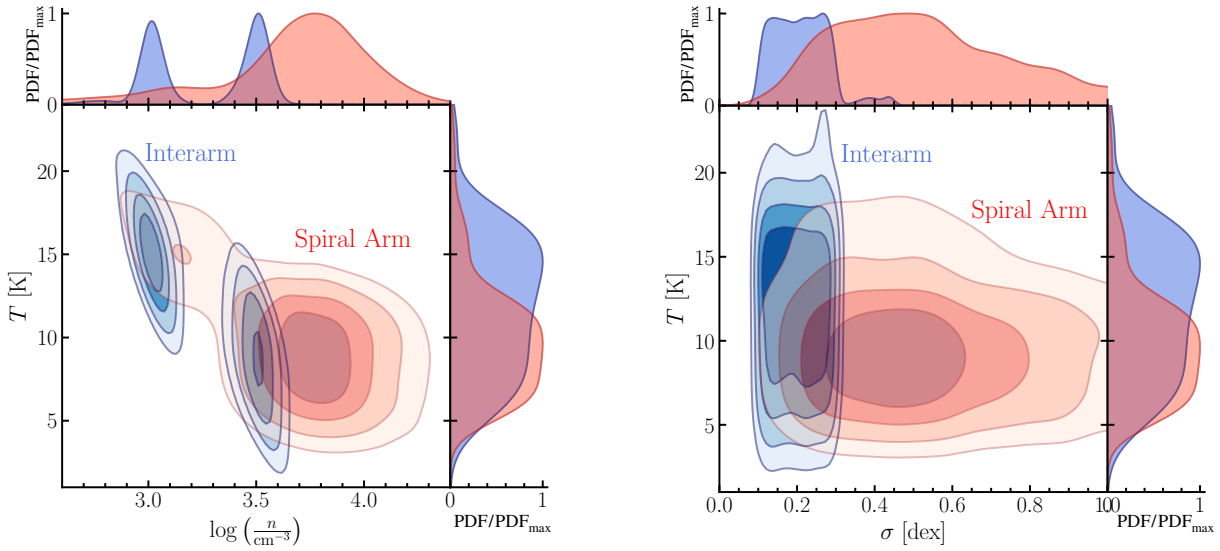

Figure 7.3: **Probability Density Distribution for M51's Arm and Interarm region.** The panels show the DGT-derived PDF of temperature-density (*left*) and temperature-density width (*right*) in terms of 25%, 50%, 75% and 90% inclusion area (indicated by colored contours). The histogram show the normalized PDF for the different parameters.

The bimodal distribution of molecular gas conditions clearly indicates that the spiral arm and interarm region do not constitute a homogeneous region. Instead, temperature and density can also vary within these environments. With our kpc-scale observations, we are limited. At such resolution, we cannot accurately resolve the internal structure of the different environments, and there is evidence that the dynamical range of the molecular line ratio changes with spatial scale (see Section 7.2). Recent IRAM NOEMA large program observations (PI: Eva Schinnerer and Frank Bigiel) at higher resolution (~2″) will shed light on the internal variations within the different environments in M51.

7.1.3 Line Modelling: Next Steps

So far, we only modeled the molecular gas conditions for two regions: the spiral arm and interarm. However, as indicated already by the bimodal distribution of the densities, these environments generally are not homogeneous but contain gas under varying physical and chemical conditions. Ideally, we want to model the conditions for individual sightlines. As such, we can investigate resolved variation of the molecular gas conditions on kpc or even sub-kpc scales. A logical first step consists of expanding the analysis presented in this section to the individual sightlines of the CLAWS survey observations in M51, for which we have multiple CO isotopologue emission. However, due to the faintness of some of the CO isotopologue lines, such as $C^{18}O$ (2−1) and $C^{18}O$ (1−0), stacking remains an essential tool for obtaining significant line detection for selected regions beyond the nuclear region.

In addition, it will be crucial to compare results not just from the DGT but also from other line emission modeling techniques and tools. This includes pipelines build on `RADEX` (e.g., Teng et al., 2022, A. Garcia-Rodriguez et al., in prep) which focus on fixing and varying different key parameters of the molecular gas conditions. Such a model cross-comparison will help to benchmark the various tools and improve constraints on molecular gas parameters across different environments.

7.2 High-Resolution CO Excitation: NGC3627

Several times throughout the thesis, we have alluded to the fact that ^{12}CO (2−1) emission is increasingly used over ^{12}CO (1−0) to trace the distribution and kinematics of molecular gas. For instance, it is more efficient and faster to observe the $J = 2 \rightarrow 1$ line, particularly with ALMA. For example, the *Physics at High Angular resolution in Nearby GalaxieS* (PHANGS; Leroy et al., 2021b) mapped approximately 90 nearby galaxies in ^{12}CO (2−1) emission at a resolution of ≤150 pc. A key goal of the PHANGS project is to understand the connection of molecular gas within the baryonic life cycle of the ISM. However, to accurately trace the molecular gas mass distribution, it is essential to understand variation in R_{21} and the conversion factor X_{CO}. However, R_{21} variation is not yet fully understood across different physical scales in galaxies. Similar to our research described in Chapter 4, most work so far focused on resolved large-scale (> 1 kpc) variation across external galaxies (e.g. Yajima et al., 2021; Leroy et al., 2022) or comparable small-scale observations of molecular clouds within the Milky Way (e.g. Sawada et al., 2001; Yoda et al., 2010). With large programs, like PHANGS, we nowadays achieve angular resolutions that can resolve scales of a similar order to the largest GMC size found in the Milky Way (e.g. Colombo et al., 2014; Miville-Deschênes et al., 2017). Figure 7.4 shows a comparison of the two scales in question. The left panel shows IRAM 30m observations of the spiral galaxy NGC3627 at ~27″ (< 2 kpc) resolution. At this resolution, we can distinguish different morphological features of the galaxy, such as the center and bar-ends. The right panel shows ALMA observations at a higher angular resolution of 3″. At these scales, we can start to see and study line emission variation within certain regions of the galaxy, such as along the spiral arms or within the center and bar-ends. For future studies, it becomes increasingly relevant to link, understand and close the bridge regarding any potential variation on large galactic and small GMC scales. Furthermore, the push toward higher angular resolution will help connect extragalactic to Galactic molecular gas studies.

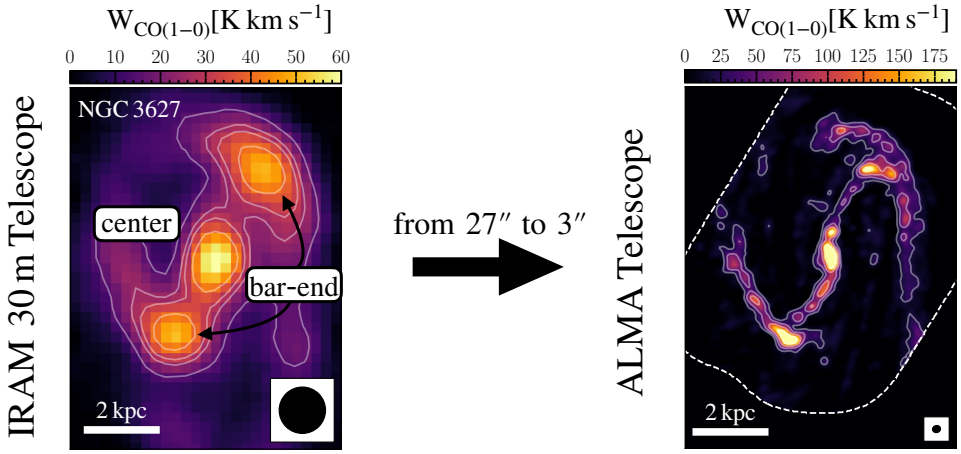

Figure 7.4: **From IRAM 30m to ALMA resolution.** (*Left*) IRAM 30m observations of CO(1-0) as part of EMPIRE (Jiménez-Donaire et al., 2019). The angular resolution is at 27″ (~1.5 kpc). While coarse, this resolution is sufficient to distinguish between the morphological features of the galaxy, including its center, the bar-ends, and the spiral arm. (*Right*) ALMA CO(1-0) moment-0 map for the same field-of-view. The white outline shows the ALMA observed field-of-view. The native resolution is at 3″. We probe scales comparable to the largest GMCs in our Milky Way at such a resolution. With this map, we can study the internal variation of the emission within the center, bar-ends, or spiral arms.

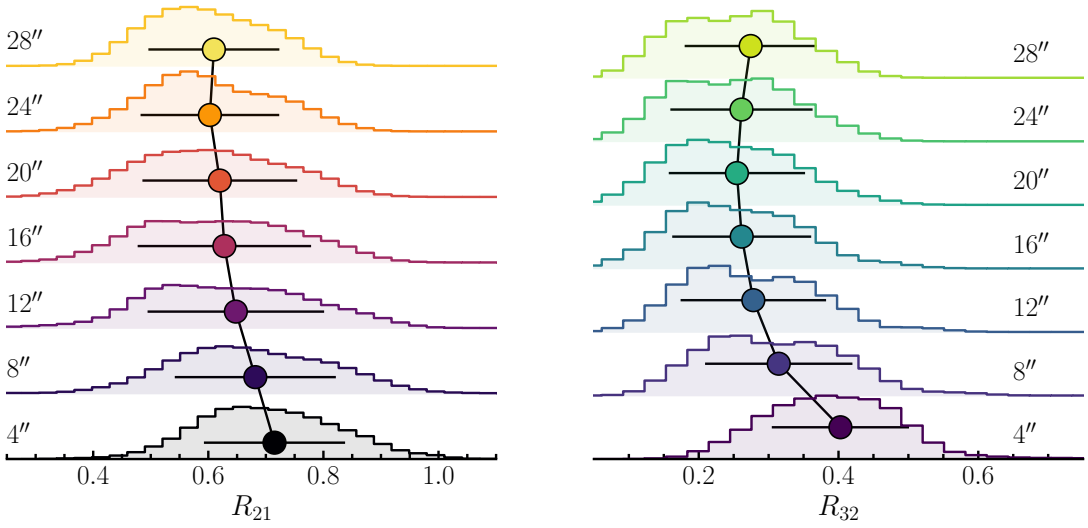

Figure 7.5: **Scale-dependent Line Ratio Distribution.** These panels show the total line ratio (left R_{21} and right R_{32}) distribution across NGC 3627 at various resolutions (indicated at the left or right of the distribution). Only sightlines for which all three lines are detected above 10σ are considered. The circles indicate the median line ratio per resolution. The bars show the 1σ scatter as measured using the median absolution deviation (and correcting by a factor of 1.4 to convert to a standard deviation).

7.2.1 CO Observations of NGC 3627: Bridging the Gap across Different Scales

For the galaxy NGC 3627, we have high-resolution emission line maps (common beamsize of $\leq 4''$) for ^{12}CO (1−0) from Gallagher et al. (2018), (2−1) from the PHANGS-ALMA sample (Leroy et al., 2022), and (3−2) (PI: J. Puschnig). The average 1σ sensitivity of the data per 5 km s^{-1} channel width at $4''$ angular resolution amounts to 56 mK for ^{12}CO (1−0), 25 mK for ^{12}CO (2−1), and 32 mK for ^{12}CO (3−2). The following section provides a short summary where we address the relevant question of scale-dependent R_{21} and R_{32} variation. Future work will dive much further into detail.

With the help of these maps, we can start to assess CO excitation variation across different scales by convolving the observations to various coarser resolutions. Figure 7.5 shows the pixel-wise R_{21} and R_{32} distribution across the full galaxy for different resolutions. Only sightlines for which all three emission lines are at S/N>10 are considered. A clear trend towards smaller average values for both R_{21} and R_{32} with coarser resolutions is evident. At $4''$, we find an average line ratio of $\langle R_{21}^{4''} \rangle = 0.71 \pm 0.12$ and $\langle R_{32}^{4''} \rangle = 0.40 \pm 0.11$. In contrast, at $28''$ we find a significantly lower average of $\langle R_{21}^{28''} \rangle = 0.60 \pm 0.11$ and $\langle R_{32}^{28''} \rangle = 0.27 \pm 0.11$.

Such scale-dependent variation has implications when relying on line ratios obtained from datasets at different physical resolutions. The fact that the line ratio decreases at a coarser resolution suggests that regions with high line ratios get averaged out. At low resolutions, the beam will encompass an ensemble of clouds, averaging the line emission from different origins. For example, we expect the line ratios to increase toward the galactic center, where more active star formation occurs, leading to a higher interstellar radiation field, which enhances the CO excitation (e.g., Narayanan et al., 2012). At coarser resolutions, however, the central regions will be convolved with surrounding regions, which leads to a decrease of the

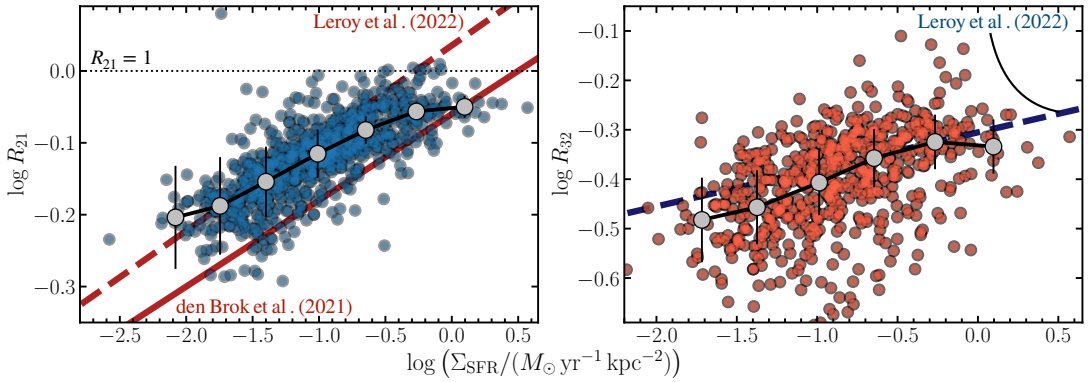

Figure 7.6: **Line Ratio Variation with SFR Activity.** (*Left*) R_{21} as a function of SFR surface density. The blue points show individual sightlines at 4″ with S/N>10 for both lines. The grey points show the binned values. The red lines show the trends found by den Brok et al. (2021) (see Chapter 4) and Leroy et al. (2022). (*Right*) R_{32} as function of SFR surface density. Description identical to the left panel.

observed line ratio average.

In addition, we note that Peñaloza et al. (2017) found a bimodal R_{21} distribution of R_{21} after performing smooth particle hydrodynamic simulations of a single molecular cloud. The lower line ratio values go along with less dense, more diffuse emission. This emission is less bright and requires more sensitive observations to capture. The trend towards lower line ratios might also reflect the fact that we pick up more of the fainter diffuse emission due to the increase in sensitivity with coarser resolution.

This brief overview section focuses on the overall line ratio distribution across the different regions of NGC 3627. However, to fully assess the degree and origin of the line ratio variation at different scales, it is crucial to study changes of R_{21} and R_{32} within the different environments, such as center, bar, arm, and inter-arm regions. We expect that these environments impact the molecular gas conditions in different ways (Colombo et al., 2014). In addition, the SFR also varies as a function of the galaxy morphology (Calvi et al., 2018), reflecting another driver for line ratio variation. Future work will address the line ratio at various scales as a function of different galactic morphology in further detail.

7.2.2 Tracing and Understanding Line Ratio Variation at High-Angular Resolutions

In Chapter 4, we describe a way to parameterize R_{21} variation using the SFR surface density, $\Sigma_{\rm SFR}$. We find a linear expression for both variables in logarithmic space (see Equation 4.1). Similarly, Yajima et al. (2021) and Leroy et al. (2022) find a trend in R_{21} and R_{32} with SFR surface density. However, all of the aforementioned findings are based on kpc-scale resolution. With our observations of NGC 3627, we can test if and how the scaling relation change with different angular scales. We can potentially connect the variation to changes in excitation temperature, collider density, and the CO column density by studying the connection of R_{21} with the star formation activity, which acts as a heating source for low-J CO lines (e.g. Peñaloza et al., 2017; Leroy et al., 2017).

Figure 7.6 shows the R_{21} and R_{32} line ratios as function of the SFR surface density. The figure shows all sightlines with S/N>10 for the three CO transitions. For comparison, we also highlight the R_{21} and R_{32} trend found in den Brok et al. (2021) and Leroy et al. (2022). Based on binning by SFR surface density (grey points), we find a clear correlation between line ratios and star formation activity. For R_{21}, the trend spans between both prescriptions from den Brok et al. (2021) and (Leroy et al., 2022). The line ratio

clearly does not exceed R_{21}>1. Also, the trend seems to converge toward $R_{21} \sim 0.9$ at $\log \Sigma_{\rm SFR} > -0.5$. Regarding R_{32}, it seems to follow more closely the trend found by Leroy et al. (2022). The result underlines that indeed the excitation conditions, as traced by the SFR surface density, lead to higher line ratios. In particular, we expect warmer gas as a result of more intense star-forming activity due to stronger radiation fields, higher cosmic-ray densities, and higher-density gas (e.g. Usero et al., 2015; Gallagher et al., 2018).

Again, we can trace the impact of using different scales for this analysis. Figure 7.7 shows the trend of R_{21} with SFR surface densities for different resolutions of the NGC 3627 data. We note, in particular, that the steepness of the correlation seems to increase with coarser resolutions. Furthermore, with higher angular resolutions, we trace a larger dynamical range of SFR surface densities, in particular at the higher-value end. Especially with higher angular resolutions of $\leq 4''$, we start to resolve individual star-forming complexes. With observations reaching molecular cloud scale resolution ($\leq$100 pc) we start to directly probe the dynamical and physical features (Meidt et al., 2013; Schinnerer et al., 2013; Forbrich et al., 2020; Muraoka et al., 2020). This is impossible for lower-resolution observations because such features get washed out. Hence, we can start to test the underlying drivers, such as UV radiation, cosmic ray ionization rate, gas density, and gas dynamics, which all affect line ratio variation as expected from simulations (e.g., Peñaloza et al., 2018; Gong et al., 2020).

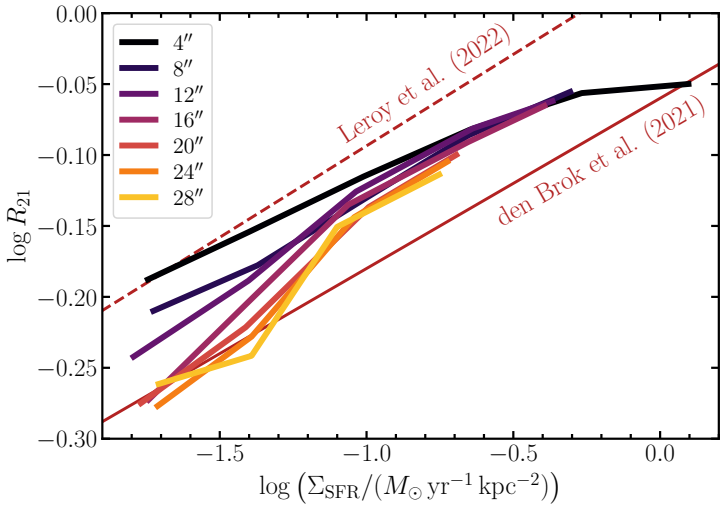

Figure 7.7: **R_{21} Line Ratio Trends with SFR Activity.** The colored lines show trends of R_{21} binned by SFR surface density for different resolutions of the NGC 3627 dataset. The red solid and dashed lines show the predicted line ratio trend according to den Brok et al. (2021) and Leroy et al. (2022). We see that the trend gets steeper with coarser resolution.

7.2.3 Molecular Cloud-Scale CO Ratio Variation: Next Steps

The previous summary and discussion of the R_{21} and R_{32} line ratio variation mark just a first look at a possible future direction of thesis-related research. Also, so far, we only looked at general line ratio trends across the galaxy, without separating by morphology, such as center, arm or bar-end. As part of the PHANGS collaboration, we aim to obtain high-angular resolution ($\leq 4''$) ALMA ^{12}CO (1−0) and (3−2) data for a larger subset of the full 90 galaxy sample to complement with the already available ^{12}CO (2−1) observations. The sources will be selected to span a larger range of total stellar mass ($\log(M_\star/M_\odot)$=9.5−11)

and SFR ($\log(\mathrm{SFR}/(\mathrm{M}_\odot\,\mathrm{yr}^{-1})) = (-1) - 1$), representative of the nearby star-forming galaxy population. With this larger dataset, we hope to obtain robust constraints on high-resolution R_{21} variations, which will help to improve ^{12}CO (2−1) derived parameters, such as the molecular gas mass, which usually relies on fixed R_{21} values. Key future science steps will include:

- **How can we describe the overall structure and distribution of CO excitation conditions in nearby galaxies?**
  So far, we only looked at overall R_{21} and R_{32} distribution and correlation with Σ_{SFR}. However, with high-resolution observations, we can go beyond radial and azimuthal variations and inspect the internal variation within the spiral arm, center, bar-ends, and interarm region. The aim will be to obtain a calibrated and homogeneously measured census of low-J CO excitation, which will help to predict CO line ratio variation for nearby spiral galaxies.

- **How is CO gas excitation connected to molecular cloud properties?**
  Using the ^{12}CO (2−1) data, the GMC cloud properties, such as density, line width, and brightness, have been characterized (Sun et al., 2018; Rosolowsky et al., 2021). Hence we can start to connect the observed line ratios to GMC properties. With this analysis, we aim to understand molecular gas and macroscopic GMC properties are related, which will help to reveal and understand the true drivers of CO excitation variation.

While the kpc-scale study provides valuable insight into the large-scale variation of molecular gas conditions, it is evident that connecting it to cloud-scale physics on which star formation takes place is key to obtaining a complete picture of processes regulating galaxy evolution.

7.3 Further Open Questions

The focus on multi-CO line emission modeling to obtain insight into the molecular gas physics and chemistry on kpc-scale and the push towards GMC-scale resolution low-J observations constitute only the tip of the iceberg of further open questions. Numerous directions for possible future research exist, covering both kpc-scale and GMC-scale research.

1. **Beyond a single Type/Morphology of Galaxy**
   Throughout the thesis, the main focus lay on the study of nearby massive star-forming spiral galaxies, such as M51, M101, or the EMPIRE sample (see Chapter 4). However, the nearby galaxy population includes a wide variety of galaxy types, such as metal-poor dwarfs, starburst galaxies, luminous infrared galaxies, or elliptical galaxies, to name a few. Such galaxies usually host molecular gas under many different conditions. For example, starburst galaxies hold molecular gas at much higher volume and column densities compared to regular spiral galaxies (e.g. Jackson et al., 1995; Iono et al., 2007). In addition, the gas is also observed to be warmer, leading to enhanced emission of higher-J CO transitions (e.g. Bradford et al., 2003; Ward et al., 2003; Rangwala et al., 2011; Narayanan et al., 2012). In contrast, metal-poor galaxies show very little CO emission. For instance, low-mass dwarf irregular galaxies with metallicities lower than $12 + \log(\mathrm{O/H}) \leq 8$ show almost no CO emission (e.g. Elmegreen et al., 1980; Tacconi and Young, 1987; Taylor et al., 1998). And finally, it has become evident that also elliptical galaxies, despite not showing any active star formation, also host certain amounts of molecular gas (e.g. Lees et al., 1991; O'Sullivan et al., 2015; Temi et al., 2018). In such elliptical galaxies, it is suggested that the origin of the gas comes from accumulation during mergers events and material ejected from stars (Davis et al., 2011).

The increased gas temperature in starburst galaxies or the low metallicity gas in dwarf galaxies will impact derived molecular gas properties using relations calibrated on normal spiral galaxies. For example, following the discussion in Subsection 1.4.1, we expect the conversion factor, $X_{\rm CO}$, to decrease in warmer gas. But the case is not straightforward for starburst galaxies since the increased density of the gas could compensate for the temperature-dependent decrease of $X_{\rm CO}$. In addition, we expect an increase in the conversion factor in low-metallicity environments. Low metallicities lead to low C and O abundances and a low dust-to-gas ratio (Draine et al., 2007; Muñoz-Mateos et al., 2009a). Less dust will reduce the shielding of CO from far-UV radiation. In addition, at lower column densities, the CO cannot effectively self-shield from the ambient UV radiation field anymore. As a result, the molecular cloud will become more CO-faint, hence increasing the $X_{\rm CO}$ factor.

So given the implications, a sample of a wider range of galaxy types is essential to expand the dynamical range of various key physical and chemical parameters (such as SFR, stellar mass, brightness, metallicity, etc). A key goal is to perform a benchmark study by combining the investigation of various galaxy types systematically within a single study. Going beyond the investigation of regular nearby spiral galaxies is also relevant for connecting with high-redshift studies. In the past, most high-redshift observations have focused on CO observations toward brighter luminosity sources, such as so-called submillimeter galaxies (SMGs) and quasi-stellar object (QSO) hosts. Over the course of the last decade, also more regular main-sequence galaxies have been targeted by high-z studies (e.g. Daddi et al., 2010; Tacconi et al., 2010; Uzgil et al., 2019). Connecting to the nearby galaxy sample will make it possible to fine-tune derived properties from CO emission for high-z observations.

2. **Connecting Galactic and Extragalactic Multi-CO Studies**
In recent years, extragalactic studies of nearby spiral galaxies have pushed toward increasingly higher angular resolutions of CO observations around $\sim 1-2$ pc (e.g. Schruba et al., 2017; Tokuda et al., 2020; Krieger et al., 2020; Sano et al., 2021). With the help of such high angular resolutions, it becomes possible to draw parallels between extragalactic and Galactic molecular gas studies. In the Milky Way, molecular clouds get regularly studied at sub-pc resolutions (e.g. Indebetouw et al., 2013; Heyer and Dame, 2015; Lane et al., 2016; Bron et al., 2018). At these scales, we can address the question of cloud lifetimes and investigate the role of stellar feedback and its impact on molecular clouds. However, it is difficult to reconcile how sub-pc cloud properties connect to the global GMC and galactic (kpc) scales since our perspective on the MW makes it hard to obtain its larger-scale properties. The question regarding the connection of different physical scales is also tightly linked to assessing the validity and universality of the Kennicutt-Schmidt law across different scales (see Subsection 1.5.1).

3. **Different $\alpha_{\rm CO}$ Estimation Methodology**
In section Subsection 1.4.2, different techniques to estimate the conversion factor, $X_{\rm CO}$, are introduced. In order to calibrate the conversion factor, the molecular gas mass must be determined robustly and independently from CO emission. To summarize the section in the introduction of this thesis, the major ways to estimate the molecular mass are as follows (see also Bolatto et al., 2013): (i) using dust emission and relating it to the gas column with a dust-to-gas ratio, (ii) determining the virial mass of spatially resolved molecular clouds with measurements of their size and kinematics, (iii) with the help of an optically thin gas tracer, such as ^{13}CO , or (iv) using γ-ray emission from the interaction of cosmic rays with the nucleons.

So far, only for the Milky Way do $X_{\rm CO}$ estimates exist from all these four techniques. For other galaxies, studies usually rely on one of the techniques mentioned above (e.g. Nakai and Kuno, 1995; Sandstrom et al., 2013; Cormier et al., 2018; Teng et al., 2022). Generally, the $X_{\rm CO}$ found with different

methods are loosely consistent within a specific galaxy. Nonetheless, a large scatter of values exists both between galaxies and between methods. A significant challenge for a systematic study of different $X_{\rm CO}$ estimation techniques is that one needs to rely on data from numerous surveys that have probed the galaxy at different sensitivities and scales. So far, no systematic study has been performed that applies multiple methods simultaneously in a sample of nearby galaxies. In particular, with the M51 and M101 observations, it will be possible in a future study to perform methods (i-iii) simultaneously and assess the performance of the different $X_{\rm CO}$ conversion factor estimation techniques.

CHAPTER 8

Conclusion

Per aspera ad astra.

Latin Proverb

Overview

In this thesis, we investigate the content, distribution, and conditions of the bulk molecular gas in the ISM and study its relation to star formation within and across nearby galaxies. This includes a detailed and systematic analysis of multi-CO line observations in the mm wavelength regime. We address questions regarding the state and conditions of the molecular gas, such as temperature, density, and opacity. The ^{12}CO line and its rotational transitions trace the overall distribution of the gas and, via their ratio, the subsequent excitation conditions. Furthermore, the optical thin CO isotopologues, such as ^{13}CO and C^{18}O, offer valuable insight into their relative abundances and allow us to study the chemical enrichment of the gas. To achieve a robust and systematic investigation, we rely on large program observations that were made with state-of-the-art instruments, such as ALMA and the IRAM 30m telescope. The focus lies on studying the nearby massive star-forming galaxy population (with $d \leq 10$ pc). Studying such extragalactic sources, as opposed to molecular gas in our own Milky Way, comes at the expense of coarser angular resolution. However, because we can study the emission across entire galactic disks, we can explore a broad range of relevant processes and conditions. In contrast, since we are situated right within, we cannot achieve a similar perspective within the Milky Way.

The thesis can be separated into four major parts: The 30m telescope performance analysis, the CO line ratio analysis of the EMPIRE sample, the M51 CLAWS survey analysis, and the M101 wide-field multi-CO analysis. Here, we reflect again on the main research questions of the individual projects and the most relevant conclusions we draw.

1.) IRAM 30m Telescope Performance

Chapter 3 analyzes the flux calibration uncertainty and error beam contribution of the IRAM 30m telescope. It is crucial to understand the associated uncertainties for an adequate analysis and interpretation of the observations. We rarely find such an analysis in the literature, despite its importance for correctly interpreting observed line emission trends. The chapter presents IRAM 30m DDT observations that

we obtained for six selected pointings across M51 (two spiral arm and two interarm pointings). We simultaneously observed ^{12}CO (1−0) at ∼115 GHz and (2−1) at ∼230 GHz. These observations aim to specifically analyze the flux calibration performance and understand previously observed CO line emission variation within and across nearby galaxies. A multitude of factors related to the instrument, receiver, and telescope can affect the subsequent robustness of an observing run. For example, the system noise temperature can vary, there might be scanning artifacts, or the intensity calibration can go wrong. In addition, external factors, such as varying atmospheric conditions, also play a role.

For the 30m observing run, we iteratively observed the six selected pointing several times throughout the night. This way, we obtain several scans per pointing. The chapter investigates how the line emission varies from scan to scan. We can analyze if the uncertainties are systematic and similar for both frequency regimes that we targeted simultaneously. Indeed, we find significant scan-to-scan variation, particularly for the pointings of the faint regions, with a variation of >50% in integrated intensity. Analyzing various potential sources that could drive such variation, we conclude that the pointing accuracy of the telescope or the source's elevation does not seriously affect the performance. However, with the help of line calibrator observations from the two different nights, we find that the flux calibration stability can vary up to 15%. Hence, our analysis suggests that ∼15% of uncertainty should be expected when comparing data from different IRAM 30m observing runs. However, when studying line ratios observed within the same observing run and spectral setup, the uncertainty will be lower (around ∼5%).

Furthermore, the chapter provides a detailed mathematical description for treating emission contribution from the telescope's error beams. The beam pattern of a telescope can be described using the main beam component and a set of side lobes, via which emission can enter the observation. In particular, for faint regions that are embedded in brighter regions, such contribution can significantly enhance the observed emission (e.g., the interarm region sitting between two spiral arms). So, improper error beam handling can lead to wrongly assuming too much flux from certain regions. Assessing and quantifying the impact is difficult since the exact beam shape varies with the frequency and orientation of the telescope. However, for the IRAM 30m telescope, the beam pattern has been measured. Hence, we can perform a first-order estimate of the error beam impact. The chapter presents two techniques to estimate the contribution: (i) the direct method using a Fourier transform approach and (ii) the iterative method by subtracting the convolved data using only the error beam pattern from the original data. Overall, we find that the ^{12}CO (2−1) emission from the interarm region can suffer by ∼20% for IRAM 30m telescope observations. For ^{12}CO (1−0) emission from the interarm region, the error beam contribution is smaller, with only ∼10%. We only perform this analysis for IRAM 30m telescope observations. Such error beam contribution also affects other single dish telescope observations (e.g., 45m Nobeyama radio telescope). However, it is not feasible to quantify the impact without estimates of the beam pattern.

2.) CO Line Ratio Across EMPIRE Sample

Over the course of the last decade, it has become increasingly common to rely on ^{12}CO (2−1) emission, instead of ^{12}CO (1−0), as a main tracer of molecular gas amount, distribution, and kinematics in nearby galaxies. The advantage of ^{12}CO (2−1) is that it can be mapped faster, in particular given the performance capabilities of ALMA. Furthermore, due to its higher frequency, it can be observed at a higher resolution relative to ^{12}CO (1−0) when observing with the same telescope. Studies that rely on ^{12}CO (2−1) as their molecular gas tracer then commonly use a constant $R_{21} \equiv {}^{12}\mathrm{CO}\,(2-1)/(1-0)$ ratio to down-convert the measured intensity to the lowest-J ^{12}CO (1−0) transition. However, from theoretical consideration and

previous empirical studies in the Milky Way, we expect the CO excitation conditions, and hence the R_{21} line ratio, to vary within and across nearby galaxies.

Chapter 4 presents the results from the published study analyzing kpc-scale R_{21} line ratio variation across a set of nine nearby massive star-forming spiral galaxies drawn from the EMPIRE sample. The goal is to benchmark and quantify the degree of R_{21} variation within and across nearby galaxies. While similar studies exist that investigate resolved low-J CO line ratio variation within individual galaxies, we lay the focus on expanding the sample to a set of several galaxies. We use a homogeneous dataset of the best observations available in flux stability and calibration. Overall, we find significant R_{21} variation within the individual galaxies as well as significant galaxy-to-galaxy offsets. The galaxy-to-galaxy offset can amount to a 0.3 dex global difference. Regarding internal trends, particularly barred galaxies show an enhancement of R_{21} toward the central region with 10−20% higher values than their galaxy-wide average. Some galaxies also show further significant internal variation, such as arm-interarm variation. M51, for instance, shows higher line ratios in the interarm region (R_{21}~$0.9-1$) than the spiral arm region (R_{21}~$0.8-0.9$). Averaged over all sightlines of the nine galaxies, we find an intensity-weighted mean line ratio of $\langle R_{21} \rangle = 0.64 \pm 0.09$, which is slightly lower than the canonical value of $R_{21} = 0.7$ used before. Based on the trend with SFR, we can provide a prescription of R_{21} as a function of $\Sigma_{\rm SFR}$.

The observed variation and scatter in R_{21} implies a significant degree of uncertainty for accurate molecular gas mass estimates derived from ^{12}CO(2-1) intensities alone. The large galaxy-to-galaxy offsets likely originate, to some degree, from flux calibration uncertainties. So far, the focus of the study was on kpc-scale variation. The picture might be different at higher angular resolution, where we can resolve individual GMCs. Finally, the derived scaling relations, such as the Kennicutt-Schmidt law, could also be affected when relying on inaccurate or fixed R_{21} values. However, since the conversion factor, $X_{\rm CO}$ likely varies as well, we cannot accurately quantify the impact on the molecular gas scaling relations from R_{21} alone.

3.) CLAWS: Multi CO Isotopologue Survey of M51

Chapter 5 presents the published *CO Line Atlas of the Whirlpool Galaxy Survey* (CLAWS) paper. CLAWS is an IRAM 30m telescope large program. As part of the project, we targeted the entire disk of M51 and obtained faint CO isotopologue emission for different transitions in the 1.3 mm and 3 mm wavelength regime. For the first time, we can assess resolved ^{13}CO, C^{18}O, and even C^{17}O emission across a regular star-forming galaxy other than our Milky Way. With the wealth of CO isotopologue, we address various relevant science questions related to understanding the chemical enrichment of the molecular gas and gaining insight into the kpc-scale conditions. This is possible because the CO isotopologue line emission is mostly optically thin, as opposed to the optically thick ^{12}CO emission. With the help of optically thin lines, we can assess relative abundance variation, while contrasting optically thin to optically thick lines yields further insight into opacity changes.

The various CO isotopologue line ratios show clear trends with the environment (i.e., center–disk, arm–interarm) and SFR surface density. We use these trends to qualitatively assess and identify potential galaxy-wide drivers that explain the observed changes in the line ratio. In particular, the decreasing $R_{12/13}$ and $R_{12/18}$ J=1 $\rightarrow$ 0 line ratio trends suggest that a combination of selective nucleosynthesis and changes in the opacity act as the major drivers for the overall CO line ratio variation across M51. Regarding the arm-interarm difference, the higher CO excitation in the interarm, as traced by higher R_{21} values, likely links to more diffuse molecular gas at higher temperatures.

In summary, with its measured line ratios, the survey provides a benchmark for future isotopologue studies in extragalactic systems. Similar studies have so far only focused on brighter starburst galaxies or the nuclear region inside regular galaxies. With the wealth of CO isotopologue lines that the survey targeted, it is possible to obtain a quantitative description of how the molecular gas conditions connect to the observed line ratio trends (see Section 7.1). With the eight CO isotopologue lines, we can constrain various parameters, such as temperature, volume density, or the density distribution width, using non-LTE radiative transfer modeling across a regular nearby galaxy.

4.) M101 Wide-Field Observations: CO and the Conversion Factor

Chapter 6 presents an in-progress manuscript of IRAM 30m wide-field CO observations of M101 and the subsequent analysis. The study focuses on two main science questions related to the kpc-scale molecular gas physics and chemistry in M101 and also draws on M51 for a comparison. First, the study addresses how well CO isotopologue line emission captures the variation of the molecular gas characteristics. Secondly, the investigation analysis how $\alpha_{\rm CO}$ varies with environmental parameters across the galaxy.

The CO isotopologue line emission variation in M101 again hints at changes in abundances due to nucleosynthesis as the major driver on galaxy-wide scales. Of peculiarity is also the faint $C^{18}O$ emission. We only detect it via stacking since it is much fainter than anticipated based on line ratios from other nearby spiral galaxies. The low $R_{18/13}$ line ratio suggests a very low relative abundance of this isotopologue, setting strong constraints on the selective nucleosynthesis enrichment history.

In addition to the CO isotopologue analysis, the chapter investigates the variation of the CO-to-H_2 conversion factor, $\alpha_{\rm CO}$, across M101. We estimate the conversion factor with a modified scatter minimization technique that uses dust mass surface density measurements, H I 21 cm, ^{12}CO (1−0) and (2−1) emission line maps to determine the molecular gas content. For comparison, we also perform an $\alpha_{\rm CO}$ estimation using an LTE-modelling approach based on the predominantly optically thin ^{13}CO (1−0) line emission. For M101, we find a flat $\alpha_{\rm CO}$ value across the disk with both $\alpha_{\rm CO}$-estimation techniques. From the scatter minimization technique, we find $\langle\alpha_{\rm CO}\rangle = 4.4 \pm 0.9\,M_\odot\,{\rm pc}^{-2}({\rm K\,km\,s}^{-1})$, while the LTE approach yields a lower $\alpha_{\rm CO}$ by a factor 2−3. Toward the central region, the conversion factor drops significantly by a factor ∼10. The conversion factor has been systematically analysed in previous studies before. However, in this project, we expand the previous work by combining the analysis of the conversion factor with the study of the variation in the R_{21} line ratio and investigating the implications if both parameters vary.

The observed CO line ratio and $\alpha_{\rm CO}$ variation across the galaxy has implications on molecular gas mass scaling relations that are commonly derived when using a fixed $\alpha_{\rm CO}$ and R_{21} value. Accounting for the variation, we find that the Kennicutt Schmidt relation index increases by ∼50% in the case of M51. In addition, we investigate how the molecular gas depletion time, $\tau_{\rm dep}$, varies: Not accounting for $\alpha_{\rm CO}$ and R_{21} seems to be significantly overestimated in the center. Such low depletion times suggest high star forming efficiencies in the galactic center region.

Finally, we also perform a parameterization attempt to describe the variation of $\alpha_{\rm CO}$ with a set of commonly observed feature variables, such as the SFR surface density, metallicity, CO line ratios, etc. From theoretical consideration, we expect two major physical drivers that will affect the conversion factor: the presence of CO-dark gas and enhanced molecular gas temperature or opacity, which will impact the CO emissivity. Using a feature selection technique based on *lasso* regression and the Bayesian Inference Criterion (BIC) model, we find that 80% of the observed variation, in particular the depression of $\alpha_{\rm CO}$ toward the center, can be described by three feature variables. Using a power-law model, we find that the

most relevant features are stellar mass surface density, $\Sigma_\star$, SFR surface density, $\Sigma_{\rm SFR}$, and the CO kpc-scale velocity dispersion, σ_v, which all in combination mostly trace the change of $\alpha_{\rm CO}$ due to temperature and opacity variation. We find that by applying the derived model from M101, we predict correctly the overall $\alpha_{\rm CO}$ values found in M51 across the disk. However, the model also predicts a depression of $\alpha_{\rm CO}$ in M51, which we do not see via the scatter minimization technique. This suggests the existence of another *hidden* parameter that needs to be taken into account when assessing the lower central conversion factor values.

In summary, this study contributes to our general understanding of $\alpha_{\rm CO}$ variation within and across nearby galaxies on kpc-scales. The investigation concludes that care needs to be taken in particular when assessing molecular gas properties derived from CO toward the center of galaxies, where the depression of the conversion factor can seriously impact the derived molecular gas properties.

Closing Remarks

Understanding the conditions that regulate the cold molecular gas in the ISM constitute an essential piece of the puzzle to unraveling star formation processes and galaxy evolution. The research presented in this thesis is among the first studies that open the window of resolved CO isotopologue line emission to investigate the molecular gas conditions across nearby regular star-forming galaxies, which before was only possible in galactic centers of the Milky Way. As such, it offers an important step toward closing the gap between extragalactic and Galactic studies. The previous chapters outline how we can use multi-CO line ratios to trace different aspects of the molecular gas, such as its temperature, density, or relative species abundances. The potential further research paths are far from being exhausted. New and exciting science questions are waiting to be tackled and addressed. Two major directions seem to stand out as immediate next steps: (i) Pushing toward higher resolution CO isotopologue observations across nearby extragalactic systems and bridging the small and large-scale processes that regulate star formation. And (ii) using the wealth of observed CO isotopologue lines to obtain robust quantitative constraints on the molecular gas conditions across different environments within nearby galaxies using non-LTE line modeling. The effort to complete the picture connecting molecular gas and star formation throughout the Universe and cosmic time will remain an active field of research. Therefore, I like to think that with my research described in the previous chapters, I contribute to the overarching effort with a piece of the puzzle. Because even the most complex puzzles are solved piece by piece.

Appendix

APPENDIX A

EMPIRE CO(2-1)/(1-0) Line Ratio Paper

The paper *den Brok et al. MNRAS (2021), 504, 3221* is reproduced below in its original form with permission by Oxford University Press.

Monthly Notices of the ROYAL ASTRONOMICAL SOCIETY

MNRAS **504,** 3221–3245 (2021) doi:10.1093/mnras/stab859
Advance Access publication 2021 March 31

New constraints on the ^{12}CO(2–1)/(1–0) line ratio across nearby disc galaxies

J. S. den Brok [1]★ D. Chatzigiannakis,[1] F. Bigiel,[1] J. Puschnig [1] A. T. Barnes [1] A. K. Leroy,[2] M. J. Jiménez-Donaire,[3,4] A. Usero,[3] E. Schinnerer,[5] E. Rosolowsky [6] C. M. Faesi,[7] K. Grasha [8] A. Hughes [9,10] J. M. D. Kruijssen [11] D. Liu,[5] L. Neumann,[1] J. Pety,[12,13] M. Querejeta,[3] T. Saito,[5] A. Schruba[14] and S. Stuber [5]

[1]*Argelander-Institut für Astronomie, Universität Bonn, Auf dem Hügel 71, D-53121 Bonn, Germany*
[2]*Department of Astronomy, The Ohio State University, 4055 McPherson Laboratory, 140 West 18th Avenue, Columbus, OH 43210, USA*
[3]*Observatorio Astronómico Nacional (IGN), C/Alfonso XII 3, E-28014 Madrid, Spain*
[4]*Centro de Desarrollos Tecnológicos, Observatorio de Yebes (IGN), E-19141 Yebes, Guadalajara, Spain*
[5]*Max Planck Institute for Astronomy, Königstuhl 17, D-69117 Heidelberg, Germany*
[6]*University of Alberta, 4-183 CCIS, Edmonton AB T6G 2E1, Alberta, Canada*
[7]*Department of Astronomy, University of Massachusetts Amherst, 710 N. Pleasant Street, Amherst, MA 01003, USA*
[8]*Research School of Astronomy and Astrophysics, Australian National University, Canberra, ACT 2611, Australia*
[9]*Université de Toulouse, UPS-OMP, F-31028 Toulouse, France*
[10]*CNRS, IRAP, Av. du Colonel Roche BP 44346, F-31028 Toulouse cedex 4, France*
[11]*Astronomisches Rechen-Institut, Zentrum für Astronomie der Universität Heidelberg, Mönchhofstraße 12-14, D-69120 Heidelberg, Germany*
[12]*IRAM, 300 rue de la Piscine, F-38406 Saint Martin d'Hères, France*
[13]*Sorbonne Université, Observatoire de Paris, Université PSL, École normale supérieure, CNRS, LERMA, F-75005 Paris, France*
[14]*Max-Planck Institut für Extraterrestrische Physik, Giessenbachstraße 1, D-85748 Garching, Germany*

Accepted 2021 March 12. Received 2021 March 9; in original form 2020 May 6

ABSTRACT

Both the CO(2–1) and CO(1–0) lines are used to trace the mass of molecular gas in galaxies. Translating the molecular gas mass estimates between studies using different lines requires a good understanding of the behaviour of the CO(2–1)-to-CO(1–0) ratio, R_{21}. We compare new, high-quality CO(1–0) data from the IRAM 30-m EMIR MultiLine Probe of the ISM Regulating Galaxy Evolution survey to the latest available CO(2–1) maps from HERA CO-Line Extragalactic Survey, Physics at High Angular resolution in Nearby Galaxies-ALMA, and a new IRAM 30-m M51 Large Program. This allows us to measure R_{21} across the full star-forming disc of nine nearby, massive, star-forming spiral galaxies at 27 arcsec (∼1–2 kpc) resolution. We find an average $R_{21} = 0.64 \pm 0.09$ when we take the luminosity-weighted mean of all individual galaxies. This result is consistent with the mean ratio for disc galaxies that we derive from single-pointing measurements in the literature, $R_{21,\mathrm{lit}} = 0.59^{+0.18}_{-0.09}$. The ratio shows weak radial variations compared to the point-to-point scatter in the data. In six out of nine targets, the central enhancement in R_{21} with respect to the galaxy-wide mean is of order of ∼10−20 per cent. We estimate an azimuthal scatter of ∼20 per cent in R_{21} at fixed galactocentric radius but this measurement is limited by our comparatively coarse resolution of 1.5 kpc. We find mild correlations between R_{21} and carbon monoxide (CO) brightness temperature, infrared (IR) intensity, 70–160 μm ratio, and IR-to-CO ratio. All correlations indicate that R_{21} increases with gas surface density, star formation rate surface density, and the interstellar radiation field.

Key words: ISM: molecules – galaxies: ISM – radio lines: galaxies.

1 INTRODUCTION

Carbon monoxide (CO) is the most abundant molecule in the interstellar medium (ISM) after molecular hydrogen (H_2). Unlike H_2, CO has a permanent dipole moment and its rotational transitions can be excited at low temperatures. The two lowest rotational transitions of the main CO molecule, $^{12}C^{16}O$ $J = 1 \rightarrow 0$, hereafter CO(1–0), and $^{12}C^{16}O$ $J = 2 \rightarrow 1$, hereafter CO(2–1), are among the brightest millimetre-wave spectral lines emitted by galaxies. They have critical densities of $n_{\mathrm{crit},1-0} \sim 2000$ cm^{-3} and $n_{\mathrm{crit},2-1} \sim 10\,000$ cm^{-3} for a fully molecular gas with a temperature of $T = 10$ K and optically thin transitions. Given typical optical depths for CO(1–0) of $\tau \sim$ 5–10, line trapping effects lower the effective critical density even further, to ∼100–1000 cm^{-3}. This is comparable to the mean density of molecular gas in galaxies (for more, see reviews by Bolatto, Wolfire & Leroy 2013; Heyer & Dame 2015; Shirley 2015). As a result of their brightness, low excitation requirement, and locations at favourable frequencies for observations from the ground, both transitions are often used to trace the mass of molecular gas in galaxies.

★ E-mail: jdenbrok@astro.uni-bonn.de

ALMA, NOEMA, and other mm-wave facilities now regularly map both CO(2–1) and CO(1–0) line emission across large areas and large samples of galaxies. It is increasingly important to be able to quantitatively compare results obtained using these different lines. Physically, the CO(2–1)-to-CO(1–0) line ratio, R_{21}, should depend on the temperature and density of the gas and on the optical depths of the lines (see e.g. Sakamoto et al. 1994, 1997; Peñaloza et al. 2017, 2018). Thus, understanding how R_{21} varies in response to the local environment also has the prospect to provide information regarding the physical conditions of the molecular gas.

The R_{21} ratio has been studied in both the Milky Way (e.g. Hasegawa 1997; Hasegawa et al. 1997; Sakamoto et al. 1997; Sawada et al. 2001; Yoda et al. 2010) and nearby galaxies (e.g. Eckart et al. 1990; Casoli et al. 1991a; Lundgren et al. 2004; Crosthwaite & Turner 2007; Leroy et al. 2009, 2013; Koda et al. 2012, 2020; Druard et al. 2014; Saintonge et al. 2017; Law et al. 2018; Yajima et al. 2021). Milky Way studies highlight a correlation between the R_{21} ratio and density, with R_{21} dropping with decreasing gas density from the centres to the edges of molecular clouds (e.g. Hasegawa 1997).

Studies of individual other galaxies often find higher R_{21} in the central kpc compared to the outer parts (e.g. Braine & Combes 1992; Leroy et al. 2009, 2013; Koda et al. 2020; Yajima et al. 2021). This radial behaviour could be explained if the average temperature and/or density of molecular gas drops with galactocentric radius. Independent evidence suggests that both temperature and density are often enhanced in galaxy centres (e.g. Mangum et al. 2013; Gallagher et al. 2018a; Sun et al. 2018; Jiménez-Donaire et al. 2019). Other work has focused on azimuthal variations in well-resolved galaxies with strong spiral arms, especially M51. There studies indicate enhanced excitation in the spiral arms and bar ends compared to the interarm regions (Koda et al. 2012, 2020; Vlahakis et al. 2013; Law et al. 2018).

However, our quantitative knowledge of how R_{21} varies across galaxies remains limited. Extensive CO(2–1) mapping has only been possible for ∼10 yr and there have been only a limited number of mapping surveys that cover both CO(1–0) and CO(2–1) in the same sample of galaxies. As a result, the magnitude of the observed variations in R_{21} remains fairly weak, with the typical range of values found in spiral galaxies spanning from 0.5 to 0.9 and often much less inside a single galaxy. This is easily within the range where even modest calibration uncertainties and heterogeneous data can obscure real astrophysical signal. Furthermore, much of the extragalactic mapping work has been confined to single-galaxy studies (e.g. Crosthwaite & Turner 2007; Koda et al. 2012, 2020; Vlahakis et al. 2013; Law et al. 2018).

In this paper, we present the full disc mapping of CO(1–0) and CO(2–1) observations. CO(1–0) is obtained with the IRAM 30-m telescope, from the EMIR MultiLine Probe of the ISM Regulating Galaxy Evolution (EMPIRE; Bigiel et al. 2016; Jiménez-Donaire et al. 2019) and for CO(2–1) we use the latest available data, selecting from the HERA CO-Line Extragalactic Survey (HERACLES; Leroy et al. 2009), the Physics at High Angular resolution in Nearby Galaxies (PHANGS) survey (Leroy et al. 2021b), or the IRAM 30-m M51 Large Program (den Brok et al., in preparation). Thus, each line is covered by a homogeneous, deep, wide-area mapping survey. Together they probe R_{21} across a sample of nine nearby spiral galaxies. Our main goals are to derive robust galaxy-wide mean values of the R_{21} ratio and to investigate how R_{21} varies systematically across the discs of these galaxies.

In Section 2, we present the data and define the physical quantities we use. Our analysis of the R_{21} ratio is presented in Section 3, where we examine the distribution of the ratio, its radial and azimuthal variations, and the possible correlations between R_{21} and physical properties such as CO brightness temperature and infrared (IR) emission. We discuss our results and compare them to results from previous observations in Section 4. We summarize our findings in Section 5.

Table 1. Galaxy sample.

Name	RA (J2000)	Dec. (J2000)	D (Mpc)	i (deg)	PA (deg)
NGC 0628	01:36:41.8	15:47:00	9.0	7	20
NGC 2903	09:32:10.1	21:30:03	8.5	65	204
NGC 3184	10:18:17.0	41:25:28	13.0	16	179
NGC 3627	11:20:15.0	12:59:30	9.4	62	173
NGC 4254	12:18:50.0	14:24:59	16.8	32	55
NGC 4321	12:22:55.0	15:49:19	15.2	30	153
NGC 5055	13:15:49.2	42:01:45	8.9	59	102
NGC 5194	13:29:52.7	47:11:43	8.4	20	172
NGC 6946	20:34:52.2	60:09:14	7.0	33	243

Note. Adopted from Jiménez-Donaire et al. (2019).

2 OBSERVATIONS

2.1 Galaxy sample

Our sample consists of the nine nearby star-forming disc galaxies targeted by the EMPIRE survey (Bigiel et al. 2016; Jiménez-Donaire et al. 2019). We list their names, orientations, and adopted distances in Table 1. For a more detailed description of the properties of our sample, we refer to Jiménez-Donaire et al. (2019). Summarizing, our targets are all massive, star-forming disc galaxies, with stellar masses of $10 < \log_{10}(M_\star/\mathrm{M}_\odot) < 10.6$, metallicities from half-solar to solar, and star formation rate (SFR) surface densities in the range $2.8-21 \times 10^{-3}\,\mathrm{M}_\odot\,\mathrm{yr}^{-1}\,\mathrm{kpc}^{-2}$.

2.2 EMPIRE CO(1–0) data

EMPIRE mapped the entire optical discs of these galaxies in several 3 mm emission lines using the EMIR receiver. One main goal of EMPIRE is to understand how the dense gas fraction depends on the environment within and among galaxies. To achieve this goal, EMPIRE obtained deep, extended maps of high critical density lines that trace dense gas, such as HCN (1–0), HCO^+ (1–0), and HNC(1–0). In order to measure the dense gas fraction, EMPIRE also required a high-quality tracer of the total molecular gas. This was accomplished by mapping the ^{12}CO(1–0) and ^{13}CO(1–0) lines.

We employ the ^{12}CO(1–0) data from EMPIRE for eight galaxies (PI Jiménez-Donaire, projects 061-51 and 059-16, Jiménez-Donaire et al. 2019; PI Cormier, project D15-12 for NGC 5055, Cormier et al. 2018). For NGC 5194, we use the ^{12}CO(1–0) data from the PdBI Arcsecond Whirlpool Survey (PAWS; Pety et al. 2013; Schinnerer et al. 2013). This was also obtained by the IRAM 30-m using an almost identical strategy to the EMPIRE project.

These CO(1–0) maps cover the full disc of each galaxy, with an angular resolution of 27 arcsec (∼1–2 kpc).[1] They have rms noise

[1]When we quote the beam of single-dish maps, we refer to the effective beam size, which combines the primary beam of the telescope and that of the gridding kernel. All observations used short dump times that critically sampled the beam along the scan direction. See Mangum, Emerson & Greisen (2007) for general information on gridding kernels and see Leroy et al. (2009), Jiménez-Donaire et al. (2019), and Herrera et al. (2020) for information on the HERACLES, EMPIRE, and PHANGS-ALMA maps.

between 13 and 24 mK in each 4 km s^{-1} channel. For full details regarding the observing strategy, reduction, and data products, see Jiménez-Donaire et al. (2019).

We estimate the overall calibration uncertainty of EMPIRE to be ∼5 per cent and we expect this to mostly be a multiplicative factor that scales the whole map. Most EMPIRE maps were made by combining many observing sessions that each covered the whole galaxy. Therefore, we expect the maps to be well-calibrated internally. We regularly observed line calibrators as part of the EMPIRE observing strategy. Cormier et al. (2018) and Jiménez-Donaire et al. (2019) showed that the absolute flux calibration of the EMPIRE data showed rms variation of ∼4−8 per cent from session to session.

Given the overall brightness of the CO(1–0) line, this calibration term represents the dominant source of uncertainty over the inner region of many galaxies.[2]

2.3 CO(2–1) data

We compare the EMPIRE CO(1–0) data to CO(2–1) maps from the IRAM 30-m and ALMA. In each case, we picked the highest quality available CO(2–1) map. All of the CO(2–1) data have higher native resolution than the CO(1–0) maps. We convolved them to the resolution of EMPIRE using a Gaussian kernel with width determined by subtracting the current beam from the target beam in quadrature. We then aligned the CO(2–1) data to the EMPIRE astrometric grid and rebinned to 4 km s^{-1} channels.

For NGC 5194 (M51), we use observations from a new IRAM 30-m Large Program (PI: Toshiki Saito, project 055-17; den Brok et al., in preparation). The goal of this programme is to obtain sensitive observations of 1-mm and 3-mm CO isotopologue transitions and thereby to improve constraints of ISM physical quantities. These observations were carried out using the EMIR instrument at the IRAM 30-m telescope with a total of 172 h. The programme included new CO(2–1) observations, which we use here. At 27 arcsec resolution and 4 km s^{-1} channel width, this new CO(2–1) cube has rms noise 5.6 mK.

The observing strategy and instrument for the M51 EMIR maps closely resemble that of EMPIRE. Therefore, we expect that the uncertainty in the amplitude calibration of the M51 EMIR CO(2–1) map is also similar to that of the EMPIRE maps and consider ∼5 per cent a good estimate.

ALMA observed CO(2–1) emission from NGC 0628, NGC 2903, NGC 3627, NGC 4254, and NGC 4321 part of the PHANGS-ALMA survey (Leroy et al. 2021b). PHANGS-ALMA is using ALMA's 12-m, 7-m and total power antennas to observe CO(2–1) emission from a large sample of nearby. We begin with the cubes made from combining the 12-m, 7-m, and total power observations. Because we convolve the data to 27 arcsec for our analysis and the ALMA single dishes have a ∼27 arcsec beam, the total power data contribute almost all of the information for our analysis. As a result, the details of interferometric imaging are secondary. The PHANGS-ALMA total power pipeline is described by Herrera et al. (2020). After convolving to 27 arcsec, the PHANGS-ALMA cubes have on average an rms noise of 1–2 mK in each 4 km s^{-1} channel.

[2]For CO(1–0), considering all individual lines of sight, we find 839/5416 points have S/N > 20, compared to 3528/5416 points with S/N > 3. For CO(2–1) on the other hand, we have 1130 points with S/N > 20 compared to 4134 with S/N > 3.

The PHANGS-ALMA data are calibrated using observations of solar system objects or Galactic star forming regions that are pinned to the ALMA interferometric calibration scheme. The overall uncertainty in the flux calibration should be about 5 per cent at 1 mm. The flux of total power observations targeting the same PHANGS-ALMA galaxy on different days scatter from one another by ±3 per cent (Leroy et al. 2021a), in good agreement with the aforementioned 5 per cent (Bonato et al. 2018).

For the remaining three sources, NGC 3184, NGC 5055, and NGC 6946, we take observations from HERACLES (Leroy et al. 2009). HERACLES surveyed CO(2–1) emission from 48 nearby galaxies. These maps have appeared previously in Schruba et al. (2011, 2012), Leroy et al. (2013), and Sandstrom et al. (2013). After gridding, the HERACLES maps have a native resolution of 13.3 arcsec. After matching to the EMPIRE 27 arcsec beam and velocity grid, the HERACLES cubes have rms noise between 5 and 11 mK per 4 km s^{-1} channel.

The overall flux scale of HERACLES is uncertain at the ∼6−20 per cent level (see Leroy et al. 2009, and Appendix C). Also, the HERACLES maps combine information from multiple receiver pixels that can have gain uncertainties relative to one another. We investigate the internal gain variations of the HERA pixels and compare HERACLES, ALMA, and EMIR data for galaxies with multiple maps in Appendix C. This analysis yields the gain uncertainty mentioned above and also leads us to prefer ALMA or EMIR maps when available because their calibration should be more stable (i.e. their calibration uncertainties are likely to be well described by a single gain factor).

As with the CO(1–0) data, the high signal-to-noise ratio of the CO(2–1) data means that calibration often represents the dominant source of uncertainty. Anywhere that the HERACLES data exceed S/N = 5–10, and anywhere that the ALMA and EMIR data exceed S/N = 20, calibration will dominate our uncertainty on the brightness temperature. Below the S/N threshold, the uncertainty is dominated by the random noise.

We need the best intensity accuracy possible for this study. Comparing ALMA/EMIR to HERACLES, ALMA/EMIR has both lower absolute and relative flux uncertainty across the map. Although all the galaxies have been also observed with HERA, we therefore choose the ALMA/EMIR over HERACLES where possible in our analysis. In summary, the associated uncertainties for the CO(2–1) emission line from ALMA are 5 per cent, from EMIR are 5–10 per cent, and from HERA are 6–20 per cent (see Appendix C for more details).

2.4 Far-infrared data

We compare the R_{21} ratio to IR maps at wavelengths of 70, 160, and 250 μm from the *Herschel* space telescope. These were compiled and processed to match the EMPIRE beam and astrometric grid by Jiménez-Donaire et al. (2019). For seven of our targets, the data come from the KINGFISH survey (Kennicutt et al. 2011). For NGC 5194, the data come from the Very Nearby Galaxies Survey (Parkin et al. 2013). NGC 2903 lacks *Herschel* data. As a result we cannot determine the 70–160 μm ratio or the total IR (TIR) luminosity surface brightness in Section 3.4 for this galaxy.

2.5 Measured quantities

We follow a similar analysis path to the ^{13}CO-focused study of Cormier et al. (2018) and the HCN-focused study of Jiménez-Donaire et al. (2019). We measure the R_{21} ratio as a function of galactocentric

radius, the 70–160 μm ratio, CO brightness temperature, TIR surface brightness, and the TIR-to-CO ratio.

CO(2–1)/(1–0) ratio, R_{21}: We define R_{21} as the line-integrated CO(2–1) surface brightness divided by the line-integrated CO(1–0) surface brightness. For both lines, the line-integrated surface brightness has units of K km s^{-1}.

Note that our brightness temperature-based definition of R_{21} differs from the flux density based values often quoted in the high-redshift literature (e.g. Aravena et al. 2010, 2014, 2016; Daddi et al. 2010; Bothwell et al. 2013). Using the velocity-integrated flux density definition, one would expect thermalized lines to show a ratio of about four. Using the brightness temperature scale, the line ratio for a thermalized line will be about unity (see e.g. Solomon & Vanden Bout 2005) or slightly lower due to deviations from the Rayleigh–Jeans approximation.

R_{21} for individual lines of sight: We calculate R_{21} for each line of sight. When doing so, we use exactly the same velocity range for the integral over both lines. To define this velocity range, we use for sightlines outside of the 0.23 r_{25} aperture the velocities covered by H I 21-cm line emission (mostly from THINGS; Walter et al. 2008) as an independent estimate for the velocity range likely to be covered by CO. For lines of sight within the 0.23 r_{25} aperture, where the ISM is mostly molecular, we use the CO(2–1) emission as a proxy for the velocity range. This way we make sure that the broad, central CO lines are fully included. We chose the CO(2–1) line instead of the CO(1–0) because our CO(2–1) maps have higher S/N than our CO(1–0) maps.

Note that because our sampling scheme oversamples the beam by a factor of 4, measurements for R_{21} from adjacent lines of sight are correlated and not independent. We take this into account in our presentations of results.

R_{21} from spectral stacking: In addition to measuring R_{21} for individual lines of sight, we employ a spectral stacking method to explore possible correlations between the R_{21} ratio and various physical quantities. In this approach, we bin the data by some other quantity, for example, TIR surface brightness. We construct an average CO(2–1) and CO(1–0) spectrum for each bin. We estimate the mean R_{21} in that bin by dividing the integrated brightness temperature calculated from each binned spectrum.

The method is described in detail by Schruba et al. (2011), Jiménez-Donaire et al. (2017), and Cormier et al. (2018). We regrid each spectrum so that the local mean velocity now corresponds to $v = 0$ km s^{-1}. For this application, we use the velocity field derived from the H I 21-cm data to estimate the local mean velocity. After regridding the spectra, we average together all spectra in each bin. Because the large-scale velocity gradient has been removed, spectra from different parts of the galaxy average coherently.

We derive the integrated brightness temperature from each stacked spectrum. We pick the velocity range for this integral by first fitting the spectrum. We use either a single-Gaussian profile or a double-horn profile, whichever fits better. The double-horn profile offers a better description of the broad, flat-topped emission lines found in some of our galaxy centres. We set the velocity range for direct integration of the spectrum to cover everywhere that the fit exceeds 1 per cent of the peak brightness temperature. Note that the fit is *only* used to set boundaries over which we integrate the spectrum.

We only present stacked measurements of R_{21} when both lines have an integrated emission above 3σ of the rms noise. In practice, our stacks almost always achieve much higher signal-to-noise ratio than this. In Table D1, we summarize the signal-to-noise ratio for our stacks as a function of galactocentric radius. Inside $r_{\rm gal} < 9$ kpc > 95 per cent of the stacked R_{21} measurements have signal to noise >11 for both emission-line brightness temperature measurements, comparable to the very high, pixel based signal-to-noise threshold values used by Koda et al. (2012, 2020).

Uncertainties on R_{21}: We compute the uncertainties on the integrated brightness temperature, $\sigma_{\rm Int}$, using the following formula:

$$\sigma_{\rm Int} = \sigma_{\rm rms} \times \Delta v_{\rm chan} \times \sqrt{n_{\rm chan}}, \quad (1)$$

where $\sigma_{\rm rms}$ is the 1σ rms value of the noise in K measured from the signal-free part of the spectrum, $\Delta v_{\rm chan}$ is the channel width in km s^{-1}, and $n_{\rm chan}$ is the number of channels that are integrated together.

When we apply equation (1) to the stacked spectra, we measure the noise, $\sigma_{\rm rms}$, from the signal-free region of the stacked spectrum itself. As a result, this approach properly accounts for the fact that our original pixels oversample the beam.

After estimating $\sigma_{\rm Int.}$ for each line, we estimate the uncertainties on R_{21} by propagating the errors of the CO(1–0) and CO(2–1) integrated brightness temperature.

Because of the high signal-to-noise ratio in our CO observations, the systematic uncertainty due to flux calibration often dominates the overall uncertainty in R_{21}. For example, in Table D1 we report the median signal-to-noise ratio for stacks within 9 kpc is >30. This $\sim$3 per cent uncertainty is lower than the systematic uncertainty due to calibration. Our EMPIRE-ALMA or EMPIRE-EMIR galaxies have R_{21} calibration uncertainties $\sim$7 per cent. For our three EMPIRE-HERACLES targets, this may be as high as $\sim$20 per cent, and at least 10−15 per cent. At least in the EMIR-ALMA targets, we expect this calibration uncertainty to act as a single multiplicative factor for the map. Thus, it will affect the mean value, but not the internal distribution in each galaxy. For the EMPIRE-HERACLES cases, we expect the primary uncertainty to be an overall scaling, but there may be second-order local variations due to the differences in the pixel gains discussed in Appendix C.

70–160 μm ratio: We compare R_{21} to the 70–160 μm ratio. This ratio traces the temperature of interstellar dust (e.g. Draine et al. 2007). Because most of the large grains in a galaxy are in thermal equilibrium with the local interstellar radiation field (ISRF; see textbook by Draine 2011), this ratio also acts as a tracer of the ISRF. Note that at the average densities and temperatures of molecular clouds traced by CO emission, we do not expect the dust and gas to collisionally couple and share the same temperature (Draine 2011), so we do expect the IR colour to directly trace the ISRF by not the gas temperature. We measure the 70–160 μm ratio after convolving the *Herschel* 70 and 160 μm maps to match the EMPIRE resolution.

TIR surface brightness: We compare R_{21} to the TIR luminosity per unit area. We use the TIR surface brightness as an observational proxy for the amount of embedded recent star formation. This tracer has the advantage compared to other SFR tracers, as it traced the embedded SFR, which means the recent SFR might affect the state of the molecular ISM. We follow the same approach as our previous work (e.g. Usero et al. 2015; Bigiel et al. 2016; Jiménez-Donaire et al. 2017; Cormier et al. 2018).

We combine *Herschel* 70, 160, and 250 μm data in order to estimate the TIR surface brightness. First, we convolve each band to our common resolution of 27 arcsec and place them on to the EMPIRE astrometric grid. Then we combine the bands, following Galametz et al. (2013),

$$S_{\rm TIR} = \sum c_i S_i, \quad (2)$$

where $S_{\rm TIR}$ refers to the TIR surface brightness, S_i to the brightness in the given *Herschel* band i, and c_i to the calibration coefficient from

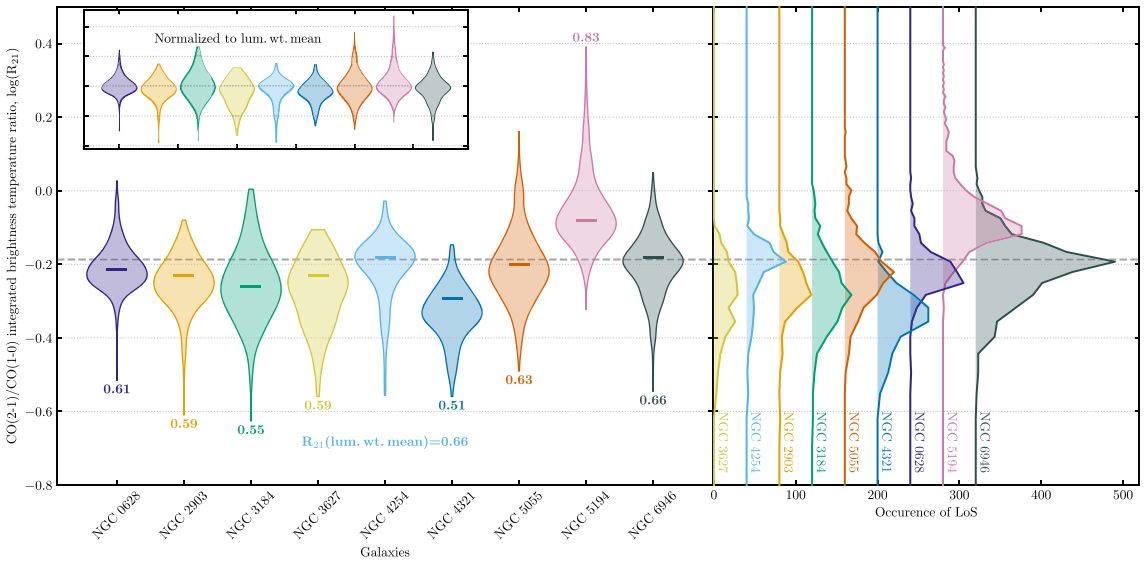

Figure 1. Histograms of the CO(2–1)/CO(1–0) integrated brightness temperature ratio, log(R_{21}), for nine nearby star-forming spiral galaxies. The *left-hand panel* shows distributions of log(R_{21}) as violin histograms. These histograms only show results for the positions that have S/N > 3 integrated brightness temperature detections in both the CO(1–0) and CO(2–1) maps. These histograms treat each line of sight equally. The *luminosity-weighted mean* R_{21} value for each galaxy appears as a coloured horizontal line inside each histogram, with the value reported above or below each violin histogram. All data, regardless of S/N, are included within the calculation of the luminosity-weighted mean, as shown in Table 2. We note that the uncertainty incorporates physical galaxy-to-galaxy scatter as well as uncertainties in flux scale calibration. The *inset* within the left-hand panel shows the R_{21} violin histograms for each galaxy normalized to their luminosity-weighted mean R_{21} values. The *right-hand panel* shows the histogram of the combined R_{21} distribution for all targets. The dashed grey line extending across all panels shows $\langle R_{21} \rangle = 0.65$, the non-weighted mean of R_{21} if including all lines of sight with S/N > 3 (see last column of Table 2).

combined brightness. We use the specific calibration coefficients provided for each galaxy, with the exception of NGC 5194 where we use the generic calibration provided by Galametz et al. (2013), since this galaxy was not explicitly studied.

We focus on TIR surface brightness because it represents a simple, reproducible quantity that is closely related to the local surface density of recent star formation. We do not implement any specific conversions or consider second-order effects like IR cirrus. Our analysis also does not hinge on any numerical conversion of TIR surface brightness to an SFR. For a detailed discussion of the use of TIR as an SFR proxy and a quantitative comparison to other star formation tracers (e.g. Cormier et al. 2018; Gallagher et al. 2018b; Jiménez-Donaire et al. 2019).

3 RESULTS

3.1 Overall distribution of R_{21}

We estimate the line ratio, R_{21}, for each line of sight that has a measured brightness temperature for both CO(2–1) and CO(1–0) lines. In total, this yields 5416 measurements across nine galaxies at 27 arcsec (∼1–2 kpc) resolution.

Fig. 1 shows the R_{21} distribution of all individual lines of sight for each galaxy, as well as a histogram of the combined R_{21} distribution for the entire sample. These histograms visualize results only for lines of sight with S/N > 3 in both lines. We do not find many cases where only one of the two lines is detected, highlighting that the two lines follow similar distributions and the data sets are well matched. The individual sightlines are arranged in a hexagonal grid (see Fig. 2), where the points have a half-beam separation distance. Consequently, the beam size is oversampled by four hexagonal grid pixels.

Table 2 reports the luminosity-weighted mean value for each galaxy, as well as the 16th/84th and 5th/95th percentiles. Here, 'luminosity weighted' means averaging over the individual R_{21} values weighted by the corresponding CO (1–0) brightness temperature. We prefer to use these intensity-weighted values for our quantitative results because they map straightforwardly to the results expected from galaxy-integrated measurements.

For individual galaxies, we find luminosity-weighted mean R_{21} ratios ranging between ∼0.51 and 0.87. In our view, the best characteristic sample-wide value for R_{21} is the mean of the luminosity-weighted mean ratios for the individual galaxies. This is $\langle R_{21}^{\rm mean} \rangle = 0.64 \pm 0.09$ with 0.10 rms scatter from galaxy to galaxy. The uncertainty is the standard deviation between the galaxies. The value of the ratio agrees well with previous measurements of a wider population of galaxies, which tend to lie in the range 0.5–0.8 (Sections 1 and 4). We verified that no significant effects are found when different weighting schemes are used.

In principle, our choice of method could affect our derived mean R_{21} if, e.g. a few very bright regions show different R_{21} than the rest of the galaxy or there is a large diffuse component with different R_{21}. The small differences among different approaches in Fig. 1 and Table 2 show that this is mostly not the case for our sample. The galaxy-wide mean and intensity-weighted mean show good agreement for most galaxies. Moreover, we find an average ratio of $\langle R_{21}^{\rm mean,norm} \rangle = 0.62$ and a standard deviation of 0.12 when weighting

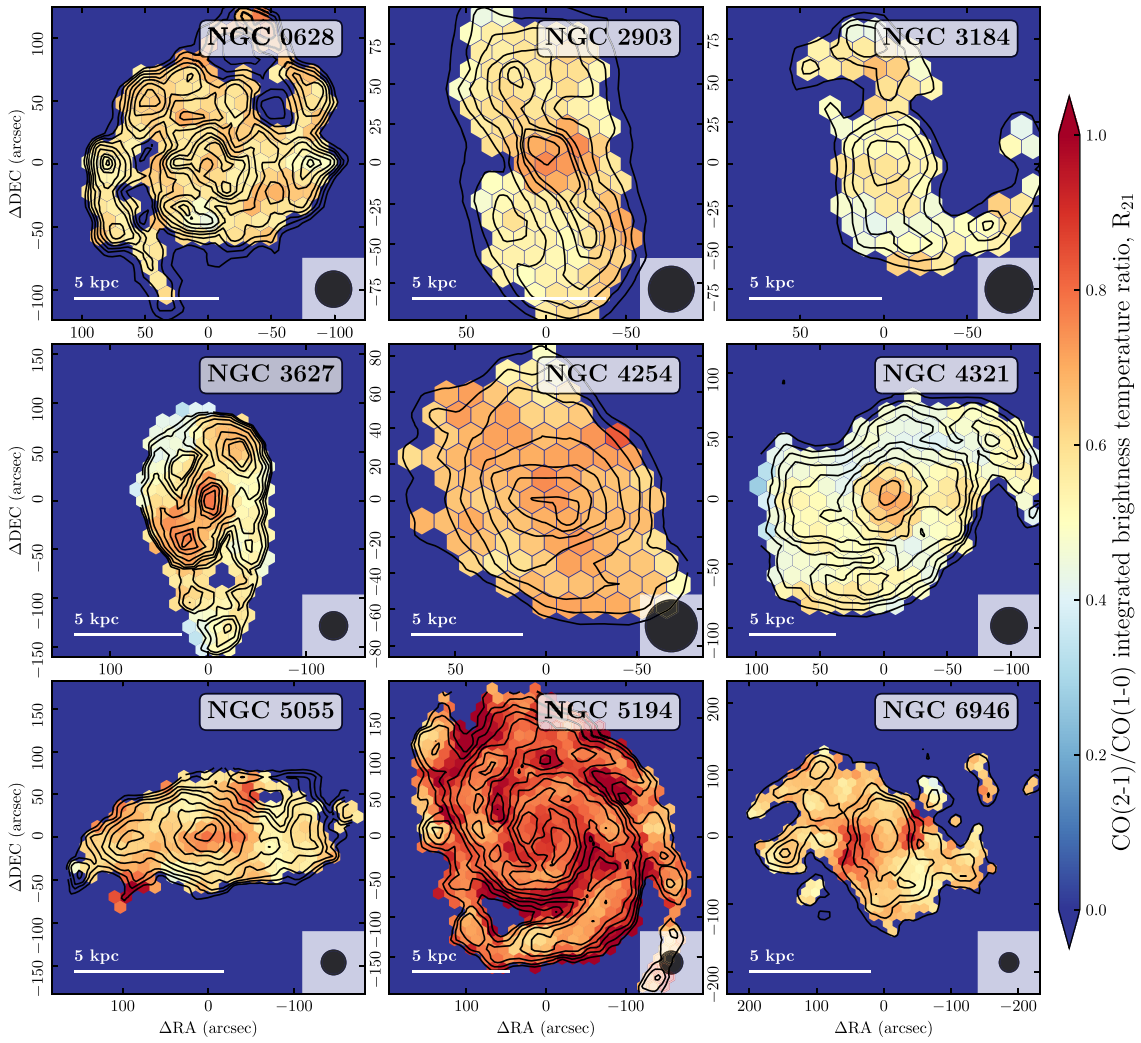

Figure 2. Maps of the CO(2–1)/CO(1–0) integrated brightness temperature ratio, $\log(R_{21})$, for nine nearby star-forming spiral galaxies. These maps show R_{21} for all positions that have S/N > 10 integrated brightness temperature in both the CO(2–1) and CO(1–0) maps. The overlaid contours show the CO(1–0) integrated brightness temperature, with levels showing 20, 30, 40, 50, 60, 70, 80, 90, 95, 97.5, and 99.5 per cent of the peak value in the map (see Fig. A1). The white scale bar in the bottom left corner of each panel shows a linear scale of 5 kpc, without accounting for inclination, at the distance of each source (see Table 1). The black circle in the bottom right corner indicates the beam size of 27 arcsec. Note that the hexagonal grid shows points critically sampling the beam, i.e. adjacent points are spaced by one-half the beam size.

all lines of sight equally, compared to $\langle R_{21}^{\rm mean} \rangle = 0.64 \pm 0.09$ when weighting by the luminosity-weighted mean of each galaxy.

Fig. 2 shows the maps of the distribution of the CO line brightness temperature ratio R_{21} across the individual galaxies. We do find evidence for both radial and azimuthal variations. We explore the systematic variation of the ratio within and between individual galaxies in the following sections.

3.2 Radial variations of R_{21}

Many quantities, including the SFR, molecular gas fraction, and gas density vary as a function of galactocentric radius. In Fig. 3, we present radial profiles of R_{21} for our sample. We plot all individual lines of sight at 27 arcsec (∼1–2 kpc) resolution. Recall that for these data, adjacent points are spaced by one-half beam so that the points are not independent. Filled points show measurements with a signal-to-noise ratio, S/N > 3, on the line ratio, propagated. Open symbols indicate measurements with S/N < 3.

Coloured points in Fig. 3 show radial profiles of azimuthal-averaged ratios, with error bars indicating the uncertainty on this mean R_{21}. For these stacked profiles, we use all of the data, regardless of S/N. We plot all of the stacked profiles together in Fig. 4.

In Figs 3 and 4, our azimuthally averaged measurements of R_{21} show only a small dynamical range across individual galaxy discs for

Table 2. The CO(2–1)/CO(1–0) integrated brightness temperature ratio, R_{21}, for nine nearby star-forming spiral galaxies. The upper half of the table shows luminosity-weighted statistics (R_{21}). The lower half of the table shows number statistics, which treat each pixel equally ($R_{21}^{\rm num}$). We tabulate the galaxy name, values of the mean, and 5th, 16th, 50th (i.e. median), 84th, and 95th percentile ranges of R_{21} for our target galaxies. The second to last column gives the mean value and associated standard deviation of R_{21} across the whole sample. The last column lists the mean and percentiles when considering all significant (S/N > 3) lines of sight across the whole sample. Note that all values within this table have been calculated for positions with a significant detection in both the CO(1–0) and CO(2–1) integrated brightness temperature maps (i.e. S/N > 3). The bottom rows indicate the number of lines of sight (l.o.s.) for the individual galaxies. The number of all l.o.s. as well as those l.o.s that have both the CO(1–0) and CO(2–1) above the threshold of 3σ and 10σ.

NGC	0628	2903	3184	3627	4254	4321	5055	5194	6946	Galaxy average	All sightlines ($>3\sigma$)
$R_{21}^{\rm mean}$	0.61	0.59	0.55	0.59	0.66	0.51	0.63	0.83	0.66	0.63 ± 0.09	0.66
$R_{21}^{5\%}$	0.5	0.48	0.41	0.41	0.49	0.38	0.48	0.68	0.51		0.49
$R_{21}^{16\%}$	0.55	0.52	0.46	0.48	0.61	0.44	0.54	0.74	0.58		0.56
$R_{21}^{50\%}$	0.6	0.58	0.54	0.59	0.66	0.5	0.62	0.81	0.65		0.71
$R_{21}^{84\%}$	0.67	0.7	0.64	0.71	0.71	0.6	0.72	0.91	0.73		0.85
$R_{21}^{95\%}$	0.75	0.72	0.78	0.76	0.74	0.68	0.79	1.02	0.83		0.94
$R_{21}^{\rm num.mean}$	0.62	0.57	0.57	0.54	0.63	0.47	0.64	0.9	0.65	0.62 ± 0.12	0.65
$R_{21}^{\rm num.5\%}$	0.52	0.44	0.4	0.37	0.42	0.34	0.44	0.66	0.47		0.42
$R_{21}^{\rm num.16\%}$	0.55	0.49	0.46	0.43	0.53	0.4	0.51	0.73	0.54		0.49
$R_{21}^{\rm num.50\%}$	0.61	0.57	0.55	0.54	0.65	0.47	0.61	0.84	0.64		0.63
$R_{21}^{\rm num.84\%}$	0.7	0.65	0.68	0.66	0.71	0.54	0.75	1.06	0.74		0.82
$R_{21}^{\rm num.95\%}$	0.79	0.72	0.82	0.73	0.77	0.59	0.97	1.37	0.85		1.01
$N_{\rm l.o.s}^{\rm all}$	328	319	741	239	288	318	410	947	1824	5414	
$N_{\rm l.o.s}^{>3\sigma}$	292	188	302	200	207	304	370	705	884	3452	
$N_{\rm l.o.s}^{>10\sigma}$	153	101	65	136	95	162	201	475	321	1709	

some cases while for other sources the ratio tends to show a negative or positive gradient. In Table 3, we report the power-law fit relating R_{21} to galactocentric radius in each galaxy. We also report the p-value (of a linear relation in logarithmic space), which allows us to gauge the significance (p-value) of the radial gradient.

Six out of the nine galaxies show radial variations. Four show stronger radial variations. NGC 2903 shows an initial radial decline then a rise in R_{21} with increasing radius. NGC 3184 shows increasing R_{21} with increasing radius. NGC 3627 and NGC 4321 show a strong while NGC 4254 shows a moderate decreasing trend as a function of the radius.

Fig. 4 also shows that in six of our nine targets, R_{21} appears higher in the central kpc than at intermediate radii, ∼1–6 kpc. This central enhancement is most prominent in NGC 2903, NGC 3627, NGC 4321, and NGC 5055. Other galaxies, for example NGC 4254, show little or no central enhancement. On average, the central R_{21} bin (0–1.5 kpc) for our targets is 16 per cent higher (median is 15 per cent) compared to the luminosity-weighted average of the rest of the galaxy.

Outside a galactocentric radius of about 6 kpc, we find highly variable behaviour among our sample, with some galaxies showing increasing R_{21}, some showing decreasing R_{21}, and some being flat. Fig. 3 shows that these breaks in the profile often coincide with the emergence of a large amount of low signal-to-noise data. Using different techniques to bin the data and estimate the binned ratio yield large discrepancies. We are therefore hesitant to overinterpret them. Sensitive multiline observations of outer discs will help illuminate whether CO excitation does change dramatically in the outer parts of disc galaxies.

3.3 Azimuthal variations of R_{21}

Fig. 2 also shows variation in R_{21} at fixed galactocentric radius. The SFR surface density and gas column density also vary azimuthally, with the most striking features due to the influence of spiral arms and bars. NGC 3627, 5194, NGC 6946, and to some extent NGC 2903, 4321, and 5055 show clear spatial variations in the CO line ratio. NGC 5194 shows higher R_{21} ratios in the interarm. We note that this stands in contrast to previous findings. Koda et al. (2012) found a higher line ratio in the arm region as opposed to the interarm region in this galaxy. For NGC 3627, we find a higher line ratio in the centre and at the bar ends. NGC 6946 shows regions with enhanced line ratio towards the east and west of the centre. NGC 2903, 4321, and 5055 all show an increase of the CO line ratio in the central ∼1–2 kpc region. The other three sources do not show any clear spatial variations.

At 27 arcsec resolution, our ability to distinguish arm and interarm regions is limited, especially in the inner parts of galaxies where most of the molecular gas resides. The most straightforward imprint of azimuthal R_{21} variations on our data is to increase the observed scatter in R_{21} at fixed radius, e.g. as suggested in Fig. 3.

To quantify these azimuthal variations in R_{21}, we measure the scatter in the ratio at a fixed galactocentric radius. We disentangle the physical variation from scatter due to observational noise using a forward modelling process, which we describe in Appendix B. Briefly, we use a Monte Carlo approach and the known observational errors to determine how much physical variation must be present in each radial bin to match the observed scatter. We plot the results of this calculation in Fig. 5, where we repeat the modelling routine for every individual galaxy. We show best-fitting physical variation in R_{21} as a function of radius for each galaxy.

On average, the intrinsic scatter rises from $\lesssim$10 per cent in the inner bins to $\gtrsim$20 per cent outside a galactocentric radius of 6 kpc. This has roughly the same magnitude as the observed galaxy-to-galaxy scatter. Note, however, that we do not expect calibration uncertainties to play as large a role in the scatter observed *within* a galaxy. Taking this into account, the physical scatter within galaxies may be larger than the physical scatter among galaxies. Also note that our azimuthal scatter calculations consider each pixel equally. A luminosity-weighted calculation would suppress faint regions and lower the magnitude of the measured scatter. A reasonable overall conclusion from this is that in our data, point-to-point scatter has a magnitude greater than or equal to galaxy-to-galaxy variations, and appears stronger than radial variations.

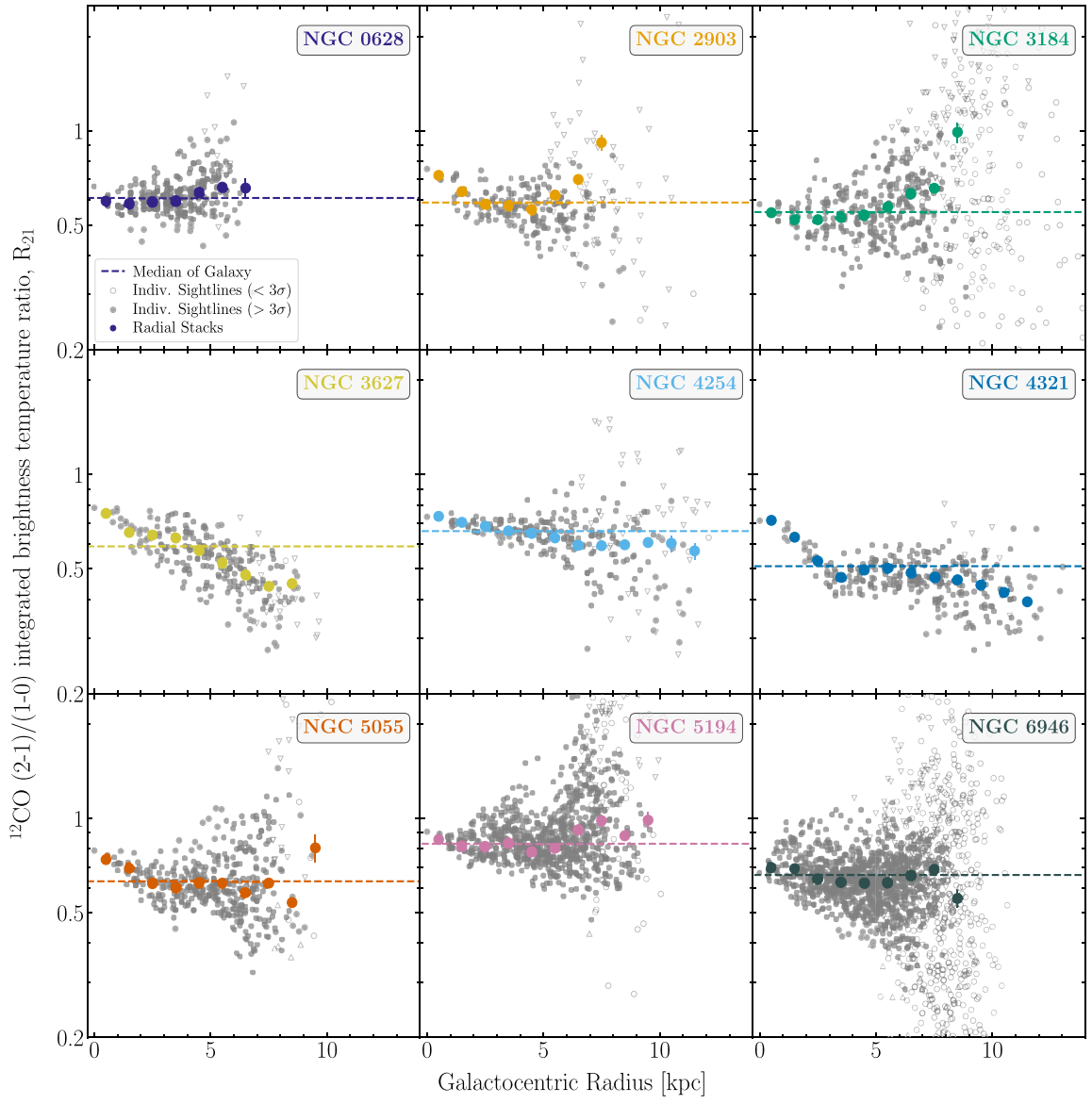

Figure 3. Radial profiles of the R_{21} ratio. The grey points correspond to individual sightlines with adjacent lines of sight spaced by one half the beamwidth. The line ratio is plotted on a logarithmic scale. Filled circles indicate data points where both lines have a signal-to-noise ratio above 3. Data with lower signal-to-noise ratio appear either as upper or lower limits. Open triangles show where one line is below S/N = 3. Open circles show points where both lines are below the S/N threshold of 3. Coloured circles present the stacked values of the line ratio calculated in 27 arcsec-wide radial bins following the method described in in Section 2.5. The galaxy-wide median value for each individual galaxy appears as a coloured dashed line. Six of our nine targets show clear central enhancements in R_{21}, but otherwise the stacked profiles show relatively small deviation from the galaxy-wide median.

We also applied the same Monte Carlo based analysis on the complete data of all lines of sights as a whole. This way we can estimate the overall physical scatter. The physical scatter estimated after accounting for different calibration uncertainties for the individual instruments is about 8 per cent.

As stated before, for NGC 5194 (M51) we measure spatial variations that have the opposite sense of those reported by Koda et al. (2012). In the arm region, we find a R_{21} value ∼0.8, which is in agreement with the value found by Koda et al. (2012) in the arm region. However, in the interarm region, we find larger values (R_{21} ∼ 0.9–1), while they find lower values (R_{21} ∼ 0.4–0.6). We examine in detail and discuss possible causes for the difference in Appendix E, and find the disagreement to stem from differences in the CO (1–0) maps used for the analysis. In particular, the NRO map used by Koda

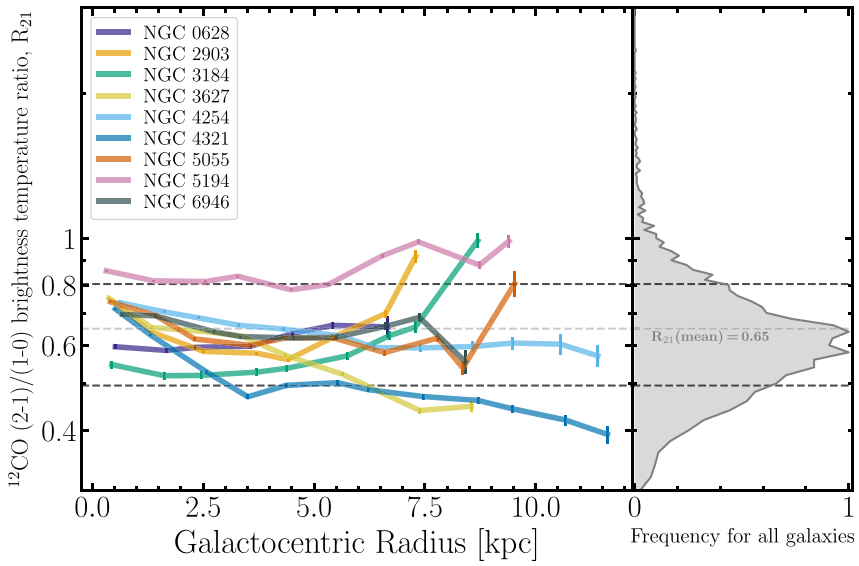

Figure 4. Stacked profiles of the CO line brightness temperature ratio, R_{21}, as a function of galactocentric radius, plotted using a y-axis logarithmic scale. Stacked radial profiles use a bin width of 1.5 kpc. We only plot stacked bins where both CO(1–0) and CO(2–1) integrated, stacked lines are detected above an S/N > 3, but otherwise include all data. Error bars indicate the propagated uncertainty of the integrated brightness temperature of the stacked spectra. The histogram, reproduced from Fig. 1, indicates the distribution of all lines of sight were both the CO(1–0) and CO(2–1) integrated line emissions are significantly (S/N > 3) detected. The light grey, dashed line indicates the sample-wide mean ratio when considering all lines of sight with S/N > 3. The darker, dashed lines indicate the 1σ scatter over all sightlines. The figure illustrates the galaxy-to-galaxy scatter that accounts for a large fraction of the overall variation of R_{21} in the sample.

et al. (2011) shows more emission in the interarm region than the IRAM 30-m PAWS CO(1–0) map. Beyond a galactocentric radius of 2 kpc, NGC 5194 shows the highest scatter in our sample and Fig. 2 does show the strongest arm–interarm contrast. At our resolution, this contrast manifests as rms physical scatter of 15−20 per cent between $r_{gal} = 2$ and 6 kpc. Koda et al. (2012) report a standard deviation of ∼0.1–0.15 and mean $R_{21} \approx 0.7$, so our numbers for both the mean line ratio and scatter appear to be overall slightly larger than theirs, which is mostly driven by the differing values within the interarm region.

As Fig. A1 shows, our 27 arcsec resolution only coarsely resolves the dynamical features in our targets. Spiral arms and bars are visible at large radii in many targets. However, we cannot distinguish the upstream and downstream sides of these features and they can be almost entirely suppressed in the inner galaxies. Physical conditions can vary dramatically across a spiral arm (e.g. Schinnerer et al. 2010, 2017). Thus, we expect our large beam to blur together regions with a wide range of temperature and densities, especially in the inner parts of galaxies. This effect is expected to be even stronger, when a bright arm region lies next to a faint interarm region, the wider spacing between, e.g. arms and other discrete regions in the outer parts of galaxies may partially explain the increased scatter at large radii. Future work at higher physical scales offers the prospect to give much more insight on local variations of R_{21}.

3.4 Correlations with CO brightness temperature and IR emission

We also compare R_{21} to the local intensities of CO(1–0) and CO(2–1) emission, the local TIR surface brightness, and the local 70–160 μm ratio. These observed quantities indirectly trace physical conditions that should affect CO excitation, so that this analysis can highlight the physical drivers of the R_{21} variations observed in the previous two sections.

We compare to these specific quantities because they are directly observable and also indirectly related to conditions which we expect to affect excitation. Though we observe at coarse physical resolution, we expect that CO(1–0) and CO(2–1) emission trace the molecular gas surface density and more indirectly trace gas volume density. High gas densities will be associated with thermalization and a higher R_{21}. The IR colour traces the dust temperature, which in turn is set by strength of the interstellar radiation field (Draine 2011). The radiation field also illuminates photon-dominated regions and should play a key role in heating the gas. All other things equal, we expect warmer gas to be more nearly thermalized. Along similar lines, the TIR surface brightness indicates the level of star formation activity. We expect that this indirectly relates to both the heating of the gas and the gas density, with denser gas forming more stars, on average.

Fig. 6 shows the mean normalized R_{21} (normalized with respect to the galaxy-internal luminosity-weighted mean; see Table 2) calculated from spectral stacks as a function of each quantity of interest. We show results for each galaxy separately and show results stacking the data in bins of CO(1–0) brightness temperature, CO(2–1) brightness temperature, TIR surface density, and 70–160 μm ratio. Table 3 reports the results form fitting a power law relating R_{21} to each quantity for all individual points. In addition, the p-value is indicated for the correlation in log-space, describing the tightness of the correlation. Finally, we also report the Spearman's rank correlation coefficient, r_s. For the stacking, we only included sightlines with S/N > 10 in both the CO(1–0) and CO(2–1) data to make sure that the

Table 3. Fits and correlation coefficients for individual galaxies. Results from fitting a power law of form $R_{21,\mathrm{norm}}^{\mathrm{fit}} = C \cdot x^m$ to the stacked ratios in Figs 6 and 7. The fit is performed as a linear fit in logarithmic space. We normalized the line ratio by the luminosity-weighted, galaxy wide mean (see Table 2). The Pearson p-value indicates the significance of the linear correlation in logarithmic space. We only performed the fit, if the p value is below 0.05. Furthermore, the Spearman's rank correlation coefficient, r_s, is given. For CO(1–0) the fitting range was set to exclude points below $I_{\mathrm{CO(1-0)}} < 10$ K km s^{-1}. A minus indicates that no fit could be made. For NGC 0628 and NGC 3184, we do not have $I_{\mathrm{CO(1-0)}} > 10$ K km s^{-1} data and for NGC 2903 we do not have IR data from *Herschel*.

		NGC 0628	NGC 2903	NGC 3184	NGC 3627	NGC 4254	NGC 4321	NGC 5055	NGC 5194	NGC 6946
CO(1–0)	m	–	0.17	–	0.23	0.73	0.18	0.16	–	–
[K km s^{-1}]	C	–	0.61	–	0.46	0.82	0.62	0.62	–	–
	p	–	0.048	–	0.030	0.035	6.4×10^{-4}	0.026	0.26	0.24
	r_s	–	1.0	–	1.0	1.0	1.0	1.0	0.60	0.80
CO(2–1)	m	−0.0027	0.14	0.13	0.24	0.14	0.17	0.076	–	–
[K km s^{-1}]	C	1.0	0.70	0.86	0.56	0.74	0.69	0.82	–	–
	p	0.0	0.0050	0.0	0.0016	0.034	0.0053	0.029	0.08	0.06
	r_s	−1.0	1.0	1.0	1.0	1.0	1.0	0.9	0.68	0.77
PACS 70/160	m	0.15	–	0.19	0.43	–	0.40	0.21	0.20	0.20
	C	1.2	–	1.3	1.5	–	1.6	1.3	1.2	1.2
	p	0.039	–	0.047	2.8×10^{-6}	0.07	0.00033	0.0083	0.00046	0.03
	r_s	0.9	–	1.0	1.0	1.0	1.0	0.82	1.0	0.83
Σ_{TIR}	m	–	–	–	0.20	0.080	0.20	0.082	0.020	0.1
[W kpc^{-1}]	C	–	–	–	6.7×10^{-8}	0.0016	1.1×10^{-7}	0.0014	0.20	0.00025
	p	0.40	–	0.27	0.00082	0.034	0.0023	0.0073	0.037	0.026
	r_s	0.4	–	0.8	1.0	1.0	1.0	0.94	0.86	0.94
$\Sigma_{\mathrm{TIR}}/\mathrm{CO}(1-0)$	m	0.24	–	0.2	–	0.11	–	–	0.17	–
[(W kpc^{-1})/(K km s^{-1})]	C	–	–	9.8×10^{-8}	–	0.00021	–	–	1.3×10^{-6}	–
	p	0.15	–	0.0	0.70	0.0	0.20	0.13	0.011	0.088
	r_s	1.0	–	1.0	1.0	1.0	1.0	1.0	1.0	0.8
$\Sigma_{\mathrm{TIR}}/\mathrm{CO}(2-1)$	m	–	–	−0.063	0.12	−0.053	–	–	–	–
[(W kpc^{-1})/(K km s^{-1})]	C	–	–	1.4×10^{2}	7.4×10^{-5}	64	–	–	–	–
	p	0.25	–	0.0	0.0	0.0	0.60	0.54	0.24	0.18
	r_s	1.0	–	−1.0	1.0	−1.0	−0.50	0.5	1.0	−1.0

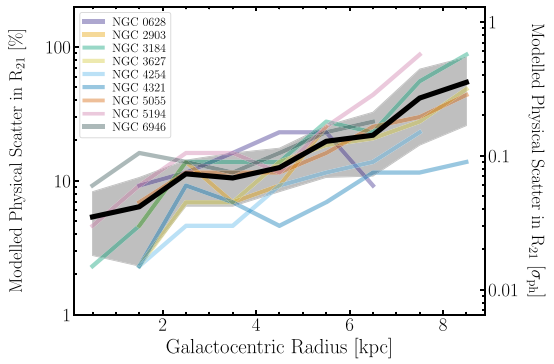

Figure 5. Inferred physical scatter in the R_{21} ratio for each radial bin. The plot shows the physical scatter in each radial bin inferred from our modelling. We have already removed the effects of observational noise from the plotted scatter via a forward modelling Monte Carlo calculation. The left y-axis indicates the scatter in percentage of the line ratio, while the right y-axis describes the scatter's actual value (converting using a fixed $R_{21} = 0.65$). Coloured lines show individual galaxies. The black line and grey region show the median and $\pm 1\sigma$ range combining all galaxies. We observe increasing scatter in R_{21} towards large galactocentric radii, with scatter $\gtrsim$20 per cent typical at radii >6 kpc. This increase in scatter may reflect a large variation in physical conditions at large radius or the inability to separate physically distinct regions at the 27 arcsec (∼1–2 kpc) resolution of our measurements.

trends in the ratio are not noise dominated. The black line indicates the binned mean line ratio and the grey band describes the binned standard deviation. Table 4 lists the results from fitting a power law to the binned mean line ratio indicating the strength of the trend.

CO(1–0) brightness temperature: The top left panel of Fig. 6 shows the stacked, normalized R_{21} as a function of CO(1–0) brightness temperature. The bin width of the stacks is set to 0.25 in logarithmic space. At higher intensities, we observe a tendency to find higher R_{21} in the highest brightness temperature bins. The highest CO(1–0) brightness temperature almost always appears in the galaxy centre, so this reflects the same central enhancements noted in the radial profiles. Overall, Fig. 6 reveals a positive relationship between R_{21} and CO(1–0) brightness temperature.

Because of the correlated axes, low signal-to-noise CO(1–0) measurements will lead to an artificial upturn at the low brightness temperature end driven by sorting predominantly noise measurements, as it can be seen in the top left panel. Supporting this view, no such feature appears in the radial, CO(2–1), or IR intensity plots.

CO(2–1) brightness temperature: The top right panel of Fig. 6 shows stacked R_{21} as a function of CO(2–1) brightness temperature. We also chose a bin width of 0.25 in logarithmic space. As with CO(1–0), we observe a positive correlation between R_{21} and CO(2–1). In general, we tend to find moderately higher R_{21} in high brightness temperature regions.

TIR luminosity surface brightness: The bottom left panel of Fig. 3 shows stacked R_{21} as a function of TIR surface brightness. The bin width for the TIR surface brightness is 0.3 in logarithmic space. TIR surface brightness traces embedded star formation activity and

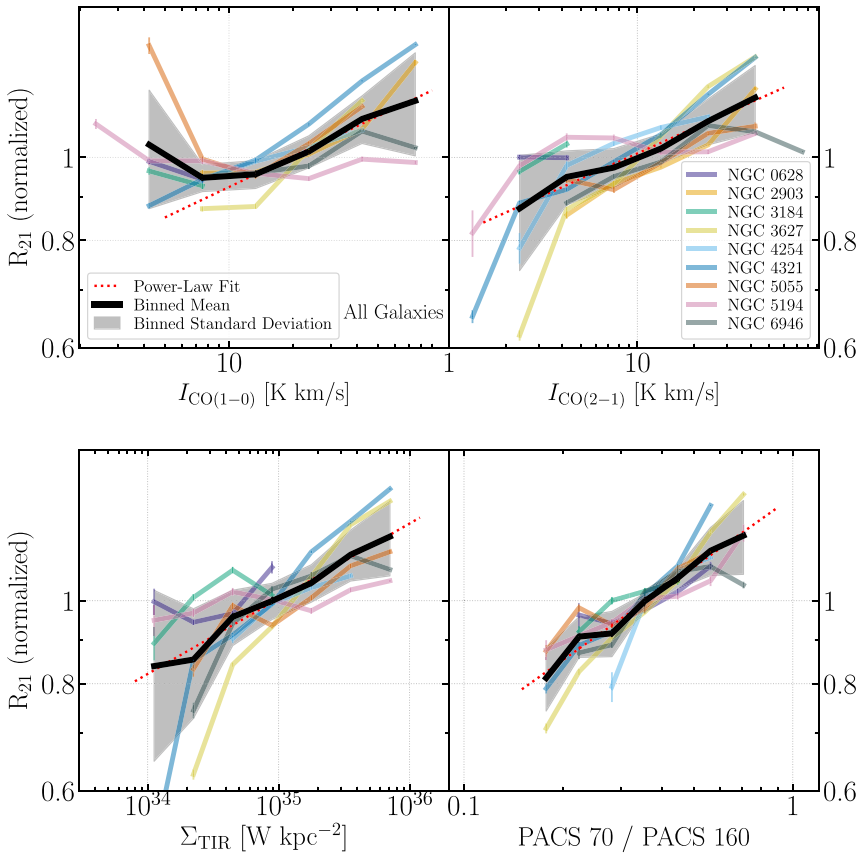

Figure 6. Stacked measurements of R_{21} on a logarithmic scale in bins of CO(1–0), CO(2–1) brightness temperature, TIR surface brightness, and IR colour. In each panel, we bin each galaxy by the quantity on the *x*-axis. Then, we measure stacked line ratios in each bin for each galaxy. For stacking in bins of CO(1–0), CO(2–1) brightness temperature, TIR surface brightness, and IR colour, we only included lines of sight with an S/N > 10 for both CO(1–0) and CO(2–1) in order to reduce noise effects and make the trend more robust. The individual lines are normalized by the median stacked CO ratio value of the corresponding galaxy. The black line is the binned mean combining all galaxies. Only bins with at least a stacking result from three galaxies are included in the mean line. We observe positive correlations between R_{21} and CO brightness temperature, IR surface brightness, and IR colour. These have the sense that R_{21} increases along with gas surface density, star formation activity, and dust temperature. The red dotted line indicates the power-law fit. The fitting range and results are listed in Table 4. We also report rank correlation coefficients in Table 3.

Table 4. Fitting results for stacked, normalized profiles combining all galaxies. Results from fitting a power law of form $R^{\rm fit}_{21,\rm norm} = C \cdot x^m$ to the mean of the stacked, normalized quantities in Figs 6 and 7 (black line in figure). The fitting range indicates the range along the *x*-axis over which the fit is performed.

Parameter (*x*-axis)	Fitting range (units of param.)	C	m	r_s
CO(1–0)	10–75	0.70	0.12	1.0
CO(2–1)	2–43	0.81	0.099	1.0
PACS 70/ PACS 160	0.2–0.7	1.3	0.27	1.0
$\Sigma_{\rm TIR}$	10^{34}–$10^{35.85}$	8.5×10^{-4}	0.088	1.0
$\Sigma_{\rm TIR}$/CO(1–0)	$10^{33.45}$–$10^{34.05}$	5.2×10^{-8}	0.20	1.0
$\Sigma_{\rm TIR}$/CO(2–1)	$10^{33.75}$–$10^{34.35}$	0.15	0.025	0.5

scales with molecular gas surface density, so we expect similar results to stacking by CO brightness temperature. Again, we observe a positive correlation where the IR-bright parts of our sample show moderately higher R_{21}. Because TIR tends to be measured at high signal-to-noise ratio and represents an independent quantity from CO(2–1) and CO(1–0) this correlation spans a larger dynamic range than the CO(1–0) and CO(2–1)-based stacks and should be less subject to systematics. As in the previous panels, we observe a positive correlation between TIR surface brightness and R_{21}. In regions with more star formation per unit area, R_{21} tends to be higher.

70–160 μm ratio: In the bottom right panel of Fig. 6, we plot R_{21} stacked as a function of IR colour. The stacks have a bin with of 0.1 in logarithmic space. IR colour traces dust temperature and the interstellar radiation field. The axes are not correlated, though the lowest bin may again suffer from some sampling and signal-to-noise concerns.

As above, we find a positive correlation between 70–160 μm ratio and R_{21}. R_{21} tends to be higher with stronger interstellar radiation field. This fits with an overall pattern that systems with more intense star formation activity also tend to have higher dust temperatures, denser gas, and more nearly thermal excitation in their CO lines. A higher dust temperature does correspond to a higher R_{21}.

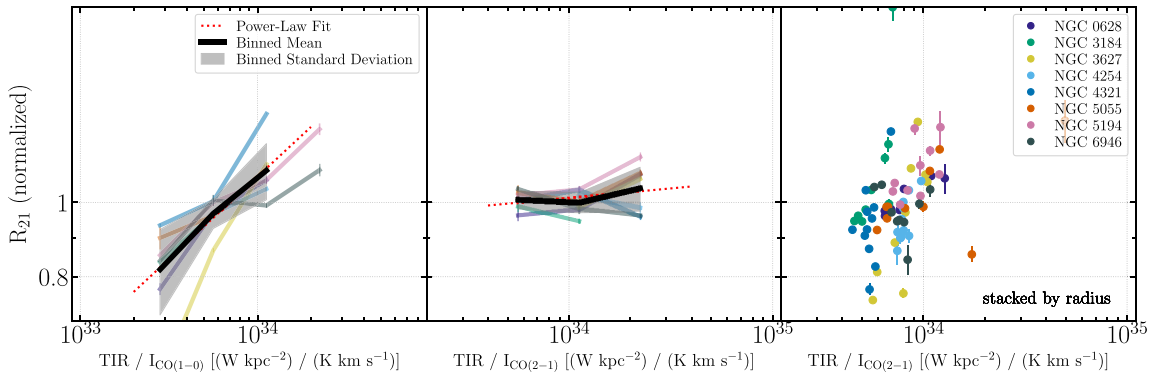

Figure 7. Stacked measurements of the R_{21} ratio as a function of TIR-to-CO ratios. The TIR-to-CO ratio is closely related to the SFR per unit gas mass, a key figure for many studies using both lines. The figure shows three plots of stacked R_{21} as a function of TIR-to-CO(1–0) and TIR-to-CO(2–1). In the left-hand panel, we show R_{21} as a function of TIR-to-CO(1–0), stacking by TIR-to-CO(1–0). In the middle panel, we show R_{21} as a function of TIR-to-CO(2–1), stacking by TIR-to-CO(2–1). In both of these stacks, the quantity being stacked correlates with the quantity used for stacking. However, the correlation with the CO(2–1) integrated brightness temperature is much weaker. In the right-hand panel, we show R_{21} as a function of TIR-to-CO(2–1), but now stacked by radius, an independent quantity, to remove this bias in the stacks. The underlying trend appears to be a moderate positive correlation between R_{21} and TIR-to-CO(2–1), consistent with the results in Fig. 6. The inner, high density parts of galaxies both show higher star formation per unit gas and higher excitation.

Taken together, the CO-bright, IR-bright, high 70–160 μm ratio regions of our targets show moderately higher R_{21} than the cooler, fainter regions. These trends appear significant, with most galaxies showing a trend with these external parameters. The overall magnitude of the trends is a ∼20−30 per cent change in the ratio across the sample.

Perhaps surprisingly, these trends appear *internal* to galaxies. They do not appear to explain the observed galaxy-to-galaxy offset in R_{21}. They can explain some of the internal radial and azimuthal variations observed. The residual galaxy-to-galaxy offsets must either be driven by different physics or be due to flux calibration uncertainties.

We also note, that while R_{21} in NGC 5194 shows discrepancies in spatial variation with previous findings (Koda et al. 2012), the trends discussed in this subsection are actually in agreement. The discrepancy is mostly due to differences in the fainter, interarm region, thus an agreement in the trends with environmental parameters spanning the entire galactic radial range is not unexpected.

3.5 TIR-to-CO ratio and R_{21}

Many CO surveys over the last two decades have focused on measuring the gas depletion time, star formation scaling relations, or related quantities. In these studies, the figure of merit is often the SFR per unit molecular gas mass. Both CO(1–0) and CO(2–1) line emissions are commonly used to estimate the molecular gas mass. We use a simple observational proxy, the TIR-to-CO ratio, to explore how R_{21} depends on the SFR per unit molecular gas. For the bin width, we chose 0.3 in logarithmic space.

In Fig. 7, we plot R_{21} stacked by the TIR-to-CO(1–0) ratio, the TIR-to-CO(2–1) ratio, and galactocentric radius. We explore all three stacks because of the correlated nature of the axes. We might expect an artificial correlation between R_{21} and TIR-to-CO(1–0) when stacking by TIR-to-CO(1–0). In noisy or scattered data, low CO(1–0) data points will scatter to both high R_{21} and high TIR-to-CO(1–0) values, potentially creating an artificial correlation. A similar effect could introduce an artificial anticorrelation comparing R_{21} to TIR-to-CO(2–1). Because the stacking approach uses values for individual data points to assign them to bins, it will not necessarily reduce this effect via averaging.

In the left-hand panel of Fig. 7, we plot R_{21} stacked by the TIR-to-CO(1–0) ratio. The profiles show a clear positive correlation between R_{21} and TIR-to-CO(1–0) for all galaxies. Correlated axes could, however, be tilting the trend in this direction.

In the central panel of Fig. 7, we instead plot R_{21} as a function of TIR-to-CO(2–1), binned using the TIR-to-CO(2–1) ratio. That is, we change the line used for the stack. Again, the correlated axes potentially affect the stack, this time producing a mild correlation between R_{21} and TIR-to-CO(2–1) for most galaxies.

With this in mind, the right-hand panel of Fig. 7 where R_{21} is plotted as a function of the TIR-to-CO(2–1) ratio, i.e. the same axes as in the left-hand panel, but now stacked by galactocentric radius. Radius represents an independent variable that should minimize bias in the stacks. This figure shows more scatter and a somewhat smaller dynamic range compared to the previous two stacks. When stacking by radius, there is an overall tendency for TIR-to-CO(2–1) and R_{21} to be positively correlated. The behaviour is less universal than we saw when stacking by TIR-to-CO(2–1).

Overall, this result appears consistent with the results in the previous section. We tend to find high R_{21}, TIR-to-CO(1–0), 70–160 μm ratio, and CO brightness temperature in the inner parts of galaxies.

4 DISCUSSION

4.1 Comparison to single-pointing literature measurements

In order to compare our results to literature values, we compiled and homogenized single-pointing CO observations from a number of publications (Boselli et al. 1994; Wiklind, Combes & Henkel 1995; Chini, Kruegel & Lemke 1996; Leon, Combes & Menon 1998; Lavezzi et al. 1999; Curran, Aalto & Booth 2000; Böker, Lisenfeld & Schinnerer 2003; Albrecht et al. 2004; Strong et al. 2004; Evans et al. 2005; Albrecht, Krügel & Chini 2007; Combes, Young & Bureau 2007; Ocaña Flaquer et al. 2010; Cappellari et al. 2011). To create a set of reference measurements:

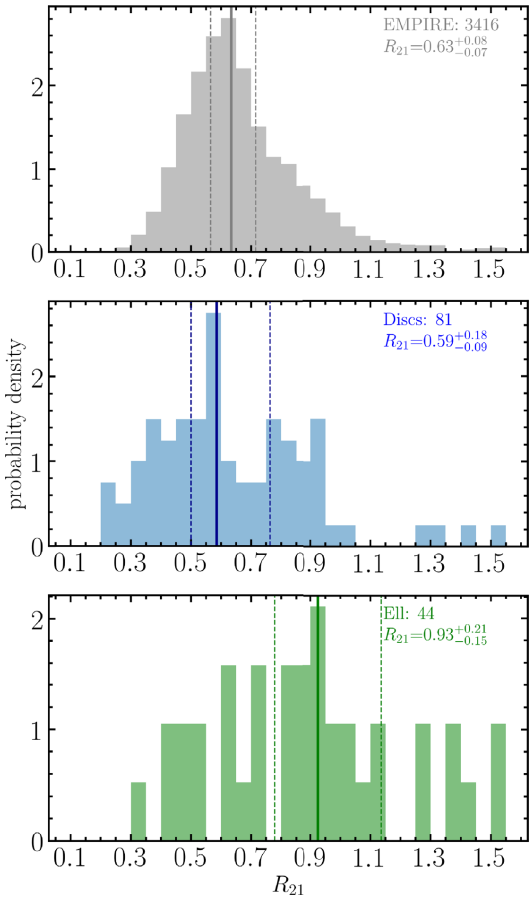

Figure 8. Distributions of R_{21} from literature studies. The distribution of R_{21} for individual lines of sight in EMPIRE (top panel) and a compilation of R_{21} estimates from the literature broken into late-type disc (middle panel) and early-type elliptical (bottom) galaxies (Data from Boselli et al. 1994; Wiklind et al. 1995; Chini et al. 1996; Leon et al. 1998; Lavezzi et al. 1999; Curran et al. 2000; Böker et al. 2003; Albrecht et al. 2004, 2007; Strong et al. 2004; Evans et al. 2005; Combes et al. 2007; Ocaña Flaquer et al. 2010; Cappellari et al. 2011).

(i) We first tabulate CO(1–0) and CO(2–1) line brightness temperatures, errors, and beam sizes for 659 galaxies drawn from the references above. When necessary, we converted from antenna temperature scale to main beam temperature scale using the efficiencies provided in the respective publication. Note that we further limited our compilation of measurements using the criteria below. Our final number of reference galaxies in Fig. 8 is 125.

(ii) For each target, we obtained optical blue band 25 mag arcsec^{-2} isophotal diameters (D_{25}), axial ratios from RC3 (de Vaucouleurs et al. 1991), and morphological types through the *NASA Extragalactic Database* (NED).

(iii) We filtered the data to only include significant detections (S/N > 3) where the beam covered an appreciable part of the galaxy. Some values in the literature are upper limits only, and we do not consider these here. We further require that the full width at half-maximum of the smaller beam, typically CO(2–1), covers at least 40 per cent of a CO scale length (see next point). This typically amounts to requiring that the CO beam covers at least 0.1 D_{25}.

(iv) From D_{25}, we estimate a CO scale length (r_{CO}), assuming: $r_{CO} = 0.23\,D_{25}/2$ (Young et al. 1995; Leroy et al. 2008, 2009; Lisenfeld et al. 2011; Davis et al. 2013). From this scale length and the known beam sizes, we assume an exponential disc and performed an aperture correction to estimate the full luminosity of the galaxy in each line (see e.g. Puschnig et al. 2020). Note that because we focus on the line ratio, the accuracy of the extrapolation to the full galaxy is not important. Only matching the effective area covered by the beams matter.

(v) We calculate R_{21} as the ratio of the estimated full-galaxy CO(2–1) luminosity to the full-galaxy CO(1–0) luminosity. After the cuts based on signal-to-noise ratio and extent, this leaves us with 125 measurements, 81 for late-type ('disc') galaxies and 44 for early-type ('elliptical') galaxies.

Fig. 8 shows histograms of these literature R_{21} measurements. In the figure, we divide the literature sample into disc-like and elliptical galaxies. For disc galaxies we find $R_{21} = 0.59^{+0.18}_{-0.09}$. This agrees well with our results for the EMPIRE sample, though the literature distribution appears much broader. Some of this additional scatter likely reflects uncertainty in calibration. Another part of the scatter reflects the comparatively lower signal-to-noise ratio of these data compared to EMPIRE. A full meta-analysis disentangling the sources of physical and observational scatter for the literature measurements is beyond the scope of this paper. Here, we emphasize the general good agreement between our smaller set of high-quality, resolved measurements and the literature.

The lower panel in Fig. 8 shows that elliptical galaxies exhibit higher excitation. This might be expected if the deeper potential well leads to wider line profiles and thus lower optical depth. Regardless of the explanation, literature observations of early-type galaxies indicate higher apparent R_{21} but also enormous scatter.

Recently, Saintonge et al. (2017) studied R_{21} in 28 galaxies that are part of the xCOLDGASS galaxy sample. Combining IRAM and APEX observations they found a mean ratio of $R_{21} = 0.79 \pm 0.03$ with scatter of 0.15–0.23. xCOLDGASS includes both disc-like and elliptical galaxies, so the relevant comparison is to our full compilation. For all literature data, we find a mean $R_{21} = 0.72$ with a scatter of ± 0.15. This agrees reasonably well with the xCOLDGASS results, especially given the heterogeneous nature of the literature data. The EMPIRE results have lower mean R_{21} compared to the xCOLDGASS IRAM–APEX overlap sample. As discussed by Saintonge et al. (2017), this may somewhat reflect the central focus of the xCOLDGASS pointings. Or it may reflect a greater contribution of early-type galaxies to their sample. Future larger mapping surveys will be needed to help synthesize our knowledge of resolved and galaxy-integrated R_{21}.

4.2 Comparison to previous mapping results

Combining HERACLES with previously existing CO(1–0) data, Leroy et al. (2009) initially found a mean $R_{21} \approx 0.8$ with evidence for central enhancements. Subsequently, improved main beam efficiencies for the IRAM 30-m telescope became available and Usero et al. (2015) carried out pointed spectroscopy using the IRAM 30-m that obtained improved CO(1–0) comparison data. Based on comparing HERACLES to the Usero et al. (2015) data and a collection of earlier CO(1–0) measurements, Leroy et al. (2013) found a median $R_{21} \approx 0.67$ with a large scatter of 0.16 dex or ∼40 per cent among individual measurements. Our mean R_{21} has an almost identical value to that in

Leroy et al. (2013), but the measured scatter using EMPIRE CO(1–0) is smaller. This likely reflects the much better calibration using EMIR compared to the archival CO(1–0) data, though the smaller sample size may also play a role. Also using HERACLES, but now attempting to homogenize literature mapping data, Rosolowsky et al. (private communication) found that a ratio of ∼0.7 was typical of the inner parts of galaxies, while 0.5 was more common in outer discs (see also Rosolowsky et al. 2015). Our results yield slightly higher R_{21} at large galactocentric radius (see Fig. 4). Again, we expect the EMPIRE CO(1–0) data to be of higher quality than the HERACLES maps, but the EMPIRE sample size is small.

Our results also agree reasonably well with previous mapping-based results for other nearby galaxies. For example, Crosthwaite & Turner (2007) found $R_{21} \approx 0.8$ in the central 1 arcmin × 1 arcmin of NGC 6946, while we find a value of $R_{21} = 0.7$ for the same galaxy centre. Our measured value of 0.7 for NGC 5194 (M51) agrees with the typical ratio found by Koda et al. (2012) while studying the arm/interarm contrast of the ratio. Other resolved mapping results include $R_{21} \approx 0.8$ for M33 (Druard et al. 2014) with no obvious radial trends. Lundgren et al. (2004) and Koda et al. (2020) found $R_{21} \approx 0.77$ for M83 which closely resembles the EMPIRE targets in morphology and stellar mass, showing a similar decreasing trend in R_{21} with galactocentric radius. Again, our EMPIRE results tend towards the low side of the literature value, but well within the previously measured range.

4.3 R_{21} variations in EMPIRE

We measure the characteristic value, scatter, and dependence of R_{21} on environment. We do find scatter in R_{21} from galaxy-to-galaxy and within galaxies. In certain galaxies, we identify significant correlations with galactocentric radius and other observable quantities.

One recurring theme in our analysis is that the magnitude of these variations is weak. Put simply, the dynamic range in R_{21} across our sample remains small compared to many of the uncertainties associated with measuring the ratio. The small magnitude of these variations somewhat diminish the utility of R_{21} as a diagnostic of the physical conditions in the gas. Of course, CO(2–1) and CO(1–0) both still represent the most widely used tracers of molecular gas at low redshift. Detailed knowledge of how R_{21} behaves is crucial to our knowledge of molecular gas in galaxies.

With that caveat in mind, we discuss the major sources of R_{21} variation in EMPIRE:

Observed galaxy-to-galaxy scatter: In each of our analyses, galaxy-to-galaxy scatter in R_{21} appears to play a role. The galaxy being considered appears to matter independent of radial gradients, correlation with local conditions, or azimuthal variations.

We checked for correlations between global galaxy properties and R_{21} that might explain the galaxy-to-galaxy scatter, including comparing to stellar mass, SFR, metallicity, inclination, distance, and morphological type. We found no significant correlation that could explain the observed galaxy-to-galaxy scatter. We emphasize, however, that EMPIRE represents an extremely small sample with a limited range of stellar mass, SFR, and metallicity values. EMPIRE is fundamentally a mapping project, not a representative survey of the local galaxy population.

One plausible explanation for much of the observed galaxy-to-galaxy is uncertainty in the flux calibration, which we discuss in Section 2.3 and Appendix C. Given the estimated uncertainties in the amplitude calibration of each data set, ∼6 per cent for EMPIRE, ≈ 5 per cent for PHANGS-ALMA and M51 Large Program, and ∼20 per cent for HERACLES, we expect ∼7−20 per cent scatter in R_{21} based on calibration uncertainty alone. We measure rms scatter of 10−15 per cent from galaxy-to-galaxy, so it seems highly likely that much of the galaxy-to-galaxy scatter that we observe is caused by flux calibration uncertainties.

Building a quantitative understanding of galaxy-to-galaxy variations in R_{21} places strong requirements on the data. Given the small dynamic range in the ratio, one needs high signal-to-noise ratio and high precision absolute flux calibration. To avoid uncertain aperture corrections, one needs to observe and cover the same area in both lines. Although EMPIRE and the IRAM–APEX subset from xCOLDGASS (Saintonge et al. 2017) represent good first steps, obtaining such carefully calibrated, high signal-to-noise data sets still represents a future goal.

Trends within galaxies: Within galaxies, we find a clear, but weak systematic variation of R_{21} as a function of environment. We examined correlations with CO brightness temperature, TIR surface brightness, IR colour, and TIR-to-CO ratio. After accounting for biases and disregarding low signal-to-noise regions, these all show the same trend, i.e. higher R_{21} values in regions with higher gas surface density, hotter dust, and more star formation.

Galaxy centres: One major driver for these trends is that we observe a higher R_{21} in the centre of galaxies compared to the discs. The average enhancement is 15 per cent compared to the galaxy-wide luminosity-weighted mean, but several individual cases show much stronger nuclear enhancements. NGC 2903, NGC 327, NGC 4321, and NGC 5055 all show strong (∼50 per cent) central enhancements in R_{21}.

Though not uniquely associated with bars, these central enhancements do seem strongest in the strongly barred members of our sample. NGC 2903, NGC 3627, and NGC 4321 all have prominent bars that visibly interact with the molecular gas. In these cases our coarse resolution likely causes us to underestimate the strength of the R_{21} enhancement, because the nuclear star-forming regions, where we expect the R_{21} enhancements to be strongest, are compact (often ∼0.5 kpc) compared to our 27 arcsec (∼1–2 kpc) beam.

In unbarred galaxies, we often observe flatter R_{21} profiles, e.g. in NGC 628, NGC 3184, or NGC 4254. NGC 5194 (M51) remains an ambiguous case, with our newer EMIR mapping data showing evidence for a flatter R_{21} profile than the HERA maps (see Appendix C).

A similar drop in R_{21} from the centre of the galaxies towards their discs has also been found by many previous studies. Milky Way studies show values close to unity in the central kpc of the Galaxy, dropping to 0.75 at 4 kpc and to ∼0.6 at 8 kpc from the Galaxy centre (Sakamoto et al. 1997; Sawada et al. 2001). Similarly, Casoli et al. (1991b) report a value of ∼1 in the nuclei of nearby spirals (at ∼500 pc scales) compared to 0.5–7 in their discs. Studying the nearby spiral IC 342, Eckart et al. 1990) found a drop from $R_{21} \approx 1.1$ to $R_{21} \approx 0.7$–0.8 around 500 pc from the starburst nucleus. A high average ratio of ∼0.9 is also found by Braine & Combes (1992) in the central kpc of 36 nearby galaxies. Similar radial trends have been found by Saito et al. (2017) when studying the spatially resolved R_{21} ratio in NGC 1614. Using RADEX modelling they find a radial kinetic temperature gradient that mirrors the observed R_{21} trend. Using HERACLES with lower quality CO(1–0) data but a larger sample, Leroy et al. (2009, 2013) noted a similar trend in resolved maps of nearby galaxies.

Furthermore, variation in the CO line ratio could be driven to some parts by the presence of an active galactic nuclei (AGNs) within the galaxy. Four of the galaxies in our sample, NGC 3627, 4321, 5055, and 5194, are know to host an AGN.

Correlation with physical conditions: We observe positive correlations of R_{21} with CO brightness temperature, TIR surface

brightness, and IR colour. All of these quantities tend to decrease with increasing galactocentric radius, so these trends likely express the same underlying physics as the radial gradients.

Physically, the IR colour reflects the interstellar radiation field heating the dust. At the typical densities associated with molecular clouds, gas and dust have different temperatures and are not collisionally coupled (e.g. Draine 2011). However, the radiation field traced by the dust temperature should also relate to the radiation field illuminating molecular clouds and so indirectly relate to excitation of the gas. We would expect more intensely illuminated clouds to have high temperatures and be more nearly thermalized.

Similarly, the TIR surface density traces the heating of the ISM because it indicates the amount of reprocessed, mostly ultraviolet emission. High TIR surface density may also indirectly trace gas density, because high gas densities tend to be associated with high SFRs (see e.g. more discussion in Jiménez-Donaire et al. 2019). We would expect denser, higher temperature gas to be more nearly thermalized and show a higher R_{21}.

As mentioned above, optical depth effects may also play a role. The line ratio of optically thin gas exceeds unity and a component of diffuse, optically thin gas will drive R_{21} to higher values.

A systematic dependence of R_{21} on, e.g. $\Sigma_{\rm TIR}$ has implications for the slope of derived scaling relations. For example, the scaling relation between $\Sigma_{\rm TIR}$ and $I_{\rm CO}$ corresponds to the molecular version of the Kennicutt–Schmidt law. If R_{21} varies systematically with $\Sigma_{\rm TIR}$ then one expects to derive different slopes if using CO(1–0) or CO(2–1).

Our results show that this is the case, but also that the effect is modest. For example, in Fig. 6, R_{21} changes by ∼40 per cent as $\Sigma_{\rm TIR}$ changes by a factor of 100. This would translate to a difference in slope of ∼0.07 for a power law relating the two quantities. It seems reasonable to infer that using CO(2–1) instead of CO(1–0) will change the slope of the $I_{\rm CO}$–$\Sigma_{\rm TIR}$ relation by 0.05–0.1.

We caution that the implications of R_{21} for the underlying physical scaling relation, e.g. between $\Sigma_{\rm mol}$ and $\Sigma_{\rm SFR}$, are less clear. The sensitivity of R_{21} to these local physical conditions implies that physical conditions in the molecular gas are changing. Variations in density, temperature, and optical depth will imply changes in the CO-to-H_2 conversion factor, $\alpha_{\rm CO}$, for both CO(1–0) and CO(2–1). Unfortunately, on its own R_{21} does not heavily constrain $\alpha_{\rm CO}$. Future work using a large set of lines and independent constraints on $\alpha_{\rm CO}$ will help map R_{21} variations to $\alpha_{\rm CO}$ variations for both lines.

Scatter at fixed radius and resolved patterns: Density and radiation field also vary at fixed galactocentric radius, e.g. due to the effects of spiral density waves and stellar bars. The arm–interarm contrast and small-scale structure of R_{21} have been the focus of several recent papers (Koda et al. 2012; Law et al. 2018). Though our ∼1–2 kpc resolution limits our ability to isolate small-scale variations in R_{21}, we attempt to quantify the scatter in R_{21} at fixed galactocentric radius in our sample using a forward modeling technique.

NGC 5194 (M51) shows the largest intrinsic scatter of any target, presumably due to its well-defined grand-design structure. Past studies have already highlighted a strong arm–interarm contrast in the CO line ratio in M51 (Koda et al. 2012; Vlahakis et al. 2013). The contrast is also strongly visible in our analysis, but we find an opposite trend (we find a high interarm and low arm R_{21} ratio; see Section 3.3 and Appendix E). Among the literature there is disagreement between the relative and quantitative trend of R_{21} between arm versus interarm. Interestingly, when studying NGC 6946, Crosthwaite & Turner (2007) found $R_{21} > 1$ in the interarm as opposed to smaller values in the molecular arm regions. While we cannot confirm such large average absolute values with our observations, the regions that show enhancement in our data overlaps with theirs (we find an average $R_{21} \sim 0.9$ in the interarm, with 35 per cent of the points in that region with S/N > 3 showing $R_{21} > 1$, and only 8 per cent have $R_{21} > 1.2$). Furthermore, Crosthwaite et al. (2002) and Lundgren et al. (2004) have investigated M83 and both report higher line ratio values in the interarm region as well. However, the validity of this trend within M83 has recently been disputed by Koda et al. (2020), who studied the source with ALMA observations. Differences of R_{21} between arm and interarm have been found in several galaxies, however, different studies have presented opposing trends. We believe that this is caused at least partially by coarse spatial resolution and insufficient data quality, and should be investigated in more detail in the future.

From point of view of the data, our study differs from Koda et al. (2012) in that we use both new CO(1–0) and CO(2–1) maps obtained using the IRAM 30-m EMIR receiver. The primary difference appears to come from the use of the new CO(1–0) map. We defer a detailed comparison among M51 data sets to the presentation of the new IRAM LP (den Brok et al., in preparation) and new Submillimeter Array observations (Jimenez Donaire et al., in preparation). As emphasized in Section 2.2 and Appendix E, we use what we consider the best available map.

Interpreting in terms of ISM physics and molecular cloud conditions, our finding of enhanced R_{21} in interarm regions as compared to arm regions implies more excited, perhaps more diffuse, warm and optically thin gas in the interarm regions. In the interarm region, the heating is most likely more efficient due to different cloud composition. Furthermore, Lundgren et al. (2004) suggest that photon-dominated regions (PDRs) around cool stars could be responsible for bright CO emission. This is, because the PDR radiation field is softer, thus the CO can be heated photoelectrically at lower A_V (Spaans et al. 1994). Another possibility would be 'CO-loud' gas (Lundgren et al. 2004). Small amounts of optically thin gas could already cause strong emisivity in CO(2–1) (Wiklind et al. 1990). These explanations might be consistent with the extended diffuse component identified in M51 by Pety et al. (2013). They find that ∼50 per cent of the total CO emission originates from larger spatial scales (>1.3 kpc), which would be consistent with emission from a diffuse disc of gas at a scale height of ∼200 pc. A similar fining was made by Caldú-Primo & Schruba (2016) studying M31. The large scatter found may also reflect the influence of M51's ongoing interaction with the companion galaxy NGC 5195.

Uncertain behaviour at large radii: Despite our use of spectral stacking, many of our R_{21} estimates remain uncertain at low brightness temperature and large radius. In the stacked radial profiles, we see suggestions of large deviations to both low and high R_{21} in some of our targets. Similarly, in the lowest brightness temperature bins of IR colour and TIR surface brightness we see hints of significant deviations. It could well be that molecular gas in the outer parts of galaxies is either optically thin, leading to high R_{21}, or cool, leading to low R_{21}. More sensitive observations of both lines will be required to ascertain the behaviour of the ratio in the faint CO emission from the outer discs of galaxies.

4.4 Comparison to radiative transfer models

Following up the work of Leroy et al. (2017), Puschnig et al. (in preparation) have established a set of molecular radiative transfer models, i.e. the `Dense Gas Toolbox` (Puschnig 2020), which predicts line ratios for a medium with an underlying density distribution (e.g. a lognormal distribution rather than from a single density).

Using CO line optical depths as previously published by Cormier et al. (2018) for EMPIRE galaxies (they find $\tau^{12} \approx 6$ for 12CO(1–0)), we now examine the impact of three physical quantities on R_{21}: temperature, mean density, and width of the lognormal density distribution. The interplay between these quantities can be studied through an interactive tool.[3] The models show that R_{21} is most sensitive to regimes with mean densities lower than $\sim 10^3$ cm^{-3}. Below that value all three quantities are degenerate. However, above that density the line ratio may only be driven further up by higher temperatures, regardless of the width of the density distribution (that is proportional to line width or Mach number). We also recognize that values of $R_{21} > 0.8$ are only predicted for temperatures above 35 K, regardless of the mean gas density. For NGC 5194, we may thus conclude that the mean gas density and temperature must be $n_{H_2} > 10^3$ cm^{-3} and $T_{kin} > 35$ K, throughout the whole disc.

5 SUMMARY

We measure the ^{12}CO(2–1)/^{12}CO(1–0) brightness temperature ratio, R_{21}, across the star-forming discs of nine nearby galaxies. We measure CO(1–0) emission from maps obtained by the IRAM 30-m telescope in the context of the EMPIRE survey (Bigiel et al. 2016; Jiménez-Donaire et al. 2019) and CO(2–1) emission from a mixture of ALMA and IRAM 30-m data (den Brok et al., in preparation). We use IRAM 30-m CO (2–1) maps obtained as part of HERACLES (Leroy et al. 2009) and a new IRAM Large Program targeting M51. We use ALMA maps obtained as part of the PHANGS-ALMA survey (Leroy et al. 2021b). We measure the distributions and mean values of R_{21} across individual lines of sight, integrated over galaxies, stacking by radius, and stacking as a function of other local conditions. Our main results are:

(i) The luminosity-weighted mean R_{21} for individual galaxies ranges from 0.48 to 0.73. Within individual galaxies, we observe a typical range of ± 0.1. Over the whole sample, treating galaxies equally we find a mean R_{21} of 0.63 ± 0.09.

(ii) We compiled and homogenized a set of CO observations from the literature. For 81 disc galaxies, these literature measurements yield $R_{21} = 0.59^{+0.18}_{-0.09}$, in good agreement with our mean value.

(iii) Seven of our nine targets show a central enhancement in R_{21} compared to the disc-averaged value (median enhancment $\sim$15 per cent). The magnitude of the deviation varies from galaxy-to-galaxy, but variation at larger radii can be much larger than the ones found towards the centre. Both central enhancements and radial gradients in R_{21} are in agreement with previous work.

(iv) We find significant correlations between R_{21}, CO brightness temperature, TIR surface density, and 70–160 μm ratio. All of these have the expected trend of an increasing ratio when the gas density and radiation field increase.

(v) R_{21} also shows azimuthal variation. Using a forward modelling approach, we estimate the intrinsic scatter in R_{21} at fixed galactocentric radius to be $\sim$ 20 per cent at our $\sim$1–2 kpc resolution.

(vi) These physical trends are not sufficient to explain the majority of the galaxy-to-galaxy variations observed. Given the scale of our calibration uncertainties, we cannot completely rule them out as one of the dominant drivers for these trends. Instead, the magnitude of this scatter appears consistent with being driven by absolute flux calibration uncertainties.

[3] http://www.densegastoolbox.com/explorer/

ACKNOWLEDGEMENTS

The IRAM 30-m large programme EMPIRE was carried out under project number 206-14 (PI Bigiel), the ^{12}CO(1–0) observations under projects 061-15 and 059-16 (PI Jiménez-Donaire) and D15-12 (PI Cormier). IRAM is supported by INSU,CNRS (France), MPG (Germany), and IGN (Spain). MJJD acknowledges support from the Smithsonian Institution as a Submillimeter Array (SMA) Fellow. FB, JPu, AB, and JdB acknowledge funding from the European Union's Horizon 2020 research and innovation programme (grant agreement No 726384/Empire). AU acknowledges support from the Spanish funding grants AYA2016-79006-P (MINECO/FEDER), PGC2018-094671-B-I00 (MCIU/AEI/FEDER), and PID2019-108765GB-I00 (MICINN). The work of AKL and MJG is partially supported by the National Science Foundation under Grants No. 1615105, 1615109, and 1653300. AKL also acknowledges partial support from NASA ADAP grants NNX16AF48G and NNX17AF39G. ES, DL, and ST acknowledge funding from the European Research Council (ERC) under the European Union's Horizon 2020 research and innovation programme (grant agreement No. 694343). CMF acknowledges support from the National Science Foundation under Award No. 1903946. JMDK gratefully acknowledges funding from the Deutsche Forschungsgemeinschaft (DFG) through an Emmy Noether Research Group (grant number KR4801/1-1) and the DFG Sachbeihilfe (grant number KR4801/2-1), as well as from the European Research Council (ERC) under the European Union's Horizon 2020 research and innovation programme via the ERC Starting Grant MUSTANG (grant agreement number 714907). JPe acknowledges support by the Programme National 'Physique et Chimie du Milieu Interstellaire' (PCMI) of INSU,CNRS with INC/INP, co-funded by CEA and CNES. Furthermore, we thank J. Koda for making available the NRO 45-m CO(1–0) data of NGC 5194.

DATA AVAILABILITY

The HERACLES and EMPIRE survey data used in this article are publicly available in IRAM repository, at https://www.iram.fr/ILPA/LP001/ and https://www.iram.fr/ILPA/LP015/, respectively. The PHANGS-ALMA CO maps will be available as part of the first public data release in the first half of 2021 and will be available from the ALMA archive and https://www.phangs.org. The M51 IRAM Large Program will be publicly available during the first half of 2021 via the IRAM Large Program Archiva. The remaining data underlying this article will be shared on reasonable request to the corresponding author.

REFERENCES

Albrecht M., Chini R., Krügel E., Müller S. A. H., Lemke R., 2004, A&A, 414, 141
Albrecht M., Krügel E., Chini R., 2007, A&A, 462, 575
Aravena M. et al., 2010, ApJ, 718, 177
Aravena M. et al., 2014, MNRAS, 442, 558
Aravena M. et al., 2016, MNRAS, 457, 4406
Bigiel F. et al., 2016, ApJ, 822, L26
Böker T., Lisenfeld U., Schinnerer E., 2003, A&A, 406, 87
Bolatto A. D., Wolfire M., Leroy A. K., 2013, ARA&A, 51, 207
Bonato M. et al., 2018, MNRAS, 478, 1512
Boselli A., Gavazzi G., Combes F., Lequeux J., Casoli F., 1994, A&A, 285, 69
Bothwell M. S. et al., 2013, MNRAS, 429, 3047
Braine J., Combes F., 1992, A&A, 264, 433
Caldú-Primo A., Schruba A., 2016, AJ, 151, 34

Cappellari M. et al., 2011, MNRAS, 413, 813
Carter M. et al., 2012, A&A, 538, A89
Casoli F., Boisse P., Combes F., Dupraz C., 1991a, A&A, 249, 359
Casoli F., Dupraz C., Combes F., Kazes I., 1991b, A&A, 251, 1
Chini R., Kruegel E., Lemke R., 1996, A&AS, 118, 47
Combes F., Young L. M., Bureau M., 2007, MNRAS, 377, 1795
Cormier D. et al., 2018, MNRAS, 475, 3909
Crosthwaite L. P., Turner J. L., 2007, AJ, 134, 1827
Crosthwaite L. P., Turner J. L., Buchholz L., Ho P. T. P., Martin R. N., 2002, AJ, 123, 1892
Curran S. J., Aalto S., Booth R. S., 2000, A&AS, 141, 193
de Vaucouleurs G., de Vaucouleurs A., Corwin H. G. Jr., Buta R. J., Paturel G., Fouque P., 1991, Third Reference Catalogue of Bright Galaxies. Springer, New York
Daddi E. et al., 2010, ApJ, 713, 686
Davis T. A. et al., 2013, MNRAS, 429, 534
Draine B. T., 2011, Physics of the Interstellar and Intergalactic Medium. Princeton Univ. Press, Princeton, NJ
Draine B. T. et al., 2007, ApJ, 663, 866
Druard C. et al., 2014, A&A, 567, A118
Eckart A., Downes D., Genzel R., Harris A. I., Jaffe D. T., Wild W., 1990, ApJ, 348, 434
Evans A. S., Mazzarella J. M., Surace J. A., Frayer D. T., Iwasawa K., Sanders D. B., 2005, ApJS, 159, 197
Galametz M. et al., 2013, MNRAS, 431, 1956
Gallagher M. J. et al., 2018a, ApJ, 858, 90
Gallagher M. J. et al., 2018b, ApJ, 868, L38
Hasegawa T., 1997, in Latter W. B., Radford S. J. E., Jewell P. R., Mangum J. G., Bally J., eds, Proc. IAU Symp. 170, The CO 2-1/1-0 Ratio. Kluwer, Dordrecht, p. 39
Hasegawa T. et al., 1997, in Okuda H., Matsumoto T., Rollig T., eds, ASP Conf. Ser. Vol. 124, Diffuse Infrared Radiation and the IRTS. Astron. Soc. Pac., San Francisco, p. 244
Herrera C. N. et al., 2020, A&A, 634, A121
Heyer M., Dame T. M., 2015, ARA&A, 53, 583
Jiménez-Donaire M. J. et al., 2017, ApJ, 836, L29
Jiménez-Donaire M. J. et al., 2019, ApJ, 880, 127
Kennicutt R. C. et al., 2011, PASP, 123, 1347
Koda J. et al., 2011, ApJS, 193, 19
Koda J. et al., 2012, ApJ, 761, 41
Koda J. et al., 2020, ApJ, 890, L10
Lavezzi T. E., Dickey J. M., Casoli F., Kazès I., 1999, AJ, 117, 1995
Law C. J., Zhang Q., Ricci L., Petitpas G., Jiménez-Donaire M. J., Ueda J., Lu X., Dunham M. M., 2018, ApJ, 865, 17
Leon S., Combes F., Menon T. K., 1998, A&A, 330, 37
Leroy A. K., Walter F., Brinks E., Bigiel F., de Blok W. J. G., Madore B., Thornley M. D., 2008, AJ, 136, 2782
Leroy A. K. et al., 2009, AJ, 137, 4670
Leroy A. K. et al., 2013, AJ, 146, 19
Leroy A. K. et al., 2017, ApJ, 835, 217
Leroy A. K. et al., 2021a, ApJS, preprint (arXiv:2104.07665)
Leroy A. K. et al., 2021b, preprint (arXiv:2104.07739)
Lisenfeld U. et al., 2011, A&A, 534, A102
Lundgren A. A., Wiklind T., Olofsson H., Rydbeck G., 2004, A&A, 413, 505
Mangum J. G., Emerson D. T., Greisen E. W., 2007, A&A, 474, 679
Mangum J. G., Darling J., Henkel C., Menten K. M., MacGregor M., Svoboda B. E., Schinnerer E., 2013, ApJ, 779, 33
Ocaña Flaquer B., Leon S., Combes F., Lim J., 2010, A&A, 518, A9
Parkin T. J. et al., 2013, ApJ, 776, 65
Peñaloza C. H., Clark P. C., Glover S. C. O., Shetty R., Klessen R. S., 2017, MNRAS, 465, 2277
Peñaloza C. H., Clark P. C., Glover S. C. O., Klessen R. S., 2018, MNRAS, 475, 1508
Pety J. et al., 2013, ApJ, 779, 43
Puschnig J., 2020, Dense Gas Toolbox. Available at: http://www.densegastoolbox.com/ (accessed April 10, 2021)
Puschnig J. et al., 2020, A&A, 644, A10
Rosolowsky E., Leroy A. K., Usero A., Loeppky J., Walter F., Wilson C., Heracles Team N. T., 2015, American Astronomical Society Meeting Abstracts #225, p. 141.25
Saintonge A. et al., 2017, ApJS, 233, 22
Saito T. et al., 2017, ApJ, 835, 174
Sakamoto S., Hayashi M., Hasegawa T., Handa T., Oka T., 1994, ApJ, 425, 641
Sakamoto S., Hasegawa T., Handa T., Hayashi M., Oka T., 1997, ApJ, 486, 276
Sandstrom K. M. et al., 2013, ApJ, 777, 5
Sawada T. et al., 2001, ApJS, 136, 189
Schinnerer E., Weiß A., Aalto S., Scoville N. Z., 2010, ApJ, 719, 1588
Schinnerer E. et al., 2013, ApJ, 779, 42
Schinnerer E. et al., 2017, ApJ, 836, 62
Schruba A. et al., 2011, AJ, 142, 37
Schruba A. et al., 2012, AJ, 143, 138
Schuster K. F., Kramer C., Hitschfeld M., Garcia-Burillo S., Mookerjea B., 2007, A&A, 461, 143
Shirley Y. L., 2015, PASP, 127, 299
Solomon P. M., Vanden Bout P. A., 2005, ARA&A, 43, 677
Spaans M., Tielens A. G. G. M., van Dishoeck E. F., Bakes E. L. O., 1994, ApJ, 437, 270
Strong M., Pedlar A., Aalto S., Beswick R. J., Curran S., Booth R., 2004, MNRAS, 353, 1151
Sun J. et al., 2018, ApJ, 860, 172
Usero A. et al., 2015, ApJ, 150, 115
Vlahakis C., van der Werf P., Israel F. P., Tilanus R. P. J., 2013, MNRAS, 433, 1837
Walter F., Brinks E., de Blok W. J. G., Bigiel F., Kennicutt R. C., Jr, Thornley M. D., Leroy A., 2008, AJ, 136, 2563
Wiklind T., Rydbeck G., Hjalmarson A., Bergman P., 1990, A&A, 232, L11
Wiklind T., Combes F., Henkel C., 1995, A&A, 297, 643
Yajima Y. et al., 2021, PASJ, 73, 257
Yoda T. et al., 2010, PASJ, 62, 1277
Young J. S. et al., 1995, ApJS, 98, 219

APPENDIX A: OVERVIEW OF MAPS

Fig. A1 displays maps of our nine target galaxies. The leftmost column shows $\log_{10}R_{21}$, the CO(2–1)/(1–0) integrated brightness temperature ratio (see Section 3.1). Columns two and three show the integrated CO(1–0) and CO(2–1) brightness temperature maps (see Sections 2.2 and 2.3). Columns four and five show the *Herschel* 70 and 160 μm intensity maps (see Section 2.4). The last column shows the TIR surface brightness (see Section 2.5).[4]

All of the maps have already been convolved to share the same, 27 arcsec angular resolution. They have all been projected on to a hexagonal grid with a grid spacing equal to half the beamsize (13.5 arcsec). The maps in Fig. A1 only show sightlines that have significant ($S/N > 3$) integrated brightness temperature detections in both CO(2–1) and CO(1–0).

[4]NGC 2903 lacks *Herschel* data.

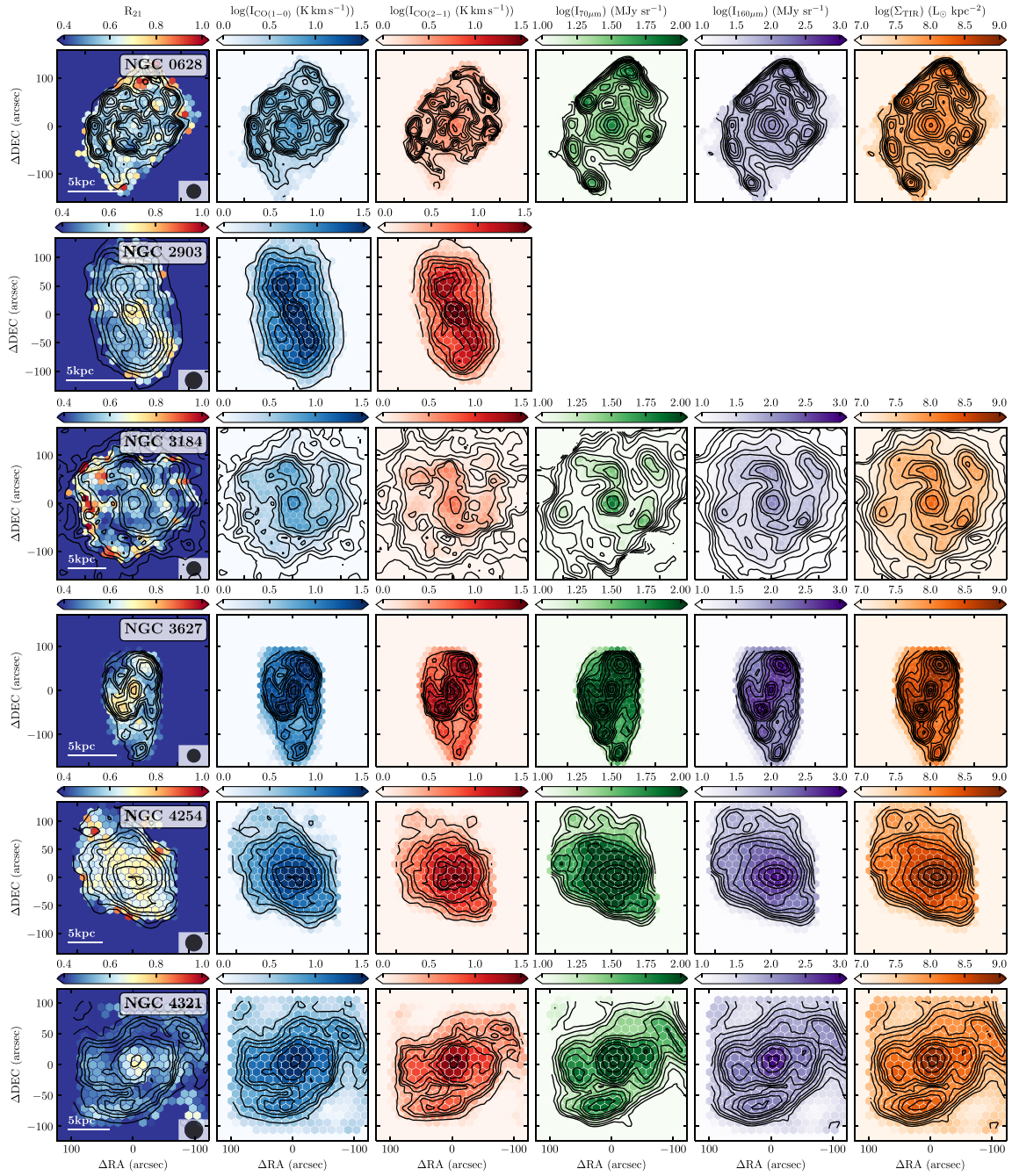

Figure A1. Multiwavelength maps used in this paper. From left to right, each row shows maps of the CO(2–1)/CO(1–0) integrated brightness temperature ratio, $\log(R_{21})$, CO(1–0) and CO(2–1) integrated brightness temperature, *Herschel* 70 and 160 μm fluxes, and the TIR surface brightness. There are no *Herschel* data available for NGC 2903. We plot values for positions that have significant ($S/N > 3$) integrated brightness temperature detections within both the CO(2–1) and CO(1–0) maps. For reference, we overlay CO(1–0) integrated brightness temperature contours on the R_{21} map. The remaining panels have contours of their respective colour scale, in levels of 20, 30, 40, 50, 60, 70, 80, 90, 95, 97.5, and 99.5 of the peak value.

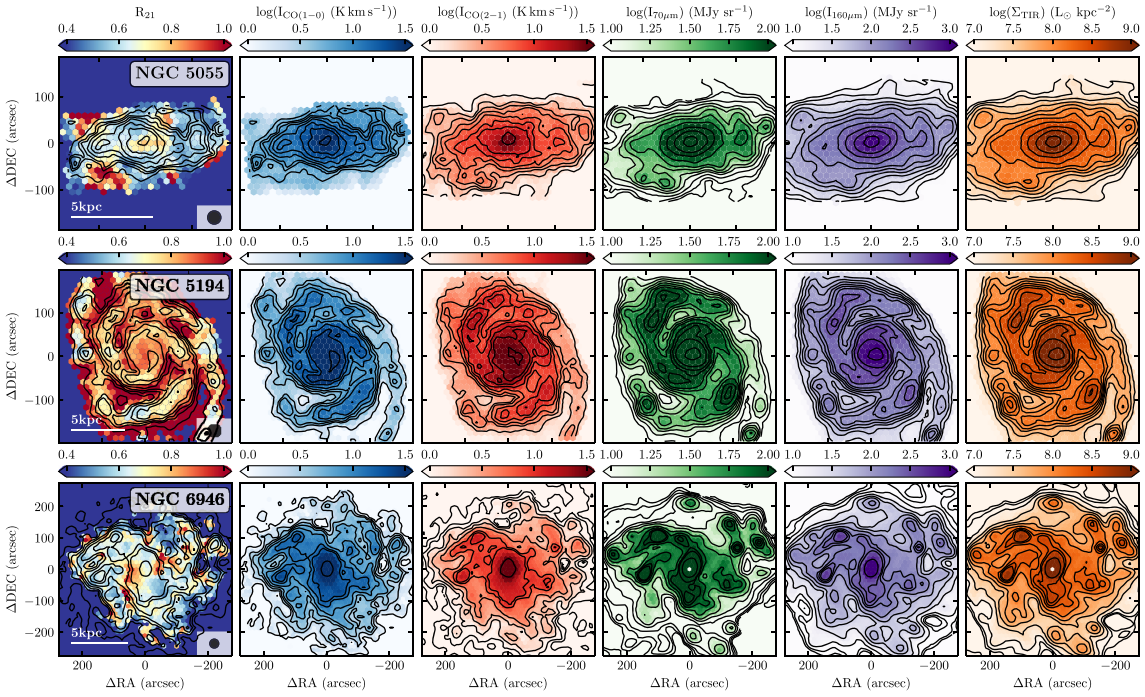

Figure A1 – *continued*

APPENDIX B: FORWARD MODELLING TO INFER PHYSICAL SCATTER IN R_{21}

This section presents our modelling used to estimate the scatter of the R_{21} ratio at a fixed galactocentric radius. In our modelling, we choose to disentangle the intrinsic scatter per radial bin from the observational noise, and model the value of the scatter that best describes our data separately.

The observed scatter in R_{21} reflects a combination of statistical and physical scatter. Fortunately, we have accurate estimates of the statistical uncertainties. To estimate the physical scatter, we carry out a forward modelling analysis that leverages this knowledge.

To do this, we assume that the true physical distribution of R_{21} is lognormal. This appears to be a reasonable assumption based on the observed distributions, e.g. in Fig. 1. The lognormal distribution has strictly speaking no physical meaning, but gives a simple representation of the scatter. Then, our modelling process proceeds as follows:

(i) We normalize all measured R_{21} ratios to the median value of the ratio in the distribution.

(ii) We simulate a set of new data. Each data set has a known physical scatter between 0 and 2 dex. We add Gaussian noise to each new data set based on the known observational uncertainties for the measurement in the data set.

(iii) We compare the observed distribution to the simulated distribution and select the simulated data set that best matches our observational data. To selected the best match, we use the Kolmogorov–Smirnov statistics.

(iv) We adopt the physical scatter in the best-matching model distribution as our best estimate of the true physical scatter.

This estimate accounts for the known scatter due to statistical uncertainties, which can be substantial.

APPENDIX C: CALIBRATION UNCERTAINTIES IN HERACLES

In the main text, we emphasize the importance of knowing the calibration uncertainties for accurate R_{21} estimation. Here, we revisit topics related to the calibration of the HERACLES CO(2–1) maps. Table C1 shows the list of sources for which we have complementary CO(2–1) data besides HERACLES.

HERACLES was obtained using the HERA receiver array on the IRAM 30-m telescope (Schuster et al. 2007). HERA consists of two nine-receiver arrays, one for each polarization, for a total of 18 pixels. HERACLES was calibrated using the standard IRAM 30-m chopper wheel calibration and converted from antenna temperature to main beam temperature using best estimates for the IRAM forward and main beam efficiencies. The bandwidth of HERA does not allow observations of a Galactic line calibrator. The overhead to observe a flux calibrator with every pixel during each few-hour observing block was prohibitive.

Measured gain variations: Leroy et al. (2009) assessed the uncertainty in the HERACLES calibration by building maps from different polarizations and observing sessions. By comparing the intensity of bright-point sources, they estimated an overall calibration uncertainty of 20 per cent.

After that, a more rigorous check was added to the HERACLES pipeline to assess the relative flux calibration of the individual receiver pixels. We took the final cube created from all pixels. Then, we took the location of each observation for each individual receiver

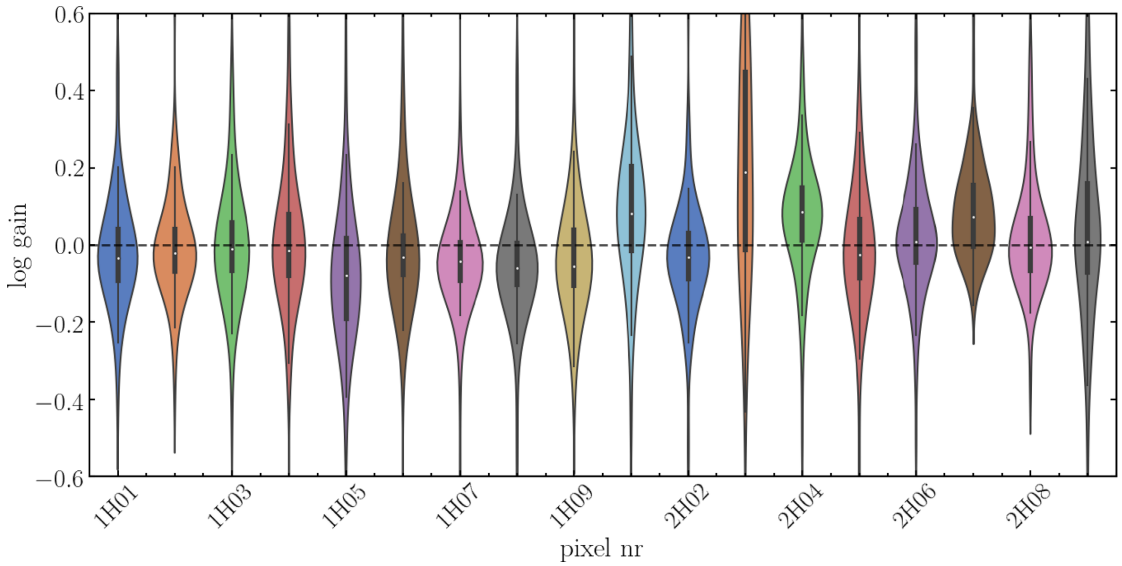

Figure C1. Histograms of log gains per HERA pixel and polarization.

Table C1. Overview of adopted CO(2–1) single dish data sets that we use as complimentary to EMPIRE CO(1–0) for the CO line brightness temperature ratio.

Galaxy	HERA[a]	ALMA[b]	EMIR[c]
NGC 0628	✓	✓	
NGC 2903	✓	✓	
NGC 3184	✓		
NGC 3627	✓	✓	
NGC 4254	✓	✓	
NGC 4321	✓	✓	
NGC 5055	✓		
NGC 5194	✓		✓
NGC 6946	✓		

[a]Part of HERACLES (Leroy et al. 2009).
[b]Part of PHANGS-ALMA-survey (Leroy et al. 2021b).
[c]Part of M51 IRAM 30-m Large Program (den Brok et al., in preparation).

pixel. In this way, we simulated the spectrum that we would expect to observe with that pixel. We compared this expected spectrum to the real observed spectrum for that pixel. Based on this comparison, we calculate the best-fitting multiplicative factor, the 'pixel gain', to match that pixel to the overall cube. The accuracy of the gain measurements is accessible via the χ^2 values obtained from the comparison between simulated and observed spectrum. We measured a gain for each array pixel and observing session, labelling the observing session by the day of the observations.

The measured pixel gain represents the offset in calibration between that pixel and the overall array. This factor does not capture absolute variations in the calibration, it measures how internally well calibrated the pixels are relative to one another.

Fig. C1 shows histograms of the pixel gain for each pixel. We only plot pixel gains with high accuracy, i.e. their χ^2 values lie within $\pm 1\sigma$ of the Gaussian log-χ^2 distribution. Lower signal-to-noise cases typically represent observations of faint galaxies or empty sky and do not contain the signal needed to fit for the pixel gain.

The figure displays that the gain shows typical rms variation of ± 0.10 dex. Some pixels are less stable than others, with the second polarization (HERA2, labelled '2H') showing more scatter than the first polarization.

If the pixel gains were uncorrelated, random, and the coverage of each pixel were spread evenly across the maps, then we expect that the pixel gain uncertainties should average and the calibration uncertainty associated with individual receiver variations would be $\sqrt{18} \approx 4.2$ times lower than the mean individual pixel gain. This represents a lower limit to the calibration uncertainty, which we estimate at ± 0.024 dex or ± 6 per cent.

In fact, the gains do show some correlation, so that there do not appear to be 18 truly independent realizations. As mentioned, the two polarizations often appear offset from one another, with the typical offset on any given day of 0.08 dex.

Based on this, we find an upper and lower limit uncertainty of ± 0.10 and ± 0.024 dex, respectively, corresponding to a flux calibration uncertainty between ± 6 and ± 25 per cent. This will not include any additional terms that are covariant among all pixels, like correction for the atmosphere and beam efficiency effects.

Note that although the HERACLES observing strategy attempted to maximize the number of different pixels observing each part of the sky, local variations in the calibration will be worse due to the fact that not all pixels see all locations.

As an aside, note that we already used these calculated pixel gains to identify and flag the worst receiver-day combinations before producing the maps made publicly available and used in Schruba et al. (2011, 2012), Leroy et al. (2013), and Sandstrom et al. (2013).

Comparisons in Galaxy with two maps: As a more direct, alternative check, we took the overlap between PHANGS-ALMA, HERACLES, and the new IRAM 30-m map of M51 in our sample and directly calculated how these CO(2–1) maps compared to one another (see Figs C2 and C3).

On average, we find consistent results for the mean CO(2–1)/CO(1–0) line ratio when we change the CO(2–1) data set used in the overlapping data set (HERA: $\langle R_{21} \rangle = 0.62 \pm 0.14$; ALMA:

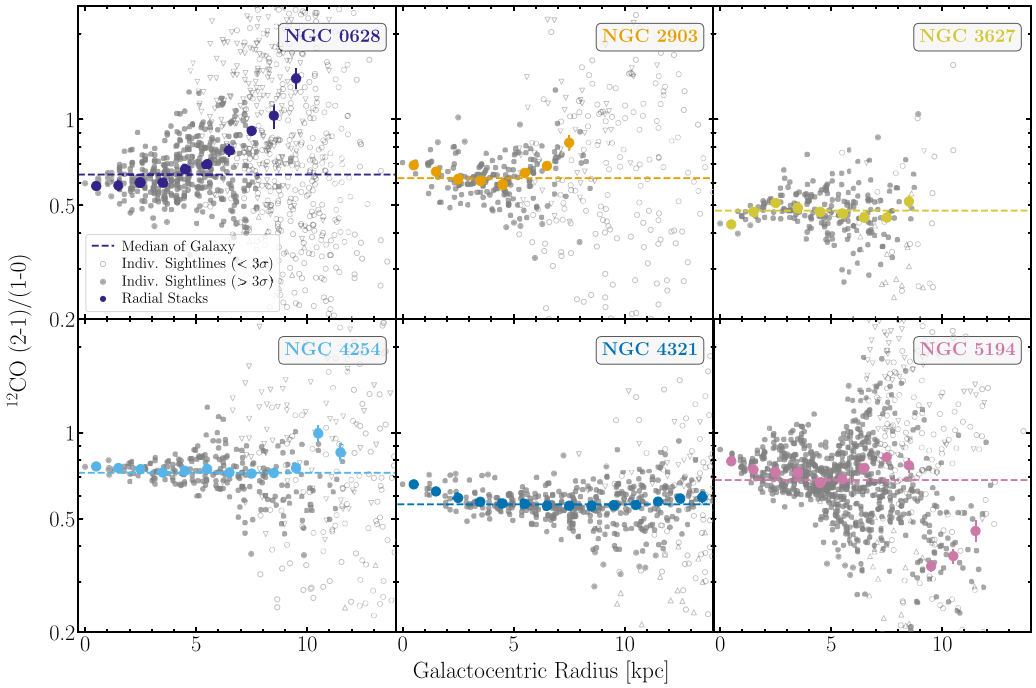

Figure C2. Radial profiles of the CO line brightness temperature ratio, R_{21}, as a function of galactocentric radius for all the galaxies in the EMPIRE sample, similar to Fig. 3. Here, we substituted the CO(2–1) data from HERACLES for ALMA or the new M51 Large Program data. Upper and lower limits of individual sightlines are indicated by upward and downward triangles. We present the stacked values of the ratio per 27 arcsec radial bin. The dashed line gives the mean line ratio within the galaxy.

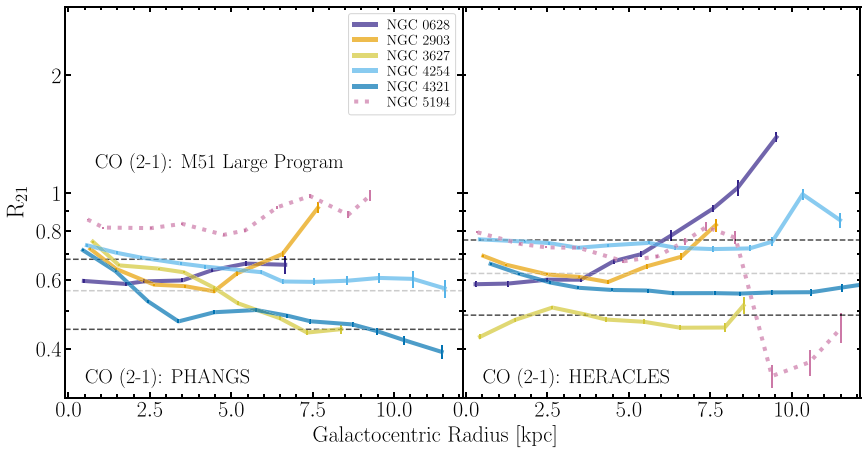

Figure C3. Radial profiles of the CO ratio, R_{21}, as a function of galactocentric radius for all the galaxies in the EMPIRE sample, similar to Fig. 4. The grey, dashed line gives the mean line ratio across all galaxies plotted, while the black, dashed lines indicate the 1σ deviation. For the CO(2–1) data set, HERA data were substituted by ALMA and in the case of NGC 5194 with EMIR 1-mm observations.

$\langle R_{21} \rangle = 0.56 \pm 0.11$). That is, there does not seem to be strong evidence that the overall amplitude scale of HERA is biased relative to ALMA or the new 30-m observations obtained with EMIR.

We do find relatively strong discrepancies in the maps for two galaxies: NGC 3627 and NGC 5194 (see Fig. C4). Compared to the new EMIR map by den Brok (in preparation), the HERACLES map of NGC 5194 is low by a factor of 0.89. Meanwhile the NGC 3627 shows an offset of 0.73 from the ALMA map on average, but also a qualitatively different radial structure.

These were the two earliest galaxies observed with HERA. NGC 5194 was observed as part of commissioning (Schuster et al. 2007) and NGC 3627 as part of a pilot programme that explored the viability of HERACLES. As a result, they did not yet adopt the rotation, cross-scanning, and offset that became part of the later

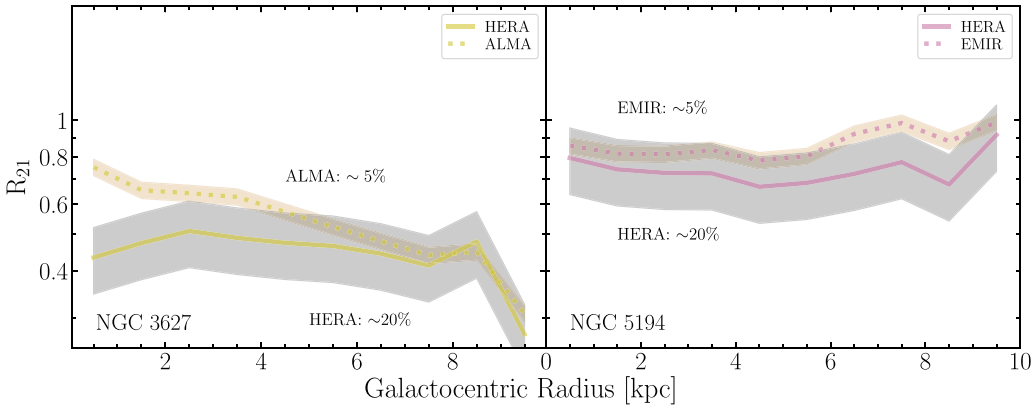

Figure C4. Side-by-side comparison when substituting HERA CO(2–1) with ALMA or EMIR data in the case of NGC 3627 and NGC 5194. The calibrational uncertainties for HERA are estimated to be around 20 per cent (Leroy et al. 2009), while for EMIR (Carter et al. 2012) and ALMA (Bonato et al. 2018) it is around 5 per cent. We note that the HERA maps in particular of NGC 5194 are less reliable, as this constitutes a commission observation under difficult observing conditions. The two cases show the strongest discrepancies when substituting the CO(2–1) data sets.

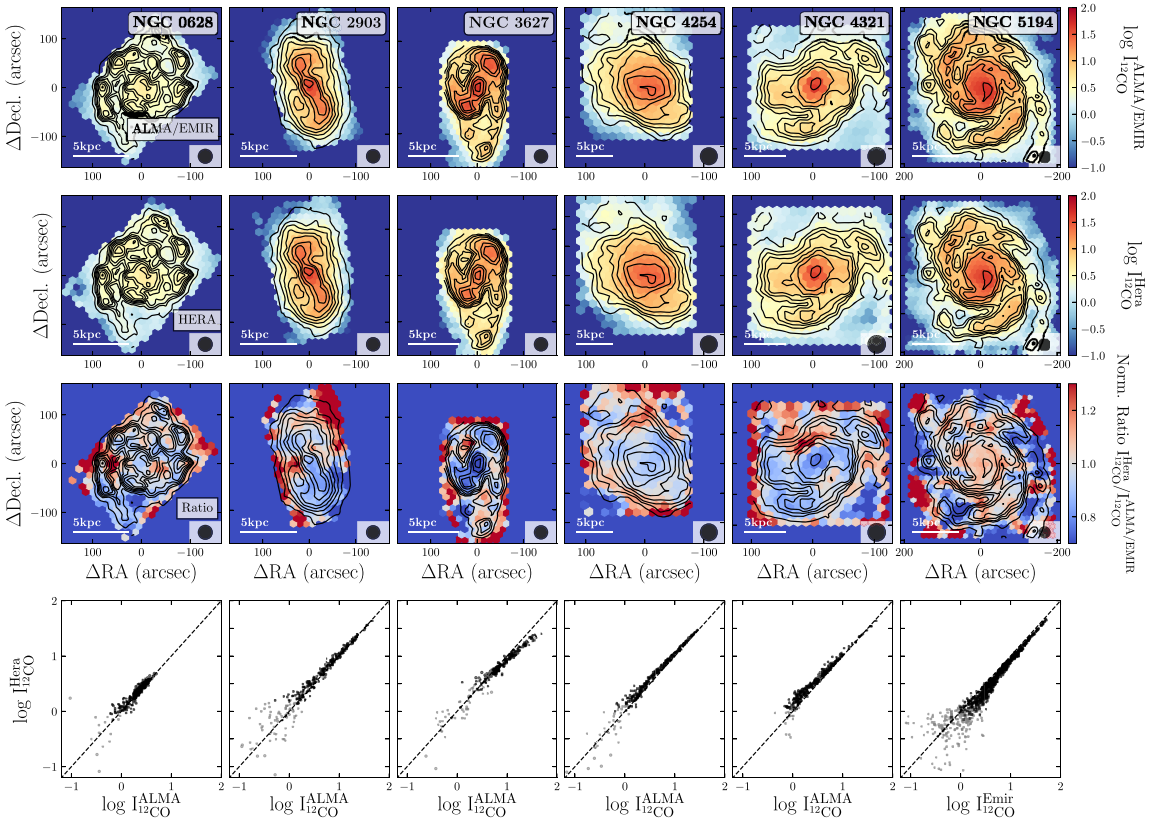

Figure C5. In-depth analysis and comparison of the the sources for which we have two CO(2–1) data sets. The top row shows the latest available CO(2–1) data sets (from ALMA or EMIR in the case of NGC 5194). The second row shows the HERACLES CO(2–1) 2D maps. The third row shows the relative spatial variation of the ratio of the two CO(2–1) observations. In the bottom row, the integrated brightness temperatures of individual sightlines are plotted against each other. The dotted line indicates the 1:1 relation. Black points indicate data points for which both CO(2–1) data are detected with S/N > 3.

HERACLES observing strategy. Our recommendation is that the new EMIR and ALMA maps supersede the HERA data for these targets, and we have adopted this approach in this paper.

For the remaining galaxies with two maps, NGC 628, NGC 2903, NGC 4254, and NGC 4321, we find better agreement. A more detailed comparison is shown in Fig. C5, where the spatial variation in 2D of the ratio of the two different CO(2–1) observations is shown. Overall pairs of CO(2–1) maps mostly show similar morphologies. The global offset in calibration for NGC 3627 and NGC 5194 discussed above is striking. We also see some second-order variations in morphology between the maps, e.g. in the centre of NGC 3627 and NGC 4321. Our best estimate is that these reflect pixel gain variations in HERA, which are inducing second-order local calibration uncertainties.

APPENDIX D: STACKED CO LINE MEASUREMENTS

We apply a stacking technique to improve the S/N when measuring R_{21} as a function of other quantities. This technique is summarized in Section 2.5 and described in more detail by Schruba et al. (2011), Jiménez-Donaire et al. (2017), and Cormier et al. (2018). In Figs D1 and D2, we show one application, the stacked CO(1–0) and CO(2–1) brightness temperature as a function of galactocentric radius in NGC 0628. This illustrates the procedure used to stack other galaxies and to stack by other quantities. It also highlights some of the uncertainty associated with the lowest brightness temperature bins, an issue raised in the main text.

Table D1. Signal-to-noise ratio for the radial stack bins (see Fig. D1 for an example showing the individual radial bins for one galaxy). The median of a given bin over the nine galaxies is taken, as well as the 5 and 95 percentiles. Each radial bin has a width of 1 kpc.

Center radial bin (kpc)	0.5	1.5	2.5	3.5	4.5	5.5	6.5	7.5	8.5	9.5	10.5	11.5
Median SNR	142	110	103	96	89	67	54	40	28	9.5	4.1	10.1
5 perc.	54	60	62	59	63	49	23	20	11	6.5	0.8	0.8
95 perc.	323	215	157	148	97	94	99	78	59	47	36	28

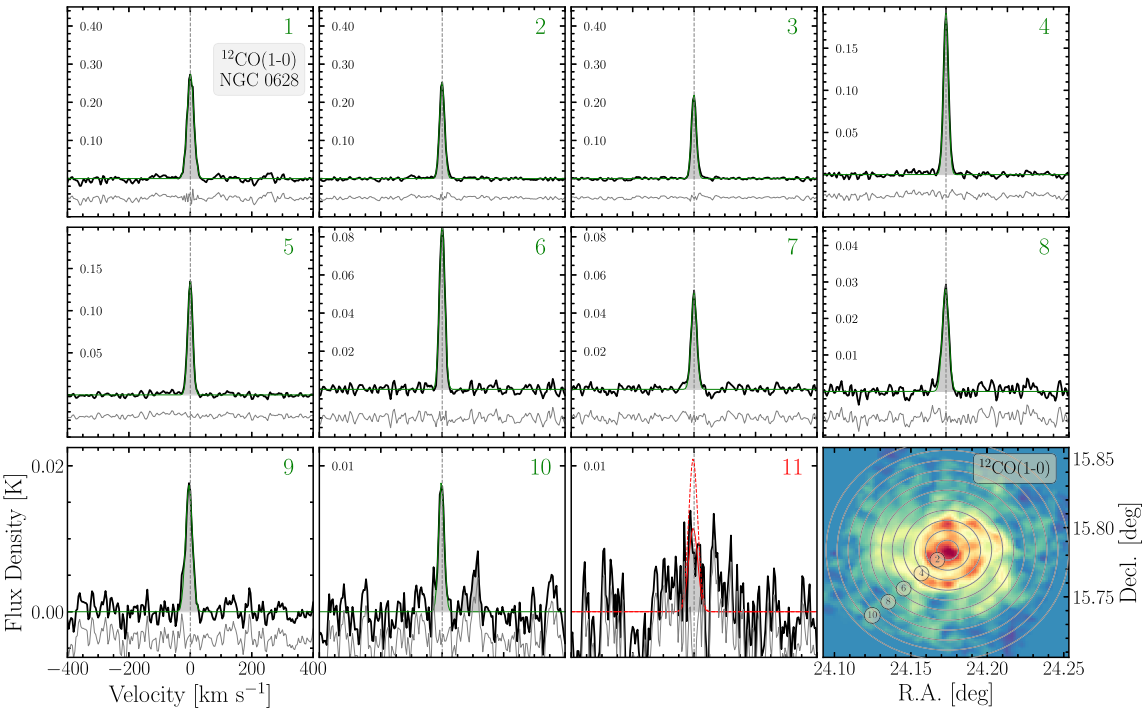

Figure D1. Illustration of spectral stacking. Spectra of CO(1–0) brightness temperature stacked as function of galactocentric radius in NGC 0628. The outer radius, in kpc, of each kpc-wide ring is given in the top right corner, with the colour indicating whether the line peak has S/N > 5 (green) or not (red). Shaded area shows the region over which we integrate to determine the line flux. The light grey dotted line indicates $v = 0\,\mathrm{km\,s^{-1}}$ position. The bottom right panel illustrated the rings used for the stack.

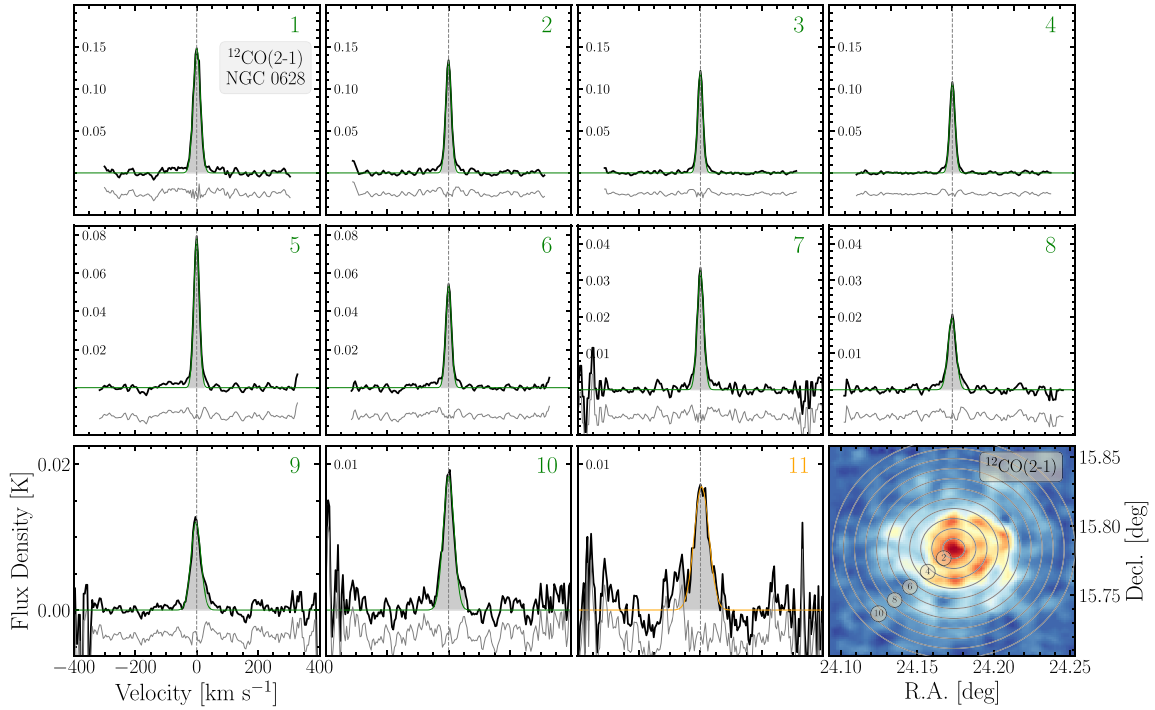

Figure D2. Illustration of spectral stacking**.** As Fig. D1 but now showing the CO(2-1) line stacked in bins of galactocentric radius.

Both figures show that stacked by the local H I velocity produced high signal-to-noise ratio, coherent spectra out to ∼10 kpc. The grey region shows the integration area used to determine the integrated brightness temperature. This clearly corresponds to all real astrophysical signal out to 9 kpc, with the algorithm used to identify the line width doing a good job.

Outside 9 kpc, we begin to see some breakdowns in the approach. In the 10th radial bin, which covers $r_{\rm gal}$ = 9–10 kpc, the CO(1–0) spectrum includes a second, fainter, CO(1–0) emission peak to the right of the main emission line. This second peak appears displaced by approximately 100 km s^{-1} from the main peak. This could represent a noise spike, a problem with the H I velocity field, a problem with baseline subtraction, or real signal. No analogous feature appears in the CO(2–1) spectrum. In this case, we manually extended the integration range to cover the additional emission line, but the profile becomes uncertain in this bin. This uncertainty is higher than the statistical uncertainty. In the next panel, we see that by 10–11 kpc, uncertainties in the baseline produce large 'ripples' in the spectrum for both CO(1–0) and CO(2–1). Though formally the S/N of the data remain high (there is extended emission over a large velocity range), these results remain uncertain.

These sorts of systematic uncertainties tend to crop up in the outer parts of the binned data. These breakdowns in the stacking procedure and baseline uncertainties contribute to some of the scatter in profiles at low intensity but are not necessarily reflected in the statistical scatter.

APPENDIX E: AZIMUTHAL R_{21} VARIATION IN NGC 5194

In this study, we investigated the spatial variation of the CO line brightness temperature ratio across the full discs of the galaxies. The source NGC 5194 is not only unique in the sense that it shows strong differences between the arm and interarm regions, but the trend we find disagrees with a previous study by Koda et al. (2012). We find larger R_{21} values (∼0.9–1) in the interarm region compared to the molecular arm region (∼0.7–0.8). This trend stands in contrast to the one reported in Koda et al. (2012). Here, we investigate the origin of the discrepancy. As we used different observations than the previous study, it is essential to determine, which data set causes the discrepancy. In particular, we used CO(1–0) observations from the PAWS survey (Pety et al. 2013) and CO(2–1) observations from the M51 Large Program (den Brok et al., in preparation). Koda et al. (2012) on the other hand used CO(1–0) observations from NRO (Koda et al. 2011) and CO(2–1) observations from HERACLES (Leroy et al. 2009).

To properly analyse the azimuthal variation, we followed the same procedure as described in Koda et al. (2012) to determine the variation of R_{21} as a function of the spiral phase. Fig. E1 shows (left-hand panel) the result, where we looked at the line ratio using all possible permutations of the CO(1–0) (PAWS and NRO) with CO(2–1) (M51 LP and HERACLES) data sets. All observations were convolved to a common resolution of 24 arcsec. The red and blue hashed regions indicate the location of the spiral arm, as given in Koda et al. (2012) (see also right-hand panel of Fig. E1; molecular arm: blue, ψ = 60–100° and 230–270°; leading edge: red, ψ = 80–120° and 250–290°). Note that the *y*-axis shows the normalized line

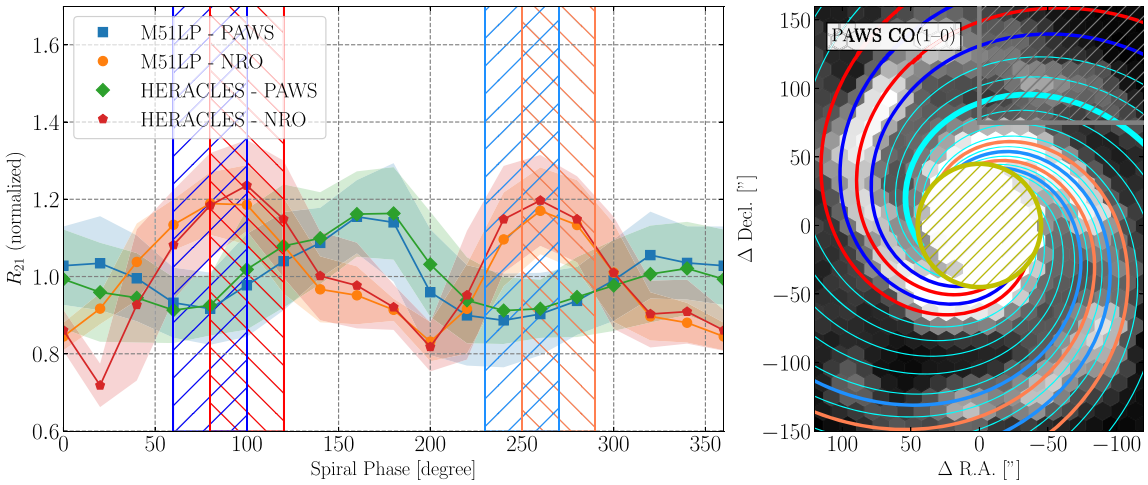

Figure E1. Normalized CO line ratio as function of spiral phase. We follow the spiral phase analysis of the integrated CO line brightness temperature ratio, as described in Koda et al. (2012), to study the azimuthal variation. (*Left-hand panel*) Here, we show all four permutations of the two different CO data sets for both transitions. Each line ratio is normalized by the corresponding mean. The shaded area shows the standard deviation of the line ratio binned by spiral phase. The blue, hashed band shows the molecular arm and the red, hashed band indicates the trailing star-forming arm, as provided by Koda et al. (2012). It is evident, that upon changing the CO(1–0) data set (PAWS versus NRO), the trend of the line ratio changes, while changing the CO(2–1) data sets (M51 LP versus HERACLES), has no effect. (*Right-hand panel*) The CO(1–0) brightness temperature map showing the PAWS data. The spiral phases are plotted in increments of 20°. Points within the central hashed inner 45 arcsec area as well as the hashed region in the north-west are excluded from the spiral phase bins. We applied an S/N = 10 threshold.

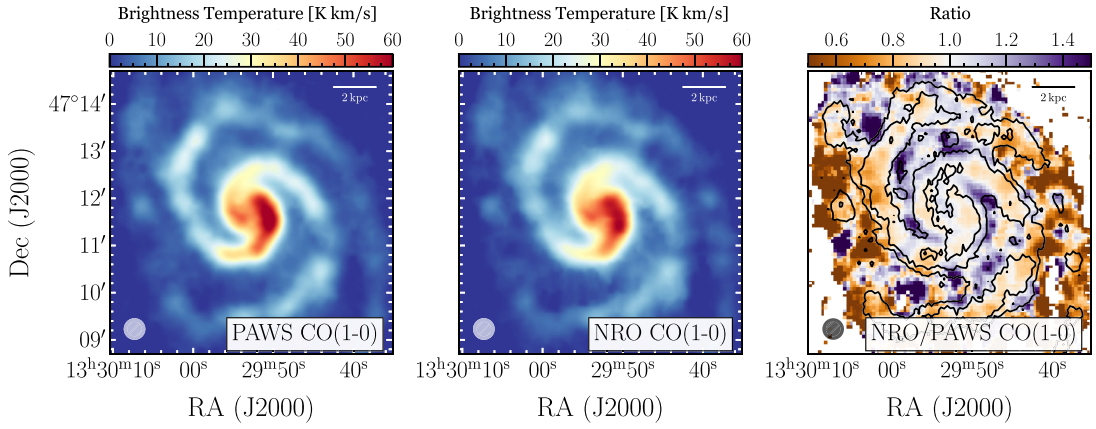

Figure E2. CO(1–0) line brightness temperature maps. Side-by-side comparison of (*left*) the PAWS CO(1–0) line brightness temperature map (Pety et al. 2013) and (*right*) the NRO 45-m map (from Koda et al. 2011). Both show similar line brightness temperature values, but the NRO map shows a weaker contrast between arm and interarm region (especially at the position of the outer arms), which we believe causes the discrepancy in the azimuthal line brightness temperature trend discussed in Section 3.3 and Appendix E. Both maps were created by integrating the full cube over the same masked velocity range. (*right*) The ratio of the CO(1–0) line of the NRO map and the PAWS map. The contours are drawn at S/N = 20, 40, and 100 of the PAWS CO(1–0) map. The discrepancy is strong in the interarm region, where the ratio is clearly >1.

ratio. It is evident from this plot, that the discrepancy is caused by the use of a different CO(1–0) data set. Substituting the CO(2–1) HERACLES data with the M51 LP observations does not change the azimuthal trend at all. Fig. E2 shows the two different CO(1–0) maps side by side. The left-hand panel shows the PAWS brightness temperature map, while the map on the right illustrates the NRO map. The NRO map has a native resolution of 19.7 arcsec. For the comparison, we convolved it to the resolution of the PAWS CO(1–0) map at 24 arcsec. We integrated both the NRO and PAWS cube over the same velocity range. Already from visual inspection, it is evident that the contrast between arm and interarm is higher in the PAWS than in the NRO map (especially for the position of the outer arms). The discrepancy can be caused by inproper error beam handling, different or unstable T_{sys}, variable S/N, or scanning artefacts. To investigate the exact cause for the discrepancy is beyond the scope of this project.

This paper has been typeset from a TEX/LATEX file prepared by the author.

APPENDIX B

CLAWS Survey Paper

The paper *den Brok et al. A&A (2022), 662, A89* is reproduced below in its original form with permission by ESO.

A&A 662, A89 (2022)
https://doi.org/10.1051/0004-6361/202142247

Astronomy & Astrophysics

A CO isotopologue Line Atlas within the Whirlpool galaxy Survey (CLAWS)

Jakob S. den Brok[1], Frank Bigiel[1], Kazimierz Sliwa[2], Toshiki Saito[2,3,4], Antonio Usero[5], Eva Schinnerer[2], Adam K. Leroy[6], María J. Jiménez-Donaire[5,7], Erik Rosolowsky[8], Ashley T. Barnes[1], Johannes Puschnig[1], Jérôme Pety[9,10], Andreas Schruba[11], Ivana Bešlić[1], Yixian Cao[11], Cosima Eibensteiner[1], Simon C. O. Glover[12], Ralf S. Klessen[12,13], J. M. Diederik Kruijssen[14], Sharon E. Meidt[15], Lukas Neumann[1], Neven Tomičić[16], Hsi-An Pan[2,17], Miguel Querejeta[5], Elizabeth Watkins[14], Thomas G. Williams[2], and David Wilner[18]

[1] Argelander-Institut für Astronomie, Universität Bonn, Auf dem Hügel 71, 53121 Bonn, Germany
e-mail: jdenbrok@astro.uni-bonn.de
[2] Max-Planck-Institut für Astronomie, Königstuhl 17, 69117 Heidelberg, Germany
[3] Department of Physics, General Studies, College of Engineering, Nihon University, 1 Nakagawara, Tokusada, Tamuramachi, Koriyama, Fukushima, 963-8642, Japan
[4] National Astronomical Observatory of Japan, 2-21-1 Osawa, Mitaka, Tokyo 181-8588, Japan
[5] Observatorio Astronómico Nacional (IGN), C/ Alfonso XII 3, 28014 Madrid, Spain
[6] Department of Astronomy, The Ohio State University, 4055 McPherson Laboratory, 140 West 18th Avenue, Columbus, OH 43210, USA
[7] Centro de Desarrollos Tecnológicos, Observatorio de Yebes (IGN), 19141 Yebes, Guadalajara, Spain
[8] 4-183 CCIS, University of Alberta, Edmonton, Alberta T6G 2E1, Canada
[9] Institut de Radioastronomie Millimétrique (IRAM), 300 Rue de la Piscine, 38406 Saint Martin d'Hères, France
[10] LERMA, Observatoire de Paris, PSL Research University, CNRS, Sorbonne Universités, 75014 Paris, France
[11] Max-Planck-Institut für extraterrestrische Physik, Giessenbachstraße 1, 85748 Garching, Germany
[12] Universität Heidelberg, Zentrum für Astronomie, Institut für Theoretische Astrophysik, Albert-Ueberle-Str 2, 69120 Heidelberg, Germany
[13] Universität Heidelberg, Interdisziplinäres Zentrum für Wissenschaftliches Rechnen, Im Neuenheimer Feld 205, 69120 Heidelberg, Germany
[14] Astronomisches Rechen-Institut, Zentrum für Astronomie der Universität Heidelberg, Mönchhofstraße 12–14, 69120 Heidelberg, Germany
[15] Sterrenkundig Observatorium, Universiteit Gent, Krijgslaan 281 S9, 9000 Gent, Belgium
[16] INAF-Osservatorio Astronomico di Padova, Vicolo Osservatorio 5, 35122 Padova, Italy
[17] Department of Physics, Tamkang University, No.151, Yingzhuan Rd., Tamsui Dist., New Taipei City 251301, Taiwan
[18] Center for Astrophysics | Harvard & Smithsonian, 60 Garden St., Cambridge, MA 02138, USA

Received 17 September 2021 / Accepted 22 December 2021

ABSTRACT

We present the CO isotopologue Line Atlas within the Whirpool galaxy Survey (CLAWS), which is based on an IRAM 30 m large programme that provides a benchmark study of numerous faint CO isotopologues in the millimetre-wavelength regime across the full disc of the nearby grand-design spiral galaxy M 51 (NGC 5194). The survey's core goal is to use the low-J CO isotopologue lines to constrain CO excitation and chemistry, and therefrom the local physical conditions of the gas. In this survey paper, we describe the CLAWS observing and data reduction strategies. We map the $J = 1 \rightarrow 0$ and $2 \rightarrow 1$ transitions of the CO isotopologues ^{12}CO, ^{13}CO, C^{18}O, and C^{17}O, as well as several supplementary lines within the 1 mm and 3 mm window (CN (1−0), CS (2−1), CH_3OH (2−1), N_2H^+ (1−0), and HC_3N (10−9)) at ∼1 kpc resolution. A total observation time of 149 h offers unprecedented sensitivity. We use these data to explore several CO isotopologue line ratios in detail, study their radial (and azimuthal) trends, and investigate whether changes in line ratios stem from changes in interstellar medium properties such as gas temperatures, densities, or chemical abundances. For example, we find negative radial trends for the ^{13}CO/^{12}CO, C^{18}O/^{12}CO, and C^{18}O/^{13}CO line ratios in their $J = 1 \rightarrow 0$ transitions. We also find variations with the local environment, such as higher ^{12}CO (2−1)/(1−0) or ^{13}CO/^{12}CO (1−0) line ratios in interarm regions compared to spiral arm regions. We propose that these aforementioned variations in CO line ratios are most likely due to a variation in the optical depth, though abundance variations due to selective nucleosynthesis on a galaxy-wide scale could also play a role. We also study the CO spectral line energy distribution (SLED) using archival JCMT ^{12}CO (3−2) data and find a variation in the SLED shape with local environmental parameters, suggesting changes in the optical depth, gas temperatures, or densities.

Key words. galaxies: ISM – ISM: molecules – radio lines: galaxies

A&A 662, A89 (2022)

1. Introduction

A key to our understanding of the interstellar medium (ISM) and its chemical evolution is the study of emission from carbon monoxide (CO), the second most abundant molecule after H_2, and its isotopologues. Such isotopologue studies allow us to examine the physical conditions within the gas, study the enrichment of the ISM, and open up the potential of deciphering the star formation history of a galaxy. Due to CO's permanent dipole moment and low mass, it has low-energy rotational transitions. Consequently, the emission from these rotational transitions is excited and can be observed at low temperatures (<10 K) – unlike for H_2, which is hardly excited and thus not observable under typical ISM conditions. While the low-J CO transitions of the main isotopologue, ^{12}CO, are known to be optically thick, a relation of their emission with the molecular gas mass has been found via the CO-to-H_2 conversion factor, α_{CO} (e.g. Solomon et al. 1987; Nakai & Kuno 1995; Leroy et al. 2011a; Sandstrom et al. 2013; or see review by Bolatto et al. 2013).

The ^{12}CO line brightness temperature ratios between different rotational transitions are generally of great interest. High-z observations typically observe higher-J ^{12}CO lines (Carilli & Walter 2013). By assuming line ratios, such studies can calculate an equivalent ^{12}CO (1–0) brightness temperature (e.g. Tacconi et al. 2008; Genzel et al. 2012; Cañameras et al. 2018) and then convert to physical parameters, such as the molecular gas mass, using α_{CO}. Such studies often adopt CO line ratios and a CO-to-H_2 conversion factor measured in the local universe (e.g. Tacconi et al. 2008; Schruba et al. 2012; Sandstrom et al. 2013, see also reviews by Solomon & Vanden Bout 2005; Carilli & Walter 2013). However, recent studies find variations in the line ratio within and among nearby spiral galaxies (den Brok et al. 2021; Yajima et al. 2021; Leroy et al. 2022), which have consequences for the down-conversion of high-J CO transitions and the conversion to ISM physical parameters. Such variations are also expected from simulations. Modelling individual giant molecular clouds, Peñaloza et al. (2018) found variations in the ^{12}CO line brightness temperature ratios of order 0.3 dex and attributed these changes to varying environmental conditions, including cloud mass and density, the interstellar radiation field (ISRF), and the cosmic ray ionisation rate (CRIR). Furthermore, the CO-to-H_2 conversion factor itself is subject to environmental variations (e.g. Young & Scoville 1982; Sandstrom et al. 2013; Accurso et al. 2017; see also simulations, e.g. Shetty et al. 2011a,b; Gong et al. 2018, 2020). The value for α_{CO} is empirically calibrated using many Milky Way clouds (Solomon et al. 1987), from CO, H I, and dust mass observations in external galaxies (Sandstrom et al. 2013), or using [C II] emission (Madden et al. 2020). When comparing α_{CO} to other galaxies, the metallicity, the presence of CO-dark gas, and temperature variations relative to the Milky Way should be taken into account. Thus, it is important to constrain variations in the CO line ratio and conversion factor and understand their dependences on the galactic environment and ISM conditions.

CO isotopologue transitions help us study the conditions of the ISM. Whereas the low ^{12}CO transitions usually remain optically thick, C^{18}O and C^{17}O lines stay optically thin over large parts of the galaxy. By contrast, the ^{13}CO emission can be optically thin or have a moderate optical depth, depending on its relative abundance (see the review by Heyer & Dame 2015). Comparing two optically thick lines provides insight into the physical conditions of the emitting gas, such as its temperature or density (Leroy et al. 2017; Jiménez-Donaire et al. 2019; den Brok et al. 2021). Contrasting optically thin to optically thick lines allows us to analyse the optical depth of the gas and investigate the gas column and volume densities of the molecular gas (Young & Scoville 1982; Pineda et al. 2008; Wilson et al. 2009). Finally, studying the ratio of two optically thin lines can be used to study abundance variations within the Milky Way (Langer & Penzias 1990; Milam et al. 2005) or across galaxy discs (Jiménez-Donaire et al. 2017b).

The study of CO isotopologues can also be used to investigate the chemical enrichment of the molecular gas. C and O isotopes – and consequently CO isotopologues – are a direct byproduct of stellar evolution via the CNO cycle. By studying their abundances, the physical processes that generate the various CO isotopologue species can be analysed. For instance, the ^{13}C isotope is primarily produced in low-mass stars (Wilson & Rood 1994), while ^{18}O is mainly replenished due to massive stars (Henkel et al. 1994). This makes the CO isotopologues a useful diagnostic tool for studying stellar populations (Sliwa et al. 2017; Sliwa & Downes 2017; Zhang et al. 2018; Brown & Wilson 2019). Previous studies of CO isotopologues and other C, N, and O isotope ratios have already been extensively carried out for the Milky Way (Langer & Penzias 1990; Wilson & Matteucci 1992; Wilson & Rood 1994; Henkel et al. 1994; Milam et al. 2005). The past decade has also seen an increase in the study of CO isotopologues in extragalactic sources (Martín et al. 2010; Henkel et al. 2014; Meier et al. 2015; Cao et al. 2017; Jiménez-Donaire et al. 2017a,b, 2019; den Brok et al. 2021; Yajima et al. 2021).

The low-J ^{12}CO transitions produce the brightest molecular lines (e.g. at 30 arcsec, we find brightness temperatures of around 60 K km s^{-1} in the centre of M 51) and consequently have been covered in numerous previous studies carried out with the Institut de Radioastronomie Millimétrique (IRAM) 30 m telescope, the IRAM Northern Extended Millimeter Array (NOEMA), the Atacama Large Millimeter/submillimeter Array (ALMA), and other millimetre-wavelength observatories (Hasegawa et al. 1997; Hasegawa 1997; Sakamoto et al. 1997; Leroy et al. 2009; Koda et al. 2011, 2020). CO isotopologue ratios are harder to observe since, due to their lower abundance, the emission is of order ~10 and ~50 times fainter for ^{13}CO and C^{18}O, respectively, compared to the ^{12}CO emission. Therefore, in the past these transitions were usually either studied in the Milky Way (Langer & Penzias 1990; Wilson & Rood 1994; Sawada et al. 2001; Yoda et al. 2010) or in strongly active star-forming galaxies, such as starburst galaxies or ultra-luminous infrared galaxies (ULIRGs; Meier & Turner 2004; Costagliola et al. 2011; Aladro et al. 2013; Sliwa et al. 2017; Brown & Wilson 2019). Only in recent years, thanks to the advancement of state-of-the-art receivers and large programmes, have we seen an increase in CO isotopologue line surveys of star-forming spiral galaxies.

The EMIR Multiline Probe of the ISM Regulating Galaxy Evolution (EMPIRE) survey targeted nine galaxies and covered the ^{13}CO and C^{18}O $J = 1 \rightarrow 0$ transitions (Jiménez-Donaire et al. 2019). It has been found, for example, that the ^{13}CO to C^{18}O line ratio is much lower in ULIRGs and star-bursting systems than compared to the Milky Way or nearby normal star-forming galaxies (Greve et al. 2009; Matsushita et al. 2009; Jiménez-Donaire et al. 2017b; Brown & Wilson 2019), consistent with recent or ongoing star formation as well as a top-heavy stellar initial mass function (Brown & Wilson 2019). Furthermore, Cormier et al. (2018) used the optically thin ^{13}CO (1–0) line from EMPIRE to derive a spatially resolved ^{13}CO-to-H_2 conversion factor for nearby galaxies.

With the CO Isotopologue Line Atlas within the Whirlpool galaxy Survey (CLAWS), we use the IRAM 30 m telescope to provide an in-depth analysis of low-J transitions of CO and

several isotopologues (^{13}CO, C^{18}O, and C^{17}O) over the entire star-forming and molecular disc (6.6 arcmin × 6.6 arcmin) of the grand-design spiral galaxy M 51 (NGC 5194). Due to its relative proximity (D = 8.6 Mpc; McQuinn et al. 2016) and high surface density, it is routinely observed from high-energy X-ray to radio wavelengths, thus providing a wealth of ancillary data. Previous wide field-of-view imaging observations have targeted different low-J ^{12}CO and ^{13}CO emission line transitions (e.g. Koda et al. 2011; Pety et al. 2013; Schinnerer et al. 2013 as part of PAWS; Jiménez-Donaire et al. 2019 as part of EMPIRE) and even C^{18}O was observed towards a few bright regions inside M 51 (see Schinnerer et al. 2010; Tan et al. 2011; Watanabe et al. 2014, 2016). We complement these studies and provide the currently most complete extragalactic CO isotopologue line atlas.

The main goal of this project is to use the large number of CO isotopologues to study the dependence of excitation on galactic environment and investigate isotopic abundance variations. In addition, we use the CO isotopologues to constrain the spatial variation in the CO-to-H_2 conversion factor.

This paper is organised as follows: In Sect. 2, we present and describe the IRAM 30 m observations as well as the ancillary data that are used in this paper. Section 3 explains how we convert observational measurements to physical quantities. The main results of the paper, which include the different CO line ratios as well as their spatial variations, are presented in Sect. 4. Finally, Sect. 5 discusses our findings and provides an outlook on future projects that can be conducted with the data from this project.

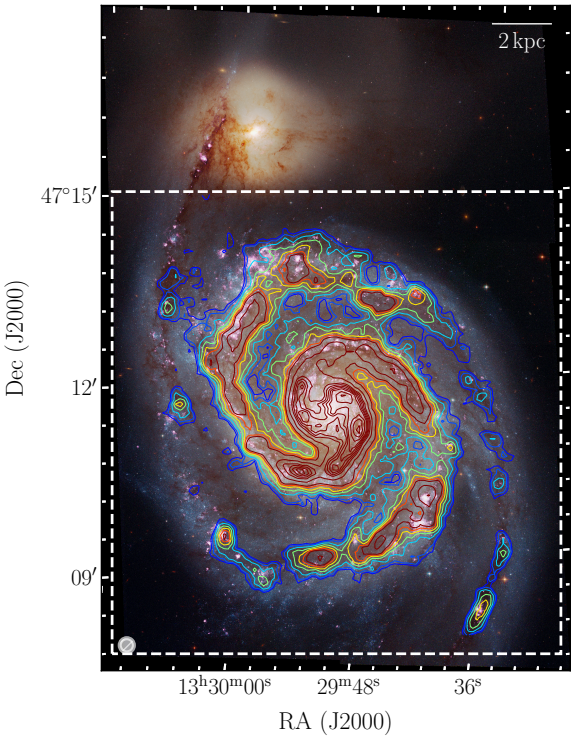

Fig. 1. Red, green, and blue (RGB) image of M 51 with ^{12}CO emission, a colour HST plate composed of B, V, and I filter images taken from Mutchler et al. (2005). Overlaid as contours are the IRAM 30 m ^{12}CO (2−1) integrated line brightness temperatures (at a resolution of 13 arcsec, indicated by the circle in the lower-left corner). The contours show signal-to-noise levels from 8 to 70, from blue to brown. The beam size of the ^{12}CO (2−1) observations is indicated at the bottom left of the figure. The dashed region shows the field-of-view of the IRAM 30 m observations.

2. Observations and data reduction

2.1. Target

M 51 (NGC 5194) is a prime target for the study of faint CO isotopologues in extragalactic systems. With a distance of $D \approx 8.6$ Mpc (McQuinn et al. 2016) – so an angular scale of 1 arcsec corresponds to physical scale of ∼40 pc – it is one of the brightest nearby grand-design spiral galaxies. It is a tidally interacting, active star-forming galaxy, with the molecular gas dominating the inner ∼5−6 kpc (Schuster et al. 2007; Leroy et al. 2008) Furthermore, the galaxy hosts an active galactic nucleus (Querejeta et al. 2016). Figure 1 shows the galaxy in the optical using a *Hubble* Space Telescope (HST) image. The ^{12}CO (2−1) emission observed as part of this programme is overlaid. The galaxy is close-to face on (i = 22°; Colombo et al. 2014) and the target's key parameters are listed in Table 1. M 51 is a template for active star-forming galaxies, where we can resolve discrete environments, know molecular cloud properties (e.g. from PAWS; Colombo et al. 2014) and have a wealth of ancillary data and observations from all wavelength regimes. The ancillary data used in this study are provided and described in the following sections.

2.2. Observations

As part of an IRAM 30 m large programme (#055-17), the EMIR receiver was used to map emission lines in the 1 mm (220 GHz) and 3 mm (100 GHz) windows in dual polarisation from the entire disc of M 51 for a total of 149 h (109.2 h on-source time) between 2017 and 2019. The receiver has an instantaneous bandwidth of 15.6 GHz per polarisation. The observations were split into two parts by implementing E90 LO/LI + UI/UO (Setup 1) as well as E230 LO/LI + UI/UO (Setup 2). The first setup covers the 3 mm range and was carried out under good atmospheric conditions (1.8 mm of precipitable water vapour (pwv) and mean $T_{\rm sys}$ = 111 K [$T_{\rm a}^{\star}$]). The total on-source time accumulated to 65.9 h. The second setup observes $J = 2 \rightarrow 1$ lines in the 1 mm regime. For this setup, good winter conditions were required (1.7 mm pwv and $T_{\rm sys}$ = 217 K [antenna temperature $T_{\rm a}^{\star}$] mean) and the final total on-source time amounted to 43.3 h. The fast Fourier transform spectrometers with 195 kHz spectral resolution (FTS200) were used for both setups to provide a spectral resolution of ∼0.5 km s^{-1} for the E090 and ∼0.2 km s^{-1} for the E230 band. Table 2 lists the lines covered.

A field of 6.6 arcmin × 6.6 arcmin (around 44 arcmin^2) was mapped in the on-the-fly–position switching (OTF-PSW) mode and included two emission-free reference positions nearby. The mapping approach is similar to the one used in the EMPIRE survey (see Jiménez-Donaire et al. 2019). For each spectral setup, a scan of 8 arcsec s^{-1} is performed using multiple paths that are each offset by 8 arcsec from each other. For each execution of the mapping script, the scanned box is shifted by $\sqrt{2} \times (0, 2, 4, 6)$ along the diagonal. So in the end, M 51 is covered with a much finer, 2 arcsec instead of 8 arcsec, grid. The read-out dump time is 0.5 s, the final spacing between data points is 4 arcsec. The focus of the telescope was determined using observations of bright quasars or planets at the beginning of each observation

A&A 662, A89 (2022)

Table 1. M 51 source description.

Property	Value
Name	NGC 5194 (M 51)
RA (J2000) [(a)]	$13^{h}29^{m}52\overset{s}{.}7$
Dec (J2000) [(a)]	47°11′43″
i [(b)]	22°
PA [(c)]	172°
r_{25} [(d)]	3.9′
D [(e)]	8.6 Mpc
$V_{\rm hel}$ [(f)]	456.2 km s^{-1}
Metallicity [(g)] [12 + log(O/H)]	8.55
Morphology [(h)]	SAbc
$\langle\Sigma_{\rm SFR}\rangle$ [(i)]	20×10^{-3} $M_\odot$ yr^{-1} kpc^{-2}
$\log_{10}(M_\star/M_\odot)$ [(j)]	10.5

Notes. [(a)]Coordinates of the centre of the galaxy adopted from the NASA Extragalactic Database (NED) from Shetty et al. (2007). [(b)]Inclination of the galaxy with respect to the plane of the sky from Colombo et al. (2014). [(c)]Position angle of the galaxy. [(d)]25th magnitude isophote radius of the B-band taken from the Extragalactic Distance Database (EDD; Tully et al. 2009). [(e)]Distance to the galaxy from McQuinn et al. (2016). [(f)]Heliocentric systemic velocity from Walter et al. (2008). [(g)]Metallicity averaged across the full galaxy from Moustakas et al. (2010). [(h)]Morphological type as given in Leroy et al. (2013). Adopted from Dale et al. (2009). [(i)]The average SFR surface density within $0.75r_{25}$. [(j)]Integrated stellar mass derived from 3.6 µm emission.

session, which had typical lengths of 2−3 h. In the case of longer sessions, the focus was corrected every 3 h, and in addition after sunset and sunrise. Every 1−1.5 h, the pointing of the telescope was adjusted using either a nearby quasar or planet. In order to properly perform the antenna temperature ($T_{\rm a}^\star$) calibration, a chopper-wheel calibration was done repeatedly every 10−15 minutes using a hot- and a cold-load absorber and sky measurements. Finally, line calibrators (IRC+10216, W3OH, and W51D) were routinely observed to monitor systematic error in amplitude and the flux calibration.

2.3. Data reduction

The data reduction was performed automatically using the scripts and pipeline used for the EMPIRE survey (see description in Jiménez-Donaire et al. 2019). Basic calibration was done using `MRTCAL`[1]. The first step consists of converting the spectrum to the antenna temperature scale. For this, each science scan is combined with the last previous calibration scan. Next, we subtract from the calibrated spectrum the OFF measurement. These steps constitute the most basic calibration. The target lines are then extracted using the Continuum and Line Analysis Single-dish Software (`CLASS`[2]). A zeroth-order baseline is subtracted, omitting the range of 50–300 km s^{-1} around the centre of the line in the fit. The individual spectra are then re-gridded to have a 4 km s^{-1} channel width across the full bandpass. The spectra are saved as FITS files for further processing.

In order to monitor the stability of the flux calibration, the spectra of line-calibrator sources (e.g. IRC+10216) were further obtained. From these we find a maximum day-to-day variation in amplitude of ∼7.5% over all observations. The 1σ variation is ∼2.4% only.

Subsequent data reduction is performed using a custom `IDL` routine based on the HERA CO-Line Extragalactic Survey (HERACLES) data reduction pipeline (Leroy et al. 2009). This routine removes pathological data such as bad scans or spectra. Platforming correction at the edges of the FTS units is also corrected for in the EMPIRE pipeline. The baseline fitting is performed again excluding a generous line window using the ^{12}CO (1−0) line emission from PAWS as a prior: Around the mean ^{12}CO (1−0) velocity, a window is placed, the full width of which ranges between 50 and 300 km s^{-1} depending on the width of the line for each pixel. Two further windows of the same width are defined adjacent to the central window and a second-order polynomial fit of the baseline is performed in these windows. The resulting baseline is subtracted from the entire spectrum.

After these steps, we check for further pathological spectra. These are rejected by sorting the remaining spectra by their rms, which is calculated from the line-free windows after the baseline subtraction, and the highest 10% are rejected. Upon careful inspection by eye, additional spectra were discarded if they showed platforming or other potential issues.

The antenna temperature scale ($T_{\rm a}^\star$) is converted to main beam temperature ($T_{\rm mb}$) using a cubic interpolation of the forward ($F_{\rm eff}$) and beam ($B_{\rm eff}$) efficiencies from the IRAM documentation[3] as a function of the observing frequency. In particular, the conversion is performed using the following equation:

$$T_{\rm mb} = \frac{F_{\rm eff}}{B_{\rm eff}} T_{\rm a}^\star. \quad (1)$$

The $F_{\rm eff}/B_{\rm eff}$ ratio adopted for our observing programme was 1.2 for Setup 1 (3 mm regime) and 1.6 for Setup 2 (1 mm regime). In this study, we exclusively use the main beam temperature $T_{\rm mb}$.

The final data cube is generated by gridding the spectra onto a 2 arcsec spaced Cartesian grid. Consequently, the final resolution is coarser than the IRAM 30 m native resolution due to the gridding kernel by a factor of 1.2.

We do not correct for the contribution from the IRAM 30 m error beam to the observed main beam temperature. We discuss this effect in Appendix A. In short, emission can enter our detection via the telescope's error beam, thus increasing the observed flux. Regions with faint emission in the galaxy are most likely affected by this. The exact shape of the IRAM 30 m error beam is difficult to determine and it fluctuates depending on the telescope's elevation. Consequently, we can only estimate the impact. We see that in the 3 mm regime, the contribution leads to an additional 10% increase in flux in faint regions. In the 1 mm regime, the impact is larger with a contribution of up to 30 to 40% in certain regions. For a more detailed discussion of the estimation of error beam contributions, we refer the reader to Appendix A.

2.4. Ancillary data

2.4.1. PAWS ^{12}CO (1–0) emission line data

The PdBI Arcsecond Whirlpool Survey (PAWS)[4] covers the ^{12}CO (1−0) line emission at 1 arcsec (≈40 pc) resolution across the full disc of M 51 (Schinnerer et al. 2013). The survey

[1] https://www.iram-institute.org/medias/uploads/mrtcal-check.pdf
[2] https://www.iram.fr/IRAMFR/GILDAS/doc/html/class-html/class.html
[3] The online IRAM documentation can be found at http://www.iram.es/IRAMES/mainWiki/Iram30mEfficiencies
[4] Data can be downloaded from https://www2.mpia-hd.mpg.de/PAWS/PAWS/Data.html

Table 2. Summary of the lines covered in CLAWS, the key observational parameters, and key characteristics of the extracted data products.

Setup	Band	Line	$\nu_{\rm rest}$ (GHz)	Beam size ($''$) (1)	Beam size (kpc) (1)	On-source time (h) (2)	$\langle T_{\rm sys}\rangle$ (K) (3)	$\langle$pwv$\rangle$ (mm) (4)
1	E0 (3 mm)	CN (1−0)	113.250	26.1	1.1	44.5	111	1.8
		$C^{17}O$ (1−0)	112.359	26.3	1.1			
		^{13}CO (1−0)	110.201	26.8	1.1			
		$C^{18}O$ (1−0)	109.782	26.9	1.1			
		CS (2−1)	97.981	30.2	1.3			
		CH_3OH (2−1)	96.700	30.6	1.3			
		N_2H^+ (1−0)	93.173	31.7	1.3			
		HC_3N (10−9)	90.897	32.5	1.4			
2	E2 (1.3 mm)	^{12}CO (2−1)	230.538	12.8	0.53	20.9	217	1.7
		^{13}CO (2−1)	220.399	13.4	0.56			
		$C^{18}O$ (2−1)	219.560	13.5	0.56			

Notes. (1) Beam size of the final data cube after reduction. (2) Total on-source time (spectral time) excluding additional telescope overheads. (3) Average system temperature. (4) Average precipitable water vapour (pwv) during observations.

combines observations from IRAM's Plateau de Bure Interferometer (PdBI) and the IRAM 30 m single dish telescope. We only use the IRAM 30 m observations for this work, as we do not require high spatial resolution. The data reduction is described in Pety et al. (2013). Observations were carried out in 2010 and the data have a native spatial resolution of 23 arcsec (≈1.0 kpc) with an 1σ noise level of 16 mK at 5 km s^{-1} spectral resolution.

2.4.2. NGLS ^{12}CO (3–2) emission line data

As part of the *James Clerk Maxwell* Telescope (JCMT) Nearby Galaxy Legacy Survey (NGLS; Wilson et al. 2012), the ^{12}CO (3−2) emission across the full disc of M 51 was mapped (Vlahakis et al. 2013). Observations with an angular resolution of 14.5 arcsec (≈600 pc) were carried out with the 16 pixel array receiver HARP-B at the JCMT between 2007 and 2009.

2.4.3. THINGS 21 cm H I emission line data

The H I data[5] from the H I Nearby Galaxy Survey (THINGS; Walter et al. 2008) is used to map the atomic gas content across the full disc of M 51. The H I emission is of particular interest, as it is very extended, making it a good prior for masking emission regions outside the central region of the galaxy. The survey employed the Very Large Array (VLA). The natural weighted data used in this study have an angular resolution of ∼10 arcsec (≈400 pc) and a spectral resolution of ∼5 km s^{-1}.

2.4.4. High-density EMPIRE emission line data

The EMPIRE survey (Jiménez-Donaire et al. 2019) covered the emission of a number of high-density emission lines in the 3 mm regime, such as HNC (1−0), HCN (1−0) or HCO^+ (1−0), across the entire star-forming disc of a sample of nine nearby spiral galaxies. The survey uses observations[6] carried out with the EMIR receiver at the IRAM 30 m single dish telescope. The science goal of the survey was to take deep and extended intensity maps of high critical density lines tracing the dense gas content in the galaxy. While the $J = 1 \rightarrow 0$ transition of ^{13}CO is also covered in the survey, we only consider the high-density lines HCN (1−0) HNC (1−0), and HCO^+ (1−0) in our study and rely on our own ^{13}CO (1−0) observation (since our observations are deeper).

2.4.5. VNGS infrared data

Infrared broadband data in the range of 3.6 to 500 µm are taken from the Very Nearby Galaxy Survey (VNGS; Parkin et al. 2013). These observations were carried out using the Multiband Imaging Photometer for *Spitzer* (MIPS) instrument on board the *Spitzer* Space Telescope, as well as Photodetector Array Camera & Spectrometer (PACS) and the Spectral and Photometric Imaging Receiver (SPIRE) instruments on board the *Herschel* Space Observatory. The infrared bands are used to estimate the total infrared (TIR) emission and star formation rate (SFR; see Sect. 3.3).

2.5. Final data products

Due to the large wavelength range covered, we have a variety of spatial resolutions for our observations, ranging from 12.8 arcsec/500 pc for ^{12}CO (2−1) to 32.5 arcsec/1.3 kpc for HC_3N (10−9). To properly match and compare observations of different emission lines, we convolve to the same working resolution and re-project all data to a common grid. In this study we use three different working resolutions: (i) 15 arcsec/600 pc, analysis involving ^{12}CO (2−1) and (3-2); (ii) 27 arcsec/1.1 kpc, analysis involving all CO isotopologues; and (iii) 34 arcsec/1.4 kpc, analysis involving all molecular lines.

Table 3 lists the working resolutions used for every line in our sample. The data are finally resampled onto a hexagonal grid with a grid size of half the beam size (see Fig. 2, note that lines observed as part of other programmes than CLAWS are marked with an asterisk). Re-gridding onto a hexagonal grid is commonly done in the literature (see e.g. Bigiel et al. 2011; Leroy et al. 2013; Sandstrom et al. 2013; Cormier et al. 2018). One advantage over a Cartesian grid is the

[5] Available at https://www2.mpia-hd.mpg.de/THINGS/Data.html

[6] Details on the survey and the data can be found at https://empiresurvey.webstarts.com/index.html

A&A 662, A89 (2022)

Table 3. Lines covered as part of CLAWS with measurements re-gridded onto the same hexagonal grid and convolved to a common working resolution: 15, 27, or 34 arcsec.

					35″/1.4 kpc aperture [(a)]			60″/2.4 kpc aperture [(a)]		
Band	Line	Resolution (″)	T_{peak} (mK)	⟨rms⟩ (mK)	W_{line} (K km s^{-1})	S/N_{line}	$W_{line}/W_{^{12}CO\,(2-1)}$	W_{line} (K km s^{-1})	S/N_{line}	$W_{line}/W_{^{12}CO\,(2-1)}$
		(1)	(2)	(3)	(4)	(5)	(6)	(7)	(8)	(9)
3 mm	CN (1−0)	34	32	4.4	1.7	66	0.05	1.1	50	0.04
	$C^{17}O$ (1−0)	27	26	5.8	0.23	10	0.006	0.1	11	0.007
		34	20	4.2						
	^{13}CO (1−0)	27	142	4.9	5.5	250	0.15	4.2	280	0.15
		34	116	3.6						
	$C^{18}O$ (1−0)	27	40	4.7	1.2	52	0.033	0.9	47	0.030
		34	33	3.4						
	CS (2−1)	34	15	3.0	0.6	35	0.016	0.4	36	0.014
	CH_3OH (2−1)	34	13	2.8	0.2	9	0.004	0.1	7	0.004
	N_2H^+ (1−0)	34	14	3.0	0.3	19	0.007	0.2	11	0.006
	HC_3N (10−9)	34	16	3.7	0.2	10	0.006	0.2	15	0.007
1 mm	^{12}CO (2−1)	15	1420	20	37	710	1.0	29	750	1.0
		27	850	10.6						
		34	730	8.8						
	^{13}CO (2−1)	15	185	17.6	3.3	67	0.09	2.3	73	0.08
		27	103	9.2						
		34	88	7.7						
	$C^{18}O$ (2−1)	15	88	18.3	0.9	21	0.03	0.6	21	0.02
		27	51	9.4						
		34	41	7.8						

Notes. [(a)]Emission of the central region convolved to the given aperture size. (1) Working resolutions used for each molecular line. (2) Maximum peak temperature observed across the full map of M 51 for a given emission line at a given working resolution. (3) Average channel rms sensitivity at 4 km s^{-1} channel width. (4, 7) Velocity-integrated brightness temperature within the central aperture. (5, 8) S/N within the central aperture. (6, 9) line ratio of a given line with respect to the velocity-integrated ^{12}CO (2−1) brightness temperature.

equidistance to the neighbouring pixels allowing for a more uniform sampling. Furthermore, since the beam shape is circular, given that the neighbourhood for a hexagonal grid also grows with some circularity, beam effects are captured. Using a half beam-sized hexagonal grid, we have an oversampling factor[7] of $N_s = 4.p6$. The spectra for all lines, sampled in the aforementioned way, are combined into a final data structure for further analysis.

We determine the velocity-integrated brightness temperature by integrating masked spectra of individual sight lines. For the innermost part of the galaxy up to a galactocentric radius of a CO scale length of $0.23r_{25}$ (Leroy et al. 2008; Lisenfeld et al. 2011; Puschnig et al. 2020)[8], we use the ^{12}CO (2−1) emission line as a prior for masking. For larger radii, where the CO emission becomes faint, we use the 21 cm H I emission line. By only integrating over the masked velocity region, we can improve the S/N significantly, which is essential to capture also the fainter line emission. The mask is produced by first flagging high S/N voxels in the ^{12}CO (2−1) or H I data, respectively ($S/N > 4$ for both). An additional, lower S/N mask (S/N>2) is produced using the same lines and voxels from the high mask, which are then expanded into the low mask. The velocity-integrated brightness temperature and its uncertainty, for both we are adopting units of K km s^{-1} throughout this work, are given by:

$$W_{line} = \sum^{n_{chan}} T_{mb}(v) \cdot \Delta v_{chan} \quad (2)$$

$$\sigma_W = \sqrt{n_{chan}} \cdot \sigma_{rms} \cdot \Delta v_{chan}, \quad (3)$$

where n_{chan} is the masked number of channels along a line of sight, T_{mb} is the surface brightness temperature of a given channel in K, σ_{rms} is the position-dependent 1σ root-mean-squared (rms) value of the noise in K, and Δv_{chan} is the channel width in km s^{-1}. We calculated σ_{rms} over the signal-free part of the spectrum using the `astropy` function `mad_std`. It calculates the median absolute deviation and scales the result by a factor 1.4826 to yield a standard deviation (the factor follows from the assumption that noise follows a Gaussian distribution).

Table 3 provides a summary of the lines observed by CLAWS, as well as information about the data such as the average rms or the S/N of the line detection over a certain aperture. Figure 3 shows spectra of all these lines stacked over the central 1.5 kpc region. All the data of this project are made publicly available on the IRAM Large Programme website[9].

[7] We define the oversampling factor by the ratio of the beam area over the pixel size: $N_s = (1.13 \times \theta^2_{FWHM})/A^{hex}_{pix}$. Since we sample the data hexagonally, the pixels have a hexagonal shape with the long diagonal being equal to half the beam full width at half maximum.

[8] At a radial distance of $0.23r_{25}$, it has been found that the CO surface brightness has dropped, on average, by a factor of $1/e$ (see for more details Puschnig et al. 2020).

[9] https://www.iram-institute.org/EN/content-page-434-7-158-240-434-0.html

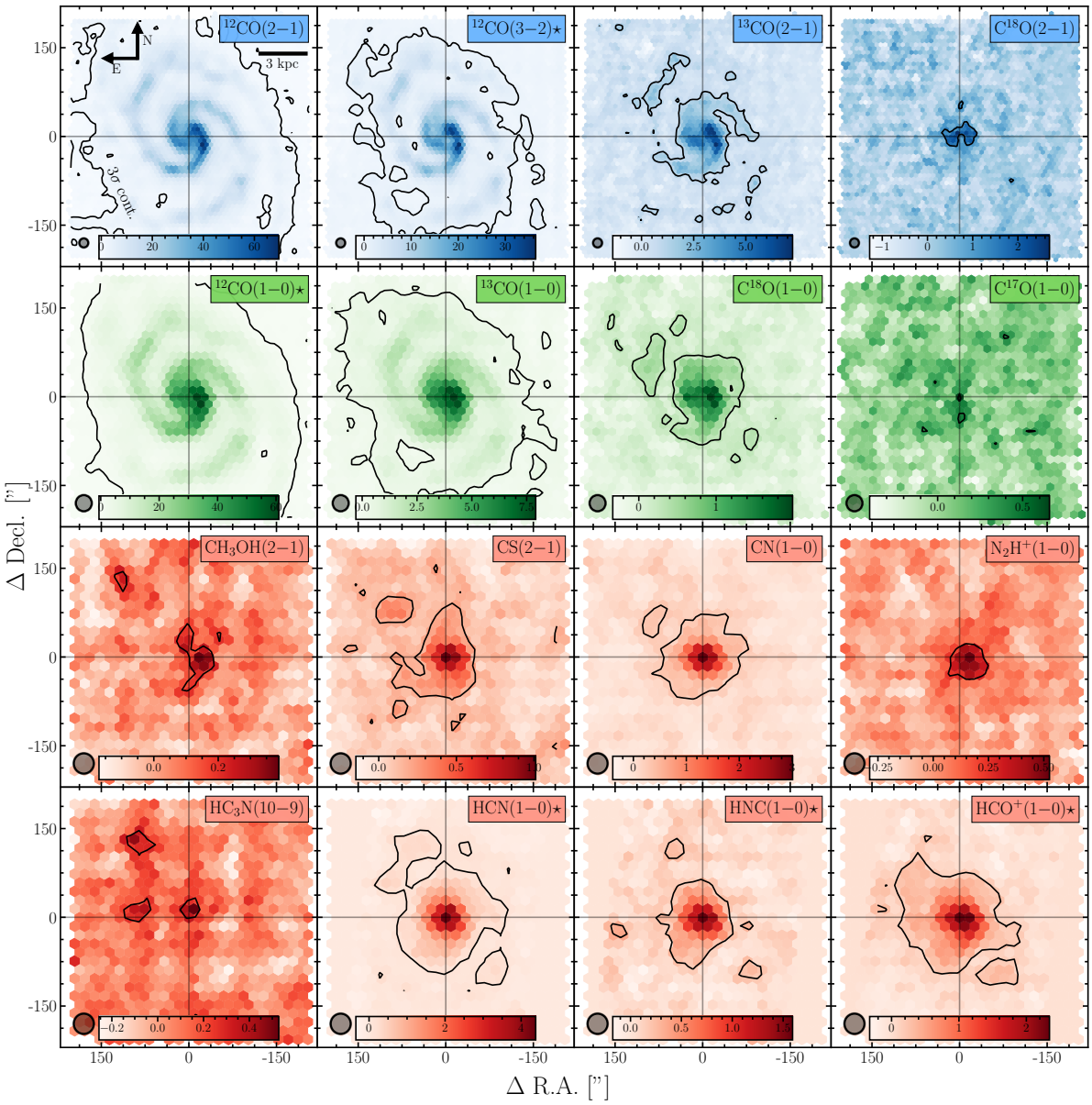

Fig. 2. Maps of the velocity-integrated brightness temperature for all lines used in this study. The maps are convolved to certain common beam sizes and re-gridded onto a common hexagonal grid, which allows a more uniform sampling. The top row (blue) is at 15 arcsec resolution, the second row (green) at 27 arcsec, and the remaining two rows (red) are convolved to 34 arcsec (corresponding to 0.62, 1.1, and 1.4 kpc, respectively). The grid spacing is chosen to be half the beam size. The velocity-integrated brightness temperature is in units of K km s^{-1}. The coordinates are relative to the centre coordinates given in Table 1. The black line indicates the $S/N = 3$ contour. Lines observed by other programmes are indicated by an asterisk after the line name in each panel. ^{12}CO (1−0) is part of the PAWS survey (Schinnerer et al. 2013; Pety et al. 2013), ^{12}CO (3−2) is taken from the NGLS survey (Wilson et al. 2012), and HCN (1−0), HNC (1−0), and HCO$^+$ (1−0) are emission lines obtained by the EMPIRE survey (Jiménez-Donaire et al. 2019).

3. Physical parameter estimation

We largely follow the methodology described in Cormier et al. (2018) investigating ^{13}CO line emission in EMPIRE galaxies and the EMPIRE survey paper by Jiménez-Donaire et al. (2019). The line ratios are measured as a function of galactocentric radius, ^{12}CO (2−1) brightness temperature and TIR surface brightness. For completeness, we also include the derived physical quantities of the molecular gas mass surface density ($\Sigma_{\rm mol}$) and the SFR surface density ($\Sigma_{\rm SFR}$), which we corrected for the inclination of M 51 by applying the factor cos(i). We note, however, that the conversion from observed to physical quantity is subject to

A&A 662, A89 (2022)

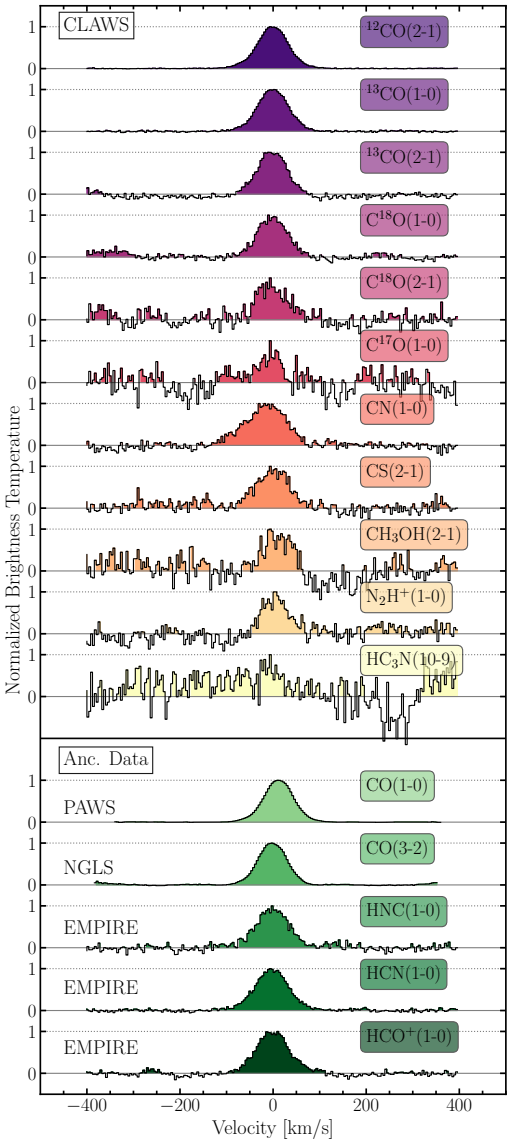

Fig. 3. Spectra of emission lines covered by this programme stacked over the central 1.5 kpc region at 34″. The emission lines are normalised to the maximum in the spectrum. The five bottom spectra are taken from different observing programmes (see Sect. 2.4), while the spectra above come from this project. For the absolute intensities, we refer the reader to Table 3. We note that we employ a hexagonal, half-beam-sized sampling. The angular resolution of 34″ corresponds to a physical scale of around 1.4 kpc. Therefore, the stacked spectra over the central 1.5 kpc region are thus the combination of the spectra of the seven most central sampling points.

uncertainties (see e.g. Kennicutt & Evans 2012; Bolatto et al. 2013; Usero et al. 2015).

3.1. Line ratio

Line ratios are determined by taking the velocity-integrated brightness temperatures of two lines, in units of K km s^{-1}, and dividing them. This is done for every line of sight as well as for the stacked spectra (see Sect. 3.2). The uncertainty of a line ratio, $R = W_1/W_2$, is given by the propagated uncertainty of the two lines:

$$\sigma_R = \frac{W_1}{W_2}\sqrt{\left(\frac{\sigma_{W_1}}{W_1}\right)^2 + \left(\frac{\sigma_{W_2}}{W_2}\right)^2}. \tag{4}$$

We generally express the average line ratio, $\langle R \rangle$, in terms of the ^{12}CO (2−1) brightness temperature weighted median, which is equivalent to the weighted 50th percentile. Given the ordered set of line ratios R for N lines of sight, with associated (but not necessarily ordered) ^{12}CO (2−1) surface brightness of $W_{^{12}\mathrm{CO}\,(2-1)}$

$$\left\{\left(R^i, W^i_{^{12}\mathrm{CO}\,(2-1)}\right)\right\}_{i=1,\ldots,N} \quad \text{for} \quad R^{i+1}_{^{12}\mathrm{CO}\,(2-1)} \geq R^i_{^{12}\mathrm{CO}\,(2-1)}, \tag{5}$$

and defining the relative weight as

$$w_i = \frac{W^i_{^{12}\mathrm{CO}\,(2-1)}}{\sum_{i=1}^{N} W^i_{^{12}\mathrm{CO}\,(2-1)}}, \tag{6}$$

the weighted pth percentile is given by the element R^k:

$$Q^w_p(R) = R^k \quad \text{satisfying} \quad \sum_{i=1}^{k} w_i \leq p \text{ and } \sum_{i=k+1}^{N} w_i \leq 1 - p. \tag{7}$$

Following this definition, we defined the ^{12}CO (2−1) brightness temperature weighted median line ratio as

$$\langle R \rangle \equiv Q^w_{0.5}(R). \tag{8}$$

The uncertainty of the weighted average line ratio is given by the 16th and 84th weighted percentile range throughout the study.

We constructed the line ratios such that the generally brighter line is in the denominator and the, overall, fainter line is in the numerator. As a consequence, we generally find upper limits, while lower limits are very rare.

Furthermore, because we compare lines with different S/N, we try to estimate the region in the plot in which we cannot obtain any measurements. Such a censored region occurs, for example, if we investigate the line ratio of a fainter line to a brighter line. Given that we have the same observed sensitivity, lower line ratios will be 'censored' since we reach the detection threshold for the faint line, while larger line ratios can still be observed, as they could originate from points with brighter emission of the faint line. To estimate the censored region, we first bin the line ratios by a certain quantity (such as the galactocentric radius). Since we constructed the line ratios such that the (generally) fainter line is in the numerator, we estimate the censored 1σ (or 3σ) region by dividing the average rms (or three times this value) of the faint line per bin by the average brightness temperature of the brighter line. We notice that because the rms and the line brightness vary across the survey field, we do find also points within the censored region.

3.2. Spectral stacking

In order to improve the S/N, which is especially crucial for fainter emission lines, we apply a spectral stacking technique. A detailed description of the stacking technique is given in several previous studies (e.g. Cormier et al. 2018; Jiménez-Donaire et al. 2019; den Brok et al. 2021). In short, the spectral axis of each

cube is re-gridded such that the emission line of each sight line is centred at $v = 0\,\mathrm{km\,s^{-1}}$. At $r_{\rm gal} < 0.23r_{25}$, ^{12}CO (2−1) is used as the reference line, while at $r_{\rm gal} \geq 0.23r_{25}$, H I is used. We note that for sight lines with both H I and CO detection, we find good agreement between their centroid velocities. With this approach, we can stack the lines of sight by a predefined quantity (for example galactocentric radius or ^{12}CO brightness temperature) and obtain an average spectrum for every bin. We stacked all lines of sight, irrespective of their individual S/N. We note that by stacking we disregard the intrinsic scatter of the data. Line ratios are then calculated from the velocity-integrated brightness temperatures of two (separately) stacked emission lines. Again, for an illustration of stacked spectra, we refer the reader to Fig. 3, which shows stacked spectra of the observed emission lines for the central region ($r_{\rm gal} < 1.5\,$kpc). With the exception of HC_3N (10−9), all emission lines are significantly detected at $S/N > 3$ within the centre.

3.3. Total infrared surface brightness

The TIR surface density can be used as a proxy of the local surface density of star formation. Following Galametz et al. (2013), the TIR surface brightness ($\Sigma_{\rm TIR}$) takes the subsequent form:

$$\Sigma_{\rm TIR} = \sum_i c_i \Sigma_i, \tag{9}$$

with Σ_i being the surface brightness of the *Herschel* bands and c_i coefficients depending on the number of infrared bands available (see Table 3 in Galametz et al. 2013 for numerical values of the coefficients). We take the same approach as previous studies (e.g. Usero et al. 2015; Jiménez-Donaire et al. 2017b; Cormier et al. 2018) by combining the *Herschel* 70, 100, and 160 µm bands to estimate the TIR surface brightness. The maps are first convolved to the common beam size of 30 arcsec using the kernels described in Aniano et al. (2011). In their study, Galametz et al. (2013) indicated that the combination of the *Herschel* 70, 100, and 160 µm bands has a coefficient of determination[10] of $R^2 = 0.97$, meaning that the calibration we use accounts for 97% of the total variation in the TIR surface brightness.

From the TIR surface brightness we can estimate the SFR surface density. We adopted the calibration given by Murphy et al. (2011):

$$\left(\frac{\Sigma_{\rm SFR}}{M_\odot\,\mathrm{yr^{-1}\,kpc^{-2}}}\right) = 1.48\times10^{-10}\left(\frac{\Sigma_{\rm TIR}}{L_\odot\,\mathrm{kpc^{-2}}}\right). \tag{10}$$

It can been seen that, compared to the far-ultraviolet (FUV) plus 24 µm SFR prescription, a scatter of 40% is expected based on comparisons between the two prescriptions using resolved measurements in M33 (Williams et al. 2018).

3.4. Molecular gas mass surface density

The molecular gas mass surface density can be estimated from the ^{12}CO (1−0) line emission or from ^{12}CO (2−1) data using the well calibrated CO line ratio, $R_{21}^{^{12}\rm CO}$ (which we measure in this project). The conversion from CO emission to gas mass surface density relies on the CO-to-H_2 conversion coefficient, $\alpha_{\rm CO}$, as

$$\begin{aligned}\left(\frac{\Sigma_{\rm mol}}{M_\odot\,\mathrm{pc^{-2}}}\right) &= \alpha_{\rm CO} W_{\rm CO\,(1-0)}\cos(i)\\ &= \alpha_{\rm CO}\frac{W_{\rm CO\,(2-1)}}{R_{21}^{^{12}\rm CO}}\cos(i).\end{aligned} \tag{11}$$

For the $\alpha_{\rm CO}$ parameter usually the Milky Way value of is chosen $\alpha_{\rm CO} = 4.4\ M_\odot\,\mathrm{pc^{-2}}\ (\mathrm{K\,km\,s^{-1}})^{-1}$ (which includes a factor 1.36 for helium) in the case of massive galaxies with solar metallicity (Bolatto et al. 2013). Galaxy-to-galaxy as well as galaxy-internal variations in the conversion factor have been observed, but studies of nearby main sequence galaxies find largely values of similar order to those in the Milky Way (Sandstrom et al. 2013; Cormier et al. 2018). We note, however, that these $\alpha_{\rm CO}$ calibrations may not account for CO-dark gas, which could significantly impact the conversion factor in certain regions (see e.g. Gratier et al. 2017; Chevance et al. 2020; Madden et al. 2020).

4. Results

4.1. CLAWS line emission

Figure 2 shows the velocity-integrated brightness temperature maps of the lines covered as part of this programme (see coloured panels), all convolved to a common working beam size of 15, 27, or 34 arcsec (corresponding to 0.62, 1.1, or 1.4 kpc, respectively). The ^{12}CO and ^{13}CO emission, and to some extent the C^{18}O (1−0) emission are clearly extended and M 51's spiral structure is visible by eye. The fainter C^{18}O (2−1) and C^{17}O (1−0) isotopologue lines are only detected in the centre of the galaxy. Besides the CO isotopologues, the other molecular lines are all confined to the centre of the galaxy. This is most likely just attributed to a lack of S/N at larger radii and not necessarily evidence of the molecule being truly more centrally concentrated. We explore radial trends for the CO lines in the following sections. Regarding emission from the centre, we see that for the CO isotopologues, the emission peaks are slightly offset towards the western spiral arm of the galaxy. By contrast, for the dense gas tracers, the emission seems to peak directly in the centre. Radial stacking improves the significant detections of faint emission lines. Among the non-CO lines part of CLAWS, with the reached sensitivity of $1\sigma_{\rm rms}\sim4$ mK at 4 km s^{-1}, only the CN (1−0) and CS (2−1) emission show radial extension out to $r_{\rm gal} \sim 3$ kpc (see Fig. 2).

4.2. CO emission line ratios

Line ratios can give insight into the physical conditions of the gas from which the emission originates. For example, under local thermodynamic equilibrium (LTE) conditions, contrasting optically thin and thick lines allows us to draw conclusions about the optical depth, while comparing two optically thin lines allows for investigating molecular abundances.

In Fig. 4, we inspect spatial variations for a selection of four CO line ratios with a large number of significantly detected sight lines. The figure shows the line ratio maps for ^{12}CO (2−1)/(1−0), ^{12}CO (3−2)/(2−1), ^{13}CO/^{12}CO (1−0), and C^{18}O/^{12}CO (1−0) (only for sight lines detected above 5σ in both lines). On the one hand, the ^{12}CO lines are generally optically thick so their line ratios relate to gas density or temperature as well as optical depth. (For ^{12}CO (2−1)/(1−0), we find also a non-negligible fraction of values with line ratios >1 at the edges

[10] The coefficient of determination is equal to the square of Pearson's linear correlation coefficient.

A&A 662, A89 (2022)

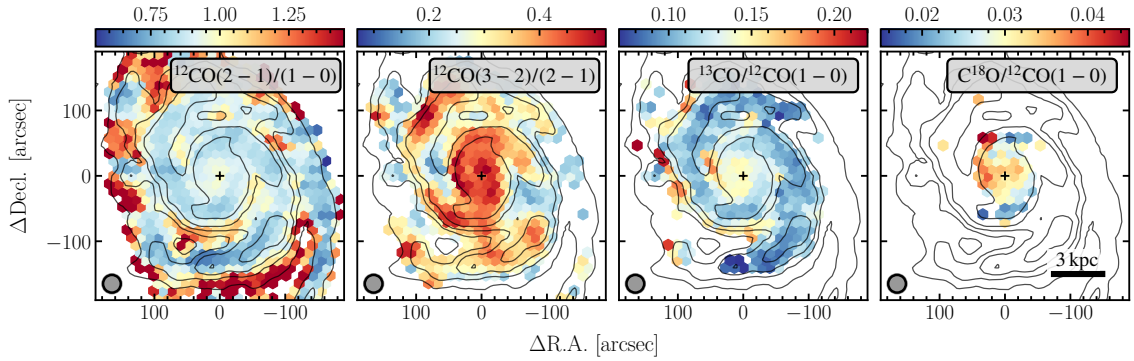

Fig. 4. CO line ratio maps for four selected ratios. All panels show the data convolved to 27 arcsec (indicated by circles in the lower-left corners). Only lines of sight with $S/N > 5$ in both lines are shown. Contours in each panel show the ^{12}CO (2−1) emission at 2, 4, 6, 10, and 20 K km s^{-1}. A local enhancement of the line ratio in the centre of the galaxy (indicated by a plus sign) is clearly visible for ^{12}CO (3−2)/(2−1) *(second to left panel)* and to some extent also for ^{12}CO (2−1)/(1−0) *(left and second to right panels)*. The C^{18}O (2−1)/^{12}CO (1−0) *(right panel)* is only significantly detected in the centre of the galaxy.

Table 4. CO line ratios and galactic environment.

Line ratio	Global	Central 45″	Arm	Interarm
^{12}CO (2−1)/(1−0)	$0.89^{+0.11}_{-0.07}$	$0.91^{+0.03}_{-0.05}$	$0.85^{+0.09}_{-0.05}$	$0.93^{+0.11}_{-0.07}$
^{12}CO (3−2)/(2−1)	$0.37^{+0.09}_{-0.11}$	$0.42^{+0.04}_{-0.05}$	$0.31^{+0.06}_{-0.07}$	$0.26^{+0.07}_{-0.05}$
^{13}CO/^{12}CO (1−0)	$0.12^{+0.02}_{-0.02}$	$0.14^{+0.01}_{-0.02}$	$0.11^{+0.01}_{-0.02}$	$0.12^{+0.03}_{-0.02}$

Notes. The CO (2−1) brightness temperature weighted mean line ratios and weighted 16th and 84th percentiles are given for different galactic environments.

of the map. Such line ratios would require optically thin ^{12}CO gas. However, at the edge of the map, S/N effects can drive up the ratio as well.) On the other hand, ^{13}CO and C^{18}O are generally optically thinner, thus making it possible to investigate their optical depths. Just qualitatively assessing the spatial variations and trends, we see that there is a tendency of higher line ratios in the centre. Furthermore, ^{12}CO (2−1)/(1−0) shows clear arm–interarm differences. Along spiral arms, the ratio is lower (∼0.85) than in interarm regions (∼0.93; see Table 4). We note that this finding is opposite to the results from Koda et al. (2012), who found a larger line ratio in spiral arm regions (see Sects. 4.4 and 5.1 for more details). For the C^{18}O/^{12}CO (1−0) line ratio, we only detect significant sight lines in the centre. With the help of stacking, we can get significant detections also at larger galactocentric radii ($r_{\rm gal} < 6$ kpc), showing a moderate negative radial trend.

In Fig. 5, we investigate the distributions of all CO isotopologue line ratios. These line ratios span a range of around 2 dex. ^{12}CO (2−1)/(1−0) shows the highest line ratio with CO (2−1) brightness temperature weighted mean of $0.89^{+0.11}_{-0.07}$. The lowest line ratio is given by C^{18}O/^{12}CO (1−0) with weighted mean of $0.031^{+0.004}_{-0.006}$. The individual ratios show a 95% inclusion region of ∼0.5 to 1 dex. The inset panel shows the effect of increasing the S/N cut of the ^{12}CO(2−1)/(1−0) line ratio. We do not find a significant difference in terms of the mean line ratio with increasing S/N cut.

We also studied the line ratios binned by galactocentric radius, CO (2−1) brightness temperature and TIR surface brightness. We ordered the CO line ratios into three categories: (i) fixed CO isotopologue, different transition (Fig. 6); (ii) different CO isotopologue, fixed $J = 1 \rightarrow 0$ (Fig. 7); and different CO isotopologue, fixed $J = 2 \rightarrow 1$ (Fig. 8).

We used the highest working resolution possible for each line ratio. For ratios involving the C^{17}O (1−0) line, we use the lowest resolution of 34 arcsec to maximise sensitivity. We define all line ratios such that the fainter line is in the numerator and the brighter one in the denominator. As a consequence, line ratios in faint regions may (frequently) appear as upper limits, while lower limits are very rare.

In Figs. 6, 7, and 8, we present our measurements in two ways: (i) we plot the line ratios of individual sight lines as a function of galactocentric radius, CO (2−1) brightness temperature and TIR surface brightness, and (ii) we stack the emission line spectra within bins of galactocentric radius, CO (2−1) brightness temperature and TIR surface brightness, and plot the line ratio of these stacked spectra. We note that the sample of sight lines usually differs between case (i) where only those sight lines are shown for which both lines have $S/N > 5$ and case (ii) where all sight lines are included in the stacked spectra while (again) only those line ratios are shown for which both stacked lines have $S/N > 5$. We stress that extrapolating these trends based on the stacked points to the individual lines of sight should be done with caution, as by stacking, we discard the intrinsic scatter of the data. This difference in sample implies that frequently the line ratio from stacked spectra does not coincide with the 'middle' of the line ratio distribution for individual sight lines (which provide a biased view as long as non-detections are neglected). The censored regions are described in Sect. 3.1 and show regions in the ratio space that we cannot sample due to the limited sensitivity. In these censored regions line ratios from stacked

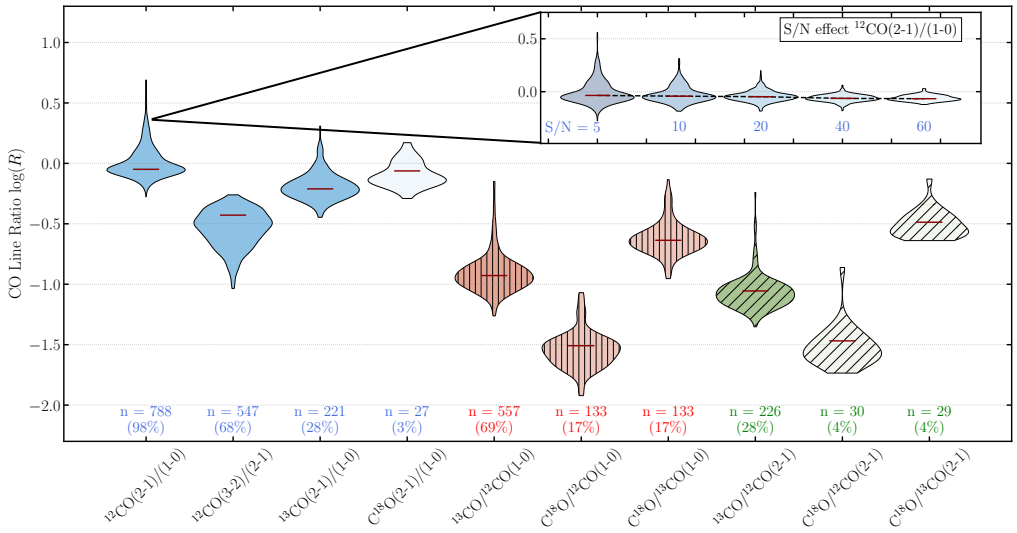

Fig. 5. Distribution of CO line ratios at 27 arcsec. The violin plots are colour-coded: blue indicates ratios of fixed CO isotopologue but different transitions, while red (vertically hatched) and green (diagonally hatched) show ratios of different CO isotopologue but fixed transition. The number of significant data points ($S/N > 5$) for each line ratio is indicated with n and the saturation of the colour of each violin. The percentage in terms of total detection is also indicated (with respect to $S/N > 5$ detected ^{12}CO(1–0) data points). In the inset panel, we show the effect of increasing the S/N cut from $S/N = 5$–60 for the ^{12}CO(2–1)/(1–0) line ratio. We do not find a significant difference in terms of the mean line ratio with increasing S/N.

spectra should be considered as these provide a robust and unbiased measurement (since they include non-detected sight lines).

Table 5 lists the Kendall's τ rank correlation coefficient as well as its significance, the p-value, of various line ratios based on the stacked data points that have $S/N > 5$. We employed the Kendall's τ rank correlation coefficient to measure a monotonic increasing, non-linear relationship in our data. It is more robust to error and discrepancies in the data (Croux & Dehon 2010) than the widely used Spearman's rank correlation coefficient. We also do not use the Spearman's rank correlation coefficient, since it is more sensitive to our choice of binning of the stacked data points. For the calculation of the coefficients for the CO line ratios as a function of galactocentric radius, we only included stacked points at $r_{\rm gal} \leq 5$ kpc. Since ^{12}CO (1−0) has the highest sensitivity and this transition appears in the denominator of our line ratios, this leads to line ratio for individual sight lines to turn upwards at larger radii or at fainter CO (2−1) brightness temperatures. To avoid this, we only include stacks with $W_{\rm CO\,(2-1)} > 2\,{\rm K\,km\,s^{-1}}$ for computation of Kendall's τ for the CO line ratios as a function of CO (2−1) brightness temperature. We do not compute the correlation coefficients for CO line ratios with only two or less significantly stacked points.

4.2.1. Fixed CO isotopologue – different transitions

Figure 6 shows fixed CO isotopologue line ratios for the three lowest rotational transitions. Such line ratios can give insight into the excitation state of the ISM. Looking at the line ratios as a function of galactocentric radius, we see that especially the stacked measurements of ^{12}CO (3−2)/(2−1) and ^{13}CO (2−1)/(1−0) show negative trends with both having a Kendall's rank correlation coefficient of $\tau = -0.80$ ($p = 0.083$). Within the central region ($r_{\rm gal} < 1$ kpc), the line ratios are enhanced by 37% for ^{12}CO (3−2)/(2−1) and 45% for ^{13}CO (2−1)/(1−0) as compared to the average stacked line ratio for $r_{\rm gal} < 5$ kpc. An increase in the line ratio within the centre of the galaxy is also qualitatively visible in Fig. 4 (see second to left panel for ^{12}CO (3−2)/(2−1)). Conversely, the ^{12}CO (2−1)/(1−0) line ratio does not show a significant trend with galactocentric radius, it shows only a slight enhancement of 5% in the centre over the average within 5 kpc. For C^{18}O (2−1)/(1−0), we do not have enough significantly detected stacked spectra to investigate a trend with radius.

For the line ratios as a function of the ^{12}CO (2−1) brightness temperature, only ^{12}CO (3−2)/(2−1) shows a significant positive trend with Kendall's $\tau = 1.00$ ($p = 0.003$). However, we note that especially for lower CO brightness temperatures, the effect of correlated axes might enhance such a trend. Both the ^{12}CO (2−1)/(1−0) and ^{13}CO (2−1)/(1−0) line ratios do not show any clear trend with CO brightness temperature. However, for ^{13}CO (2−1)/(1−0), we find a positive trend in the range $W_{\rm CO\,(2-1)} > 2\,{\rm K\,km\,s^{-1}}$.

Finally, considering the line ratios as a function of the TIR surface brightness, we again find positive trends for ^{12}CO (3−2)/(2−1) with $\tau = 1.0$ ($p = 0.083$). While, for ^{12}CO (2−1)/(1−0), we find a flat trend with respect to $\Sigma_{\rm TIR}$. Due to the faintness of the C^{18}O (2−1) line, we do not have enough significant points for the C^{18}O (2−1)/(1−0) line ratio to determine if any trend exists.

Of particular conspicuousness is the fact that the stacked ^{12}CO (3−2)/(2−1) line ratio shows opposite trends in every column (i.e. with galactocentric radius, CO brightness temperature and TIR surface brightness) compared to the ^{12}CO (2−1)/(1−0) line ratio. This is opposite to the notion that both ratios show a similar behaviour, but could be coupled to the fact that ^{12}CO (3−2) is more constrained to the denser regions of the molecular ISM.

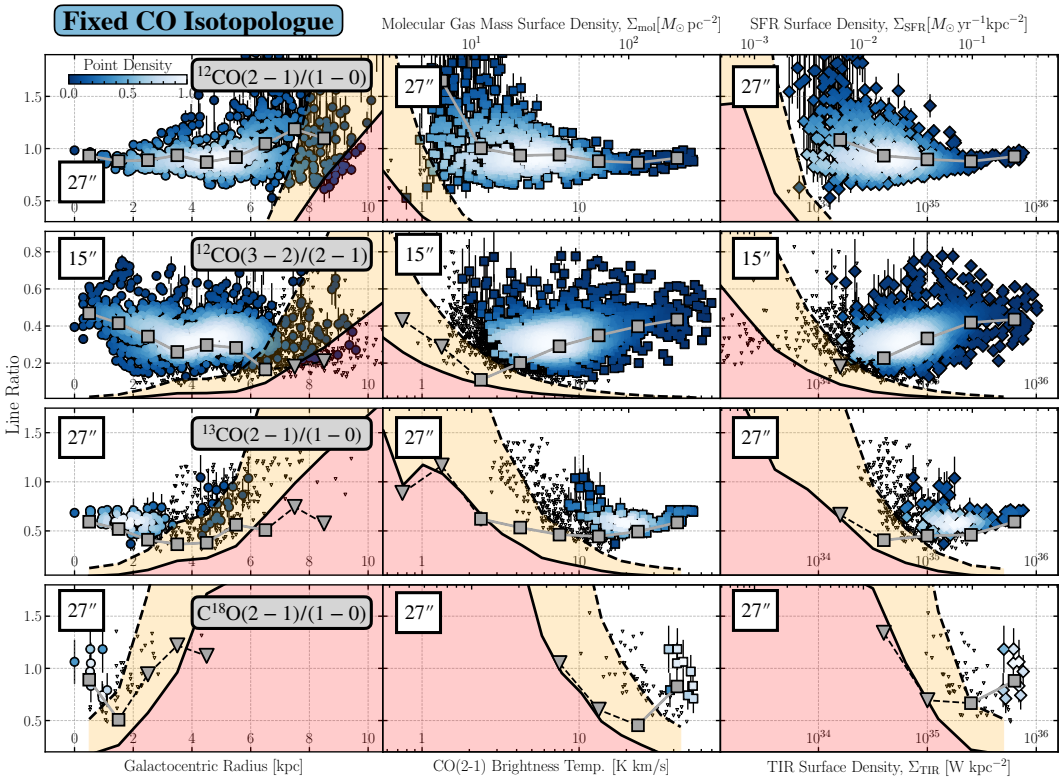

Fig. 6. CO line ratios as a function of galactocentric radius, CO (2−1) brightness temperature, and TIR surface brightness. Each row shows the line ratio for individual lines of sight for fixed CO isotopologues but different transitions. Each column shows the CO line ratio as a function of galactocentric radius, CO (2−1) brightness temperature, and TIR surface brightness. The coloured data points show the individual lines of sight with a $S/N > 5$, and the small black downward triangles indicate 3σ upper limits. To illustrate the point density in the figure, we colour-code the points using a 2D KDE. Values are normalised to the peak density and range from most dense (1; white) to least dense (0; blue) The shaded area in each panel shows the 1σ (red) and 3σ (orange) censored regions for the individual lines of sight. They are an estimate of where we expect to no longer be able to detect line ratios (due to the low S/N of one of the lines). Marked in grey are the line ratios derived from the stacked spectra (downward triangles again mark upper limits). Error bars for significant points are indicated (for the stacked data points, the error bars are generally not visible due to the plotted point size being larger). For each line ratio, we used the highest resolution possible (indicated in the upper-left corner of the panel). To convert to Σ_{mol}, which we provide for comparison on the top x axis of each panel, we assume a constant $R_{21} = 0.89$. We note that the x and y axes are correlated if the ^{12}CO (2−1) emission is used in the line ratio. The stacked points allow us to probe the line ratios in fainter regions, which sometimes confirms the trend suggested by the individual (significantly detected) sight line measurements (e.g. the ^{12}CO (2−1)/(1−0) in the top panel row) and sometimes reveals trends that could not be identified from the sight line measurements (e.g. the trend in the ^{12}CO (3−2)/(2−1) ratio in the second row).

4.2.2. Different CO isotopologue – fixed-*J* transition

Looking at different CO isotopologue line ratios with fixed rotational transitions can give insight into various physical quantities such as the abundance of the molecule or its optical depth, depending on whether the emission line is optically thin or thick (Davis 2014; Jiménez-Donaire et al. 2017b; Cormier et al. 2018). Figures 7 and 8 show CO line ratios for different CO isotopologues but at fixed-J transition. The ^{13}CO/^{12}CO line ratio shows for both the (1−0) and (2−1) transition the same significant correlation with galactocentric radius (negative), ^{12}CO brightness temperature (positive) and TIR surface brightness (positive). The (1−0) line ratio shows also indication of an enhancement in the centre of the galaxy of order 20% (see also centre right panel in Fig. 4). The C^{18}O/^{12}CO (1−0) line ratio shows a negative trend with galactocentric radius, but positive trends with ^{12}CO brightness temperature and TIR surface brightness. For the C^{17}O line, we only have two sight lines with significant detection at 34 arcsec resolution. We are very limited by the censored region and from the individual sightlines alone, we cannot infer any trends with radius, CO brightness and/or the TIR surface density. For C^{17}O/^{12}CO(1–0) we find an average value of ∼0.02, for C^{17}O/^{13}CO(1–0) ∼0.15, and for C^{17}O/C^{12}O(1–0) we find ∼0.7. Using stacking, we identify a positive trend with radius out to 4 kpc for the C^{17}O/^{12}CO(1–0), C^{17}O/^{13}CO(1–0) and C^{17}O/C^{18}O(1–0) ratios. Since the individual sightlines are affected by the censoring, we also provide the average line ratios using the stacked spectra: For stacked C^{17}O/^{12}CO(1–0) we find 0.009 ± 0.002, for the stacked C^{17}O/^{13}CO(1-0) we have 0.07 ± 0.03 and for the stacked C^{17}O/C^{18}O(1–0) we measure 0.4 ± 0.1.

4.2.3. Comparing different CO line ratios

As previously highlighted, different CO line ratios trace different gas characteristics and physical properties, depending on the

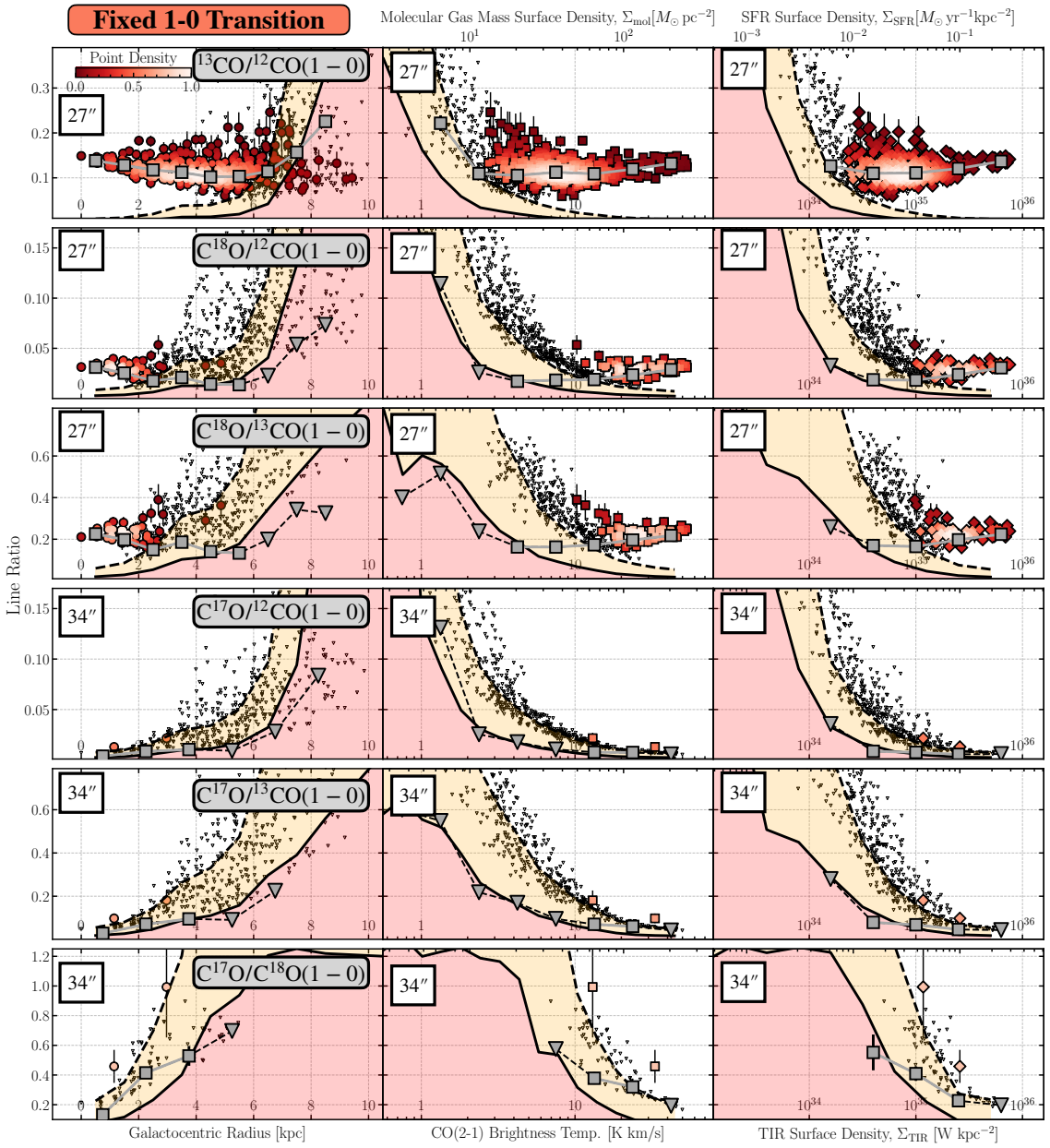

Fig. 7. CO line ratios with a fixed (1−0) transition but different CO isotopologues. For a description of the panels, see Fig. 6.

optical depth of the two lines. By comparing different line ratios that trace different conditions (e.g. the optical depth or the chemical abundance), we can gain insight into the relation between various physical conditions. Figure 9 shows a corner plot comparing different CO isotopologue line ratio combinations against each other. Plotted are the individual sight lines that show significantly detected line ratios in both axes, as well as the 50% and 75% inclusion contours using a kernel density estimation (KDE). We note that we do not account for censoring effects that can affect the wider distribution of the data points. To test for a linear correlation between the different line ratios, we computed the Pearson's r_p coefficient.

We do not find a clear linear trend for most combinations of line ratios at our working resolution of 1 to 2 kpc. A moderate trend ($|r_P| > 0.4$) of high significance ($p < 0.05$) can only be seen for $^{12}CO\,(2-1)/(1-0)$ versus $^{13}CO/^{12}CO\,(1-0)$, $^{12}CO\,(2-1)/(1-0)$ versus $C^{18}O/^{12}CO\,(1-0)$ and $^{13}CO/^{12}CO\,(1-0)$ versus $C^{18}O/^{12}CO\,(1-0)$ (ratio comparisons in question are marked in Fig. 9). However, these are the combinations that both have the $^{12}CO\,(1-0)$ line in the

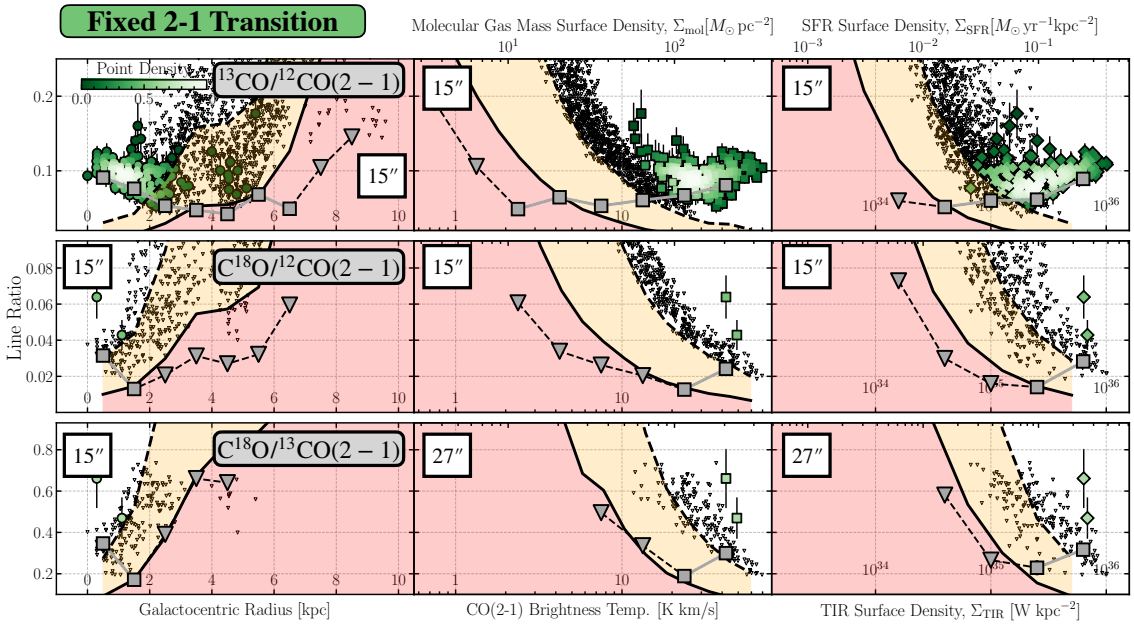

Fig. 8. CO line ratio with a fixed (2−1) transition but different CO isotopologues. For a description of the panels, see Fig. 6.

Table 5. Mean values and Kendall's τ rank correlation coefficient (p-value given in parentheses).

	Line Ratio	$\langle R\rangle$	$\langle R\rangle^{equal}$	Kendall's τ rank correlation coefficient		
				Radius	$W_{CO\,(2-1)}$	Σ_{TIR}
		(1)	(2)	(3)	(4)	(5)
	$^{12}CO\,(2-1)/(1-0)$	$0.89^{+0.11}_{-0.07}$	$0.9^{+0.3}_{-0.1}$	−0.20 (0.82)	−0.6 (0.14)	−0.6 (0.23)
	$^{12}CO\,(3-2)/(2-1)$	$0.37^{+0.09}_{-0.11}$	$0.32^{+0.10}_{-0.09}$	−0.80 (0.083)	1.0 (0.003)	1.0 (0.083)
	$^{13}CO\,(2-1)/(1-0)$	$0.61^{+0.09}_{-0.08}$	$0.61^{+0.10}_{-0.08}$	−0.80 (0.083)	−0.2 (0.7)	1.0 (0.083)
	$C^{18}O\,(2-1)/(1-0)$	$0.87^{+0.24}_{-0.15}$	$1.0^{+0.2}_{-0.2}$	–	–	–
fixed-J $1\rightarrow0$	$^{13}CO/^{12}CO$	$0.12^{+0.02}_{-0.02}$	$0.12^{+0.02}_{-0.02}$	−1.0 (0.017)	0.6 (0.13)	0.40 (0.48)
	$C^{18}O/^{12}CO$	$0.031^{+0.004}_{-0.006}$	$0.031^{+0.004}_{-0.008}$	−0.80 (0.083)	1.0 (0.017)	0.67 (0.33)
	$C^{18}O/^{13}CO$	$0.23^{+0.02}_{-0.03}$	$0.23^{+0.02}_{-0.03}$	−0.80 (0.083)	0.80 (0.083)	0.67 (033)
	$C^{17}O/^{12}CO$	–	–	1.0 (0.3)	–	−1.0 (0.33)
	$C^{17}O/^{13}CO$	–	–	1.0 (0.3)	–	−1.0 (0.33)
	$C^{17}O/C^{18}O$	–	–	1.0 (0.3)	–	−1.00 (0.33)
fixed-J $2\rightarrow1$	$^{13}CO/^{12}CO$	$0.09^{+0.01}_{-0.02}$	$0.09^{+0.02}_{-0.02}$	−1.0 (0.017)	0.73 (0.056)	1.0 (0.083)
	$C^{18}O/^{12}CO$	$0.034^{+0.006}_{-0.008}$	$0.034^{+0.008}_{-0.005}$	–	–	–
	$C^{18}O/^{13}CO$	$0.36^{+0.06}_{-0.06}$	$0.33^{+0.08}_{-0.04}$	–	–	–

Notes. They are measured for the line ratios of stacked spectra as a function of galactocentric radius, CO (2−1) brightness temperature, and TIR surface brightness (see Figs. 6, 7, and 8). Only stacked points with $S/N > 5$ are considered. A dash indicates that only two or fewer significant measurements exist for the specific line ratio. (1) $\langle R\rangle$ indicates the average line ratio weighted by $^{12}CO\,(2-1)$ brightness temperature (see Eq. (8)). The uncertainty for each line ratio is given by the weighted 16th and 84th percentiles. (2) The volume weighted median line ratio and 16th and 84th percentiles (since all pixel have the same size, this corresponds to weighing all points equally). (3) For the correlation coefficient computation, we only include stacked points at $r_{gal} < 5$ kpc. (4) Only includes stacked points with $W_{CO\,(2-1)} > 2$ K km s^{-1}. (5) The correlation coefficient computation does not include any additional constraints.

denominator. Consequently, the trends may hint more at a correlation between the two numerators. Such trends are expected, given that all CO isotopologues have a similar spatial distribution within the galaxy, so we expect a correlation in the strength of their emission. For all other combinations, no significant linear trend can be determined.

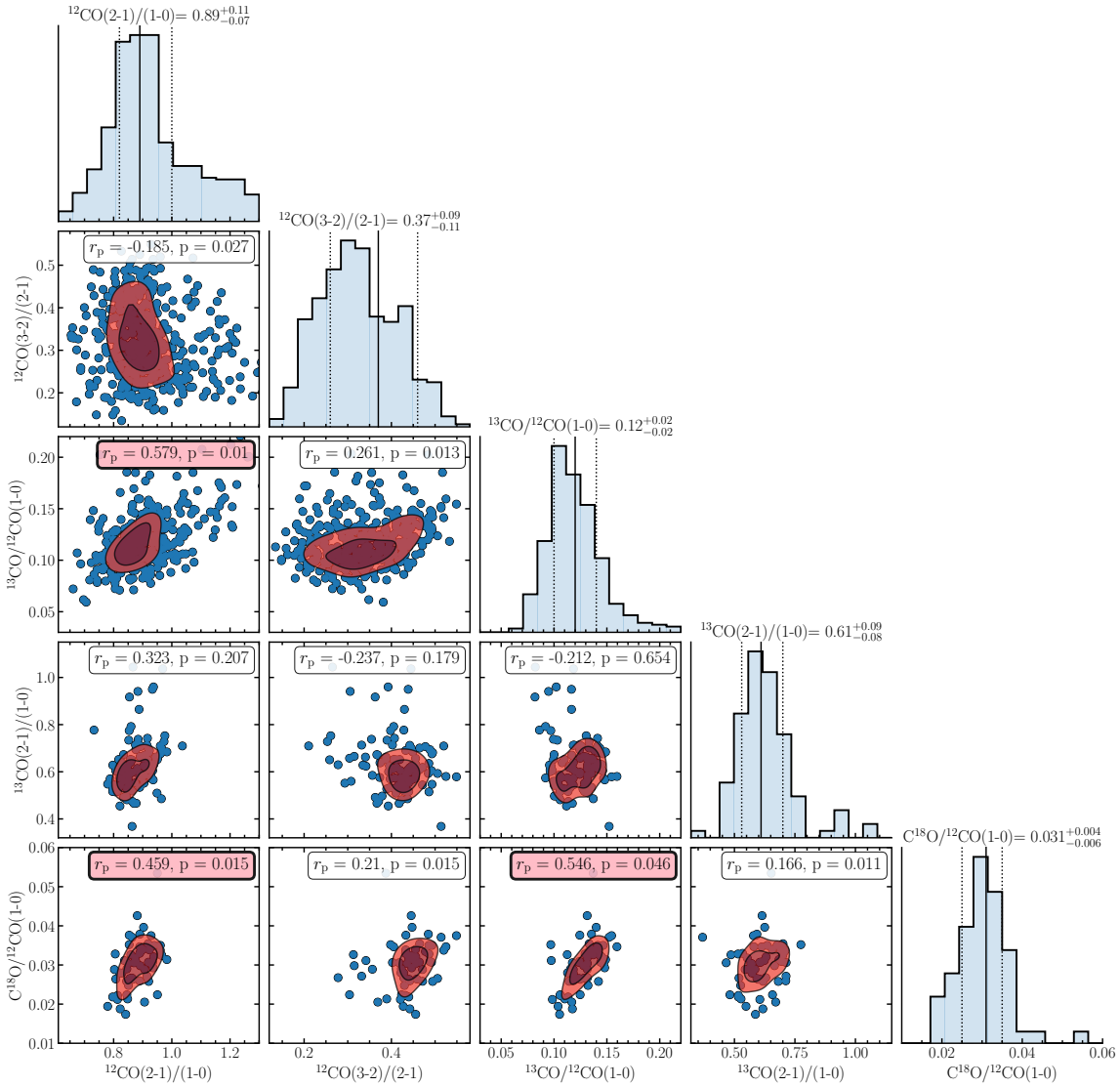

Fig. 9. Comparing different CO line ratios against one another at 27 arcsec. Individual sight lines and significantly detected CO line ratios vs. other line ratios are shown. Contours show the 50% and 75% inclusion region based on a KDE. For each line ratio comparison, Pearson's r_P correlation coefficients and its p-value are indicated in the panel. The histograms indicate the distribution of each line ratio using all significant data points. The CO (2−1) weighted mean and weighted 16th and 84th percentiles are also shown. We find a moderate, significant linear correlation ($|r_P| > 0.4$ and $p < 0.05$; panel labels are colour-coded in the case of a moderate linear correlation) for ratio comparison in panels (b), (g), and (i) only.

4.3. Line ratios and the galactic environment

For several CO line ratios, an enhancement towards the centre of the galaxy is observed (see Sect. 4.2). To analyse whether galaxy morphological features, such as the galactic centre, spiral arms or interarm regions, have an impact on the molecular gas properties, we classify each sight line as centre, spiral arm, interarm or general disc (see Fig. 10). This classification is based on visual inspection of optical HST data as well as the extent of the ^{12}CO (2−1) emission. In our study, the 'centre' refers to the central ($r_{gal} \leq 45$ arcsec $\approx$2 kpc) region of the galaxy.

Figure 11 shows histograms of the CO line ratio distributions for ^{12}CO (2−1)/(1−0), ^{12}CO (3−2)/(2−1) and ^{13}CO (2−1)/(1−0), separated by the different environments. These three line ratios show significant pixel detections in the centre, spiral arm and interarm regions. The numerical values of the mean and 16th and 84th percentiles for each environment are given in Table 4. We find again that all three line ratios show higher values in the central region, but this enhancement is significant only in the case of ^{12}CO (3−2)/(2−1). Furthermore, we find evidence for a difference in the line ratios between arm and interarm regions for ^{12}CO (2−1)/(1−0) and ^{12}CO (3−2)/(2−1). We note that the line ratios in the interarm regions are higher for ^{12}CO (2−1)/(1−0) and lower for ^{12}CO (3−2)/(2−1) than the spiral arm regions. For the ^{13}CO/^{12}CO (1−0) line ratio, we also find a larger average

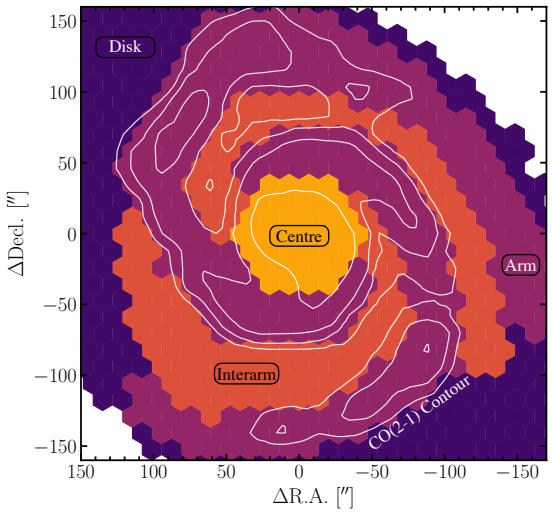

Fig. 10. Environmental mask of M 51. Based on a visual inspection of optical HST data and ^{12}CO (2−1) emission, we generated the following environmental mask. The pixels are colour-coded by their associated region. This includes the centre (bright orange), interarm (dark orange), spiral arm (magenta), and disc (purple). The centre includes data points within a 45 arcsec aperture. White contours indicate ^{12}CO (2−1) emission at 7, 10, 15, and 30 K km s^{-1}.

value in the interarm ($0.12^{+0.03}_{-0.02}$) than in the spiral arm region ($0.11^{+0.01}_{-0.02}$), though the two medians lie within the margin of error of each other.

4.4. Spiral arm and interarm variations

In the following section, we further investigate the arm-interarm contrast, as it stands against previous studies, which found a larger ^{12}CO (2−1)/(1−0) line ratio in the spiral arm region than the interarm region (Koda et al. 2012). To further study the systematic variations in the ^{12}CO (2−1)/(1−0), ^{12}CO (3−2)/(2−1), and ^{13}CO/^{12}CO (1−0) line ratios across the spiral arm and interarm regions, we use a similar approach as described in Koda et al. (2012). The method is illustrated for the ^{12}CO (2−1)/(1−0) line ratio in Fig. 12, while a comparison of all four line ratios is shown in Fig. 13. The data are binned using logarithmic spirals, which are described by

$$r = e^{k \cdot \psi}, \tag{12}$$

where $k \equiv \tan(\theta)$ with the pitch angle θ and the spiral phase ψ. For M 51, we use a pitch angle[11] of $\theta = 20°$. Each segment spans over 40° and we increment in steps of $\Delta\psi = 20°$ anti-clockwise. For the analysis, we exclude the central ($r_{\rm gal} \leq 45$ arcsec) region and only bin points with $S/N > 5$. The logarithmic spiral segments can be seen in the left and central panels of Fig. 12. The red and blue lines indicate the molecular spiral arms (ψ = 40°−100° and 220°−290°). We note that the shaded regions in the upper-right and bottom-left corners are also excluded, as there the molecular arm starts to deviate significantly from a simple logarithmic spiral.

The right panel of Fig. 12 shows the result of the line ratios binned by spiral phase angle. The two spiral arms are based on molecular gas emission. The figure shows the binned arithmetic average of each logarithmic spiral arm segment. Using the same data, we can confirm the larger ^{12}CO (2−1)/(1−0) line ratios in the interarm regions compared to the arm regions found by den Brok et al. (2021). The average line ratio in the central segment of the molecular arm region is 0.85, while in the interarm region the average is ∼0.93. We note that the enhancement of the line ratio in the interarm is more concentrated towards the downstream, convex part of the spiral region. A similar variation is also seen in the ^{13}CO/^{12}CO (1−0) ratio (see Fig. 13). We note that Table 4 also lists the line ratios separated into arm and interarm. But the value in the table are ^{12}CO (2−1) weighted and combine data points spanning a wider range of spiral phases. Consequently, we concentrate the analysis of the azimuthal variation on the analysis plotting the line ratios as a function of the spiral phase.

To make sure the trend we find is not due to higher line ratios at larger radii, we vary the S/N threshold and also add a constraint to only include sight lines within a given galactocentric radius. The results are shown in Fig. 14, where besides the $S/N > 5$ threshold (which is used in Fig. 12), we also include thresholds of $S/N > 10, 15, 20$. For the radial thresholds, we include $r_{\rm gal} < 6, 5, 4$ kpc. We see that the finding of larger ^{12}CO (2−1)/(1−0) line ratios in the interarm region is independent of the threshold implemented.

We note that in particular the 3 mm lines in the interarm region are subject to significant error beam contribution, which to some degree can drive the larger ^{12}CO (2−1)/(1−0) line ratio in the interarm region. We discuss the effect in more detail in Appendix A.

5. Discussion

The rich dataset of different CO isotopologues allows us to address a multitude of science questions. First, in Sect. 5.1 we look at the various trends we find in the CO isotopologue line ratios. We compare them to the literature and then, in Sect. 5.4, investigate what the observed trends in the line ratios may imply. In Sect. 5.1 we also look into a particular environmental variation in the line ratio – the arm–interarm differences we find most notably in the ^{12}CO (2−1)/(1−0) line ratio – and constrain the cause for this variation. The galactic environment appears to have an impact on the line ratio, so we also investigate how environment affects the CO spectral line energy distribution (SLED) in Sect. 5.5.

5.1. Comparing R_{21} with previous studies

The first questions to address are whether the galaxy M 51 conforms to the trends seen in other galaxies regarding the CO line ratios and what we can learn from such trends. When looking at the ^{12}CO line ratios, a few peculiarities are evident for M 51. The well-studied line ratio of ^{12}CO (2−1)/(1−0) (denoted hereafter as $R_{21}^{^{12}\rm CO}$) is rather high, with a luminosity-weighted average value of $R_{21}^{^{12}\rm CO} = 0.89^{+0.11}_{-0.07}$. The question of how this compares to findings from other studies using different datasets then arises. In their ^{12}CO line ratio study, comparing literature values of a larger set of spiral disc galaxies, den Brok et al. (2021) found a common

[11] To be consistent with the study of Koda et al. (2012), we used the value of 20° for the pitch angle. This value is similar to the value of 21.°1 given by Shetty et al. (2007) and the value of 18.°5 found in Pineda et al. (2020).

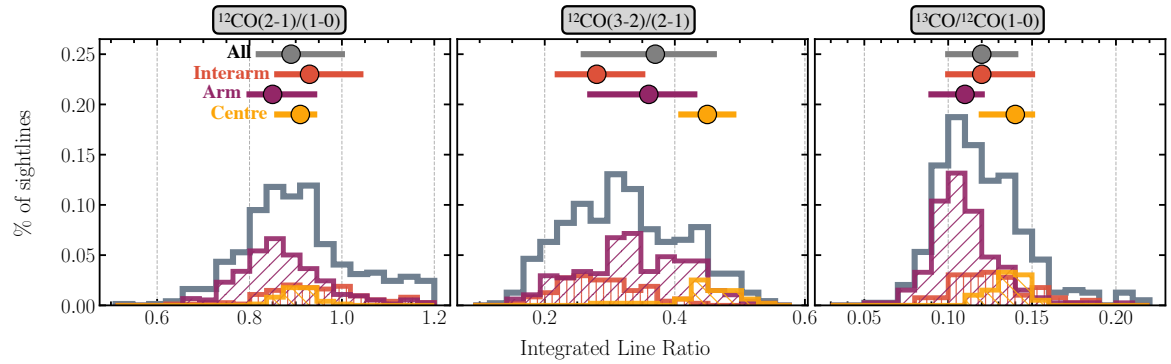

Fig. 11. Distributions for three selected CO line ratio in different galactic environments. The locations of the various galactic regions are shown in Fig. 10. For each region, the CO (2−1) brightness temperature weighted median (see Eq. (8)) is indicated by the circle and the 16th and 84th percentile range by the bars. The numerical values are given in Table 4. For the ^{12}CO (2−1)/(1−0) line ratio, we find evidence of larger values in the interarm than in the spiral arm. For ^{12}CO (3−2)/(2−1) we find the opposite trend. ^{12}CO (3−2)/(2−1) and ^{13}CO/^{12}CO (1−0) show a clear enhancement of the line ratio in the galaxy centre.

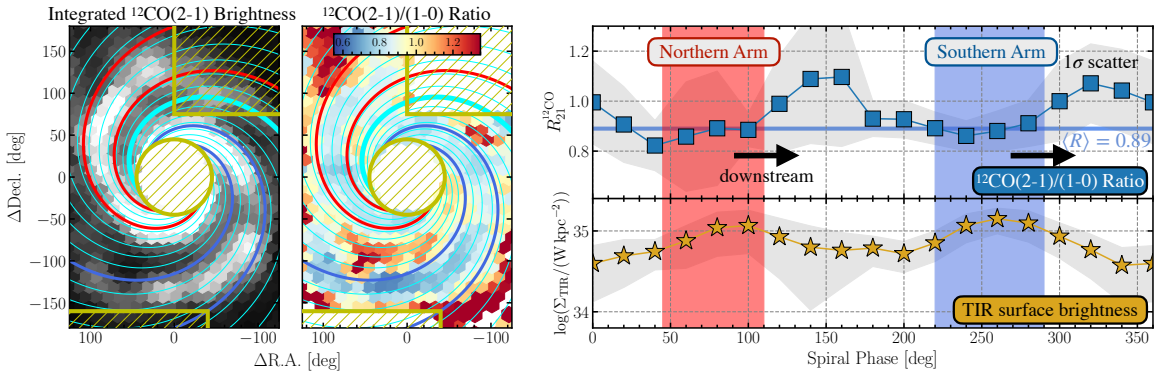

Fig. 12. Spiral arm–interarm CO line ratio variation. This figure closely follows the layout of Fig. 4 in Koda et al. (2012). *Left*: ^{12}CO (2−1) brightness temperature map with the logarithmic spiral pattern. The logarithmic spiral has a pitch angle of 20°. The bold cyan line indicates the starting spiral phase (ψ = 0°). The spiral phases increase anti-clockwise in 20° increments. The red and blue spirals indicate the bounds of the molecular gas spiral arm (at ψ = 45°−110° and 220°−290°). We ignore the top-right and bottom-left regions, where the molecular arm deviates from the logarithmic spiral pattern, in our analysis. Furthermore, we exclude the central region (radius of 45 arcsec, indicated by the yellow hashed region). *Centre*: ^{12}CO (2−1)/(1−0) line ratio map. We only show sight lines at $S/N > 5$ and not within the exclusion regions. *Right*: Average line ratio for each spiral phase bin on top (which has a width of 40° and increases by 20° every step). The blue horizontal line shows the galaxy-wide, luminosity weighted median line ratio of $\langle R_{21}^{^{12}\mathrm{CO}} \rangle$. The bottom panel shows the TIR surface density (which is proportional to the SFR surface density) to highlight the spiral arm. The grey shaded area indicates the standard deviation. The locations of the northern (red) and southern (blue) spiral arm are indicated. The downstream direction of the spiral arm is indicated by the black arrow.

line ratio of $R_{21}^{^{12}\mathrm{CO}} = 0.59 \pm 0.1$, making the line ratio we find for M 51 clearly stand out. Similarly, Leroy et al. (2022), studying the low-J ^{12}CO line ratios using single-dish CO mapping surveys and the Physics at High Angular resolution in Nearby Galaxies (PHANGS) survey find a mean value and respective 16th and 84th percentile of $R_{21}^{^{12}\mathrm{CO}} = 0.65^{+0.18}_{-0.14}$. Other studies that investigated this line ratio in M 51 found lower global values. Koda et al. (2012) found an average value of $R_{21}^{^{12}\mathrm{CO}} \approx 0.7$, but they identified enhanced values in the spiral arm regions that are closer to our mean value. Vlahakis et al. (2013) also investigated the spatial variation in the ^{12}CO line ratios in M 51. They found an overall higher median $R_{21}^{^{12}\mathrm{CO}}$ of 0.8, which is close to our luminosity-weighted value.

In Fig. 12, we study the spatial variation in the ^{12}CO (2−1)/(1−0) line ratio across the arm and interarm regions of M 51. The main result is the higher line ratios in the interarm regions (∼0.93) as opposed to the arm regions (∼0.85), as also seen in Table 4. This trend stands against previous findings from, for example, Sakamoto et al. (1997), who found the opposite trend in the Milky Way. Koda et al. (2020) reported higher line ratios in arm as opposed to interarm regions for the spiral galaxy M83. In fact, Koda et al. (2012) and Vlahakis et al. (2013) (using the same data) studied the arm–interarm variation in M 51 and found opposing trends with respect to this study.

We investigated in detail the origin of this discrepancy of the arm–interarm variation in den Brok et al. (2021). The study by Koda et al. (2012) used different CO (1−0) and CO (2−1) data than used here. Their CO (2−1) data were taken from the HERACLES survey (Leroy et al. 2011b), and the CO (1−0) data came from the Nobeyama Radio Observatory (NRO) observations (Koda et al. 2011). Performing the same analysis as shown

A&A 662, A89 (2022)

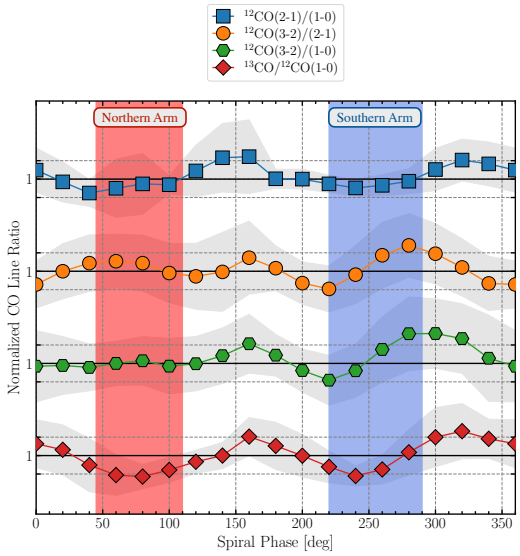

Fig. 13. Spiral arm–interarm line ratio variations for three different CO line ratios. We only include sight lines with $S/N > 5$ for each of the emission lines of the respective line ratio. We use a working resolution of 27 arcsec. We normalise the line ratio by the median value. The horizontal grey dotted lines indicate ±15% deviations from the median value.

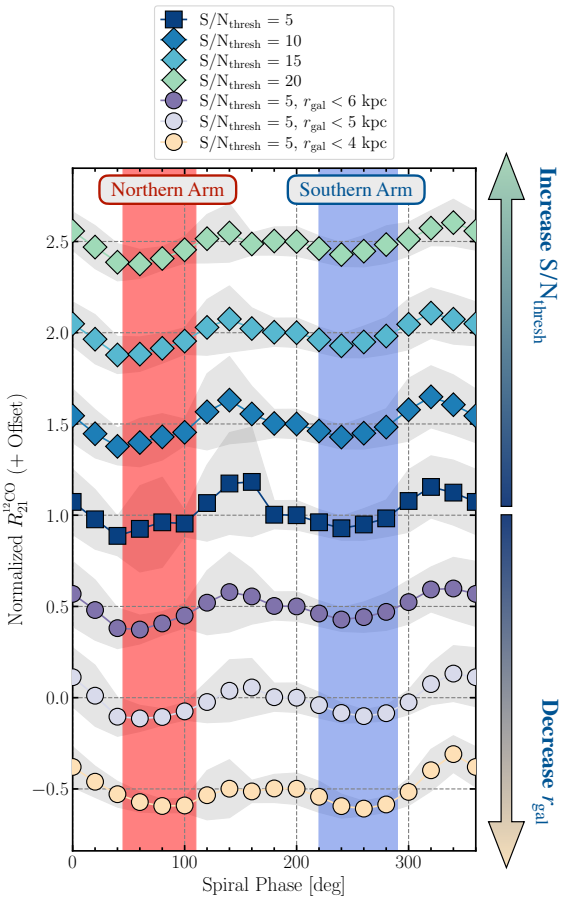

Fig. 14. Spiral arm–interarm CO line ratio variation consistency. For the arm–interarm variation in Fig. 12, we include all sight lines with $S/N > 5$. Here, we increase the S/N threshold from 5 to 20 in steps of 5 to investigate whether the higher line ratios are still preserved in the interarm region. Furthermore, we add a radial constraint, only including sight lines within a given galactocentric radius of 4, 5, and 6 kpc. We normalise the line ratios by the global CO (2−1) brightness weighted median. We offset different line ratios in steps of 0.5 (in the positive direction for increasing S/N and in negative steps for decreasing radial constraint). We see that the trend of higher line ratios in the interarm region is persistent for all computations shown in this figure.

in Fig. 12 for all the different combinations of the CO (1−0) and CO (2−1) datasets, den Brok et al. (2021) found that the cause of the discrepancy comes from substituting the CO (1−0) data and not from substituting CO (2−1) data. This demonstrates that the opposite arm–interarm trend is not an artefact of the new CO (2−1) data taken with the IRAM 30 m telescope as part of this programme and that care should be taken combining datasets from different telescopes and receivers when carrying out measurements of molecular line ratios.

To verify if using ^{12}CO (2−1) with a different sensitivity and flux calibration uncertainty changes the outcome, we substituted the CLAWS CO (2−1) data with the HERACLES CO (2−1) data (Leroy et al. 2009) as an experiment. We also find a lower line ratio ($R_{21}^{12CO} \approx 0.7$; see Appendix B). Such a dependence of the absolute value on the specific dataset has been discussed in den Brok et al. (2021) by comparing HERACLES, ALMA, IRAM 30 m, and NRO CO (1−0) and CO (2−1) data. A variation of order 20% has been found between observations of the same line from different telescopes. This variation is attributed to uncertainties in the absolute flux calibration of the individual telescopes, which can vary between 5% to 20%. However, the flux calibration generally affects the observational data globally, so while the absolute values may differ, we would not expect to find different galaxy-wide trends when comparing CO ratios using different single-dish telescope data (e.g. den Brok et al. 2021 find the same arm–interarm R_{21}^{12CO} (i.e. higher values in the interarm region relative to the arm region) trend in M 51 when substituting CLAWS with HERACLES data).

The discrepancy could also be explained due to instrumental reasons. As previously mentioned, uncertainties in the absolute flux calibration of order up to 20% can lead to differences in the absolute value found when comparing observations from different telescopes and/or observing runs. Such variations are, however, expected to lead to global differences, so we do not expect local variation. Furthermore, contributions from the error beam might significantly affect the detected emission, in particular when observing interarm positions, if emission from brighter spiral arm regions enters via the error beam. In Appendix A, we investigate these effects for this survey and show that we still find the same arm–interarm trend even when taking account of these instrumental effects.

The CO (2−1)/(1−0) line ratio is a tracer of both the gas density and excitation temperature. There is strong evidence that interarm regions do not host higher-density molecular gas (Sun et al. 2020). Consequently, a higher line ratio in interarm regions would indicate the presence of molecular gas with a higher excitation temperature. If the UV and optical attenuation is lower in a certain region, one can assume that the gas is

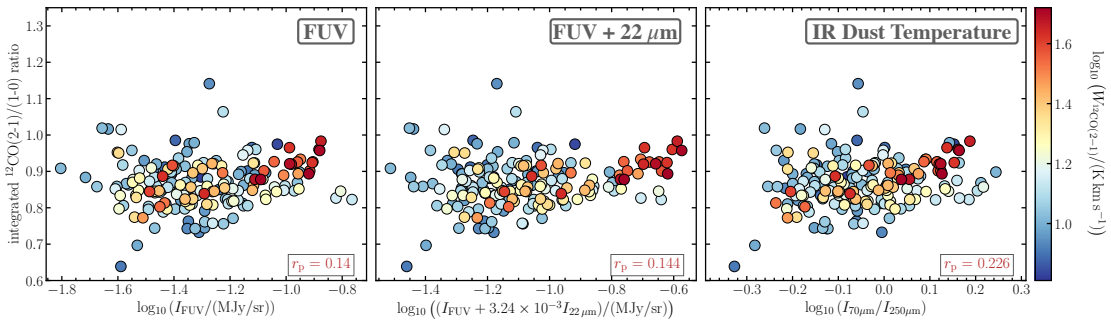

Fig. 15. ^{12}CO (2−1)/(1−0) line ratio compared to FUV intensity (*left*), FUV+22 μm (*centre*), and infrared colour (*right*). We only include sight lines with $S/N > 5$ for the line ratio to minimise scatter from faint ^{12}CO lines. We use a working resolution of 27 arcsec. FUV emission follows to some extent young (≤100 Myr) stellar populations. Because FUV can be heavily obscured, we correct using 22 μm data from *WISE* band-4 observations. To combine FUV and 22 μm, we multiply the 22 μm by a factor 3−24 × 10^{-3}. The resulting sum is proportional to the SFR surface density (Leroy et al. 2019). The infrared 70 μm/250 μm colour is a proxy for the dust temperature. We provide the Pearson's linear correlation coefficient, r_p, in each panel. We do not find any evident correlation of the line ratio with either quantity.

less shielded and the molecular gas can reach higher excitation temperatures, producing a higher line ratio. By contrast, regions with higher-density gas are better shielded and thus showing a lower excitation temperature. We note, however, that Koda et al. (2020) did not exclusively found larger line ratios in spiral arm regions in M83. To be more precise, they found larger $R_{21}^{^{12}CO}$ ratios towards the downstream, convex part of the spiral arm, spanning into the interarm region (see Fig. 1 in Koda et al. 2020). We also find enhanced line ratios more towards the downstream, convex part of the spiral arm. Further, they postulated that there is a direct or indirect link between dust heating via the ISRF and molecular cloud conditions, which may explain the trend. The large CO line ratio could then potentially be explained due to the evolution of massive stars after leaving the spiral arm downstream and consequently contributing more heavily to the dust heating because they are no longer obscured by their birth cloud. Based on the timescales of this evolution, we would expect the location to vary within spiral arm and interarm regions. Looking at Fig. 15, we do not find any apparent global correlation between FUV and the sum[12] FUV+22 μm with dust colour or $R_{21}^{^{12}CO}$. Consequently, the explanation provided by Koda et al. (2020) for the M83 is at least not straightforward to apply to explain the arm–interarm line ratio variations observed in M 51. Alternatively, the presence of diffuse emission can impact the line ratio. The result of a lower $R_{21}^{^{12}CO}$ in the spiral arm region could suggest the presence of a diffuse CO gas component, which boosts the ^{12}CO (1−0) emission (Cormier et al. 2018). Such a diffuse component would be in accordance with the diffuse component found by Pety et al. (2013).

5.2. Interpreting variations in other line ratios

For the ^{12}CO (3−2)/(2−1) line ratio, Vlahakis et al. (2013) found a global value of $R_{32}^{^{12}CO} = 0.5 \pm 0.14$, which is higher than the value we find ($R_{32}^{^{12}CO} = 0.37^{+0.09}_{-0.11}$), but within the margin of error. Similar to our finding, they identified a trend of larger values in the arm (0.5) than in the interarm (0.4), but their absolute values again are higher than the values we find.

Due to the high sensitivity of the observations we also significantly detect C^{17}O (1−0) emission towards the centre of the galaxy, if we use the 34″ spatial resolution data (see Fig. 7). While we find a positive trend with the galactocentric radius for the C^{17}O/^{12}CO (1−0), C^{17}O/^{13}CO (1−0), and C^{17}O/C^{18}O (1−0) ratios, we note the caveat that this could also be an artefact due to the fact that they are constrained by data points within the censored region. For C^{17}O/C^{18}O (1−0), when stacking by radius, we find an average value of 0.4 ± 0.1. This is slightly larger than, but of similar order of, the value of 0.24 ± 0.01 found for the solar neighbourhood (Wouterloot et al. 2005).

We also compared the azimuthal trend for the ^{12}CO (3−2)/(2−1) ^{12}CO (3−2)/(1−0), and ^{13}CO/^{12}CO (1−0) line ratios. We select these line ratios because we already investigated them in Fig. 11. For all three line ratios in Fig. 13, we only include sight lines that have $S/N > 5$ for both lines for each spiral phase. We notice that particularly the ^{13}CO/^{12}CO (1−0) line ratio clearly shows larger values in interarm regions compared to spiral arm regions. Again, such a trend could be attributed to either an increased ^{13}CO abundance or variation in the optical depth of the gas. Based on our discussion in Sect. 5.4, in which we argue that ^{13}CO abundance variations cannot explain the variation in the different CO isotopologue line ratios, we therefore conclude that most likely changes in the optical depth explain the observed difference in the arm–interarm values for the ^{13}CO/^{12}CO line ratio.

The ^{12}CO (3−2)/(2−1) line ratio also shows clear azimuthal variations. We see that the line ratio also peaks in the interarm region at spiral phase of ∼150° (see Fig. 13). We note that from the lines analysed in the figure, it is the only one that does not have ^{12}CO(1-0) in the denominator. The fact that the line ratio also peaks in the interarm region further underlines the presumption that the discrepancy to previous results comes from the use of different ^{12}CO(1–0) datasets (PAWS and NRO; see discussion in Sect. 5.1). But for ^{12}CO (3−2)/(2−1), the line ratio value also peaks in the spiral arm regions. Vlahakis et al. (2013) attributed the larger values in spiral arm compared to interarm regions to the presence of warmer and/or denser molecular gas. This is consistent with the detection of HCN (1−0) in spiral arms (Querejeta et al. 2019), but it does not explain the opposite trend for the ^{12}CO (2−1)/(1−0) line ratio. We have also seen opposite stacked ^{12}CO (3−2)/(2−1) ratio trends with galactocentric radius, ^{12}CO (2−1) brightness temperature, and TIR surface brightness when comparing to stacked ^{12}CO (2−1)/(1−0) ratio trends (see Fig. 6). This could be explained by the fact that, because of its higher excitation, ^{12}CO (3−2) emission is more

[12] We use *WISE* band-4 22 μm observations. For the sum, we normalise the infrared intensity by a factor 3.24 × 10^{-3}. The resulting sum is proportional to the SFR surface density (Leroy et al. 2019).

A&A 662, A89 (2022)

constrained to denser regions within the molecular gas and the detected emission does not have a large diffuse component.

In Fig. 9, we compare different CO line ratios with one another. We do not find any clear ratio-to-ratio trends. We recognise that in particular noise effects and uncertainties (e.g. flux calibration uncertainty) can wash out any minor existing trends. Furthermore, due to the censoring effect of line ratios with a low value, potential correlations could non-trivially be suppressed in this analysis.

5.3. Comparing CO line ratios to simulations

To better understand what we can learn from specific CO isotopologue lines, we compare our findings to simulations. Peñaloza et al. (2017) studied the utility of the ^{12}CO (2−1)/(1−0) line ratio for uncovering the physical and chemical properties of molecular clouds. In their study, they carried out a high resolution smoothed particle hydrodynamics (SPH) simulation of an isolated molecular cloud using the `GADGET-2`) SPH code supplemented with a model for the time-dependent H_2 and CO chemistry. The results of this simulation were resampled onto a hierarchical Cartesian mesh and then post-processed with the `RADMC-3D` radiative transfer code (Dullemond et al. 2012) to generate synthetic maps of ^{12}CO (2−1) and (1−0) line emission. We note that the spatial resolution used in the study is on parsec scale, while our observations are on kiloparsec scales. Consequently, any comparison has to be taken with caution, since differences in the spatial scale can also impact the relations. Peñaloza et al. (2017) found a bimodality in $R_{21}^{^{12}\mathrm{CO}}$, with one peak at ∼0.4 and another one at ∼0.7, which are below the value we see (∼0.89). They attributed the high peak to emission from cold ($T \leq 40$ K) and denser ($n \geq 10^3$ cm^{-3}) molecular gas, and the lower peak to faint emission from warmer ($T \geq 40$ K) and diffuse ($n \leq 10^3$ cm^{-3}) molecular gas. We do not see such a bimodality in $R_{21}^{^{12}\mathrm{CO}}$ (see e.g. Fig. 5). However, we cannot resolve individual giant molecular clouds with our resolution (27 arcsec or ∼1–2 kpc). As the lower ratio peak comes from diffuse emission, we would need high sensitivity observations for a secure detection of this component and high spatial resolution to separate it from molecular clouds. In a follow-up study, Peñaloza et al. (2018) investigated the impact of the galactic environment on 'cloud-averaged' CO line ratios $R_{21}^{^{12}\mathrm{CO}}$ and $R_{32}^{^{12}\mathrm{CO}}$. They performed simulations similar to Peñaloza et al. (2017), but involving a much broader range of model clouds, and analysed the post-processed CO emission. For $R_{32}^{^{12}\mathrm{CO}}$, they reported larger values (∼0.6) than what we find (∼0.4). However, their inferred scatter is ±0.2 for both $R_{21}^{^{12}\mathrm{CO}}$ and $R_{32}^{^{12}\mathrm{CO}}$ when averaging the line ratio over whole clouds. Based on their simulations, they suggested that the scatter is mainly driven by variations in the ISRF and the CRIR. Our data show a similar range of scatter, despite the large difference in spatial scale, so variations in the ISRF and CRIR could be a potential explanation for the observed change in $R_{21}^{^{12}\mathrm{CO}}$ and $R_{32}^{^{12}\mathrm{CO}}$.

The ratios of $R_{21}^{^{12}\mathrm{CO}}$ and $R_{32}^{^{12}\mathrm{CO}}$ across galactic environments were also investigated in the recent study by Bisbas et al. (2021). They rely on 3D thermochemical simulations and synthetic observations of magnetised, turbulent, self-gravitating molecular clouds. They found a remarkably flat trend for both $R_{21}^{^{12}\mathrm{CO}}$ and $R_{32}^{^{12}\mathrm{CO}}$ with respect to several galactic parameters, such as CRIR, FUV emission, and metallicity. They suggested that the flat trend is mainly due to the fact that all the environmental factors they investigated affect the ^{12}CO transitions equally. Matching to this prediction, we do not find any significant systematic variation for $R_{21}^{^{12}\mathrm{CO}}$ (see Fig. 6). However, we see a clear negative trend with galactocentric radius and SFR surface density for $R_{32}^{^{12}\mathrm{CO}}$. Consequently, this hints at another driving factor besides changes in ISRF and CRIR. But we note that Bisbas et al. (2021) only simulated molecular clouds and not the diffuse medium, which could explain the observed discrepancy or it can again be attributed to the fact that in their study they used a much higher spatial scale (approximately parsec scales).

So far, we have only discussed ^{12}CO line ratios. In our further analysis, we now include the other CO isotopologue lines and study the impact of the galactic environment.

5.4. Implications from CO isotopologue line ratio trends

As discussed in the previous section, we find clear evidence for variations within the galaxy for several combinations of different CO isotopologue line ratios (see Figs. 6, 7 and 8). We remind as a caveat that our observations have a spatial resolution of ∼1–2 kpc. Consequently, we study beam-averaged emission, so sub-beam variations can play a role (see Sect. 5.6). In the subsequent discussion, we focus on the following line ratios: ^{12}CO (2−1)/(1−0), ^{13}CO (2−1)/(1−0), ^{13}CO/^{12}CO (1−0), C^{18}O/^{12}CO (1−0), and C^{18}O/^{13}CO (1−0).

There are several potential explanations for the observed variations and trends. In a study of the ^{13}CO/^{12}CO line ratio variations in a sample of early-type galaxies, Davis (2014) offers three major explanations for systematic changes in the line ratio between different isotopologues. Summarised, variations can be explained by (i) different excitation processes for the individual CO isotopologues, (ii) fractional abundance variations in ^{13}CO and C^{18}O relative to ^{12}CO, and (iii) changes in the optical depth of the gas for one of the CO isotopologues. We note that, while ^{12}CO is generally optically thick, ^{13}CO and C^{18}O are mostly optically thin (Cormier et al. 2018), so changes in abundance will impact the emission of these lines. Using data from our survey, we can, to first order, try to isolate the main driver for the observed line ratio variations.

CO is mainly excited to higher rotational states by collisions with H_2 or He, or through photon trapping (Narayanan & Krumholz 2014). We do assume that the excitation is subthermal for most parts of our observations. Because all CO isotopologues seem to trace the same spatial region at the spatial resolution of this study (∼20 arcsec/1 kpc) and because the ^{13}CO/^{12}CO (1−0) and (2−1) line ratios both exhibit negative trends with galactocentric radius and positive trends with CO brightness temperature and TIR surface brightness, it is unlikely that different excitation processes that we investigate in more detail below cause the observed variations.

Potential mechanisms that can cause variations in the relative fractional abundance of ^{13}CO and C^{18}O are selective photodissociation, chemical fractionation or selective nucleosynthesis. In a recent letter, Jiménez-Donaire et al. (2017b) argued that CO isotopologue trends with galactocentric radius and SFR surface density, found across a sample of nearby spiral galaxies, are consistent with fractional abundance variations expected due to fractionation. Chemical fractionation is a process that can enrich ^{13}CO, but it is highly temperature dependent (Watson et al. 1976; Keene et al. 1998) and favourable in cold conditions. This process occurs in cold regions, such as the outskirts of galaxies. If this were the main cause of the observed variations, we would find lower ^{13}CO abundances in warmer regions. Due to more heating from young stars, it is expected that the SFR surface density correlates to a certain degree with gas temperature. Consequently, we expect a decrease in ^{13}CO abundance

with increasing Σ_{SFR}. As $C^{18}O$ is not affected by fractionation, the decreasing radial trend that we find for the $^{13}CO/C^{18}O$ line ratio, is in agreement with this explanation. However, we also see an increasing trend with increasing Σ_{SFR} for the $^{13}CO/^{12}CO$ line ratio, which contradicts the explanation that abundance variations are due to chemical fractionation alone, as we would expect the opposite trend: A larger line ratio at larger radii and smaller SFR surface densities would be due to an increase in the abundance of ^{13}CO in these environments.

Additionally, selective photodissociation cannot explain the observed trend in $^{13}CO/^{12}CO$. The process occurs in strong ISRFs. While on the one hand, ^{12}CO more shielded, ^{13}CO on the other hand is less well protected over large areas, so strong UV radiation will destroy the molecule (van Dishoeck & Black 1988). As high star formation is linked to the presence of OB stars, a negative trend with SFR would have been expected. Abundance variations due to selective nucleosynthesis could explain the observed decreasing trend in the $^{13}CO/C^{18}O$ line ratio with SFR surface density. While ^{12}C and ^{18}O are mainly produced in massive stars, ^{13}C is primarily produced in low-mass stars (Sage et al. 1991), as it is converted further to ^{14}N in high-mass stars (>8 $M_\odot$), which would lead to only a very small replenishing rate of ^{13}C in the ISM (Prantzos et al. 1996). But in low- and intermediate-mass stars ^{13}C can surface, due to convection, during the red giant phase and consequently enhance the abundance (Wilson & Matteucci 1992). In their study, Brown & Wilson (2019) attributed the extremely low $^{13}CO/C^{18}O$ line ratio in ULIRGs to an excess in massive star formation. Furthermore, an increase in $^{12}C/^{13}C$ and $^{16}O/^{18}O$ with galactic radius is observed (Langer & Penzias 1990; Milam et al. 2005). Such a trend arises if we assume an inside-out formation scenario for galaxies (Tang et al. 2019). If M 51 exhibits similar carbon and oxygen isotope trends, also the observed $^{13}CO/^{12}CO$ and $C^{18}O/^{12}CO$ variation can be explained.

Finally, variations in the optical depth or changes in physical conditions (e.g. gas temperature or density) of the CO isotopologues will also cause variations in the observed line ratios. For example, in LTE, the ^{12}CO optical depth depends on the gas column density, N_c, the gas velocity dispersion, σ, and the gas kinetic temperature, T_k, via $\tau \propto N_c/(\sigma T_k)$ (Paglione et al. 2001). Increased turbulence in the centre, for example, could decrease the optical depth of $^{12}CO\,(1-0)$. The trends we observe in the CO isotopologue line ratios are all consistent with changes in the optical depth.

Given the trends we find in the $^{13}CO/C^{18}O$ and $^{13}CO/^{12}CO$ line ratios, we reach a similar conclusion to Cormier et al. (2018): Abundance variations due to nucleosynthesis (assuming similar isotope trends as in the Milky Way) and/or changes in the physical conditions (temperature, density, opacity) of the gas can explain the global observed CO isotopologue line ratio variations. We recognise that most likely we are seeing a combination of effect that depends further on the SF history and chemical enrichment.

5.5. CO spectral line energy distribution

In the previous sections, we have discussed variations we find in the CO line ratios. Here, we want to further analyse in particular ^{12}CO excitation, which is relevant, for example, to accurately estimate molecular gas masses at high redshift where CO low-J transitions are difficult to obtain. Converting CO luminosities to H_2 gas masses generally relies on observations of the $^{12}CO\,(1-0)$ transition, or via down-conversion of observed higher-J observations. In particular high redshift studies rely on such down-conversions (Solomon & Vanden Bout 2005; Carilli & Walter 2013). A proper down-conversion requires a good understanding of the CO SLED. Using the three rotational transitions of ^{12}CO presented in this study, $J = 1 \rightarrow 0$, $2 \rightarrow 1$ and $3 \rightarrow 2$, we can investigate the CO SLED. As described by Narayanan & Krumholz (2014), the CO excitation, and thus the precise shape of the SLED, is expected to depend on gas temperatures, densities, and optical depth within the ISM. Consequently, we do not expect that the CO SLED is constant across the galaxy. In their study, Narayanan & Krumholz (2014) provided a parametrisation of the CO SLED as a function of SFR surface density. In Fig. 16, we investigate variations in the CO SLED with galactocentric radius, galactic morphology and SFR surface density. We see that, with the exception of sight lines within the central 1 kpc radius (which are also impacted by the central active galactic nucleus), the CO SLED has reached its turning point already at $J = 2 \rightarrow 1$. The shapes of the CO SLEDs for arm and interarm regions are very similar. But we see that variations in the CO SLED as a function of Σ_{SFR} do not follow the model presented in Narayanan & Krumholz (2014), as in particular the $^{12}CO\,(3-2)$ line seems to be fainter than the predictions of the models (see right panel in Fig. 16). In their study, they compared their model mainly to high-z sub-millimetre galaxies (SMGs). As SMGs exhibit more extreme star formation, the ISM conditions are very likely different in terms of gas temperature and density from the conditions present in M 51, which could explain the discrepancy of the CO SLED in M 51 and predicted by the models.

We note that there are also other explanations for a depression of the CO SLED relative to the models. If the beam filling factor differs significantly between the three ^{12}CO transitions, with the beam filling factor for $^{12}CO\,(3-2)$ being the smallest, beam dilution could drive down the CO SLED. The model presented in Narayanan & Krumholz (2014) takes into account different beam filling factors for the different CO transitions. In the case of the three ^{12}CO transitions we analyse, the effect is a decrease of order 10% if we apply the model that accounts for beam filling factors. Only for higher-J transitions, the effect will increase as their emission is coming from more compact regions due to the larger excitation. For confirmation that the assumed differences in beam filling factors of the model are appropriate in the case of M 51, we would need higher resolution observations for all the three low-J transitions. Narayanan & Krumholz (2014) described other effects that may lead to discrepancy between model and observation. In particular, dust extinction, which affects the very high-J transitions more, can explain the depression of the CO SLED relative to the prediction from the model. However, as our CO lines are observed in the millimetre regime, dust effects will be minimal in a normal star-forming disc galaxy such as M 51. Consequently, we do not believe that the divergence of the observations from the model can be attributed to the effects of dust.

5.6. Molecular lines and systematic density variation

In our discussion so far, we have only focused on the CO isotopologue lines. However, molecular line ratios that include denser gas tracers (such as HCN, HNC, or HCO^+) can also be used to study the underlying molecular gas density. The picture is complex: Our working resolution of >15 arcsec/600 pc is substantially larger than the dense star-forming cores, which have sizes of 0.1−1 pc (e.g. Lada & Lada 2003; André et al. 2014). Consequently, within our beam, a large range of gas volume densities are included. Therefore, the sub-beam density distribution

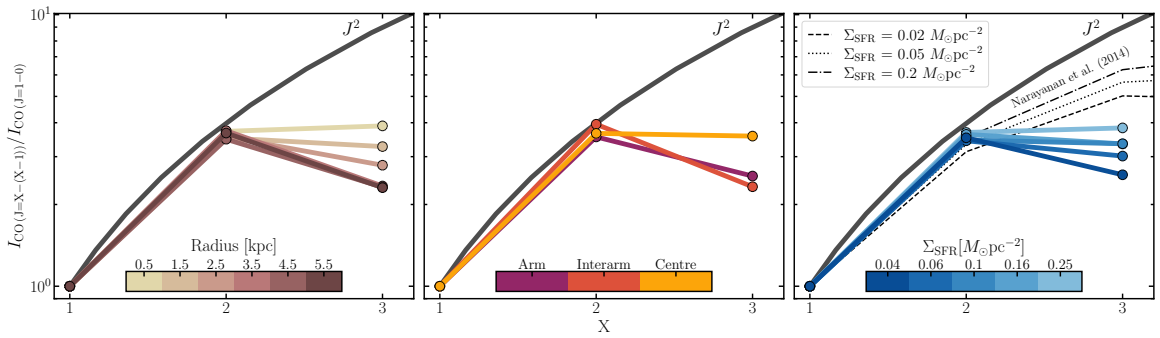

Fig. 16. CO SLED variation in M 51. *Left*: CO SLED binned by 1 kpc radial bins ranging up to 6 kpc. With the exception of the most central 1 kpc bin, we see that the CO SLED peak is already reached for $J = 2 \rightarrow 1$. *Middle*: Variation with galactic environment. The spiral arm and interarm regions show a similar CO SLED shape. *Right*: Variation as a function of SFR surface density. We include predictions for $\Sigma_{SFR} = 0.2, 0.05$, and $0.02\,M_\odot\,pc^{-2}$ based on the model code provided in Narayanan & Krumholz (2014). We use their unresolved model, which takes different beam filling factors into account for the three CO transitions. For this analysis, we use the data at a 27 arcsec working resolution.

affects the overall emission averaged over the full beam size, because certain lines emit more efficiently for a particular density distribution. Generally speaking, emission lines originate not just at or above the critical density, but the wide density distribution within our coarse observations has to be taken into account.

Leroy et al. (2017) showed by applying non-LTE radiative transfer models on a range of underlying density distributions that the line ratios of high-to-low critical density lines (i.e. emission lines with higher critical density[13]) are more sensitive to changes in gas density. For such lines, a substantial fraction of the emission can originate from regions that have a density below the nominal critical density. They based their predictions on basic radiative transfer models and a parametrised density probability distribution to characterise the effect of sub-beam density variations on the observed beam-averaged emission. The crucial point is that a line can still be emitted at densities much below the critical density, just with a reduced emissivity. Consequently, a slight increase in the gas density can significantly increase the emissivity of the emission line. This is not the case for lines with low critical density. The gas density generally exceeds the critical density already for such lines, so a variation in the gas density will not significantly impact the emissivity of the emission line.

The lines observed as part of our sample as well as the ancillary lines can be used to test whether lines with higher critical density show a larger scatter in the line ratio with respect to CO (1–0). We stack the data by CO (1–0) brightness temperature and compute the line ratio with respect to CO (1–0). In Fig. 17, we normalise the line ratios by the median value for each line ratio. Lines with a higher critical density are shown towards the right end of the plot. We colour-code the points by binned CO (1–0) brightness temperature, which we use as a shorthand for gas density. There is a distinct increase in the variation (a 'flaring') in the line ratio pattern towards higher-density tracers, in agreement with the predictions from Leroy et al. (2017), as these lines are more sensitive to variations in the sub-beam gas density distribution. This is already apparent from looking at the ^{12}CO transitions. The critical density of

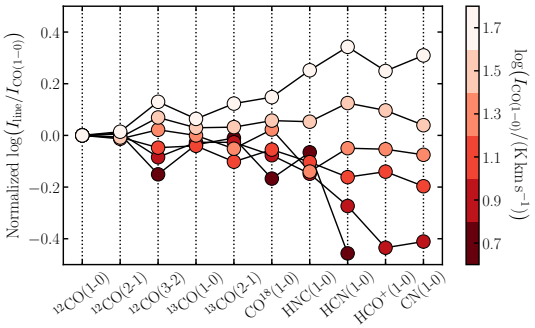

Fig. 17. Patterns of molecular line ratios for M 51. Each molecular line is stacked by CO (1–0), and the line ratio is normalised by the mean stacked line ratio with CO (1–0). We colour-coded by the CO (1–0) line brightness of the stacked bin. The line ratios are roughly ordered from left to right by increasing critical density of the line entering in the numerator. We find an increase in the line ratio variations towards the right end of the plot. Such a trend is in agreement with the results from the models presented in Leroy et al. (2017).

^{12}CO (3–2) is about an order of magnitude larger than for the (2–1) and (1–0) transitions (in the optically thin case; Carilli & Walter 2013) and we clearly find a larger variation in the ratio with ^{12}CO (3–2)/(1–0) than in the ^{12}CO (2–1)/(1–0) line ratio.

With this analysis, we thus find a larger dynamical range of line ratios of lines with a large difference in critical density. This supports the idea that the flaring pattern seen in Fig. 17 is in agreement with the higher sensitivity of these line ratios with respect to the mean gas density. Line ratio patterns of such a diverse suite of lines are thus a powerful tool for constraining the molecular gas physical conditions.

6. Conclusion

In this paper, we present observations of several CO isotopologues in the galaxy M 51 obtained with the IRAM 30 m telescope. Besides $J = 1 \rightarrow 0$ and $J = 2 \rightarrow 1$ transitions of ^{13}CO and C^{18}O, we also detect C^{17}O (1–0) emission as well as supplementary lines, such as CN (1–0), CS (2–1), N_2H^+ (1–0), and CH_3OH (2–1):

[13] For our qualitative discussion in this section, we do not go into detail regarding the various definitions of critical densities. See Leroy et al. (2017) or Shirley (2015) for a more in-depth discussion of the various definitions and their advantage and disadvantages in describing the conditions of efficient line emission.

1. We study the CO isotopologue line ratios as a function of galactocentric radius, ^{12}CO (2−1) intensities (which translates to molecular mass surface density), and TIR surface brightness (which is correlated with the SFR surface density). Several line ratios, such as ^{12}CO (2−1)/(1−0), ^{12}CO (3−2)/(2−1), and ^{13}CO (2−1)/(1−0), show a significant increase of order 5 to 40% towards the centre of the galaxy compared to their disc-averaged line ratios;
2. Galactic morphology, such as spiral arm and interarm regions, seems to affect several line ratios. In addition to increased line ratios in the centre, ^{12}CO (2−1)/(1−0) and ^{13}CO/^{12}CO(1−0) show indications of larger values in interarm regions than in spiral arm regions. Previous studies attributed an increase in the ^{12}CO (2−1)/(1−0) line ratio to the more efficient dust heating by bright, young stars (<100 Myr) at the convex, downstream end of the spiral arm. We do not, however, see any trend in the line ratio with either UV or infrared radiation;
3. We investigate the potential cause for the observed variations in the ^{13}CO/^{12}CO, C^{18}O/^{12}CO, and C^{18}O/^{13}CO line ratios. A change in optical depth most likely explains the trend seen with galactocentric radius and TIR surface density, which indicates that abundance variations in the CO isotopologues are not the cause;
4. The shape of the CO spectral energy distribution varies with galactic environment. We find a relation between the shape of the CO SLED and the SFR surface density, but the turning point of the CO SLED shape is at a lower J than predicted by recent models, which are mostly calibrated on high-z SMGs.

As a potential future study, high-quality observations at low spatial resolutions can be combined with higher spatially resolved observations to also study the diffuse CO component for the CO isotopologues and furthermore investigate line ratio variation at different spatial scales. In addition, by performing non-LTE analyses using modelling tools, it can be possible to gain further constraints on the CO-to-H_2 conversion factor or – in combination with dense gas data from EMPIRE (HCN, HCO$^+$, and HNC (1–0)) – the probability density function. This will improve constraints on the average volume density, which constituted one of the major science goals of the EMPIRE survey.

Acknowledgements. J.dB., F.B., J.P., A.T.B. and I.B. acknowledge funding from the European Research Council (ERC) under the European Union's Horizon 2020 research and innovation programme (grant agreement no.726384/Empire). T.S., E.S., H.A.P. and T.G.W. acknowledge funding from the European Research Council (ERC) under the European Union's Horizon 2020 research and innovation programme (grant agreement no. 694343). H.A.P. further acknowledges the Ministry of Science and Technology (MOST) of Taiwan under grant 110-2112-M-032-020-MY3. The work of AKL is partially supported by the National Science Foundation under Grants No. 1615105, 1615109 and 1653300. A.U. acknowledges support from the Spanish grants PGC2018-094671-B-I00, funded by MCIN/AEI/10.13039/501100011033 and by "ERDF A way of making Europe", and PID2019-108765GB-I00, funded by MCIN/AEI/10.13039/501100011033. E.R. acknowledges the support of the Natural Sciences and Engineering Research Council of Canada (NSERC), funding reference number RGPIN-2017-03987. C.E. acknowledges funding from the Deutsche Forschungsgemeinschaft (DFG) Sachbeihilfe, grant number BI1546/3-1. SCOG and RSK acknowledge support from the DFG via SFB 881 "The Milky Way System" (sub-projects B1, B2 and B8) and from the Heidelberg cluster of excellence EXC 2181-390900948 "STRUCTURES: a unifying approach to emergent phenomena in the physical world, mathematics, and complex data", funded by the German Excellence Strategy. R.S.K. furthermore thanks for financial support from the European Research Council via the Synergy Grant "ECOGAL" (grant 855130). J.M.D.K. gratefully acknowledges funding from the Deutsche Forschungsgemeinschaft (DFG, German Research Foundation) through an Emmy Noether Research Group (grant number KR4801/1-1) and the DFG Sachbeihilfe (grant number KR4801/2-1), as well as from the European Research Council (ERC) under the European Union's Horizon 2020 research and innovation programme via the ERC Starting Grant MUSTANG (grant agreement number 714907). For our research, we made use of Astropy and affiliated packages. Astropy is a community-developed core Python package for Astronomy (Astropy Collaboration 2018). Furthermore, we employed the Python package NumPy (Harris et al. 2020), SciPy (Virtanen et al. 2020), and APLpy, an open-source plotting package for Python (Robitaille & Bressert 2012).

References

Accurso, G., Saintonge, A., Catinella, B., et al. 2017, MNRAS, 470, 4750
Aladro, R., Viti, S., Bayet, E., et al. 2013, A&A, 549, A39
André, P., Di Francesco, J., Ward-Thompson, D., et al. 2014, in Protostars and Planets VI, eds. H. Beuther, R. S. Klessen, C. P. Dullemond, & T. Henning, 27
Aniano, G., Draine, B. T., Gordon, K. D., & Sandstrom, K. 2011, PASP, 123, 1218
Astropy Collaboration (Price-Whelan, A. M., et al.) 2018, AJ, 156, 123
Bensch, F., Panis, J. F., Stutzki, J., Heithausen, A., & Falgarone, E. 1997, in Astronomische Gesellschaft Abstract Series, 13, 205
Bigiel, F., Leroy, A. K., Walter, F., et al. 2011, ApJ, 730, L13
Bisbas, T. G., Tan, J. C., & Tanaka, K. E. I. 2021, MNRAS, 502, 2701
Bolatto, A. D., Wolfire, M., & Leroy, A. K. 2013, ARA&A, 51, 207
Brown, T., & Wilson, C. D. 2019, ApJ, 879, 17
Cañameras, R., Yang, C., Nesvadba, N. P. H., et al. 2018, A&A, 620, A61
Cao, Y., Wong, T., Xue, R., et al. 2017, ApJ, 847, 33
Carilli, C. L., & Walter, F. 2013, ARA&A, 51, 105
Chevance, M., Madden, S. C., Fischer, C., et al. 2020, MNRAS, 494, 5279
Colombo, D., Meidt, S. E., Schinnerer, E., et al. 2014, ApJ, 784, 4
Cormier, D., Bigiel, F., Jiménez-Donaire, M. J., et al. 2018, MNRAS, 475, 3909
Costagliola, F., Aalto, S., Rodriguez, M. I., et al. 2011, A&A, 528, A30
Croux, C., & Dehon, C. 2010, Stat. Meth. Appl., 19, 497
Dale, D. A., Cohen, S. A., Johnson, L. C., et al. 2009, ApJ, 703, 517
Davis, T. A. 2014, MNRAS, 445, 2378
den Brok, J. S., Chatzigiannakis, D., Bigiel, F., et al. 2021, MNRAS, 504, 3221
Dullemond, C. P., Juhasz, A., Pohl, A., et al. 2012, RADMC-3D: A multi-purpose radiative transfer tool
Galametz, M., Kennicutt, R. C., Calzetti, D., et al. 2013, MNRAS, 431, 1956
Genzel, R., Tacconi, L. J., Combes, F., et al. 2012, ApJ, 746, 69
Gong, M., Ostriker, E. C., & Kim, C.-G. 2018, ApJ, 858, 16
Gong, M., Ostriker, E. C., Kim, C.-G., & Kim, J.-G. 2020, ApJ, 903, 142
Gratier, P., Braine, J., Schuster, K., et al. 2017, A&A, 600, A27
Greve, T. R., Papadopoulos, P. P., Gao, Y., & Radford, S. J. E. 2009, ApJ, 692, 1432
Harris, C. R., Millman, K. J., van der Walt, S. J., et al. 2020, Nature, 585, 357
Hasegawa, T. 1997, in IAU Symposium, ed. W. B. Latter, S. J. E. Radford, P. R. Jewell, J. G. Mangum, & J. Bally, 170, 39
Hasegawa, T., Morino, J., Sorai, K., et al. 1997, in Astronomical Society of the Pacific Conference Series, Diffuse Infrared Radiation and the IRTS, eds. H. Okuda, T. Matsumoto, & T. Rollig, 124, 244
Henkel, C., Wilson, T. L., Langer, N., Chin, Y. N., & Mauersberger, R. 1994, Interstellar CNO Isotope Ratios, (Springer), 439, 72
Henkel, C., Asiri, H., Ao, Y., et al. 2014, A&A, 565, A3
Heyer, M., & Dame, T. M. 2015, ARA&A, 53, 583
Jiménez-Donaire, M. J., Bigiel, F., Leroy, A. K., et al. 2017a, MNRAS, 466, 49
Jiménez-Donaire, M. J., Cormier, D., Bigiel, F., et al. 2017b, ApJ, 836, L29
Jiménez-Donaire, M. J., Bigiel, F., Leroy, A. K., et al. 2019, ApJ, 880, 127
Keene, J., Schilke, P., Kooi, J., et al. 1998, ApJ, 494, L107
Kennicutt, R. C., & Evans, N. J. 2012, ARA&A, 50, 531
Koda, J., Sawada, T., Wright, M. C. H., et al. 2011, ApJS, 193, 19
Koda, J., Scoville, N., Hasegawa, T., et al. 2012, ApJ, 761, 41
Koda, J., Sawada, T., Sakamoto, K., et al. 2020, ApJ, 890, L10
Kramer, C., Peñalver, J., & Greve, A. 2013, Observational examples of spectral line calibration at the 30m telescope with MRTCAL and MIRA
Lada, C. J., & Lada, E. A. 2003, ARA&A, 41, 57
Langer, W. D., & Penzias, A. A. 1990, ApJ, 357, 477
Leroy, A. K., Walter, F., Brinks, E., et al. 2008, AJ, 136, 2782
Leroy, A. K., Walter, F., Bigiel, F., et al. 2009, AJ, 137, 4670
Leroy, A. K., Bolatto, A., Gordon, K., et al. 2011a, ApJ, 737, 12
Leroy, A. K., Walter, F., Schruba, A., et al. 2011b, in American Astronomical Society Meeting Abstracts, 217, 246.14
Leroy, A. K., Walter, F., Sandstrom, K., et al. 2013, AJ, 146, 19
Leroy, A. K., Walter, F., Martini, P., et al. 2015, ApJ, 814, 83
Leroy, A. K., Usero, A., Schruba, A., et al. 2017, ApJ, 835, 217
Leroy, A. K., Sandstrom, K. M., Lang, D., et al. 2019, ApJS, 244, 24
Leroy, A. K., Rosolowsky, E., Usero, A., et al. 2022, ApJ, 927, 149
Lisenfeld, U., Espada, D., Verdes-Montenegro, L., et al. 2011, A&A, 534, A102

Lundgren, A. A., Wiklind, T., Olofsson, H., & Rydbeck, G. 2004, A&A, 413, 505
Madden, S. C., Cormier, D., Hony, S., et al. 2020, A&A, 643, A141
Marka, C., Pety, J., Bardeau, S., & Sievers, A. 2017, Improvement of the IRAM 30mTelescope Beam Pattern, Tech. Rep. 2013-1
Martín, S., Aladro, R., Martín-Pintado, J., & Mauersberger, R. 2010, A&A, 522, A62
Matsushita, S., Iono, D., Petitpas, G. R., et al. 2009, ApJ, 693, 56
McQuinn, K. B. W., Skillman, E. D., Dolphin, A. E., Berg, D., & Kennicutt, R. 2016, ApJ, 826, 21
Meier, D. S., & Turner, J. L. 2004, AJ, 127, 2069
Meier, D. S., Walter, F., Bolatto, A. D., et al. 2015, ApJ, 801, 63
Milam, S. N., Savage, C., Brewster, M. A., Ziurys, L. M., & Wyckoff, S. 2005, ApJ, 634, 1126
Moustakas, J., Kennicutt, Robert C., J., Tremonti, C. A., et al. 2010, ApJS, 190, 233
Murphy, E. J., Condon, J. J., Schinnerer, E., et al. 2011, ApJ, 737, 67
Mutchler, M., Beckwith, S. V. W., Bond, H., et al. 2005, in American Astronomical Society Meeting Abstracts, Vol. 206, 13.07
Nakai, N., & Kuno, N. 1995, PASJ, 47, 761
Narayanan, D., & Krumholz, M. R. 2014, MNRAS, 442, 1411
Paglione, T. A. D., Wall, W. F., Young, J. S., et al. 2001, ApJS, 135, 183
Parkin, T. J., Wilson, C. D., Schirm, M. R. P., et al. 2013, ApJ, 776, 65
Peñaloza, C. H., Clark, P. C., Glover, S. C. O., Shetty, R., & Klessen, R. S. 2017, MNRAS, 465, 2277
Peñaloza, C. H., Clark, P. C., Glover, S. C. O., & Klessen, R. S. 2018, MNRAS, 475, 1508
Pety, J., Schinnerer, E., Leroy, A. K., et al. 2013, ApJ, 779, 43
Pineda, J. E., Caselli, P., & Goodman, A. A. 2008, ApJ, 679, 481
Pineda, J. L., Stutzki, J., Buchbender, C., et al. 2020, ApJ, 900, 132
Prantzos, N., Aubert, O., & Audouze, J. 1996, A&A, 309, 760
Puschnig, J., Hayes, M., Östlin, G., et al. 2020, A&A, 644, A10
Querejeta, M., Schinnerer, E., García-Burillo, S., et al. 2016, A&A, 593, A118
Querejeta, M., Schinnerer, E., Schruba, A., et al. 2019, A&A, 625, A19
Robitaille, T., & Bressert, E. 2012, APLpy: Astronomical Plotting Library in Python
Sage, L. J., Mauersberger, R., & Henkel, C. 1991, A&A, 249, 31
Sakamoto, S., Hasegawa, T., Handa, T., Hayashi, M., & Oka, T. 1997, ApJ, 486, 276
Sandstrom, K. M., Leroy, A. K., Walter, F., et al. 2013, ApJ, 777, 5
Sawada, T., Hasegawa, T., Handa, T., et al. 2001, ApJS, 136, 189
Schinnerer, E., Weiß, A., Aalto, S., & Scoville, N. Z. 2010, ApJ, 719, 1588
Schinnerer, E., Meidt, S. E., Pety, J., et al. 2013, ApJ, 779, 42
Schruba, A., Leroy, A. K., Walter, F., et al. 2012, AJ, 143, 138
Schuster, K. F., Kramer, C., Hitschfeld, M., Garcia-Burillo, S., & Mookerjea, B. 2007, A&A, 461, 143
Shetty, R., Vogel, S. N., Ostriker, E. C., & Teuben, P. J. 2007, ApJ, 665, 1138
Shetty, R., Glover, S. C., Dullemond, C. P., & Klessen, R. S. 2011a, MNRAS, 412, 1686
Shetty, R., Glover, S. C., Dullemond, C. P., et al. 2011b, MNRAS, 415, 3253
Shirley, Y. L. 2015, PASP, 127, 299
Sliwa, K., & Downes, D. 2017, A&A, 604, A2
Sliwa, K., Wilson, C. D., Aalto, S., & Privon, G. C. 2017, ApJ, 840, L11
Solomon, P. M., Rivolo, A. R., Barrett, J., & Yahil, A. 1987, ApJ, 319, 730
Solomon, P. M., & Vanden Bout, P. A. 2005, ARA&A, 43, 677
Sun, J., Leroy, A. K., Schinnerer, E., et al. 2020, ApJ, 901, L8
Tacconi, L. J., Genzel, R., Smail, I., et al. 2008, ApJ, 680, 246
Tan, Q.-H., Gao, Y., Zhang, Z.-Y., & Xia, X.-Y. 2011, Res. Astron. Astrophys., 11, 787
Tang, X. D., Henkel, C., Menten, K. M., et al. 2019, A&A, 629, A6
Tully, R. B., Rizzi, L., Shaya, E. J., et al. 2009, AJ, 138, 323
Usero, A., Leroy, A. K., Walter, F., et al. 2015, AJ, 150, 115
van Dishoeck, E. F., & Black, J. H. 1988, ApJ, 334, 771
Virtanen, P., Gommers, R., Oliphant, T. E., et al. 2020, Nat. Methods, 17, 261
Vlahakis, C., van der Werf, P., Israel, F. P., & Tilanus, R. P. J. 2013, MNRAS, 433, 1837
Walter, F., Brinks, E., de Blok, W. J. G., et al. 2008, AJ, 136, 2563
Watanabe, Y., Sakai, N., Sorai, K., & Yamamoto, S. 2014, ApJ, 788, 4
Watanabe, Y., Sakai, N., Sorai, K., Ueda, J., & Yamamoto, S. 2016, ApJ, 819, 144
Watson, W. D., Anicich, V. G., & Huntress, W. T., J. 1976, ApJ, 205, L165
Westerhout, G., Wendlandt, H. U., & Harten, R. H. 1973, AJ, 78, 569
Williams, T. G., Gear, W. K., & Smith, M. W. L. 2018, MNRAS, 479, 297
Wilson, T. L., & Matteucci, F. 1992, A&ARv, 4, 1
Wilson, T. L., & Rood, R. 1994, ARA&A, 32, 191
Wilson, T. L., Rohlfs, K., & Hüttemeister, S. 2009, Tools of Radio Astronomy (Springer)
Wilson, C. D., Warren, B. E., Israel, F. P., et al. 2012, MNRAS, 424, 3050
Wouterloot, J. G. A., Brand, J., & Henkel, C. 2005, A&A, 430, 549
Yajima, Y., Sorai, K., Miyamoto, Y., et al. 2021, PASJ, 73, 257
Yoda, T., Handa, T., Kohno, K., et al. 2010, PASJ, 62, 1277
Young, J. S., & Scoville, N. 1982, ApJ, 260, L11
Zhang, Z.-Y., Romano, D., Ivison, R. J., Papadopoulos, P. P., & Matteucci, F. 2018, Nature, 558, 260

Appendix A: IRAM 30 m error beam contribution

In this appendix we analyse the impact of the IRAM 30-m error beam on the detection of extended emission in our dataset. The response of the telescope to a point source is not a single perfect Gaussian, but has an additional contribution from the so-called error beams. Greve et al. (2009) characterised these error beams as a series of 2D Gaussians broader than the main beam but with a lesser contribution to the telescope power. The telescope beam patter was characterised again by Kramer et al. (2013) after the last major upgrade. The most recent characterisation implies that a point source of 1 Jy will only provide about 0.8 and 0.6 Jy in the telescope main beam at 3 and 1 mm, respectively, the flux remainder being scattered in the error beams. The image of a point source by the telescope will appear fainter at its actual position and the point source will contribute a faint extended brightness halo around it. This can be potentially critical when observing fainter positions inside a galaxy (e.g. interarm positions), as emission from brighter central parts of the galaxy will boost the detected line brightness. For similar observations with the IRAM 30 m telescope, Pety et al. (2013) first modelled the contributions of bright M 51 sources on the interarm signal (see their appendix C), and Leroy et al. (2015) proposed a first iterative deconvolution solution. We note that other deconvolution schemes had been proposed in the past (e.g. Westerhout et al. 1973; Bensch et al. 1997; Lundgren et al. 2004). We describe here the method we use to extract the contribution of the error beam to the emission and investigate its extent. This method will be precised in P. Tarrio et al. (in prep.). It should be noted that we perform the succeeding error beam estimation after attempt to correct for the main beam efficiency, but that this correction had assumed a signal free error beam, which may not be correct. So here we account for what happens when there is emission from the galaxy in the (assumed empty) error beam.

Appendix A.1: Model of the error beam

The exact pattern and shape of the error beam is hard to measure. It evolves as a function of the telescope's elevation because of gravitational deformation of the primary dish. It also depends on the evolution of the thermal environment, in particular at sunrise and sunset. We relied on the beam pattern characterisation by Kramer et al. (2013). This characterisation comes from on-the-fly measurements of the Moon edge at the IRAM 30 m optimal elevation of ∼50 deg. Table A.1 lists the details of the error beam parameters used here.

In essence, we are interested in the underlying, ideal, error beam corrected main brightness temperature $\hat{T}_{\rm mb}$. The main brightness temperature is not to be confused with the intrinsic brightness temperature in the sky, T. They are related via

$$\hat{T}_{\rm mb} = G_0 \otimes T, \tag{A.1}$$

where we indicate the main beam, which has a shape of a 2D circular Gaussian, by G_0. Similarly, following Kramer et al. (2013), we assumed that the error beam also consists of a set of wide 2D Gaussian beams, indicated by G_i, where $i = 1, 2, 3$ (see Table A.1).

With the telescope, we only have access to the measured brightness in $T_{\rm A}^{\star}$ unit, which we initially converted to $T_{\rm mb}$ (the brightness temperature we use in the main text) under the simplifying assumption of an empty error beam:

$$\frac{F_{\rm eff}}{B_{\rm eff}} \times T_{\rm A}^{\star} = T_{\rm mb}, \tag{A.2}$$

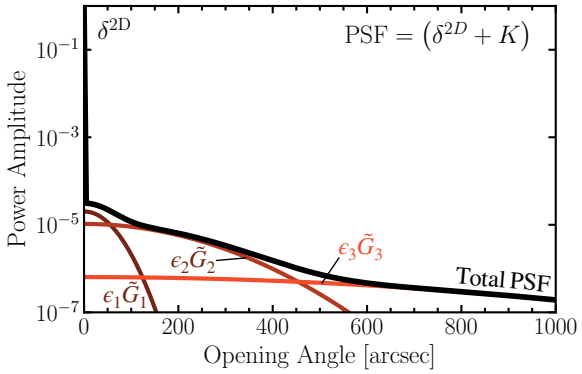

Fig. A.1. IRAM 30 m full kernel for the error beam contribution analysis after deconvolution of the main beam, G_0, for 3 mm. The kernel includes the three components of the error beam ($\tilde{G}_i$ indicates the Gaussian 2D profile after deconvolution with G_0). The ratio of the relative beam power (P_i) with respect to the relative main beam power (P_0) is indicated by $\epsilon_i = P_i/P_0$.

with the forward efficiency $F_{\rm eff}$ and the beam efficiency $B_{\rm eff}$.

The error beam corrected brightness temperature $\hat{T}_{\rm mb}$ is related to $T_{\rm mb}$ via the convolution kernel K as follows (see Figure A.1):

$$T_{\rm mb} = (\delta^{\rm 2D} + K) \otimes \hat{T}_{\rm mb}\,, \tag{A.3}$$

where $\delta^{\rm 2D}$ is the Dirac 2D distribution and the kernel K is the sum of the error beams components, after deconvolution by the main beam:

$$K = \sum_{i=1}^{3} \epsilon_i \tilde{G}_i\,, \tag{A.4}$$

where $\epsilon_i = P_i/P_0$ with P_i being the relative beam power and $\tilde{G}_i$ the deconvolution with the main beam ($G_i = \tilde{G}_i \otimes G_0$, $\tilde{\theta}_i^2 = \theta_i^2 - \theta_0^2$). Because the error beam consists of very wide 2D Gaussians, we can deconvolve the narrower main beam and get a well behaved function. Finally, to estimate the error beam contribution we have to perform a further deconvolution on Equation A.3 to determine $\hat{T}_{\rm mb}$.

Appendix A.2: Deconvolution

There are two ways in which we can approximate the error beam free source brightness temperature $\hat{T}_{\rm mb}$. The first is an iterative solution in the image plane. This approach, first described in Leroy et al. (2015), elaborates on the statement by Pety et al. (2013) that the bright intensity part of a galaxy can be approximated by the measured brightness in $T_{\rm mb}$ unit. It is possible to determine the error beam contribution by convolving the measured brightness in $T_{\rm mb}$ unit with the error beam part of the point spread function of the telescope. This gives another estimation of the source brightness that can be then used iteratively to improve the solution. In particular, we define the $N^{\rm th}$ approximate solution via the following recursion:

$$\hat{T}_{{\rm mb}|N} = T_{\rm mb} - K \otimes \hat{T}_{{\rm mb}|N-1}, \tag{A.5}$$

with $\hat{T}_{{\rm mb}|0} \equiv T_{\rm mb}$. This iterative process is stopped when the difference between two estimations becomes smaller than a give criterion.

A&A 662, A89 (2022)

Table A.1. Error beam parameters based on a cubic interpolation from Table 1 in Kramer et al. (2013).

	Main Beam	1. Error Beam	2. Error Beam	3. Error Beam
115.3 GHz				
Beam Width θ	21″	113″	434″	1518″
Integrated relative power P [%]	84	1	9	6
230.5 GHz				
Beam Width θ	10″	56″	217″	759″
Integrated relative power P [%]	69	5	13	13

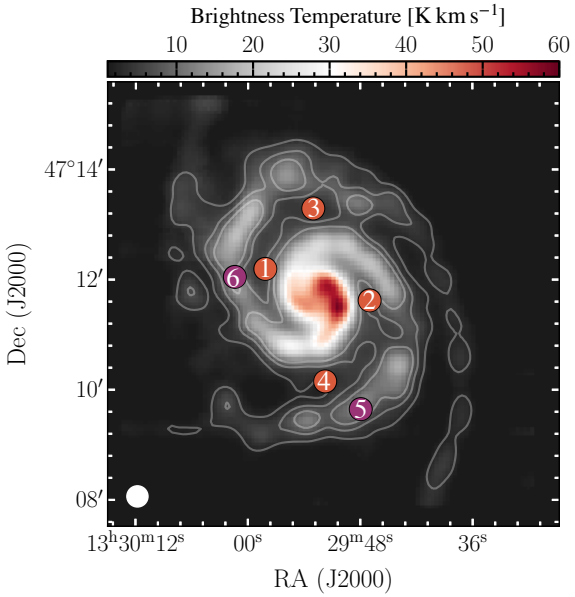

Fig. A.2. CO (2−1) line brightness temperature map. Indicated are the six pointings for which we performed the error beam correction analysis in Figure A.3. Pointings 1–4 are located in interarm regions (marked in orange). Pointings 5 and 6 are located in spiral arm regions (marked in purple). Contours are drawn at S/N = 10, 20, 30. For the IRAM 30 m DDT project E02-20, we observed these six pointings (see Appendix B.1).

The second is the Fourier plane solution. Performing a 2D Fourier transform, it follows from Equation A.3 that

$$\hat{T}_{\rm mb} = {\rm FT}^{-1}\left(\frac{{\rm FT}(T_{\rm mb})}{1+{\rm FT}(K)}\right). \quad \text{(A.6)}$$

We implemented the approach in `Python` using the unsupervised Wiener-Hunt deconvolution (based on the Wiener-Hunt approach and estimating the hyperparameters automatically).

Appendix A.3: Result and implication

We perform the error beam contribution analysis for both the PAWS ^{12}CO (1−0) and CLAWS ^{12}CO (2−1) observations. To see the effect on the spectrum, we investigate six pointings with a 23 arcsec aperture (see Figure A.2). Four pointings (1–4) are located in the fainter interarm region and two pointings (5 and 6) are situated in the brighter spiral arm region. The result of the deconvolution can be seen in Figure A.3 for the six pointings. The blue and green spectra show $T_{\rm mb}$ (the brightness temperature we derive from $T_{\rm A}^{\star}$ assuming no error beam contributions) for ^{12}CO (1−0) and ^{12}CO (2−1) respectively. In red, we indicate the contribution to the spectrum from the error beam (i.e. $T_{\rm mb} - \hat{T}_{\rm mb}$). We indicated the percentage contribution to the $T_{\rm mb}$ integrated intensity for each pointing. This contribution is calculated only for the spectral range where S/N > 3. We performed both methods described in the Appendix A.2. Both methods yield a similar percentage contribution (< 1% point difference). We continue using the exact approach via Fourier deconvolution, since it is easier to implement. We find that for the ^{12}CO (1−0) line, the impact is minor, with the contribution ranging from ∼15 per cent in the interarm and to only 4 per cent in the spiral arm region. For the ^{12}CO (2−1) emission, because the main beam efficiency is smaller ($B_{\rm eff}^{230\,\rm GHz} \approx 60$ per cent), the contribution is more significant. In the interarm, the contribution is up to 40 per cent. This is mainly due to emission from the brighter regions in the galaxy, such as the central region, entering the observation via the different error beam components. Figure A.4 shows the full 2D map. For every pixel, we computed the error beam contribution along its spectral axis. We again see a larger effect for the ^{12}CO (2−1) emission, in particular for the interarm regions (up to 30−35 per cent).

Because the 1 mm lines are affected more than the 3 mm lines by the error beam contribution, we expect the corrected $R_{21}^{^{12}\rm CO}$ to be lower. In Table B.1, we indicate the line ratio before and after correcting for the error beam. Except for pointing 4, we still find larger $R_{21}^{^{12}\rm CO}$ values in the interarm than in the spiral arm. Consequently, even though in certain instances the error beam contribution is far from negligible, it alone cannot explain the arm/interarm trend.

We reiterate that the preceding error beam analysis is subject to many uncertainties: The exact shape of the error beam is difficult to measure and subject to temporal and positional (e.g. the elevation of the telescope) variation. Furthermore, the approach we described will generally in fact overestimate the effect of the error beam in the case of single dish maps of a galaxy. Since the error beam will be comparable to the size of the galaxy, the individual spectra will include a component consisting of a strongly convolved spectrum of the full galaxy. The baseline fitting procedure we performed will then subtract such low and broad emission in resolved observations of galaxies. So the estimated value for the error beam contribution for the different positions should be interpreted with caution. However, we believe that our measurement constitute a reasonable upper limit for the order of magnitude of the error beam contribution. We refrain from suggesting a particular constant percentage uncertainty value for general observations since the error beam contribution is not constant across the galaxy and depends strongly on the galaxy morphology. But generally, one should be aware that an additional uncertainty of order 20%-40% can be possible.

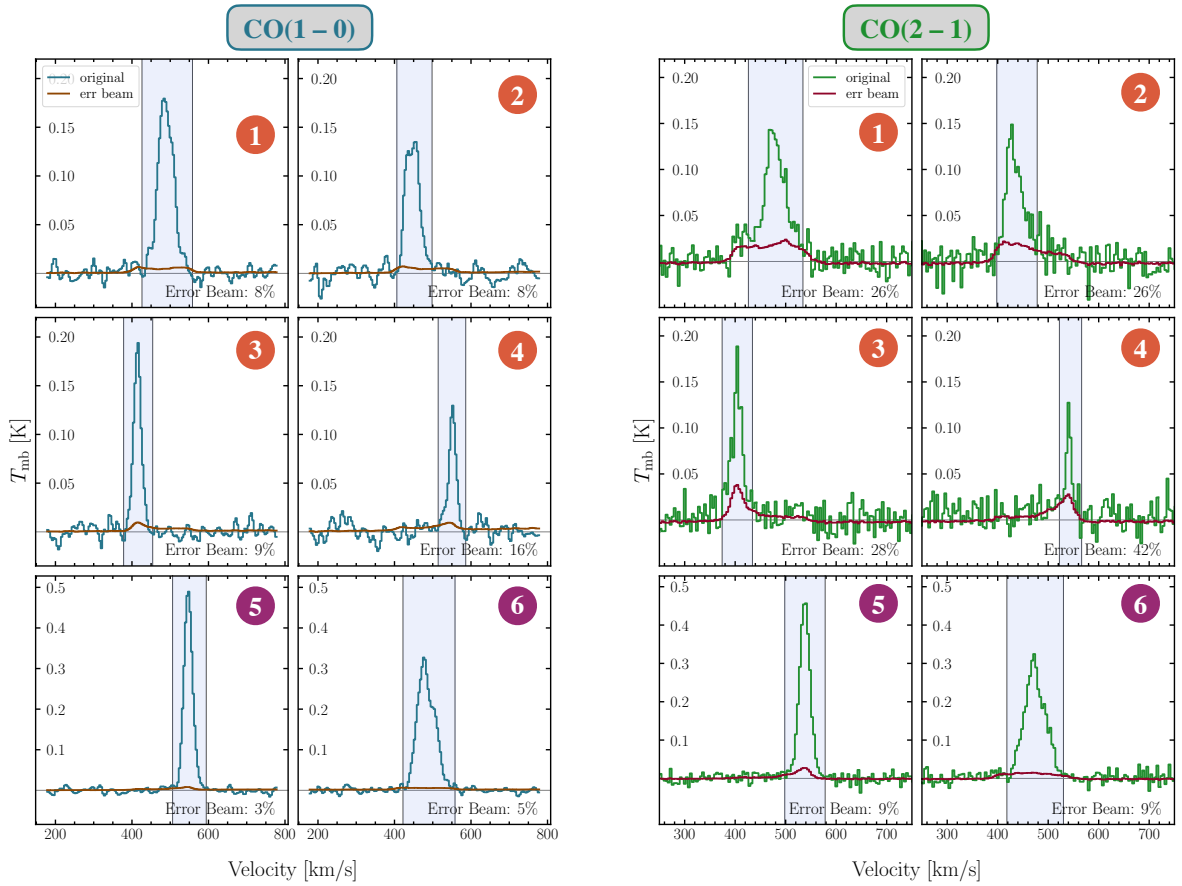

Fig. A.3. Error beam contribution analysis for individual pointings. We performed the deconvolution using the exact approach via Fourier deconvolution. After deconvolution, we performed a baseline correction. In the panels, we show the observed line brightness (T_{mb}) as well as the contribution from the error beam, $T_{mb} - \hat{T}_{mb}$. For each panel, we indicate the contribution from the error beam to the emission with S/N > 3 (see masked region). The position of the pointings is indicated in Figure A.2.

Appendix B: Flux calibration uncertainties

The flux measurements from various telescopes are subject to various degrees of calibrational uncertainties. den Brok et al. (2021) discuss in detail the impact such calibrational uncertainties can have by comparing ALMA, IRAM 30 m and NRO data. Jiménez-Donaire et al. (2019) find a flux calibration uncertainty rms of order 7 per cent for the EMIR observations from line calibrator monitoring. Finally, based on jackknifing several Heterodyne Receiver Array (HERA) datasets, Leroy et al. (2009) estimate that their HERACLES CO (2–1) observations are subject to up to a typical 20 per cent uncertainty in rms. As the data for CLAWS were observed using the EMIR instrument, which has more stable calibration than HERA, we assume our data to have an uncertainty under 10 per cent, as reported by IRAM.[14]

In this section we describe the results from the IRAM 30 m director's discretionary time (DDT) proposal, in which we observed the six pointings shown in Figure A.2 to address the flux stability in the arm and interarm to understand its impact on the arm–interarm CO line ratio.

[14] https://publicwiki.iram.es/EmirforAstronomers#Telescope_efficiencies

Appendix B.1: DDT proposal E02-20

As we have seen in the previous section, comparing datasets from different telescopes/instruments taken at different times needs extra care as uncertainties in the flux calibration can affect absolute values of line emission and ratios. den Brok et al. (2021) determined that the arm–interarm CO line ratio discrepancy contrast (and the line ratio itself) is sensitive to combining datasets from different telescopes and instruments. For example, Koda et al. (2012) find a different line ratio in the interarm region of M 51 using NRO ^{12}CO (1–0) compared to den Brok et al. (2021) and this study. Here we address the question of whether the stability of the flux calibration could explain this discrepancy.

To address this question we obtained 6 h DDT IRAM 30 m time to observe six carefully selected pointings (see Figure A.2), four in the interarm and two in the spiral arm region. As we observe CO (1–0) and ^{12}CO (2–1) simultaneously, any time dependence is removed when investigating the line ratio.

Observations were carried out on 2021 February 27 and on the night of 2021 March 8. We cannot simply take the line ratio, as the ^{12}CO (2–1) beam is smaller than the ^{12}CO (1–0) beam. To estimate how to scale the high resolution ^{12}CO (2–1) spectrum when convolving it to the resolution of ^{12}CO (1–0), we first

A&A 662, A89 (2022)

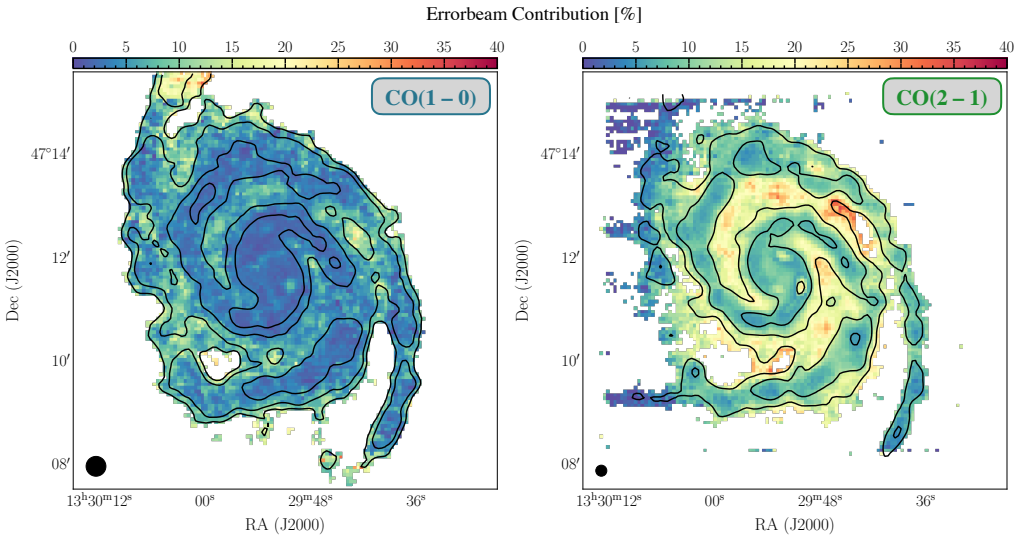

Fig. A.4. 2D distribution of the error beam contribution. (*Left*) ^{12}CO (1−0) map. Contours are drawn at S/N = 10, 20, 30 of CO (1−0) emission. (*Right*) ^{12}CO (2−1) map. We see that the error beam contribution is more pronounced for CO (2−1), in particular in the interarm regions of the galaxy.

extract a spectrum using a 11.5 arcsec (i.e. beam-sized) aperture from the CLAWS ^{12}CO (2–1) map. We then convolve the CLAWS ^{12}CO (2–1) to the lower angular resolution of 23 arcsec (i.e. PAWS resolution). We now extract a ^{12}CO (2–1) from the same position in the convolved CLAWS map, but use a 23 arcsec aperture. By comparing the two extracted ^{12}CO (2–1) spectra, we can determine a scaling factor, which we can apply to the ^{12}CO (2–1) spectrum obtained from the DDT programme.

The comparison of the line ratios is shown in Figure B.1 and the numerical values are listed in Table B.1. Circles represent the line ratio using the PAWS and CLAWS data. We notice that the line ratio is elevated in the positions of the spiral arm (1–4). Blue rectangles indicate the line ratio using the acquired DDT observations. While there is a global offset between the ratios measured in both experiments, the trend of larger line ratios in the interarm region still remains. The offset of order 20 to 30 per cent between the two datasets is mainly due to an overall calibration difference. We find that the CO (1−0) line intensities are systematically higher by 20 to 30 per cent for the DDT EMIR observations compared to the CO (1−0) data from PAWS, which reduces the line ratio overall. We note that the discrepancy between NRO and the PAWS CO (1−0) is still greater. Especially in the interarm region, the NRO data are larger by a factor of ∼2. This is related to a change of the calibration strategy of the EMIR receivers, which happened in February 2017 when the calibration software swapped from `MIRA` to `MRTCAL`. To first order, the calibration factor applied to the spectrometer data is proportional to the measured system temperature computed on the calibration scan. While `MIRA` was computing this system temperature on spectral chunks of 4 GHz, `MRTCAL` computes it every 20 MHz. Marka et al. (2017) shows that this leads to an overestimation of the system temperature for lines that lies at the edges of the atmospheric windows as this is the case for ^{12}CO (1−0) whose rest frequency lies inside the wings of the di-oxygen telluric line. In this case, calibrating the PAWS data with `MRTCAL` would lead to higher (and more accurate) system temperature, and thus higher line brightnesses.

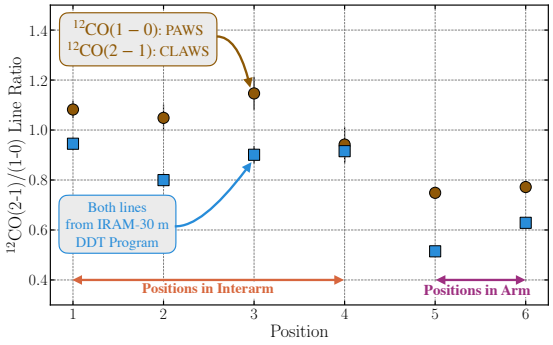

Fig. B.1. Arm–interarm CO line ratio analysis. Circles indicate the ^{12}CO (2−1)/(1−0) line ratio for lines extracted over the apertures shown in Figure A.2. The squares show the CO line ratio from the IRAM 30 m DDT project E02-20. Positions 1–4 are within the interarm of the galaxy, and positions 5 and 6 are in the spiral arm region. We see that both show larger line ratios in the interarm regions, leading us to conclude that the trend we find is not due to issues with the flux calibration uncertainties. The numerical values of the individual points are listed in Table B.1.

Relative flux calibration can be significant. But our analysis leads us to conclude that relative flux calibration is not the main cause of the arm–interarm trend, since we find also larger line ratio values in the interarm region using the newer IRAM 30 m DDT observations.

Appendix C: Products for public data release

Along with this survey paper, we provide several data products for the various spectral lines. The data products are stored on

Table B.1. Comparison of the ^{12}CO (2–1)/(1–0) line ratio within the selected positions, 1–6, using either the CLAWS ^{12}CO (2−1) and PAWS ^{12}CO (1−0) dataset or the newly acquired IRAM 30 m data from project E02-20.

	Position	R_{21}^{12CO}		
		CLAWS/PAWS data		E02-20 data
		raw	e.b. corrected	
Interarm	1	1.08 ± 0.03	0.94 ± 0.03	0.87 ± 0.02
	2	1.05 ± 0.05	0.84 ± 0.05	0.80 ± 0.03
	3	1.15 ± 0.07	0.91 ± 0.06	0.90 ± 0.04
	4	0.94 ± 0.07	0.65 ± 0.05	0.92 ± 0.05
Arm	5	0.75 ± 0.01	0.70 ± 0.01	0.52 ± 0.01
	6	0.77 ± 0.02	0.74 ± 0.01	0.63 ± 0.01

Notes. For the CLAWS/PAWS R_{21}^{12CO}, we provide the value without (raw) and with error beam correction (based on the error beam contribution indicated in Figure A.3).

the IRAM server.[15] The data have been processed following the methodology adopted for the IRAM Large Programmes EMPIRE (Jiménez-Donaire et al. 2019) and HERACLES (Leroy et al. 2009). The IRAM repository for Large Programmes provides the following, non-error beam corrected data products: (i) for all lines: the 3D data cubes, the rms and uncertainty maps, and the integrated brightness temperature (moment-0) maps; and (ii) for ^{12}CO (2−1) and ^{13}CO (1−0) only: the intensity-weighted velocity (moment-1) maps, the equivalent width maps, and the peak temperature maps.

We refer the reader to the `Readme` file at the IRAM data repository for more detailed information. We ask that when using this dataset or parts of it, this paper be cited.

[15] https://www.iram-institute.org/EN/content-page-434-7-158-240-434-0.html

APPENDIX C

M101 Wide-Field CO Paper

Overview

The following sections constitute the appendix of Chapter 6, *Wide-Field Multi-CO Emission Across M101*.

C.1 Single Dish Scale Factor Estimation

The scatter minimization technique uses total gas mass estimates derived from dust mass measurements. With the help of atomic gas mass estimates via H I observations, we can separate the total gas in to an atomic and a molecular gas component, from which we can deduce α_{CO}. For the analysis, we use H I 21cm

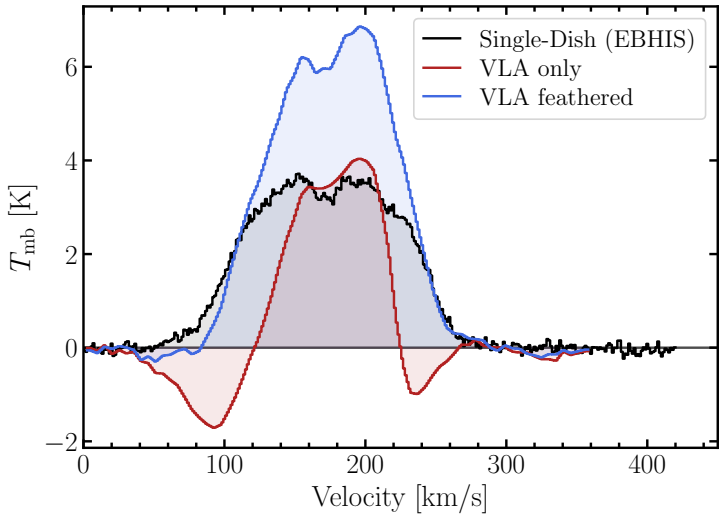

Figure C.1: **H I Short Spacing Correction** The THINGS H I data cube for M101 is seriously affected by filtering and bowling artifacts. The red spectrum illustrates the spectrum for an arbitrarily selected line of sight at 650″ spatial resolution (angular resolution of the Effelsberg single-dish data). The black spectrum shows the same sightline spectrum obtained from the Effelsberg single-dish data (EBHIS survey). We used the `uvcombine` package to determine a single-dish scale factor of 1.7. The blue spectrum shows the resulting feathered observation for the selected sightline.

cubes from the TINGS survey (Walter et al., 2008). The observations for M101 are, however, severely limited by filtering issues (see). In order to correct these issues, we feathered the data using H I observations from the Effelsberg-Bonn HI Survey (EBHIS; Winkel et al., 2016).

Figure C.1 illustrates the need for correctly feathering the interferometric VLA data from the THINGS survey. The red spectrum indicates the VLA-only data. Clear bowling on both sides of the spectral line seriously hampers integrated intensity measurements. The black spectrum shows the single-dish data in the figure. Using the Python package `uvcombine` we determine a single-dish factor of 1.7. We use the `casa-feather` tool to feather the data. Not correcting the VLA-only data would significantly underestimate the total H I emission (total intensity lower by 70% before feathering).

C.2 Censored Line Ratio Regions

As a consequence of how we have constructed the line ratio (fainter lines in the numerator), we can also estimate the censored region in the ratio plane. If we observe lines observed with different sensitivity, the noise levels will differ for each line. Since we compare lines of varying brightness, we will obtain many upper limits. We expect to obtain significantly fewer line ratios at lower values since the line in the numerator has reached the sensitivity. Larger line ratios are still possible because this can happen due to either lower line brightness in the denominator (since we have not yet reached the sensitivity limit) or larger brightness of the line in the numerator. We bin the line ratios by a certain quantity. We then estimate the censored 1σ (or 3σ) region in the following way: We divide the average rms (or $3\times$ this value) of the faint line per bin by the average brightness temperature of the brighter line. We reiterate that this approach is only valid when constructing the line ratio to have the fainter line in the numerator. Since rms and the line brightness vary across the survey field, we expect to find a certain number of significantly detected data points within the censored region.

C.3 CO Line Stacks

In order to improve the S/N – which allows for the detection of fainter emission lines – we stack the spectra after binning by a certain quantity (e.g., radius, star formation rate surface density, etc.). By shifting the spectrum of each line of sight to the zero velocity, we ensure that the spectra are added coherently. In general, the combination of N independent sightlines will enhance the S/N by a factor $\sqrt{N}$.

Figure C.2 shows the individual radial stacks for the ^{12}CO (1–0) and ^{13}CO (1–0) molecular transition lines. Each panel indicates the S/N ratio for the integrated ^{13}CO (1–0) intensity. We require a detection with S/N > 3 to classify it as *significant*. Significant stacks are shown in green, while non-significant line detections are framed in red. We note that with the help of stacking, we do significantly detect ^{13}CO (1–0) out to 8 kpc (i.e., second to last bin).

When we perform radial stacking (with a bin with of ~1.3 kpc, we still do not recover a significant detection of C^{18}O (1–0). However, we detect significant emission in our data if we stack over a larger part of the galaxy. When we stack over the full ^{12}CO (1–0) mask (illustrated by the solid contour in Figure C.3), we do not find significant line emission. But in contrast, if we stack over the ^{13}CO (1–0) mask (illustrated by the dashed contour line), we detect C^{18}O (1–0) emission with S/N = 3. This detection is valuable, since it provides a constraint on the $R_{18/13} \equiv$ C^{18}O/^{13}CO (1–0) line intensity ratio. Since both these lines are optically thin, that particular line ratio traces the relative abundance ratio of the two CO isotopologues.

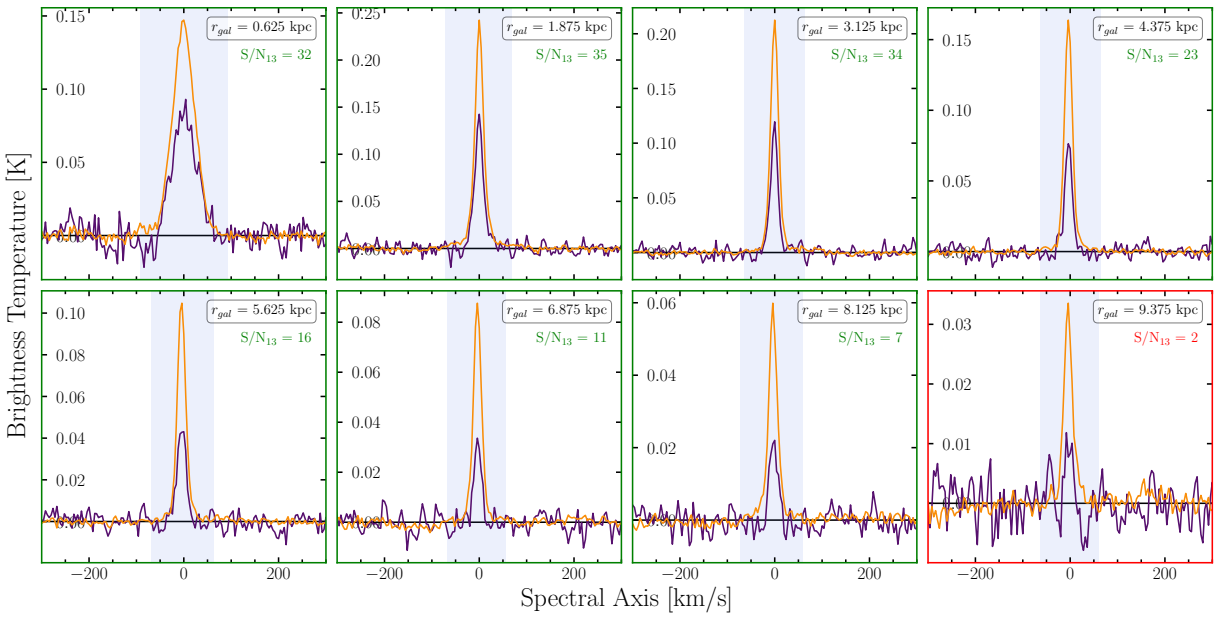

Figure C.2: **Radially stacked ^{12}CO (1–0) (orange) and ^{13}CO (1–0) (purple) spectra.** For a better comparison, we scale the ^{13}CO (1–0) brightness temperature up by a factor 5. The S/N of the ^{13}CO (1–0) is indicated in each panel (green indicates spectra where S/N$_{13}$ > 5. We stack in radial bins of size 1.25 kpc. The shaded region indicates the spectral range over which we integrate the spectra. We detect significant ^{13}CO (1–0) emission out to $r_{gal} \sim 8$ kpc.

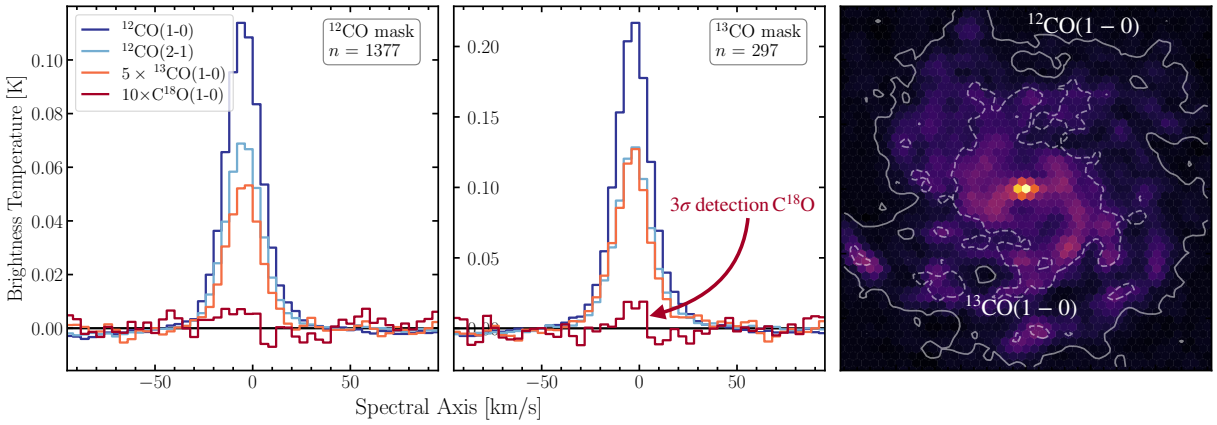

Figure C.3: **Stacked CO spectra over the full galaxy** (*Left*) Stacked spectra over the ^{12}CO (1–0) 3σ mask. ^{13}CO (1–0) spectrum scaled up by a factor of 5, C^{18}O (1–0) by a factor of 10. We mark the number of sightlines per mask with n. (*Middle*) Similar to left panel, but stacked over the ^{13}CO (1–0) 3σ mask. We do not detected significant C^{18}O (1–0) emission. (*Right*) moment 0 map of ^{12}CO (1–0). The S/N = 3 contour of ^{12}CO (1–0) is illustrated by the solid line, while for ^{13}CO (1–0) it is indicated by the dashed line.

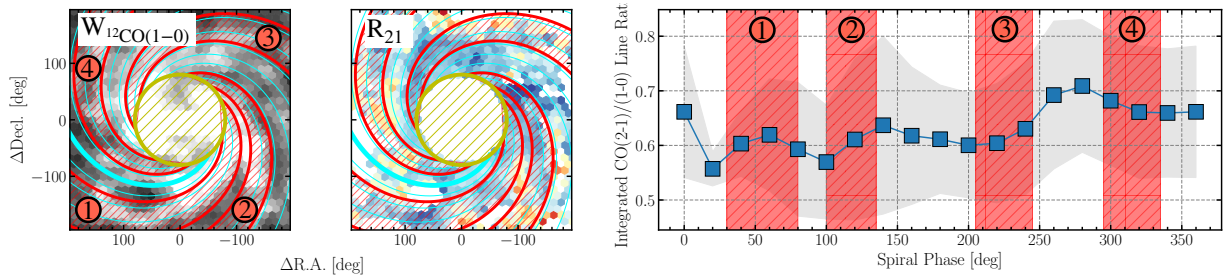

Figure C.4: **Azimuthal Variation of R_{21} in M101.** (*Left*) The ^{12}CO (1−0) integrated intensity map with the logarithmic spirals with a pitch angle of $\theta = 23^{\circ}$ overlayed. The spirals increment with a spiral phase $\Delta\psi = 20^{\circ}$ and increment in the counter-clockwise direction. The spiral bins have a with of 40°. The thick cyan line indicates $\psi = 0$. The four spiral arms are accordingly labeled and colored in red. For the spiral binning, we exclude the central $80'$ (in diameter), belonging to the central region of the galaxy (indicated by the golden-hatched region in the middle). (*Center*) The map shows the R_{21} variation across the galaxy. Spiral bins follow the description on the left panel. (*Right*) The line ratio is binned by the spiral phase. The grey shaded region shows the 1σ scatter per bin. The red shaded region indicates the spiral phases of a particular spiral arm.

C.4 Azimuthal Variation in M101

Koda et al., 2012 provide a prescription of decomposing sightlines by their corresponding spiral phase. We can bin the data using a logarithmic spiral of the following form:

$$R = e^{k \times \psi} \tag{C.1}$$

where R indicates the galactocentric radius distance of a selected point, $k = \tan(\theta)$ encapsulates the galaxy's pitch angle θ, and ψ describes the spiral phase. For M51, we use a pitch angle of $\theta = 20^{\circ}$, which is close to the values found by Shetty et al. (2007) ($\theta = 21^{\circ}.1$) and Pineda et al. (2020) ($\theta = 18^{\circ}.5$).

The spiral arms in M51 could be described using two components: a northern and a southern spiral arm (see Figure 6.12). In the case of M101, however, we opted for four spiral arms. We use a pitch angle $\theta^{\mathrm{M101}} = 23^{\circ}$ (Abdeen et al., 2020). Figure C.4 shows the spiral phases (left and central panel) as well as the decomposition of R_{21} (right panel). We bin the data by segments that span over 40° and we increment in steps of $\Delta\psi = 20^{\circ}$. The phase angle increase in a counter-clockwise direction. We find a slightly higher line ratio between spiral arms 3 and 4 (R_{21}~0.7). But generally, we do not find any significant arm or interarm variation.

C.5 Different Data Sets

The galaxy M101 is also amongst the galaxies studied by Sandstrom et al. (2013). Compared to our CO-to-H_2 conversion factor estimate in the disk of the galaxy ($\langle\alpha_{\mathrm{CO}}\rangle = 4.4\pm0.9$), they find a lower value of $\alpha_{\mathrm{CO}} = 2.3^{+2.6}_{-1.2}$. The value is lower even though they also use the scatter minimization technique. We note that we employed different datasets in this study. To ensure that the discrepancy is not related to our implementation of the scatter minimization technique, we compare the result using different permutations of the different datasets. In particular, we suspect that the discrepancy can stem from

1. *Feathered H I data*: As discussed in Appendix C.1, the THINGS data cubes are seriously affected by filtering and bowling issues. In this study, we have feathered the data cube to improve the H I data.

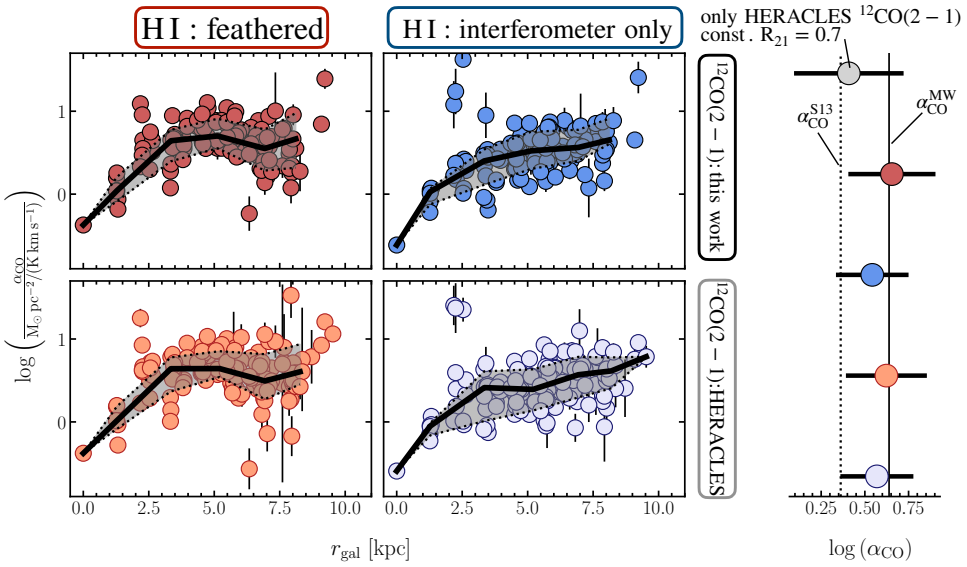

Figure C.5: **Comparing the Impact of Different Datasets on α_{CO} Estimates.** We compare the results after substituting feathered H I (left column) and non-feathered H I (right column) observations as well as different ^{12}CO (2–1) observations (data from this project and HERACLES). The points show the resulting α_{CO} value for the different solution pixels. The black line indicates the binned trend, and the shaded region illustrates the 1σ scatter per bin. The right panel shows the average values of the different permutations (color-coded). The grey point is based on using the ^{12}CO (2–1) data only (and deriving the ^{12}CO (1–0) data using a fixed R_{21}). This approach reproduced the method by Sandstrom et al. (2013). The solid line indicates the average MW α_{CO} value, and the dashed line shows the average value found by Sandstrom et al. (2013) for M101.

Using the VLA data without a correction could impact the resulting α_{CO}.

2. *Different* ^{12}CO (2–1) *Datasets:* As discussed in den Brok et al., 2021, the mm single-dish datacubes can suffer from flux calibration issues. For observations with HERA on the IRAM 30m telescope, the flux calibration can account up to 20% difference. We hence compare the result when substituting our ^{12}CO (2–1) data to the observations from HERACLES (Leroy et al., 2009).

3. *Fixed* R_{21}: Sandstrom et al. (2013) rely on the HERACLES ^{12}CO (2–1) observations and apply a constant R_{21} to convert to a ^{12}CO (1–0) intensity. The discrepancy could hence also be related to the use of a constant and a variable R_{21}.

Figure C.5 illustrates the comparison for the radial α_{CO} trends when using different permutations of dataset. The top row (orange and blue) use the ^{12}CO (2–1) observations from this project. The bottom rows (pink and green) use the HERACLES ^{12}CO (2–1) data. The columns differ by the use of H I data (the left column shows the results based on the feathered and the right column the interferometric only H I data). The right panel shows the α_{CO} mean and scatter for the various data set permutations. The grey point shows when only using ^{12}CO (2–1) data from HERACLES and a constant R_{21} value (i.e., reproducing result from Sandstrom et al. 2013).

Overall, we find that α_{CO} values are ~ 0.1 lower when using the non-feathered H I data. Furthermore, only relying on the HERACLES ^{12}CO (2–1) data only indeed reproduced an even lower α_{CO} value that is in agreement with the finding by Sandstrom et al. (2013).

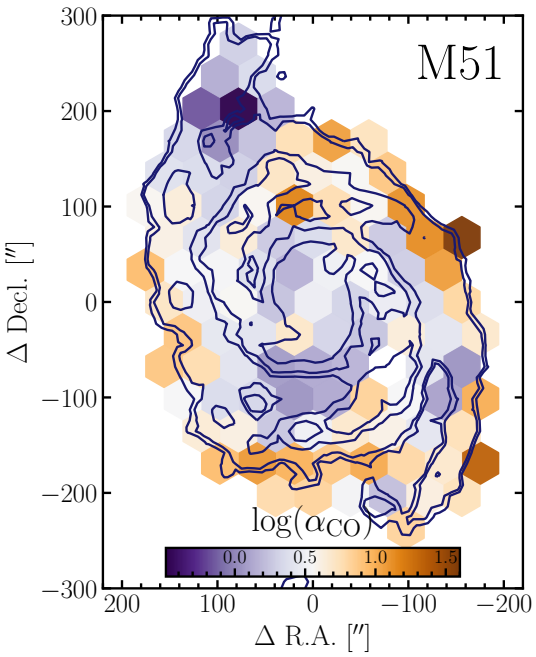

Figure C.6: **Distribution of α_{CO} across M51** Solution pixels of M51 color-coded by their respective α_{CO} value. Contours are drawn at S/N = 7, 10, 30, 50, 100 and help visualize the extent and structure of the galaxy.

C.6 DGR and α_{CO} in M51

In this project, we compare α_{CO} estimates across M101 to values and trends we find across M51. Figure C.6 shows the α_{CO} distribution across M51. The solution pixels are color-coded according to their value of α_{CO}. For reference, the ^{12}CO (1−0) S/N contours show the extent and morphology of the galaxy.

C.7 Lasso Regression

We try to identify a set of features that best describe the variation observed in α_{CO} and that can be used to parameterize the CO-to-H_2 conversion factor. We use a *lasso* regression (Tibshirani, 1996) and *BIC*-based (Schwarz, 1978) model to select the most relevant variables. In this section, we provide a brief overview of the methodology. Overall, we closely follow the variable selection methodology performed by Sun et al. (2022).

The goal is to express the target variable (in our case α_{CO}) in terms of the feature variables as a linear combination (in logarithmic space):

$$\hat{y}_i = \beta_0 + \sum_{j=1}^{m} \beta_j X_{ji} \tag{C.2}$$

We have a set of m different features and $i = 1, 2, ..., n$ are the indices of the data points (e.g. sightlines). The *lasso* regression method consists of minimizing the following cost function:

$$\frac{1}{2n} \sum_{i=1}^{n} (y_i - \hat{y}_i)^2 + \alpha \sum_{j=1}^{m} |\beta_j| \tag{C.3}$$

The non-negative parameter α is introduced as a penalty term in order to eliminate feature variables that do not have a significant contribution to the variation in the target value y_i. Due to this feature of a *penalty* term, we can use the *lasso* regression to select relevant variables. We use the Python function `LassoLarsIC`, which is part of the `scikit-learn` package. The function returns a best-fit model for different α values after it iteratively increments the number of features with a non-zero slope.

We evaluate the performance of the *lasso* regression using the Bayesian Inference Criterion (BIC; Schwarz 1978):

$$\mathrm{BIC} \equiv \mathrm{n} \ln\left(2\pi\sigma^2\right) + \frac{\sum_{\mathrm{i}=1}^{\mathrm{n}} (\mathrm{y_i} - \hat{\mathrm{y}}_\mathrm{i})^2}{\sigma^2} + \mathrm{d} \ln(\mathrm{n}) \tag{C.4}$$

where σ indicates the noise variance of the target variable (in our case α_{CO}) and d describes the number of features with $\beta_j \neq 0$.

For α_{CO} we use $\sigma = 0.2$ dex, which corresponds to the scatter in the conversion factor after subtracting the radial trend. Generally, one would select the candidate with the smallest BIC. However, we choose the model that satisfies $\Delta\mathrm{BIc} \equiv \mathrm{BIC} - \mathrm{BIC}_{\mathrm{min}} \leq 10$ and corresponds to the largest α value (i.e. contains the least amount of non-zero feature values). The threshold justification of $\Delta\mathrm{BIC} \leq 10$ follows from the description in Kass and Raftery (1995).

Bibliography

Abdeen, S. et al. (2020), *Determining the co-rotation radii of spiral galaxies using spiral arm pitch angle measurements at multiple wavelengths*, MNRAS **496** 1610.

Abdo, A. A. et al. (2010), *Fermi Observations of Cassiopeia and Cepheus: Diffuse Gamma-ray Emission in the Outer Galaxy*, ApJ **710** 133.

Ahumada, R. et al. (2020), *The 16th Data Release of the Sloan Digital Sky Surveys: First Release from the APOGEE-2 Southern Survey and Full Release of eBOSS Spectra*, ApJS **249**, 3 3.

Allen, R. J., D. E. Hogg and P. D. Engelke (2015), *The Structure of Dark Molecular Gas in the Galaxy. I. A Pilot Survey for 18 cm OH Emission Toward $l \approx 105°$, $b \approx +1°$*, AJ **149**, 123 123.

Amorin, R., C. Muñoz-Tuñon, J. A. L. Aguerri and P. Planesas (2016), *Molecular gas in low-metallicity starburst galaxies:. Scaling relations and the CO-to-H_2 conversion factor*, A&A **588**, A23 A23.

Anand, G. S. et al. (2021), *Distances to PHANGS galaxies: New tip of the red giant branch measurements and adopted distances*, MNRAS **501** 3621.

André, P. et al. (2014), "From Filamentary Networks to Dense Cores in Molecular Clouds: Toward a New Paradigm for Star Formation", *Protostars and Planets VI*, ed. by H. Beuther, R. S. Klessen, C. P. Dullemond and T. Henning 27.

André, P. et al. (2010), *From filamentary clouds to prestellar cores to the stellar IMF: Initial highlights from the Herschel Gould Belt Survey*, A&A **518**, L102 L102.

Asplund, M., N. Grevesse, A. J. Sauval and P. Scott (2009), *The Chemical Composition of the Sun*, ARA&A **47** 481.

Azeez, J. H., C. .-. Hwang, Z. Z. Abidin and Z. A. Ibrahim (2016), *Kennicutt-Schmidt Law in the Central Region of NGC 4321 as Seen by ALMA*, Scientific Reports **6**, 26896 26896.

Bacon, F. and W. Rawley (1670), *Sylva Sylvarum: Or, A Natural History, in Ten Centuries. Whereunto is Newly Added the History Natural and Experimental of Life and Death, Or of the Prolongation of Life*, Early English Books Online / EEBO, J.R., URL: https://books.google.de/books?id=5gU2AQAAMAAJ.

Bally, J. and W. D. Langer (1982), *Isotope-selective photodestruction of carbon monoxide.*, ApJ **255** 143.

Bayet, E., M. Gerin, T. G. Phillips and A. Contursi (2009), *Are ^{12}CO lines good indicators of the star formation rate in galaxies?*, MNRAS **399** 264.

Bensch, F., J. Stutzki and A. Heithausen (2001), *Methods and constraints for the correction of the error beam pick-up in single dish radio observations*, A&A **365** 285.

Berg, D. A. et al. (2015), *CHAOS I. Direct Chemical Abundances for H II Regions in NGC 628*, ApJ **806**, 16 16.

Berg, D. A. et al. (2020), *CHAOS IV: Gas-phase Abundance Trends from the First Four CHAOS Galaxies*, ApJ **893**, 96 96.

Bertoldi, F. and C. F. McKee (1992), *Pressure-confined Clumps in Magnetized Molecular Clouds*, ApJ **395** 140.

Bicalho, I. C., F. Combes, M. Rubio, C. Verdugo and P. Salome (2019), *ALMA CO(2-1) observations in the XUV disk of M83*, A&A **623**, A66 A66.

Bigiel, F. et al. (2008), *The Star Formation Law in Nearby Galaxies on Sub-Kpc Scales*, AJ **136** 2846.
Bigiel, F. et al. (2010), *Extremely Inefficient Star Formation in the Outer Disks of Nearby Galaxies*, AJ **140** 1194.
Bigiel, F. et al. (2011), *A Constant Molecular Gas Depletion Time in Nearby Disk Galaxies*, ApJ **730**, L13 L13.
Bigiel, F. et al. (2016), *The EMPIRE Survey: Systematic Variations in the Dense Gas Fraction and Star Formation Efficiency from Full-disk Mapping of M51*, ApJ **822**, L26 L26.
Binney, J. and M. Merrifield (1998), *Galactic Astronomy*.
Bisbas, T. G., J. C. Tan and K. E. I. Tanaka (2021), *Photodissociation region diagnostics across galactic environments*, MNRAS **502** 2701.
Blitz, L. (1987), "The structure of molecular clouds.", *Physical Processes in Interstellar Clouds*, ed. by G. E. Morfill and M. Scholer, vol. 210, NATO Advanced Study Institute (ASI) Series C 35.
Bolatto, A. D., M. Wolfire and A. K. Leroy (2013), *The CO-to-H_2 Conversion Factor*, ARA&A **51** 207.
Bolatto, A. D., A. K. Leroy, E. Rosolowsky, F. Walter and L. Blitz (2008), *The Resolved Properties of Extragalactic Giant Molecular Clouds*, ApJ **686** 948.
Bradford, C. M. et al. (2003), *CO (J=7–>6) Observations of NGC 253: Cosmic-Ray-heated Warm Molecular Gas*, ApJ **586** 891.
Braine, J. and F. Combes (1992), *A CO(1-0) and CO(2-1) survey of nearby spiral galaxies. II - Physical conditions in the nuclear gas*, A&A **264** 433.
Bron, E. et al. (2018), *Clustering the Orion B giant molecular cloud based on its molecular emission*, A&A **610**, A12 A12.
Brown, T. and C. D. Wilson (2019), *Extreme CO Isotopologue Line Ratios in ULIRGS: Evidence for a Top-heavy IMF*, ApJ **879**, 17 17.
Burke, B. F. and F. Graham-Smith (2014), *An Introduction to Radio Astronomy*.
Burton, W. B., M. A. Gordon, T. M. Bania and F. J. Lockman (1975), *The overall distribution of carbon monoxide in the plane of the Galaxy.*, ApJ **202** 30.
Byrne, L., C. Christensen, M. Tsekitsidis, A. Brooks and T. Quinn (2019), *Implementing Dust Shielding as a Criteria for Star Formation*, ApJ **871**, 213 213.
Calvi, R. et al. (2018), *Morphology rather than environment drives the SFR-mass relation in the local universe*, MNRAS **481** 3456.
Cañameras, R. et al. (2018), *Planck's dusty GEMS. VI. Multi-J CO excitation and interstellar medium conditions in dusty starburst galaxies at $z = 2$-4*, A&A **620**, A61 A61.
Carruthers, G. R. (1971), *Far-Ultraviolet Spectra and Photometry of Perseus Stars*, ApJ **166** 349.
Carter, M. et al. (2012), *The EMIR multi-band mm-wave receiver for the IRAM 30-m telescope*, A&A **538**, A89 A89.
Casoli, F., C. Dupraz and F. Combes (1992), *The case of missing 13CO in mergers.*, A&A **264** 55.
Chastenet, J. et al. (2021), *Benchmarking Dust Emission Models in M101*, ApJ **912**, 103 103.
Chevance, M. et al. (2020), *The lifecycle of molecular clouds in nearby star-forming disc galaxies*, MNRAS **493** 2872.
Chiang, I.-D. et al. (2018), *The Spatially Resolved Dust-to-metals Ratio in M101*, ApJ **865**, 117 117.
Chiang, I.-D. et al. (2021), *Resolving the Dust-to-Metals Ratio and CO-to-H_2 Conversion Factor in the Nearby Universe*, ApJ **907**, 29 29.
Choudhuri, A. R. and G. Smoot (2011), *Astrophysics for Physicists*, Physics Today **64** 57.
Cicone, C. et al. (2017), *The final data release of ALLSMOG: a survey of CO in typical local low-M_* star-forming galaxies*, A&A **604**, A53 A53.

Colombo, D. et al. (2014), *The PdBI Arcsecond Whirlpool Survey (PAWS): Multi-phase Cold Gas Kinematic of M51*, ApJ **784**, 4 4.

Condon, J. J. and S. M. Ransom (2016), *Essential Radio Astronomy*.

Cormier, D. et al. (2014), *The molecular gas reservoir of 6 low-metallicity galaxies from the Herschel Dwarf Galaxy Survey. A ground-based follow-up survey of CO(1-0), CO(2-1), and CO(3-2)*, A&A **564**, A121 A121.

Cormier, D. et al. (2018), *Full-disc ^{13}CO(1-0) mapping across nearby galaxies of the EMPIRE survey and the CO-to-H_2 conversion factor*, MNRAS **475** 3909.

Crosthwaite, L. P. and J. L. Turner (2007), *CO(1-0), CO(2-1), and Neutral Gas in NGC 6946: Molecular Gas in a Late-Type, Gas-Rich, Spiral Galaxy*, AJ **134** 1827.

Croxall, K. V., R. W. Pogge, D. A. Berg, E. D. Skillman and J. Moustakas (2016), *CHAOS III: Gas-phase Abundances in NGC 5457*, ApJ **830**, 4 4.

Daddi, E. et al. (2010), *Very High Gas Fractions and Extended Gas Reservoirs in $z = 1.5$ Disk Galaxies*, ApJ **713** 686.

Daddi, E. et al. (2015), *CO excitation of normal star-forming galaxies out to $z = 1.5$ as regulated by the properties of their interstellar medium*, A&A **577**, A46 A46.

Dale, D. A. et al. (2007), *An Ultraviolet-to-Radio Broadband Spectral Atlas of Nearby Galaxies*, ApJ **655** 863.

Dale, D. A. et al. (2009), *The Spitzer Local Volume Legacy: Survey Description and Infrared Photometry*, ApJ **703** 517.

Dame, T. M., D. Hartmann and P. Thaddeus (2001), *The Milky Way in Molecular Clouds: A New Complete CO Survey*, ApJ **547** 792.

Davis, T. A. (2014), *Systematic variation of the ^{12}CO/^{13}CO ratio as a function of star formation rate surface density*, MNRAS **445** 2378.

Davis, T. A. et al. (2011), *The ATLAS^{3D} project - X. On the origin of the molecular and ionized gas in early-type galaxies*, MNRAS **417** 882.

De Cia, A., C. Ledoux, P. Petitjean and S. Savaglio (2018), *The cosmic evolution of dust-corrected metallicity in the neutral gas*, A&A **611**, A76 A76.

de los Reyes, M. A. C. and R. C. Kennicutt (2019), *Revisiting the Integrated Star Formation Law. I. Non-starbursting Galaxies*, ApJ **872**, 16 16.

Demyk, K. (2011), "Interstellar dust within the life cycle of the interstellar medium", *European Physical Journal Web of Conferences*, vol. 18, European Physical Journal Web of Conferences 03001 03001.

den Brok, J. S. et al. (2021), *New constraints on the ^{12}CO(2-1)/(1-0) line ratio across nearby disc galaxies*, MNRAS **504** 3221.

den Brok, J. S. et al. (2022), *A CO isotopologue Line Atlas within the Whirlpool galaxy Survey (CLAWS)*, A&A **662**, A89 A89.

Dickman, R. L. (1978), *The ratio of carbon monoxide to molecular hydrogen in interstellar dark clouds.*, ApJS **37** 407.

Downes, D. and P. M. Solomon (1998), *Rotating Nuclear Rings and Extreme Starbursts in Ultraluminous Galaxies*, ApJ **507** 615.

Draine, B. T. (1978), *Photoelectric heating of interstellar gas.*, ApJS **36** 595.

Draine, B. T. et al. (2007), *Dust Masses, PAH Abundances, and Starlight Intensities in the SINGS Galaxy Sample*, ApJ **663** 866.

Draine, B. T. (2011), *Physics of the Interstellar and Intergalactic Medium*, Princeton University Press.

Dwek, E. (1998), *The Evolution of the Elemental Abundances in the Gas and Dust Phases of the Galaxy*, ApJ **501** 643.

Eckart, A. et al. (1990), *Warm gas and spatial variations of molecular excitation in the nuclear region of IC 342*, ApJ **348** 434.

Eibensteiner, C. et al. (2022), *A 2-3 mm high-resolution molecular line survey towards the centre of the nearby spiral galaxy NGC 6946*, A&A **659**, A173 A173.

Einstein, A. (1916), *Strahlungs-Emission und Absorption nach der Quantentheorie*, Deutsche Physikalische Gesellschaft **18** 318.

Elmegreen, B. G., M. Morris and D. M. Elmegreen (1980), *On the abundance of carbon monoxide in galaxies - A comparison of spiral and Magellanic irregular galaxies*, ApJ **240** 455.

Elmegreen, B. G. (2002), *Star Formation from Galaxies to Globules*, ApJ **577** 206.

Esposito, F. et al. (2022), *AGN impact on the molecular gas in galactic centres as probed by CO lines*, MNRAS **512** 686.

Ewen, H. I. and E. M. Purcell (1951), *Observation of a Line in the Galactic Radio Spectrum: Radiation from Galactic Hydrogen at 1,420 Mc./sec.*, Nature **168** 356.

Fazio, G. G. et al. (2004), *The Infrared Array Camera (IRAC) for the Spitzer Space Telescope*, ApJS **154** 10.

Field, G. B., D. W. Goldsmith and H. J. Habing (1969), *Cosmic-Ray Heating of the Interstellar Gas*, ApJ **155** L149.

Forbrich, J., C. J. Lada, S. Viaene and G. Petitpas (2020), *First Resolved Dust Continuum Measurements of Individual Giant Molecular Clouds in the Andromeda Galaxy*, ApJ **890**, 42 42.

Francis, L., D. Johnstone, G. Herczeg, T. R. Hunter and D. Harsono (2020), *On the Accuracy of the ALMA Flux Calibration in the Time Domain and across Spectral Windows*, AJ **160**, 270 270.

Franeck, A. et al. (2018), *Synthetic [C II] emission maps of a simulated molecular cloud in formation*, MNRAS **481** 4277.

Frankel, N., J. Sanders, H.-W. Rix, Y.-S. Ting and M. Ness (2019), *The Inside-out Growth of the Galactic Disk*, ApJ **884**, 99 99.

Frisch, P. C. and J. D. Slavin (2003), *The Chemical Composition and Gas-to-Dust Mass Ratio of Nearby Interstellar Matter*, ApJ **594** 844.

Galametz, M. et al. (2009), *Probing the dust properties of galaxies up to submillimetre wavelengths. I. The spectral energy distribution of dwarf galaxies using LABOCA*, A&A **508** 645.

Galametz, M. et al. (2013), *Calibration of the total infrared luminosity of nearby galaxies from Spitzer and Herschel bands*, MNRAS **431** 1956.

Gallagher, M. J. et al. (2018), *Do Spectroscopic Dense Gas Fractions Track Molecular Cloud Surface Densities?*, ApJ **868**, L38 L38.

Garcia-Burillo, S., M. Guelin and J. Cernicharo (1993), *CO in Messier 51. I. Molecular spiral structure.*, A&A **274** 123.

Gauss, C. F. (1816), *Bestimmung der Genauigkeit der Beobachtungen*, Zeitschrift für Astronomie und Verwandte Wissenschaften **1** 187.

Genzel, R. et al. (2012), *The Metallicity Dependence of the CO $\rightarrow$ H_2 Conversion Factor in z >= 1 Star-forming Galaxies*, ApJ **746**, 69 69.

Glover, S. C. O. and M. .-. Mac Low (2011), *On the relationship between molecular hydrogen and carbon monoxide abundances in molecular clouds*, MNRAS **412** 337.

Goldsmith, P. F., T. Velusamy, D. Li and W. D. Langer (2010), *Molecular Hydrogen Emission from the Boundaries of the Taurus Molecular Cloud*, ApJ **715** 1370.

Goldsmith, P. F. et al. (2008), *Large-Scale Structure of the Molecular Gas in Taurus Revealed by High Linear Dynamic Range Spectral Line Mapping*, ApJ **680** 428.

Gong, M., E. C. Ostriker, C.-G. Kim and J.-G. Kim (2020), *The Environmental Dependence of the X_{CO} Conversion Factor*, ApJ **903**, 142 142.

Gordon, K. D. et al. (2014), *Dust and Gas in the Magellanic Clouds from the HERITAGE Herschel Key Project. I. Dust Properties and Insights into the Origin of the Submillimeter Excess Emission*, ApJ **797**, 85 85.

Gordon, K. D. et al. (2007), *Absolute Calibration and Characterization of the Multiband Imaging Photometer for Spitzer. II. 70 μm Imaging*, PASP **119** 1019.

Gratier, P. et al. (2010), *The molecular interstellar medium of the Local Group dwarf NGC 6822. The molecular ISM of NGC 6822*, A&A **512**, A68 A68.

Grenier, I. A., J.-M. Casandjian and R. Terrier (2005), *Unveiling Extensive Clouds of Dark Gas in the Solar Neighborhood*, Science **307** 1292.

Greve, T. R. et al. (2014), *Star Formation Relations and CO Spectral Line Energy Distributions across the J-ladder and Redshift*, ApJ **794**, 142 142.

Griffin, M. J. et al. (2010), *The Herschel-SPIRE instrument and its in-flight performance*, A&A **518**, L3 L3.

Haffner, L. M. et al. (2009), *The warm ionized medium in spiral galaxies*, Reviews of Modern Physics **81** 969.

Hasegawa, T. et al. (1997), "The CO 2-1/1-0 ratio in the southern Milky Way and the Large Magellanic Cloud", *Diffuse Infrared Radiation and the IRTS*, ed. by H. Okuda, T. Matsumoto and T. Rollig, vol. 124, Astronomical Society of the Pacific Conference Series 244.

Heiderman, A., I. Evans Neal J., L. E. Allen, T. Huard and M. Heyer (2010), *The Star Formation Rate and Gas Surface Density Relation in the Milky Way: Implications for Extragalactic Studies*, ApJ **723** 1019.

Heiles, C. and T. H. Troland (2003), *The Millennium Arecibo 21 Centimeter Absorption-Line Survey. II. Properties of the Warm and Cold Neutral Media*, ApJ **586** 1067.

Henkel, C. and R. Mauersberger (1993), *C and O nucleosynthesis in starbursts : the connection between distant mergers, the galaxy and the solar system.*, A&A **274** 730.

Henkel, C., T. L. Wilson, N. Langer, Y. .-. Chin and R. Mauersberger (1994), "Interstellar CNO Isotope Ratios", *The Structure and Content of Molecular Clouds*, ed. by T. L. Wilson and K. J. Johnston, vol. 439 72.

Henkel, C. et al. (2014), *Carbon and oxygen isotope ratios in starburst galaxies: New data from NGC 253 and Mrk 231 and their implications*, A&A **565**, A3 A3.

Hennebelle, P. and S.-i. Inutsuka (2019), *The role of magnetic field in molecular cloud formation and evolution*, Frontiers in Astronomy and Space Sciences **6**, 5 5.

Heyer, M. and T. M. Dame (2015), *Molecular Clouds in the Milky Way*, ARA&A **53** 583.

Heyer, M., C. Krawczyk, J. Duval and J. M. Jackson (2009), *Re-Examining Larson's Scaling Relationships in Galactic Molecular Clouds*, ApJ **699** 1092.

Hollenbach, D. J. and A. G. G. M. Tielens (1999), *Photodissociation regions in the interstellar medium of galaxies*, Reviews of Modern Physics **71** 173.

Hoyle, F. and G. R. A. Ellis (1963), *On the Existence of an Ionized Layer about the Galactic Plane*, Australian Journal of Physics **16** 1.

Hu, C.-Y., A. Sternberg and E. F. van Dishoeck (2021), *Metallicity Dependence of the H/H_2 and C^+/C/CO Distributions in a Resolved Self-regulating Interstellar Medium*, ApJ **920**, 44 44.

Huggins, W. (1865), *On the Spectrum of the Great Nebula in the Sword-Handle of Orion*, Proceedings of the Royal Society of London Series I **14** 39.

Huggins, W. and W. A. Miller (1864), *On the Spectra of Some of the Nebulae. By William Huggins, F.R.A.S. A Supplement to the Paper "On the Spectra of Some of the Fixed Stars William Huggins F.R.A.S., and W. A. Miller, M.D., LL.D., Treas. and V.P.P.S."*, Philosophical Transactions of the Royal Society of London Series I **154** 437.

Hughes, A. et al. (2010), *Physical properties of giant molecular clouds in the Large Magellanic Cloud*, MNRAS **406** 2065.

Indebetouw, R. et al. (2013), *ALMA Resolves 30 Doradus: Sub-parsec Molecular Cloud Structure near the Closest Super Star Cluster*, ApJ **774**, 73 73.

Iono, D. et al. (2007), *High-Resolution Imaging of Warm and Dense Molecular Gas in the Nuclear Region of the Luminous Infrared Galaxy NGC 6240*, ApJ **659** 283.

Israel, F. P. (1997), *H_2 and its relation to CO in the LMC and other magellanic irregular galaxies*, A&A **328** 471.

– (2009a), *CI and CO in nearby galaxy centers. The bright galaxies NGC 1068 (M 77), NGC 2146, NGC 3079, NGC 4826 (M 64), and NGC 7469*, A&A **493** 525.

– (2009b), *CI and CO in nearby galaxy centers. The star-burst galaxies NGC 278, NGC 660, NGC 3628 NGC 4631, and NGC 4666*, A&A **506** 689.

– (2020), *Central molecular zones in galaxies: ^{12}CO-to-^{13}CO ratios, carbon budget, and X factors*, A&A **635**, A131 A131.

Jackson, J. M., T. A. D. Paglione, J. E. Carlstrom and N.-Q. Rieu (1995), *Submillimeter HCN and HCO + Emission from Galaxies*, ApJ **438** 695.

Jakob, H. et al. (2007), *The cooling of atomic and molecular gas in DR21*, A&A **461** 999.

Jansky, K. G. (1933), *Electrical phenomena that apparently are of interstellar origin*, Popular Astronomy **41** 548.

Jenkins, E. B. (2009), *A Unified Representation of Gas-Phase Element Depletions in the Interstellar Medium*, ApJ **700** 1299.

Jiang, X.-J., Z. Wang, Q. Gu, J. Wang and Z.-Y. Zhang (2015), *Sub-millimeter Telescope CO (2-1) Observations of Nearby Star-forming Galaxies*, ApJ **799**, 92 92.

Jiménez-Donaire, M. J. et al. (2017a), *^{13}CO/C^{18}O Gradients across the Disks of Nearby Spiral Galaxies*, ApJ **836**, L29 L29.

Jiménez-Donaire, M. J. et al. (2017b), *Optical depth estimates and effective critical densities of dense gas tracers in the inner parts of nearby galaxy discs*, MNRAS **466** 49.

Jiménez-Donaire, M. J. et al. (2019), *EMPIRE: The IRAM 30-m Dense Gas Survey of Nearby Galaxies*, arXiv e-prints, arXiv:1906.08779 arXiv:1906.08779.

Kakkad, D. et al. (2017), *ALMA observations of cold molecular gas in AGN hosts at $z \sim 1.5$ - evidence of AGN feedback?*, MNRAS **468** 4205.

Kamenetzky, J., N. Rangwala, J. Glenn, P. R. Maloney and A. Conley (2014), *A Survey of the Molecular ISM Properties of Nearby Galaxies Using the Herschel FTS*, ApJ **795**, 174 174.

Kass, R. E. and A. E. Raftery (1995), *Bayes Factors*, Journal of the American Statistical Association **90** 773, ISSN: 01621459, URL: http://www.jstor.org/stable/2291091 (visited on 28/06/2022).

Kawana, Y. et al. (2022), *Multiwavelength and Multi-CO View of the Minor Merger Driven Star Formation in the Nearby LIRG NGC 3110*, ApJ **929**, 100 100.

Keene, J. et al. (1998), *Detection of the $^3P_2$ –> $^3P_1$ Submillimeter Transition of ^{13}C I in the Interstellar Medium: Implication for Chemical Fractionation*, ApJ **494** L107.

Kennicutt, R. C. et al. (2011), *KINGFISH-Key Insights on Nearby Galaxies: A Far-Infrared Survey with Herschel: Survey Description and Image Atlas*, PASP **123** 1347.

Kennicutt, R. C. (1989), *The Star Formation Law in Galactic Disks*, ApJ **344** 685.

– (1998), *The Global Schmidt Law in Star-forming Galaxies*, ApJ **498** 541.

Kennicutt, R. C. and M. A. C. De Los Reyes (2021), *Revisiting the Integrated Star Formation Law. II. Starbursts and the Combined Global Schmidt Law*, ApJ **908**, 61 61.

Kennicutt, R. C. and N. J. Evans (2012), *Star Formation in the Milky Way and Nearby Galaxies*, ARA&A **50** 531.

Kennicutt, R. C. et al. (2003), *SINGS: The SIRTF Nearby Galaxies Survey*, PASP **115** 928.

Kennicutt, R. C. et al. (2007), *Star Formation in NGC 5194 (M51a). II. The Spatially Resolved Star Formation Law*, ApJ **671** 333.

Kewley, L. J., D. C. Nicholls and R. S. Sutherland (2019), *Understanding Galaxy Evolution Through Emission Lines*, ARA&A **57** 511.

Kim, C.-G., W.-T. Kim and E. C. Ostriker (2011), *Regulation of Star Formation Rates in Multiphase Galactic Disks: Numerical Tests of the Thermal/Dynamical Equilibrium Model*, ApJ **743**, 25 25.

Klessen, R. S. and S. C. O. Glover (2016), *Physical Processes in the Interstellar Medium*, Saas-Fee Advanced Course **43** 85.

Koda, J. et al. (2011), *CO(J = 1-0) Imaging of M51 with CARMA and the Nobeyama 45 m Telescope*, ApJS **193**, 19 19.

Koda, J. et al. (2012), *Physical Conditions in Molecular Clouds in the Arm and Interarm Regions of M51*, ApJ **761**, 41 41.

Koda, J. et al. (2020), *Systematic Variations of CO J = 2-1/1-0 Ratio and Their Implications in The Nearby Barred Spiral Galaxy M83*, ApJ **890**, L10 L10.

Köhler, M., N. Ysard and A. P. Jones (2015), *Dust evolution in the transition towards the denser ISM: impact on dust temperature, opacity, and spectral index*, A&A **579**, A15 A15.

Komugi, S., Y. Sofue, H. Nakanishi, S. Onodera and F. Egusa (2005), *The Schmidt Law at High Molecular Densities*, PASJ **57** 733.

Kramer, C., J. Peñalver and A. Greve (2013), *Improvement of the IRAM 30m telescope beam pattern*, IRAM, URL: https://www.iram-institute.org/medias/uploads/eb2013-v8.2.pdf.

Krieger, N. et al. (2017), *The Survey of Water and Ammonia in the Galactic Center (SWAG): Molecular Cloud Evolution in the Central Molecular Zone*, ApJ **850**, 77 77.

Krieger, N. et al. (2020), *The Molecular Interstellar Medium in the Super Star Clusters of the Starburst NGC 253*, ApJ **897**, 176 176.

Kruijssen, J. M. D. and S. N. Longmore (2014), *An uncertainty principle for star formation - I. Why galactic star formation relations break down below a certain spatial scale*, MNRAS **439** 3239.

Krumholz, M. R. (2015), *Notes on Star Formation*, arXiv e-prints, arXiv:1511.03457 arXiv:1511.03457.

Krumholz, M. R., A. Dekel and C. F. McKee (2012), *A Universal, Local Star Formation Law in Galactic Clouds, nearby Galaxies, High-redshift Disks, and Starbursts*, ApJ **745**, 69 69.

Krumholz, M. R. and C. F. McKee (2005), *A General Theory of Turbulence-regulated Star Formation, from Spirals to Ultraluminous Infrared Galaxies*, ApJ **630** 250.

Lada, C. J., A. A. Muench, J. Rathborne, J. F. Alves and M. Lombardi (2008), *The Nature of the Dense Core Population in the Pipe Nebula: Thermal Cores Under Pressure*, ApJ **672** 410.

Lane, J. et al. (2016), *The JCMT Gould Belt Survey: Dense Core Clusters in Orion A*, ApJ **833**, 44 44.

Langer, W. D. and A. A. Penzias (1990), *12C/ 13C Isotope Ratio across the Galaxy from Observations of 13C 18O in Molecular Clouds*, ApJ **357** 477.

– (1993), *12C/ 13C Isotope Ratio in the Local Interstellar Medium from Observations of 13C 18O in Molecular Clouds*, ApJ **408** 539.

Larson, R. B. (1981), *Turbulence and star formation in molecular clouds.*, MNRAS **194** 809.

Law, C. J. et al. (2018), *Submillimeter Array Observations of Extended CO (J = 2 - 1) Emission in the Interacting Galaxy NGC 3627*, ApJ **865**, 17 17.

Lebrun, F. et al. (1983), *Gamma-rays from atomic and molecular gas in the first galactic quadrant*, ApJ **274** 231.

Lees, J. F., G. R. Knapp, M. P. Rupen and T. G. Phillips (1991), *Molecular Gas in Elliptical Galaxies*, ApJ **379** 177.
Leroy, A. K. et al. (2008), *The Star Formation Efficiency in Nearby Galaxies: Measuring Where Gas Forms Stars Effectively*, AJ **136** 2782.
Leroy, A. K. et al. (2009), *Heracles: The HERA CO Line Extragalactic Survey*, AJ **137** 4670.
Leroy, A. K. et al. (2013), *Molecular Gas and Star Formation in nearby Disk Galaxies*, AJ **146**, 19 19.
Leroy, A. et al. (2007), *The Spitzer Survey of the Small Magellanic Cloud: Far-Infrared Emission and Cold Gas in the Small Magellanic Cloud*, ApJ **658** 1027.
Leroy, A. K. et al. (2011), *The CO-to-H_2 Conversion Factor from Infrared Dust Emission across the Local Group*, ApJ **737**, 12 12.
Leroy, A. K. et al. (2015), *The Multi-phase Cold Fountain in M82 Revealed by a Wide, Sensitive Map of the Molecular Interstellar Medium*, ApJ **814**, 83 83.
Leroy, A. K. et al. (2017), *Millimeter-wave Line Ratios and Sub-beam Volume Density Distributions*, ApJ **835**, 217 217.
Leroy, A. K. et al. (2019), *A $z = 0$ Multiwavelength Galaxy Synthesis. I. A WISE and GALEX Atlas of Local Galaxies*, ApJS **244**, 24 24.
Leroy, A. K. et al. (2021a), *PHANGS-ALMA Data Processing and Pipeline*, ApJS **255**, 19 19.
Leroy, A. K. et al. (2021b), *PHANGS-ALMA: Arcsecond CO(2-1) Imaging of Nearby Star-forming Galaxies*, ApJS **257**, 43 43.
Leroy, A. K. et al. (2022), *Low-J CO Line Ratios from Single-dish CO Mapping Surveys and PHANGS-ALMA*, ApJ **927**, 149 149.
Li, Q., D. Narayanan, R. Davè and M. R. Krumholz (2018), *Dark Molecular Gas in Simulations of $z \sim 0$ Disk Galaxies*, ApJ **869**, 73 73.
Liszt, H. S. and J. Pety (2012), *Imaging diffuse clouds: bright and dark gas mapped in CO*, A&A **541**, A58 A58.
Liszt, H. S., J. Pety and R. Lucas (2010), *The CO luminosity and CO-H_2 conversion factor of diffuse ISM: does CO emission trace dense molecular gas?*, A&A **518**, A45 A45.
Lodders, K. (2003), *Solar System Abundances and Condensation Temperatures of the Elements*, ApJ **591** 1220.
Loomis, R. A. et al. (2021), *An investigation of spectral line stacking techniques and application to the detection of $HC_{11}N$*, Nature Astronomy **5** 188.
Lundgren, A. A., T. Wiklind, H. Olofsson and G. Rydbeck (2004), *Molecular gas in the galaxy M 83. I. The molecular gas distribution*, A&A **413** 505.
Magnani, L. and J. S. Onello (1995), *A New Method for Determining the CO to H 2 Conversion Factor for Translucent Clouds*, ApJ **443** 169.
Maloney, P. and J. H. Black (1988), *I CO/N(H 2) Conversions and Molecular Gas Abundances in Spiral and Irregular Galaxies*, ApJ **325** 389.
Mangum, J. G., D. T. Emerson and E. W. Greisen (2007), *The On The Fly imaging technique*, A&A **474** 679.
Mangum, J. G. and Y. L. Shirley (2015), *How to Calculate Molecular Column Density*, PASP **127** 266.
Mangum, J. G. et al. (2019), *Fire in the Heart: A Characterization of the High Kinetic Temperatures and Heating Sources in the Nucleus of NGC 253*, ApJ **871**, 170 170.
Martin, D. C. et al. (2005), *The Galaxy Evolution Explorer: A Space Ultraviolet Survey Mission*, ApJ **619** L1.
Martin, S., R. Aladro, J. Martin-Pintado and R. Mauersberger (2010), *A large $^{12}C/^{13}C$ isotopic ratio in M 82 and NGC 253*, A&A **522**, A62 A62.

Martin, S. et al. (2021), *ALCHEMI, an ALMA Comprehensive High-resolution Extragalactic Molecular Inventory. Survey presentation and first results from the ACA array*, A&A **656**, A46 A46.

McKee, C. F. and J. P. Ostriker (1977), *A theory of the interstellar medium: three components regulated by supernova explosions in an inhomogeneous substrate.*, ApJ **218** 148.

McKee, C. F. and E. C. Ostriker (2007), *Theory of Star Formation*, ARA&A **45** 565.

McKee, C. F. and J. C. Tan (2003), *The Formation of Massive Stars from Turbulent Cores*, ApJ **585** 850.

McQuinn, K. B. W., E. D. Skillman, A. E. Dolphin, D. Berg and R. Kennicutt (2016), *The Distance to M51*, ApJ **826**, 21 21.

Meidt, S. E. et al. (2013), *Gas Kinematics on Giant Molecular Cloud Scales in M51 with PAWS: Cloud Stabilization through Dynamical Pressure*, ApJ **779**, 45 45.

Meier, D. S. and J. L. Turner (2004), *Dynamically Influenced Molecular Clouds in the Nucleus of NGC 6946: Variations in the CO Isotopic Line Ratios*, AJ **127** 2069.

Meier, D. S., J. L. Turner and S. C. Beck (2001), *Molecular Gas and Star Formation in NGC 3077*, AJ **122** 1770.

Meier, D. S., J. L. Turner and R. L. Hurt (2008), *Nuclear Bar Catalyzed Star Formation: ^{13}CO, $C^{18}O$, and Molecular Gas Properties in the Nucleus of Maffei 2*, ApJ **675** 281.

Meyer, B. S., L. R. Nittler, A. N. Nguyen and S. Messenger (2008), *Nucleosynthesis and Chemical Evolution of Oxygen*, Reviews in Mineralogy and Geochemistry **68** 31.

Meyerdierks, H. and A. Heithausen (1996), *Diffuse molecular gas in the Polaris flare.*, A&A **313** 929.

Milam, S. N., C. Savage, M. A. Brewster, L. M. Ziurys and S. Wyckoff (2005), *The $^{12}C/^{13}C$ Isotope Gradient Derived from Millimeter Transitions of CN: The Case for Galactic Chemical Evolution*, ApJ **634** 1126.

Miville-Deschênes, M.-A., N. Murray and E. J. Lee (2017), *Physical Properties of Molecular Clouds for the Entire Milky Way Disk*, ApJ **834**, 57 57.

Morokuma-Matsui, K. and K. Muraoka (2017), *Kennicutt-Schmidt Relation Variety and Star-forming Cloud Fraction*, ApJ **837**, 137 137.

Muñoz-Mateos, J. C. et al. (2009a), *Radial Distribution of Stars, Gas, and Dust in Sings Galaxies. II. Derived Dust Properties*, ApJ **701** 1965.

– (2009b), *Radial Distribution of Stars, Gas, and Dust in Sings Galaxies. II. Derived Dust Properties*, ApJ **701** 1965.

Muraoka, K. et al. (2020), *ALMA Observations of Giant Molecular Clouds in M33. II. Triggered High-mass Star Formation by Multiple Gas Colliding Events at the NGC 604 Complex*, ApJ **903**, 94 94.

Murphy, E. J., T. A. Porter, I. V. Moskalenko, G. Helou and A. W. Strong (2012), *Characterizing Cosmic-Ray Propagation in Massive Star-forming Regions: The Case of 30 Doradus and the Large Magellanic Cloud*, ApJ **750**, 126 126.

Murray, N. (2011), *Star Formation Efficiencies and Lifetimes of Giant Molecular Clouds in the Milky Way*, ApJ **729**, 133 133.

Nakai, N. and N. Kuno (1995), *The CO-to-H_2 Conversion Factor in the Galaxy M51*, PASJ **47** 761.

Narayanan, D. and M. R. Krumholz (2014), *A theory for the excitation of CO in star-forming galaxies*, MNRAS **442** 1411.

Narayanan, D., M. R. Krumholz, E. C. Ostriker and L. Hernquist (2011), *The CO-H_2 conversion factor in disc galaxies and mergers*, MNRAS **418** 664.

– (2012), *A general model for the CO-H_2 conversion factor in galaxies with applications to the star formation law*, MNRAS **421** 3127.

Nelson, E. J. et al. (2012), *Spatially Resolved Hα Maps and Sizes of 57 Strongly Star-forming Galaxies at z ~1 from 3D-HST: Evidence for Rapid Inside-out Assembly of Disk Galaxies*, ApJ **747**, L28 L28.

Noble, A. G. et al. (2019), *Resolving CO (2-1) in z ~ 1.6 Gas-rich Cluster Galaxies with ALMA: Rotating Molecular Gas Disks with Possible Signatures of Gas Stripping*, ApJ **870**, 56 56.

Nordmann, C. (1905), *Essai Sur le Role des Ondes Hertziennes en Astronomie Physique et Sur Diverses Questions Qui S'y Rattachent*, Annales de l'Observatoire de Nice **9** A.1.

Nyquist, H. (1928), *Thermal Agitation of Electric Charge in Conductors*, Physical Review **32** 110.

O'Sullivan, E. et al. (2015), *Cold gas in group-dominant elliptical galaxies*, A&A **573**, A111 A111.

Oka, T., T. Hasegawa, M. Hayashi, T. Handa and S. Sakamoto (1998), *CO (J = 2–1) Line Observations of the Galactic Center Molecular Cloud Complex. II. Dynamical Structure and Physical Conditions*, ApJ **493** 730.

Oka, T. et al. (2001), *Statistical Properties of Molecular Clouds in the Galactic Center*, ApJ **562** 348.

Onodera, S. et al. (2010), *Breakdown of Kennicutt-Schmidt Law at Giant Molecular Cloud Scales in M33*, ApJ **722** L127.

Ostriker, E. C., C. F. McKee and A. K. Leroy (2010), *Regulation of Star Formation Rates in Multiphase Galactic Disks: A Thermal/Dynamical Equilibrium Model*, ApJ **721** 975.

Ostriker, E. C. and R. Shetty (2011), *Maximally Star-forming Galactic Disks. I. Starburst Regulation Via Feedback-driven Turbulence*, ApJ **731**, 41 41.

Paglione, T. A. D. et al. (2001), *A Mapping Survey of the ^{13}CO and ^{12}CO Emission in Galaxies*, ApJS **135** 183.

Papadopoulos, P. P., P. van der Werf, E. Xilouris, K. G. Isaak and Y. Gao (2012), *The Molecular Gas in Luminous Infrared Galaxies. II. Extreme Physical Conditions and Their Effects on the X_{co} Factor*, ApJ **751**, 10 10.

Paradis, D., J. .-. Bernard and C. Mény (2009), *Dust emissivity variations in the Milky Way*, A&A **506** 745.

Paturel, G. et al. (2003), *HYPERLEDA. I. Identification and designation of galaxies*, A&A **412** 45.

Peñaloza, C. H., P. C. Clark, S. C. O. Glover and R. S. Klessen (2018), *CO line ratios in molecular clouds: the impact of environment*, MNRAS **475** 1508.

Peñaloza, C. H., P. C. Clark, S. C. O. Glover, R. Shetty and R. S. Klessen (2017), *Using CO line ratios to trace the physical properties of molecular clouds*, MNRAS **465** 2277.

Penzias, A. A. and C. A. Burrus (1973), *Millimeter-Wavelength Radio-Astronomy Techniques*, ARA&A **11** 51.

Pereira-Santaella, M. et al. (2021), *Physics of ULIRGs with MUSE and ALMA: The PUMA project. II. Are local ULIRGs powered by AGN? The subkiloparsec view of the 220 GHz continuum*, A&A **651**, A42 A42.

Pessa, I. et al. (2021), *Star formation scaling relations at ~100 pc from PHANGS: Impact of completeness and spatial scale*, A&A **650**, A134 A134.

Pety, J. et al. (2013), *The Plateau de Bure + 30 m Arcsecond Whirlpool Survey Reveals a Thick Disk of Diffuse Molecular Gas in the M51 Galaxy*, ApJ **779**, 43 43.

Pety, J. et al. (2017), *The anatomy of the Orion B giant molecular cloud: A local template for studies of nearby galaxies*, A&A **599**, A98 A98.

Pilbratt, G. L. et al. (2010), *Herschel Space Observatory. An ESA facility for far-infrared and submillimetre astronomy*, A&A **518**, L1 L1.

Pineda, J. E., P. Caselli and A. A. Goodman (2008), *CO Isotopologues in the Perseus Molecular Cloud Complex: the X-factor and Regional Variations*, ApJ **679** 481.

Pineda, J. L. et al. (2020), *A SOFIA Survey of [C II] in the Galaxy M51. II. [C II] and CO Kinematics across the Spiral Arms*, ApJ **900**, 132 132.

Planck Collaboration et al. (2011a), *Planck early results. XIX. All-sky temperature and dust optical depth from Planck and IRAS. Constraints on the "dark gas" in our Galaxy*, A&A **536**, A19 A19.

Planck Collaboration et al. (2011b), *Planck early results. XXI. Properties of the interstellar medium in the Galactic plane*, A&A **536**, A21 A21.
Planck Collaboration et al. (2016a), *Planck intermediate results. XXXIV. The magnetic field structure in the Rosette Nebula*, A&A **586**, A137 A137.
Planck Collaboration et al. (2016b), *Planck intermediate results. XXXV. Probing the role of the magnetic field in the formation of structure in molecular clouds*, A&A **586**, A138 A138.
Poglitsch, A. et al. (2010), *The Photodetector Array Camera and Spectrometer (PACS) on the Herschel Space Observatory*, A&A **518**, L2 L2.
Pokhrel, R. et al. (2018), *Hierarchical Fragmentation in the Perseus Molecular Cloud: From the Cloud Scale to Protostellar Objects*, ApJ **853**, 5 5.
Prantzos, N., O. Aubert and J. Audouze (1996), *Evolution of the carbon and oxygen isotopes in the Galaxy.*, A&A **309** 760.
Puschnig, J. et al. (2020), *The Lyman Alpha Reference Sample XI: Efficient Turbulence Driven Lya Escape and the Analysis of IR, CO and [C II]158 um*, arXiv e-prints, arXiv:2004.09142 arXiv:2004.09142.
Puschnig, J. (2020), *Dense Gas Toolbox*, version v1.2.
Querejeta, M. et al. (2016), *AGN feedback in the nucleus of M 51*, A&A **593**, A118 A118.
Rangwala, N. et al. (2011), *Observations of Arp 220 Using Herschel-SPIRE: An Unprecedented View of the Molecular Gas in an Extreme Star Formation Environment*, ApJ **743**, 94 94.
Reach, W. T., B.-C. Koo and C. Heiles (1994), *Atomic and Molecular Gas in Interstellar Cirrus Clouds*, ApJ **429** 672.
Reach, W. T., W. F. Wall and N. Odegard (1998), *Infrared Excess and Molecular Clouds: A Comparison of New Surveys of Far-Infrared and H I 21 Centimeter Emission at High Galactic Latitudes*, ApJ **507** 507.
Rebolledo, D. et al. (2015), *Scaling Relations of the Properties for CO Resolved Structures in Nearby Spiral Galaxies*, ApJ **808**, 99 99.
Reynolds, R. J. (1985), *S II lambda 6716 in the galactic emission-line background.*, ApJ **294** 256.
– (1989), *The Column Density and Scale Height of Free Electrons in the Galactic Disk*, ApJ **339** L29.
Rickard, L. J., P. Palmer, M. Morris, B. Zuckerman and B. E. Turner (1975), *Detection of extragalactic carbon monoxide at millimeter wavelengths.*, ApJ **199** L75.
Rieke, G. H. et al. (2004), *The Multiband Imaging Photometer for Spitzer (MIPS)*, ApJS **154** 25.
Roman-Duval, J., J. M. Jackson, M. Heyer, J. Rathborne and R. Simon (2010), *Physical Properties and Galactic Distribution of Molecular Clouds Identified in the Galactic Ring Survey*, ApJ **723** 492.
Roman-Duval, J. et al. (2016), *Distribution and Mass of Diffuse and Dense CO Gas in the Milky Way*, ApJ **818**, 144 144.
Rosen, A. L. et al. (2020), *Zooming in on Individual Star Formation: Low- and High-Mass Stars*, Space Sci. Rev. **216**, 62 62.
Rosolowsky, E. and L. Blitz (2005), *Giant Molecular Clouds in M64*, ApJ **623** 826.
Rosolowsky, E. and A. K. Leroy (2006), *Bias-free Measurement of Giant Molecular Cloud Properties*, PASP **118** 590.
Rosolowsky, E. et al. (2021), *Giant molecular cloud catalogues for PHANGS-ALMA: methods and initial results*, MNRAS **502** 1218.
Roueff, A. et al. (2021), *$C^{18}O$, ^{13}CO, and ^{12}CO abundances and excitation temperatures in the Orion B molecular cloud. Analysis of the achievable precision in modeling spectral lines within the approximation of the local thermodynamic equilibrium*, A&A **645**, A26 A26.
Roussel, H. et al. (2007), *Warm Molecular Hydrogen in the Spitzer SINGS Galaxy Sample*, ApJ **669** 959.
Rubio, M., J. Lequeux and F. Boulanger (1993), *Results of the ESO-SEST key programme: CO in the Magellanic clouds. III. Molecular gas in the small Magellanic Cloud.*, A&A **271** 9.

Sage, L. J., R. Mauersberger and C. Henkel (1991), *Extragalactic 18O/17O ratios and star formation : high-mass stars preferred in starburst systems ?*, A&A **249** 31.

Saintonge, A. et al. (2017), *xCOLD GASS: The Complete IRAM 30 m Legacy Survey of Molecular Gas for Galaxy Evolution Studies*, ApJS **233**, 22 22.

Saito, T. et al. (2017), *Spatially resolved CO SLED of the Luminous Merger Remnant NGC 1614 with ALMA*, ApJ **835**, 174 174.

Sakamoto, S., T. Hasegawa, T. Handa, M. Hayashi and T. Oka (1997), *An Out-of-Plane CO (J = 2-1) Survey of the Milky Way. II. Physical Conditions of Molecular Gas*, ApJ **486** 276.

Sakamoto, S., M. Hayashi, T. Hasegawa, T. Handa and T. Oka (1994), *A large area CO (J = 2 goes to 1) mapping of the giant molecular clouds in Orion*, ApJ **425** 641.

Salpeter, E. E. (1952), *Nuclear Reactions in Stars Without Hydrogen.*, ApJ **115** 326.

Sanchez-Garcia, M. et al. (2022), *Spatially resolved star-formation relations of dense molecular gas in NGC 1068*, A&A **660**, A83 A83.

Sanders, D. B., N. Scoville and P. M. Solomon (1985), *Giant molecular clouds in the galaxy. II. Characteristics of discretefeatures.*, ApJ **289** 373.

Sandstrom, K. M. et al. (2013), *The CO-to-H_2 Conversion Factor and Dust-to-gas Ratio on Kiloparsec Scales in Nearby Galaxies*, ApJ **777**, 5 5.

Sano, H. et al. (2021), *ALMA CO observations of a giant molecular cloud in M 33: Evidence for high-mass star formation triggered by cloud-cloud collisions*, PASJ **73** S62.

Santosa, F. and W. W. Symes (1986), *Linear Inversion of Band-Limited Reflection Seismograms*, SIAM Journal on Scientific and Statistical Computing **7** 1307, URL: https://doi.org/10.1137/0907087.

Sawada, T. et al. (2001), *The Tokyo-Onsala-ESO-Calán Galactic CO J=2-1 Survey. I. The Galactic Center Region*, ApJS **136** 189.

Schinnerer, E., A. Weiß, S. Aalto and N. Scoville (2010), *Multi-transition Study of M51'S Molecular Gas Spiral Arms*, ApJ **719** 1588.

Schinnerer, E. et al. (2013), *The PdBI Arcsecond Whirlpool Survey (PAWS). I. A Cloud-scale/Multi-wavelength View of the Interstellar Medium in a Grand-design Spiral Galaxy*, ApJ **779**, 42 42.

Schmidt, M. (1959), *The Rate of Star Formation.*, ApJ **129** 243.

Schruba, A. et al. (2011), *A Molecular Star Formation Law in the Atomic-gas-dominated Regime in Nearby Galaxies*, AJ **142**, 37 37.

Schruba, A. et al. (2012), *Low CO Luminosities in Dwarf Galaxies*, AJ **143**, 138 138.

Schruba, A. et al. (2017), *Physical Properties of Molecular Clouds at 2 pc Resolution in the Low-metallicity Dwarf Galaxy NGC 6822 and the Milky Way*, ApJ **835**, 278 278.

Schuster, K. F., C. Kramer, M. Hitschfeld, S. Garcia-Burillo and B. Mookerjea (2007), *A complete ^{12}CO 2-1 map of M 51 with HERA. I. Radial averages of CO, H I, and radio continuum*, A&A **461** 143.

Schuster, K. F. et al. (2004), *A 230 GHz heterodyne receiver array for the IRAM 30 m telescope*, A&A **423** 1171.

Schwarz, G. (1978), *Estimating the Dimension of a Model*, Annals of Statistics **6** 461.

Scoville, N. and P. M. Solomon (1975), *Molecular clouds in the Galaxy.*, ApJ **199** L105.

Seifried, D., S. Haid, S. Walch, E. M. A. Borchert and T. G. Bisbas (2020), *SILCC-Zoom: H_2 and CO-dark gas in molecular clouds - the impact of feedback and magnetic fields*, MNRAS **492** 1465.

Shetty, R., S. N. Vogel, E. C. Ostriker and P. J. Teuben (2007), *Kinematics of Spiral-Arm Streaming in M51*, ApJ **665** 1138.

Shetty, R. et al. (2011), *Modelling CO emission - II. The physical characteristics that determine the X factor in Galactic molecular clouds*, MNRAS **415** 3253.

Shirley, Y. L. (2015), *The Critical Density and the Effective Excitation Density of Commonly Observed Molecular Dense Gas Tracers*, PASP **127** 299.

Shu, F. H., F. C. Adams and S. Lizano (1987), *Star formation in molecular clouds: observation and theory.*, ARA&A **25** 23.

Shull, J. M. and S. Beckwith (1982), *Interstellar molecular hydrogen*, ARA&A **20** 163.

Sliwa, K., C. D. Wilson, S. Aalto and G. C. Privon (2017), *Extreme CO Isotopic Abundances in the ULIRG IRAS 13120-5453: An Extremely Young Starburst or Top-heavy Initial Mass Function*, ApJ **840**, L11 L11.

Snow, T. P. and B. J. McCall (2006), *Diffuse Atomic and Molecular Clouds*, ARA&A **44** 367.

Sobolev, V. V. (1960), *Moving envelopes of stars*.

Sofue, Y. et al. (1999), *Central Rotation Curves of Spiral Galaxies*, ApJ **523** 136.

Sokolov, V. et al. (2018), *Subsonic islands within a high-mass star-forming infrared dark cloud*, A&A **611**, L3 L3.

Solomon, P. M. and R. de Zafra (1975), *Carbon monoxide in external galaxies.*, ApJ **199** L79.

Solomon, P. M., A. R. Rivolo, J. Barrett and A. Yahil (1987), *Mass, Luminosity, and Line Width Relations of Galactic Molecular Clouds*, ApJ **319** 730.

Solomon, P. M., N. Scoville, A. A. Penzias, R. W. Wilson and K. B. Jefferts (1972), *Molecular Clouds in the Galactic Center Region: Carbon Monoxide Observations at 2.6 Millimeters*, ApJ **178** 125.

Spitzer Lyman, J. (1956), *On a Possible Interstellar Galactic Corona.*, ApJ **124** 20.

Stanke, T. et al. (2022), *The APEX Large CO Heterodyne Orion Legacy Survey (ALCOHOLS). I. Survey overview*, A&A **658**, A178 A178.

Strong, A. W. and J. R. Mattox (1996), *Gradient model analysis of EGRET diffuse Galactic γ-ray emission.*, A&A **308** L21.

Sun, J. et al. (2018), *Cloud-scale Molecular Gas Properties in 15 Nearby Galaxies*, ApJ **860**, 172 172.

Sun, J. et al. (2020), *Molecular Gas Properties on Cloud Scales across the Local Star-forming Galaxy Population*, ApJ **901**, L8 L8.

Sun, J. et al. (2022), *Molecular Cloud Populations in the Context of Their Host Galaxy Environments: A Multiwavelength Perspective*, arXiv e-prints, arXiv:2206.07055 arXiv:2206.07055.

Szűcs, L., S. C. O. Glover and R. S. Klessen (2014), *The $^{12}CO/^{13}CO$ ratio in turbulent molecular clouds*, MNRAS **445** 4055.

– (2016), *How well does CO emission measure the H_2 mass of MCs?*, MNRAS **460** 82.

Tacconi, L. J. et al. (2008), *Submillimeter Galaxies at z ~2: Evidence for Major Mergers and Constraints on Lifetimes, IMF, and CO-H_2 Conversion Factor*, ApJ **680** 246.

Tacconi, L. J. et al. (2010), *High molecular gas fractions in normal massive star-forming galaxies in the young Universe*, Nature **463** 781.

Tacconi, L. J. and J. S. Young (1987), *The CO Contents of Dwarf Irregular Galaxies*, ApJ **322** 681.

Tan, J. C. et al. (2014), "Massive Star Formation", *Protostars and Planets VI*, ed. by H. Beuther, R. S. Klessen, C. P. Dullemond and T. Henning 149.

Tan, Q.-H., Y. Gao, Z.-Y. Zhang and X.-Y. Xia (2011), *^{12}CO, ^{13}CO and $C^{18}O$ observations along the major axes of nearby bright infrared galaxies*, Research in Astronomy and Astrophysics **11** 787.

Tang, X. D. et al. (2019), *ALMA view of the $^{12}C/^{13}C$ isotopic ratio in starburst galaxies*, A&A **629**, A6 A6.

Taylor, C. L., H. A. Kobulnicky and E. D. Skillman (1998), *CO Emission in Low-Luminosity, H I-rich Galaxies*, AJ **116** 2746.

Temi, P. et al. (2018), *ALMA Observations of Molecular Clouds in Three Group-centered Elliptical Galaxies: NGC 5846, NGC 4636, and NGC 5044*, ApJ **858**, 17 17.

Teng, Y.-H. et al. (2022), *Molecular Gas Properties and CO-to-H_2 Conversion Factors in the Central Kiloparsec of NGC 3351*, ApJ **925**, 72 72.

Thronson Harley A., J., D. A. Hunter, C. M. Telesco, M. Greenhouse and D. A. Harper (1988), *The Magellanic Irregular Galaxy NGC 4214: Star Formation and the Interstellar Medium*, ApJ **334** 605.

Tibshirani, R. (1996), *Regression Shrinkage and Selection via the Lasso*, Journal of the Royal Statistical Society. Series B (Methodological) **58** 267, ISSN: 00359246, URL: http://www.jstor.org/stable/2346178 (visited on 28/06/2022).

Tielens, A. G. G. M. (2010), *The Physics and Chemistry of the Interstellar Medium*.

Tielens, A. G. G. M. et al. (1993), *Anatomy of the Photodissociation Region in the Orion Bar*, Science **262** 86.

Timmes, F. X., S. E. Woosley and T. A. Weaver (1995), *Galactic Chemical Evolution: Hydrogen through Zinc*, ApJS **98** 617.

Tokuda, K. et al. (2020), *ALMA Observations of Giant Molecular Clouds in M33. I. Resolving Star Formation Activities in the Giant Molecular Filaments Possibly Formed by a Spiral Shock*, ApJ **896**, 36 36.

Usero, A. et al. (2015), *Variations in the Star Formation Efficiency of the Dense Molecular Gas across the Disks of Star-forming Galaxies*, AJ **150**, 115 115.

Utomo, D. et al. (2017), *The EDGE-CALIFA Survey: Variations in the Molecular Gas Depletion Time in Local Galaxies*, ApJ **849**, 26 26.

Uzgil, B. D. et al. (2019), *The ALMA Spectroscopic Survey in the HUDF: Constraining Cumulative CO Emission at $1 \lesssim z \lesssim 4$ with Power Spectrum Analysis of ASPECS LP Data from 84 to 115 GHz*, ApJ **887**, 37 37.

van de Hulst, H. C. (1945), *Radiogolven uit het wereldruim: II. Herkomst der radiogolven (Radio waves from space).*, Nederlandsch Tijdschrift voor Natuurkunde **11** 210.

van der Tak, F. F. S., J. H. Black, F. L. Schöier, D. J. Jansen and E. F. van Dishoeck (2007), *A computer program for fast non-LTE analysis of interstellar line spectra. With diagnostic plots to interpret observed line intensity ratios*, A&A **468** 627.

van Dishoeck, E. F. and J. H. Black (1988), *The Photodissociation and Chemistry of Interstellar CO*, ApJ **334** 771.

– (1989), *Interstellar C 2, CH, and CN in Translucent Molecular Clouds*, ApJ **340** 273.

Verley, S., E. Corbelli, C. Giovanardi and L. K. Hunt (2010), *Star formation in M 33: the radial and local relations with the gas*, A&A **510**, A64 A64.

Vizgan, D. et al. (2022), *Tracing Molecular Gas Mass in $z = 6$ Galaxies with [C II]*, ApJ **929**, 92 92.

Vlahakis, C., P. van der Werf, F. P. Israel and R. P. J. Tilanus (2013), *A CO J = 3-2 map of M51 with HARP-B: radial properties of the spiral structure*, MNRAS **433** 1837.

Vogel, S. N., F. Boulanger and R. Ball (1987), *Giant Molecular Clouds in M31*, ApJ **321** L145.

Wakelam, V. et al. (2017), *H_2 formation on interstellar dust grains: The viewpoints of theory, experiments, models and observations*, Molecular Astrophysics **9** 1.

Waller, W. H. et al. (1997), *Ultraviolet Signatures of Tidal Interaction in the Giant Spiral Galaxy M101*, ApJ **481** 169.

Walsh, C. et al. (2016), *First Detection of Gas-phase Methanol in a Protoplanetary Disk*, ApJ **823**, L10 L10.

Walter, F. et al. (2008), *THINGS: The H I Nearby Galaxy Survey*, AJ **136** 2563.

Wannier, P. G. et al. (1993), *Warm Neutral Halos around Molecular Clouds. V. OH (1665 and 1667 MHz) Observations*, ApJ **407** 163.

Ward, J. S., J. Zmuidzinas, A. I. Harris and K. G. Isaak (2003), *A ^{12}CO J=6-5 Map of M82: The Significance of Warm Molecular Gas*, ApJ **587** 171.

Watanabe, Y., N. Sakai, K. Sorai, J. Ueda and S. Yamamoto (2016), *Molecular Distribution in the Spiral Arm of M51*, ApJ **819**, 144 144.

Watanabe, Y., N. Sakai, K. Sorai and S. Yamamoto (2014), *Spectral Line Survey toward the Spiral Arm of M51 in the 3 and 2 mm Bands*, ApJ **788**, 4 4.

Watson, W. D., V. G. Anicich and J. Huntress W. T. (1976), *Measurement and significance of the reaction $^{13}C^{+}+^{12}CO \rightarrow {}^{12}C^{+}+^{13}CO$ for alteration of the $^{13}C/^{12}C$ ratio in interstellar molecules.*, ApJ **205** L165.

Weizsäcker, C. von (1937), *Über Elementumwandlungen im Inneren der Sterne. I*, S. Hirzel.

– (1938), *Über Elementumwandlungen im Inneren der Sterne. II*, S. Hirzel.

Werner, M. W. et al. (2004), *The Spitzer Space Telescope Mission*, ApJS **154** 1.

White, G. J. (1997), *Using CO isotopes to probe the ISM.*, IAU Symposium **170** 101.

Whitworth, D. J. et al. (2022), *Is the molecular KS relationship universal down to low metallicities?*, MNRAS **510** 4146.

Wiklind, T., G. Rydbeck, A. Hjalmarson and P. Bergman (1990), *Arm and interarm molecular clouds in M 83.*, A&A **232** L11.

Williams, D. (1999), *Hydrogen molecules in the cosmos*, Astronomy and Geophysics **40** 10.

Williams, D. A. and S. Viti (2014), *Observational Molecular Astronomy*.

Wilsing, J. and J. Scheiner (1896), *Ueber einen Versuch, eine electrodynamische Sonnenstrahlung nachzuweisen, und über die Aenderung des Uebergangswiderstandes bei Berührung zweier Leiter durch electrische Bestrahlung*, Annalen der Physik **295** 782.

Wilson, C. D. et al. (2012), *The JCMT Nearby Galaxies Legacy Survey — VIII. CO data and the $L_{CO(3-2)}$-L_{FIR} correlation in the SINGS sample*, MNRAS **424** 3050.

Wilson, C. D., N. Scoville, W. L. Freedman, B. F. Madore and D. B. Sanders (1988), *Observations of Individual Star-forming Regions in the Nucleus of M33*, ApJ **333** 611.

Wilson, R. W., K. B. Jefferts and A. A. Penzias (1970), *Carbon Monoxide in the Orion Nebula*, ApJ **161** L43.

Wilson, T. L. and F. Matteucci (1992), *Abundances in the interstellar medium*, A&ARv **4** 1.

Wilson, T. L. and R. Rood (1994), *Abundances in the Interstellar Medium*, ARA&A **32** 191.

Wilson, T. L., K. Rohlfs and S. Hüttemeister (2013), *Tools of Radio Astronomy*.

Wilson, W. J. et al. (1974), *Observations of Galactic Carbon Monoxide Emission at 2.6 Millimeters*, ApJ **191** 357.

Winkel, B. et al. (2016), *The Effelsberg-Bonn H I Survey: Milky Way gas. First data release*, A&A **585**, A41 A41.

Wolfire, M. G., D. Hollenbach and C. F. McKee (2010), *The Dark Molecular Gas*, ApJ **716** 1191.

Wolfire, M. G., C. F. McKee, D. Hollenbach and A. G. G. M. Tielens (2003), *Neutral Atomic Phases of the Interstellar Medium in the Galaxy*, ApJ **587** 278.

Wong, T. et al. (2008), *Molecular line mapping of the giant molecular cloud associated with RCW 106 - II. Column density and dynamical state of the clumps*, MNRAS **386** 1069.

Wong, T. and L. Blitz (2002), *The Relationship between Gas Content and Star Formation in Molecule-rich Spiral Galaxies*, ApJ **569** 157.

Wootten, A. and A. R. Thompson (2009), *The Atacama Large Millimeter/Submillimeter Array*, IEEE Proceedings **97** 1463.

Wouterloot, J. G. A., J. Brand and C. Henkel (2005), *The interstellar $C^{18}O/C^{17}O$ ratio in the solar neighbourhood: The ρ Ophiuchus cloud*, A&A **430** 549.

Wright, E. L. et al. (2010), *The Wide-field Infrared Survey Explorer (WISE): Mission Description and Initial On-orbit Performance*, AJ **140** 1868.

Wyder, T. K. et al. (2009), *The Star Formation Law at Low Surface Density*, ApJ **696** 1834.

Wyrowski, F. et al. (2016), *Infall through the evolution of high-mass star-forming clumps*, A&A **585**, A149 A149.

Yajima, Y. et al. (2021), *CO Multi-line Imaging of Nearby Galaxies (COMING). IX.* ^{12}*CO(J = 2-1)/*^{12}*CO(J = 1-0) line ratio on kiloparsec scales*, PASJ **73** 257.

Yates, R. M., G. Kauffmann and Q. Guo (2012), *The relation between metallicity, stellar mass and star formation in galaxies: an analysis of observational and model data*, MNRAS **422** 215.

Yoda, T. et al. (2010), *The AMANOGAWA-2SB Galactic Plane SurveyI. Data on the Galactic Equator*, PASJ **62** 1277.

Young, J. S. and N. Scoville (1982), *Extragalactic CO : gas distribution which fillow the light in IC 342 and NGC 6946.*, ApJ **258** 467.

– (1991), *Molecular gas in galaxies.*, ARA&A **29** 581.

Zhang, Z.-Y., D. Romano, R. J. Ivison, P. P. Papadopoulos and F. Matteucci (2018), *Stellar populations dominated by massive stars in dusty starburst galaxies across cosmic time*, Nature **558** 260.

List of Figures

List of Tables

Acronyms

AGN	**A**ctive **G**alactic **N**ucleus
ALMA	**A**tacama **L**arge **M**illimetre/submillimetre **A**rray
BIC	**B**ayesian **i**nference **c**riterion
CLAWS	**C**O **L**ine **A**tlas of the **W**hirlpool Galaxy **S**urvey
CMB	**C**osmic **m**icrowave **b**ackground
CNM	**C**old **N**eutral **M**edium
DDT	**D**irector's **d**iscretionary **t**ime
DGT	**D**ense **G**as **T**oolbox
EMIR	**E**ight **Mi**xing **R**eceiver
EMPIRE	**E**MIR **M**ultiline **P**robe of the **I**SM **R**egulating Galaxy **E**volution Survey
FIR	**F**ar-**i**nfra**r**ed
FoV	**F**ielf-**o**f-**v**iew
FT	**F**ourier **t**ransform
FWHM	**F**ull-**w**idth at **h**alf **m**maximum
GMC	**G**iant **M**olecular **C**loud
HERA	**HE**terodyne **R**eceiver **A**rray
HERACLES	The **HERA** **C**O-**L**ine **E**xtragalactic **Survey**
IF	**I**ntermediate **f**requency
IRAM	**I**nstitut de **R**adio**a**stronomie **M**illimètrique
ISM	**I**nter**s**tellar **m**edium
ISRF	**I**nter**s**tellar **r**adiation **f**ield
JWST	**J**ames **W**ebb **s**pace **t**elescope
KS	**K**ennicutt-**S**chmidt
LO	**L**ocal **o**scillator
LOS	**L**ine **o**f **s**ight
LSB	**L**ower **s**ide **b**and
LSR	**L**ocal **s**tandard of **r**est
LTE	**L**ocal **t**hermodynamic **e**quilibrium
MCMC	**M**onte **C**arlo **M**arkov **c**hain
MW	**M**ilky **W**ay
NIR	**N**ear-**i**nfra**r**ed
NOEMA	**NO**rthern **E**xtended **M**illimeter **A**rray
NRO	**N**obeyama **R**adio **O**bservatory
OTF	**O**n-**t**he-**F**ly Mapping
PACS	**P**hotodetector **A**rray **C**amera and **S**pectrometer

PAWS	**P**dBI **A**rcsecond **W**hirlpool **S**urvey
PdBI	**P**lateau **d**e **B**ure **I**nterferometer
PDF	**P**robability **d**ensity **f**unction
PDR	**P**hoto**d**issociation **r**egions
PHANGS	**P**hysics at **H**igh **A**ngular resolution in **N**earby **G**alaxie**S**
PI	**P**rinciple **I**nvestigator
PSF	**P**oint **s**pread **f**unction
pwv	**P**ercipitable **w**ater **v**apour
rms	**R**oot-**m**ean-**s**quared
SED	**S**pectral **e**nergy **d**istribution
SDSS	**S**loan **D**igital **S**ky **S**urvey
SFR	**S**tar **f**ormation **r**ate
SFE	**S**tar-**f**orming **e**fficiency
SMA	**S**ub**m**illimeter **A**rray
SPIRE	**S**pectral and **P**hotometric **I**maging **Re**ceiver
S/N	**S**ignal-to-**n**oise
THINGS	**T**he **HI** **N**earby **G**alaxy **S**urvey
TIR	**T**otal **i**nfra**r**ed
USB	**U**pper **s**ide **b**and
UV	**U**ltra **v**iolet
VIF	**V**ariance **i**nflation **f**actor
VLA	**V**ery **L**arge **A**rray
WIM	**W**arm **i**onised **m**edium
WNM	**W**arm **n**eutral **m**edium

Physical Definitions and Constants

Physical Constants

Boltzmann's constant	$k_B = 1.38 \times 10^{-23}\,\mathrm{J\,K^{-1}}$
Mass of hydrogen atom	$m_\mathrm{H} = 1.673 \times 10^{-21}\,\mathrm{kg}$
Planck's constant	$h = 6.626 \times 10^{-34}\,\mathrm{J\,s}$
Speed of light (in vacuum)	$c = 2.998 \times 10^{8}\,\mathrm{m\,s^{-1}}$

Astronomical Definitions and Constants

Local CO-to-H_2 Factor	$\alpha_\mathrm{CO} = 4.35\,M_\odot\,\mathrm{pc^{-2}}\,(\mathrm{K\,km\,s^{-1}})^{-1}$
Jansky	$\mathrm{Jy} = 10^{26}\,\mathrm{W\,Hz^{-1}\,m^{-2}}$
Parcec	$\mathrm{pc} = 3.086 \times 10^{16}\,\mathrm{m}$
Astronomical Unit	$\mathrm{AU} = 1.496 \times 10^{11}\,\mathrm{m}$
Solar mass	$M_\odot = 1.989 \times 10^{30}\,\mathrm{kg}$
Solar luminosity	$L_\odot = 3.828 \times 10^{26}\,\mathrm{W}$
Solar metallicity	$Z_\odot = 0.02$

Front Cover: *Galaxy M51 with CO(2-1) contours over HST image (Credit: NASA/ESA)*
Back Cover: *Orion Nebula (Credit: NASA, ESA, M. Robberto)*